Numerical Modelling of the Micromechanical Behaviour of Catastrophic Long Run-Out Rock Avalanches

Kim L. de Graaf

A thesis submitted in partial fulfillment of the requirements

for the degree of

Doctor of Philosophy

in Civil Engineering

Department of Civil and Natural Resources Engineering

University of Canterbury

30 November 2016

Abstract

Long runout rock avalanches occur in steep mountainous areas, typically due to the effects of heavy rain, freeze-thaw cycles or seismic shaking among others. The runout is renowned for travelling a large horizontal distance in comparison to the vertical fall height and the extent is largely determined by the volume of source rock. The material dynamically disintegrates during runout depositing angular fragments surrounded by rock flour and preserving the original stratigraphy.

The propagation mechanism of long runout rock avalanches has been debated for over a century. The majority of the mechanical theories suggested to explain the long runout behaviour may focus on a particular aspect noted from one or several events, however, do not properly explain the angularity of the grains within the deposit or the possible internal behaviour of the avalanche.

This thesis aims to investigate the fragmentation theory of rock avalanche propagation from a soil mechanics perspective. The rapid application of load and high speed shearing is postulated to cause the dynamic fragmentation of debris, where the rapid movement of fragments and fines reduces effective stress and therefore friction, increasing mobility. Material then moves rapidly until all available kinetic energy has been dissipated or no further dynamic fragmentation can occur. The potential influence of multiple dynamic fragmentation events occurring at once provides useful information for the prediction and extent of rock avalanches, along with micro scale behaviour of rock under rapid loading and high speed shearing for mining purposes.

Discrete Element Modelling (DEM) via the use of PFC^{3D} has been utilised to undertake oedometer and shear box testing of idealised samples. These tests are used to represent dominant mechanisms that occur in the two key periods of a long runout rock avalanche — the fall (modelled by high strain rate oedometer testing) and the runout (modelled by high speed shear box testing). Synthetic and fully calibrated bonded particle models are used to investigate the response of rock boulders under these conditions. The calibrated materials of sandstone, weak chalk and extremely weak chalk were chosen to represent typical large and small scale long runout events.

Numerical oedometer testing reveals that the application of high strain rates normal to the ground surface produces fast and significant breakage along with a noticeable response in kinetic energy and a reduction in mobilised friction. The additional kinetic energy remains available in the system for a longer period of time than that produced by semi-static strain rates. The high

strain rate oedometric tests suggest that dynamic fragmentation occurs under fast loading rates. It is plausible that dynamic fragmentation in a sturzstrom due to rapid loading at the transition point from fall to runout can enhance mobility.

High speed shear box testing indicates a significant rise in normal and shear stresses resulting in intense crushing and dilation rather than dynamic fragmentation. Kinetic energy produced from breakages is quickly dissipated through dilation and does not remain in the system long enough to influence mobility. The majority of the shearing is likely to occur in a small zone at the base of the debris. The minimal mixing of layers during the shear testing and substantial dilation supports the observed preservation of stratigraphy and increase in debris volume seen at the majority of sturzstrom sites.

Acknowledgements

I would like to thank my supervisors Elisabeth Bowman, Cedric Lambert and Misko Cubrinovski for their contributions through out my thesis and toward improving my knowledge and understanding of geotechnical engineering. In particular, Lis Bowman during our initial chats considered this thesis topic was a great opportunity for me to utilise my math background and interest in natural hazards. I truly appreciate the opportunities that have been provided throughout this thesis process.

I would also like to acknowledge the support of the Department of Civil and Natural Resources Engineering for this research, in particular the support staff who have ensured a smooth experience. Thanks also must be given to EQC for additional funding along with the Federation of Graduate Women and the Claude McCarthy Fellowship for funding support to travel to conferences overseas.

My family, friends and colleagues over the last several years have been unfailing in their solidarity and support of my goals to complete this research. I would like to thank them all for supporting me in reaching the conclusion of this research.

"If you're trying to achieve, there will be roadblocks. I've had them; everybody has had them. But obstacles don't have to stop you. If you run into a wall, don't turn around and give up. Figure out how to climb it, go through it, or work around it."

Michael Jordan

Contents

List of Figures

List of Tables

Chapter 1

Introduction

1.1 Introduction

Catastrophic long run-out rock avalanches, named sturzstroms or 'stream-fall' by Albert Heim, are large volume avalanches occurring in steep mountainous areas that can begin as rock slides or rock falls. Long run-out rock avalanches are renowned for travelling at excessive speeds, and travel large horizontal distances in comparison to their vertical fall height. The failure debris typically dynamically disintegrates during runout, producing angular fragments of various sizes and fines. These avalanches stop as quickly as they begin, leaving an often inversely graded deposit that preserves the original stratigraphy.

The runout of sturzstroms typically occurs along flat or gently inclined valley floors, often for several kilometres, and appears to violate rules based on simple frictional models of a block mass sliding downslope. This is due to the spreading and mobility of the material that is not described by simple block slide models. A large volume of source rock providing substantial potential energy is required in order to reach long runout as noted by Dade and Huppert (1998). This large volume is calculated as $1x10^6 m^3$ McSaveney and Davies (1999), an order above which long runout appears to occur. A reduced runout in a sturzstrom is only apparent where the avalanche is confined by topography, the runout path is rough or there is a reduced fall height Hsu (1978).

Multiple theories have been advanced over the last century to attempt to explain the unusual behaviour of sturzstroms. In general, these theories include dynamic fragmentation (Davies et al., 1999; Davies and McSaveney, 2008), undrained loading (Legros, 2002) and acoustic fluidisation (Melosh, 1983). The concept of dynamic fragmentation in sturzstroms is postulated by Davies and McSaveney (2008) and encapsulates the angularity and structure of sturzstrom deposits. Dynamic fragmentation coupled with the collisional forces within an avalanche may provide a good explanation of sturzstrom behaviour.

This thesis aims to examine the micromechanical behaviour of sturzstrom using Discrete El-

ement Modelling (DEM) via PFC^{3D}, to investigate the localised effects of fragmentation in a sturzstrom. The fall and runout of a sturzstrom is examined using conventional and simple geotechnical testing methods in PFC^{3D}, and the associated soil mechanics response is analysed. The results are referenced back to the fragmentation theory and sturstrom behaviour to provide further insight into the mechanics of the fragmentation and runout of the debris.

1.2 Research Background

Sturzstroms typically occur in heavily fractured material in steep mountainous areas and can begin due to tectonic activity, freeze-thaw cycles and heavy rain. Instances of sturzstroms have occurred across the world for example Elm, Switzerland (1881), Frank, Alberta, Canada (1905), Falling Mountain, New Zealand (1929), Nevados Huascarán, Peru (1970), Mt Haast, Aoraki/Mt Cook National Park, New Zealand (2013). These examples are outlined in more detail in Chapter 2, Section 2.1.2.

Collectively the examples show similarities in behaviour and deposits, resulting in a generalised description of a typical sturzstrom as outlined in Section 2.1.2. In general, sturzstroms are highly mobile, travel at rapid speeds and cease quickly. They are difficult to predict and therefore occurrences are normally unexpected and can be life threatening in both populated areas such as around the Himalayas, Andes and Alps, and in areas containing lifeline routes such as the South Island of New Zealand. The resulting deposits show angularity in particle shape and preserved stratigraphy. At times deposits can also indicate an inverse grading.

In addition to sturzstroms occurring in steep mountainous areas, it has been suggested that chalk flows mimic sturzstrom behaviour at a far smaller scale (Bowman and Take, 2014). A chalk flow is a giant failure of a chalk cliff or slope that has runout of up to 6 times the fall height (Hutchinson, 2002). Chalk flows have been noted to occur in high porosity, extremely weak chalks, largely along the Kent coastline in the UK and the northwest coast of France. The surface of chalk flows is typically blocky with stratigraphy retained, and some chalk flows have travelled out to sea and created groynes. There are distinct similarities between sturzstroms and chalk flow characteristics (Williams et al., 2004).

Mechanics

Following the Elm sturzstrom in 1881, Albert Heim suggested that the material had flowed and behaved like a fluid, resulting in a mechanical fluidisation. The angularity of the deposit was likely to be the result of the disintegration of a very large rock mass. Hsu (1978) agrees with Heim's suggestions, however believes that sturzstroms follow Bagnoldian grain flow theory. According to his hypothesis, the collisions between the grain layers cause oscillations in the material with

repulsive pressures likely occurring between contacting grains.

The preservation of stratigraphy suggests that a sturzstrom flow either has high viscosity (McSaveney, 1978), or there is little agitation of the debris outside of the basal layer (Cleary and Campbell, 1993). Violent collisions with a roughened base produces a dilative energy in simple computational models run by Cleary and Campbell (1993), with the mass halting once all kinetic energy has been consumed by the collisions. It appears that the initial velocity in the model particles provides kinetic energy to the basal layer.

The collision of rock clasts causes fragmentation of rock according to Davies and McSaveney (2008) which produces the fractured angular debris typical in sturzstrom deposit areas. Explosive fragmentation of rock is postulated to produce high velocity fragments that travel in all directions, dilating the sturzstrom debris and resulting in an isotropic dispersive stress. As explained further in Section 2.1.2 the intricacies of this theory are yet to be properly detailed as the micromechanics have proven difficult to establish.

Various other mechanical theories have been proposed to explain the unusual behaviour of sturzstroms. These include fluidisation resulting in a cushion of air or gas, self-undrained loading where a reduction in effective stress within an alluvial layer due to excess pore pressure carries the debris, and melted rock creating a fluid base during a sturzstrom flow. Melosh (1986) suggests that acoustic waves generated from vibrations in the shear flow transmit pressure fluctuations that relieve the overburden pressure. Each of these theories can relate to a specific sturzstrom or can be shown to occur under specific laboratory conditions, however none of them can explain the features and characteristics seen across all sturzstroms. In particular, the angularity and structure of the deposits is not explained by all of these theories.

Discrete Element Modelling

Discrete element modelling allows for the analysis of mechanisms that occur at small scale in large displacement geomechanics problems. The early discrete element models, such as BALL from Cundall and Strack (1979), were first created to improve the analysis of rock mechanics and granular soils. Microscale behavours can be monitored closely during discrete element modelling, thus the micromechanical behaviour of a sturzstrom can be investigated.

PFC^{3D} is a soft sphere DEM where the discrete elements are spheres that are rigid but can overlap at contact points. The introduction of parallel bonds allows for the creation of bonded particle models that can be calibrated to standard laboratory tests to produce a realistic, albeit synthetic, version of soil or rock. This material can then be used to produce a specimen for testing in whatever form is desired. For more detailed information on PFC^{3D} refer to Chapter 2, Section 2.3.

DEM models have begun to be used fairly widely for geomechanics and particulate research.

2D and 3D shear box tests have been performed in DEM with similarity between the numerical and experimental results. Shearing produced strong anisotropy in 3D models with particle rotation increasing with breakage. The 2D DEM models of Liu (2006), Zhang and Thornton (2007) and Cheng et al. (2008) produced macroscopic behaviour similar to that seen in experimental shear box tests, where dense material dilates and loose material contracts. DEM modelling has also been used to model granular flows, to predict the runout of potential rock avalanches and to examine the collapse of volcanic edifices (see Section 2.3.3). In all cases DEM models have been shown to produce realistic results and to be capable of handling geophysical processes.

1.3 Scope

The long runout of sturzstroms, preservation of stratigraphy and angularity of the debris, is not yet adequately explained by the mechanical theories proposed so far. The production of fines is readily explained by grinding or crushing resulting from the shearing of material, however does not result in large quantities of angular fragments of varying sizes. The dynamic fragmentation of material during the key phases of a sturzstrom, the fall and the runout, is likely to produce the angular material seen throughout the deposit. The significant question here is whether dynamic fragmentation can be responsible for long runout. The mechanics of sturzstroms can provide insight into unusual mechanical behaviours of rock, and thus may be useful for the prediction of sturzstrom extents for life and lifeline developments in steep mountainous areas, as well as provide additional information into rock mechanics for mining.

Many discussions have occurred within the landslides research community regarding the underlying behaviour of sturzstroms. Such a large rock avalanche cannot simply be explained with frictional sliding theories. The collision of grains is suggested as a possible explanation for long runout, with the presence of interstitial dust and small debris reducing friction or effective normal pressure to allow for the extensive movement. Turbulence however cannot occur during runout or else stratigraphy would not be preserved due to material mixing, and jig-saw boulders would not be so prevalent. The suggestion is that turbulence occurs only within the basal layer of the avalanche producing a dilative energy and little dissipation. More recent discussions have resulted in the suggestion that fragmentation of rock under high overburden stresses produces high velocity fragments that dilate the debris resulting in an isotropic dispersive stress. This dispersive stress however, will likely increase the porosity of the debris and allow for greater frictional dissipation of energy than contended.

There is no real consensus within the research community at this stage as to the propogation mechanism responsible for such unusual and extreme behaviour. Sturzstroms are difficult to predict and occur quickly, thus there is a large degree of impracticality in applying instrumentation in a

notional sturzstrom prone area to obtain real time information. The macroscale characteristics of sturzstroms can be postulated reasonably accurately from deposits and witness accounts. However, the microscale characteristics that would assist with explaining the long runout and angularity of fragments are difficult to obtain from these same sources, and unable to be fully replicated using laboratory techniques. The application of numerical modelling is of benefit in this situation.

Dynamic fragmentation of rock during the fall and runout of a sturzstrom produces kinetic energy that is then available to drive runout. A rapid application of load through contact forces causes intense fragmentation due to the fast extension of critical cracks, allowing for a high stress state to be achieved before the flaws coalesce and the material disintegrates. The kinetic energy induced in a material by a dynamic load is the fuelling energy for dynamic fragmentation events. Substantial amounts of kinetic energy are available after fragmentation to move material within the system. The fragmentation of the material and subsequent kinetic energy increase are postulated here to reduce the mobilised friction within the system and thus reduce effective stress. This collectively allows for an increase in the mobility of the material when multiple events occur simultaneously.

The application of soil mechanics theory to the large scale and unusual behaviour of sturzstroms, by considering the micro-scale effects of fragmentation on a system, is expected to provide clarity to the landslides community as to the influence of fragmentation on long runout behaviour. The micro-scale behaviour of sturzstroms has not been properly investigated to date, with suggestions for the macro-scale response explained largely from conjecture surrounding deposit formation and witness accounts.

Extreme velocity, appropriate instrumentation and specimen arrangement makes laboratory testing difficult. The ideal method to explore the micro-scale behaviour is using numerical modelling. As the fragmentation theory is being considered, the most appropriate numerical model to use will provide detailed information of breakage, energy and material movement. A discrete element model is clearly the most appropriate for exploring the micro-scale behaviour of sturzstroms.

1.4 Research Objectives

The objectives for the micromechanical modelling of sturzstrom in this thesis are outlined below:

- Establish a model to account for the normal application of load (oedometer type test) under quasi-static and dynamic conditions
- Establish a model to account for the application of shear (shear box type test) under quasi-static and dynamic conditions
- Consider idealised and synthetic rock materials as encountered in the field in particular, hexagonal close packed aggregates, greywacke sandstone and chalk

- Determine the key micromechanical responses to consider in the oedometer and shear tests
- Consider the applicability of the results to the long runout of sturzstrom

1.5 Thesis Layout

This thesis first discusses the background literature of the topic in Chapter 2. This includes outlining several examples of known long runout rock avalanches, as well as chalk flows to highlight typical behaviours seen from these events. This is followed by a discussion of the mechanical theories postulated to explain the overall behaviour of long runout avalanches. Highlighted in Chapter 2, Section 2.1.5, is a summary of why sturzstroms are being studied and the significance of the long runout behaviour. Chapter 2 also briefly outlines conventional laboratory soil testing, and discusses the fracture and fragmentation of rock as these tests and behaviours are important in the studies undertaken.

The theory behind discrete element modelling as is implemented in PFC^{3D} is outlined in detail in Chapter 2, Section 2.3, in order to explain the usefulness and relevance of these types of numerical models for investigating the behaviour of sturzstroms. Sections 2.3.2 and 2.3.3 discuss recent geomechanics research and avalanche and landslide modelling using discrete element models. This information is very useful for the later application of the PFC^{3D} model to the micro-scale behaviours in sturzstroms. Following the review of material on discrete element modelling, continuum numerical models and physical models (laboratory and otherwise) are discussed for their capacity to provide useful information on the microscale behaviour of long runout rock avalanches.

The initial testing in Chapter 3 follows on from discrete element modelling research outlined in Chapter 2, and focuses on the use of hexagonal close packed specimens to represent rock boulders. These boulders are placed in an oedometer under varying strain rates as a singular boulder and a larger cuboid arrangement, to investigate the possible behaviour that can be modelled using PFC^{3D}. The tests are also used to consider the response of a synthetic rock specimen to high strain rates that represent the impact or transition point of a sturzstrom from fall to runout. Following these tests, sandstone and chalk materials are fully calibrated in PFC^{3D} using the methods outlined in the BPM by Potyondy and Cundall (2004). The results of these calibrations are outlined in Chapter 4.

The strain rate testing performed in Chapter 3 is continued in Chapter 5 using the calibrated sandstone and chalk materials. Varying strain rates are applied to specimens of greywacke sandstone, weak chalk and extremely weak chalk. The results are analysed in a similar manner to those of Chapter 3, so that comparisons can be made between fully synthetic and calibrated materials under high strain rates.

Runout of a sturzstrom is represented in this thesis through shear box testing of the calibrated

materials at high velocity. The test specimen is arranged in the same manner as debris is anticipated to be found in the runout portion of a sturzstrom. Boulders of material are surrounded by fines and fragments of the same material, with an overburden pressure to represent the carapace of debris at various stages of the runout. The description and results of the shear box tests are enclosed in Chapter 6.

A full discussion of the results obtained in Chapters 3 to 6 is formed in Chapter 7. This discussion considers the results of the high strain rate oedometer and high velocity shear box tests, and relates the results to the theory of fragmentation and the behaviour of materials during fragmentation. Key findings are outlined and limitations of the testing are stated. Finally, in Chapter 8 the thesis is drawn to a close with conclusions following from the discussion, and recommendations for further research and applications of numerical modelling to long runout rock avalanche behaviour.

Chapter 2

Literature Review

2.1 Rock Avalanches

2.1.1 Introduction

Giant catastrophic rock avalanches are large volume, generally dry avalanches that can begin as rock slides or rock falls. They typically occur in steep mountainous areas where the initial rock material is thought to be heavily pre-fractured and subject to tectonic activity (Friedmann et al., 2003). During the avalanche runout, the material begins to dynamically disintegrate. Giant rock avalanches are renowned for travelling a horizontal distance upwards of 5 - 10 times the vertical distance they fall, at extremely high speeds across relatively flat land (Hsu, 1978; McSaveney et al., 2000). Witnesses typically recount stories of a round bulging head at the front of the avalanche, wind whirling at the sides and the total destruction of property in the path of the material (Hsu, 1978).

These giant rock avalanches stop as quickly as they begin and the deposited material is normally dry or unsaturated (Hsu, 1978). The final deposit is often inversely graded (that is, the material at the base is fine silt or rock flour overlain by a silt matrix supporting rock clasts, all covered by large boulders), preserves the original stratigraphy and contains a large amount of silt or rock flour (McSaveney et al., 2000). Evidence of giant rock avalanches in New Zealand appears confined to the mountainous Alp regions which are distant from human habitation (e.g. Falling Mountain (McSaveney et al., 2000) or Mt Ashburton (Davies and McSaveney, 1999) both located in the Southern Alps) although they are potentially still a threat to highways, railways and other important lifeline structures. Elsewhere in the world, giant rock avalanches have shown the propensity to be fatal (e.g. Nevado Huascarán in Peru (Plafker and Ericksen, 1978) and Elm in Switzerland(Hsu, 1978)) where there are villages, towns and in some cases cities, built in valley areas that may be directly in the path of the hazard, or built on sites where rock avalanches have

occurred in the geologic record. The following section provides a few accounts of well known rock avalanches that have occurred throughout the world.

2.1.2 Rock Avalanche Examples

Elm, Switzerland 1881 (Hsu, 1978)

In 1881 the town of Elm in the canton of Glarus, Switzerland, was wealthy due to mining slate from the Elm Plattenberg mountains directly behind the town. The mining ceased in early 1881 as the majority of the high quality slate had been removed and the mountain side was showing signs of movement. Several supporting columns of original material were left in place. Later in the same year some local townsfolk set forth and removed some of the column support structures (Anna Brühwiler, pers. comm.). The mountainside eventually failed. The failure would prove to be so spectacular and unusual that Elm would become famous for this disaster and initiate research into giant rock avalanches, worldwide.

The first failure at Elm was a large rock fall, followed by a secondary rock fall 17 minutes later on the opposite side of what would become the final failure surface (see Figure 2.1, Fromm (1981)). These initial failures killed four people. The Elm Plattenberg failed catastrophically another 4 minutes later falling from between the two initial failures. The resultant material fell as a block, collided with the ledge created by the slate mine entrance and began to disintegrate. The collision with the ledge caused the material to become airborne over the local stream before impacting with the valley floor. Momentum was so great that some of the material travelled up the opposite side of the valley toward the hamlet of Düneberg where some of the survivors of the first two failures had escaped and would ultimately die. This material then fell back to the valley floor to join the main flow toward Untertal and the northern part of Elm. The runout material travelled along a relatively flat valley floor for another 1,500 m before finally coming to a halt. 114 people were killed in total.

Albert Heim was Professor of Geology in Zürich at the time and was asked to investigate the event in Elm. He spent time interviewing local townsfolk as well as geologically mapping the site and making detailed observations. The thorough work performed by Heim (Heim, 1882) has provided great detail as to the behaviour of the material during the rock avalanche and led to Heim developing theories of avalanche motion. Crucially, Heim concluded that the material had flowed like a river. He coined the term âĂIJstürzstromâĂİ or “stream-fall" (Hsu, 1975) to describe this type of event. Heim calculated the approximate speed of the stürzstrom as 180 kmh^{-1} (50 ms^{-1}) from witness statements. The whole event lasted 45 seconds and travelled around 2,000 m. (Since Hsu (1975) published his discussion on Heim’s work, it has become common place in English to describe these types of rock avalanche as sturzstrom, dropping the umlaut.)

Figure 2.2 shows photos taken after the cessation of the Elm sturzstrom. These photos clearly

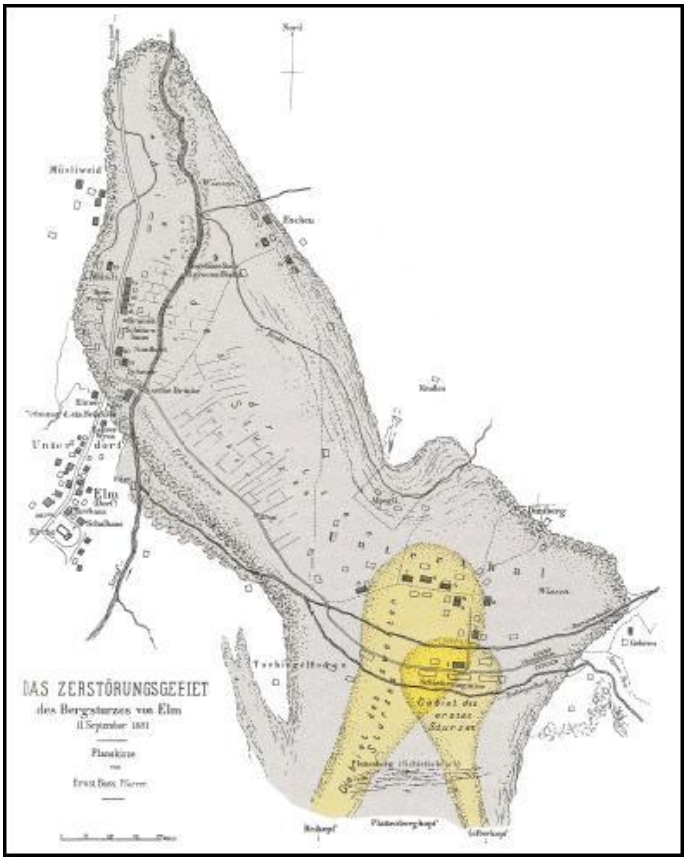

Figure 2.1: Diagram of the Elm rock avalanches (Fromm, 1981, pg 23).

show large boulders on the carapace with angular edges typical of fragmented rock. Mounds of small rock fragments suspended within a fine matrix material can be seen on top of larger rock fragments. In Figure 2.3 are photographs taken at Elm in 2010 of the typical angular boulders seen on the slope and the internal deposit shown by a walking track cutting just above the local stream. The figures clearly support the observations made of sturzstrom deposit characteristics, in particular the angular shape of the rock debris and the fine rock flour as a matrix supporting rock clasts.

The key points Heim made from his observations were:

- The material flowed and was dry – “the turbulent flow of a dispersion of cohesionless grains" (Hsu, 1975, pg81)
- Stratigraphic sequence was preserved in the deposit
- The sturzstrom stopped as quickly as it began
- The material had travelled 1.5 km along a flat valley floor (4 °)
- Rear blocks impacted forward blocks transmitting kinetic energy with the material flowing

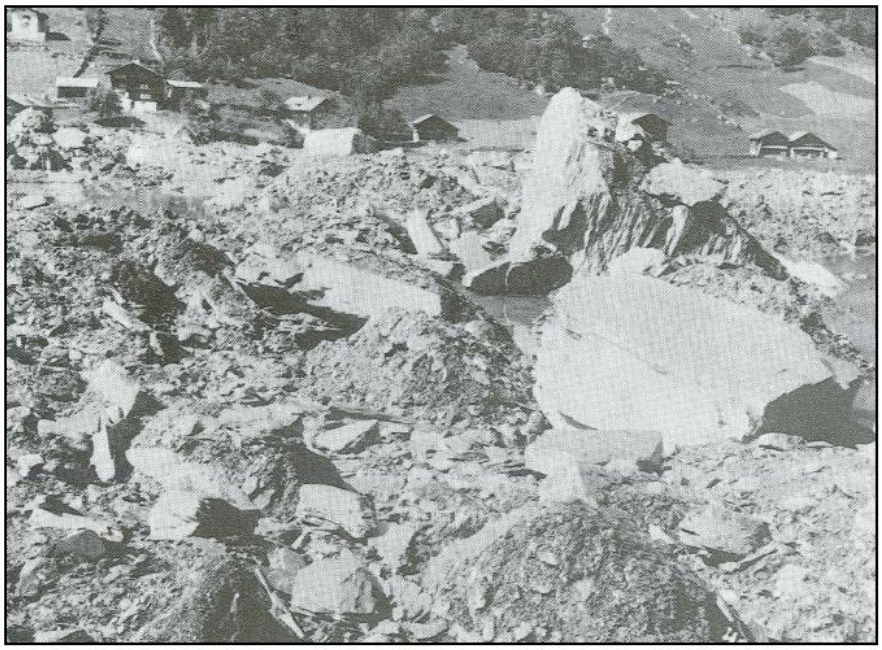

(a) Elm Debris

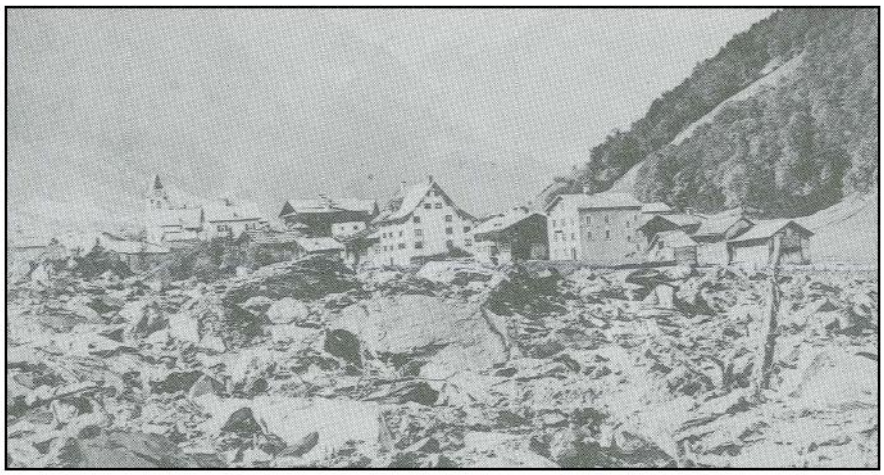

(b) Elm from Untertal

Figure 2.2: Views of debris at Elm 1881 (Fromm, 1981, pg 51-52)

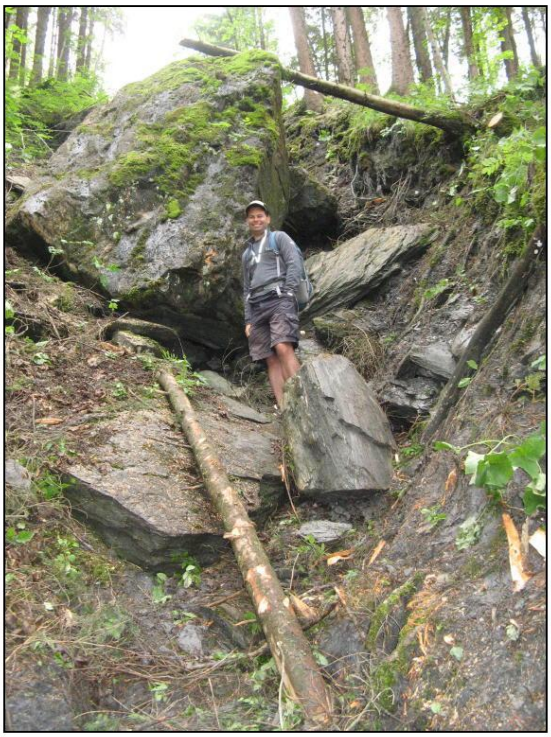

(a) Elm Upper Deposit

(b) Elm Lower Deposit

Figure 2.3: Views of Elm deposit 2010

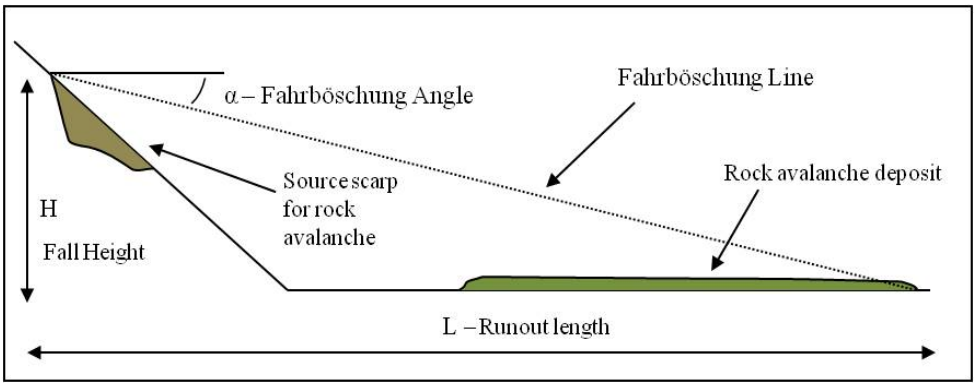

Figure 2.4: Heim's description of the Fahrböschung from his investigations at Elm after (Hsu, 1978, Figure 4, pg 79)

as a stream

- Fahrböschung or the energy line is described by the height of the fall and length of travel (see Figure 2.4 and Section 2.1.6 for a detailed explanation of this concept).

Frank Rockslide, Alberta, Canada 1903 (Cruden and Hungr, 1986; Pirulli and Mangeney, 2008; Moreno et al., 2011)

On April 29 1903, the East face of Turtle Mountain collapsed and travelled across the entrance to the Frank coal mine, traversed the Crowsnest River, destroyed the southern part of the town of Frank killing 70 people, and damaged both roadways and railways. The rockslide avalanche appears to have travelled along bedding planes initially as a block and then began to disintegrate. Cruden and Krahn (1978) note from the investigation by McConnell and Brock (1904) that the original rock mass volume was estimated at 27.5-30.5 x 10^6 m^3 with a runup of 120 m on the opposite side of the valley. The whole event is estimated to have taken 20-100 s. In the years that followed the Frank Slide, Brock revisited numerous times showing concern as to the stability of the mountain, a result of which was the creation of a commission to study Turtle Mountain (Cruden and Krahn, 1978). Studies of Turtle Mountain continued over the next few decades highlighting the complex geology of the area and concluding that the bedding planes and discontinuities contributed to the Frank Slide failure (Cruden and Krahn, 1978). Multiple discontinuities and a highly fractured anticline continue to cause instabilities today (Moreno et al., 2011).

The debris of the slide shows highly angular limestone grains through to blocks, with large blocks apparent across the whole surface area of the deposit (see Figure 2.5). The reconstructed railway line cutting through the deposit shows a cross section of the debris that indicates inverse grading with crushed limestone of sand size in the basal area.

Figure 2.5: View of the Frank Slide debris carapace looking toward Turtle Mountain.

Nevados Huascarán, Peru 1970 (Plafker and Ericksen, 1978)

Two giant rock avalanches occurred in the Peruvian Andes, one in 1962 and the other in 1970. There are indications that prior giant avalanches have occurred in the geologic record. The 1970 avalanche is the most catastrophic on record as more than 18,000 people were killed. This rock avalanche was triggered by an earthquake and travelled for almost 4km before joining the Rio Santa and becoming a debris flow. The total distance travelled was 16 km (16,000 m) at an average velocity of 280 kmh^{-1} (78 ms^{-1}).

Witnesses state that a fall of rock and ice fell first from the face followed immediately by a complete collapse. During the initial drop from the face, the debris entrained and/or melted a substantial amount of snow which would later provide water for mud deposits. Water is believed to have been incorporated also from streams and irrigation channels. An abundance of blocks of ice were found deposited in the debris lobes and were also carried down the Rio Santa. A large number of rocks were thrown beyond the margins of the avalanche area, some for almost 4 km (4,000 m). The avalanche mobility is suggested as being due to the steep slopes in the source area, glacial ice below the source, and the great amounts of water gathered along the way.

Although water was involved in this avalanche, some of the behavioural characteristics are comparable to those of the Elm sturzstrom. Eye witnesses describe the motion as wavelike with the avalanche preceded by a severe wind. An enormous cloud of dust rose from the base of the peak obscuring it from view a few seconds after the fall occurred. The first wave involved rocks bouncing and rolling, the second wave wet debris due to the interaction with snow and water as the material travelled downslope. Debris swept up valley walls and fell back to join the main flow. The deposit was mainly mud and boulders with angular shaped rock fragments. The matrix mud was described as being soft for several days and when finally dry was as hard as adobe.

Flims, Switzerland Holocene (Pollet et al., 2005)

The Flims rock avalanche is one of the 10 largest recorded terrestrial landslides in the world with an estimated volume of 12 km^3 (12 x 10^9 m^3). Occurring approximately 8-9,000 years ago, it mobilized a large part of the Flimmerstein on the northern banks of the Rhine River and travelled around 16 km to the farthest point of rock deposition. The rock avalanche blocked the Rhine River and caused a large lake to occur, however this dam was soon over-topped and the river eroded a channel through the debris which is now known as the Swiss canyon. The central part of the deposit shows large intact rock slabs; at the ground surface and margins are angular rock blocks embedded in a fine silty matrix (see Figure 2.6). This deposit shows jigsaw style broken rock structures as described by Shreve (1968). Very large limestone blocks have been mapped at 12 km (12,000 m) distance from the source site.

Pollet et al. (2005) state that the Flims rockslide never fully evolved into a real sturzstrom and suggest this was due to topographic constraints – the material impacted with the southern bank of the Rhine River dissipating a substantial amount of energy. Disintegration took place at the base and exterior reaches of the debris which is suggested by Pollet et al. (2005) to have occurred through grain-to-grain collisions from the shear or translational movement of the sturzstrom, and the confining forces of the rock mass above.

Falling Mountain, Arthur's Pass, New Zealand 1929 (McSaveney and Davies, 1999)

In 1929, a M6.9 earthquake struck in Arthur's Pass near to what is now known as Falling Mountain. This near source shaking caused the unusually strong greywacke that comprised Falling Mountain to fail. Approximately 55 x 10^6 m^3 of highly indurated (hard and well cemented) greywacke fell 1200 m and travelled around 4.5 km down the Otehake Valley to the west. The mountain shows many different rock-mass defects and the abrupt truncation of the Otehake Valley by Tarn Col suggests that this was not the first time a large rock avalanche had occurred in the area. Figure 2.7 shows the extent of the failure and subsequent sturzstrom runout.

The runup on Mt Franklin and elevation on valley walls due to the deflection by topography provided data to estimate the speed of the sturzstrom. At Mt Franklin this speed was approximately 70 ms^{-1} while further down the valley at the deflection points the speed is estimated at 24-46 ms^{-1}.

The upper part of the deposit appears like a normal granular deposit — it is thin and drapes over the landscape with abundant boulders on the surface up to 10 m in diameter. There is also around 1,000 m^2 of former mountain surface that has been shattered, yet not disaggregated in the same area. Further down the Otehake Valley debris of cobble or boulder size becomes less apparent. The interior of the deposit is comprised of fine pulverised rock, and the stratigraphy of the original source is preserved. Figure 2.8 illustrates part of the interior of the deposit where

(a) Large angular rock slab at Flims

(b) Field in Flims where angular boulders can be seen today

Figure 2.6: Views of Flims deposit 2010

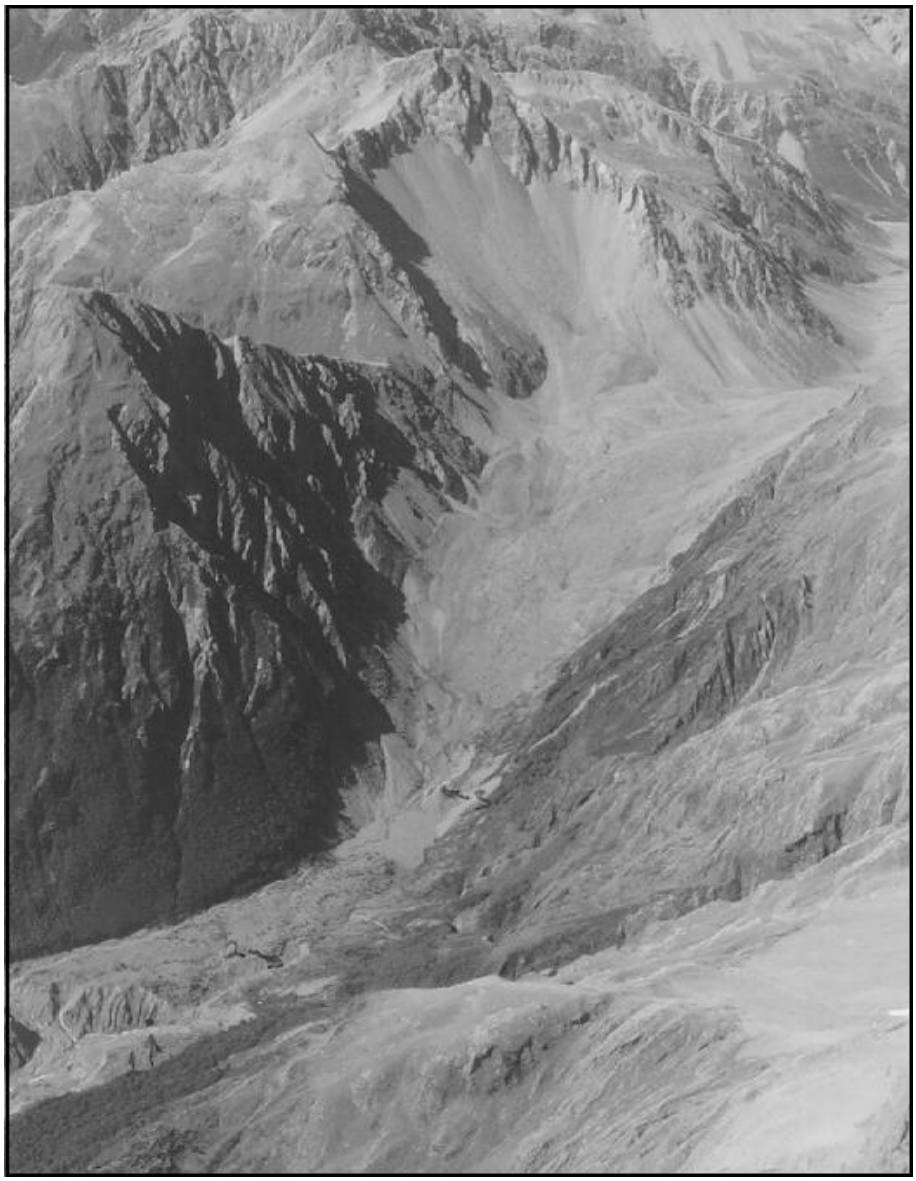

Figure 2.7: Aerial view of Falling Mountain sturzstrom runout area (McSaveney and Davies, 1999, Figure 5)

Figure 2.8: Falling Mountain deposit (McSaveney and Davies, 1999, Figure 13)

broken rock clasts and a jigsaw fractured rock are supported within a fine matrix. McSaveney and Davies (1999) note that there is no evidence of erosion of the bedrock, however the sturzstrom did strip the soil and vegetative cover with some of the vegetation displaced and now growing further down the valley.

Mt Haast, Aoraki/Mt Cook National Park, New Zealand, Jan 2013 (Hancox and Thomson, 2013; Dunning et al., 2015)

Multiple rock avalanches have occurred in the Mt Cook National Park, most notably the Mt Cook avalanche of 1991 that reduced the top of the mountain by 10m (10-15 million m^3 of rock) and the Vampire Peak rock avalanche of 2008 which saw 150,000 m^3 of rock topple from the summit of Vampire Peak and runout across the Mueller Glacier for 1,700m. A similar avalanche had occurred from Vampire Peak in 2003. The area contains steeply sloping mountains under constant freeze-thaw processes and subject to high winds and heavy rain during inclement weather. The area is also crossed with various faults capable of producing enough earthquake shaking to induce avalanches.

Recently in New Zealand's Mt Cook National Park, a small rock avalanche of approximately 1 million m^3 of steeply dipping and heavily fractured greywacke occurred from the southern flank of Mt Haast. The debris travelled around 300 m almost vertically fragmenting as it impacted the slope and producing substantial dust clouds. The final runout of the avalanche was approximately 500 m wide and 3 km in length from scarp to toe along the Grand Plateau glacier reaching to within 200 m of a mountaineering hut. One climber at that hut managed to take video of the

(a) Rock avalanche runout

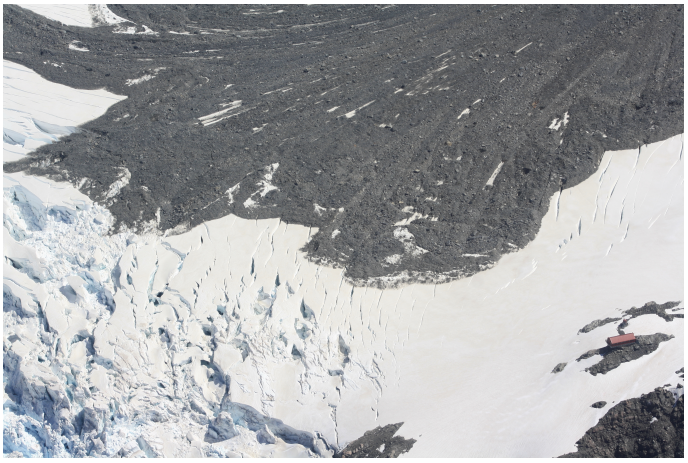

(b) Debris lobes with Plateau Hut in the foreground

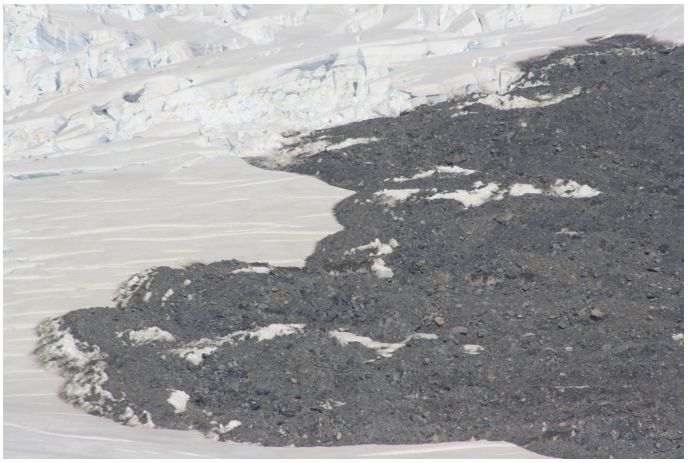

(c) Close up view of debris

Figure 2.9: Mt Haast rock avalanche Jan 2013

avalanche which can be viewed online (`http://www.youtube.com/watch?v=E28_3uj9K0g`). From this video the velocity of the rock avalanche is estimated at up to 150 kmh^{-1} over a period of 65 s with the turbulence at the flow front clearly visible. The resulting debris filled numerous crevasses across the snow field with some of the debris large enough to bridge them (pers. comm. local mountain guides). The avalanche and debris can be seen in Figures 2.9. Large angular boulders are noticeable on the surface of the debris, snow has been ploughed around the lobe margins and the majority of the debris appears well fragmented. The runout debris is estimated at up to 5m high in some places. The landslide runout appears to have followed the topography of the area and flowlines are noticeable in the deposit as the entrained snow is spread.

Morphology and Sedimentology of Rock Avalanches

In a recent review of the sedimentology of rock avalanches, Dufresne et al. (2016) outlines key markers of rock avalanche deposits that are noted by the majority of field geologists. These markers include the size and shape of the deposit material, stratigraphy, structure of the deposit, and facies within the deposit.

The initial observation often noted by those at the site of a rock avalanche is related to the angularity of the debris due to intense fragmentation (Dufresne et al., 2016; Weidinger et al., 2014; McSaveney and Davies, 1999; Cruden and Krahn, 1978; Plafker and Ericksen, 1978; McSaveney, 1978). It is frequently noted that there are large angular boulders on the surface and fractured angular boulders throughout, with Weidinger et al. (2014) noting shattered grains at thin section scale. Dufresne et al. (2016) notes that jigsaw fractured clasts are found at all scales along with large intact blocks within a fine-grained matrix.

Dufresne et al. (2016) also suggest that rock avalanche deposits are typically formed from several facies: carapace, blocky facies, body facies and basal facies. The facies can vary spatially suggesting varying degrees of fragmentation have occurred throughout the material. The blocky facies is described by Dufresne et al. (2016) as a transition zone from the carapace to the body, comprising angular clasts supported in a finer matrix. The greatest variation in particle sizes occurs between the carapace and body facies as noted by McSaveney and Davies (2007).

The geological structures on the surface of the deposits are reasonably consistent across many events. For instance, Coe et al. (2016) notes hummocks are seen in many deposits along with shear zones and small faults, structures also noted by Dufresne et al. (2016), Weidinger et al. (2014) and Robinson et al. (2014). McSaveney (1978) notes that the Sherman Glacier rock avalanche formed longitudinal grooves that clearly showed the direction of flow, and which could also be used to determine the flow sequence.

The basal zone of the deposit is often represented by a sharp unconformity (Dufresne et al., 2016; Robinson et al., 2014; McSaveney and Davies, 1999). Dufresne et al. (2016) suggest that this

indicates an erosional contact, however McSaveney and Davies (1999) suggest there is no evidence of basal erosion at Falling Mountain even though the contact is sharp. It is also noted that the basal area of the deposit is typically comprised of fine grains with large clasts considered rare (McSaveney and Davies, 1999).

2.1.3 Chalk Flows

Chalk

Chalk is a pure limestone, metastable and generally weak (Bell et al., 1990). Microscopic coccoliths are deposited beneath the ocean and under diagenesis form chalk (Omdal, 2010). Following uplift the chalk deposits can become cliffs such as those found in south-east England and north-west France. Typically chalks have high porosity and weaker chalk is known to have smaller grains in relation to the pore size. Chalk is regarded as a low permeability material and needs to be loaded sufficiently slowly in order to obtain drained conditions; as such there is rate dependent behaviour (Omdal, 2010).

Omdal (2010) notes that the breakage of coccoliths or alternatively the rearrangement of the matrix under compression have both been suggested as responsible for the reduction in porosity observed when chalk is compressed. However, the experimental results of Omdal (2010) support the nucleus of failure concept; where the load is carried by the microstructure of the chalk with load transferring to surrounding parts of the microstructure during localised failure. Pore collapse becomes a cascading transfer of load throughout the microstructure. Omdal (2010) further notes that Andersen (1995) suggests that during static loading, deformation is driven partly by the load and partly by the cascading failure. If the loading rate is reduced, then the cascading effect will catch up to the loading rate and if loading is halted, then deformation is solely driven by the cascading process.

Millar (2000) found in triaxial tests that high porosity chalks have contractive behaviour at high stress (due to the stretching of pores in a sideways direction under high confining stress) with dilatant behaviour at low stress. Low porosity chalks were found to have dilatant yielding behaviour although they did not behave rigidly. Clayton (1990) noted that chalk can behave like a rock if it is hard and like undrained clay if it is soft. In soft chalks it is known that “putty" or fully remoulded chalk can be produced with pile driving and that static loading can cause considerable settlement (Hutchinson, 2002).

Flows

Chalk flows are classified by Mortimore et al. (2004) as giant failures of a chalk cliff or slope where the debris can run upward of six times in horizontal distance to the fall height. An atypical chalk cliff collapse will produce a conical shaped fan of debris (Mortimore et al., 2004) or can form a

wet slurry (Hutchinson, 2002). The greatest concentration of chalk flows are based along the Kent coastline in the UK with some occurring in a similar chalk succession along the northwest coast of France. In hard chalk areas (for example the Isle of Wight) there have been no reports of chalk flows. Triggering factors include a high water table, heavy rainfall and frost (Duperret et al., 2002).

Following are some examples of chalk flows:

- Puys Rockfall, France (Duperret et al., 2002) – the rockfall occurred in May 2000 and was followed by a large dust cloud. A secondary fall occurred around 1 hour after the first. The total volume of rock is estimated at around 85,000 m^3. The oldest chalk strata are located the furthest from the cliff and have undergone the longest runout. Stratigraphy is retained, the largest blocks are in the most distant part of the deposit (from the cliff) and the surface of the rockfall is quite blocky. The authors calculate the H/L ratio at 0.5 and find that this falls within the Hsu (1975) range of H/L<0.6 to indicate a long runout rock avalanche. (See Figure 2.10.)

- Beachy Head and Monkey's Cliff (west of Beachy Head), England (Hutchinson, 2002) – around 1848, a volume of approximately 150,000 m^3 failed from Monkey's Cliff and travelled so far out to sea that it created a groyne that persisted for years. At Beachy Head where the cliffs are around 160 m high, there have been several failures. In 1813 around 235,000 m^3 fell and in 1999 around 150,000 m^3 collapsed after prolonged heavy rainfall and frost (Duperret et al., 2002). The 1999 failure is not classified as a sturzstrom comparable flow as H/L>1.0 due to a small runout distance.

- St Margaret's Bay, Kent, England (Hutchinson, 2002) – multiple chalk flows have occurred in the St Margaret's Bay area with a significantly large flow noted in 1895. The largest fall known of the complete face occurred in 1970 with runout of 405 m into the ocean from a fall height of approximately 68 m. In 1905, 130,000 m^3 of chalk fell leaving debris up to 9 m thick in places and extending 370 m out into the ocean. Additional large chalk flows have occurred from the north eastern side of the bay at Leathercote Point. The geologic record indicates that multiple chalk flows have occurred in this area in the past along with multiple smaller chalk falls.

Hutchinson (2002) proposed that an impact mechanism is responsible for chalk flows. Soft, highly porous and saturated chalk can reach a dynamic pore-collapse threshold on impact resulting in a cascading failure through the micro-structure. The impact of falling chalk against the shore platform causes the pores to crush producing excess pore-water pressure which leads to a high temporary mobility via undrained loading. The longest flows occur in the lowest dry density material with 40% porosity indicated as a possible transition point from chalk fall to chalk flow (Hutchinson, 2002).

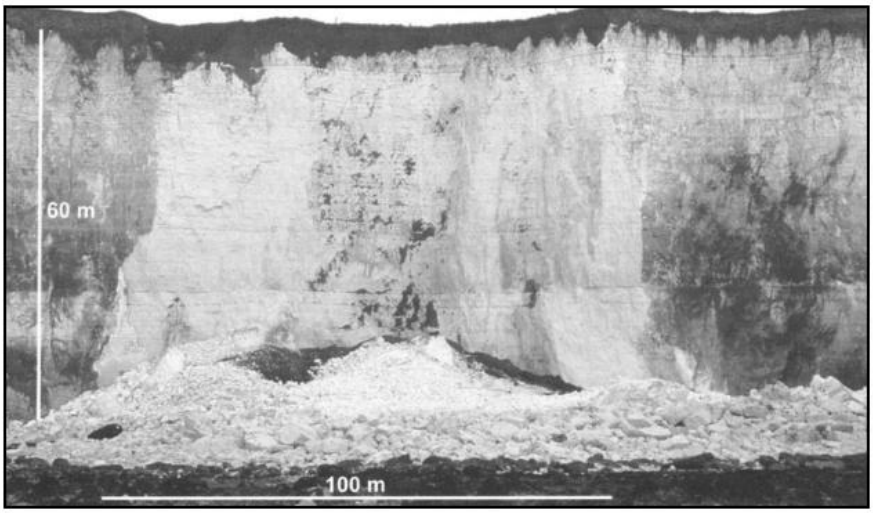

(a) Puys cliff

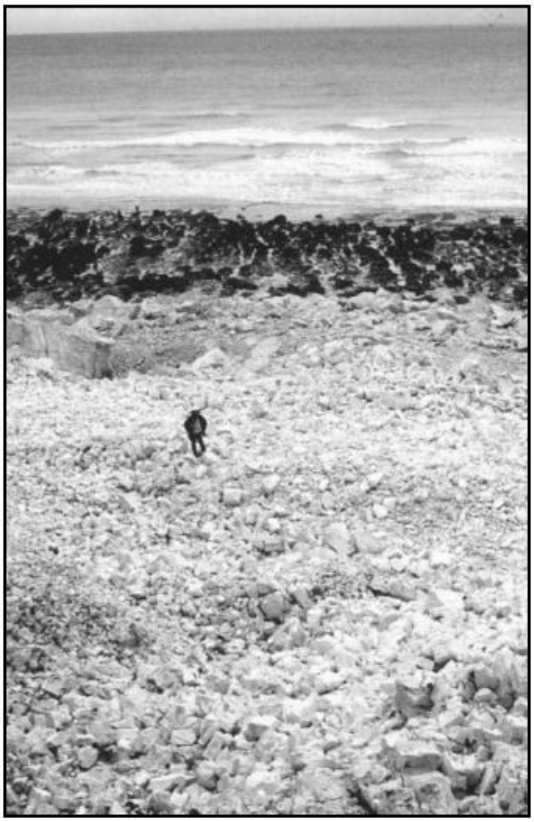

(b) Puys deposit

Figure 2.10: Puys cliff collapse (Duperret et al., 2002, Figure 2, pg 54 and Figure 5, pg 56)

Mortimore et al. (2004) suggest that chalk flows match alpine dry rock avalanches in behaviour albeit at a smaller magnitude. This resemblance includes that the H/L or Fahrboschung decreases with the event volume, fragmentation is evident in the debris, stratigraphy is preserved, clouds of dust occur at impact and the mass dilates during runout (Bowman and Take, 2014). Bowman and Take (2014) note that the occurrence of dust clouds suggests that the chalk is not fully saturated and indicate that a minor amount of moisture is required to reduce the strength of chalk toward that of a saturated chalk. The experimental results of Bowman and Take (2014) suggest that increased moisture in chalk cliffs is potentially more important for triggering collapse than as an influence on the runout behaviour. They go on to note that chalk cliff collapses behave like sturzstroms in terms of the propagation and deposition behaviours although chalk flows fall from a much smaller height with a simple and shorter runout zone.

2.1.4 Summary of Typical Sturzstrom Characteristics

- Typically occur in steep mountainous areas that may be tectonically active and have pre-fractured material
- Highly mobile and travel at very high speeds
- Can travel up to 30 times horizontally the distance fallen and often travel up valley sides during runout
- Characteristically dry or unsaturated
- Are capable of entraining or releasing material
- Cease quickly
- Deposit material shows angularity in particle shape and at times inverse grading
- Deposit shows preserved stratigraphy
- Life threatening in populated areas

2.1.5 Why Study Sturzstroms?

Table 2.1 outlines the key information from the above examples and includes additional sturzstroms that have been researched or discussed in the literature, however the table is not exhaustive. Along with the summary of behavioural characteristics above, several striking items appear, as mentioned by prior authors such as Hsu (1978), McSaveney (1978), McSaveney and Davies (2007) and Hungr (1995).

There is a clear relationship between volume and distance travelled as seen in Figure 2.11 produced by Dade and Huppert (1998). Extraterrestrial events are likely to travel much further

h

Table 2.1: Summary of key characteristics of example rock avalanches. Note: * I=Igneous, M=Metamorphic, S=Sedimentary.

Name	Year	Volume (m^3)	Rock Type*	Fall Height (m)	Run Out (km)	Run Up (m)	Comments	Reference
Flims, Switzerland	Holocene	12 x 10^9	Limestone (S)	500	16.5	None	Glacial unloading, earthquake and karstic dissolution possible causes.	Pollet et al. (2005)
Avalanche Lake, Canada	1440 A.D. 1220	200 x 10^6	Dolomite (M)		4	640m	Entrained and ejected material.	Evans et al. (1994)
Elm, Switzerland	1881	10 x 10^6	Slate (M)	1500	2	100	Slope undercut by mining; duration approximately 45s with 114 killed.	Hsu (1978)
Frank Slide, Canada	1903	30 x 10^6	Limestone (S)	2200	2.5	120	Failure of Turtle Mountain possibly due to freeze/thaw and mining operations; duration approximately 100s with 70 killed.	Cruden and Hungr (1986); Cruden and Krahn (1978); Pirulli (2009)
Falling Mountain, New Zealand	1929	55 x 10^6	Greywacke (S)	1900	4.5	250	1929 Arthur's Pass Earthquake.	McSaveney et al. (2000)
Nevados Huascarán, Peru	1962 and 1970	30-50 x 10^6	Granodiorite (I)	5400 to 6500	16	230	1970 event killed 18,000 people. Sturzstrom travelled 4 km to Rio Santa where it became a debris flow. Begun by earthquake and mobility influenced by water and ice.	Plafker and Ericksen (1978)
Sherman Glacier, Alaska	1964	10 x 10^6	Greywacke (S)	1400	4	150	Earthquake induced failure of Shattered Peak where steeply dipping faults were parallel to the bedding. Speed was estimated at 26-67 ms^{-1} probably enhanced with the presence of ice and water.	McSaveney (1978); Hungr and Evans (1996)
Val Pola, Italy	1987	5 x 10^6	Gneiss, gabbro and diorite (I)	2370	1.5	300	Heavy rain caused prehistoric landslide surface to fail as a sturzstrom killing 27 people in 70-120 s.	Crosta et al. (2007)
Denali Fault, Alaska	2002	4–20 x 10^6	Metamorphic and granitic (I)	1000+	3.2–11.5	150	Multiple sturzstrom set off by the Denali Fault earthquake.	Jibson et al. (2006); Schulz et al. (2008)
Went Hill, Sussex, UK	1914	12,500	Chalk (S)	45	0.07	None	Mobilisation like sturzstrom.	Williams et al. (2004)
Puys, France	2000	85 x 10^6	Chalk (S)	50	0.12	None	Stratigraphy retained, debris rocky and fragmented.	Duperret et al. (2002)

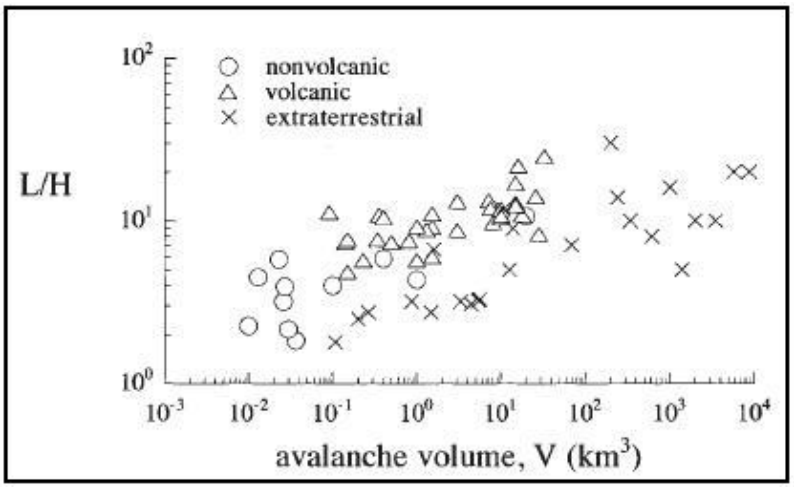

(a) Volume effect – relative runout vs volume of avalanche material

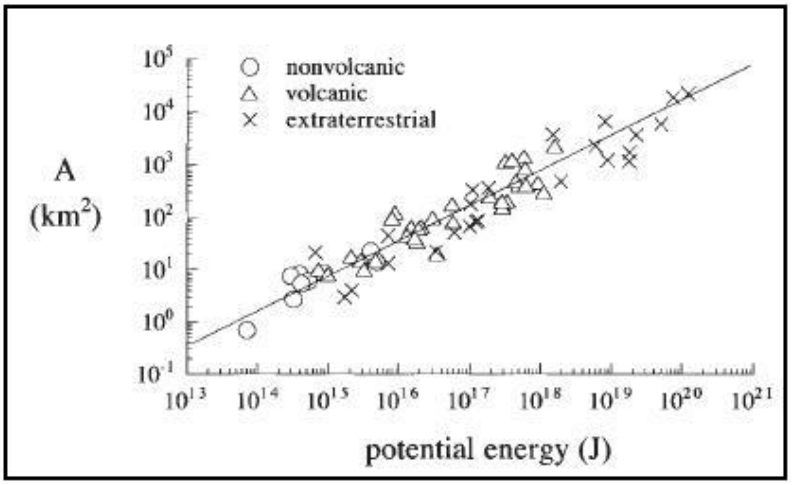

(b) Energy effect – area of avalanche runout vs potential energy

Figure 2.11: Volume and energy effects from Dade and Huppert (1998, Figure 1, pg 803 and Figure 2, pg 805).

than terrestrial events, for example, due to gravity being much less on the Moon than Earth and Martian events generally occurring from greater fall heights. If the potential energy of the estimated original mass prior to a sturzstrom is calculated then the areal distribution of the material after the event has a strong positive relationship with the potential energy, although as Dade and Huppert (1998) note, many sturzstroms are restricted by topography thus are unable to spread perhaps as far as they otherwise might on a flat plane. It also appears that a sturzstrom will not occur in 'hard' rock material unless the volume of material is greater than 1 x 10^6 m^3.

Although not exhaustive, the sturzstrom events outlined in Table 2.1 indicate that sturzstrom occur in sedimentary and metamorphic rock. Sturzstrom have also been recorded as occurring in basalts in Iceland (e.g. Mercier et al. (2012)), and subaerial basaltic lava flows that overlie

sandstones and mudstones in Greenland (e.g. Pedersen et al. (2002)), where permafrost and freeze-thaw events are frequent. It appears however, that sturzstrom events in igneous rocks are less frequent than those in sedimentary and metamorphic events, and perhaps limited to parts of the planet under extreme climatic conditions.

The deposits from sturzstroms indicate that there is little mixing between differing stratigraphic layers (Hsu, 1975; Friedmann et al., 2003; Crosta et al., 2007; Kilburn, 1999), however there is evidence of very fine rock flour material at every sturzstrom site. Rock clasts and larger fragments or boulders remain within their stratigraphic layer to maintain the sequence after failure. Detailed datasets have been collected on limited sturzstrom events. In general, the volume of material deposited is estimated and an educated guess is made as to the initial volume at source.

The volume of a sturzstrom deposit can be increased by the entrainment of material. Material entrained from the slopes is more common than during the runout (Dufresne et al., 2010) with ploughing below and ahead of the avalanche front the most common method of entrainment. Abrasion, as the sturzstrom overrides and mobilises in-situ material, can also increase the overall deposit volume. Various other methods of entrainment are also possible.

Earthquakes, heavy rain, undercut of slope, freeze/thaw and other triggering events are attributed to the failure that leads to sturzstroms. The pre-fractured nature of the material that fails is likely to be important to the susceptibility of the material to any specific event that may cause failure. Thus there is not a specific failure mode responsible for the occurrence of a sturzstrom.

The excessive speed of sturzstrom events (characterised by a large horizontal distance travelled in a very short timeframe) creates difficulties in monitoring the runout behaviour in situ. The multiple possible initiation sites of failure that result in sturzstrom also makes predicting the likelihood of a sturzstrom event very difficult unless a prior sturzstrom has occurred in the area. Witnesses who have survived sturzstroms provide good macroscopic information however it has not been possible to clearly identify the microscopic behaviour occurring during a sturzstrom.

In all sturzstrom events the material at some stage will begin dynamically disintegrating. This is supported by deposits of angular rock fragments and pulverised material or rock flour. The amount of dynamic disintegration appears to be related to the volume of source rock. More specifically the pressures that can be exerted by overburden rock weight during the initial fall of material and later runout will influence the breakage of underlying material.

The Long Runout Problem

Landslides of substantial volume can often exhibit extremely long runout that appears to violate the simple frictional rules of the mechanics of a block mass sliding downslope. McSaveney et al. (2000) note that long runout requires that material in the distal part of the deposit travels further than would normally be expected. Sturzstroms in particular produce long runout along flat or

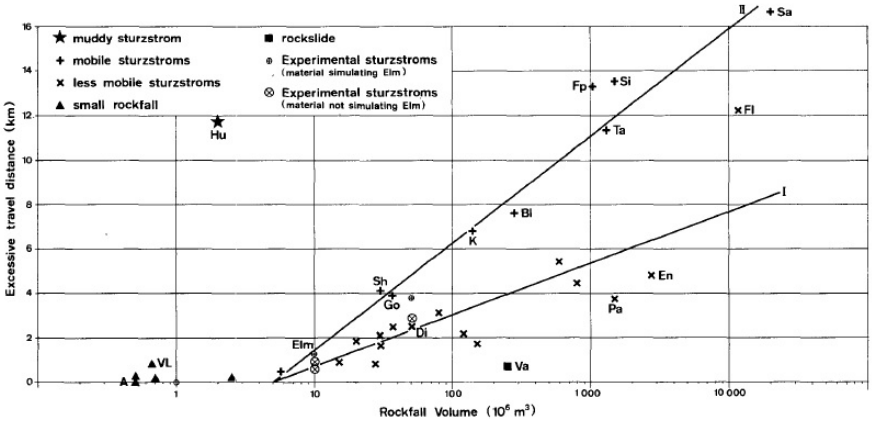

Figure 2.12: Volume and excess runout relationship from Hsu (1975, Figure 8, pg 139) for various types of sturzstrom. Line II indicates the more mobile group.

gently inclined valley floors for often several kilometres and for a far larger distance than the initial fall height. The investigation of the possible associated causes for this unusual behaviour of a sturzstrom is termed the long runout problem.

The runout distance of granular avalanches cannot simply be related to the coefficient of friction of the material (McSaveney et al., 2000) as the volume of material from the initial failure is much greater for avalanches with larger spreading (McSaveney and Davies, 1999). McSaveney and Davies (1999) suggest a minimum volume of source rock for rock avalanches with large spreading can be estimated from the multiplication of the length of the runout, which is ten times the width, which is itself around ten times the depth, or a volume of minimum 1x10^6 m^3. This volume is a level an order above which long runout appears to occur. The influence of the initial volume of rock on runout has been discussed by Hsu (1975) who noted a semilog relationship between volume and runout as shown in Figure 2.12. Hsu (1975) also noted that a reduced runout in large volume rock avalanches is only apparent where the avalanche has been confined by topography, the runout path is very rough or there is a reduced fall height.

The influence of the volume of source material on the runout behaviour of the avalanche is also noted by Melosh (1986) and Staron (2008) among others. Small rock avalanches travel horizontally around 1-2 times the vertical fall height and the flow behaviour is largely understood in terms of the influence of gravity and internal friction in debris (Melosh, 1986). The dramatic increase in horizontal distance travelled by a long runout rock avalanche suggests a substantial decrease in the internal shearing resistance which is not well understood.

Laboratory experiments of small, low velocity granular flows are noted by Dufresne et al. (2010) as complying with simple frictional behaviour. For example, the Sliding Block model presented by Newmark (1965) (Jibson et al., 2006) considers a landslide as a rigid rectangular block that slides on an inclined plane. This model is typically utilised for earthquake slope displacement analyses.

The critical acceleration of the block is known and can be twice integrated to obtain the cumulative displacement of the landslide under earthquake shaking. The critical acceleration is typically found for when the factor of safety is unity. This method does not consider internal deformation of the landslide body or permanent displacement of the block at accelerations less than the critical value. Pore pressure is also neglected in this model. Although a simple and frequently used method to determine inertial slope displacement, this type of model is not capable of explaining long runout in sturzstroms due to the influence of strain and dynamic pore pressures in these events. Other simple frictional models have similar issues and are also not appropriate for modeling sturzstroms due to their inability to represent the internal deformation behaviour.

The discussion regarding the possible reasons for long runout in sturzstroms highlights the overall lack of clarity in the landslides research community of the general underlying behaviour of sturzstroms. A giant rock avalanche with extreme volume of at least $1x10^6$ m^3 of initial material, that travels with extreme mobility across relatively flat land for up to 30 times the original vertical fall height, cannot be explained with frictional sliding theories. Many prior researchers have recognised this unusual behaviour requires a different explanation. The main theories of long runout rock avalanche mobility and mechanism are discussed in the following section.

2.1.6 Mechanics of Long Run-Out Rock Avalanches

Mechanical Fluidisation After Heim

The first mechanical theory for the behaviour of a sturzstrom was put forward by Albert Heim in 1882 after his investigations at Elm. Heim stated that sturzstroms flow and show comparable behaviours to a fluid — mechanical fluidisation. Hsu (1975) notes in his review of Heim's findings that Heim believed that the angular broken debris was generated through the disintegration of a rock mass of a very large size.

Hsu (1975) describes the debris as a flowing mass of cohesionless blocks and believes that sturzstroms follow Bagnoldian grain flow theory. Bagnold (1954) states that dispersive stresses in a shear flow are developed as a result of grain collisions that occur due to one layer of grains overtaking grains in an adjacent slower layer. The grains are assumed to be packed in an hexagonal close packing or cannon ball packing (closely packed with low porosity) and in an inertial regime where the collisions between layers cause oscillations in the material or can cause dilation (Bagnold, 1954). Bagnold (1954) indicates that if the basal layer is considered a rigid granular (rough) surface then any collision by a grain above this layer will cause an adjustment to that grain's momentum and there will occur a repulsive pressure between the two grains that contact.

Laboratory Testing

In physical laboratory tests run by Savage and Sayed (1984), it was found that collisions between glass beads generate fine powder due to grinding where the beads were clear and smooth at the start of the test to roughened and opaque at the end. The powder coated the beads and made them appear slippery, possibly reducing friction in the tests. It was also noticed that although a granular material may initially be randomly packed, under high shear stress the grains can rearrange to reduce the shear stress. Savage and Sayed (1984) also found size segregation occurring when a granular material shears. The void sizes fluctuated during shearing providing an overall higher probability of small voids than large voids. Thus smaller beads could more readily travel through the material – like a sieving effect. Overall Savage and Sayed (1984) found that in a granular material under shear, a net migration of fines in the direction of gravitational and centrifugal forces is likely.

Hsu (1975) notes that the dust cloud that surrounds a sturzstrom may provide the interstitial fluid between blocks. Hsu (1975) goes on to state that the presence of interstitial dust and small debris may be able to reduce the effective normal pressure. The laboratory tests by Savage and Sayed (1984) support this conjecture, as they suggest that fine material in a sturzstrom could sieve to the base and coat larger rock clasts reducing friction in shear.

Coulomb Equation

Heim produced a figure similar to Figure 2.4 from his investigations at Elm. From this figure the Fahrböschung angle can be calculated as follows:

$$\frac{H}{L} = tan(\alpha) \tag{2.1}$$

where α is the angle from the scarp top to the distal end of the sturzstrom deposit (see Figure 2.4, also known as the Fahrböschung angle), H is the total fall height of the debris, and L the runout length. Originally the Fahrböschung ($\frac{H}{L}$) was thought of as a coefficient of friction; however the equation itself implies that the centre of gravity shifts from the highest point on the failure slope to the distal edge of the deposit (Hsu, 1975) and represents translation due to the motion of the event (Davies and McSaveney, 2002). The Fahrböschung has also been considered an energy-line to indicate the rate of frictional dissipation of energy (Hsu, 1978).

The slow flow of granular material is well described by the Coulomb equation

$$\tau = \sigma' * tan(\phi') \tag{2.2}$$

where τ is shear stress, σ' the effective normal stress and ϕ' the effective friction angle of the soil on the plane. In comparison to the Fahrböschung Equation 2.1 the right hand side of Equation 2.2 represents frictional resistance to be overcome by the shear stress. In Equation 2.1 it is clear that

the angle of repose of the slope or Fahrböschung angle can be formed from simple trigonometry of the ensuing angle or $tan(\alpha) = \frac{opp}{adj} = \frac{H}{L}$ rather than stress parameters.

Heim's Fahrböschung is still used by most researchers to indicate the likelihood of a sturzstrom having occurred. Sturzstroms are able to maintain high velocity when $\frac{H}{L} < 1.0$ where the Fahrböschung angles observed for less energetic landslide events are typically >1.0 due to the lesser distance of travel or value of L.

Collision Concept

McSaveney (1978) reaffirms the theories of Hsu and Heim that a collision-based mechanical fluidisation is an explanation for the long run-out behaviour of a stuzstrom. Specifically **?** writes this collisional behaviour is a "mechanical fluidisation where internal friction is lowered through the statistical separation of clasts in rebounds from countless collisions." The rolling or impact of debris must reduce toward the top of the debris in motion due to the reduced confining load, therefore any deformation is confined to the basal area of the avalanche.

Turbulence can not be possible during runout or the types of structures seen in sturzstrom deposits would not be found — including jig-saw boulders, ridges and grooves. There is also a lack of mixing of material shown by textural and lithographic zones as seen in the Sherman Glacier deposit (McSaveney, 1978). Earlier work by McSaveney (1978) indicates that a sturzstrom must have high "viscosity" to prevent turbulence, thus preserving stratigraphic features. Fine rock material, postulates McSaveney (1978), may allow larger rock clasts to pass over one another creating a reduction in friction as later supported by Savage and Sayed (1984). **?** concludes from research into the Sherman Glacier rock avalanche that a sturzstrom is a "supercritical laminar flow of Bingham plastic." A Bingham plastic as defined by Darby (2001) will be solid until a certain yield stress is met at which point the material will flow and on deposit will generally show signs of a textured surface with ridges or peaks. This deposit surface texture is claimed by McSaveney (1978) to be comparable to the transverse ridge lines and other characteristic features of sturzstrom deposits.

In further support of the mechanical fluidisation theory via collision, Campbell (1989) and Cleary and Campbell (1993) state that simple particle dynamics are likely within a sturzstrom flow. Campbell (1989) states that order of strata in deposits suggests that little agitation of debris takes place outside of a basal layer of active particles passing over a roughened base. Cleary and Campbell (1993) use a simple computational plane strain model to represent a column of particles traveling at uniform velocity over flat and rough ground surfaces. They find that violent basal collisions with the roughened base within only the lower 15% of the flow supports the upper plug by producing dilative energy. Cleary and Campbell (1993) comment that energy is resupplied to the system from the load and that once all kinetic energy is consumed by the collisions that the

mass comes to a halt. This appears contradictory when the upper plug has not apparently moved from above the collisional layer, thus if load was causing the continuation of the collisions the model should not halt until the upper plug has thinned. This also suggests instead that the initial velocity in the model particles is providing kinetic energy to the lower layer.

Energy

Kilburn (1999) has suggested modifications to the application of granular flow theory to sturzstroms. He suggests that the simplest model is that significant deformation occurs within a narrow boundary at the base of a sturzstrom, so that the energy dissipation is small in relation to the energy in the whole system. Kilburn (1999) states that the overall energy in a granular avalanche is obtained from the potential energy released during descent and this energy is then consumed by friction during runout. Fragments in the debris move together as groups so that energy is only lost from the exterior fragments and this is suggested by Kilburn (1999) as a possible means of energy retention during a granular flow process.

Fragmentation

McSaveney (1978), Davies et al. (1999), Davies and McSaveney (2008) and Davies et al. (2012) state that fragmentation of rock during a sturzstrom from collisions between rock clasts is responsible for producing the very fractured and angular rubble that commonly occurs in the deposit area. Fragmented material is recognised in the deposits of most sturzstroms, and Crosta et al. (2007) suggest that there is more than one comminution process acting in the runout of a sturzstrom to produce this type of deposit.

Davies et al. (1999) define fragmentation as a parent rock with no initial jointing breaking into pieces that are each smaller than that of the parent rock. Fragmentation according to Davies et al. (1999), occurs in a sturzstrom under an overburden stress that exceeds the strength of unjointed rock. Fragmentation of a rock is suggested to produce high velocity fragments that travel in all directions dilating the debris and resulting in an isotropic dispersive stress — an effect that is additional to a collisional fluidisation (or rearward blocks impacting forward blocks) for long runout in sturzstroms. Davies et al. (1999) state that the process responsible for fragmentation is more likely to involve a crushing or grinding behaviour than grain collisions, due to the lack of free collisions possible with the debris being in close contact and under pressure.

Davies and McSaveney (2008) clarify the role fragmentation may play in the long runout of sturzstroms. Once micro-cracks completely travel through a rock clast, fragmentation occurs allowing subclasts to move under an applied stress field from the sturzstrom debris. Davies and McSaveney (2008) state that elastic strain energy from the fragments is released and converted to an outward directed force or pressure energy. So-called surface energy from the creation of the

fragments is suggested to account for only 1-30% of the potential energy from the initial sturzstrom fall which is also supported by Crosta et al. (2007) and Locat et al. (2006). Davies and McSaveney (2008) note that the work done in rapid brittle failure becomes the kinetic energy of the fragment such that when unconfined rapid failure occurs it is likely to be explosive.

In later work, Davies et al. (2012) go on to suggest that elastic strain energy is released during the disaggregation of a fragmenting grain and is delivered to the surrounding material as either kinetic energy (unconfined) or elastic body waves (confined). Studies reviewed by Davies et al. (2012) suggest that around half of the maximum strain energy of an unconfined rock will be returned as the kinetic energy of the fragments. Davies et al. (2012) go on to state that elastic body waves traveling through surrounding grains will alter internal grain stresses and the grain will break if the Griffith failure criterion is met. Failure of grains is more likely if the grain is already under high confining pressures and Davies et al. (2012) note that a confined and shearing granular flow can develop local stresses significant enough for breakage to occur. They go on to suggest that in a continuous flow where multiple grains are fragmenting and producing elastic body waves due to confinement, the waves may combine to form a complex isotropic pressure wave that may affect the flow.

Interestingly both Davies and McSaveney (2008) and Davies et al. (2012) go on to say that the grain most likely to fail in the material force-chains is one of the smallest which tends to contradict conventional geomechanics findings, where the largest grain has the highest probability of failing first due to being weaker, because of size effects (Hudson and Harrison, 1997). In addition, the fragmentation theory of Davies and McSaveney (2008) and Davies et al. (2007) appears to rely on the rock reaching the Hugoniot Elastic Limit (HEL) under high confining stress. Material that has undergone extensive damage and is above its HEL is said to behave like a cohesionless fluid providing little resistance to shear (Davies and McSaveney, 2008). It is difficult to determine whether a material could always be above its HEL throughout a sturzstrom runout or if this situation may only occur at discrete times. If the material is tightly packed, then Davies and McSaveney (2008) theory suggests that fragments provide an outward pressure, however this pressure will surely increase the porosity of the debris and thus allow for more frictional dissipation of energy than that contended. The intricacies of this theory are yet to be properly detailed as the micromechanics have so far proven difficult to establish.

It is suggested by De Blasio (2011) that a large proportion of fragmentation likely occurs during vertical impulsive stress events. He suggests that only a small fraction of energy is used for breakage and that particle-particle impact may not be an efficient mode of fragmentation, rather that force chains (refer Section 2.2.3) under dynamic forces are most important. De Blasio (2011) goes on to suggest that a relationship exists between topographic variations and the resultant fragmentation within an avalanche.

Collisional or Acoustic Fluidisation

Hungr and Morgenstern (1984) state that the theory of fluidisation by collisional flow assumes that the Coulomb relationship breaks down at high rates of shearing which is plausible given that particle contacts are quite different from slow to rapid shear. Multiple granular flow laboratory experiments were performed in a flume by Hungr and Morgenstern (1984) along a roughened base with materials stated to be of similar dimension to material in sturzstroms. The results of these experiments suggest that high rates of shearing are not sufficient to explain long runout as Hungr and Morgenstern (1984) state that even at mean velocities of 5 ms^{-1} the materials behaved according to the Coulomb equation thus they dispute the validity of a collisional flow. However, this velocity is quite low in relation to the typical speed of sturzstroms which can travel at up to 100 ms^{-1} or faster. Given this extreme difference in velocity of travel it is likely that there is a greater velocity than tested by Hungr and Morgenstern (1984) that could be considered the point of change from Coulomb relationship to a collisional flow.

According to Melosh (1983) acoustic waves are generated by vibrations from the shear flow and diffuse through the rock debris transmitting pressure fluctuations and relieving the overburden pressure, thus reducing the friction at the base of the avalanche. Melosh (1986) disagrees with the application of Bagnoldian theory to sturzstroms, claiming that it is unclear whether the impact between grains can lower the Fahrböschung value. He instead suggests that acoustic energy forms from collisions, and can regenerate itself during the motion of a sturzstrom. Melosh (1986) believes that a dispersive grain flow is a high energy end member of acoustic fluidisation.

Kelfoun and Davies (2011) state acoustic fluidisation has been shown to be 'insufficiently energetic' to cause pressure fluctuations substantial enough to relieve overburden pressure. Similarly, Davies et al. (1999) note that it has not been shown that rock avalanches would be able to generate the high frequency of vibrations that would be required to allow long runout to occur. It is also not known whether the extra motion from the acoustic vibrations can overcome those periods when the vibrations may actually prevent motion. Acoustic fluidisation and fragmentation could be considered related though as Melosh (1983) states that the acoustic waves occur due to grain collisions which are also theorised to cause fragmentation when violent.

Rather than acoustic fluidisation Khazaei et al. (2015) defines acoustic emission as an elastic wave from the rapid release of energy due to the cracking and rupture of intact rock. A correlation exists between the stress-strain curve in rock and the acoustic emission rate (Khazaei et al., 2015). Acoustic emission is therefore directly related to the fragmentation of rock. The release of energy due to multiple fragmentation events in a sturzstrom may lead to an elastic wave large enough to result in a reduction in friction and enhanced runout. In a similar vein, McSaveney (2015) states that during fragmentation a pulse of elastic strain energy moves through grain contacts altering the contact forces. This change in contact forces may cause slip to occur if the Coulomb failure criterion

is exceeded and will appear as an apparent reduced friction (McSaveney, 2015). Zhang et al. (2016) states that the acoustic portion of the “transient elastic strain energy" described by McSaveney (2015, pg 1741) results in “acoustic fluidisation" when enough material is breaking. Zhang and Thornton (2007) refer to the original concept from Melosh (1983) however their comments follow a similar view to that of Khazaei et al. (2015).

Other Theories

Further mechanical theories advanced to explain the extreme behaviour of sturzstroms include:

- Air/Gas fluidisation: air is trapped after the initial rock fall and becomes a cushion that the rock moves on due to reduced friction. The air escapes by pushing through the rock debris thus providing a reduction in internal friction (Shreve, 1968; Kent, 1966). It is likely that not all air would escape throughout the runout resulting in air bubbles being trapped within the debris upon cessation of the sturzstrom. If this occurs deposits indicate the presence of air bubbles which is only the case for pyroclastic flows and has not been seen in any nonvolcanic rock avalanches (Davies et al., 1999). This theory has also been further criticised as sturzstroms are known to have occurred on the Moon and Mars where the atmosphere is significantly less than that on Earth as discussed earlier.

- Self-undrained loading: a sturzstrom flows across a saturated alluvial layer which under shear attempts to contract. The debris movement leads to an increase in pore pressure and a reduction in effective stress so that the alluvial layer effectively carries the sturzstrom (Legros, 2002). Not all sturzstroms have occurred nor may occur where there are alluvial deposits. Additional alluvium is thought to reduce the motion of the sturzstrom (Davies et al., 1999) due to entrainment at the base of the runout material being likely to increase friction. The leading avalanche material is more likely to plough the underlying alluvium or flow over the top.

- Melting rock: the rock on which the sturzstrom flows becomes overheated due to frictional heating and melts creating a fluid base for the debris to flow on (Erismann, 1979). So-called “frictionite" has been observed at some sturzstrom sites, however as with self-undrained loading, not all sturzstrom deposits exhibit frictionite.

Although all of these theories appear to relate to one specific sturzstrom event or can be shown to occur in laboratory or numerical experiments, with the exception of Davies and McSaveney, none can explain the features and characteristics seen across all sturzstroms. The angularity and structure of the deposits is not clearly explained by the theories listed above and neither are the microscopic mechanics that lead to the macroscopic sturzstrom behaviour as seen by witnesses and described by researchers. In comparison, Davies and McSaveney’s theory of fragmentation

encapsulates the angularity and structure of sturzstrom deposits. In general, the dynamics of long runout rock avalanches are still debated with researchers as yet generally unable to reach consensus.

2.2 Material Testing and Behaviour

In any geotechnical investigation, either real world or numerical, it is crucial to understand the likely behaviour of the relevant material (soil and/or rock) in order to draw clear conclusions for the particular situation that material is found in or stress it may be placed under. Conventionally in geotechnics, laboratory stress-strain experiments are performed on samples of material and the associated results examined to determine the material behaviour. Numerical experiments are normally calibrated to the material properties such as Young's Modulus and Poisson's ratio with the macroscopic material behaviour often checked for similarity to a particular laboratory experiment (see Sections 2.4 and 2.3).

Given that the runout of rock avalanches involves overburden pressure due to the volume of rock (especially at topographic transitions) and shear forces during runout, traditional laboratory tests can be utilised to model the behaviour of sturzstroms. To this end numerical triaxial, oedometric and shear box tests have been used in order to consider calibrated material behaviour under sturzstrom equivalent conditions. The physical versions of these tests are briefly discussed below for reference.

2.2.1 Conventional Laboratory Soil Tests (Powrie, 2004)

Terzaghi's Principal of Effective Stress

The concept of effective stress was developed by Karl Terzaghi after analysing the results of a series of oedometer tests. Terzaghi and Peck (1967) found that the increase of pore pressure in soils directly resulted in a loss of strength as the soil grains are pushed away from one another. The total stress that a soil feels can be separated into a pore pressure and effective stress. Thus as the pore pressure increases the effective stress decreases and so too the overall strength. Combined with this reduction in strength is an overall decrease in the critical friction angle thus a material with increased pore pressure is more able to move under shear.

Shear Box Test

The simplest way of investigating shear strength and shear stress-strain behaviour of a saturated soil is to use the Shear Box Test. In this test a sample of soil is placed inside a box. A vertical stress is provided by weights on a hanger that places load onto the lid of the apparatus so that the load can be uniformly distributed across the sample. The lid is able to move up/down freely during the test as the material dilates or contracts. The box is separated into a top half and a bottom half, one of which is driven in shear by a horizontal ram while the other is maintained stationary. The force required to move the arm is measured by a load cell. Shearing the sample is normally done very slowly so as to avoid excess pore water pressures developing during loading

(these are not able to be measured) thus the test is analysed in terms of effective stress.

Engineering shear strain is given by $\gamma = \frac{x}{h_0}$ where x is the horizontal displacement and h_0 is the initial sample height. Similarly vertical strain (or volumetric strain) is given by $\epsilon_{vol} = -\frac{y}{h_0}$ where y is the the vertical displacement due to dilation or contraction, where contraction is positive. The results of a shearbox test are conventionally plotted as stress ratio $\frac{\tau}{\sigma'}$ where τ is the shear stress and σ' the vertical effective stress, against shear strain γ. The plot of ϵ_{vol} versus γ will generally trace the same path as that which is followed by the lid of the shear box apparatus, as the test progresses.

Volume change will normally occur as the sample attempts to reach critical void ratio to continue to shear. If the particles are more densely packed than the critical void ratio, the material will dilate until it reaches that critical value and so become more loosely packed. Loose here refers to a low relative density where contraction is expected on shearing. Thus if the material is more loosely packed than the critical void ratio, the material will densify and contract to reach the critical value. From Figure 2.13 it can be seen that an initially dense sample will show an increase in shear stress with shear strain until reaching a peak stress value before falling to a steady state value. As the stress increases there is a small period of contraction before the material dilates. A loose sample however will undergo only contraction as the shear stress rises to meet the steady state. Loose samples show no peak strength (see Figure 2.13). For dense samples as the vertical effective stress is increased the peak stress ratio is reduced and so is the specific volume although the critical stress ratio is unaffected.

One Dimensional Compression

The oedometer test is commonly performed to investigate the stress-strain-time behaviour of soil in one-dimensional vertical compression. A soil sample is confined in a steel ring and placed into a water bath. A vertical load is applied and drainage of the soil sample can occur through porous stone discs placed at the top and base of the sample. The application of total vertical stress initially causes the pore water pressure to increase prior to the beginning of drainage. Over the course of the experiment, water will drain through the porous discs reducing the pore water pressure and increasing the vertical effective stress in a process termed consolidation. The vertical effective stress is only reached once consolidation of the sample has ceased and the pore water pressures have returned to equilibrium. An oedometer test will have several states of load/unload to provide multiple points of data for investigating the effective stress-strain behaviour of the sample.

Triaxial Test

A cylindrical sample of soil is placed within a thin rubber membrane and put in a triaxial cell. The sample is then subjected to isotropic pressure through water which is pressurised around

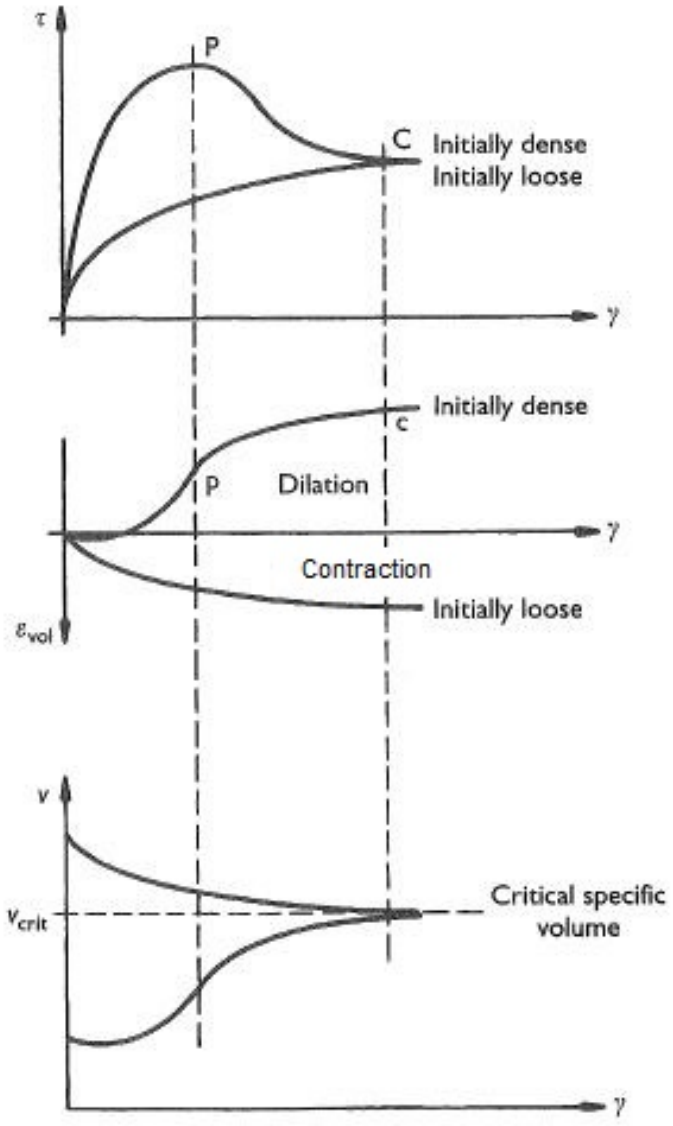

Figure 2.13: Shearbox test results as seen in Powrie (2004, Figure 2.21, pg 87)

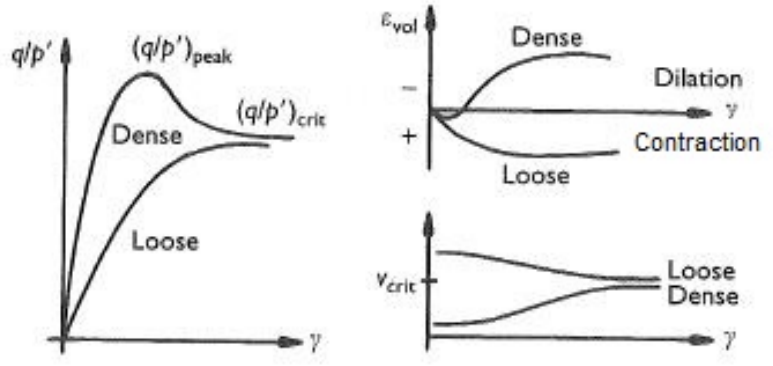

Figure 2.14: Triaxial test results as seen in Powrie (2004, Figure 5.20, pg 281)

the sample membrane. The sample is saturated then a vertical force is applied through a piston which will generally increase the vertical stress beyond that of the radial stress, thus becoming the principal stress. Drainage taps allow for water to be released from the sample under load (drained) or can be kept closed (undrained) to allow for excess pore water pressures to be developed and then measured for effective stress analysis. The mean principal effective stress p' and the deviator or distortional stress q are known as the three-dimensional stress invariants and are conventionally used to describe the behaviour of the soil sample in the triaxial test where plots of (q, p') denote the stress path of the soil with critical state line $q = Mp'$ where M is determined from the triaxial test. These invariants can be found from the measured quantities during the test:

$$\begin{aligned} p' &= \sigma_c + \frac{q}{3} - u \\ q &= \left(\frac{Q}{A_0}\right)\frac{(1-\epsilon_a)}{(1-\epsilon_{vol})} \end{aligned} \tag{2.3}$$

where σ_c is the cell pressure, u the pore pressure, Q is the ram load, A_0 is the initial cross-sectional area of the sample, ϵ_a is the axial strain and ϵ_{vol} the volumetric strain. It is important to note that the total mean stress $p = p' + u$ and therefore conventionally if the soil is dry then $u = 0$ and $p = p'$. The total mean stress p can be controlled in a triaxial test however if the material being tested is saturated, any buildup of pore pressure u will mean that $p \neq p'$.

A plot of q against ϵ_a is also commonly produced providing peak strength, critical stress and Young's Modulus (calculated from the gradient of the line to the peak strength point). The point of peak strength will normally coincide with the maximum rate of dilation.

The effect of friction in geomechanics can be measured using the three dimensional stress invariants p' and q. During a laboratory based triaxial test, the deviator stress q is measured as the ratio of loading ram force F to the cross-sectional area A of the sample and can also be calculated as the difference between axial and radial total or effective stresses. The mean effective stress is simply the average of the principal effective stresses which in a triaxial test is simply

the average of the axial and radial stresses where $\sigma'_2 = \sigma'_3 = \sigma'_r$. When q and p' are considered in respect to a cubical soil element subjected to effective normal stresses $\sigma'_{xx}, \sigma'_{yy}, \sigma'_{zz}$ and shear stresses $\tau_{yz}, \tau_{zx}, \tau_{xy}$, then the expressions for the volumetric p' and distortional stresses q for a triaxial test become (as defined by Muir Wood (1990)):

$$p' = \frac{\sigma'_{xx} + \sigma'_{yy} + \sigma'_{zz}}{3} \tag{2.4}$$

and

$$q = \left[\frac{(\sigma'_{yy} - \sigma'_{zz})^2 + (\sigma'_{zz} - \sigma'_{xx})^2 + (\sigma'_{xx} - \sigma'_{yy})^2}{2} + 3(\tau^2_{yz} + \tau^2_{zx} + \tau^2_{xy}) \right]^{\frac{1}{2}} \tag{2.5}$$

The relationship between changes in p' and changes in q is called the effective stress path where the effects of p' come from external actions on the soil. In a conventional triaxial compression test the cell pressure is maintained at a constant value and the axial load is increased so that $d\sigma'_r = 0$ and thus $dp' = \frac{1}{3}dq$ thus the stress path rises at a gradient of $\frac{1}{3}$ from the initial stress condition. If a soil contracts as it is sheared then p' must drop as q increases to keep the volume constant and if a soil dilates then p' must increase as q increases for constant volume.

The ratio of these stresses $\frac{q}{p'}$ can be plotted against the measured shear strain γ to determine the strength of the material being tested. The stress ratio $\frac{q}{p'}$ will show different values for a dense or loose sample of the same soil. A dense sample will produce a peak strength which is only maintained while the sample is dilating. The stress ratio $\frac{q}{p'}$ of a loose sample will not exhibit this peak, and will increase in value until it reaches the same value as that for the dense sample. This is called the critical value. At this critical value, the stress ratios for the dense and loose samples become constant (see Figure 2.14). At this constant state shearing can continue without any further changes in material volume or effective stresses, also known as critical state. At critical state with shearing continuing indefinitely, frictional resistance reaches its lowest value post peak.

The relationship between the stress ratio $\frac{q}{p'}$ and friction coefficient ϕ' is explained by Muir Wood (1990) as follows. Mohr Coulomb failure can be defined in terms of principal stresses which can themselves be defined in terms of p' and q. Thus Mohr Coulomb failure in terms of p' and q is:

$$\frac{q}{p' + c' cot\phi'} = \frac{6 sin\phi'}{3 - sin\phi'} \tag{2.6}$$

which in the $p' - q$ plane produces a linear relationship with gradient $M = \frac{6sin\phi'}{3-sin\phi'}$. At critical state $\frac{q}{p'} = M$ and the soil can be considered to be failing in a frictional manner.

The results of a triaxial test can be compared to that of a shearbox test as q and p' are analogous to τ and σ' respectively on the central horizontal plane in a shearbox test.

2.2.2 Fracture of Rock

As outlined in Section 2.1.2 deposits of sturzstroms generally show fractured and fragmented rock. The mechanical fluidisation theory focuses on grain collisions, and more recently the fragmentation

theory postulates the occurrence of pressure energy from explosive fragmentation events that can dilate the debris mass and cause dispersive pressures that may reduce friction. As one aim of this thesis is to determine whether fragmenting materials can in fact reduce the frictional dissipation in a sturzstrom runout, fracture and fragmentation theory are briefly introduced below for later reference.

As is commonly stated all rock is believed to contain flaws. Under a compressive, tensile or shear stress, these flaws can lead to fracture. Fracture is defined as the instance where the strength of a material is overcome and the inherent flaws have grown and created fractures or cracks. These fractures do not necessarily separate the material into pieces.

If a fractured material is placed under further stress the material may rupture, or completely fail along the pre-existing fractures produced from the initial stress. Once a material has ruptured, it will separate into fragments. These daughter fragments can then undergo loading or stress and also may fracture, and then fragment themselves. The instance where a material ruptures into multiple fragments is defined as fragmentation.

Griffith Theory

Fracture energy was originally conceived by Griffith in 1920 (Cook, 1965; Brace, 1960) who suggested that solid isotropic materials contain flaws that can grow under stress and lead to fracture. Certain flaws or cracks grow in preference to others with the highest stress occurring at the tip of the crack. SackâĂŹs (1964) extension of the Griffith theory showed that the cracks are parallel with the intermediate principal stress axis (Brace, 1960). Further modifications to this theory were made by McClintock and Walsh (Brace, 1960) who found that cracks can close and cause frictional forces as the two sides slide against one another. In compression, this modified theory coincides with Mohr-Coulomb descriptions of rock strength (Brace, 1960).

The key limitation with the Griffith theory of fracture is that it can only predict fracture initiation and cannot predict the propagation of that fracture or failure of a specimen (Hoek and Bieniawski, 1965). The fracture initiates at the tip of a pre-existing crack when the tensile stress induced exceeds the strength of the material — which is represented by the uniaxial tensile strength of the material. Hoek and Bieniawski (1965) found that a single Griffith crack will only cause a specimen to fail under uniaxial compression and that this crack will propagate parallel to the compressive stress direction. Rinehart (1966) notes that for impulsive breakage to occur, the load must reach a very high stress level in a very short period of time.

Bieniawski (1967) suggests the fracture process that a typical rock sample may follow when under compression (see Figure 2.15). Under compression, the Griffith cracks close as the sample is deformed elastically. As compression increases the cracks extend, fork and coalesce as the sample moves into plastic deformation. Ultimately one or more cracks will rupture the sample and the

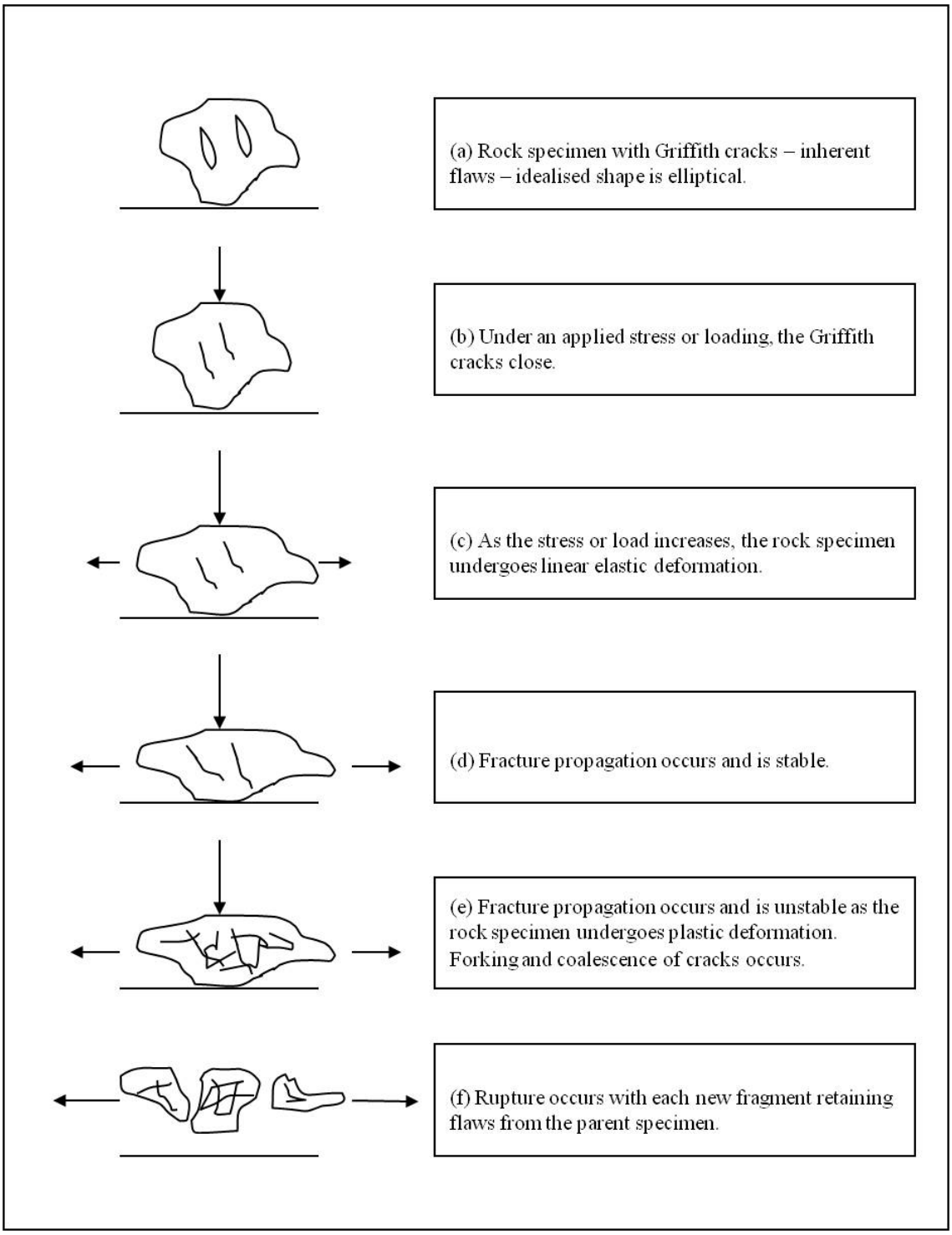

Figure 2.15: Bieniawski (1967) process of breakage under compression

daughter fragments will retain flaws from the parent.

Fracture Energy

The work done per unit area to increase the surface area of a solid is commonly called surface energy (Ruban et al., 2002). It is frequently argued that as fragmentation causes more surface area to be created, more surface energy is required and thus fragmentation is an energy sink (e.g. Hungr (2008)). The breakage or fragmentation of a rock causes energy to be expended.

Cook (1965) argues that it is important in dynamic problems to know how energy is distributed in rock during failure, especially for mining purposes. In respect of the Griffith theory, Cook suggests that elastic energy is released and surface energy absorbed as a crack extends in a material. Cook and Hodgson (1965) also state that energy is lost in the sliding process of cracks with several loading/unloading cycles occurring within the major stress-strain cycle for the rock.

McSaveney and Davies (2008) state that surface energy relates to the distribution of energy across the interface of a Griffith flaw as it is created, and that this energy is not applicable to the interface once created. They state that surface energy is in fact internal elastic strain energy that as rock fragments becomes kinetic energy (McSaveney and Davies, 2008). With a similar view Davies et al. (2012) state that breakage is not an energy sink as it creates both micro-seismic energy and a new surface. Fragmentation events cycle energy from kinetic to elastic strain via localised energy waves as rock clasts or grains break. The majority of the kinetic energy formed from breakage is expected to be transferred to the sub-fragments (Davies et al., 2007).

Meyer (1994) suggests that a very small portion of total energy is available for surface energy dissipation. A total of 15% of kinetic energy is used for "useful work" (Meyer, 1994, pg 555) of fragmentation and dispersion. Thornton et al. (1996) finds that the semi-brittle fracture of agglomerates in numerical models show a net loss of 65% of kinetic energy once steady state is reached. In numerical tests by Thornton et al. (1998) agglomerates that were shattered produced a greater steady state level of kinetic energy than for the agglomerates that were simply fractured. Therefore the agglomerates from Thornton et al. (1998) require sufficient impact forces to shatter and increase the level of kinetic energy in the system.

Fast Fracture

As noted by Ashby and Jones (2012) the critical condition for the onset of fast fracture is:

$$\sigma\sqrt{\pi a} = \sqrt{EG_c} \tag{2.7}$$

where σ is the applied stress, a is the crack length, G_c is the toughness of the material and E is Young's modulus. Fast fracture is defined as the point where a material containing a crack is sufficiently stressed that the crack becomes unstable and grows at up to the speed of sound to cause

catastrophic failure (Ashby and Jones, 2012). The material toughness represents the amount of energy required to create a unit area of crack, where a high value indicates difficulty for a crack to propagate within the material. So from Equation 2.7 it can be seen that the critical combination of stress and crack length where fast fracture will occur is reliant on material constants (Ashby and Jones, 2012). This equation is often written as $K = K_c$ (Ashby and Jones, 2012) where fast fracture will occur when the stress intensity factor K is equal to the fracture toughness K_c, where $K_c = \sqrt{EG_c}$. Thus the fracture toughness is reliant on the toughness of the material and the material elasticity. Typically the toughness G_c of rock is $O(10^{-2})$ to $O(10^{-1})kJm^{-2}$ with a fracture toughness K_c of 0.5-2 $\mathrm{MNm}^{-3/2}$ (Ashby and Jones, 2012).

Close to the tip of a crack, stress values will reach the yield stress of the material and plastic flow will occur. Ashby and Jones (2012) state that with a material such as metal that has multiple inclusions, plastic flow will occur around the inclusions creating elongated cavities that eventually join together to form a ductile tear. This process consumes a large amount of energy and leaves a very rough surface along the failure plane. In rock, cracks propagate via a cleavage process where the interatomic bonds break apart as the local stress at the crack tip exceeds the material strength; this is a process characterising brittle failure (Ashby and Jones, 2012). This results in a fairly flat surface and uses much less energy than that required for ductile tearing.

The tensile strength of a material that contains a longest crack of $2a_m$ can be calculated from the fast fracture criterion:

$$\sigma_{tensile} \approx \frac{K_c}{\sqrt{\pi a_m}} \tag{2.8}$$

The tensile strength of rock is generally around 0.2-10$\mathrm{MN/m}^2$ (Ashby and Jones, 2012). Brittle materials such as rock show a variation in tensile strength as one sample of material may have larger flaws than another. A larger sample will also generally fail at a lower stress than a small sample because there is a higher likelihood of the larger sample containing a larger flaw. Mars Ivars et al. (2011) note that brittleness in rock is not a material property but relies on the stress path the material follows before and after failure. An increase in confining stress will increase the peak strength, as this will suppress the growth of microcracks, thus the rock may behave in a more ductile fashion.

Material Class

The post stress-strain peak behaviour of rock provides distinct differences between two types of material classified as Class I and Class II by Wawersik and Fairhurst (1970). Class I behaviour is considered as the stable propagation of fractures where further work is required to reduce the strength of the material. These materials continue to retain some strength after the peak strength is surpassed. Class II materials instead show an apparent self-sustaining behaviour where the

elastic strain energy stored in the material is able to maintain fracture propagation past the peak strength until the material has lost almost all strength. Wawersik and Fairhurst (1970) notes that Class I and II rocks can potentially exhibit either behaviour under lower or higher strain rates. Fracture in Class II rocks can be arrested by removing elastic strain energy from the material for example by introducing confinement.

It has been noted by Hudson et al (1972) that non-uniform failure due to unequal loading is likely to cause failure localisation leading to Class II behaviour. Work by He et al. (1990) suggests that Class II behaviour occurs when the failure localisation is severe. They also found that if the non-elastic strain increases faster than the elastic strain decreases then Class I behaviour occurs and Class II behaviour occurs for the opposite situation. Further, He et al. (1990) note that rock showing Class II behaviour under uniaxial compression can show Class I behaviour under certain confining pressures.

2.2.3 Fragmentation

Shockey et al. (1974) claim from their experimental work that the behaviour of fragmenting rock can be predicted using measurable rock properties. They agree with the interpretation of fragmentation by Bieniawski (1967) as outlined in Figure 2.15, noting that large cracks produce large fragments, small cracks produce small fragments, and not all cracks are effective in producing a fragment. If a rock specimen is loaded such that inertial effects are negligible, then the critical crack (the crack most likely to propagate the fastest and cause fracture is generally the largest) extends very quickly in comparison to the time taken to apply the load (Lundberg, 1976). Dynamic loading however, activates large numbers of flaws almost simultaneously, to cause multiple crack growth and fractures in rock (Kipp et al., 1980).

Cracking of any element in a system causes stress to be redistributed to neighbouring elements where cracks may also occur (Sandhu and Huang, 1975). If a load is applied slowly, the cracks that are active at low stress levels coalesce and cause material failure before the load is high enough to activate other flaws, generally resulting in large fragments (Grady and Kipp, 1987). Conversely if the load is instead applied quickly, a high level of stress is achieved before the flaws coalesce so that more flaws participate and the resulting fragments are smaller (Grady and Kipp, 1987).

Inertia

One-dimensional tensile fracture of brittle bodies is shown by Passman et al. (1980) to be dependent on the inertia of the microstructure. The model built by Passman et al. (1980) utilises a balance law (relating damage to forces and crack inertia) for crack growth and is used to model fast one-dimensional deformation in rock that is elastic until the point of fracture. Damage growth under step-wise loading is controlled by two values that are determined from material properties. One of

these values specifies the intensity (or rate at which power is transferred) of the tensile load and this value was found to be the most crucial for determining the influence of inertia. The results from Passman et al. (1980) are further supported by Kipp et al. (1980) who note that in high strain rate regimes inertia may have a large influence on the behaviour of material that contains flaws due to dynamic stress wave propagation.

Strain Rate Effects

If brittle materials are subjected to rapid compressive loading the resulting peak strength is higher than that of the static strength, which suggests an apparent strain rate effect (Janach, 1976). Increasing the compressive load leads to greater breakage and separation of the fragments. Janach (1976) states that the separation of the fragments leads to dilation of the material or bulking and that inertial forces become important as the fragments move away from one another.

From a series of triaxial tests on various rock types, Donath and Fruth (1971) found that the fabric of rock is important in its response to varying strain rates. Rocks deforming through intergranular slip and recrystallisation were found to be affected by large changes in strain rate as opposed to rocks that deform through fracturing where there was little effect from changes in strain rate. Donath and Fruth (1971) found that the strength of marble and limestone, both ductile materials, can decrease or increase with decreasing strain rate depending on the strain hardening response of the material. For ductile rocks, the rate effects are more pronounced and the effects become greater with increasing confining pressure (Lajtai et al., 1991). Moderately ductile and brittle materials were found to fail by fracturing under low confining pressure and uniform flow under high confining pressures with a clear increase in strength under high strain rates. At high strain rates, Donath and Fruth (1971) found that intergranular deformation cannot take place fast enough resulting in a higher yield stress.

Kipp et al. (1980) define fracture stress as the stress at which fracture occurs and find that there is a strain-rate dependency. The static fracture stress of some rock, such as oil shale, shows an order of magnitude increase in strength from static loading to high strain rate. During dynamic loading the fracture stress becomes independent of the crack size as shown in Figure 2.16 (Kipp et al., 1980). Kipp et al. (1980) note that this insensitivity of fracture stress to flaw size in a constant-loading situation suggests that the inherent flaws in the material are responsible for the strain-rate dependent fracture stress.

In early work, Grady et al. (1977) states that under dynamic loading of dolomite significant shear overstress occurs, which effectively prohibits fracture as a mechanism of failure. Brittle fracture under quasi-static strain rates may revert to intracrystalline plasticity under dynamic loads with the dynamic stress path ultimately controlled by the strength of the internal structure of the material. This is further explained by Grady (1998), who states that stress levels consistent

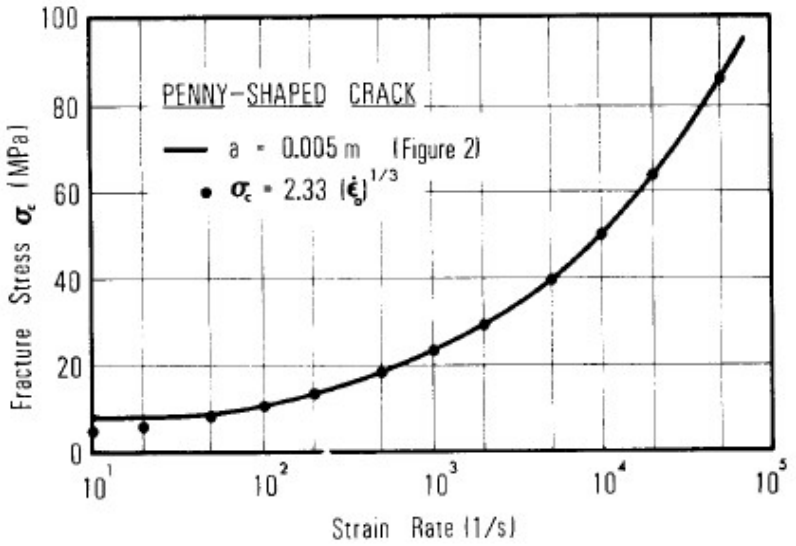

Figure 2.16: Strain rate dependent fracture response of an elastic solid containing a crack from Kipp et al. (1980, Figure 3, pg 475).

with the yield strength of material can be reached with negligible fracture damage under very high strain rates. **?** goes on to suggest that there is a “strain-rate dependent brittle-to-ductile transition" where kinetics control the failure of material under low strain rates transitioning to a “rate-insensitive" failure process under high strain rates.

Zhang and Zhao (2014) present a graph, shown in Figure 2.17, containing the normalised UCS versus strain rate from data obtained from decades of research. The figure shows an increase in the UCS of rock materials under dynamic loading. However, Zhang and Zhao (2014) note that there is not an agreed strain rate at which this increase in strength becomes significant. Zhang and Zhao (2014) therefore divide their figure based on loading techniques and specimen sizes, both of which influence the UCS. Region I corresponds to quasi-static tests with a maximum strain rate of 10 s^{-1}, and here the normalised UCS increases linearly with strain rate. Outside of this region the normalised UCS increases very quickly with strain rate.

Dynamic Fragmentation

Dynamic fragmentation or an extreme energy fragmentation event is defined by Grady (1982) as any intense impulsive process that partitions a body of material into discrete domains. Dynamic fragmentation of a material can occur due to a rapid deposition of energy through contact forces from a dynamic tensile stress (Grady, 1981). Impact or explosive induced fragmentation is of great interest to numerous rock breakage applications including oil recovery from oil shale, deep drilling, quarrying and mining. Fragmentation is also suggested as a basic process in cliff erosion by ocean waves, volcanic eruptions and even the impact of a rain-drop (Grady, 1981).

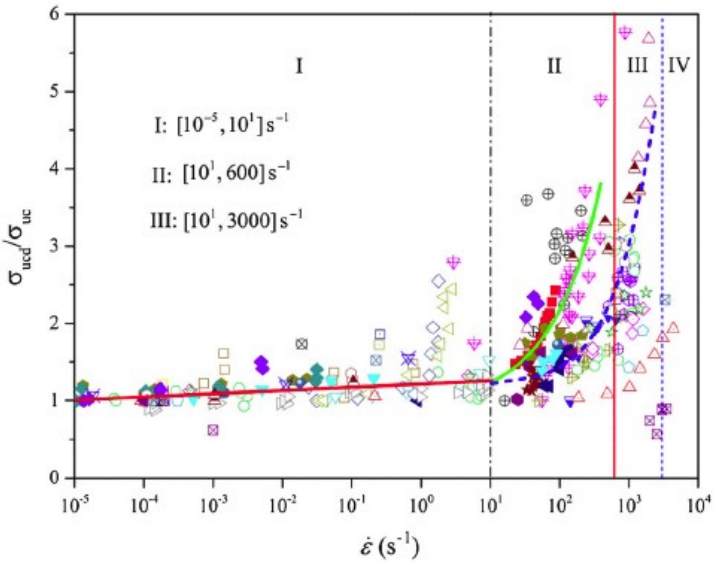

Figure 2.17: Normalised UCS versus strain rate for an assortment of rock materials from Zhang and Zhao (2014, Figure 26, pg 1442). (Refer to legend in original paper for rock types.)

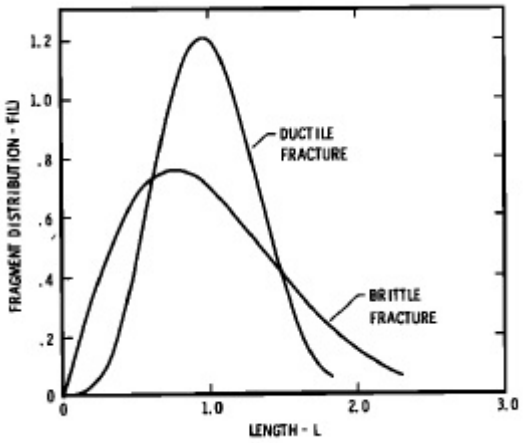

Figure 2.18: Example brittle and ductile fracture curves from the method of Grady (1981, Figure 7, pg 1051).

Initiation

Following the statistical work of Mott in 1947, Grady (1981) introduces survival statistics (a time-varying Poisson process) to investigate fracture initiation. Mott's theory as applied to a cylinder of material, suggests that there is a distribution of fracture-producing flaws surrounding the cylinder and that once a fracture has been initiated, stress relief will occur as release waves that travel away from the fracture point (Grady, 1981). The release waves stop any further fracture from occurring in the area where they propagate, with fragmentation complete once the release waves

propagate around the entire cylinder (Grady and Olsen, 2003). The propagation of these plastic release waves is combined with the randomness of the fracture process to form the 'Mott method' and is used to predict fragment size and distribution. Grady (1981) notes that the activation of flaws during tensile loading will depend on strain rate, thus activation is coupled directly with the loading conditions. The modified Mott method described by Grady (1981) provides a better match to fragmentation data of impulse loaded aluminium rings than is shown by the original Mott method and Grady (1981) notes that this is likely explained by the use of a different nucleation law.

The application of the Grady (1981) method provides very different solutions for brittle or ductile fracture. In particular the brittle fracture curve (see Figure 2.18) is skewed toward finer fragment sizes and the ductile fracture curve shows a Gaussian normal distribution shape. Grady (1981) also shows that shock loading of a material is more catastrophic than constant strain rate loading and produces finer particles and smaller fragments.

Kinetic Energy

Grady (1982) discusses the energy within an expanding fluid as an analogy to that of a brittle solid. He notes that kinetic energy is associated with fracturing forces and surface tension resists fragmentation. The production of fragment surface area is not governed solely by a balance of kinetic energy and surface energy, since a large proportion of kinetic energy remains after fragmentation (Grady, 1982). Grady (1982) introduces surface energy as providing a resistive "force" against fragmentation (to balance forces caused by kinetic energy). Surface energy however, appears to be more an energy related to surface tension due to the strength of the material. As a brittle solid is loaded in tension, elastic energy is stored, however as the fragmentation of the solid becomes more catastrophic the elastic contribution becomes negligible and Grady (1982) finds a nominal fragment diameter of:

$$d = \left(\frac{\sqrt{20} K_{1c}}{\rho c \dot{\epsilon}} \right)^{\frac{2}{3}} \tag{2.9}$$

where K_{1c} is the fracture toughness of the material, ρ is the material density, $\dot{\epsilon}$ is the linear strain rate and c is the elastic wave velocity. When an equation of this form was applied to the fracture of oil shale, the resulting relationship was found to compare well to data from experiments with the experimental models showing a decrease in the size of fragments with the increase of strain rate (Grady, 1982). Grady (1982) also tested Equation 2.9 against explosive fragmentation experiments on steel tubes and found that the equation was also consistent for this data where larger fragment size occurred for higher fracture toughness of the initial material.

Kipp and Grady (1985) draw from the earlier works of Grady (1981), Grady (1982), Kipp and Grady (1978), and Kipp et al. (1980) and restate that solids subjected to dynamic loading will

undergo divergent particle movement pulling the material into tension. These solids fail internally through the initiation, growth and coalescence of a distribution of flaws whose growth is also influenced by the available driving energy. Numerical testing based on the Mott theory for single one-dimensional fractures by Kipp and Grady (1978) indicates that stress transferred in the form of sound waves between fractures, based on the position of the fractures in the material, is at a much slower rate than that of the speed of sound. Thus, Kipp and Grady (1985) state that multiple fractures can nucleate and grow within a smaller area than had been previously thought due to the slow movement of the sound waves between fractures when compared with the speed of sound.

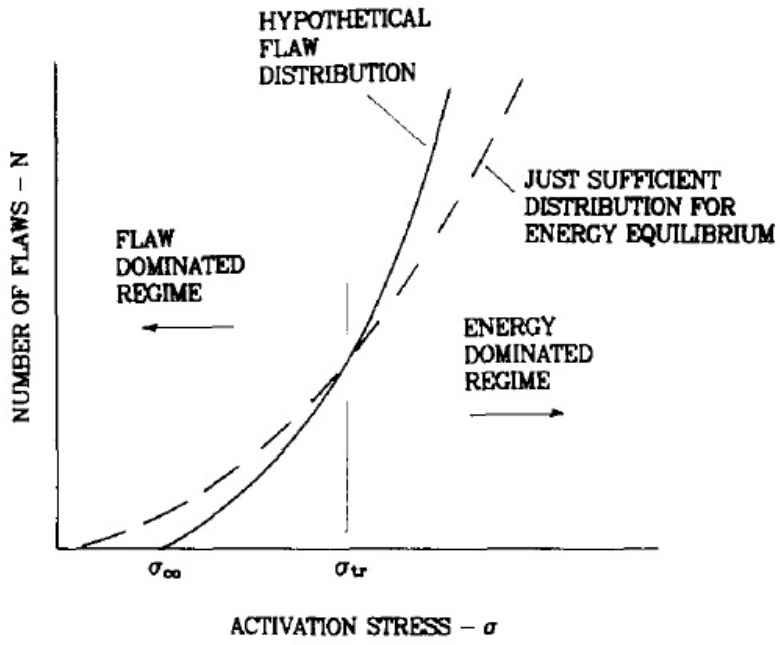

Figure 2.19: Flaw and energy dominated regimes in fragmentation from Grady and Kipp (1985, Figure 6, pg 317).

Inherent flaw growth is one concept advanced to describe the fragment size distribution from a dynamic fragmentation event. Grady and Kipp (1985) state that this concept ignores energy being consumed during the growth of the flaws. They indicate that this additional energy must come from the applied load and that there must be limitations on how many fractures are created or the amount of new area of fracture surface in order for energy balance principles to apply. The kinetic energy induced in a material by a dynamic load is considered by Grady and Kipp (1985) to be the fuelling energy for the fracture process especially in catastrophic fragmentation events. A body rapidly expanding after being compressed will have kinetic energy associated with the outward expansion that will be responsible for fracturing forces while surface tensions will resist further fracture. After fragmentation particles will continue to fly apart at high velocities and thus

a large amount of kinetic energy will still be available (Grady and Kipp, 1985). Following the work of Grady (1982), Grady and Kipp (1985) suggest from Equation 2.9 that:

$$E_{fr} = \frac{K_{1c}^2}{2\rho c \dot{\epsilon}} \tag{2.10}$$

actually represents fracture energy. Grady and Kipp (1985) suggest that there is a boundary between flaw activation and energy balance, treating each as a separate regime. Figure 2.19 suggests that for low to moderate tensile loading rates, the fragment size is flaw dominated and for high tensile loading rates the fragment size is controlled by energy equilibrium behaviour (Grady and Kipp, 1985). In both cases, flaws and energy play an important role and are interrelated (Grady and Kipp, 1985). A more complete discussion of the combined dynamic fragmentation research work produced by Grady and Kipp is provided in Grady and Kipp (1987).

Force Chains

Grains forming quasi-linear columns in the direction of maximum compression are called force chains or grain bridges (Davies et al., 2007; Dufresne et al., 2010). Force chains are considered to be a transient behaviour within granular flows as they form and fail continuously (McSaveney, 2015; De Blasio, 2011). Chains can fail through buckling or fragmentation, resulting in a shortening of the force chain and/or transfer of the stress to surrounding grains to build new force chains. Davies et al. (2007) note that under low confining pressure, less than the compressive strength of the grains, force chains are likely to buckle before grains are crushed whereas under high confining pressures force chains will fail due to crushing. Grain breakage is more likely to occur in a force chain due to the higher than average level of stress felt by these grains and thus dynamic processes are more important for the process of breakage (De Blasio, 2011).

2.2.4 Summary of Material Testing and Behaviour

Key conventional laboratory tests are outlined in this section as the same tests are used during the numerical modelling that is undertaken throughout this thesis. Theory around the fracture and fragmentation of rock, failure onset through an existing flaw, fast fracture and relevance of the material class, is outlined to prepare the reader for discussions comparing the numerical results to those in the literature. In particular, the work of Grady and Kipp (largely summarised in Grady and Kipp (1987)) regarding dynamic fragmentation in rock, is highlighted for its importance in relation to the work undertaken in this thesis. Brief discussions on the stress-strain behaviour of materials and kinetic energy response under dynamic fragmentation are included to outline some key details for comparison to the numerical modelling results of this thesis.

Fracture and Fragmentation in Sturzstroms

The theory of fragmentation in sturzstroms relies on the change of a falling mass into a collisional shearing mass where loading and confinement cause the material to fragment explosively forcing fines between the surrounding materials and reducing effective stress. Key to this theory is fragmentation and conditions in which this can become explosive, along with the distribution of energy due to fragmentation.

As outlined in the prior sections the key theoretical concepts important for investigating fragmentation in sturzstroms are:

- dynamic fragmentation is an intense impulsive process that can occur due to a rapid deposition of energy through contact forces
- fast loading of rock specimens causes critical cracks to extend quickly in comparison to the time taken to apply the load – strain-rate dependency and activation are coupled directly with the loading conditions
- fast loading causes a high stress state to be achieved before flaws coalesce so that more flaws participate in the failure of the material – fragments are smaller
- shock loading of material is more catastrophic than constant strain rate loading – produces smaller fragments and finer particles
- solids subjected to dynamic loading undergo divergent particle movement pulling the material into tension – once fragmentation occurs fragments move away from the parent specimen at high velocities
- kinetic energy induced in a material by a dynamic load is the fueling energy for catastrophic fragmentation events – as rock fragments, the internal elastic strain energy becomes kinetic energy, forcing fragments apart
- significant amounts of kinetic energy are available after fragmentation to move material within the system
- flaws and energy play an important role and are interrelated.

2.3 Continuum and Physical Models of Sturzstroms

For the purposes of this thesis, DEM is the model of choice for investigating the micromechanics of a sturzstrom (as outlined in Section 2.4), other models are utilised in the literature for modelling sturzstroms. In particular, continuum models based on the shallow-water equations and physical models using rock analogues in centrifuge experiments have been used in sturzstrom research. These research applications are outlined below for completeness.

2.3.1 Continuum Models

Continuum modelling of landslide and rock avalanche debris began in earnest after the published work of Savage and Hutter (1989). The Savage-Hutter equations for granular flow down an incline begin with the Navier-Stokes equation. The material is considered to flow along a smooth, slowly changing, base with an upper free surface flow and is regarded as an incompressible continuum of small depth. This follows the typical shallow-water or St Venant equation assumptions. The basal area of the flow is regarded as the active zone, with the depth-averaged velocity close to the actual velocity everywhere except at the very base. This basal area though is assumed to be very thin so that it is accurate to use the depth-averaged velocity for the model computations. The governing equations are thus:

$$\begin{aligned} \nabla \cdot \mathbf{u} &= 0 \\ \rho \frac{d\mathbf{u}}{dt} &= -\nabla \cdot \mathbf{p} + \rho \mathbf{g} \end{aligned} \tag{2.11}$$

where $\mathbf{u}$ is the velocity vector, ρ constant density, $\mathbf{p}$ the pressure tensor and $\mathbf{g}$ gravitational acceleration. Boundary conditions are introduced such that the upper free surface is stress-free and is part of the overall material, and that the basal boundary experiences tangential flow and is influenced by Mohr-Coulomb friction. Savage and Hutter (1989) non-dimensionalise the 2D equations and consider the system under shallow water conditions. They find that the y-momentum equation reduces to the hydrostatic equilibrium equation.

Although direct mathematical solutions can be found for the Savage-Hutter equations (see for example Chugunov et al. (2008)), more commonly the equations are solved using numerical methods. Savage and Hutter (1989) deem a Lagrangian numerical scheme as the most appropriate for solving the system of equations from (2.11) after having attempted a Eulerian approach.

Iverson (1997) describes the behaviour of debris flow phenomenon as sediments that are saturated and agitated as they travel downslope which leads to his application of continuum mixture theory as a model for debris flows by following the process outlined by Savage and Hutter (1989). Analytical solutions can be found for the system when particular dynamic variables are omitted without the loss of physical relevance. Overall, the simplifications lead to a system of equations that differ from that of Savage and Hutter (1989) only by the introduction of fluid stresses.

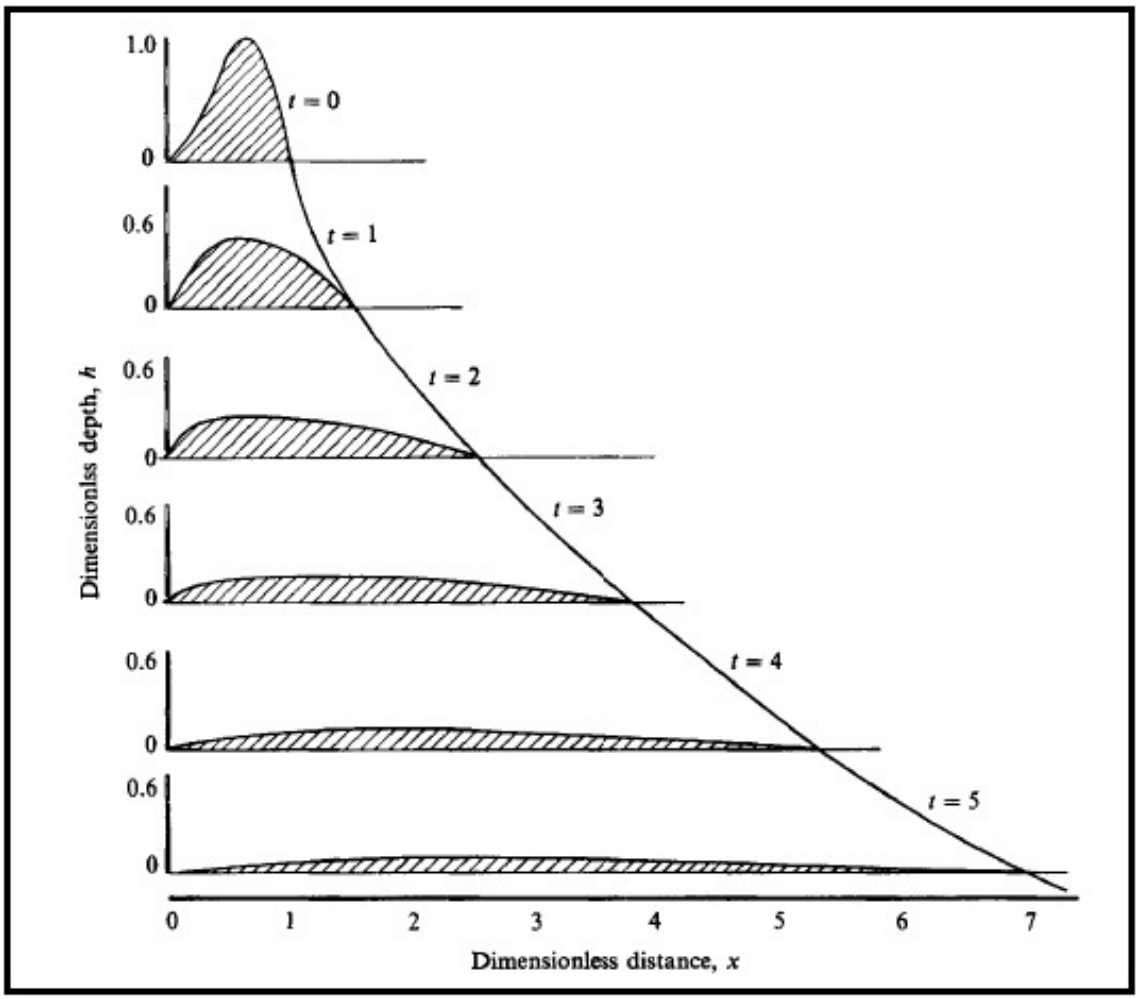

Figure 2.20: The Lagrangian numerical solution for the displacement and height of the Savage-Hutter equations as solved by Savage and Hutter (1989, Figure 13, pg 210) using data from granular flow laboratory experiments.

An hypothesis suggested by Iverson and Denlinger (2001) is that variations in flow behaviour from dry rock avalanches through to saturated debris flows occurs due to varying effects from pore fluid, topography and inertia. The model presented by Iverson (1997) is generalised for variable fluid components where a high fluid pressure may represent a viscous flood and a vanishingly small fluid stress may represent a rock avalanche. Pore pressure effects are incorporated into the model using Terzhagi's effective stress principle (Iverson and Denlinger, 2001). Iverson and Denlinger (2001) note that mixture theory equations are advantageous as they explicitly separate the solid and fluid constituents along with their influence on flow dynamics and remove the need for determining a relevant material rheology.

The hyperbolic non-linear Coulomb mixture equations from Iverson and Denlinger (2001) are tested for numerical solution and applicability to laboratory tests by Denlinger and Iverson (2001).

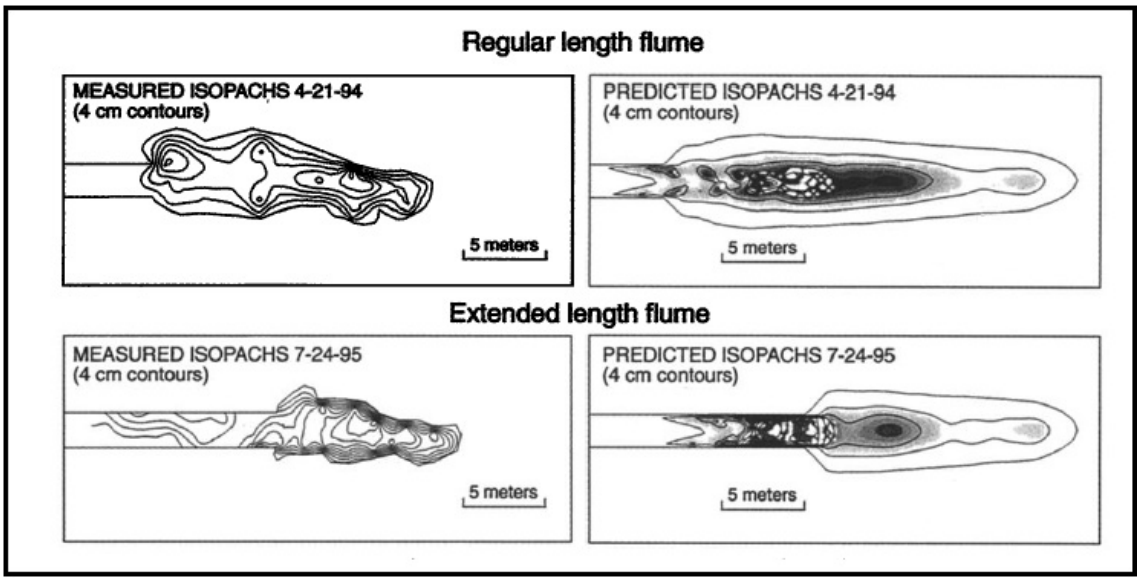

Figure 2.21: Measurements and model predictions of large scale flume debris flow experiments from Denlinger and Iverson (2001, Figure 9, pg 563).

Small granular avalanche and large debris flow experiments were performed by the authors for comparison with the model. Denlinger and Iverson (2001) find that the model predicts all flows well however it is less accurate in distal limit for large scale flows as seen in Figure 2.21. This result supports the statement by Denlinger and Iverson (2001) that it is not important to characterise rheological parameters when simulating geophysical flows.

Hungr (1995) developed the 2D model DAN (Dynamic ANalysis) to model the post failure motion of landslides and avalanches. The moving mass is replaced with an equivalent fluid with the bulk properties of the fluid set to approximate the behaviour of the mass. The material is represented as a number of blocks that contact each other and retain fixed volumes of material while descending down a vertically curving path (Hungr, 1995). The DAN model (Hungr, 1995) includes several basal rheology options such as frictional, Bingham, Voellmy and Newtonian laminar flow. Each is a function of parameters relevant to the flow which are known, and the rheology is included in the model by introducing a basal flow resistance force.

DAN3D was developed by McDougall and Hungr (2004) following from the original 2D DAN model by Hungr (1995). As with Savage and Hutter (1989), Hungr (1995) and Iverson and Denlinger (2001), McDougall and Hungr (2004) base the DAN3D model on the Lagrangian solution of the depth-averaged shallow-water equations. The principal stress axes are aligned in the direction of motion and the stress coefficients follow Savage and Hutter (1989) and are incremented at each time step when the particles are in motion. McDougall and Hungr (2004) evaluate the model against laboratory granular flow tests and back analyse the Frank slide with the model showing comparable results in run-out length, velocity and depth as indicated in Figure 2.22.

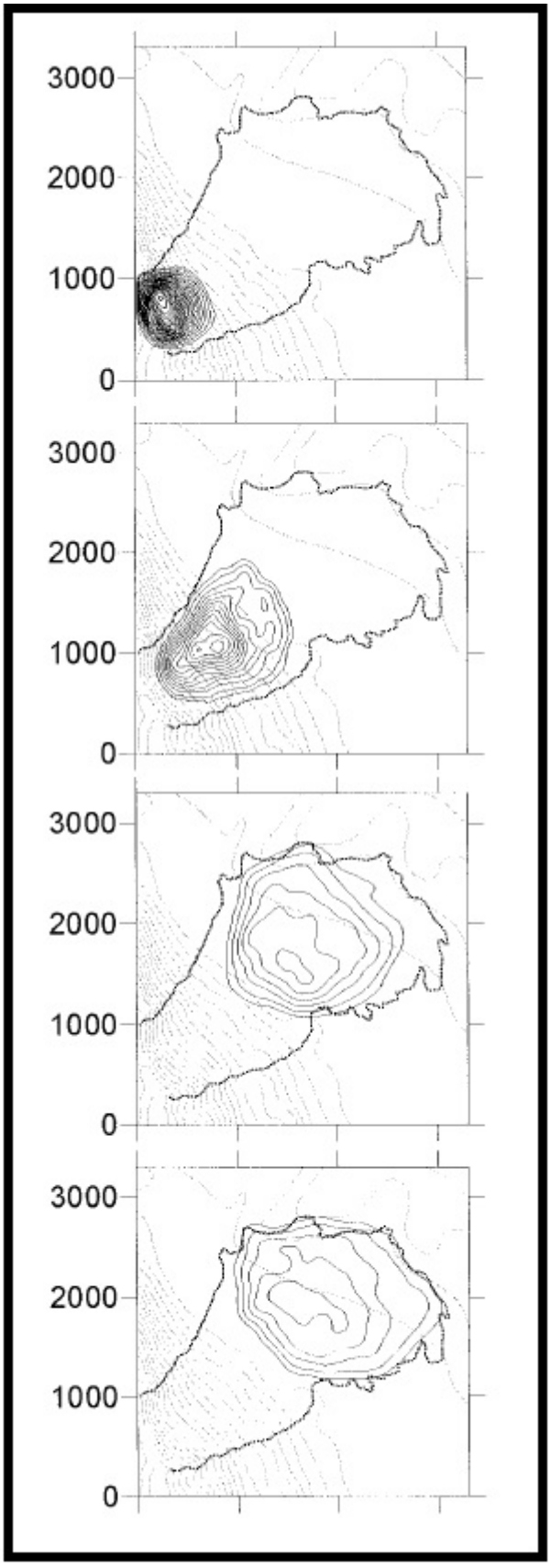

Figure 2.22: Results of the Frank Slide back analysis with DAN3D as produced by McDougall and Hungr (2004, Figure 10, pg 1095).

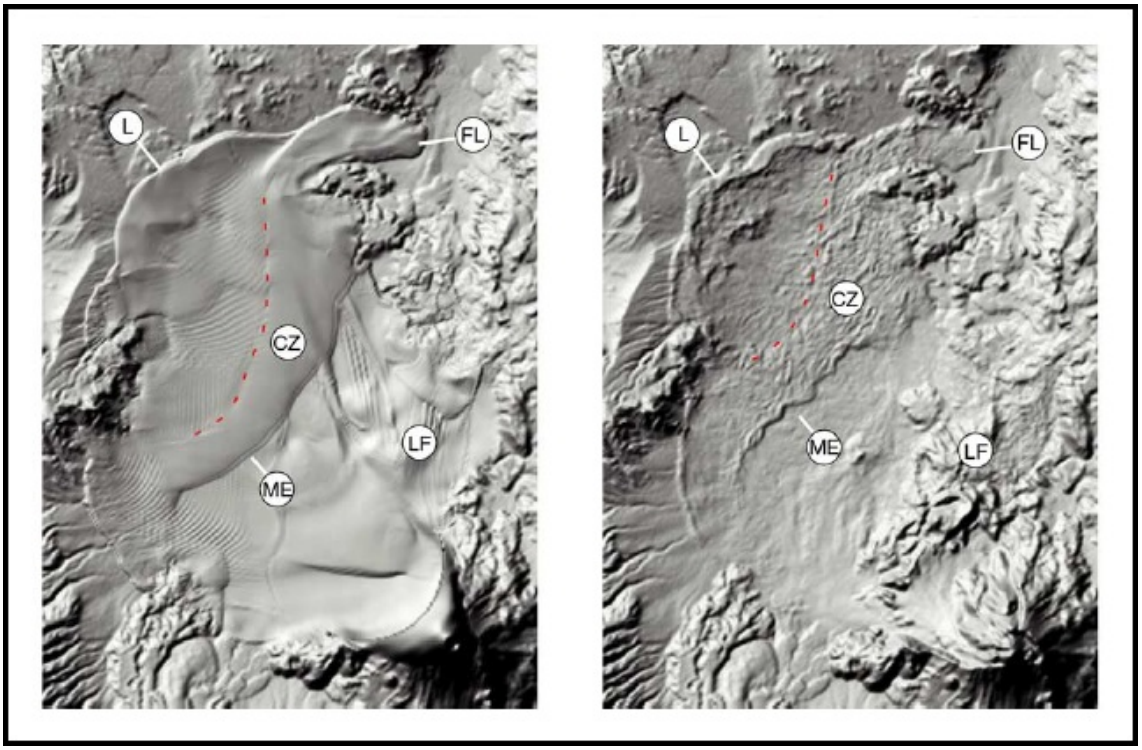

Figure 2.23: Socompa rock avalanche modelling by Kelfoun and Druitt (2005, Figure 8, pg 9).

Kelfoun and Druitt (2005) follow the shallow-water premise to derive their topography linked 3D model which is used to investigate the Socompa rock avalanche. The code was validated via application to granular flow laboratory experiments performed by other researchers (Savage and Hutter, 1991; Gray et al., 2003) and found to compare well. Field evidence is used to recreate the starting situation at Socompa with an estimation for the initial collapse volume due to uncertainty regarding the shape of the avalanche headwall scarp as it was buried during the event. The aim of the modelling by Kelfoun and Druitt (2005) was to produce a numerical model that could reasonably represent the resulting deposit from the Socompa failure including distinctive features like escarpments and lobes. They find that frictional rheology alone does not reproduce the deposit characteristics at Socompa correctly, although it does adequately represent the run-out. The introduction of a constant retarding stress of order 50-100 kPa was found to better fit the Socompa deposit characteristics, thicknesses and run-out as shown in Figure 2.23, although Kelfoun and Druitt (2005) state this is not necessarily an accurate rheology for the avalanche as the constraints on the starting conditions are crude.

2.3.2 Physical Models

As sturzstroms are rare, there is often little data available to correctly back calculate numerical variables for discrete and continuum modelling. One approach that is often utilised to improve the

understanding of rock avalanche physics and mechanics is that of small-scale physical modelling in centrifuge apparatus or in flume experiments. Manzella and Labiouse (2008) state that physical modelling advantages include the ability to control test conditions and parameters along with the repeatability of the experiments while varying particular parameters.

Manzella (2008) conducted physical experiments with sand, gravel and blocks to investigate rock avalanche propagation. The material was released from a box to travel down an inclined panel toward a sharp transition with a horizontal panel. Once the runout had completed the deposit characteristics were measured. The apparatus allowed Manzella (2008) to vary slope angle, release height and shape, material volume and to test flow behaviour with consecutive material releases. As with most experiments of this nature, Manzella (2008) made use of technology to capture the material behaviour with high speed cameras and projected topographical lines onto the deposit area for computational rendering of phase maps and determination of deposit measurements. Several series of tests were performed and Manzella (2008) and Manzella and Labiouse (2008) note in their results that the gravel tests were more representative of large scale sturzstrom. The gravel tests specifically showed that the volume of failure material appears to influence the final part of the gravel slide as this rear material pushes the front part of the deposit and transfers momentum (Manzella and Labiouse, 2008). Manzella and Labiouse (2008) noted that consecutive releases of material did not cause an extension of runout and the initial release of material determined the extent of the deposit runout.

Piled blocks were also utilised as a material by Manzella and Labiouse (2009) with random piling and ordered stacking tested separately. Tests with a higher fall height and steeper angle of inclination showed an increased runout. Ordered stacking of blocks produced a greater runout and appeared to model a rock mass with multiple discontinuities. At the transition point the blocks shattered and collided with one another producing a different flow behaviour and deposit to those of gravel and random piling of blocks. Manzella and Labiouse (2009) state that the increased runout with orderly stacked blocks could be due to the energy being retained while sliding and thus a higher velocity being maintained until the material reached the horizontal panel.

Geotechnical centrifuge experiments to reproduce fragmentation in a sturzstrom situation were performed by Imre et al. (2010). The ETH analogue rock material (ETHAR) is designed to scale the strength of rock material such that centrifuge experiments of landslides and rock avalanches can investigate fragmentation. ETHAR was utilised in cube form and blocks layered into the hopper for release into the centrifuge (Imre et al., 2010). The analogue rock masses were found to slide virtually as one block before undergoing simple shear deformation with all except the top layer of blocks experiencing intense fragmentation. However, Imre et al. (2010) claims that overburden pressure in the z-direction was found to be unimportant in the fragmentation process. The material was found to fragment in a fractal way such that particles of similar size were never

found in contact (Imre et al., 2010).

Cagnoli and Romano (2010) released dry angular volcanic rock fragments down a metallic ramp to a marble chute both of which had a trapezoidal shaped cross-section to reduce the edge effects commonly seen in laboratory tests with rectangular cross-sections. The only difference between the series of experiments was grain size where the finer grain sizes showed greater mobility and the associated overall flow involved less agitation from boundary contact due to the greater number of particles. Cagnoli and Romano (2010) suggest that this reduction in agitation would cause less dissipation of energy and thus allow a flow to travel further.

Small scale physical models to investigate the link between the length of sturzstrom runout and quantity of rock fragmentation were produced by Bowman et al. (2012). One impact or breakage step was modelled by a coal analogue travelling down a rough incline to a horizontal plane within a geotechnical centrifuge. Granular or crushed coal and regular or irregular arrangements of coal blocks were tested under centrifuge conditions with the initial arrangement and size of material found to influence the runout distance and quantity of fragmentation in the debris. The generation of an impulse velocity when the material fragmented at the base of the fall appeared to be the main influence on additional runout or spread of the debris. In particular, Bowman et al. (2012) note that even after the removal of Coriolis effects from the data (see Rait et al. (2011)) that there still exists a linear relationship between runout and degree of fragmentation as defined by Hardin's relative breakage B_r (Hardin, 1985).

2.3.3 Summary of Continuum and Physical Modelling

Continuum models following the Savage-Hutter equations have been frequently used to model granular avalanching. Improvements on this model include those from Iverson and Denlinger (2001), Hungr (1995) and McDougall and Hungr (2004) which allow for variations in rheology, inclusion of entrainment and three dimensional modelling. Continuum models are typically run to back analyse a landslide or rock avalanche failure and generally model the macroscale behaviour only. As this thesis is specifically focused on the microscale behaviour, continuum modelling was discounted as a suitable method of analysis.

Physical modelling of sturzstrom runout has so far included consideration of material type and initial failure structure. Attempts to investigate fragmentation have resulted in useful results on material behaviour at the transition zone from fall to runout. Given the difficulty in producing and measuring multiple fragmentation events within a centrifuge, and equipment constraints, it was decided that physical modelling was not a suitable method for the purposes of this thesis.

2.4 Discrete Element Modelling

The behaviour of sturzstroms can be considered in two stages - the fall and the runout. Each stage of a sturzstrom should be analysed separately in order to ascertain the influence on the total overall behaviour. In order to properly understand the mechanics existing within a stuzstrom, a tool that can model the interaction between particles and groupings of particles in each stage is crucial. The two stages can be modelled using standard laboratory tests – the fall stage can be considered an oedometer test at high strain rates and the runout stage a shear box test at high shear rates.

The main motivation for utilising Discrete Element Modelling (DEM) to model the micromechanical behaviour of sturzstrom is that this form of numerical modelling allows analysis of the mechanisms that occur at small scale in large-displacement geomechanics problems (O'Sullivan, 2011). DEM models can also be used to simulate physical laboratory testing with virtual samples where all microscale behaviours can be monitored, a result that is not directly achievable with continuum or physical models. The capabilities of DEM therefore match the requirements of this thesis for investigating fragmentation in sturzstroms. This section will discuss the theory and application of DEM to micromechanical and landslide modelling with several examples of recent work to provide background to the use of this type of model.

In 1979, Cundall & Strack wrote their benchmark paper about a new discrete element model called BALL that was designed using the distinct element method which was itself first introduced by Cundall in the early 1970s to improve the analysis of rock mechanics. This new model was specifically designed for soils where Cundall and Strack (1979) note that a granular medium is built from discrete particles that are independent and interact only where they contact. DEM calculations alternate between Newton's second law applied to the discrete elements and a force-displacement law applied at the element contact points. The time step in a DEM program is chosen to be small so that disturbances cannot propagate further than a discrete element's neighbours. Thus the resultant forces on one discrete element are determined directly from its interaction with any discrete elements it is in contact with. This removes the need for an iterative procedure and excessive computational memory for data storage.

The initial input in a DEM simulation generally involves the user input of the geometry of the system including particle coordinates and boundary conditions. Material properties are input using the contact model parameters. Often these parameters are found from simulating laboratory tests on the synthetic material. Once the behaviour of the synthetic material is similar to that of the real material, the microparameters can be identified and entered into the model. The DEM program then moves through several calculations for contact forces, external forces, particle velocities and displacements, before updating the particle positions and incrementing the time step.

There are several assumptions in DEM calculations as discussed by O'Sullivan (2011):

- particles are rigid and move independently of each other
- a contact occurs over a very small area and involves only two particles – contacts are identified automatically by the program
- particles can overlap at the contact point and this is regarded as similar to the soft deformation that can occur between real particles
- particles transmit forces at the contact points
- contacts are removed once the tensile force exceeds the maximum tensile force and particles can then move away from each other
- the time step must be sufficiently small so that the motion of a particle will only influence its immediate neighbours.

2.4.1 Particle Flow Code 3D (PFC^{3D}) (Itasca, 2008)

Over the last 30 years, DEM has been coded by various authors and utilised for many soil and rock mechanics investigations (see Section 2.4.2). Cundall formed the Itasca Consulting Group in 1981 with fellow faculty members and released the first version of the commercial software PFC^{3D} in 1995. PFC^{3D} (version 4.0) is the latest in DEM software from Itasca. Throughout the remainder of this thesis PFC^{3D} is utilised for all discrete element modelling. PFC^{3D} is a soft sphere DEM approach where the discrete elements (spheres) are rigid but can overlap at the contact points (Itasca, 2008). The contact is controlled by a force-displacement law that is dependent on the contact stiffness calculated by the (user) designated contact stiffness model. The default contact stiffness models typically used in PFC^{3D} include linear (for the interaction between two elements) and Hertz (where stiffness can vary and is a function of the particle normal and shear stiffness input values).

Contact Model

The relationship between two discrete elements (or a discrete element and boundary (i.e. wall)) is determined by a contact model at each contact point (see Figure 2.24). Any two elements (or spheres) in contact will slightly overlap, with a branch vector joining both centroids. The contact point coordinates are taken at the centre of the overlap and will exist on the branch vector. Contact normals extend from the contact point toward the centre of each sphere with the contact plane at right angles to the normal vectors and also passing through the contact point. During compression the contact normal force calculated from the particle overlap will act to repulse the spheres from one another, however if there is a gap between spheres, tensile forces can draw these together unless the limiting tensile force is exceeded. The limiting tensile force is typically set to zero in

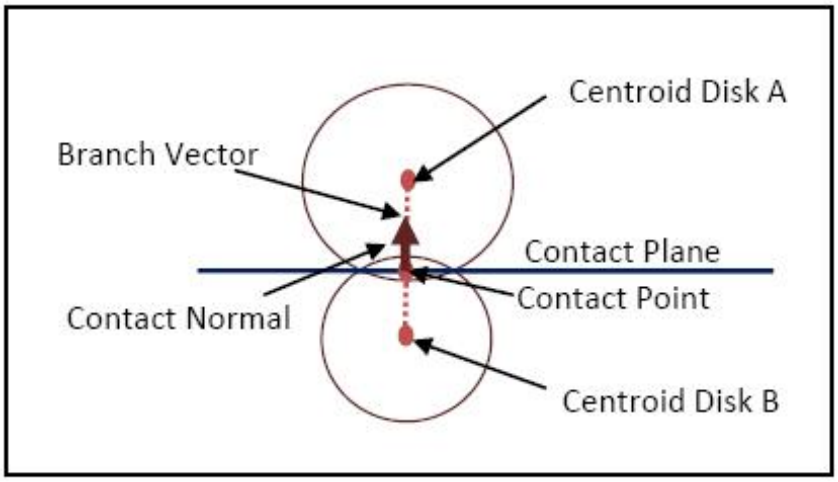

Figure 2.24: The contact model in 2D DEM after O'Sullivan (2011) also equivalent to a slice through a contact in 3D

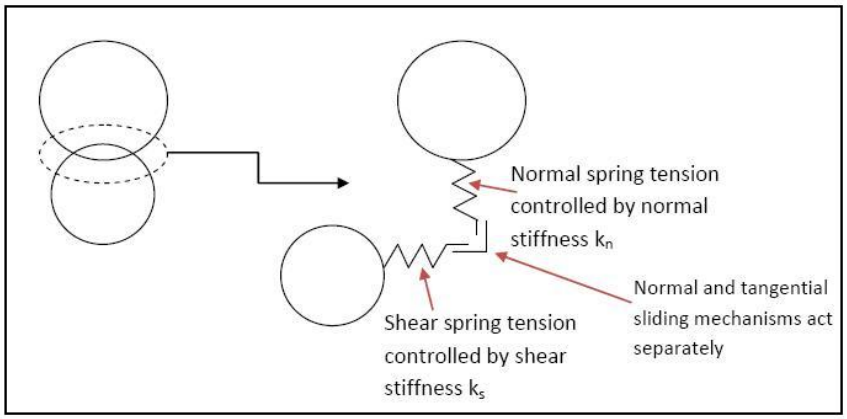

Figure 2.25: The linear contact model in DEM after O'Sullivan (2011)

geomechanics thus tensile forces cannot influence elements that are unbonded. The contact model can be thought of as a spring based at the contact point. Tangential forces induce rotation and translation on the sphere.

This contact model can be joined by two other components between the elements – a bond and a dashpot. A dashpot occurs when viscous damping is installed in the model. Viscous damping introduces a normal and shear dashpot at each contact which act parallel to the contact model and is described as *mass proportional damping* which may introduce body forces (Itasca, 2008). Conversely, local damping applies a damping force directly to the discrete element via the addition of a damping term to the equations of motion, thus only the accelerating motion is damped. Generally speaking, O'Sullivan (2011) suggests keeping the damping values low so as to provide a small reduction in any unreal physical response of the chosen contact model due to the spring behaviour.

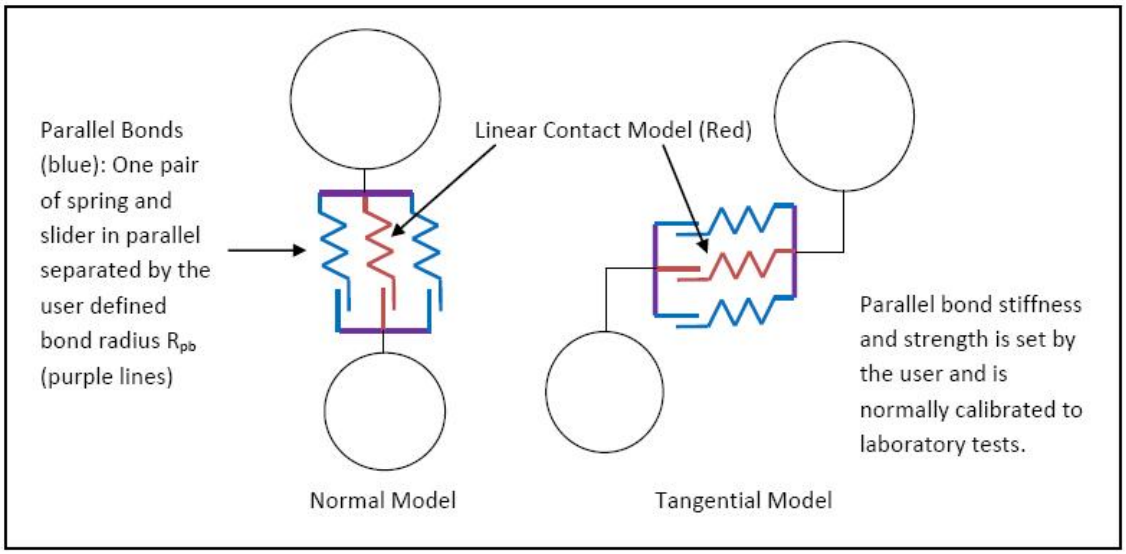

Figure 2.26: The parallel bond logic after O'Sullivan (2011). A slice through the centre of the contact point between two spheres.

The linear contact model includes component behaviour for stiffness, slip and bonding between discrete elements (see Figure 2.25). Contact stiffnesses relate contact forces in the normal and shear direction to their relative displacements and also directly control the overlap of the elements. In this model the slider will be activated when forces become tensile and hence the contacting elements will slip relative to one another. The linear contact model includes the ability to bond the discrete elements with a contact bond. A contact bond is considered to be vanishingly small and behaves like a pair of springs in the normal and shear directions. Springs have shear and tensile normal strengths which are specified by the user. The magnitude of force is limited by the strength and when the two are equal the bond breaks. This bond behaviour supersedes the slip behaviour. Once a bond is formed at a contact, that contact continues to exist until the bond is broken.

An additional bond called a parallel bond can be implemented between two discrete elements using a cement-like material as shown in Figure 2.26. The parallel bond component of the contact describes the force-displacement behaviour for the cement between the discrete elements and when this bond is in place slip can still occur. Breakage is defined by the loss of bonds at any contact. The parallel bond structure is that of a set of springs uniformly distributed across a circular cross-section which is centred at the contact point and has radius determined by the user of R_{pb}. The springs and sliders occur in parallel to each other around the perimeter of the circular section (Figure 2.26). The radius of the cement cannot be greater than the radius of the smallest element involved in the contact. Thus the parallel bond can be thought of as a disk or squat cylinder that encompasses the overlying parts of the discrete elements.

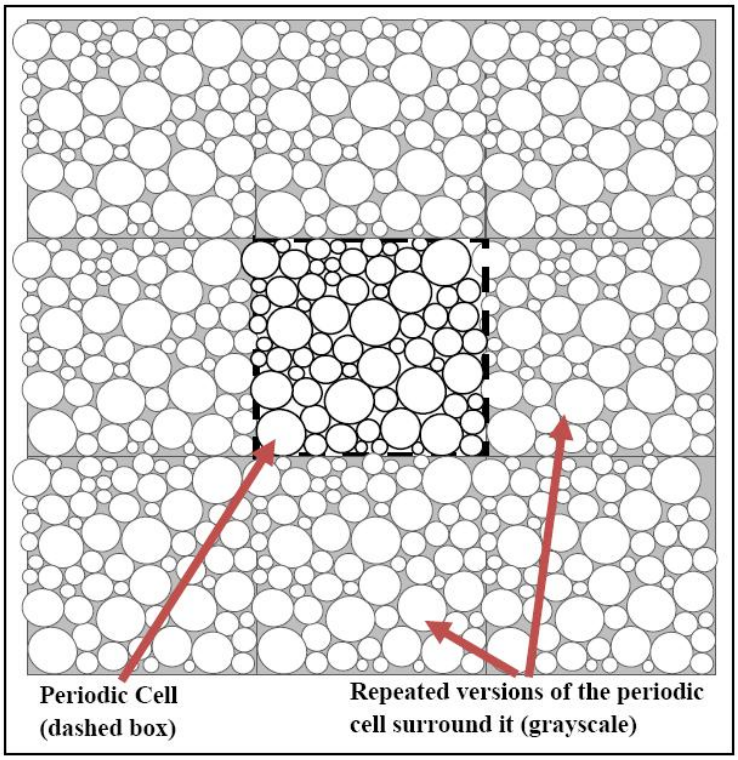

Figure 2.27: The periodic boundary logic after O'Sullivan (2011)

In PFC^{3D} there are several contact models available including Linear, Hertz-Mindlin, Simple Ductile and Smooth-Joint. For the purposes of this research the testing has been limited to the Linear model with use of contact and/or parallel bonds.

Boundary Conditions (O'Sullivan, 2011)

Displacement and/or force boundary conditions can be introduced to the model to control or create specific conditions for modelling. The most popular boundary used in DEM modelling is that of the rigid wall which can be planar or curved. The rigid wall can be used to confine material or can be utilised as a tool to impact or penetrate a material. These boundaries have no inertia and the contacts between wall and discrete element are used for the sole purpose of updating the discrete element's position. Walls can have velocities applied to them so that they impart deformation onto the material through the wall-element contacts. For example, rigid boundaries are often used to model triaxial tests. These will often be controlled by a servo (computationally controlled wall) which is set via a measured internal stress. If the stress is too high, the walls will move away from the material and if the stress is too low, the walls will move toward the material. The wall velocity is always proportional to the magnitude of the stress difference between the measured stress and required stress (O'Sullivan, 2011).

Another commonly used boundary condition in DEM is the periodic boundary. This type

of boundary is used when a selection of material is to be analysed that is representative of the surrounding material. The material is essentially infinite with the selection of material repeated in all directions normal to each of the periodic cell faces (see Figure 2.27). The periodic boundary allows for material to effectively pass through the boundary and contact the material on the opposite boundary. Thus tests can be prepared where the material is to travel in a set direction using a small representative volume which is normally a parallelepiped in 3D. Cross boundary contacts are taken into account for both contact detection and force calculation.

A flexible membrane has more recently been used by Cheung and O'Sullivan (2008) to model triaxial testing. This type of boundary is created by selecting specific discrete elements to become the membrane and applying a force to them. Cheung and O'Sullivan (2008) identify the membrane elements by choosing those that are in a membrane zone and then checking for the elements that would touch an external membrane directly. Elements are removed from the membrane group if there is another element obstructing the direct contact. The magnitude of the horizontal forces to be applied to each membrane element is determined by a Voronoi diagram of the planar surface of the membrane. The area of a Voronoi cell incorporates one discrete element, and this area multiplied by the boundary pressure required provides the force to be added to that element. During the processing of the test, the membrane must be updated as new discrete elements move to the outside of the material.

Time Step

Itasca (2008) note that a PFC^{3D} system is stable only if the timestep does not exceed a critical timestep which is related to the minimum eigen-period of the system. They indicate that it is impractical to apply eigenvalue analyses to the multiple particles within a system so instead estimate the critical timestep at the start of each cycle. In one dimension $t_{crit} = \sqrt{\frac{m}{k}}$ for translational motion and in three dimensions:

$$t_{crit} = \begin{cases} \sqrt{\frac{m}{k^{tran}}} \\ \sqrt{\frac{I}{k^{rot}}} \end{cases} \tag{2.12}$$

for translational and rotational motion where k^{tran} and k^{rot} are the translational and rotational stiffnesses, I is the moment of inertia of the particle and m is the mass of the particle. A critical timestep is found for all degrees of freedom for all bodies and the minimum of these is identified as the critical timestep for the model.

This timestep is regarded by O'Sullivan and Bray (2004) as suitable for the quasi-static type of analysis typical of geotechnical simulations where the response of the system is not sensitive to inertial effects. In these cases, mass scaling is frequently used to increase the time step and reduce the computational time. For a finite difference time-centred scheme, O'Sullivan and Bray (2004) note that the Itasca recommendation is not conservative with a more correct critical time increment of $\leq 0.17\sqrt{\frac{m}{K}}$ where m is the minimum particle mass and K the maximum contact

stiffness. The critical time step is a function of the packing configuration or fabric and number of contacts per particle or coordination number. Numerical instabilities in explicit simulations can be detected by an energy balance check where instability results in the "spurious generation of energy" (O'Sullivan and Bray, 2004, pg 297).

System Generation

The response of a material is highly dependent on its initial state. Researchers performing physical laboratory testing on a material spend a large amount of time preparing their samples for testing. In the same way, DEM modelling requires significant preparation prior to commencing testing. In a DEM simulation the material must first be created and brought to a specified stress level for the test process. It is important that, if the stresses are to be transferred throughout the system, that the packing density of the system is high enough so that the contact force chains span the system. The particle-scale responses are sensitive to the particle size distribution, thus it is worthwhile to test the system for its behaviour prior to running any DEM simulations.

Material can be explicitly created by specifying a lattice structure, however more commonly, particles are randomly generated within a set geometrical area with random central coordinates and radial size depending on the input values provided by the user. Different sized particles can be created within the same material this way. The particles once generated however, may not be in contact with one another, thus there will be no force chains present. To bring the particles into contact, the walls (or exterior boundary) could be used to compress the sample, however O'Sullivan (2011) states that this process can be time consuming. The commonly accepted approach is that suggested by Itasca (2008) in which the particle sizes are increased by expanding the radii until the desired isotropic stress is reached. After each expansion a series of cycles should be invoked to allow the material to return to an equilibrium state. It is possible during this process that some particles may experience large contact forces and this may induce an extreme velocity with the possibility that a particle could escape the geometric confines of the system, or collide with other particles and cause propagation of large velocities. Damping during the early stages of radius expansion may assist with the reduction of this problem.

Radius expansion will generate an isotropic stress state in the specimen, however if the required stress is surpassed during the method, this can lead to overconsolidation as the specimen will retain a memory of the stress history. Thus, it is suggested that the stress state be reached by monotonically increasing the radii of the particles and therefore increasing the stress from a low level to the target level. This process will allow the material to gradually meet the stress requirements without introducing a problematic stress state into the system.

Other approaches for building a system include: the advancing front method (from an initial triad of particles material is added in a clockwise circulatory fashion), the inwards packing method

(particles are placed around the boundary and particles added one-by-one alongside those on the boundary) and triangulation based methods (for example apply Delaunay triangulation to a random group of points and insert particles in the centre of each triangle, then at the vertex and so forth) which are useful in process engineering for awkward geometries. Another approach for building granular materials is by using gravitation or sedimentation. The least computationally expensive way of doing this is to produce a cloud of particles within a geometric confine and then apply gravity to them as the particles settle to the base of the confined area.

Measurement Parameters and Methods in PFC^{3D}

1. Energy Tracing

There are six predetermined energy and work terms that can be used to track the energy within a PFC^{3D} model. These are outlined in detail by Itasca (2008) in their user manuals. The six items that can be traced are:

- Body Work: the total accumulated work done by all body forces on each particle. This is based around the summation of the rotational and translational incremental movement of the particle and the associated gravity, externally applied forces and moments acting on the particle.
- Boundary Work: the total accumulated work done by all walls on the particles. This summation of the rotational and translational incremental movement of the wall by the force and moment acting on the wall is similar to the summation for the body work.
- Strain Energy: the total strain energy stored at all contacts in the system. A summation of the magnitude of the normal and shear forces in relation to the normal and shear contact stiffnesses for each contact. This energy is only valid for the linear contact-stiffness model.
- Bond Energy: the total strain energy stored in the parallel bonds. The value is found by summing the magnitude of the normal and shear forces and magnitude of the normal and shear moments in relation to the normal and shear stiffnesses of the parallel bonds across each bond.
- Frictional Work: the total energy dissipated by frictional sliding occurring at all contacts. The slip displacement is broken into an increment of displacement and an increment of shear elastic force which are combined with the average shear force in the summation.
- Kinetic Energy: the total kinetic energy of all particles from both translational and rotational motion. This results in the summation of the particle kinetic energy ($\frac{1}{2}mv^2$) with that of the particle inertia tensor and rotational velocity to represent rotational motion.

2. Measurement Spheres

Key areas of interest can be isolated by the use of measurement spheres. The centroid of the sphere is set at a user defined position with a user defined radius and encompasses a selection of particles. The measurement spheres can be used to calculate predefined quantities which are:

- Coordination Number: the ratio of the number of contacts within the measurement sphere over the number of particles to produce the average number of active contacts per particle.
- Porosity: the ratio of the void volume in the measurement sphere to the total measurement sphere volume.
- Sliding Fraction: the fraction of contacts within the measurement sphere that are not bonded and are slipping.
- Stress: the total stress in the measurement sphere is represented by the average stress within the particles. Each particle is loaded by point forces acting at discrete contact locations around the particle perimeter. The stress for each contact is simply this force multiplied by the difference between the locations of the contact and centroid of the particle. Due to the intersection of some particles by the measurement sphere and forces in the voids being zero, the total particle volume is altered by the porosity. Then the average total stress within the measurement sphere is computed as a ratio of the summation of the individual particle stress from all contacts and the volume.
- Strain Rate: the displacement and velocity differences between two points are related by a displacement gradient tensor and a velocity gradient tensor or strain rate tensor. In PFC^{3D} the strain rate tensor is calculated using a least squares approach to produce a matrix equation which can be solved for the strain-rate tensor components.

3. Individual Particles

In addition to the variables able to be calculated via the energy and measurement logic in PFC^{3D}, information regarding the state of individual particles such as velocity, displacement and force, can be extracted using the in-built FISH code.

In PFC^{3D}, the mean effective stress p$'$ and deviator stress q (as outlined in Section 2.2.1) can be measured directly for an area contained within a measurement sphere. The individual elements of the stress and strain tensors formed by the software from the measurement sphere can be accessed and used to calculate p$'$, q and therefore the stress ratio $\frac{q}{p'}$. From the symmetric stress tensor of an individual particle in PFC^{3D} and following Equations 2.4 and 2.5 we find p$'$ and q from PFC^{3D} as follows:

$$p' = \frac{s_{11} + s_{22} + s_{33}}{3}$$
$$q = \sqrt{\frac{1}{2}\left((s_{11} - s_{22})^2 + (s_{22} - s_{33})^2 + (s_{33} - s_{11})^2\right) + 3(s_{12}^2 + s_{13}^2 + s_{23}^2)} \tag{2.13}$$

It is worth noting that pore pressure is not represented in DEM models thus p=p′ where p is applied or measured externally and p′ is measured internally via the particles using Equation 2.13 above.

Bonded Particle Model of Rock (BPM) (Potyondy and Cundall, 2004)

In 2004, Potyondy & Cundall describe the use of a cemented granular material to represent rock. The BPM was introduced as a way of mimicking a rock sample by exhibiting behaviours that correspond well with those of rock. The mechanical behaviour of rock and the BPM is governed by force chains – load is carried by the grain and contact. In real world materials a sedimentary rock is bonded with a cement and a more crystalline rock bound via the interlocking of its grains. Thus all rock can be represented in DEM by particles bonded with a cement where for a crystalline rock the cement represents the strength of interlocking grains. The cement contacts can experience compressive, tensile and shear loading and can transmit a bending moment between grains. The transfer of load between grains produces a force chain which may have a high or a low load depending on the evolution of that chain. As BPM material is tested the force-chain fabric will evolve with micro-forces and micro-moments providing local loading to cause breakage. This in turn will alter the global force distribution with fractures or rupture zones eventually forming. As the material shows greater breakage, it will behave more like a granular material with unstable force chains. The BPM is a direct modelling method where the particles and bonds are related to similar items within the rock structure and allows for examining the influence of the microstructure on the macroscopic behaviour. However the BPM is still an approximation to rock using a synthetic material.

A BPM model requires several items of information about the grains to correctly build a material:

- density
- shape
- size distribution
- packing
- microproperties of the cement.

The BPM process produces a synthetic rock as a dense packing of non-uniform spherical particles that are joined at their contact points with parallel bonds (cement). The procedure to produce

the material is designed to ensure that the particles are well connected and any locked-in forces are low. A summary of the process that Potyondy and Cundall (2004) suggest to follow is:

- Compact Initial Assembly: particles are placed randomly at half of their final size within an arrangement of walls used to contain the material. The number of particles chosen to fill the material space is based on an overall porosity which can be manipulated by the user. Once all particles are created, the radii are increased to their final values and the model is cycled until equilibrium is reached.

- Isotropic Stress: the user defined radius of the particles is altered (either reduced or increased) until a user specified isotropic stress is obtained. Particle rearrangement occurs when radii values are altered and thus Potyondy and Cundall (2004) apply their radius scale factor slowly in small increments to make certain that isotropic stress is formed.

- Floating Particles: during the generation and scaling process there may evolve particles that have less than a desired number of contacts with their surrounding particles; these are called floating particles. Floating particles are removed by setting the desired number of individual particle contacts (normally 3) and scaling the radius of the floating particles until this minimum is met. This provides a denser bond network once the bonds are applied.

- Parallel Bonds: bonds are installed between all particles in the assembly with a strength and stiffness as chosen by the user. These properties are based on a mean and standard deviation with the actual values for each bond chosen from a Gaussian normal distribution.

- Release From Walls: once the above processes have concluded, the material is normally released from the boundary walls and allowed to relax to static equilibrium by cycling the model. The material will expand and generate self-equilibrating locked-in forces which Potyondy and Cundall (2004) claim are similar to locked-in stresses that may be found in a standard rock specimen.

Locked-in-forces were physically investigated by Holt (2001) using a synthetic sandstone cemented under stress to reproduce diagenesis. The same experiment was performed in PFC^{3D}, where the particles were placed under stress prior to creating bonds. The physical experiment results were well reproduced by the numerical model, supporting the BPM process in reproducing similar stresses in the model.

The BPM model described in Potyondy and Cundall (2004) was validated by the authors by building a model of Lac du Bonnett granite and comparing the numerical model results of standard geotechnical tests with those performed in a laboratory. The microproperties of the particles and bonds were calibrated with the overall short-term response of the laboratory specimen using Young's Modulus, Poisson's Ratio, the unconfined compressive strength and the failure envelope.

Ten specimens were created by varying the seed of the random number generator in PFC^{3D} allowing for each to obtain a different packing arrangement and microstrength. Potyondy and Cundall (2004) found that the PFC model using the BPM matched the macroproperties of the laboratory specimen well. The strength envelope was, however, too low and they suggest that the shape of the particles (i.e. spherical) could cause this discrepancy. A brief study of material with joined spheres (clusters) indicated an improvement on the strength behaviour of the model. Potyondy and Cundall (2004) found that particle size affected the Young's Modulus, Brazilian strength and unconfined compressive strength.

Linear Elastic Fracture Mechanics (LEFM) can be directly related to the BPM (Itasca, 2008). The properties of the BPM can be shown to represent the Mode-I fracture toughness (compare to Section 2.2.2) in the following way:

$$K_{1c} = \sigma_t' \sqrt{\pi r} \tag{2.14}$$

where r is the particle radius and σ_t' is the true tensile strength of the BPM. As particle radius enters this expression, the choice of particle size cannot be an arbitrary one when considering the fracture behaviour of a material.

Overall the BPM shows behaviour that closely resembles that of rock. Potyondy and Cundall (2004) note that the following behaviours are observed:

- Non-linear stress-strain response
- Change in behaviour depending on stress state
- Memory of prior stress or strain
- Dilatancy
- Hysteresis
- Brittle to ductile transition
- Microcracks leading to fractures and overall rupture.

2.4.2 Geomechanics Research in DEM

Impact Testing

A group of discrete element particles bonded together (called an agglomerate) may be impacted against a wall at high velocity or crushed between two platens to investigate comminution in a particle of sand or piece of rock (Thornton et al., 1996; McDowell and Harireche, 2002a). At sufficiently high impact velocity, there are generally no large fragments remaining due to the extensive shattering that occurs (Kafui and Thornton, 2000). Dense agglomerates undergoing high velocity impact will fracture or shatter, whereas loose agglomerates will simply disintegrate

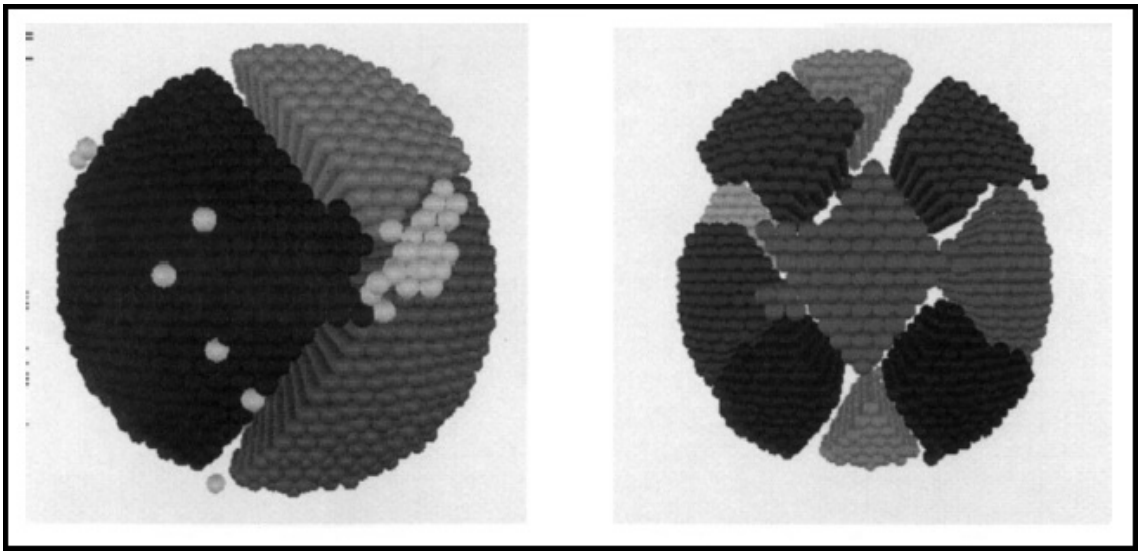

Figure 2.28: Fragmentation resulting from impacting a strong agglomerate – left at 2.0 ms^{-1} and right at 4.0 ms^{-1} – results from Kafui and Thornton (2000, Figure 13, pg 125).

(Mishra and Thornton, 2001). Thornton et al. (1996) found through their DEM experiments that a compressive wave propagates from the point of contact through the agglomerate when it impacts a wall at high velocity. If the rate of loading of an agglomerate is rapid in comparison to crack growth, many flaws will be activated to accommodate the unloading of the stress (Thornton et al., 1996), a conclusion supported by the earlier experimental work of Grady (1981) and Lundberg (1976).

Breakage increases as the velocity of impact increases however the amount of kinetic energy lost in breakage decreases according to Subero et al. (1998). This is suggested by Subero et al. (1998) as the result of cushioning occurring around the impact site due to surrounding smaller fragments. Thornton et al. (1998) found similar results noting that at a critical rate of impact, further increases in velocity will not increase the breakage in the agglomerate due to a possible cushioning effect from other fragments. Kafui and Thornton (2000) show that when a material shatters a large number of daughter fragments will be projected away from the impact location at high speed as shown in Figure 2.28 suggesting that not all kinetic energy is lost during breakage.

Moreno et al. (2003) examined agglomerate damage from oblique impacts against walls. Utilising a damage ratio constructed from the ratio of the number of broken particle bonds to the initial number of bonds, Moreno et al. (2003) found there was an increase in damage with an increase in impact velocity and as the direction of impact became more orthogonal. Wittel et al. (2008) also investigated impact fragmentation of brittle agglomerates, finding a higher strain rate caused greater crack nucleation, which in turn led to more meridional cracks. If there was enough energy available, the meridional cracks might propagate outward, fragmenting the sample into wedge

shapes with secondary oblique plane cracks causing the larger fragments to disintegrate further (Wittel et al., 2008).

Strain Rate Effects

In Section 2.2.3, the effect of strain rate on the behaviour of rock is briefly discussed. Strain rate effects can also be represented in DEM modelling and the ability of DEM to represent this behaviour supports the use of this form of modelling for geomechanics problems. Two examples of strain rate testing in DEM are outlined below.

Uniaxial laboratory tests were performed by Jackson et al. (2008) on sandstone, limestone and chalk over a range of strain rates from 2.6 x 10^{-5} s^{-1} to 0.05 s^{-1} to investigate strain rate effects and fragmentation in rock in relation to rock crushers. The physical laboratory testing concluded that the effect of strain rate on breakage was important for crusher performance. To investigate the micromechanical behaviour of the sandstone under varying strain rates, the authors prepared a calibrated sandstone specimen in PFC^{3D}. The authors increased the bond radius to be equivalent to that of the particle radius in order to fill void space in the model to reduce the porosity of the material. The results of the numerical modelling show that material brittleness decreases with increasing strain rate and that more energy is required to produce fragmentation at higher strain rates. Jackson et al. (2008) also show that breakage occurrence in relation to the stress peak varies across strain rates with more total breakage at higher strain rates.

Impact velocity tests using a specially shaped striker within a Split Hopkinson Bar (SHPB) system were modelled by Li et al. (2014) in PFC^{2D}. The full SHPB system was modelled with the rock specimen placed between the incident and transmitted bars as would be done in a laboratory. Under moderate impact velocities Li et al. (2014) found that the rock specimen deforms at a constant strain rate throughout the loading process. The higher the impact velocity, the higher the strain rate and the strength of the specimen was found to increase through an increase in the ratio between the dynamic and quasi-static UCS of the rock. Heterogeneity and lateral inertial confinement are noted as two important factors by Li et al. (2014) who state that confinement causes an increase in strength under high strain rate, as found by other authors.

Blasting

A model of shock or gas induced fractures from the blasting of rock is presented by Potyondy et al. (1996). A densely packed (face centred cubic) rectangular boulder of granite was built using PFC^{3D} with a borehole introduced through the centre. The material was bound with contact bonds and calibrated to represent granite. Varying pressures were applied to the borehole wall to model the breakage behaviour under a shock wave. Under extremely high pressure, the boulder cracked along diagonal lines leading toward the edges of the boulder which then separated into four distinct

triangular pieces. During a low pressure test, the boulder cracking remained around the borehole area. Gas pressure was introduced as forces within the cracks which were represented by areas of multiple broken contact bonds. Introducing these pressures to the prior testing, Potyondy et al. (1996) found that damage occurred much faster with the additional pressure formed within the cracks. The authors also found that their method of introducing gas pressure may cause excessive fracturing but may perform more accurately if the forces within the cracks were gradually moved toward the value of the applied borehole pressure.

In work performed by Kuhn (1999) on deformation under biaxial loading, increasing mean stress was found to push the particles together and reduce the void ratio. Low strains produced compressive behaviour and high strains produced dilatant behaviour in the experiments completed. Kuhn (1999) found that individual particles collaborated with neighbouring particles to form large deformation structures. Cundall and Strack (1979) noticed that heavily loaded contacts rarely undergo frictional slip. Kuhn (1999) indicated that where contact loadings are rapidly changing frictional slip is also unlikely.

Crushing

Fracture and crushing behaviour has also been modelled in DEM by Refahi et al. (2010) for comparison to laboratory jaw crusher tests. Refahi et al. (2010) found the fracture energy of spherical agglomerates in a jaw crusher to be well modelled using DEM, however, the delamination of cubic samples was poorly modelled. The authors suggest that the trial and error method of assigning micro properties to the BPM leads to an isotropic material whose results in breakage tests are somewhat artificial. Spherical particles accurately model tensile fracture in spherical specimens when compared to cubic specimens where shear failure is more dominant (Refahi et al., 2010). Cubic specimens are poorly modelled in PFC due to the nature of the generated material being too isotropic when using spherical elements.

Hazzard et al. (2000) noted that the response of rock under compression is controlled by the formation, growth and interaction of microcracks. Hazzard et al. (2000) state that PFC provides an adequate representation of this process as stress is redistributed when a bond breaks allowing for interaction between microcracks or broken bonds. A stress change will only cause a bond to fail if the bond is already close to failure. The authors created several BPM for granite and chalk. While processing through the trial and error process of the BPM to find the most accurate micro properties, they noted:

- The stiffness of the particle influenced the stiffness of the material
- Bond strength determined material strength and the standard deviation of the bond strength influenced the nature of failure

- Ratio of normal to shear strength influenced Poisson's Ratio.

The following study performed by Hazzard et al. (2000) focused on the evolution of cracking during loading and how the energy released from each crack influences rock behaviour. They specifically wished to know if a stress wave emitted from a crack was able to instigate cracking in nearby material. To do this, the authors looked at the change in the contact normal force after a nearby bond breakage and found that the average normal force after the first stress peak was greater than the original tensile strength of the bond. Hazzard et al. (2000) concluded that a passing stress wave can cause stress changes that can induce more cracks.

A large amount of work has been completed on crushing and breakage by Professor Malcolm Bolton and his extended research group at the University of Cambridge in the United Kingdom. McDowell et al. (1996) focused on the fractal crushing of granular materials noting that once self-similarity was achieved, that particles at all orders had the same probability of failure and thus self-similarity was maintained. They also found that a high coordination number allowed a load to be well distributed on a particle and so the probability of fracture was lower than for less well contacted particles. Utilising a Weibull distribution to model the breakage, it was found by McDowell et al. (1996) that the number of fines produced was greater for an angular sand than for a rounded sand. McDowell and Bolton (1998) explain that smaller samples are generally stronger than larger samples due to the reduction of flaws available to grow and coalesce. Although the smaller particle is generally stronger, if the coordination number is far greater than the size of the particle then it will actually have the highest probability of fracture. Therefore the yield stress of an aggregate is determined by the tensile strength of the smallest particles (McDowell and Bolton, 1998).

Hexagonal Close Packing

Robertson (2000) modelled an agglomerate in PFC^{3D} using regular packing to minimise the voids between each particle. He considered face centred cubic (FCC), body centred cubic (BCC) and hexagonal close packed (HCP) agglomerates. The FISH code produced by Robertson (2000) allowed for the agglomerate to be centred at prespecified coordinates. Parametric tests were performed during crush tests of an HCP agglomerate between platens. These tests indicated that the ratio of bond strength to ball stiffness affects the brittleness of the material. A rotated HCP agglomerate (see Figure 2.29) was found to fragment into multiple pieces as opposed to when the coordinate axes of the agglomerate were at 90^o to the platens, when the material split into two main pieces. Robertson (2000) also found that the number of particles greatly affected the peak force required to cause fracturing and the resultant number of fragments that ensued. Robertson (2000) built aggregates of agglomerates by first creating a randomly produced specimen using the radii expansion method as outlined by Itasca (2008). These particles were then deleted and each

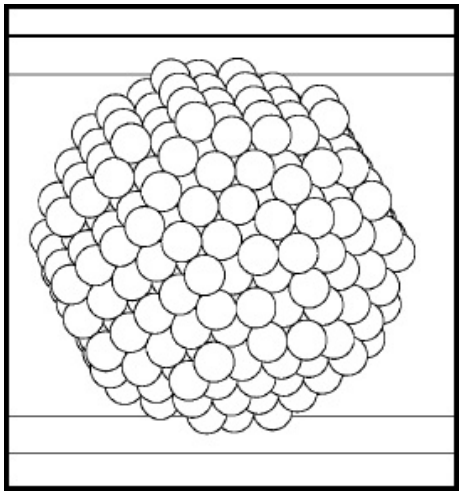

Figure 2.29: A rotated HCP agglomerate within two platens as tested by Robertson (2000, Figure 4-5, pg 4-11).

was replaced with a randomly rotated HCP agglomerate. The aggregate underwent compression tests with varying bond values to investigate breakage and pressure responses with additional testing involving load/unload/reload processes (Robertson, 2000). Robertson (2000) indicates that the results are comparable to plasticity models such as Cam Clay.

McDowell and Harireche (2002a) followed from Robertson's work and utilised hexagonal close packing with the removal of a percentage of particles to represent flaws. Multiple agglomerates built this way were crushed under a descending upper platen. They found that the strain rate on a material in PFC^{3D} must be slow enough to allow the information at one side of a sample to propagate through to the other side. McDowell and Harireche (2002b) then investigated modelling agglomerates in an oedometer by replacing spherical particles with hexagonally close packed agglomerates again with a percentage of particles removed to simulate flaws. The agglomerates were bound using contact bonds with the top platen descending to crush the material. They found that the velocity of the top platen could not descend any faster than 1 ms^{-1} as the stress on the material did not otherwise have time to propagate through the material, as found in McDowell and Harireche (2002a). Lim and McDowell (2005) used crushable agglomerates (Figure 2.30) to model railway ballast and found that the choice of damping coefficient affected fragment size distribution. A standard viscous damping coefficient of 0.015 caused the agglomerates to fail quickly and catastrophically. In a follow up paper, Lim and McDowell (2007) noted that coordination number was very important for the behaviour of an agglomerate as it is related to a size effect. One way to increase the coordination number is to increase the number of particles in an agglomerate, however this will also increase computational time. Lim and McDowell (2007) instead suggest that a scaling of the bond strengths of the agglomerate(s) can compensate for low coordination number.

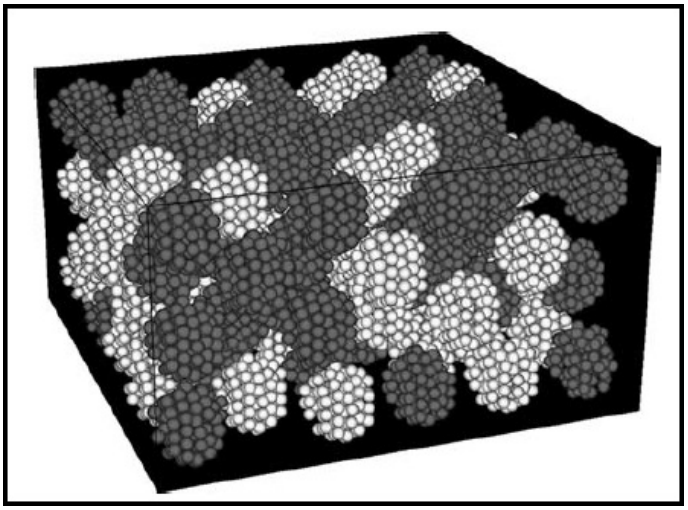

Figure 2.30: Oedometer sample of agglomerates as tested by Lim and McDowell (2005, Figure 7, pg 23).

Cheng et al. (2004, 2003) built crushable soil samples following the hexagonal close packing of Robertson (2000), and removed 20% of the particles to represent flaws. Each sample was randomly oriented and crushed between two platens. Crucial bonds in the soil element once broken allowed the agglomerate to disintegrate. Bolton et al. (2008) built a cubic box of agglomerates by moving six walls slowly inward to bring the agglomerates into contact. The samples then underwent isotropic compression which caused the agglomerates to fail where the frequency of fragmentation increased as confining pressure increased. Bolton et al. (2008) state that the elastic energy lost from bond breakage is negligible in comparison to the dissipation of crushable materials by frictional sliding due to the new surfaces created by breaking fragments.

Shear Testing

Two dimensional shear box testing in a DEM model was performed by Masson and Martinez (2001) using a loose and a dense soil sample constructed of 2-4 mm circular particles deposited randomly under gravity. The density of the soil was controlled by the use of the friction angle parameter in the DEM program during deposition. A quasi-static shear velocity of 0.05 mms^{-1} was maintained and the top plate used to apply a constant vertical force of 50 kPa. The loose sample behaved in a contractive way and the dense sample in a dilatant way as shown in Figure 2.31 – the same behaviour as seen in laboratory tests on real soil samples (Masson and Martinez, 2001). Particle rotations within a shear band (localised to a thin layer of material) were found to cause the macroscopic dilatancy seen in the dense sample while rotations in the loose sample showed a fairly uniform profile. The velocity fields of the two samples differed greatly with the upper half of the box for the dense sample showing distinct upward velocity vectors which corresponds to

the dilatancy. Masson and Martinez (2001) concluded that particle rotations are significant as indicators of strain localisation in DEM models of shear box tests.

Carolan and O'Sullivan (2006) built on the work from Masson and Martinez (2001) by producing 2D shear-box tests using crushable material (following the replacement concept of Lobo-Guerrero and Vallejo (2005)) and non-crushable material, utilising the material parameters outlined by Masson and Martinez (2001). During the shearing process the walls were moved according to a servo-controlled algorithm which Carolan and O'Sullivan (2006) noted caused challenges once crushing was introduced into the test resulting in oscillatory behaviour of the normal stress rather than maintaining a constant value, if not carefully monitored. The use of weak bonds resulted in contractant behaviour that is common in loose sand, and strong bonds resulted in dense sand behaviour or dilation. The breaking of force chain columns throughout the test impacted on the development of shear stress and the authors note that the collapse of a force chain resulted in a fluctuation in the stress-strain curve. The force chains were seen to rotate from vertical to diagonal corresponding with the shear band pattern seen in conventional shear-box tests on sand (Carolan and O'Sullivan, 2006). They state that shear bands could also be identified by considering particle rotations and incremental shear strains throughout the DEM test process.

In performing direct shear testing to model the behaviour at rock joints, Park and Song (2009) noted during a preliminary study that rock joints formed in DEM using either contact bonds or parallel bonds work fairly similarly. Thus Park and Song (2009) made the decision to work only with contact bonds due to the reduction in micro-parameters required for numerical testing. When calibrating for microparameters in PFC^{3D}, compressive and tensile strength tests are conducted. Park and Song (2009) suggested that in a BPM of rock, the ratio of tensile to compressive strength is normally 0.25 which is far greater than the suggested 0.05-0.1 for real rock. This makes calibration to both strengths difficult as this would require alterations to the bond parameters which would effectively provide two different materials in order to match the two strengths. Given Park and Song (2009) were investigating shear behaviour of rock joints and that this is described in relation to compressive strength, they determined that the stress of concern during their numerical tests was compressive. Park and Song (2009) therefore matched only the UCS characteristics to determine the microparameters. A joint curve was created and all bonds joining particles along this curve were removed to produce the joint surface (Figure 2.32a). The upper confining walls controlled all velocity and the lower walls were static with all vertical velocities controlled by a servo-mechanism. The direct shear test model compared well with laboratory tests and showed a dependency of shear behaviour on normal stress and joint roughness (Figure 2.32b). An in depth parametric study of the varying microparameters that could influence the model showed the main influencing parameter to be the friction coefficient.

Mair and Hazzard (2007) used PFC^{3D} to model contact force distributions under shear in

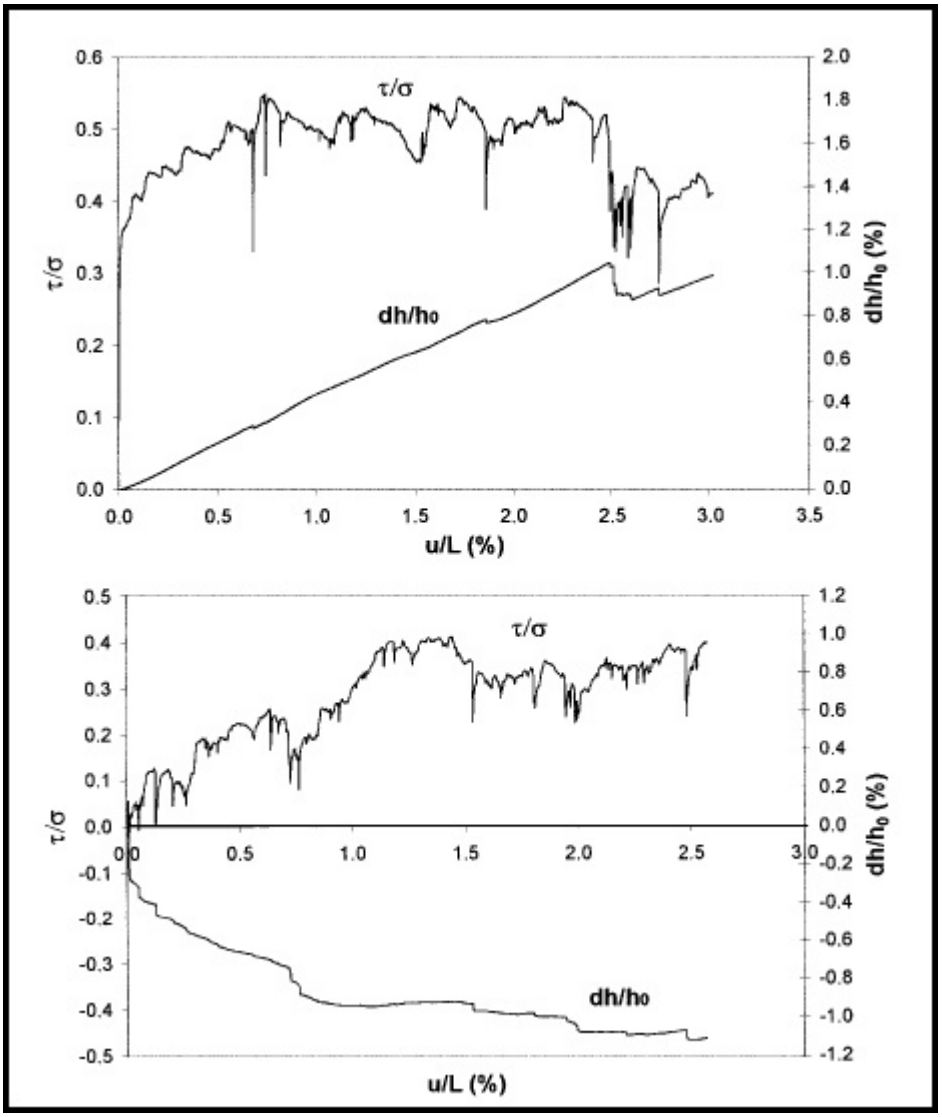

Figure 2.31: Dense (top) and loose (base) sample results from Masson and Martinez (2001, Figure 4, pg 1008) where $\frac{\tau}{\sigma}$ is the shear-to-normal stress ratio, $\frac{dh}{h_0}$ is the volume change and $\frac{u}{L}$ is the shear strain.

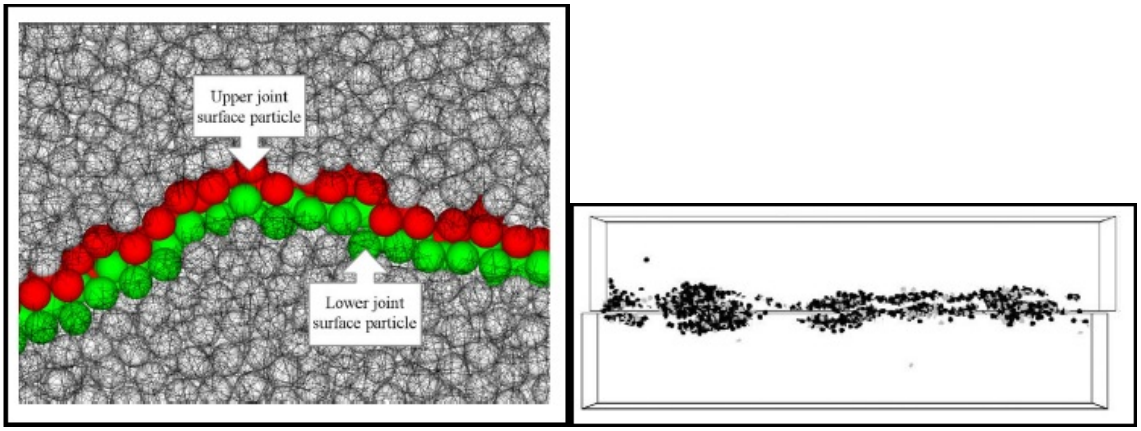

(a) Contact bond network along joint curve.

(b) Microcracks in specimen at shear displacement of 1.6mm at normal stress of 15 MPa.

Figure 2.32: The joint curve and its effect in shear from Park and Song (2009, Figure 2, pg 1317 and Figure 4(b), pg 1318).

relation to processes that may be occurring in fault zones. Varying particle size distributions were built within a parallelpiped to represent different states within fault maturity. The parallelpiped was set within a servo-controlled top wall and x-direction periodic boundaries. Shear velocity was applied only to the very top layer of particles and in one direction. The results suggested that there is a link between a strong force network and friction whereby friction reduces when the density of strong force chains reduces. The force network is also seen to move obliquely to the shearing direction over time which Mair and Hazzard (2007) suggested highlights the transient nature of force networks where the strong force network represents the dominant load bearing structure.

In a group of papers published on the evolution of fault gouge, Guo and Morgan (2004, 2006, 2007, 2008) utilised PFC^{2D} to model a fault zone boundary by building two fault blocks separated by a fault surface. Rather than confining the material with rigid walls, two boundary blocks of a few particles were created at the base and top to control the normal and shear stresses. The normal stress remained constant facing towards the fault surface and the velocity was introduced in the boundary blocks in opposite directions to create shear (see Figure 2.33). They found that the fault zone dilated at the onset of shear and friction decreased, perhaps due to the transition from interlocked grains to a dilated state. Overall, the results suggest a transition from fracture to grain rolling and sliding with the conditions of formation strongly influencing the micromechanical properties in complex ways.

2D DEM shear-box tests were also performed by Liu (2006), Zhang and Thornton (2007) and Cheng et al. (2008). All of the specimens tested by these authors were produced by random deposition with each author utilising a different process to complete the specimen creation. Liu (2006) utilised interparticle friction to create dense ($\mu = 0$) and loose samples; Zhang and Thornton

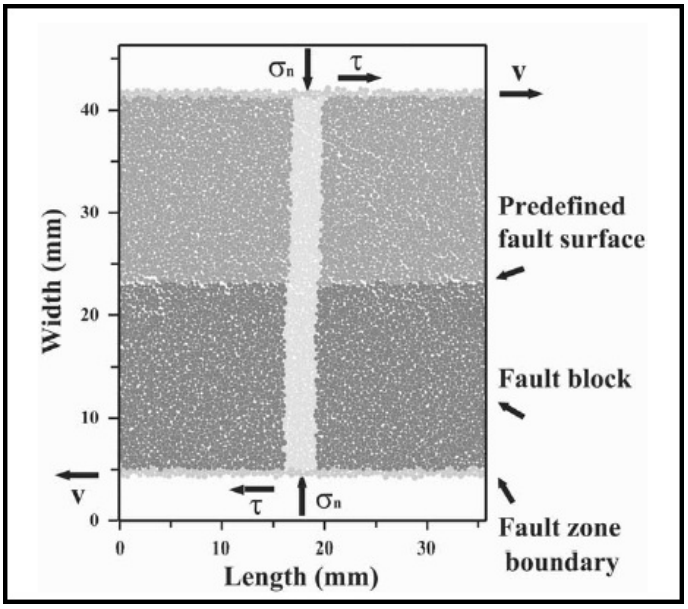

Figure 2.33: The configuration of the fault gouge numerical experiment from Guo and Morgan (2008, Figure 1, pg 3) where σ_n is the normal stress, τ is the shear stress and v the constant velocity chosen for moving the upper and lower boundaries.

(2007) used downward pressure from the top platen for consolidation of the sample, and Cheng et al. (2008) made use of the radial expansion method followed by the replacement of individual particles with three-particle agglomerates. The results of these shear-box tests are consistent with prior DEM work with soils, where dense material dilates and loose material contracts. Liu (2006) specifically investigated the effect of the frictional force that develops between the upper box and material, removing this effect in the DEM simulations by allowing the upper box to move freely in the vertical direction. Zhang and Thornton (2007) and Cheng et al. (2008) investigated the micromechanical behaviour seen in the DEM shear-box tests and found that there are several key macroscopic properties that are affected by the microscale behaviour. Higher stress levels cause more breakage which in turn leads to compression with significant bond breakages causing sudden drops in the shear stress (Cheng et al., 2008). The shear band is wider in the centre than at the edges (Zhang and Thornton, 2007), is thicker for a loose sample and the shear band width increases with crushing (Cheng et al., 2008). Particle rotation is significantly greater in the centre of the shear zone (Zhang and Thornton, 2007) and increases with breakage (Cheng et al., 2008). Zhang and Thornton (2007) also noted similar issues as Carolan and O'Sullivan (2006) with the servo-controlled wall and found the servo parameter required constant monitoring and adjustment.

3D DEM shear box tests were compared with experimental shear tests on chrome steel spheres by Cui and O'Sullivan (2006). Specimens were created by the radius expansion method to fill a predetermined box size and the behaviour of the material during the test was monitored by a central measurement sphere. Additional measurement spheres outside of this central region were

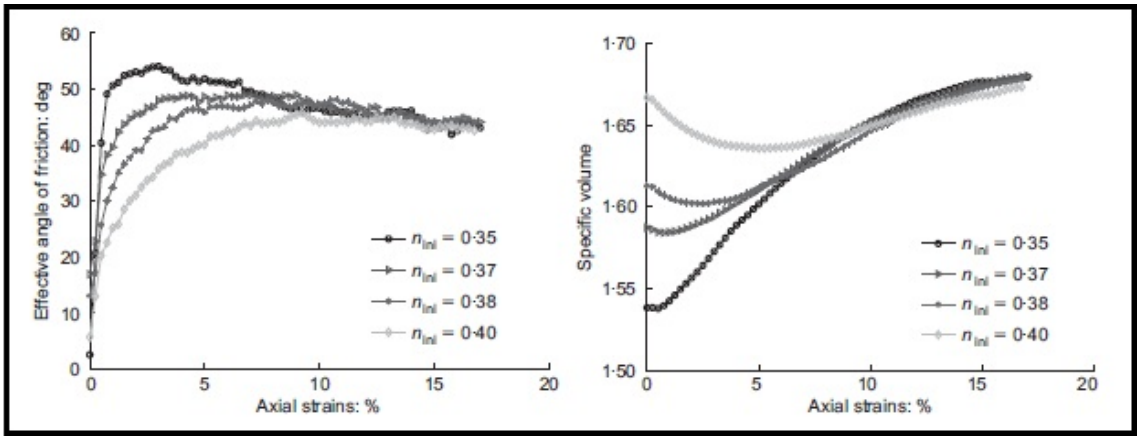

Figure 2.34: Mobilised angle of friction (left) and specific volume (right) – results from plane strain testing performed by Powrie et al. (2005, Figure 7, pg 301) with varying initial porosities.

found to produce stress values within 5% of those measured in the middle sphere. Strong anisotropy induced by the shearing was observed through the contact force distribution. Cui and O'Sullivan (2006) found differences between the experiments and DEM simulations that they believed to be related to the interparticle friction coefficient. Like Zhang and Thornton (2007) and Carolan and O'Sullivan (2006), Cui and O'Sullivan (2006) found that the top boundary servo parameters needed to be constantly adjusted.

Plane strain shear testing was introduced by Powrie et al. (2005) on a rectangular specimen where the y-direction walls were frictionless and rigid, the x-direction was constrained by a flexible membrane of particles and loading was applied in the z-direction. The soil specimen was built from particles of two bonded spheres via the radius expansion method with the particle size distribution for the material between 0.41 mm and 1.89 mm (based on the size of the larger of the two spheres in each particle) and porosity of 0.35. The z-direction loading platens were driven toward one another at 3 x 10^{-5} mm per step to almost 17% axial strain. They performed a series of simulations with different initial porosities and found that the model reproduces dependence of soil behaviour on porosity (see Figure 2.34 and refer Figure 2.13 for standard soil behaviour comparison). Powrie et al. (2005) noted that the largest particle rotations occur in the areas of most intense deformation.

Triaxial Tests

In tests of particle breakage during cyclic triaxial loading, Donohue et al. (2009) found that particles did not share equally in the bearing of load and that crushing was associated with the particles participating in the strongest force chains, as also found by McDowell and Harireche (2002a) and Cheng et al. (2003). The contact force network evolved from cycle to cycle although the process was not indefinite as the material might reach a stable state.

The standard method for modelling of triaxial tests in PFC^{3D} is to utilise a rigid cylindrical wall

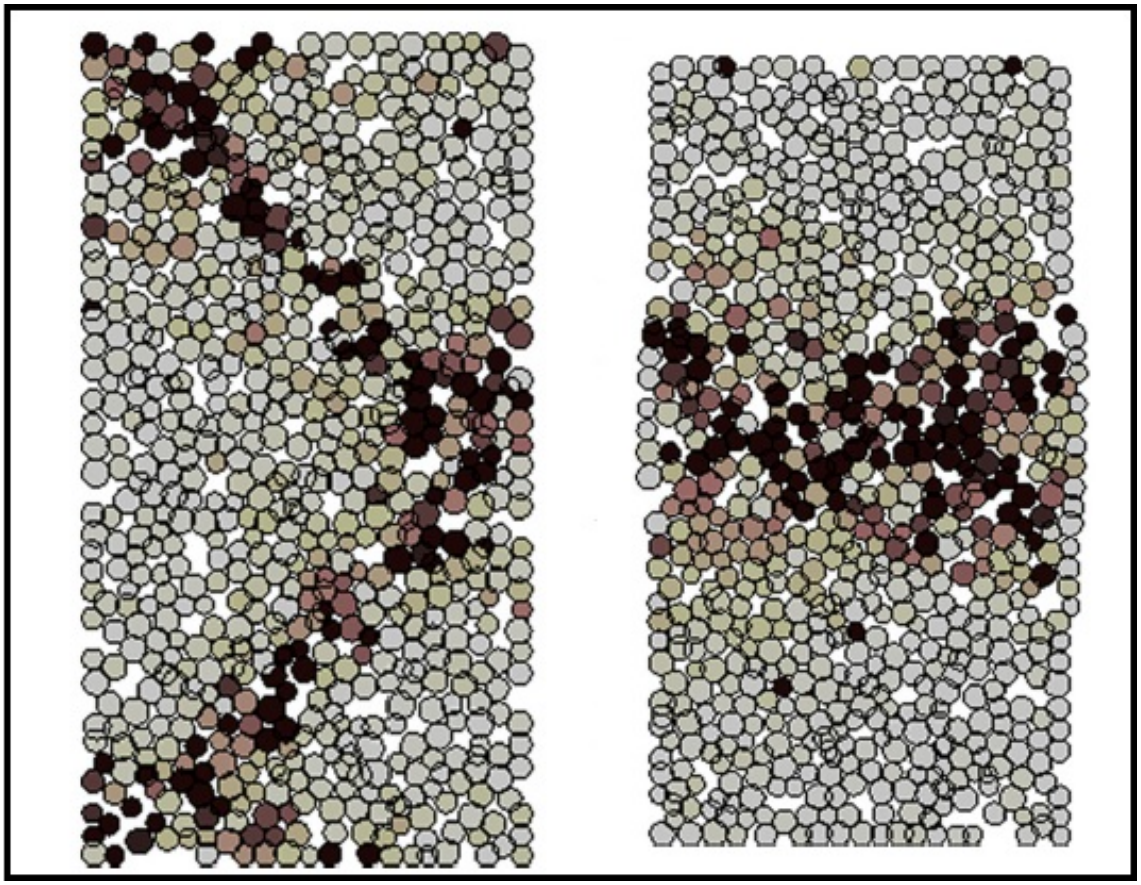

Figure 2.35: Particle rotations indicating damage to the specimen for rigid-wall (left) and flexible membrane (right) triaxial tests as performed by Cheung and O'Sullivan (2008, Figure 15, pg 495).

that can act under servo-control to pressure the material (Itasca, 2008). The membrane boundary is applied to the outermost particles and is able to be re-established as the material moves during the test. Force is exerted on the material by the membrane through an applied force on each particle in order to create and maintain the confining pressure. In contrast Cheung and O'Sullivan (2008) implemented a flexible membrane boundary for triaxial testing. When they compared the results of the standard Itasca triaxial test and that of the flexible membrane, they found that the damage was quite different. The standard Itasca test produced diagonal damage patterns whereas the membrane test produced a damage zone toward the centre of the cylindrical specimen as seen in Figure 2.35. Clearly the boundary conditions can greatly influence the failure behaviour in DEM materials.

2.4.3 Avalanche and Landslide Modelling Using DEM

DEM models are often used to validate laboratory experiments and can also be used to model large scale rock avalanches, landslides and geotechnical problems that can be thought of as grain or agglomerate based. Examples of some of the work performed using DEM to model geotechnical failure follows.

In large rock fall situations, behaviours can occur that are not generally able to be modelled in DEM type models including rolling, bouncing, sliding and free falling (Poisel and Preh, 2008). In PFC^{3D}, local damping (Section 1.8, Theory & Background, Itasca (2008)) is the default method to reduce excessive particle movement that may be unrealistic or that may occur due to the spring/slider contact model. As Poisel and Preh (2008) note however, in rock fall situations the acceleration and velocity of particles should not be corrected or damped in any way in order to correctly model the natural situation. Instead Poisel and Preh (2008) model landslide runout by deactivating all local damping and activating viscous damping, to reduce the rebound after particle-particle impacts. Application of this modified PFC^{3D} model by Poisel and Preh (2008) results in varying landslide runout times in relation to bonded and unbonded masses which Poisel and Preh (2008) state highlights the need to investigate the disintegration of the rock mass during sliding.

Staron (2008) utlised 2D Contact Dynamics (Moreau, 1994) to model the behaviour of simple laboratory granular flows. In Contact Dynamics the grains are rigid and do not overlap unlike PFC^{3D}. A rounded heap created via deposition under gravity was released down a slope transitioning to a horizontal plane (Staron, 2008). The tests were varied by adding immovable grains to the slope to investigate the effect of a rough slope on the flow. Staron (2008) investigated the Fahrböshung ($\frac{H}{L}$) theory in relation to the runout of simple laboratory granular flows that are modelled numerically. Results suggested a clear relationship between $\frac{H}{L}$ and volume of material – independent of topography. Runout is correlated with the way initial potential energy is made

available to the spreading mass so that a greater volume of source rock will typically produce a greater runout where $\frac{H}{L}$ will be low. Thus Staron (2008) concludes that the description of a granular flow in terms of $\frac{H}{L}$ is a reflection of the material quantity and properties (e.g. friction angle) and is not related to flow conditions such as topography.

Tommasi et al. (2008) modelled potential rock avalanches in the Lavini di Marco area using PFC^{2D}. In the field the fairly intact limestone dips consistently toward the local river and is interspersed with faults and buckling folds. Parameter details for PFC^{2D} were found from calibration with borehole details from the affected area. Blocks of rock taken from the field area were also tested in field rock falls to quantify energy dissipation along with restitution and friction coefficients. PFC^{2D} was then used to perform runout prediction analysis and calibrated against the material detail from the field and physical laboratory testing. The model was validated using prior rock slides in the Lavini di Marco area. Tommasi et al. (2008) found that the front of the numerical model runout fell within 10m of that from actual rock slide events in the area and that on closer inspection rock blocks (bonded aggregates) were intact on the surface with significant fragmentation at the base. The authors also noted that velocity reached a peak at the point where the avalanche reached the valley floor with a secondary peak when the rear of the avalanche arrived to push the initial material further out into the valley. When the model was applied to the specific area of interest in the Lavini di Marco, Tommasi et al. (2008) found that the top part of the slide showed greater velocity with the basal areas showing greater fragmentation. Overall Tommasi et al. (2008) conclude that PFC^{2D} is useful for the runout prediction of rock avalanches.

After completing physical laboratory testing using a rheometer, Deganutti (2008) chose to use PFC^{2D} to model a tangential slice through the rheometer. This testing was designed to investigate grain fragmentation in granular flow. Rock (where coal was used as the laboratory test analogue) grains were represented by sets of clusters with synthetic bond strengths and grain parameters calibrated against laboratory rock behaviour. The clusters could break during shear or if the stress from the external load exceeded the bond strength. Small clusters showed a lesser number of broken bonds in comparison to large clusters as large clusters tended to build large grain bridges and thus were less free to move and rotate compared with smaller clusters. Deganutti (2008) notes that there is a distinct difference in time scale between the laboratory and numerical rheometer tests, with the processes in the numerical tests occurring in a much shorter time frame than those in the physical tests, and the author suggests that this is the result of inertial effects in the numerical model. It was also found that a high external load (applied incrementally) resulted in a larger number of shear breakages and a higher fragmentation intensity (Deganutti, 2008).

Unsteady, confined granular flows were modelled by Banton et al. (2009) to simulate physical laboratory testing done by Savage and Hutter (1991) and Hutter et al. (2005). Granular DEM materials were released from rest to travel down a steep and rough incline with three types of

particle shape tested – simple sphere, two particle clump and two particle cluster. A simple 2D parametric analysis showed a shallow and long run-out granular flow with a simple sphere particle became a less dispersed and thicker deposit using a two-particle cluster. The DEM model produced very similar results to those of the laboratory tests and thus the DEM technique was found to be capable of handling the physical processes involved in granular flows.

The collapse of volcanic edifices was modelled using PFC^{2D} by Thompson et al. (2009). A portion of slope was replaced by a failure area built from discrete disk particles (2D) subjected to gravity and restrained by a flank wall. The flank wall was then deleted to set the landslide/avalanche into motion along a horizontal runout zone. As with Poisel and Preh (2008), Thompson et al. (2009) installed viscous damping which occurred only during particle contact and thus allowed free-fall and bounce to occur. Thompson et al. (2009) found that the peak stress occurred immediately following failure initiation with particles in the lower area of the flow experiencing greater stress fluctuations than particles located on the free surface with the fluctuations likely to produce fracture and disaggregation. Coloured marker particles were introduced to the model to determine the behaviour of stratigraphy under a gravity-type failure and the results show that stratigraphy is generally preserved albeit in thin layers (see Figure 2.36).

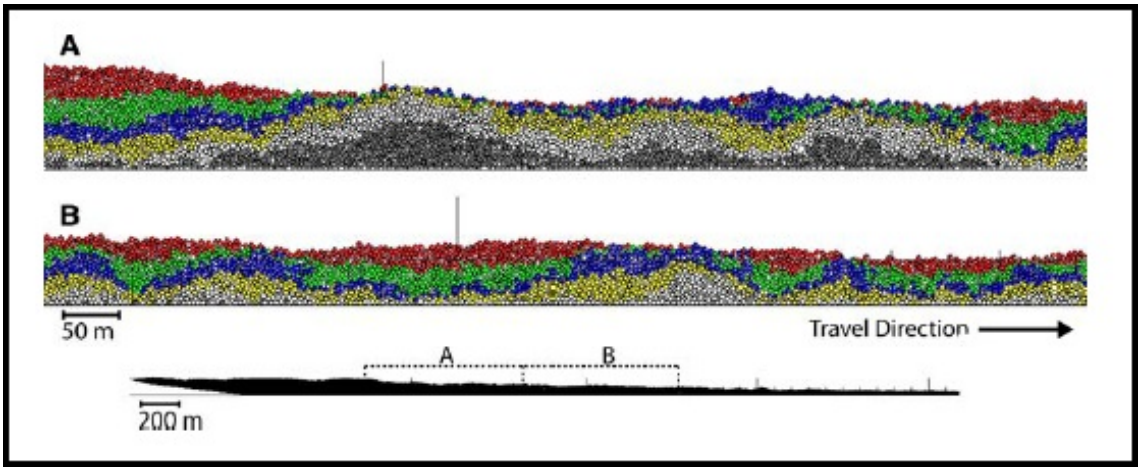

Figure 2.36: Stratigraphic layering from simulation by Thompson et al. (2009, Figure 11, pg 244) with the largest material property differences between layers.

After completing multiple flume tests using Ticino sand, Valentino et al. (2008) performed numerical simulations in PFC^{2D} to attempt to reproduce their flume tests and determine the applicability of discrete element numerical models to simulate high-speed granular flow. As with PFC^{3D}, calibration of material properties and boundary conditions occurred before testing began. The flume in the test was represented by the wall logic and the sand particles were modelled using the clump logic - where multiple discrete elements are bound together within a predetermined shape and can overlap. Biaxial tests were used to calibrate the numerical material with the Ticino

sand and multiple numerical flume tests were run to determine the appropriate damping coefficient so as to maintain as near as possible behaviour to that of the physical tests. To compare the 2D and 3D environments, Valentino et al. (2008) identified set x and y positions along the axes and checked the physical and numerical position and velocities at these positions. The numerical tests were found to match the laboratory experiments (see Figure 2.37), however as Valentino et al. (2008) explain throughout their paper, substantial amounts of calibration were required to represent this experiment with a discrete model.

Taboada and Estrada (2009) introduced a 2D Contact Dynamics approach to model a rock avalanche triggered by rain. As discussed in Cundall and Strack (1979) PFC^{3D} runs molecular dynamics and considers the particles to be soft, whereas Contact Dynamics considers the particles to be rigid, therefore removing the need for the contact model dynamics and damping. It was assumed in the model that the avalanche material is a cohesive granular material prior to fall that is subject to gravity. During the avalanche motion, Taboada and Estrada (2009) then assumed that the material became a dense flow of dry cohesive and frictional particles. The hypothetical trigger of the rock avalanche was rain and this increased the pore pressure along the dipping plane of the water table. Pore pressure was represented in the model by a volume force perpendicular to the slope which reduced the normal component of the particle weight. Once the reduction in effective normal force reached a critical value failure by way of shear rupture occurred. The layers of strata deformed and folded at the junction of slope and flat runout surface with some layers overriding the front surface. Effective normal force was found to decrease as the avalanche moved downslope and eventually stabilised at a higher value once the avalanche came to rest.

Prior numerical and experimental models discussed by Taboada and Estrada (2009) (including those of Friedmann et al. (2006) and Staron and Hinch (2007)) have identified three flow regimes

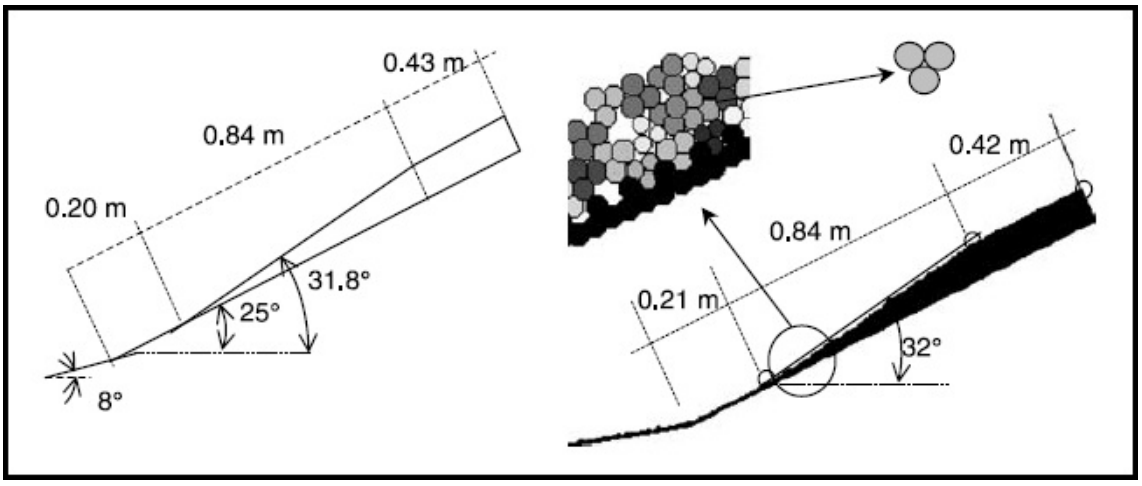

Figure 2.37: The comparison by Valentino et al. (2008, Figure 15, pg 173) between physical tests on Ticino sand (left) and the 2D DEM cluster model (right) showing a good match during runout.

that have varying velocity profiles throughout the depth of a rock avalanche. It is thought that the succession between flows is related to the dissipation of kinetic energy. At the front of a rock avalanche there is a plug flow; behind this is a simple homogeneous shear flow; at the rear is a two layer flow described as a flowing layer over a static layer. Taboada and Estrada (2009) also note that a large rockslide may transform into a rock avalanche where the slip surface exhibits dynamic weakening during the motion of the slide so long as the surface is rough or curvilinear.

Taboada and Estrada (2009) advance the hypothesis that dynamic weakening indicates a thermal pressurisation of pore fluid where, following Terzaghi's theory of effective stress, an increase in pore pressure sees a decrease in shear strength in a shear zone. The flash heating of material due to sliding causes decomposition of minerals and shear melting. They feel that this process is significant during the initiation of a rock avalanche and that large displacements and velocities enhance the process. This hypothesis draws similarities with that of frictionite proposed by Erismann (1979) as discussed in Section 2.1.6.

A DEM is used by Cagnoli and Piersanti (2015) to model laboratory chute experiments performed with granular material. Various particle shapes are used, one type per flow, to represent a more natural flow as opposed to spherical particles which have a low resistance to shear. Mead and Cleary (2015) also finds that particle shape has a major effect on the behaviour of a granular flow and the effect of friction. Cagnoli and Piersanti (2015) find that particle agitation increases downward within the flow. As grain size decreases there become more particles in the mass and any agitation due to interaction with the ground surface penetrates far less distance inside the flow.

A numerical model of the laboratory tests performed by Manzella and Labiouse (2009) is presented by Daudon et al. (2010) who found that the shape of the blocks and dissipation parameters play key roles in the numerical runout behaviour. This is also supported by Mollon et al. (2015) where larger bricks lead to a more collisonal flow while small bricks increase internal shear. A longer runout for blocks is found by Daudon et al. (2010) where the energy dissipation due to rolling after collisions is higher than the friction due to the sliding of the blocks. It was also found that gently undulating terrain disturbed the flow and that this reduced the overall runout length.

Langlois et al. (2015) utilise a 2D DEM to model the motion of a dry rock avalanche by using the collapse of a bonded granular column onto a horizontal surface as an analogue. Breakage of bonds occurs when the gap between two particles becomes larger than $\frac{1}{4}$ of the average particle radius. The results of the column collapse show that the majority of fragments are produced before 50% of the runout is reached with large blocks supported by a matrix of fine material. An increase in tensile strength leads to a decrease in runout length and Langlois et al. (2015) note that a weaker or highly weakened material will travel further. Langlois et al. (2015) state that their data suggests that runout distance increases with the degree of fragmentation, although they note that

they cannot determine if fragmentation increases the runout, if runout provides an opportunity for fragmentation, or if in fact their fragmentation model is too simplistic.

A 2D DEM model is also used by De Blasio and Crosta (2015) to consider the behaviour of blocks travelling on a smooth steep slope followed by a flat horizontal region. This topography is considered to characterise that followed by many real rock avalanches. The fragmentation of a block is allowed to occur in the model if the stress on a block is higher than a predetermined threshold value of 10 MPa, which is extrapolated from experiments of crushable aggregates. De Blasio and Crosta (2015) find that explosive fragmentation at the slope break causes a horizontal boost, the proportion of which is directly related to the amount of fragmentation. The amount of this boost decreases as the slope angle decreases. They note that most fragmentation occurs due to the effect of vertical stresses at the slope change (from the vertical component of the velocity) with grains in force chains subject to the most intense compressive stress and therefore more likely to break. De Blasio and Crosta (2015) note that fragmentation is likely dependent on normal stress and the localisation of strain.

Recent work by Johnson et al. (2016) involved the use of a two dimensional soft particle code to model a simple landslide, where the failure mass was formed into an HCP specimen and allowed to relax prior to release. This model follows directly from the work by Campbell et al. (1995) and is used to consider the mechanism that reduced friction in these earlier models. They note that the reduction of friction within a long runout landslide relies on a physical mechanism which they suggest is associated with a pressure variation, which relieves the overburden pressure. Johnson et al. (2016) noted that their results indicated short wavelength waves were the primary factor in the reduction of friction within the landslides they modelled, and that friction begins decreasing almost immediately following release. The authors considered the comparison of the effective normal stress felt at a point on the ground through the centre of mass of the landslide, versus the overburden pressure. The effective normal stress was found to oscillate around the overburden pressure. Johnson et al. (2016) state that when the effective normal stress is less than the overburden pressure, that friction is reduced and sliding will occur. The authors go on to note that the reduction in normal stress is consistent with the theory of acoustic fluidisation. The results of the testing by Johnson et al. (2016) are considered in relation to the compressional wave velocity of the pressure waves from their model, with the authors concluding that the pressure variations from their model produce low-frequency vibrations which if large enough may break particle contacts. Further, Johnson et al. (2016) state that the wave-length is determined by the particle size.

Criticism of the work by Johnson et al. (2016) has related to the lack of particle size distribution within the model and lack of consideration of prior work in relation to their results. Although these criticisms are valid for global applications of their results, Johnson et al. (2016) are careful to note that the results are interpreted only in relation to the work completed by Campbell et al. (1995).

2.4.4 Summary of Discrete Element Modelling

The theory underpinning PFC^{3D} is outlined in detail for completeness and to assist the reader with understanding the output from a DEM model. This discussion also outlines the capacity of a DEM to model events such as fragmentation and shows some of the limitations of the model, in particular, the shape of the discrete element. The BPM is used in this thesis to represent all rock materials that are modelled and therefore the process of creating a BPM is also outlined. To further support the use of PFC^{3D} for modelling rock and for micromechanical modelling of a sturzstrom, literature outlining prior research is discussed in areas relevant to this work. This includes impact testing, strain rate effects, crushing, packing of elements, shear box and triaxial testing, and granular or landslide modelling. DEM is regarded by O'Sullivan (2011) as a useful methodology for geomechanics problems and the literature reviewed in this section suggests that DEM is also a useful method for considering the fracture and fragmentation of rock.

2.5 Problem Synthesis

Small volume landslides (e.g. 1x10^5 m^3 or less), rock falls and other mass material movements are typically represented by frictional models. These models relate the behaviour of the material to Mohr Coulomb theory and presume that once the material strength is overcome, the material will move. This is seen in the Newmark Block Sliding model and also in slope displacement theory such as outlined in Jibson et al. (2006). These frictional models have been shown to represent the behaviour of small volume mass movements relatively well (e.g. Dufresne et al. (2010)). However the same models are not able to represent the movement of sturzstrom which travel further than these models would predict and contain substantial amounts of fragmented material.

Sturzstrom can travel upward of 10 times further horizontally than vertically and can travel this distance in less than 60 seconds resulting in very high speeds (e.g. >50 ms^{-1}) (see Section 2.1.2). Witness accounts note dust clouds, leaping material, boulders thrown clear and flow-like behaviour. The resulting deposits indicate little mixing with preserved stratigraphy and can sometimes show inverse grading. The deposited material is almost always angular in shape with a large amount of fines toward the basal area. Occasionally large fractured clasts and boulders can be found among the fine materials.

As discussed in Section 2.1.6 many theories to describe the behaviour of sturzstrom have been suggested and discussed within the research community with no consensus as yet on a definite concept to describe the overall phenomenon. Given that the deposited material is generally angular and has flowed as a dry avalanche, it would seem that the theory of fragmentation outlined by McSaveney and Davies has merit. The various work by Grady and Kipp (outlined in Section 2.2.3) supports the production of kinetic energy from dynamic fragmentation events and also discusses the influence of this kinetic energy on the movement of fragments away from the source of the impact.

The production of significant kinetic energy from the fragmentation of material under fast loading supports the concept of fragmentation assisting with the propagation of sturzstroms. In this thesis, the theory of fragmentation is investigated using concepts of effective stress, and hence, soil mechanics. Can the behaviour of a sturzstrom at the microscale provide evidence of a propagation mechanism? If it does, is this a localised effect or could this affect the macroscale behaviour?

In the majority of sturzstroms, and particularly in the examples outlined in Section 2.1, the avalanche failure can be broken into two or three distinct phases. Phase 1, the fall, describes the initial failure or detaching of the material and its subsequent vertical fall. This is followed by Phase 2, the runout. The runout encompasses the horizontal portion of the avalanche until the material comes to rest. Occasionally between the fall and runout may occur a leap — such as seen at Elm — when material jumps across or over an obstruction. There are situations where a sturzstrom may initially travel along a slightly inclined area (a minimum inclination of 25^o as

outlined by Heim (1932)) rather than undergo direct vertical fall. In this thesis, this situation is ignored during the initial investigations and considered later in Section 7.

Figure 2.38 outlines the behaviour considered at the fall and runout stages of a sturzstrom. The fall of a sturzstrom consists of the failed material traveling vertically until it impacts at the transition point between the vertical and horizontal, i.e. a change in topography. At this point it is anticipated that the basal material undergoes rapid loading due to the large volume of the failure with the resulting fragmentation providing propulsion for the next phase. This rapid loading occurs in a confined material producing an isotropic stress. The loads are vertical downward and normal to the horizontal plane therefore this phase of the avalanche can be readily represented by simple oedometric tests under high strain rate loading.

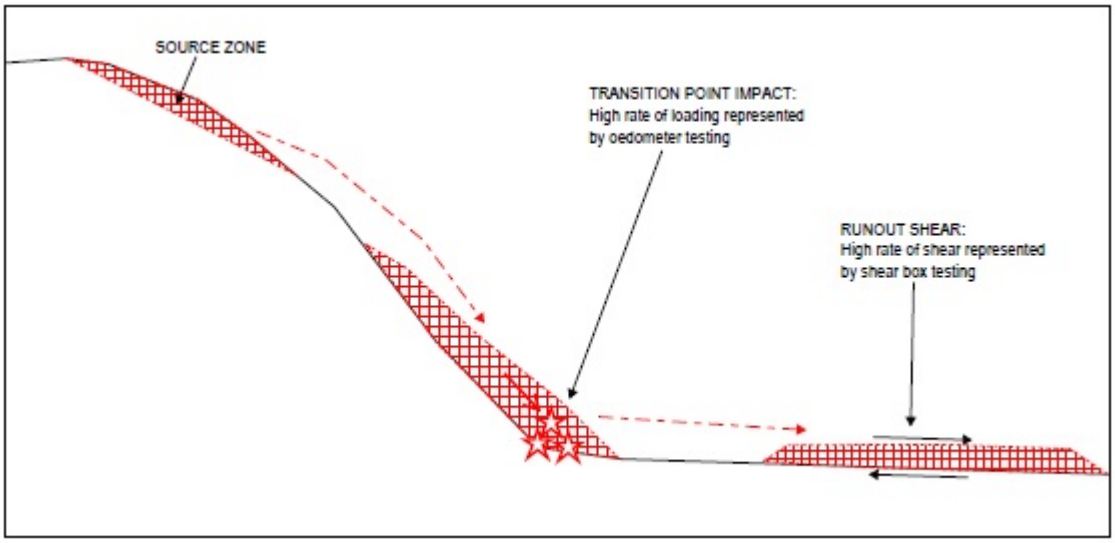

Figure 2.38: Sturzstrom runout and application of numerical testing processes.

Phase 2 of a sturzstrom results in the runout of the material along a relatively flat plane within a very short period of time. This suggests that the material is undergoing shear at high speed within its volume as runout occurs which produces a deviatoric stress. It is expected that during runout a proportion of the initial failed volume will behave as an overburden, however it is not clear what influence this overburden or the high speed shear have on the propagation of the material and what influence dynamic fragmentation may have. Shear box tests can be utlised to investigate this phase further by considering the overburden in combination with a deviatoric stress on the confined material from the shear speed.

Dynamic fragmentation in a sturzstrom is suggested to create a dispersive pressure that can reduce friction between fragments during runout. Thus for testing of the effects of shear and overburden on the runout of sturzstroms we simply need to investigate the critical state behaviour of the material. Utilising oedometer and shear box tests allows for clear inferences to be made in

relation to the critical state behaviour of material by following soil mechanics theory.

Sections 2.4 and 2.3 discuss methods commonly used to investigate material behaviour including DEM, continuum modelling and physical modelling. Rapid loading in oedometer tests and high speed shear box tests are extremely complex and difficult to perform in a laboratory setting and this approach has therefore not been considered in this thesis. Continuum modelling focuses on the macroscopic behaviour of avalanches and does not allow for consideration of the fragmentation behaviour of material which is crucial for the concept being investigated. In comparison, DEM allows for material to fragment and for the behaviour of the surrounding material to be monitored during the fragmentation process. This is very useful for the proposed investigation and DEM has therefore been chosen as the most appropriate approach for this thesis research.

2.6 Chapter Summary

Sturzstrom are catastrophic dry rock avalanches that occur around the world in steep mountainous areas. In populated areas these hazards are life-threatening and very difficult to predict. Initial research into the behaviour and mechanics of stuzstrom began after Heim investigated the Elm event of 1881. The various sturzstrom events discussed in this chapter indicate several key traits of sturzstrom:

- Excessive speed
- Long runout in comparison to fall height
- Carapace of large boulders is supported by fine rock flour incorporating broken angular rock fragments and fractured boulders
- Volume of initial material must be greater than 1 x 10^6 m^3 for a sturzstrom to occur however similar behaviour is seen in chalk flows
- Deposit shows stratigraphy from original site.

On a much smaller scale, chalk flows are noted to behave similarly to sturzstroms. The greatest concentration of chalk flows are based along the Kent coastline of England and the northeast of France. The collapse of chalk cliffs does not always result in a chalk flow. Soft, highly porous, saturated chalk is most likely to produce a chalk flow (e.g. Hutchinson (2002)). The deposit of a chalk flow retains stratigraphy like sturzstroms, and has a blocky carapace. It is thought that chalk flows could be a smaller magnitude sturzstrom event (Williams et al., 2004; Bowman and Take, 2014).

In this thesis, the long runout of sturzstroms and chalk flows will be investigated. Empirical relationships have been established between volume of material and runout distance, however, this must be based on some reduction of internal shearing resistance as the material travels, in order to reach such large distances from source.

Although the macroscopic behaviour has become clear over time as various events have been studied, the mechanics of sturzstrom behaviour are still being explored. The most recent theory postulated is that of fragmentation within the basal area of a sturzstrom contributing to its mobility, however with sturzstroms generally occurring quickly, and the impracticality of instrumentation, there is no clear evidence as yet to support this.

Fracture and fragmentation are outlined in this chapter due to the importance of both to the sturzstrom fragmentation theory and available kinetic energy to drive the runout. Dynamic fragmentation is an intense impulsive process that can occur due to a rapid deposition of energy through contact forces. The fast loading of rock specimens causes critical cracks to extend quickly

in comparison to the time taken to apply the load and causes a high stress state to be achieved before flaws coalesce so that more flaws participate in the failure of the material. Kinetic energy induced in a material by a dynamic load is the fuelling energy for catastrophic fragmentation events with significant amounts of kinetic energy available after fragmentation to move material within the system.

DEM is discussed in detail, as it is a useful method for investigating micromechanical behaviour in geomechanics problems. The Itasca PFC^{3D} program is a DEM based on a discrete spherical particle. Work outlined earlier in this chapter shows the capability of the program to model breakage and fragmentation phenomena as well as more computationally complex geotechnical laboratory tests such as shear box and triaxial testing. DEM has been used to model the macroscopic runout of landslides with reasonably similar results to experimental and real life landslides and avalanches.

The macroscopic behaviour of landslides has been modelled with continuum models largely governed by the St Venant shallow water equations, first modified by Savage and Hutter (1989). This model, which has now been extended to 3D by various authors, and DAN3D (a related model formulated by McDougall and Hungr (2004)) are both frequently cited in the literature as useful models of landslide behaviour. Continuum models are not able to provide detail of the small scale mechanics in a landslide.

Laboratory experiments have also been performed to investigate rock avalanche propagation and the fragmentation theory. Typically these experiments involve blocks of analogue rock material or large sized gravel released down a slope to a horizontal runout area, or into a geotechnical centrifuge for small scale testing of a sturzstrom. All results suggest that the more uniform the block arrangement in the release box the more fragmentation is seen in the debris. Given the limitations in size with centrifuge apparatus, it is not possible to model a full sturzstrom to test the fragmentation theory. So far, one fragmentation event has been successfully modelled in a centrifuge by Bowman et al. (2012) and Bowman and Take (2014).

The microscopic behaviour of sturzstrom has not been properly explored to date. Small scale particle and/or boulder behaviour can be idealised by using a PFC^{3D} model. PFC^{3D} models allow for the monitoring of the stress-strain response of synthesised rock material to exterior loading and shear. The remainder of this thesis fully investigates the usefulness of PFC^{3D} to model the micromechanical behaviour of sturzstrom and to determine if fragmentation is plausible as a mechanical theory of long runout.

Chapter 3

Idealised Agglomerate Modelling

3.1 Introduction

Two key events are considered here to occur during a sturzstrom — the fall and the runout — as shown in Figure 2.38. This is a simplification of the behaviour of sturzstrom used here simply to allow for the mechanics to be considered in discrete specimens. Both parts of the failure must be considered in relation to the possible influence of fragmentation on assisting the distance and spread obtained by the debris. This chapter focuses on the fall of the sturzstrom debris and in particular the impact of this debris at the transition to runout.

In order to investigate the effects of a substantial fall height on rock material, numerical oedometer tests are utilised on a synthetic rock analogue. Strengths and vertical strain rates are varied to attempt to understand how breakage and fragmentation may influence loading on and/or velocities of surrounding particles. Previous work, the test model adopted here and process are outlined and results provided for the tests performed in the following sections.

3.2 Previous Work in DEM

Synthetic representations of material are used for investigating geotechnical behaviour in 3D DEM testing (see Chapter 2). Work done by others such as Robertson (2000), Kafui and Thornton (2000), Mishra and Thornton (2001), McDowell and Harireche (2002a,b) and Cheng et al. (2004, 2003) on the crushing of particles has been considered for the initial oedometer testing. This earlier work clearly outlines methods and considerations for the use of DEM for modelling crushing and impact behaviour. The work by the individual authors is discussed in more detail below.

3.2.1 Robertson (2000)

In his thesis, Robertson (2000) considers crushing tests on singular agglomerates and aggregates or a system of agglomerates between platens using a code written by the author. The initial tests

performed were on HCP agglomerates with contact bonds and arbitrary stiffnesses. In an unusual move, Robertson (2000) chose to move the base platen upward at an arbitrary fixed rate of $1x10^{-4}$ ms^{-1} to crush the agglomerate rather than the top platen downward. The singular agglomerates typically fractured into two pieces and could rotate between the platens before crushing began. Increasing the bond strengths and ball stiffness increased the peak strength of the material and the ratio of the bond strength to ball stiffness was found to affect the brittleness of the agglomerate. Robertson (2000) also considered the variation of the rotation of the agglomerate and the removal of bonds on the fragmentation of the material.

Aggregate testing by Robertson (2000) involved building a system of agglomerates by creating a random set of particles with radius slightly smaller than the final size. The particles underwent radius expansion and the model was cycled to equilibrium. Robertson (2000) then created a list in the program memory of the central coordinates of the particles and deleted the particles whilst retaining the coordinates. Randomly rotated agglomerates centred at these coordinates were then introduced and the whole system cycled to equilibrium again. Again the base platen was moved upward to a maximum of 30% strain. Robertson (2000) indicates that constant breakage occurred from around 20% strain with the rate of bond breakage reducing as the tests proceeded and bond breakage leading to a reduction in vertical stress in some cases. Whether the agglomerate is singular or confined by other agglomerates Robertson (2000) notes that the agglomerates fracture into a number of fragments.

3.2.2 Thornton & McDowell

Using GRANULE, the Aston University version of TRUBAL from Cundall (1988), Kafui and Thornton (2000) formed face centred cubic packed agglomerates in a spherical shape by only accepting particles within that spherical region. A small centripetal gravity field was used to bring the particles together and adhesion between particles was achieved using a surface bond energy which could be varied to change the material strength. The agglomerate was then impacted against a wall with velocity imparted to all particles. The impact test ended when the wall force reached zero, no further breakage was occurring and the kinetic energy was constant.

At low velocities, no fractures occurred and the impact was considered similar to that of a solid sphere on a wall. Higher impact velocities caused breakage and deformation adjacent to the impact site with an increase in the wall forces. Kafui and Thornton (2000) found that the initial kinetic energy decreased as the impact velocity increased due to breakage, until the velocity reached a point where it was sufficient enough to produce multiple fragments; at this point kinetic energy increased due to the movement of the fragments. Increasing the strength of the material resulted in a reduction in breakage and a decrease in kinetic energy whereas decreasing the strength resulted in more fragments. Kafui and Thornton (2000) state that kinetic energy and the rate of breakage

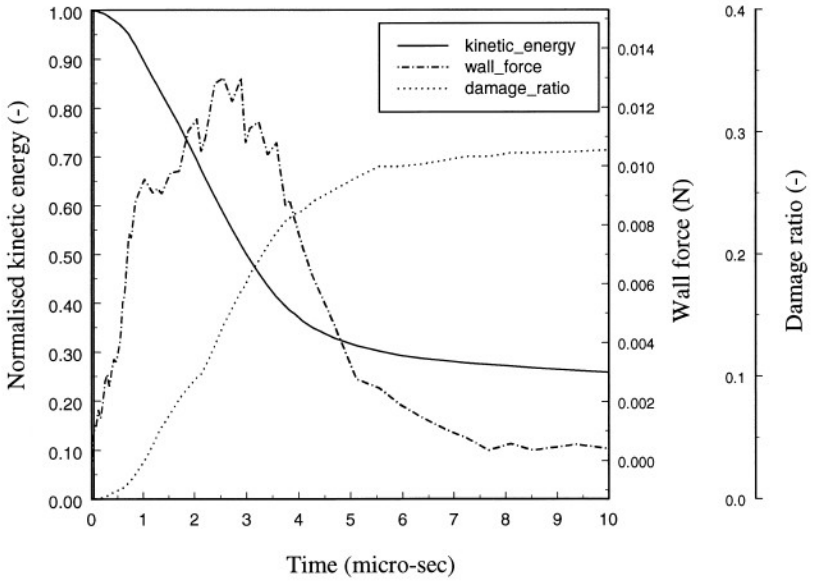

Figure 3.1: Breakage results as shown in Figure 1 from Mishra and Thornton (2001, pg 230) modelling.

are related during impact events.

Mishra and Thornton (2001) followed the process of agglomerate formation as outlined by Kafui and Thornton (2000) and considered the effects of impact velocity, bond strength, material porosity and density on breakage behaviour. An agglomerate was impacted against a wall at velocities of 0.5 - 2.0 ms^{-1} based on predetermined fall heights with the model allowed to cycle until the kinetic energy was constant. Figure 3.1 from Mishra and Thornton (2001) shows that breakage increased after impact with the wall and grew quickly during unloading as further fractures occurred. Kinetic energy reached a maximum value at impact with the majority of dissipation occurring once the wall force reached its maximum. An increase in impact velocity increased the forces on the wall and reduced the duration of the impact with the wall. They found that loose agglomerates disintegrated on impact whereas dense agglomerates or those with a higher coordination number fractured instead. Variation of the location of the impact site was found to affect only the breakage pattern.

Randomly rotated HCP agglomerates were bound with contact bonds and crushed between platens by McDowell and Harireche (2002a). The removal of particles to simulate flaws reduced the regularity of the initial specimen allowing the authors to show that PFC^{3D} could represent size effects on strength. Tests with varying platen velocities showed that at a velocity of 1.28 ms^{-1}, the velocity of the platen appeared to influence the behaviour of the material after fast fracture with a critical flaw propagating unstably through the agglomerate (McDowell and Harireche, 2002a). A platen velocity of 0.64 ms^{-1} did not appear to affect strength (axial forces for varying platen velocities are shown in Figure 3.2).

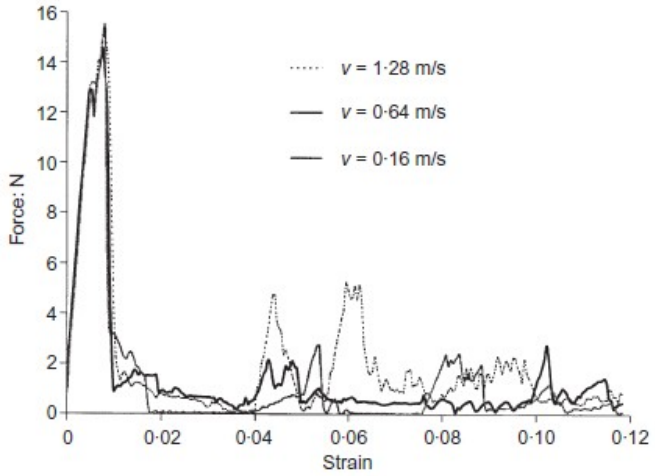

Figure 3.2: Wall force values at varying platen velocities as shown in Figure 2 from McDowell and Harireche (2002a, pg 132).

McDowell and Harireche (2002b) considered the compression of a granular material in an oedeometer using aggregates of the agglomerates described in McDowell and Harireche (2002a). They noted that the strain rate applied to the loading platen in the oedometer should be slow enough such that the stresses on the top and bottom platens are equal but also as fast as possible to produce an acceptable computational time. To ensure convergence with the time-stepping scheme in PFC^{3D}, the strain rate must be slow enough for the information at one side of the sample to propagate to the other.

3.2.3 Cheng et. al. (2003, 2004)

Following the work done by Robertson (2000) and McDowell and Harireche (2002b), research performed by Cheng et al. (2004, 2003) utilised hexagonal close packing to form clusters to represent sand grains. The introduction of flaws by removing a percentage of contact bonds, followed by crushing the flawed cluster between two rigid walls, allowed Cheng et al. (2004, 2003) to realistically model the crushing behaviour of sand grains.

Cheng et al. (2003) tested the crushing behaviour of sand grains to attempt to numerically represent the “stress level dependence of granular behaviour" (pg 634). The numerical work details the relationship between stress, crushability, yielding and plasticity as seen with sand grains. The results of the tests showed initial bursts of stress as the agglomerate rotated within the platens before breakage began. This was followed by the maximum stress occurring at the major breakage event of the test. The platens then continued to move toward one another with low stresses evident until another good contact was found to initiate the next major breakage event. Breakage is also found to occur during unloading (or disintegration) which they suggested indicates fracture

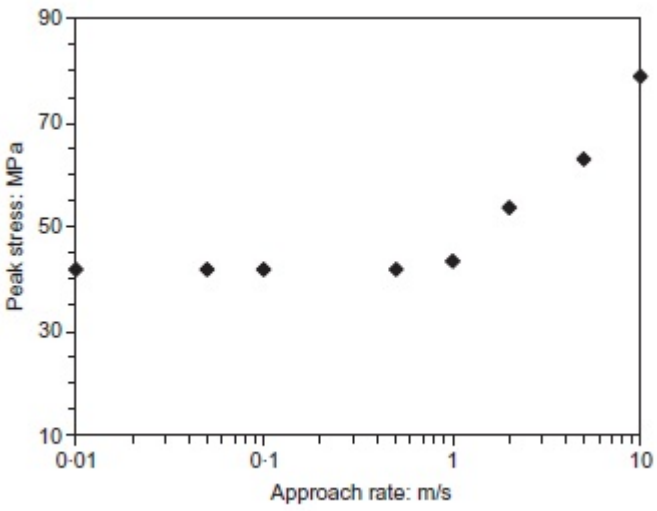

Figure 3.3: Figure 4(a) from Cheng et al. (2003, pg 635) showing peak stress against strain rate.

propagation.

Cheng et al. (2003) noted that high strain rates could produce inertia-induced crushing effects during dynamic cycling in PFC^{3D}. High strain rates as described by Cheng et al. (2003) lead to extensive breakage which is described in the dynamic fragmentation theory of Davies and McSaveney (2008) as very important for sturzstrom runout. Figure 3.3 shows the peak stress values attained by Cheng et al. (2003) in their sand grain crush tests across various platen speeds. Clearly, beyond a specific platen speed, peak stress is a function of the rate of compression, and at speeds greater than 1 ms^{-1} inertial strain rate effects occur that indicate a change of behaviour and strain rate dependence.

Cheng et al. (2003) tested their agglomerates by crushing them at 1 ms^{-1} — the speed where the pseudo-static rate of compression ended and changed to a dynamic rate of compression. This decision was made so that the material crushing would not be influenced by strain rate effects yet would allow for a higher rate of loading to reduce computational time. Testing agglomerates at a higher strain rate requires careful monitoring of the time-step and system energies to check for any signs of numerical convergence issues.

3.3 Crushable Material — Single Particle Tests

Following on from the work of Cheng et al. (2003) the testing of crushable material is extended here to the dynamic range, to determine the effects of applying a large overburden pressure via increasing strain rates. This series of tests involves synthetic material being confined and tested at increasing loading rates to determine when the change from static to dynamic breakage may occur for rock-like material and thus what additional behaviour may result in the model due to the

confinement and rate of compression. This testing regime was performed to mimic the material response to overburden pressure specifically where the topography in a typical rock avalanche changes from predominantly vertical fall to predominantly horizontal runout. Parts of this work have been published in Rait and Bowman (2010) and Rait et al. (2012) with the expanded details of the testing and results shown below and in Appendix C.

3.3.1 Measurement Parameters

The total energy of the system can be tracked in PFC^{3D} using six variables predetermined by Itasca and outlined in the Theory and Background manual (Itasca, 2008) and in Section 2. These individual variables are reintroduced here for completeness:

- Body Work – the total accumulated work done by all body forces (defined as gravity loading, applied forces and moments) on the system.
- Bond Energy – the total strain energy stored within the parallel bonds of the system.
- Boundary Work – the total accumulated work done by the walls on the system.
- Frictional Work – the total energy dissipated by sliding at all contacts within the system.
- Kinetic Energy – the total kinetic energy of all particles from both translational and rotational motion.
- Strain Energy – the total strain energy of the system stored at the contacts when using a linear contact model.

It is important to note that these variables are measured across the whole system and are therefore influenced by all particles. If particles are introduced with specific controlled behaviours, such as velocities and unbreakable bond strengths, the system energies need to be considered carefully and in some cases may be erroneous. For instance, unbreakable bonds will likely over estimate the bond energy across the system.

Another method that can be utilised in PFC^{3D} are measurement spheres which are useful, in particular, for stress-strain calculations. A measurement sphere can be placed within the system to measure the following parameters within that volume:

- Coordination Number – average number of active contacts per element
- Porosity – ratio of void volume within the measurement sphere to the overall volume of the measurement region
- Sliding Fraction – the fraction of contacts within the measurement region that are slipping

- Stress – the discrete contact forces and particle displacements are used to calculate an overall averaged stress tensor for the measurement region
- Strain Rate – a tensor representing the local strain rate within a measurement sphere.

For the tests in this chapter, the stresses in the boulder were initially monitored directly utilising the measurement sphere logic in PFC^{3D} (Itasca, 2008). As there was an interest in understanding the behaviour of the boulders according to critical state soil mechanics, the particles of the single HCP boulder and central boulder of the aggregate were considered particularly important. Therefore, because the individual particles may move away from the measurement circle once bond breakage has occurred, each particle was individually tracked. As outlined in Section 2.4.1 information regarding individual particles can be obtained using the PFC^{3D} FISH code. Following the details outlined in Section 2.4.1 the p' and q values of the boulders (Equation 2.13) could be monitored and reported on via summation of the mean and deviatoric stresses on each individual particle. System energies, breakage and overall wall stresses were also monitored throughout the testing process in order to determine the effect, if any, a fragmenting boulder may have on its surrounds.

3.4 Single Agglomerate

3.4.1 Test Process

Following Robertson (2000); McDowell and Harireche (2002b); Cheng et al. (2004, 2003), numerical modelling work was begun by testing whether an hexagonally close packed (hereafter HCP) cluster could represent a small rock boulder. The HCP code from Robertson (2000) is formatted for PFC^{3D} and was thus used to create HCP clusters of a maximum 1150 discrete spherical particles with the microparameters as shown in Table 3.1. Varying orientations were achieved by introducing a random component to the orientation of the axes when building the HCP cluster. As with the work by Cheng et al. (2004, 2003), 20% of the particles in each HCP cluster were removed to create a statistical variability in strength for each cluster and contact bonds introduced to produce material strength. Both the HCP packing and use of contact bonds produces a densely packed cluster with a high coordination number.

Itasca (2008) note in the PFC^{3D} manuals that contact bond values control fragmentation, which is the key type of failure being investigated throughout this thesis in relation to the relative exterior forces produced in a sturzstrom event. For the purposes of this section of testing on the single HCP cluster, two strengths were introduced of 4 N and 4 kN to determine the influence of bond strength on the breakage behaviour of the HCP clusters. Cheng et al. (2004) used 4 N as the bond strength of their sand grains, however as the intention here was to imitate brittle rock, 4 kN was introduced as a stronger bond strength to provide a comparison set of behaviours for a

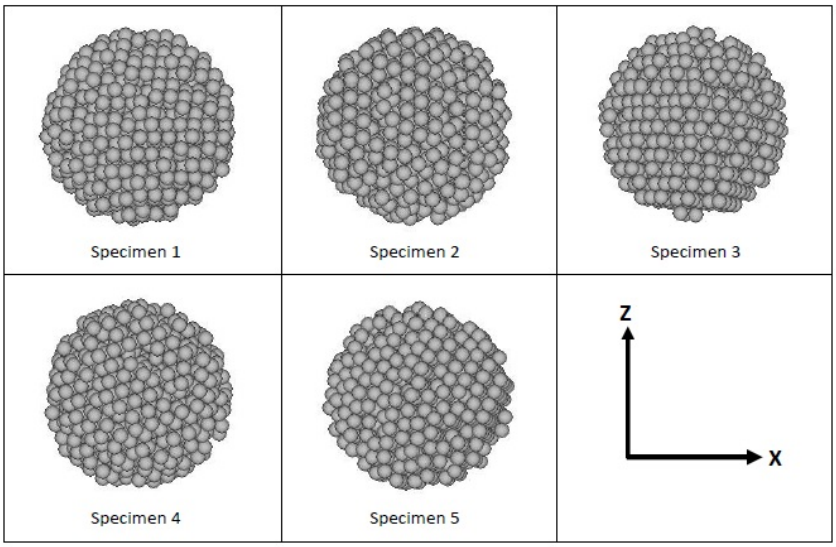

Figure 3.4: Crush test specimens

Table 3.1: HCP cluster microparameters

Parameter	Units	Value
Particle radius	m	0.002
Particle density	kgm^{-3}	2650
Cluster radius	m	0.25
Normal and shear bond strength	N	4 and 4 x 10^3
Particle normal and shear stiffness	Nm^{-1}	4 x 10^6
Particle friction coefficient		0.5
Percentage removal for flaws		20%
Number of Parallel Bonds		4050

ten times stronger material. The five randomly generated specimens are shown in Figure 3.4 with varying orientations.

Ball drop experiments with a single discrete particle were performed according to the method outlined in the Itasca Verification Problems manual (Itasca, 2008). These experiments confirmed the use of a critical damping factor of 0.2 to correspond to a coefficient of restitution of approximately 0.55 as outlined by Itasca. Rigid walls were used to represent platens and placed above and below the agglomerate before testing began (see Figure 3.5). The speed of the top platen was adjusted so that it would move downward to crush the agglomerate at various rates (see Table 3.2). The platen movement continued until 40% strain was reached at which point gravity was turned off so that there was no additional input of energy that could influence the kinetic energy already generated by the test.

As McDowell and Harireche (2002b) state, the time-stepping algorithm in PFC^{3D} requires the strain rate to be slow enough for information to travel through the specimen and for numerical convergence. Here, rather than slowing the strain rate which would nullify the intention of the

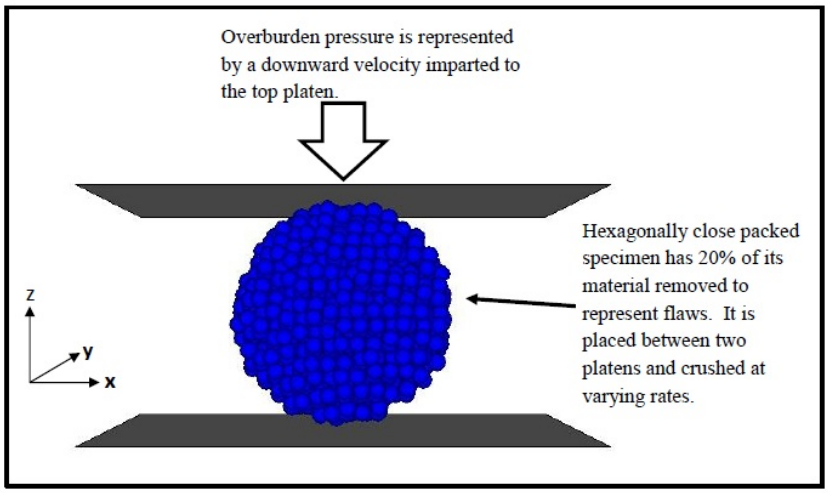

Figure 3.5: Crush test process for the HCP specimens (diameter of cluster is 0.25m).

Table 3.2: HCP crush testing platen speeds

Strain Rate (s^{-1})	Top Platen Velocity (ms^{-1})
0.1	0.05
1.0	0.50
10.0	5.00
50.0	25.00
100.0	50.00
120.0	60.00

dynamic testing, the time-step instead is manually reduced by at least two orders of magnitude. This is intended as a measure to allow for the model to capture changes in the material due to the fast advancing top platen and to reduce the likelihood of convergence issues.

3.4.2 Results

PFC^{3D} has the capacity to provide good visualisation of a model including fragmentation behaviour due to the loss of contact bonds. For the HCP agglomerate crush tests, Figures 3.6 and 3.7 were produced from the end state of the indicated strain rate models. It is clear from the lack of parallel bonds shown in Figure 3.6 that the 4 N material undergoes full breakage at all strain rates. The slower strain rates see the material collapse into a conical shape as broken particles fall under gravity. Under fast strain rates, gravity does not have time to act such that during the test the platen is able to collect the particles, so that by the time the test is completed the material has not had the opportunity to collapse.

In comparison, the 4 kN material behaves more like a brittle rock. At slow rates we see the material undergo a complete fracture causing around 3-4 fragments to develop (Figure 3.7). The larger fragments separate and come to rest on the base platen. As the strain rate increases the specimen again fragments, however here the fragments travel away from the centre of the

agglomerate rather than dropping to the base platen to settle. The fastest strain rate tests appear to be similar to the 4 N tests in that the material is crushed quickly and thus fragments do not appear to occur in the visualisation — instead, the loose particles separate the top platen from the remainder of the agglomerate which remains intact.

Figure 3.8 outlines the parallel bond breakages against strain rate for the two bond strengths tested. The graphs illustrate a clear difference in material behaviour which supports that seen in Figures 3.6 and 3.7. The 4N material undergoes complete breakage with no bonds remaining under any of the strain rates at 40% axial strain. Interestingly, the fast strain rates appear to take longer to break all of the bonds than the slow strain rates. In comparison, the 4kN material has a greater number of bond breakages under the fast strain rates, which is the behaviour expected of a rock-like material. The strain rate tests on the 4kN material result in just over 50% of the parallel bonds broken for the $120s^{-1}$ strain rate test.

The rate of breakage against shear strain is shown in Figure 3.9. Figure 3.9 (a) shows breakage from the slow strain rates occurs until a key point at around 20% strain rate, where a major breakage event happens which cleaves the material into two or more large fragments and fines. Figure 3.9 (b) for the stronger 4 kN bond strength indicates a growing number of breakages for fast strain rates, with consistent breakages throughout the test (as also seen in the 4 N case).

Appendix C contains the results for all individual specimens tested. This chapter will present the test results of one representative specimen with combined results for all specimens where appropriate. The appendix contains graphs of energy rates, breakage rates, stress paths and stress ratio for each bond strength.

There are clear differences in energy behaviour from slow strain to fast strain and between the two bond strengths. Figures 3.10 to 3.11 show the energy rates (J/time-step) against the percentage of strain for both bond strengths during the crush test of the single agglomerate. The energy rates are found from the overall energy variables outlined above in Section 3.3.1 that are available in PFC^{3D}.

Figure 3.10 show that as the strain rate increases kinetic energy increases for the 4 N test. In the slowest test, body work dominates where the other strain rate results suggest that boundary work dominates with kinetic energy increasing to noticeable levels from the strain rate test of 50 s^{-1}. At 100 s^{-1} the kinetic energy shows distinct peaks which appear to occur at the same time as a drop in the boundary work. Strain energy begins increasing as kinetic energy begins to climb.

The 4 kN crush tests produce quite a different energy behaviour. At low strain rates the energy rate values are greater than those for the 4 N tests, whereas the energy rates at high strain rates are similar (see Figure 3.11). As with the 4 N tests, kinetic energy begins to increase at 50 s^{-1} strain rate showing distinct peaks at 100 s^{-1}. The lower strain rates show a large amount of frictional dissipation energy which was not apparent in the 4 N tests, however, all strain rates show

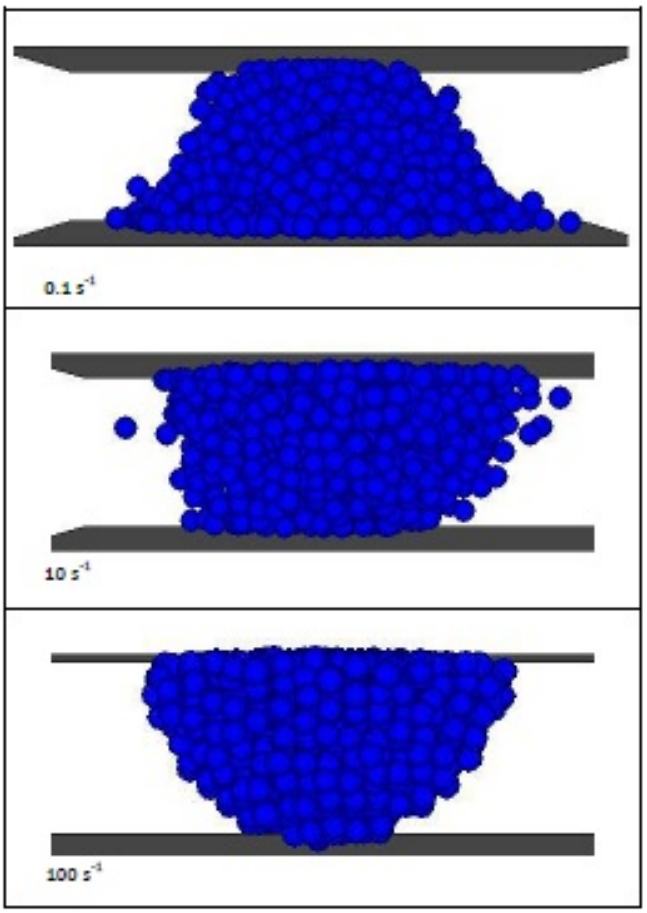

Figure 3.6: PFC^{3D} visual results for 4N HCP material at indicated strain rates. Note the complete lack of parallel bonds remaining in the agglomerate.

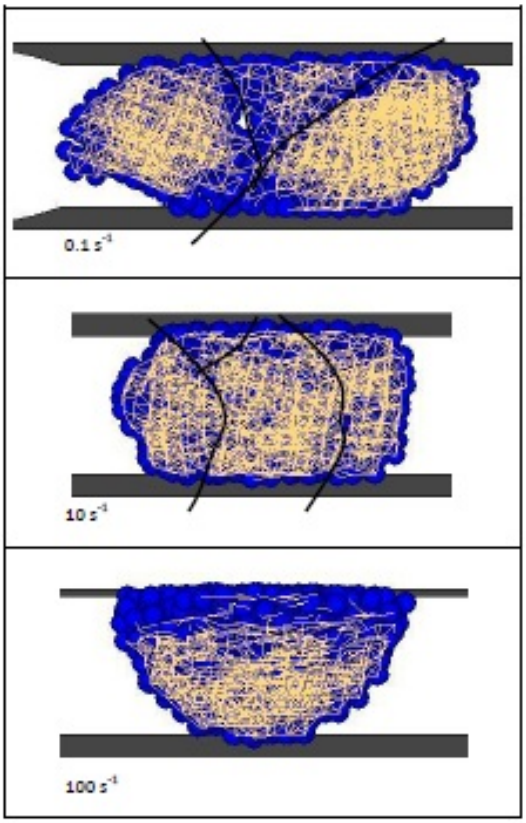

Figure 3.7: PFC^{3D} visual results for 4kN HCP material at indicated strain rates. Yellow lines show the remaining parallel bonds in the agglomerate and black lines represent possible fracture planes.

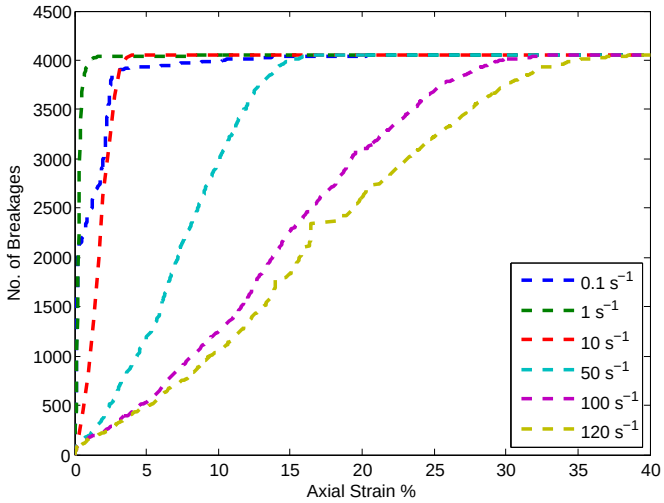

(a) 4N bond strength

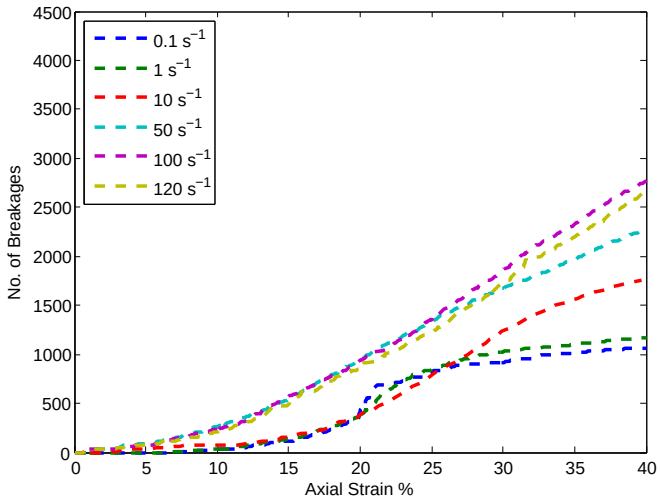

(b) 4kN bond strength

Figure 3.8: Parallel bond breakages for 4N and 4kN bond strength - Specimen 1.

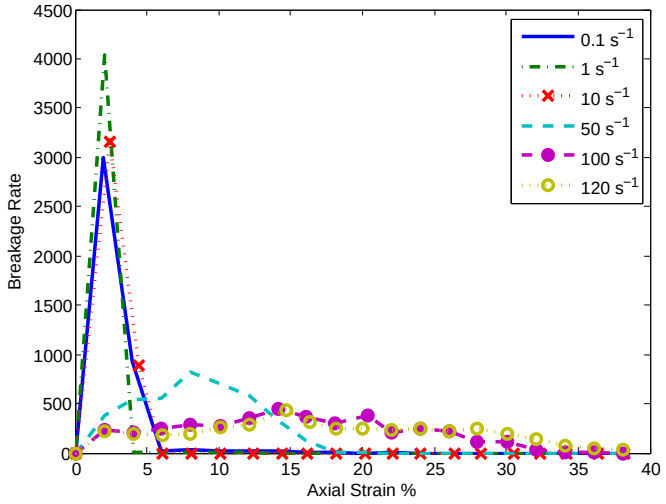

(a) 4 N bond strength

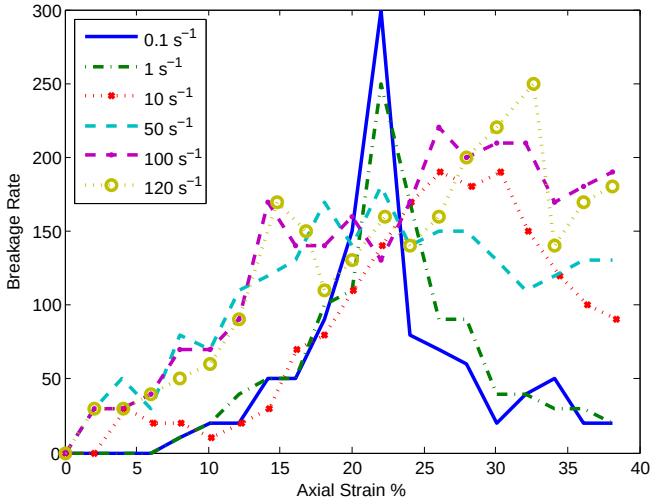

(b) 4 kN bond strength

Figure 3.9: Breakage rate of bonds at strain rates indicated - Specimen 1.

the domination of the boundary work as described above. The 120 s^{-1} test shows a substantial increase in energy over the 100 s^{-1} test, with greater increase in boundary work — a logical system response as the platen speed increases. Kinetic energy again shows distinct peaks and appears to produce more peaks for the 4 kN than the 4 N tests.

The similarity of kinetic energy response at higher strain rates appears to be related to the velocity imparted to the particles by the speed of the top platen. The lower strain rates of 0.1 s^{-1}, 1 s^{-1} and 10 s^{-1} cause fairly instantaneous breakage in the 4 N bond strength material while taking almost 20% strain to cause substantial breakage to the 4 kN material. Thus the energy

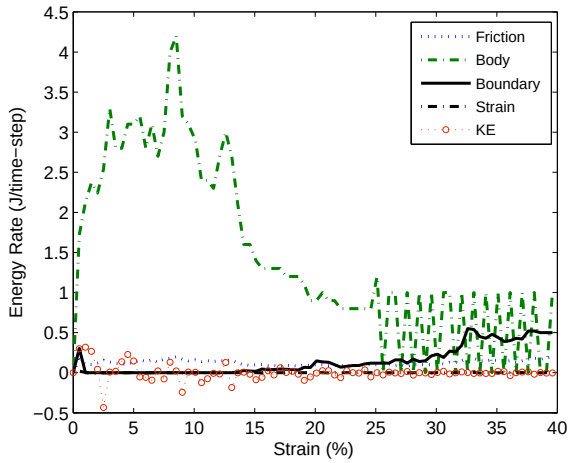

(a) 0.1 s^{-1} strain rate

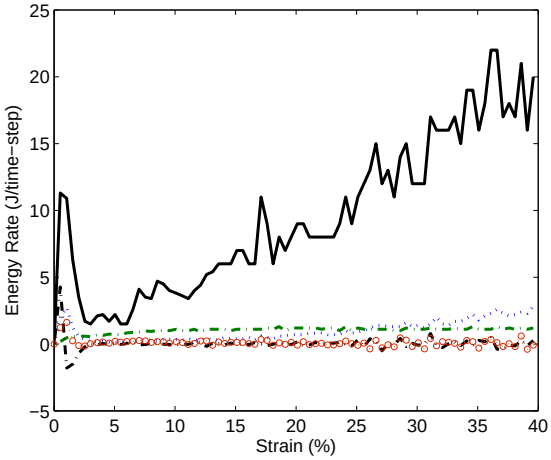

(b) 1 s^{-1} strain rate

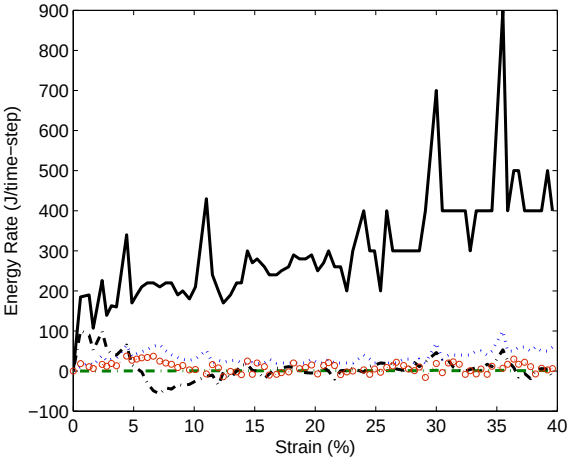

(c) 10 s^{-1} strain rate

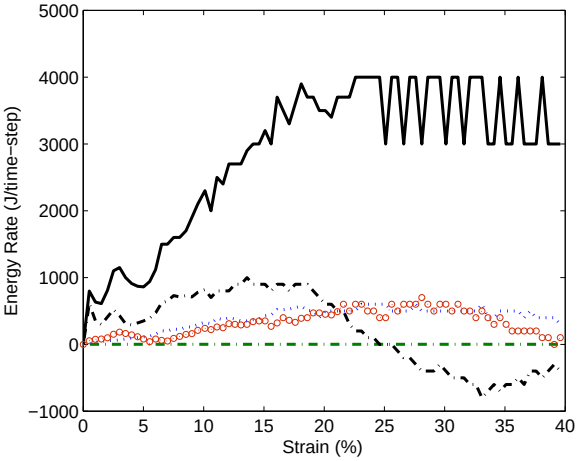

(d) 50 s^{-1} strain rate

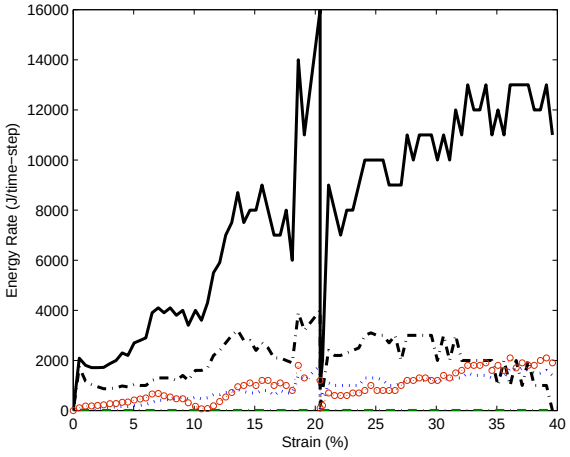

(e) 100 s^{-1} strain rate

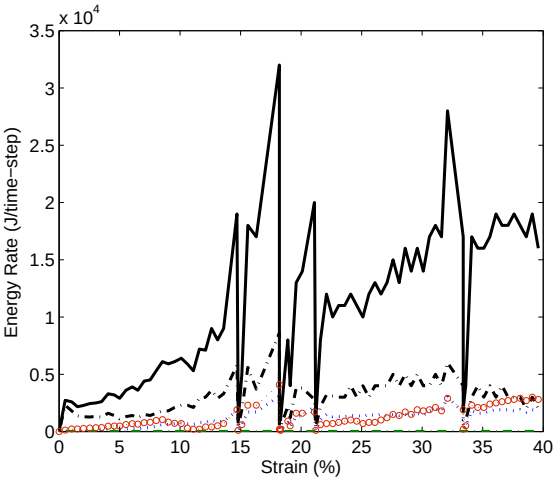

(f) 120 s^{-1} strain rate

Figure 3.10: Energy rates from all strain rate tests versus axial strain for 4 N bond strength - Specimen 1.

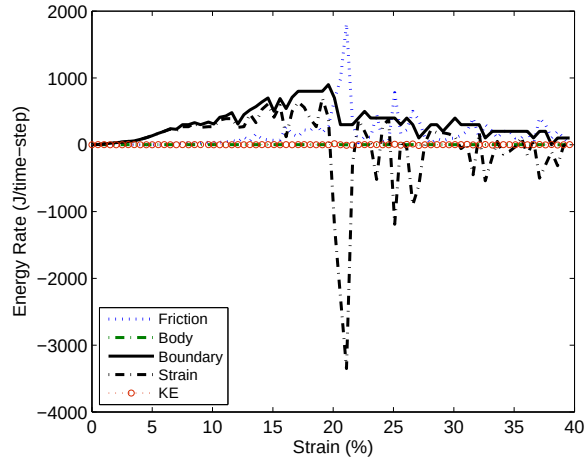

(a) 0.1 s^{-1} strain rate

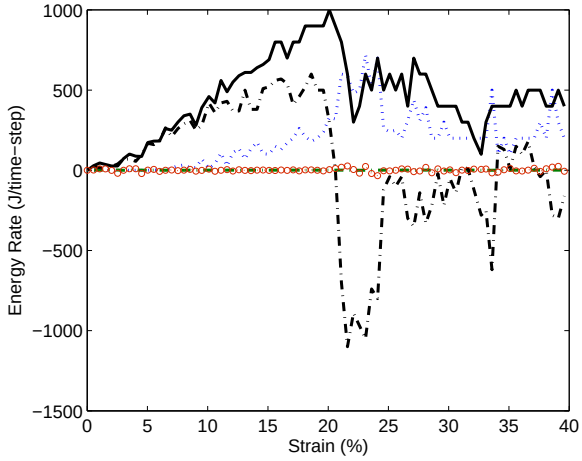

(b) 1 s^{-1} strain rate

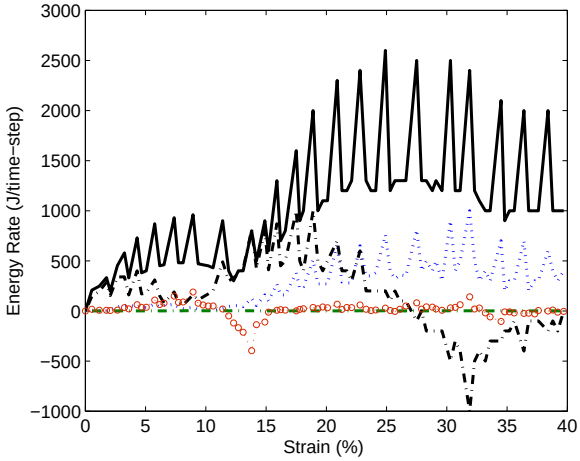

(c) 10 s^{-1} strain rate

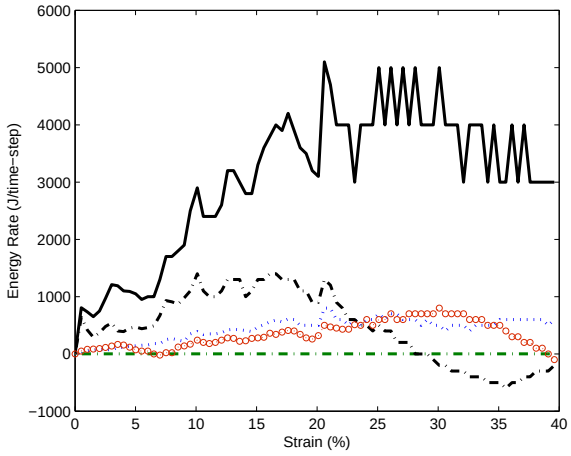

(d) 50 s^{-1} strain rate

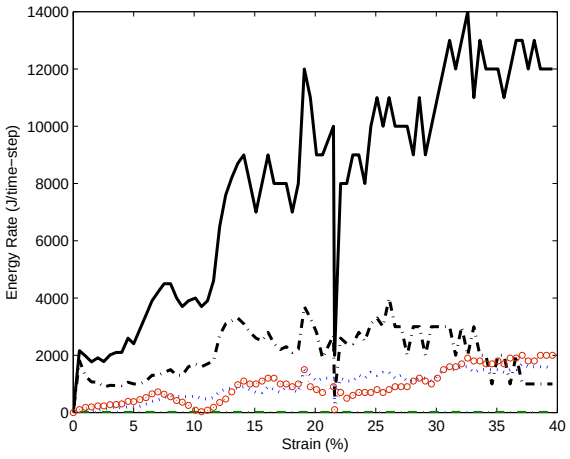

(e) 100 s^{-1} strain rate

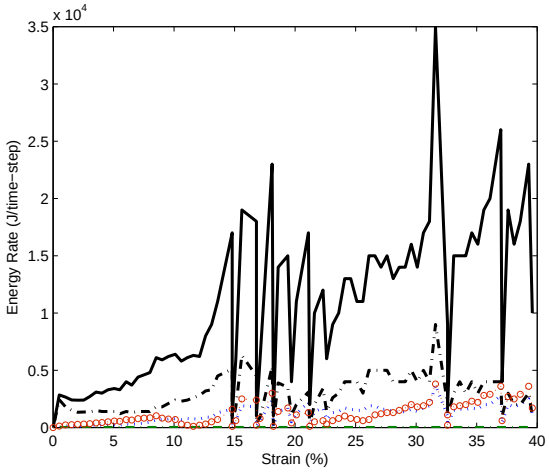

(f) 120 s^{-1} strain rate

Figure 3.11: Energy rates from all strain rate tests versus axial strain for 4 kN bond strength - Specimen 1.

rates are quite different between the materials at these strain rates, with greater kinetic energy produced in the 4 kN material once 20% strain is passed. In both the 4 N and 4 kN bond strength tests, at higher strain rates breakages occur more regularly with the kinetic energy response at approximately the same rate for both bond strength tests. At the end of the test there are no further breakages to occur in the 4 N material (Figure 3.8), however breakages can still occur in the 4 kN material. Thus, more kinetic energy is available overall from the stronger material, as would be expected.

Figure 3.13 shows the kinetic energy measured within the system from the particles and boundary work measured from the platens, for the slowest and fastest crush tests for each bond strength. The lower bond strength of 4 N indicates decreasing kinetic energy under slower strain as boundary work increases, with a few smooth oscillations over the whole test up to 40% strain. For the 4 kN bond strength under slower strain, the boundary work increases and kinetic energy sharply oscillates with a clear peak in kinetic energy at around 20% strain representing the first major breakage. Several clear peaks follow within smaller periods of oscillation perhaps suggesting that the platens gradually find additional points of contact for breakage as was also found by Cheng et al. (2003). Both bond strengths (4 N, 4 kN) show a growth in kinetic energy and boundary work for the fastest test of 120 s^{-1} and end at comparable levels.

The quantity of kinetic energy produced appears to be related to the quantity of breakage at that particular axial strain. Slow strain tests of the 4 N specimens appear to cause an instantaneous disintegration of the material, with perhaps key force chains allowing the force from the platen to travel directly through the HCP agglomerate almost immediately (see Figure 3.9 (a)). Interestingly, this fairly instant breakage of all bonds within the agglomerate does not translate to a substantial increase in kinetic energy, and with no further bond breakages throughout the test there is no additional kinetic energy introduced into the system thereafter. For the faster strain rate tests, the bond breakages occur consistently throughout the test. The kinetic energy at the fastest strain is virtually identical between the 4 N and 4 kN bond strengths and appears to be related to the velocities imparted to the particles by the platens.

Figure 3.12 is a detailed view of when kinetic energy peaks (or bursts) occur in the energy rate graphs depicted earlier in Figures 3.10 to 3.11. It can be seen that for the 4 N bond strength, each test represented in the graph has a distinct magnitude of kinetic energy achieved. The slow 0.1 s^{-1} test shows a gradual decline in the kinetic energy burst value as the axial strain increases. The 10 s^{-1} and 100 s^{-1} tests show fairly consistent kinetic energy burst value results at different orders of magnitude. The 0.1 s^{-1} test on the 4 kN bond strength specimen shows a general increase in the kinetic energy burst values, as the test proceeds the burst values reach toward the lower burst values obtained from the 10 s^{-1} test. This could be explained by the continued breakage occurring in the slower tests as seen in Figure 3.9. The 10 s^{-1} and 100 s^{-1} bursts increase over the first 10%

strain before reaching a consistent value where the kinetic energy bursts of the two strain rates are of $\mathcal{O}(2)$ in difference. The 4 N and 4 kN bond strength results show similarities in order of kinetic energy magnitude however the pattern of bursts over the axial strain of the test varies.

The stress path in terms of deviatoric stress q and mean effective stress p′ (as measured from local stresses in the boulder particles) for each test speed to 15% axial strain is shown in Figure 3.14 for the 4 N and 4 kN bond strengths for Specimen 1. (Note that a log-log relationship is plotted.) All specimens show similar linear behaviour and the graphs for the additional specimens can be viewed in Appendix C. Comparing Figure 3.14 (a) and (b), all stress paths are positive linear and the $\frac{q}{p'}$ stress ratio reduces as the strain rate increases which is more clearly seen for the 4 kN material. The low strain rate stress paths indicate a stress ratio of around 3 for both bond strengths with the high strain rate paths indicating a lower stress ratio of 1-1.5.

The individual mean and deviatoric stresses peak when the main breakage event occurs with the peak levels and behaviour being similar across all specimens (see 3.15). The overall similarity across strength and specimens at high strain rate suggests that the compression speed is partly, if not wholly, controlling the outcome of the test.

Stress ratio plots $\frac{q}{p'}$ against axial strain for the 0.1 s^{-1}, 10 s^{-1} and 100 s^{-1} tests are shown in Figure 3.16. The slower tests in general show a reduction in stress ratio over strain as the major breakages occur before settling to a critical ratio of approximately 1.5 for the 4 N bond strength and 2.5 for the 4 kN bond strength. For both bond strengths, there is a consistently decreasing trend in stress ratio with axial strain for the 100 s^{-1} test from around 3 to a critical ratio of approximately 1. This suggests a fast reduction in mobilised friction for a rapid application of overburden stress.

The 0.1 s^{-1} test for the 4 kN bond strength has very unexpected $\frac{q}{p'}$ stress ratio behaviour where at 20% axial strain the ratio increases before growing substantially after 35% axial strain. Movement in the $\frac{q}{p'}$ stress ratio is also seen in the 1 s^{-1} test after 20% axial strain, as the ratio begins to show an oscillatory behaviour. The growth in $\frac{q}{p'}$ stress ratio for the 0.1 s^{-1} strain test of the 4 kN bond strength may be attributable to a change in force chains due to the rotation of fragments between the platens, which may also occur in the 1 s^{-1} case. For instance Figure 3.17 (b) indicates that not all bonds (1060 of the 4050 bonds in the specimen) have broken at the end of the 0.1 s^{-1} test and that breakage slows at the same time that the $\frac{q}{p'}$ stress ratio begins to increase. It is possible that the platen pressure is being exerted on a very strong force chain which may take further strain to break.

Overall the increase in stress ratio for the 0.1 s^{-1} tests seems to indicate that the spherical particles (and possibly small fragments) in the model are rolling. This increase in stress ratio occurs at the same time as an increase in friction energy (refer Figure 3.11 (a)), suggesting that the rolling behaviour increases friction in the system. It appears that the slow strain rate tests

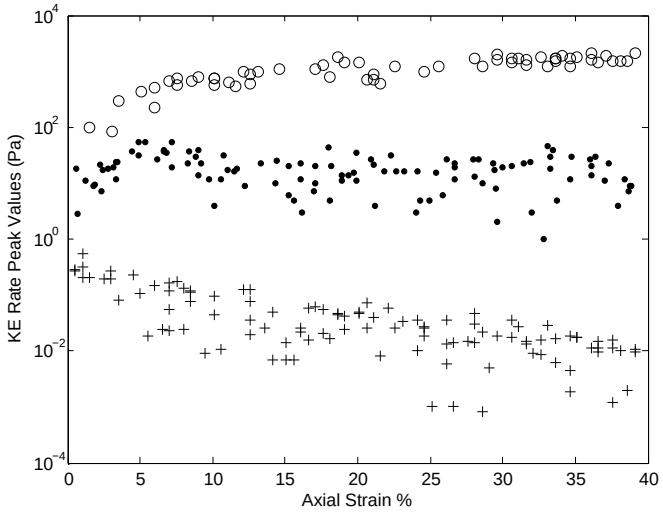

(a) 4 N bond strength

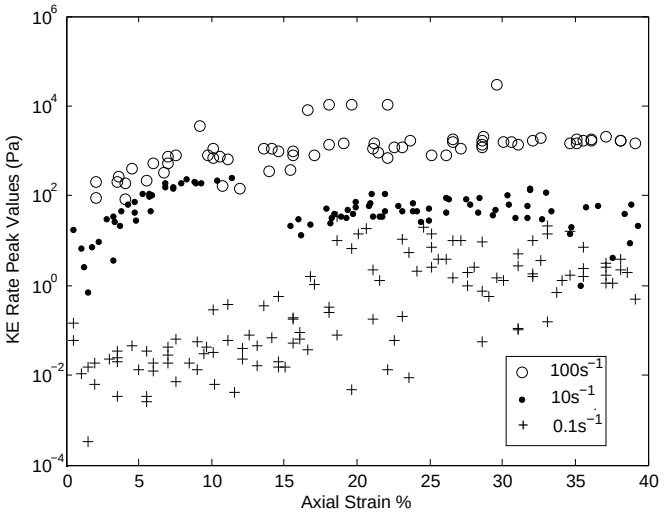

(b) 4 kN bond strength

Figure 3.12: Kinetic energy burst values from energy rates for tests 0.1 s^{-1} (cross), 10 s^{-1} (dot) and 100 s^{-1} (open circle) across all specimens.

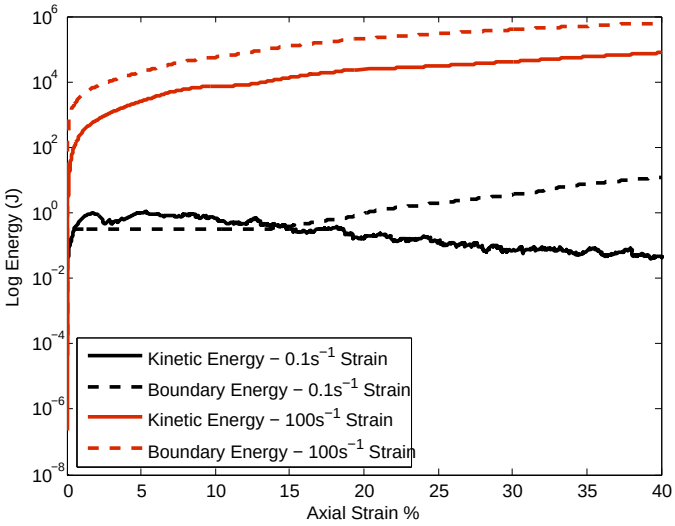

(a) 4 N bond strength

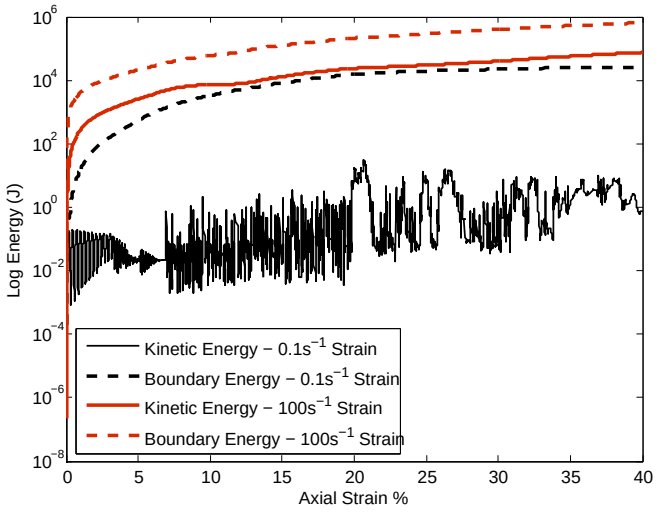

(b) 4 kN bond strength

Figure 3.13: Log of the kinetic energy and boundary work — a comparison between bond strengths for Specimen 1.

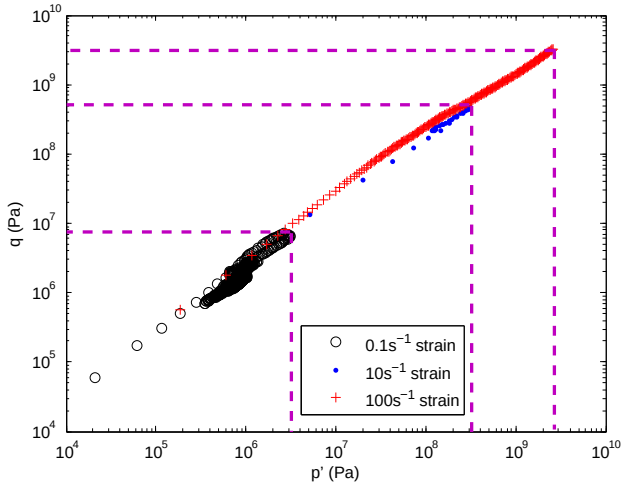

(a) 4 N bond strength

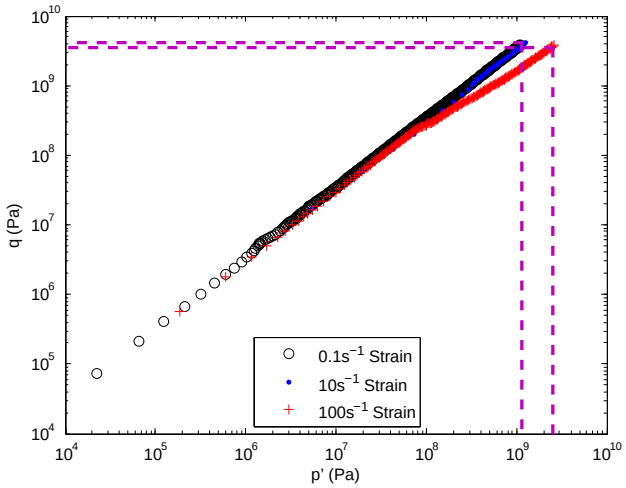

(b) 4 kN bond strength

Figure 3.14: Stress paths for 4 N and 4 kN bond strengths for Specimen 1 for indicated tests to 15% axial strain.

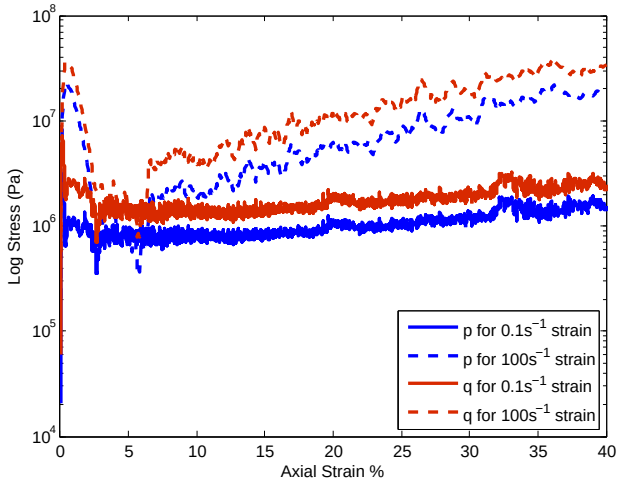

(a) 4 N bond strength

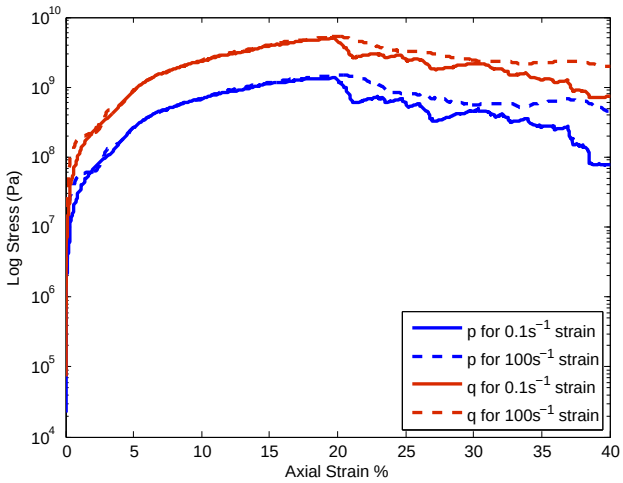

(b) 4 kN bond strength

Figure 3.15: Mean p' and deviatoric q stresses for 4 N and 4 kN bond strengths for Specimen 1 for indicated tests.

allow time for the 'broken' particles to rotate and hence attempt to dilate the system while being sheared, thus causing interparticle friction to increase.

A plot of the maximum kinetic energy values for all specimens versus strain rate is shown in Figure 3.18. Here we see a near power law relationship appear immediately for the weak material (blue) while the stronger material (black) shows similar values of kinetic energy at lower strain rates until reaching a strain rate of between 1 and 10 s^{-1}. At this point the stronger material responds with kinetic energy values similar (and in some cases almost the same) as those of the weaker material, and a power law relationship occurs at this point. Clearly the 4 kN material shows a change in regime from pseudo-static to dynamic. In the dynamic regime it appears that kinetic energy will be produced at the same value regardless of the material strength which indicates a relationship between the rate of compression and production of kinetic energy (i.e. the kinetic energy is derived from the platen speed). These results suggest that at low strain rates the regime is particle flaw dominated and at high strain rates is external energy dominated, which agrees with the work by Grady and Kipp (1987). Given that $KE = \frac{1}{2}mv^2$ the gradient of a linear line through the dynamic regime group in the log-log graph in Figure 3.18 should be 2 which is the case here.

Figure 3.19 shows the maximum axial stress achieved for each specimen during the series of oedometer tests for both the 4 N (green) and 4 kN (black) strengths. The values shown on Figure 3.19 show strong similarity to the maximum kinetic energy data in Figure 3.18. The 4 N data points are significantly lower than those of the 4 kN data until the 10 s^{-1} test when the maximum axial stress becomes similar and remains similar for the remaining tests. The 4 kN data show relative consistency for all specimens until the 10 $s^{-}1$ test, when strain starts to influence the peak axial stress reaching an inertial or dynamic regime. This suggests that prior to this test the material is showing a pseudo-static response, or that the peak axial stress is independent of the strain rate. For the 4 N bond strength tests, the peak axial stress is always a function of the strain

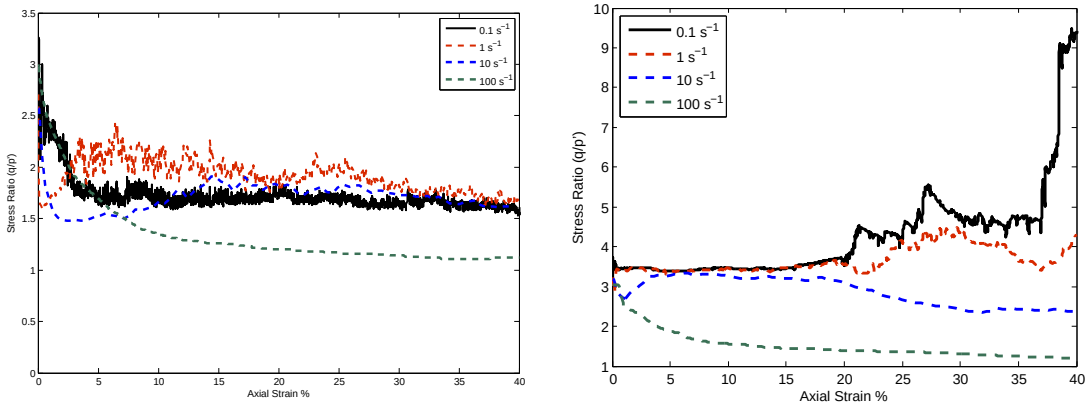

(a) 4 N bond strength

(b) 4 kN bond strength

Figure 3.16: Stress ratio comparison between bond strengths for Specimen 1.

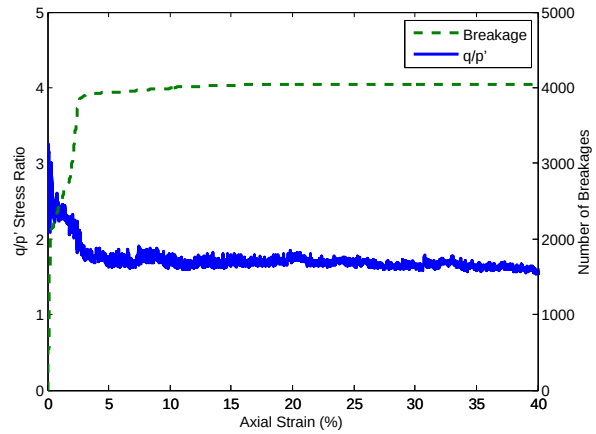

(a) 4 N bond strength at $0.1s^{-1}$ strain

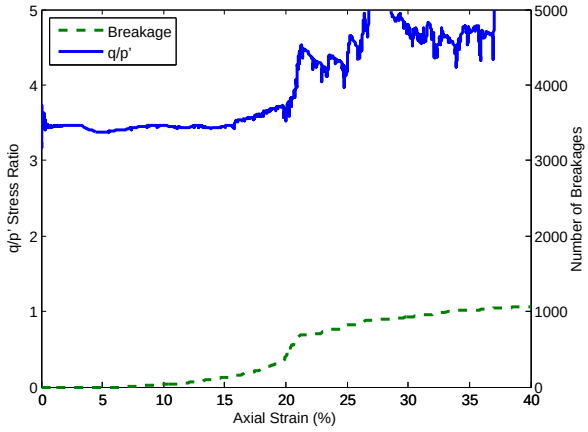

(b) 4 kN bond strength at $0.1s^{-1}$ strain

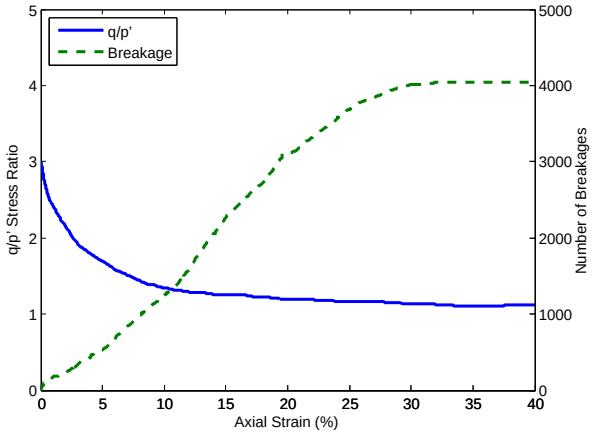

(c) 4 N bond strength at $100s^{-1}$ strain

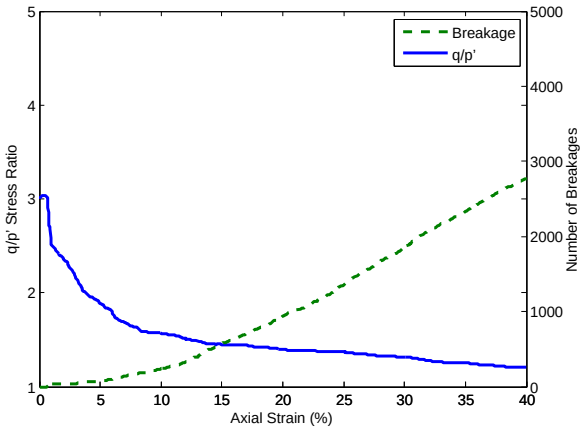

(d) 4 kN bond strength at $100s^{-1}$ strain

Figure 3.17: Comparison between stress ratio and breakage for Specimen 1.

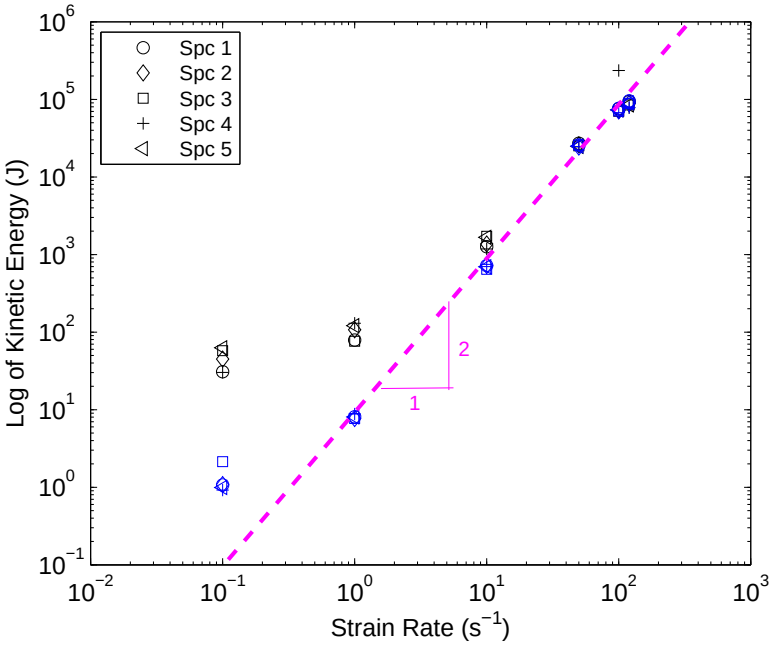

Figure 3.18: Maximum kinetic energy values for all strain rates where the blue markers represent the 4 N tests and the black markers the 4 kN tests.

rate, which suggests that even the 0.1 s^{-1} test is in the inertial regime for this bond strength. This shows that bond strength plays a role in determining the threshold for dynamic behaviour. In the 4N bond strength case, very low strain rates would be required to consider the transition from pseudo-static to dynamic.

3.4.3 Discussion

Single agglomerates crushed between two rigid platens at various strain rates have produced a clear power law relationship between strain rate and the maximum kinetic energy produced. Power law relationships for the fragmentation of material are suggested by Grady and Kipp (1987) to occur when a material is crushed at varying speeds. At high strain rates in the dynamic regime,strain rate effects begin to influence the crushing behaviour, as found by Cheng et al. (2004). Prior to the change of regime from pseudo-static to dynamic, the maximum kinetic energy produced is relatively similar across all specimens and strain rates, with small bursts of energy related to breakage of bonds. In the dynamic regime (1 s^{-1} onward for the 4 kN bond strength and from 0.1 s^{-1} for the 4 N bond strength) larger bursts of kinetic energy occur along with a more consistent breakage throughout the test period. Tests in the dynamic regime also indicate a reduction in mobilised friction.

At low strain rates once the first fracture has occurred in the agglomerate and the maximum stress is achieved, the top platen continues to descend until another contact is found on the ag-

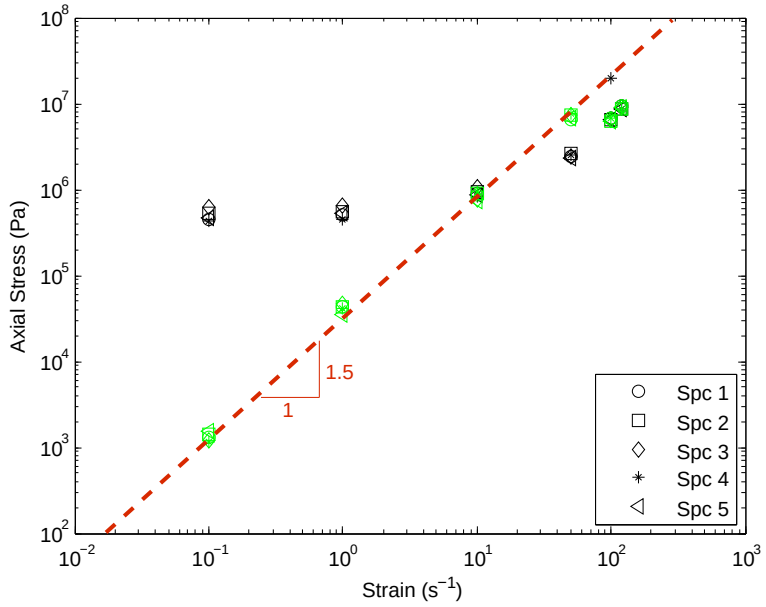

Figure 3.19: Maximum axial stress for all strain rates where the green markers represent the 4 N tests and the black markers the 4 kN tests.

glomerate — a behaviour also seen by Cheng et al. (2004). At this point another fracture may begin to occur. The breakage of the agglomerate into distinct fragments is consistent with the response found by Thornton et al. (1996) with the majority of the damage at high strain rates occurring at the impact point between the upper platen and the agglomerate.

The stronger specimen appears to behave as a more brittle material as seen by its stress and breakage response to compression, and thus is regarded as a more realistic representation of rock. The slow strain rate test of the 4 kN material takes longer to produce fracture and therefore peak kinetic energy. It appears that high strain rates are able to obtain peak kinetic energy almost instantaneously which suggests that the speed of the platen is overcoming the particles and causing an increase in the kinetic energy. However, this sharp rise in kinetic energy at the main period of breakage is also found by Mishra and Thornton (2001) as shown in Figure 3.1.

These preliminary crush tests show similarity to those performed by Cheng et al. (2004) and Mishra and Thornton (2001) and show that a fast compression rate is capable of producing larger amounts of kinetic energy from the same material than a slow compression rate. This suggests that testing the crush response of material in this manner is suitable for investigating the dynamic impact and disintegration that occurs at the topography change (vertical to horizontal) of sturzstrom events.

3.5 Agglomerate System

With the results from the crush testing supporting the hypothesis that high strain rates produce dynamic behaviour, additional testing with HCP formed agglomerate systems following from Cheng et al. (2003) was performed. In these tests a single breakable HCP agglomerate is surrounded in a cubic system by other HCP agglomerates that cannot be broken during the test. The interaction of fragments impacting the surrounding agglomerates or of fine material moving between agglomerates (that is, fully separated spherical particles that are no longer bonded to other particles) are investigated through oedometric testing of this cubic system. The oedometric strain rate test is designed to investigate the breakage behaviour of a rock when confined between other boulders as disintegration takes place.

3.5.1 Test Process

A cubic space of 0.3 m side length was formed from six rigid walls. Points within this cubic space representing the centre of 27 spheres of radius 0.05 m were placed into the memory of the model, each to represent the centre point of a future agglomerate. The memory list of the centre points was then used to form an HCP agglomerate at each position. Each HCP agglomerate was built in the same manner as the HCP clusters from Section 3.4 with details as indicated in Table 3.3 (note that the bond strengths are provided in force units). Each cluster was built in a random rotation and flaws were introduced by removing 20% of the particles (as done in Section 3.4) with material strength provided by the introduction of contact bonds. The walls were set in motion at very low velocity to bring the clusters into close contact without producing high initial stresses and the clusters were allowed to settle to equilibrium once contact was achieved.

Variation to the input to the random number generator of the program allowed for five statistically independent, yet similar, cubic specimens to be created. The cubic material was then tested in oedometric compression by assigning a velocity to the upper platen and continuing the compression until 40% strain was achieved as performed for the single agglomerate crushing tests in Section 3.3. The testing was designed to investigate how boulder fragmentation occurs under a compressive process within a sturzstrom during runout. As with the original cluster testing, the differences between each cubic specimen directly relates to the orientation of the cluster and placement of flaws – both of which are determined randomly as each HCP cluster is created. Oedometric strain rate tests were performed on each sample ranging from quasi-static compression at 0.001 s^{-1} through to fast compression at 10 s^{-1} (see Figure 3.20). The bond strength of 4 kN was utilised for this series of tests, as it was found in Section 3.4 that this bond strength allowed the HCP material to behave in a more rock-like manner.

Table 3.3: HCP agglomerate microparameters

Parameter	Units	Value
Particle radius	m	0.09
Particle density	kgm^{-3}	2650
Cluster radii	m	0.5
Normal and shear bond strength	N	4 x 10^3
Particle normal and shear stiffness	Nm^{-1}	4 x 10^6
Particle friction coefficient		0.5
Percentage removal for flaws		20%

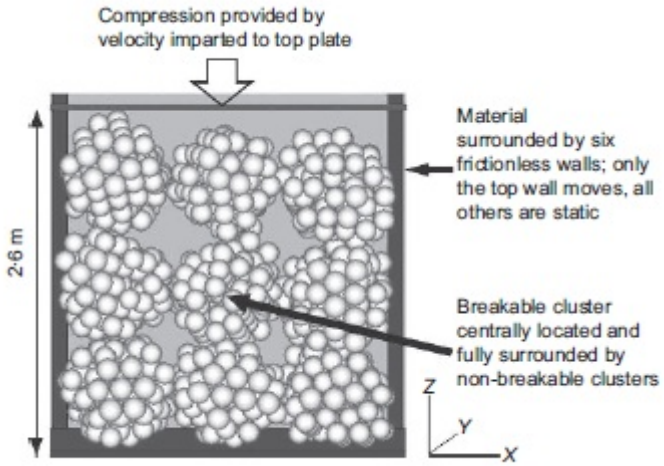

Figure 3.20: Agglomerate system testing process.

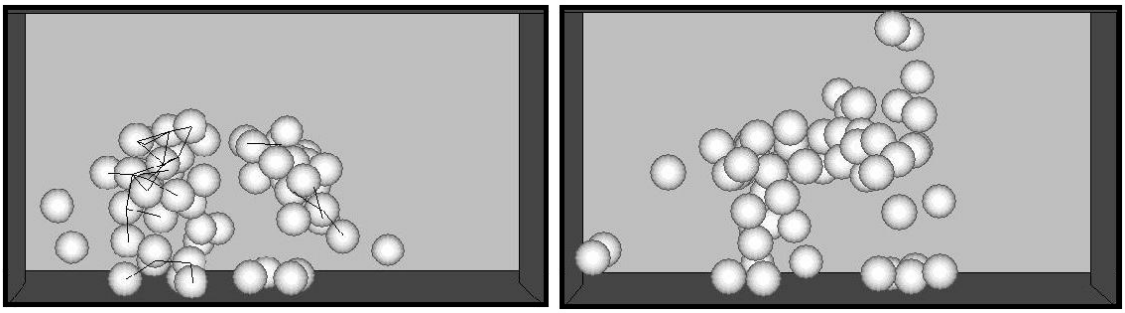

Figure 3.21: Example of the resultant breakage in the central cluster for the agglomerate system test for Specimen 3. Left at 0.001 s^{-1} and right at 10 s^{-1}. Lines between particle centres indicate intact parallel bonds.

3.5.2 Results

PFC^{3D} allows views to be taken of the central breakable cluster during the test process. Shown in Figure 3.21 are the results specifically for Specimen 3 at the end of the test (40% strain). The pictorial results show a clear difference in the breakage behaviour and movement of fragments and fines. The slow strain rate test of 0.001 s^{-1} indicates that several fragments of the central cluster remain intact with all fine material and fragments either remaining suspended within the surrounding clusters or settling toward the base platen. In comparison, the strain rate test of 10 s^{-1} shows that complete breakage has occurred with the resultant fine materials suspended between the surrounding clusters, settling on the base platen and travelling toward the top platen between clusters. This suggests that at high strain rate, fine material can move between clusters and potentially influence cluster interaction, if suitable gaps exist between clusters in which to move.

The microscopic stress paths for Specimen 3 for the strain rates of 0.001, 1 and 10 s^{-1} are shown in Figure 3.22 where the deviatoric stress q is plotted against the mean effective stress p'. These strain rates are chosen to represent pseudostatic, transitional and dynamic strain rates, respectively (see Figure 3.18 in the previous section and Figure 3.27 later in this section). The stress paths are plotted to 15% axial strain as at this point it appears that loose spherical particles may begin to influence the stress path response by rolling within the system and therefore introducing unrealistic behaviour into the system. The stress paths produce similar results in the early stages of the compression tests up to approximately 6% strain. Deviatoric stress q reaches a peak of 12 MPa at an axial strain of 15% whereas for the 10 s^{-1} strain rate q peak rises to 46 MPa at the same strain.

The maximum stress path values across all specimens are shown in Figure 3.23. All values occur at 15% axial strain and the graph shows a clear relationship between stress value and strain rate. There is a notable difference between the maximum stress path values observed with the 10

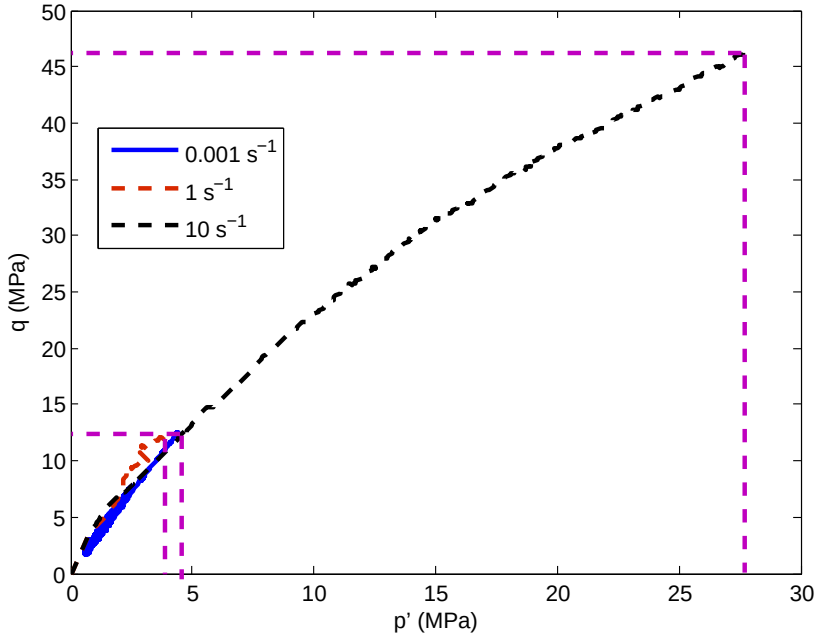

Figure 3.22: Stress paths for agglomerate system test for Specimen 3.

s^{-1} maximums substantially larger than those of the 0.001 and 1 s^{-1} rates which are comparable. Thus all specimens show a similar behaviour to that outlined above for Specimen 3.

For comparison of stress ratios, Figure 3.24 plots the macroscopic stress ratio for the central breakable boulder for Specimen 3. In this plot we see that with an increase in axial strain, the stress ratio varies quite erratically for the 0.001 s^{-1} strain rate test. Each peak that occurs throughout the test appears to be associated with large numbers of bond breakages (compare Figure 3.24 to Figure 3.25). The first large breakage event occurs at approximately 5% axial strain and produces a drop in the stress ratio while the material settles during the next phase of overburden pressure increase.

Bond breakage occurs gradually for the 1 s^{-1} test from an axial strain of around 5% where the breakage produces positive spikes in the stress ratio which are less abrupt than those seen in the 0.001 s^{-1} test. In contrast the 10 s^{-1} test shows a period of almost constant stress ratio before a decrease occurs at around 6% axial strain as breakage commences. The stress ratio for this test then continues to decrease and remains below that of the low strain rate tests until toward 25% strain rate when the stress ratio appears to meet that of 1 s^{-1}. This stress ratio behaviour suggests that the application of a high strain rate causes a reduction in interparticle friction during the main breakage period. Ultimately, the critical behaviour of all tests becomes similar as they move toward 40% strain which may be the result of particles rolling due to the loss of all bonds.

The response of the wall stresses between the varying strain rates provides an interesting comparison. In Figure 3.26 (a)-(c) the averaged wall stresses across all tests at the indicated strain

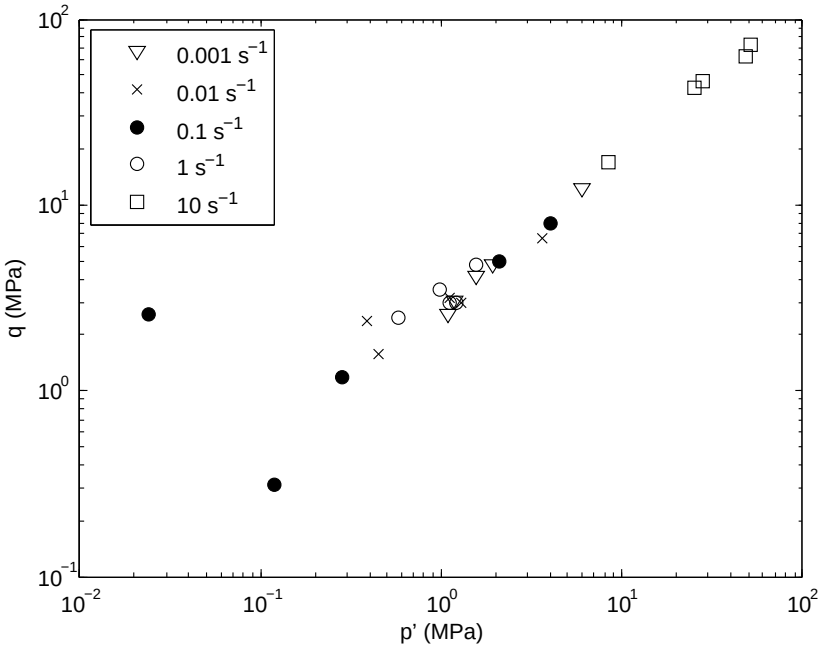

Figure 3.23: Maximum stress path values for all agglomerate system test specimens at indicated strain rates. Note that these values occur at a maximum axial strain of 15% for all tests.

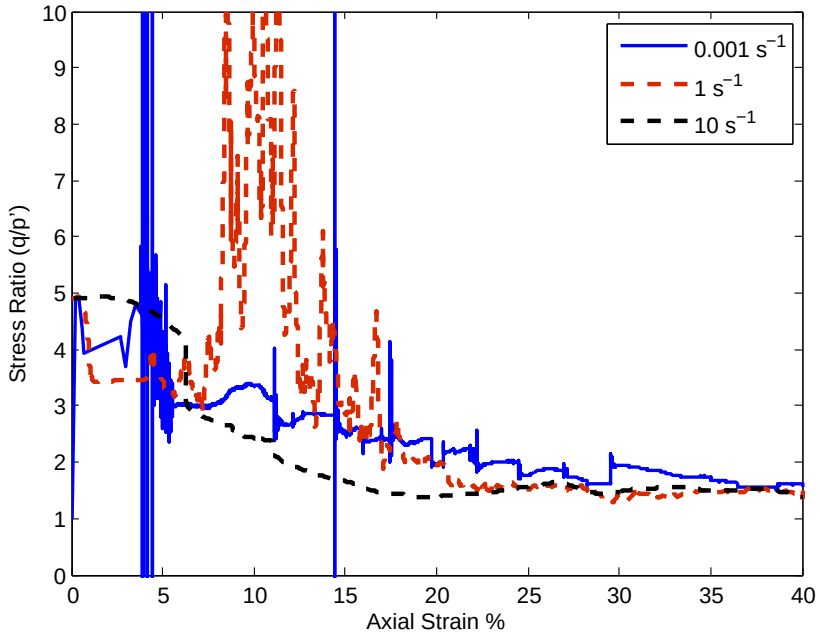

Figure 3.24: Stress ratio $\frac{q}{p'}$ plotted against axial strain for Specimen 3 in the agglomerate system test at the indicated strain rates.

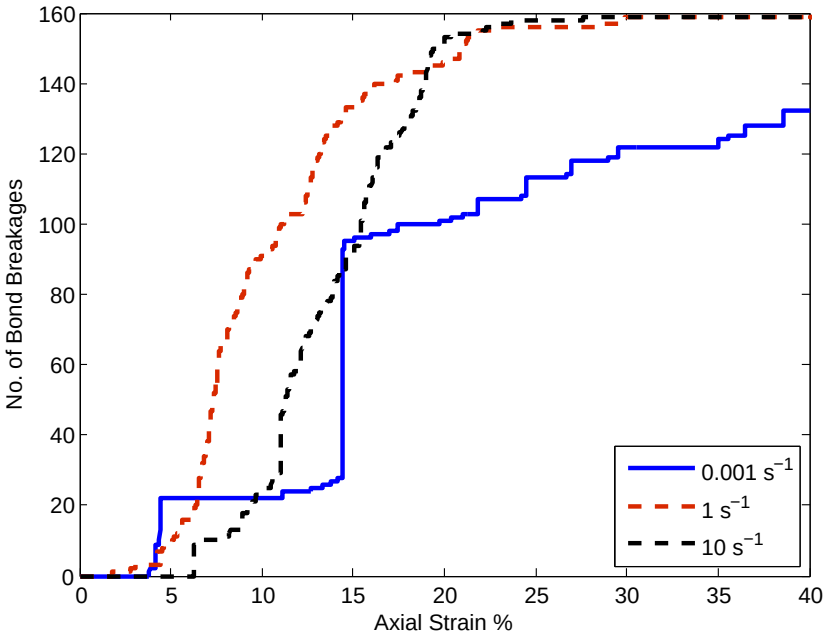

Figure 3.25: Bond breakages for agglomerate system test Specimen 3 at the indicated strain rates.

rates for the X- and Y- directions are given. The bars on the graphs represent the range of wall stress observed across all specimens which is fairly large. Figure 3.26 (d) shows results from an individual specimen. This indicates that once breakage begins, the material becomes non-isotropic and thus the X- and Y- direction wall stresses differ considerably. This non-isotropic behaviour is reflected in the graphs of Figure 3.26 (a)-(c), however, overall the maximum and minimum wall stress values are similar at all strain rates.

Looking in detail at Figure 3.26 (d) shows that the pseudostatic 0.001 s $^{-1}$ test experiences a smooth increase in wall stress as strain increases. The dynamic tests at 1 and 10 s^{-1} exhibit a distinctive “wave-like" pattern with increasing strain. As the strain on the material increases, the compression causes the material to move toward the side walls in order to alleviate the overburden stress – or deform in response to the compression. This deformation eventually reaches a point where fragmentation occurs resulting in the fragmented material moving away from its source centre. So particle movement will create a force on the side walls in both situations. When the strain rate is high the forces from the particles will not be consistently applied against the wall as the forces on the particles will be occurring more sporadically with material breakage. Therefore the wave pattern appears to occur due to an interaction between the compression effect and the response of kinetic energy associated with the rate of compression.

The maximum kinetic energy has been plotted against the applied strain rate for all five HCP specimens tested in this series and is shown in Figure 3.27. The maximum kinetic energy remains constant for the slow pseudostatic strain rates and the difference between specimens is consistent

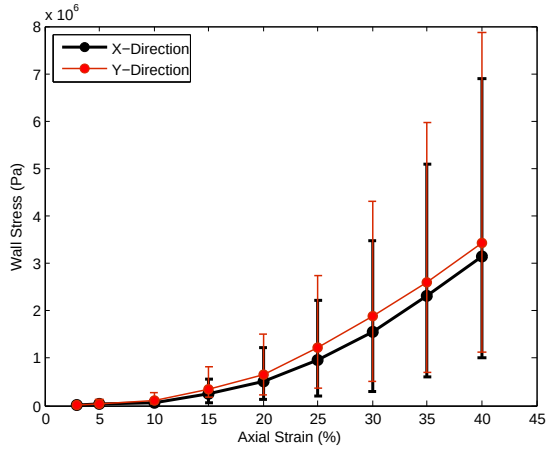

(a) 0.001 s^{-1} strain rate

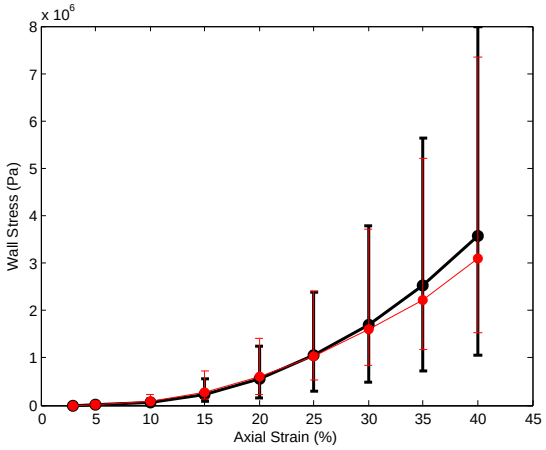

(b) 1 s^{-1} strain rate

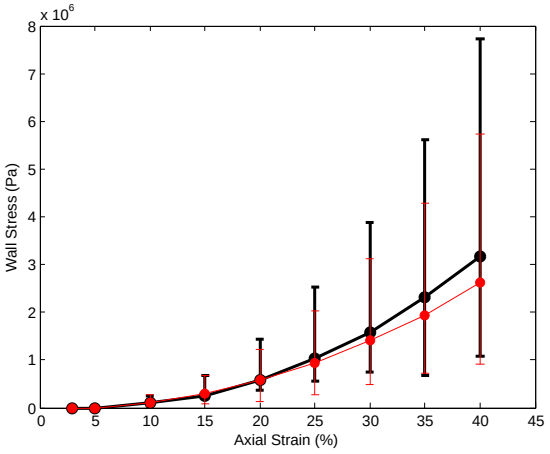

(c) 10 s^{-1} strain rate

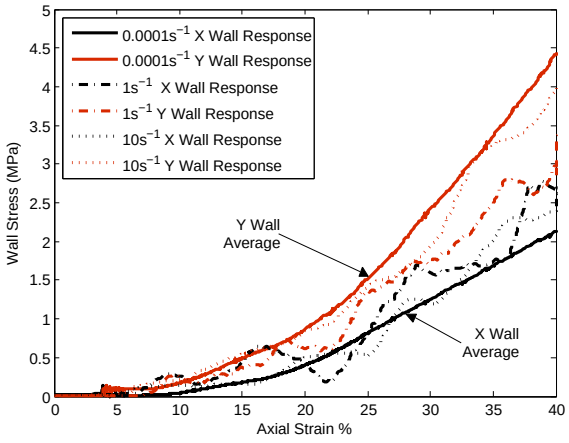

(d) Specimen 3 wall stress averages for agglomerate system test.

Figure 3.26: X and Y direction average wall stresses for all agglomerate system test specimens (a)-(c) where the error bars indicate the observed range of response. (d) The average wall stress response for agglomerate system test Specimen 3.

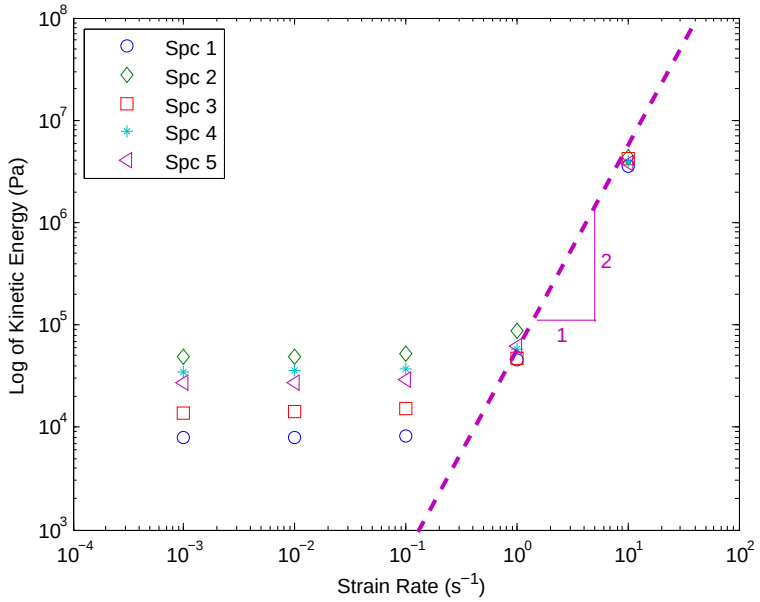

Figure 3.27: Maximum kinetic energy comparison for all agglomerate system test specimens.

until a strain rate of 1 s^{-1}. As the strain rate increases beyond 1 s^{-1} the maximum kinetic energy begins dramatically increasing. Once the strain rate reaches 10 s^{-1} it becomes difficult to discern the individual specimens on the plot. This behaviour is comparable to the initial HCP agglomerate crush tests in Section 3.4 and also follows that observed by Cheng et al. (2003). This is also in agreement with Grady and Kipp (1987) where they point out the importance of initial flaws dominating behaviour at low strain rate, which become less important at high strain rate due to the rate of application of load. As indicated for Figure 3.18, the results here also show a linear gradient of 2 above 1 s^{-1}, which again shows that structure is dominant at low strain rates and energy at high strain rates. There is likely a lack of importance of structure at high strain rates, due to the nucleation of failure at multiple points in the material resulting in fragmentation.

Multiple energies can be traced in PFC^{3D} including kinetic energy, friction energy and boundary work. The energy rates are shown in Figure 3.28 for the 0.001 s^{-1} and 10 s^{-1} tests for specimen 3. The graphs indicate that for all tests the boundary work increases as strain increases (as mentioned in Section 3.4, boundary work is formed from the work performed by the static and moving walls). The boundary work for the 0.001 s^{-1} test is converted into strain energy and also dissipated as friction energy where the kinetic energy remains very low. All specimens show similar behaviour up to 1 s^{-1} strain rate and these additional energy rate graphs can be viewed in Appendix C. A very different response occurs for the 10 s^{-1} strain rate with distinct peaks emerging in the boundary work being echoed in the kinetic energy and strain energy. There is an abrupt change at this strain rate with boundary work converted into strain energy and kinetic energy where friction

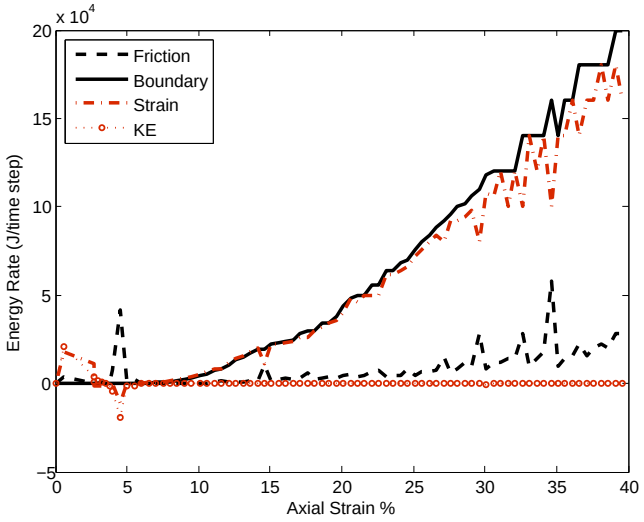

(a) 0.001 s^{-1} energy rates

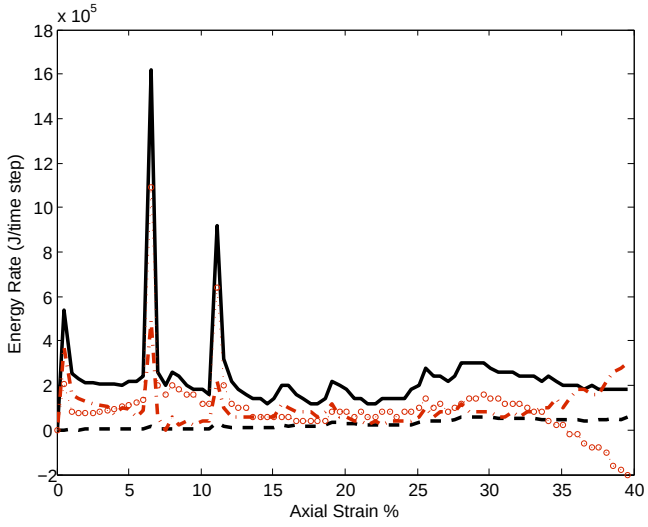

(b) 10 s^{-1} energy rates

Figure 3.28: Energy rates for the 0.001 s^{-1} and 10 s^{-1} tests for agglomerate system test Specimen 3.

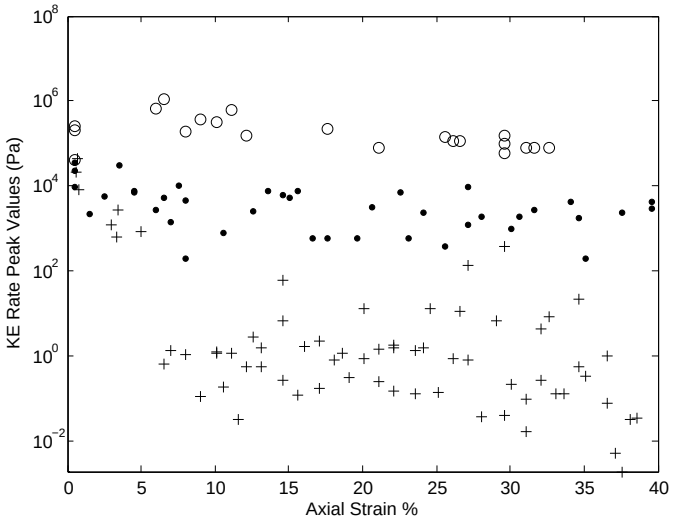

Figure 3.29: Kinetic energy burst maxima for all agglomerate system test specimens for 0.001 s^{-1}, 1 s^{-1} and 10 s^{-1} strain tests.

energy remains very low.

As mentioned in the previous section the noticeable peaks that occur in the kinetic energy output can be described as sudden 'bursts'. Figure 3.29 indicates that all specimens and tests provide an initial kinetic energy burst as the material begins to fail. As the strain increases in the tests however, bands in the graphs can be seen to occur that appear to encompass the range of burst maxima for each strain rate. These clear differences between strain rates in the maximum kinetic energy burst values suggest that kinetic energy is dependent on the strain rate, as also found in Section 3.4.

Breakage rate is compared in Figure 3.30 for three specimens at the indicated strain rates. From this figure we see that the most consistent breakage is produced by the 10 s^{-1} test with the majority of the breakage occurring between 5% and 25% strain (as is also shown in Figure 3.25). In comparison, the 0.001 s^{-1} strain rate test graph shows a few distinct peaks of high breakage rate that appear to relate to when the material cleaves into fragments. The remainder of the test sees generally low breakage rate occurrences. Figure 3.28 shows that during the breakage rate peaks there is an increase in friction energy suggesting that the released strain energy is dissipated by friction.

The maximum axial stress obtained during the tests (Figure 3.31) can be seen to follow a similar pattern to the maximum kinetic energy. The stress levels remain consistent until the 10 s^{-1} test when a minor increase in stress occurs. The increase in stress at the 10 s^{-1} strain rate may be in response to the increased kinetic energy resulting from the fragmentation of the central boulder.

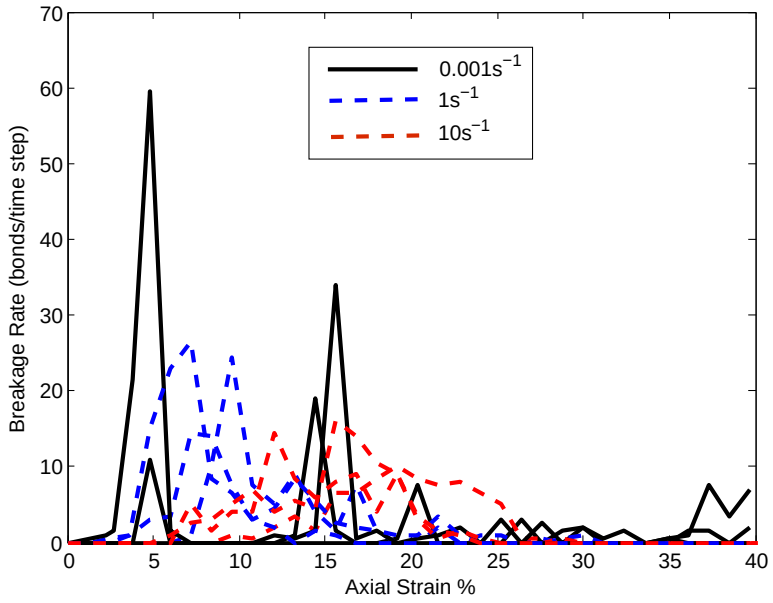

Figure 3.30: Breakage rate comparison for three agglomerate system test specimens at 0.001, 1 and 10 s^{-1} strain rates.

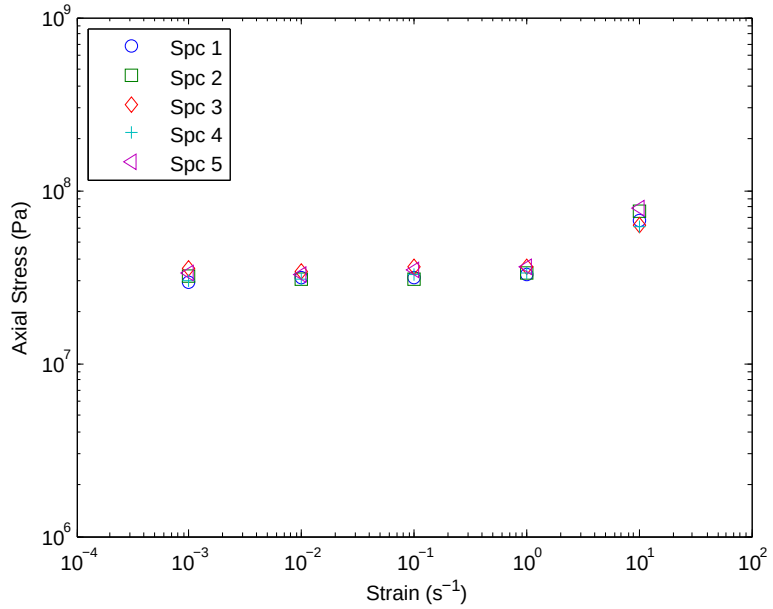

Figure 3.31: Maximum axial stress for all strain rates for the agglomerate testing.

3.5.3 Discussion

Oedometric testing of cubic HCP cluster systems has resulted in similar results to those observed for the HCP crush testing. At slower strain rates the maximum kinetic energy developed is dependent only on the initial state of the cluster based on the way the material was built – flaws and rotation of axes. Beyond 1 s^{-1} the maximum kinetic energy is similar for all specimens, thus is influenced directly by the strain rate. A rapid application of overburden load causes a large amount of damage to occur with little strain developed so long as the strength of the material can be overcome. The slower strain rates produce a kinetic energy that is around $\mathcal{O}(2)$ less than that observed for the highest strain rate. The associated breakage suggests that only the weakest bonds are breaking from which it appears little energy is released and frictional dissipation dominates.

The addition of the surrounding clusters has provided confinement to the breakable cluster, which under high strain rates completely disintegrates allowing individual spherical particles to travel throughout the confined area between the other clusters or be rebounded by them, which more closely replicates the situation in a sturzstrom. The high strain rate tests indicate a greater reduction in mobilised friction with an almost instantaneous reduction in the $\frac{q}{p'}$ stress ratio. Breakage at high strain rates is consistent throughout the tests and shows interaction with the stress ratio and kinetic energy behaviours.

The wall stress response also shows a relationship with strain rate. Wall stresses that smoothly increase at low strain rates become wave-like at high strain rates which appears to relate to the kinetic energy response. Boundary work is converted to strain energy and friction energy at low strain rates whereas at high strain rates this conversion is to strain energy and kinetic energy. Noticeable bursts of kinetic energy occur at the higher strain rates and here the maximum kinetic energy is similar across all specimens suggesting that kinetic energy is dominated by strain rate. The breakage behaviour combined with the kinetic energy burst response to the boundary work and the wave-like wall stresses suggest that at the highest strain rate the central cluster has disintegrated through dynamic fragmentation.

3.6 Chapter Summary

Crush tests of single HCP clusters (agglomerates) produce a power law relationship for the maximum kinetic energy achieved at varying strain rates. This power law relationship suggests that in the dynamic regime from 1 s^{-1} onward, material is failing through dynamic fragmentation. Alongside the substantially higher kinetic energy achieved in the dynamic regime are consistent kinetic energy bursts (some instantaneous) that appear to relate to bond breakage and a reduced stress ratio indicating a reduction in mobilised friction.

The oedometric testing results of cubically arranged clusters also indicate dynamic fragmentation events occur at high strain rates under confinement. This is supported by the interaction of breakage, kinetic energy and stress. At low strain rates, the main breakage events occur with little other breakage happening outside of these times. Kinetic energy is dominated by friction energy and wall stresses smoothly grow as the top platen lowers. Conversely, high strain rates show consistent breakage throughout the tests with kinetic energy dominating friction energy and noticeable bursts of kinetic energy that occur related to breakage events. Interestingly, the $\frac{q}{p'}$ stress ratio at high strain rates shows a reduction to a very low critical value at low strains, suggesting a reduction in mobilised friction due to dynamic fragmentation.

In both test series investigated in this chapter, high strain rate produces an interesting interrelationship between kinetic energy, breakage and stress ratio. Kinetic energy is dependent on the rate of compression and is also influenced by major breakage events. Stress imparted to the walls during high strain rate tests is also dependent on the rate of compression and appears also to be affected by the kinetic energy response to this rate of compression.

Grady and Kipp (1987) suggest a model to describe fracture damage based on the description of the failure process of a material under rapid loading. Their model relies on the use of a Weibull distribution to describe the activation of flaws within rock at varying strain rates. The resulting solution to the model describes the dependence of fracture stress on strain rate, where the value of the Weibull modulus m is central to the resulting gradient of the best fit line to the data. The axial stress versus strain rate results of the HCP and agglomerate system tests (Figures 3.19 and 3.31), for the more realistic bond strength of 4 kN, produce a best fit line with a gradient of $\frac{1}{3}$. This produces a Weibull modulus or shape parameter of $m = 6$ which is consistent with the range of values of $5 < m < 10$ noted by McDowell et al. (1996); McDowell and Bolton (1998) for cement, which can be considered as a rock-like material. Thus the bond strength of 4 kN can be considered to behave similarly to that of real rock.

Davies and McSaveney (2008) suggest that the dynamic fragmentation of material can reduce friction within a sturzstrom during runout. The oedometric tests in this chapter highlight a stress ratio response that indicates a reduction in mobilised friction as bonds break and kinetic energy peaks. The high strain rate oedometric tests suggest that dynamic fragmentation occurs under

fast loading rates. Together these results support the suggestion of Davies and McSaveney (2008) by indicating that dynamic fragmentation causing a reduction in friction is plausible particularly at the topographical change of a sturzstrom from fall state to runout.

Chapter 4

Material Calibration

In Chapter 3, the HCP oedometric tests explore the influence of the rate of application of overburden load on a purely synthetic material designed to represent closely packed rock blocks that may be found in a sturzstrom. In reality sturzstroms occur in various rock types as indicated in Table 2.1 (Chapter 2). To consider the applicability of the synthetic material testing results to sturzstrom events, it is necessary to incorporate a realistic material into the numerical test process.

To produce a rock material in PFC^{3D} requires the use of the bonded particle model (or BPM), as discussed in Chapter 2, Section 2.3.1. The BPM calibration process involves a significant amount of trial and error to determine the correct micro-parameters of the material while ensuring that the macroparameters are comparable between numerical and laboratory tests. This comparison typically occurs between numerical stress-strain results and those already determined by experimental laboratory biaxial, triaxial or UCS tests among others. The response of the BPM material is sensitive to the grain size, whose range must be carefully determined so as to make certain the model is correctly representing the material intended (Potyondy and Cundall, 2004).

As outlined in Chapter 2, two materials are considered in this thesis. First we consider the material relevant to the Falling Mountain rock avalanche in New Zealand. This failure occurred in a highly indurated (hard) and strong greywacke as identified by McSaveney and Davies (1999) and discussed earlier in Section 2.1.2. Greywacke is an interbedded rock of sandstone and mudstone layers where the sandstone typically has higher UCS (Cook, 2001). In this chapter, calibration to the stronger sandstone bed of the greywacke is performed.

The second material considered is chalk. Chalk cliff collapses are identified as commonly occurring in weak to extremely weak chalk by Mortimore et al. (2004) particularly around the chalk cliffs of Kent in England and have been suggested as possible miniature sturzstroms by Mortimore et al. (2004), Williams et al. (2004) and Bowman and Take (2014). The BPM model is also used to create synthetic weak and extremely weak chalk specimens for similar testing as the greywacke sandstone.

4.1 Size and Shape Effects

Fracture of rock results from the growth of microcracks that already exist within the sample. As outlined in Section 2.2.2, a larger sample is more likely to fail than a smaller sample. In general, a larger specimen is likely to have a more extreme flaw so as size increases, strength decreases. The compressive strength of the specimen is affected by extremes in the distribution of flaws in the sample (Hudson and Harrison, 1997). Similarly the shape of the sample can also affect the strength, whereby a standard laboratory specimen of height twice the diameter may be weaker than an insitu specimen of diameter twice the height. Figure 4.1 indicates the changing strength of material as the sample size increases and shape changes.

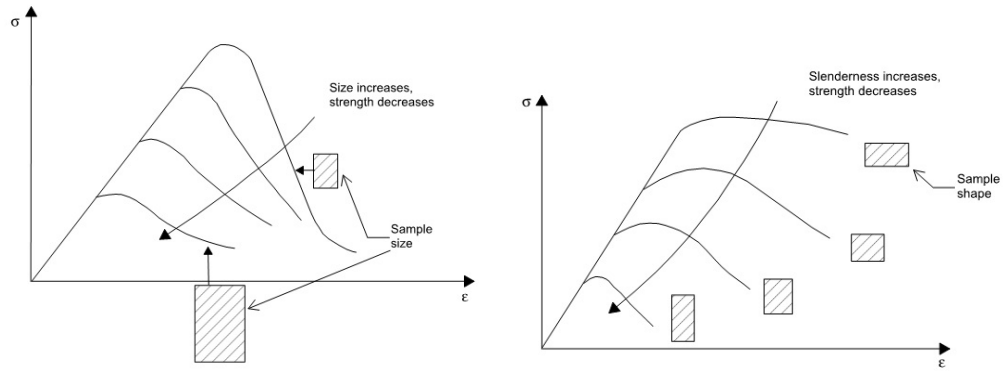

(a) Size Effect (b) Shape Effect

Figure 4.1: Size and shape effects as illustrated by Hudson and Harrison (1997, Figures 6.11 and 6.12, pg 97-98).

In PFC^{3D} the size effect must also be considered. Synthetic material must be calibrated to a comparable size as that used in the laboratory. If the size or shape of the material is to be altered, the effect of this on the strength of the synthetic material must also be taken into account. As material strength is directly related to the bond strength, the bond values can simply be increased or decreased to alter the peak strength of the sample given the relationship determined from the laboratory experiments. In this thesis, the microparameters are determined for a cylinder equivalent to that used in physical laboratory testing. The bond strengths are then adjusted to compensate for the difference in size of the cluster radius to be used in the oedometer and shear tests in the following chapters.

Particle numbers are generally reduced where possible in DEM applications due to the increase in computational time required for each step with large numbers of particles. Potyondy and Cundall (2004) indicate that the macro-response of a synthetic material in PFC^{3D} can be very sensitive to the number of particles. It is recommended that the minimum number of particles across the

radius of a cylindrical specimen be at least 4 in number for reasonable behavioural response (pers. comm. with Cedric Lambert).

As outlined in Chapter 2 (Equation 2.14), the choice of particle size cannot be arbitrary as the Mode-I fracture toughness of a synthetic material is directly related to the particle radius and tensile strength of that material. This is in comparison to the true material fracture toughness K_c, which relies on the material toughness and elasticity. In PFC^{3D} a change in particle size results in a change to the material tensile strength σ_t, and both influence the value of the Mode-I fracture toughness K_{1c}.

4.2 Strain Rate Effects

Strain rate effects in rock have been examined in the laboratory, resulting in an understanding of the strain rate sensitivity of strength and methods to offset the influence of strain rate effects such as confining pressure. Little work has been completed on strain rate effects within DEM models and the ability of the model to correctly represent this effect. Some relevant laboratory and recent DEM work is outlined below.

The paper by Jackson et al. (2008) describes uniaxial compression tests in the laboratory on a range of materials from chalk to sandstone, and over a range of strain rates from 2.6 x 10^{-5} to 0.05 s^{-1}. They found that there was an increase in the energy required to produce fragmentation as strain rate increased, with greater fragmentation at higher strain rates and greater amounts of energy required for stronger materials. Final fracture occurred at larger strains as strain rate increased and the behaviour became more plastic. Jackson et al. (2008) went on to model dynamic simulations of sandstone using PFC^{3D} for strain rates of 0.002 to 1 s^{-1}. The numerical modelling was found to replicate the physical laboratory testing relatively well, with an increase in the peak strength of the material as strain rate increased, a fairly consistent Young's modulus and a reduction in brittle behaviour as strain rate increased (see Figure 4.2). Bond breakages were found to continue throughout the post peak region of the test for high strain rates with more breakages overall as seen in the laboratory tests. Jackson et al. (2008) conclude that fragmentation is likely to be controlled, in part, by standard material parameters at high strain rates.

UCS tests on sandstone specimens with three different grain sizes were performed by Wasantha et al. (2015). Given that the strength of rock is affected by grain size, Wasantha et al. (2015) considered whether this effect was consistent under high strain rates. They noted that strain rate dependency is primarily due to the plastic strain component. At high strain rate the plastic response did not fully develop before the strain increased, causing the rock material to stiffen and thus its strength increased. Wasantha et al. (2015) collected samples of Australian sandstones and characterised the materials through thin section, scanning electron microscopy and x-ray diffraction analysis.

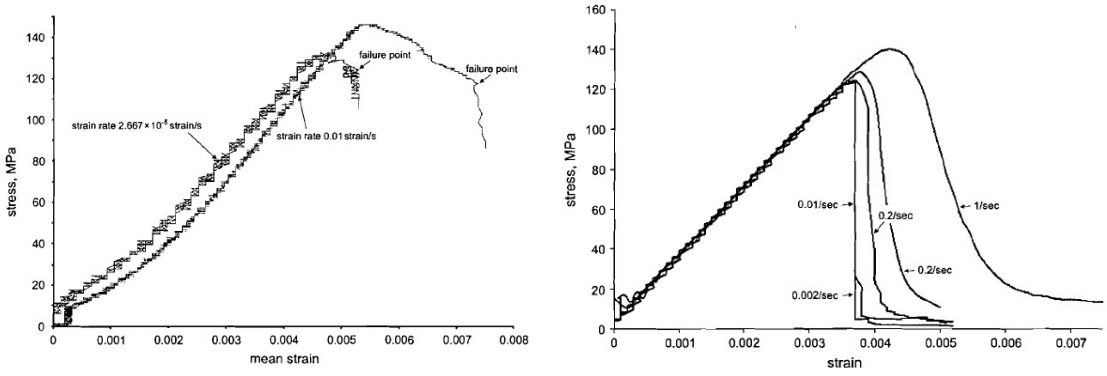

(a) Figure 2 (pg 8) - physical laboratory testing

(b) Figure 9 (pg 15) - PFC^{3D} calibration

Figure 4.2: Figures 2 and 9 from Jackson et al. (2008) showing the stress-strain curves for the sandstone from physical laboratory testing and when modelled with PFC^{3D}.

The sandstone samples were subjected to UCS tests with strain rates from 10^{-6} s^{-1} to 10^{-3} s^{-1}, and with the displacement of the loading ram used to control the strain rate. Wasantha et al. (2015) noted that they were unable to consider the post-peak behaviour in all samples, as significant damage or fracturing occurred in the specimens around the peak stress. Figure 4.3 outlines the peak strength vs strain rate results obtained for the sandstones tested by Wasantha et al. (2015).

The results of Wasantha et al. (2015) showed the finer grained sandstones were responsive to the change in strain rate, which they suggest was due to the finer grain size causing the micro-cracks to be fine and scattered through the specimen, thus dispersing the stress. The coarse grained sandstone instead failed through granular fractures, which under high stresses failed quickly with little contribution toward stress redistribution. In essence, Wasantha et al. (2015) find that rocks of different grain sizes can have different responses to increased strain rate, though in general, the stress at failure is either unaffected or increases with strain rate.

In their review of prior work, Shams Alam et al. (2015) note that a large amount of research has been performed in relation to quasi-static and dynamic compression tests below shock loading levels. The maximum strain rate they mention is a 1000 s^{-1} test on basalt by Lindholm et al. (1974) which was performed to improve drilling and fragmentation techniques in hard rock. These dynamic tests used SPHB techniques and found that the basalt fracture strength was dependent on strain rate with the greatest energy produced at the highest strain rate. Shams Alam et al. (2015) note that the research they reviewed indicates an increase in the UCS as strain rate increases. The initial threshold of dynamic compression is suggested to start at a strain rate of 1 s^{-1}. Shams Alam et al. (2015) limit their strain rate tests on Kota sandstone to the range of 0.00001 s^{-1} (low) to 1 s^{-1} (medium). The results of these tests suggest an increase in the stiffness of the material along

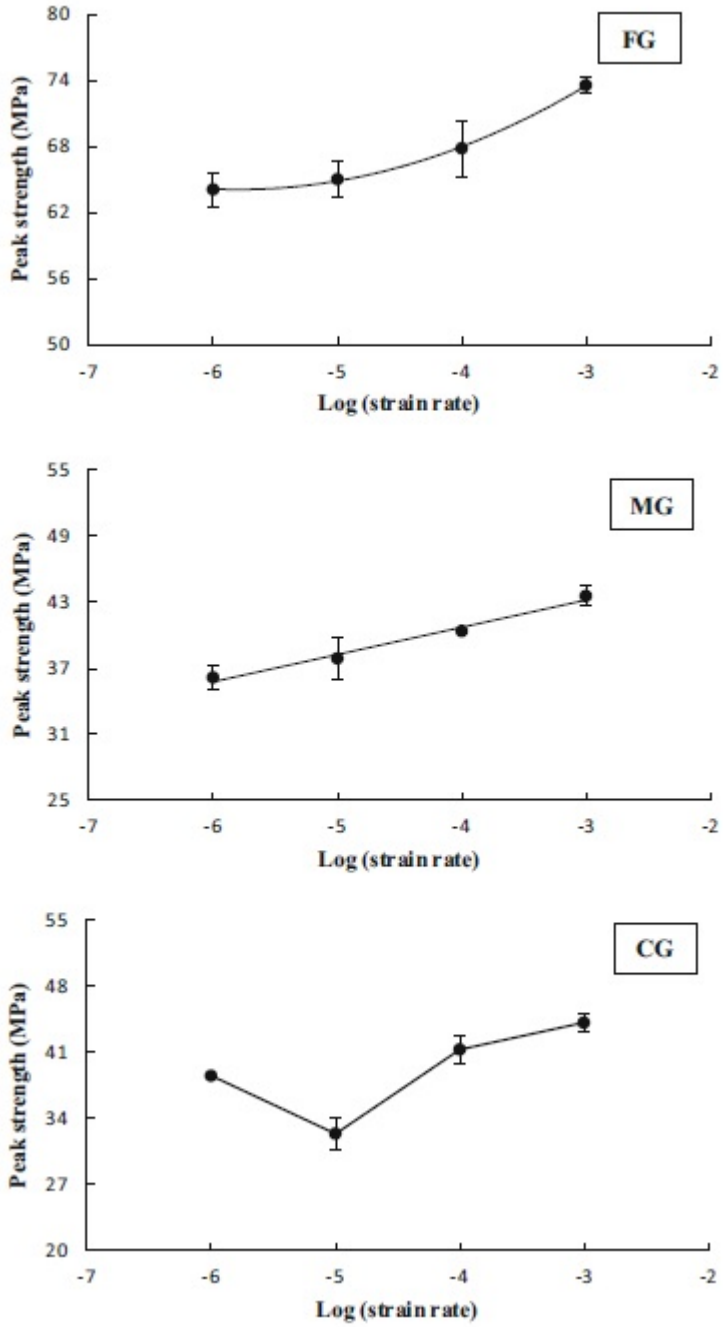

Figure 4.3: Figure 8 from Wasantha et al. (2015, pg 1891) showing the peak stress against strain rate for UCS tests on sandstone materials with varying grain sizes. FG=fine grained, MG=medium grained, CG=coarse grained.

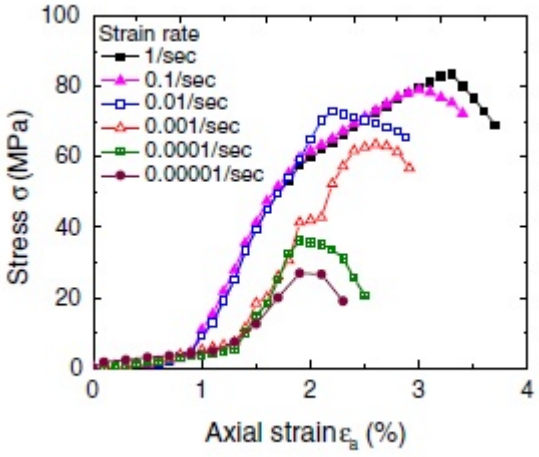

Figure 4.4: Figure 3(a) from Shams Alam et al. (2015, pg 8) showing stress-strain curves for their UCS strain rate tests on Kota sandstone.

with an increase in the peak stress (see Figure 4.4).

Zhang and Wong (2014) discuss the importance of the time step when comparing UCS loading rates on specimens of varying sizes. They undertake UCS and Brazilian tests on BPM specimens at various loading rates, in order to determine a suitable loading rate for quasi-static numerical modelling in DEM. Zhang and Wong (2014) state that of the literature they reviewed the loading rates ranged from 0.016 to 0.3 ms^{-1}, which they consider high in the physical world.

Zhang and Wong (2014) state, as also outlined earlier (Section 2.4.1), that for a stable and convergent solution in PFC (2D or 3D), the time step in the model is required to be below a critical time step. This critical time step depends on the stiffness, density and radius of the particles. The breakage of bonds within a BPM affects the time step, as bond breakage decreases the stiffness, however the effect is noted by Zhang and Wong (2014) as very small.

The comparison by Zhang and Wong (2014) of varying loading rates on different specimen sizes resulted in different mechanical responses for the same strain rate, as expected. The stress-strain curves are shown in Figure 4.5 for UCS tests at varying loading rates for one specimen. Increases in strain rate result in an increase in peak stress and peak strain, an increase in breakage and the increased ductility of the material post-peak. Zhang and Wong (2014) also found that at higher strain rates a step-wise feature appeared in the stress-strain curve within the elastic range, although they did not make suggestions as to the reason for this. Cracks were found to develop preferentially at the base of the specimen at low loading rates, and occurred more readily throughout the specimen under high loading rates. The results of Zhang and Wong (2014) are comparable to those of Jackson et al. (2008).

? note that the Itasca manual for PFC^{2D} outlines a need for "the loading rate to be low enough to ensure the specimen remains in quasi-static equilibrium." This is to ensure that inertial effects

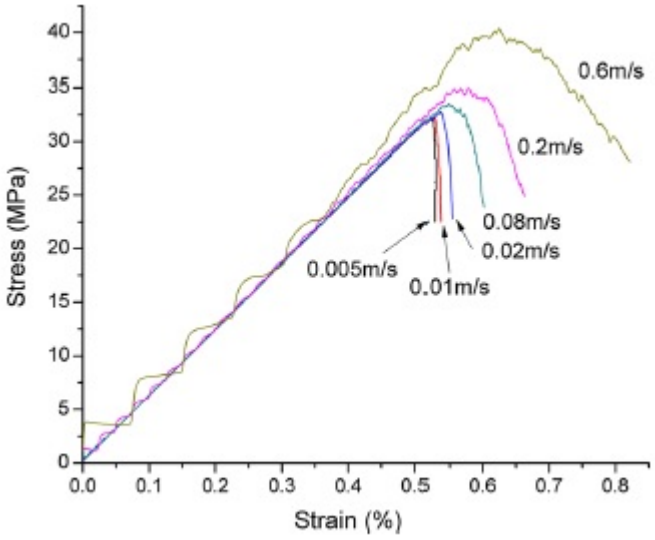

Figure 4.5: Figure 4 from Zhang and Wong (2014, pg 170) showing stress-strain curves for the UCS strain rate tests modelled with PFC^{3D}.

like premature bond breakages are avoided. Two methods are recommended by Itasca to ensuring quasi-static equilibrium:

- Stop the platens and observe if the load remains nearly constant.
- Monitor the work done by the platens and compare to the strain energy in the system; equality indicates quasi-static conditions.

In considering the second method, Zhang and Wong (2014) found that under quasi-static loading rates the strain and boundary energies were almost equivalent, and would diverge slightly due to frictional slip and the release of kinetic energy due to bond breakages. At high loading rates the energies diverged without bond breakages occurring, producing excessive kinetic energy within the system.

Zhang and Wong (2014) in summary state that a loading rate of 0.2 ms^{-1} is a threshold value between quasi-static and dynamic loading. They indicate that a loading rate of 0.02 ms^{-1}, or a maximum step strain rate of 1.1 x 10^{-8} step^{-1}, is considered to be appropriate for quasi-static uniaxial compressive tests.

As outlined in Section 2.2.2, the post-peak behaviour of rock produces two distinct classes of material. Class I behaviour involves the stable propagation of fractures during post-peak loading, with further work required to reduce the strength of the material. Some strength is retained by Class I materials after peak strength is passed. It is important to note that the rocks calibrated and tested in this thesis are considered as Class I materials.

4.3 Calibration Procedure

The calibration process for the BPM in PFC^{3D} is outlined below. The initial BPM material set-up is outlined in Chapter 2. The calibration of the material strength follows on from the preparation of a BPM that is suitable for numerical laboratory tests. The strength and stress-strain behaviour of the numerical material is compared to that of laboratory tests performed on the actual material in order to determine the micro-parameters.

The particles within a DEM model are scaled up versions of real grains, for example a particle may be up to 10 times the radius of a real grain for computational efficiency. The particle size distribution (PSD) is not often captured in DEM models as the particle sizes are evenly distributed between two limiting sizes and thus the PSD is almost uniform (Cheung, 2010). If the PSD of the synthetic material does not reflect the PSD of the actual material then the basic mechanics may not be correctly represented. Cheung (2010) indicates that the particle generation process can be altered to allow for ranges of particles sizes to be created to form a more accurate representation of a material PSD in a DEM model.

Greywacke sandstone is described by Cook (2001) as medium to coarse grained with a grain size of 0.15 mm to 0.5 mm. Thus so long as the radius extents are chosen appropriately, a uniform PSD is acceptable for modelling purposes. Chalk is formed from skeletal material and calcite secreted by marine algae or coccoliths (Bell et al., 1999). Bell et al. (1999) notes that the coccoliths and fragments thereof comprise upward of 85% of the constituents of chalk with a grain size of 0.5-20 mm with the remaining 15% of coarse material 40-100 mm in size. Therefore although chalk has a bimodal PSD, given the proportion of material classed as fine grained and with appropriate particle radius extents, a uniform PSD is considered acceptable for this material also.

The key process to follow for calibration is outlined by Cheung (2010) and Itasca (2008), and reproduced below. Parameters are defined at the beginning of the process.

- E_c the modulus of the particles; E_{pb} the modulus of the bonds; k_n the normal stiffness of the parallel bonds; k_s the shear stiffness of the parallel bonds; μ friction; s_{pb} the standard deviation of the parallel bond strengths; $\bar{x}_{pb}$ the average of the parallel bond strengths; and ν Poisson's ratio.

- Assume that the stiffness of the particles and bonds are equal ($E_c = E_{pb}$) and that $\frac{k_n}{k_s} = 1$, $\mu = 0.5$ which Cheung (2010) states is equivalent to $\phi = 27^o$. Set the bond strengths high in order to find E_c and then $\frac{k_n}{k_s}$ in order to match the laboratory E and ν values.

- Calibrate for pre-peak, peak and post-peak behaviour in order by varying appropriate parameters. Match peak strength by setting $s_{pb} = 0$ and varying $\bar{x}_{pb}$. Then match the crack initiation stress by varying s_{pb}.

- Increase stiffness to increase pre-peak stiffness – $E_c > E_{pb}$ is required for a stiffer response after the onset of breakage.
- Breakage is controlled by bond strengths – decreasing the normal strength of the parallel bonds affects post-peak behaviour. For the parallel bonds to have more influence on the stress-strain behaviour, $E_{pb} > E_c$.
- Bond strengths also influence peak mobilised stress ratio.
- Stiffness ratio $\frac{k_n}{k_s}$ is related to ν and influences the macroscopic failure mechanisms. The peak strength can be moved to any strain value by simply altering the stiffness ratio (for example, lower ratio moves the peak of the stress-strain graph to the left).
- The friction value μ adjusts the post-peak behaviour for ductile or brittle behaviour.

4.3.1 PFC^{3D} Unconfined Compressive Strength Test

The material calibration is typically performed to laboratory triaxial or unconfined compressive strength (UCS) tests. In this chapter the UCS test in PFC^{3D} is used for calibration to UCS laboratory tests. The general arrangement of this test in PFC^{3D} is similar to that performed in the laboratory and Itasca provides code with the program for the purpose of performing UCS and triaxial tests.

The Itasca code generates a cylindrical specimen for the UCS test within a rigid cylindrical wall with upper and lower end platens. User input for the cylinder shape, particle sizes and material parameters are required to form the material. Particles are created at random positions within the cylinder and the radius expansion method is used to bring the particles into close contact. Floating particles (those with less than three contacts) are gradually increased in size until the minimum number of contacts is achieved. The system is allowed to settle under gravity throughout the generation period to reduce the effects of locked-in-forces.

Prior to performing a UCS test the cylindrical wall is removed from the system resulting in a prepared specimen similar to that shown in Figure 4.6. The test is performed by applying a velocity to the top platen, where the default velocity from the Itasca code is formed from a user input value multiplied by half of the height of the specimen. For example, a 100mm tall specimen is compressed at a default velocity of 0.05 ms^{-1} using the Itasca code. For UCS tests in PFC^{3D} strain rate effects on the sample can be considered by amending the top platen velocity. The UCS test is completed once the peak stress is reached and the change in the deviatoric stress post peak is small.

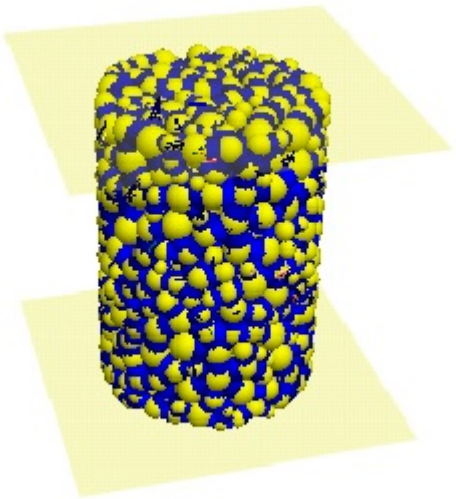

Figure 4.6: An example of a cylindrical sandstone specimen prepared for UCS testing.

4.4 Greywacke Sandstone

The Torlesse Complex rock is defined by Cook (2001) as an interbedded sandstone and mudstone commonly referred to as greywacke. The Torlesse greywacke rocks are very well indurated (hard) and in some cases slightly metamorphosed, with locality determining the depth of the alternating sandstone and mudstone beds. The sandstone is typically a medium-coarse sand of, on average, 0.5mm diameter grain size. In New Zealand, the greywacke beds are steeply dipping to almost vertical with closely spaced joints and zones of fracturing. Greywacke sandstone is described as a strong, durable material and is commonly used in New Zealand for roading and concrete. Cook (2001) sampled material from sites in both the North and South Islands of New Zealand and notes that the material is genetically similar with mass and structure differences across sites.

As outlined in Section 2.1.2, the Falling Mountain rock avalanche comprised a failure of approximately 55 x 10^6 m^3 of highly indurated (hard and well cemented) greywacke of finely alternating beds of sandstone and mudstone. The rock is understood to contain many defects, however, the rock avalanche behaved as if the material was isotropic (McSaveney et al., 2000).

4.4.1 Laboratory Tests

Due to the 'genetic' similarity found by Cook (2001) between greywacke sampling sites across New Zealand and the overall high strength of the Falling Mountain greywacke as indicated by McSaveney et al. (2000), the BPM for a Falling Mountain (Arthur's Pass National Park) greywacke sandstone equivalent material is calibrated against the tests performed by Cook (2001) for the strong Bel-

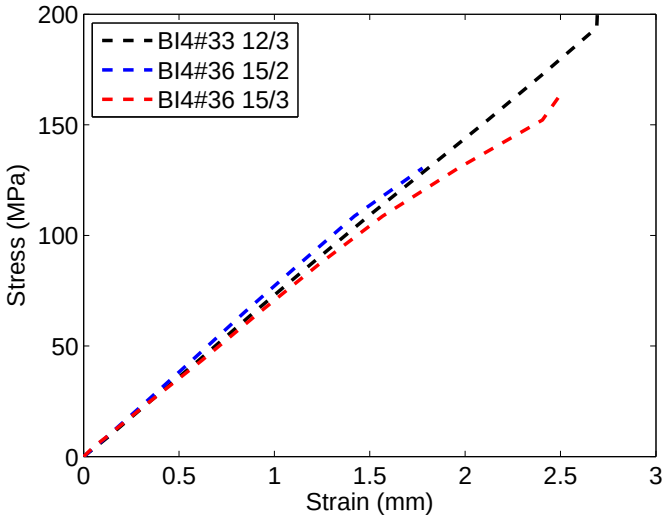

Figure 4.7: Plot of the data from the laboratory results of Cook (2001) of UCS testing of sandstone samples.

mont Quarry (Wellington) greywacke sandstone. Compressive strengths were determined by Cook (2001) using unconfined uniaxial compression and triaxial compression tests. The unconfined uniaxial compression test was utilised numerically in PFC^{3D} to match the overall macroscopic characteristics of the tested material by altering the microscopic parameters until the best match was attained.

The greywacke sandstone unconfined compressive strength (UCS) values from all New Zealand sources ranges from 144 - 347 MPa with an average of 262 MPa (Cook, 2001), where the variation is described as a result of sample selection. Such a large range of strengths is common for New Zealand greywacke sandstone and Cook (2001) states that the strength of greywacke is directly related to the mean grain size, where coarser grained sandstones are generally stronger. Cook (2001) notes that the Belmont greywacke sandstone is a strong to very strong material with an average tangential Young's modulus of 66,800 MPa.

Data from the Appendices of Cook (2001) have been used to plot stress-strain relationships (see Figure 4.7) for three uniaxial compression tests on sandstone samples labeled as BI4#33 12/3, BI4#36 15/3, BI4#36 15/2. Table 4.1 shows the results obtained by Cook (2001) for these individual tests. These results are used as the goal points for the calibration process in PFC^{3D} and the stress-strain graph for comparison to that produced by the BPM model. Laboratory tests were performed on cylindrical samples that were cut in a 2:1 height to diameter ratio with the majority of the core sample diameters around 54 mm.

Table 4.1: Uniaxial Compression Test Results from Cook (2001)

Sample	**UCS (MPa)**	**E_t (MPa)**	**Poisson's Ratio (ν)**	**Density ($\frac{kg}{m^3}$)**
BI4#33 12/3	202	70927	–	2682
BI4#36 15/3	162	68795	0.219	2673
BI4#36 15/2	144	76885	0.237	2689

4.4.2 Sandstone BPM & Calibration

After the creation of a suitably sized BPM model, the material was calibrated following the recommended process outlined above. The material is calibrated by comparing numerical UCS tests to the laboratory UCS values of Cook (2001). Approximate starting values of the microparameters can be found by using the equations outlined in the contact models section of the Itasca (2008) Theory and Background Manual. Alternatively, the calibration process outlined above requires only an estimate of E which can be found from physical laboratory testing or literature. The numerical test sample is sized to be equivalent to that of the laboratory tests.

Given the PSD of a typical greywacke sandstone can range from 0.06mm to 0.50mm and that the Cook (2001) greywacke sandstone is medium to coarse grained, the model PSD is set to contain 20-80% of the typical greywacke sandstone PSD range or 0.15 mm to 0.40 mm. For numerical efficiency this particle size range is multiplied by ten to provide a minimum radius of 1.5 mm with a radius ratio of 2.8 (where 1.5 x 2.8=4.2 mm is the largest particle size that can be formed by the material generation algorithm provided in the FISHTank).

Shown in Table 4.2 below is an excerpt of selected calibration stages outlining microparameters, test results and calibration actions.

Table 4.2: Calibration of greywacke sandstone

ID	**Properties**	**Behaviour**	**Actions**
Pre-peak behaviour must be obtained prior to determining peak strength. Set bond mean and standard deviation values to be very high and equal to one another.			
S1	Min Radius = 1.5 mm Radius Ratio = 2.8 ρ=2680 μ=0.75 $\frac{k_n}{k_s}$ =1.0 E_c=E_{pb}=20 GPa $\bar{x}_{pb}$=s_{pb}=10 GPa	E_Y=22.7 GPa, peak 2.5 GPa, too little influence from parallel bonds	E_c must be lower than E_{pb} for the parallel bonds to control failure behaviour
			Continued on next page...

Table 4.2 – continued from previous page			
ID	**Properties**	**Behaviour/Results**	**Actions**
S11	E_c=200 MPa E_{pb}=1.5 GPa	E = 780 MPa, peak 47 MPa	Continue altering the moduli
S14	E_{pb}=600 MPa	E_Y = 1 GPa, peak at 100 MPa	Bond values require adjustment
Further adjustment of bonds indicated that the order of magnitude of the elastic properties of the material was too low as the peak value could not be sufficiently increased.			
S20	E_c=8 GPa $\bar{x}_{pb}$=500 MPa	E_Y= 4 GPa with peak occurring at 535 MPa	Peak is twice the laboratory value so halve the mean parallel bond strength
S21	$\bar{x}_{pb}$=250 MPa s_{pb}=50 MPa	E_Y=4 GPa, peak at 313 MPa	Stiffness too low and peak too high - moduli and bond values require further calibration.
Alteration of the value for s_{pb} moves the peak of the stress-strain graph to the left or right. The reduction of the friction coefficient μ is responsible for the post-peak behaviour where if the value is small the behaviour appears more brittle. The stiffness ratio should be approximately 0.5 as this influences the Poisson's ratio of the material – for greywacke $\nu \approx$0.2 (Cheung, 2010, Figure 4.38, page 154).			
S30	E_c=30 GPa $\frac{k_n}{k_s}$ = 0.5 μ=0.05 E_{pb}=135 GPa $\bar{x}_{pb}$=250 MPa s_{pb}=50 MPa	E_Y=68 GPa, peak at 165 MPa at 2.6 mm of strain	Good match to laboratory tests
S30-od	E_{pb}= 135 GPa $\bar{x}_{pb}$= 275 MPa s_{pb}= 30 MPa	Peak at 164 MPa	Good match
S30-sh	Min particle radius=5 mm	Peak at 175 MPa	Good match

Model S30 was initially calibrated for use as the oedometric sandstone model specimen. Due to the particle sizes chosen, this model produces over 13,000 particles for each boulder, leading to over 350,000 particles in total for the oedometric specimen. In order to reduce the computational

time for a simple oedometric test, it was decided to recalibrate the material with increased particle sizes to reduce particle numbers. The PSD for the recalibration was maintained within a multiple of ten of the medium to coarse sand grain size range with the minimum particle radius increased from 1.5 mm to 2.25 mm, and therefore the maximum from 4.2 mm to 6.3 mm.

The recalibration for the particle size change (S30-od) resulted in an increase to the parallel bond stiffness E_{pb} in order to maintain the peak UCS at 164MPa. Without this amendment the peak UCS fell to 135 MPa using the S30 microparameters. Given that the fracture toughness in PFC^{3D} is reliant on the particle radius, it is not surprising that the overall strength of the material can also be affected by the change of particle radius or reduction in particle numbers. This was also concluded by Cheung (2010) who notes that the effects of model sensitivity to particle numbers can be minimised by using parallel bonds.

In the same way that a size effect exists with the size and shape of the specimen being tested, a size effect also exists in PFC^{3D} in relation to particle size, whereby an increased particle size reduces the material strength directly reflecting the macroscopic result from increasing the specimen size (as discussed earlier). Eberhardt et al. (1999) note that the peak strength of a material decreases in proportion to the inverse square root of the grain size. Using this relationship and the UCS results from Cook (2001), a size effect for greywacke sandstone was produced (see Figure 4.8) which was used as reference for the calibration of the sandstone material.

In a similar manner, the model was again recalibrated (S30-sh) for use in the shear testing due to excessive particle numbers causing efficiency issues. The microparameters calibrated for the oedometer testing were not altered, instead the minimum particle size was increased to 5mm and as a result the test cylinder size was also increased. Thus, the shear testing model material (S30-sh) has an associated UCS peak of 175 MPa which still falls within the bounds for the Cook (2001) data.

The fracture toughness of a sandstone greywacke material can be found from the toughness G_c and E. G_c is at most 10^{-1} kJm^{-2} for rock and from physical laboratory testing we know that E≈76 MPa. Then K_c ≈0.87 MN$\sqrt{m^{-3}}$. Tension tests in PFC^{3D} as described in Chapter 2, Section 2.3.2 require a separate calibration to that of oedometer tests and thus the material built to find the UCS and that to find σ_t require significantly different material parameters. However, the tension test in PFC^{3D} can be used to check on the effects of a change in particle size on the material fracture toughness. In the sandstone, case changing the particle size from a minimum of 1.5mm to 5mm causes a decrease in σ_t and a small (insignificant) reduction in K_c.

4.4.3 Synthetic Greywacke Material

Figure 4.9 outlines the comparison between the calibrated PFC^{3D} sandstone material and those tested by Cook (2001). The comparison is favourable for all chosen microparameter values for the

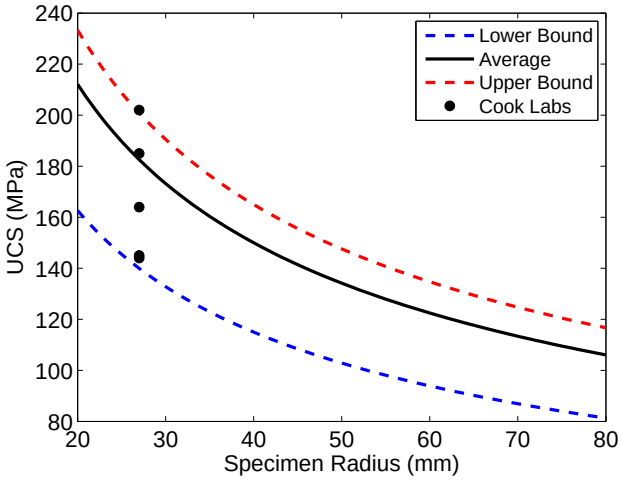

Figure 4.8: Size effect relationship for Cook (2001) data and associated boundaries from minimum and maximum UCS peaks found during testing.

oedometer and shear testing although the stiffness is slightly and consistently below that observed in the laboratory. This appears to be due to minor changes in the E_c and E_{pb} values and the resulting difference between the two.

Table 4.3: Greywacke sandstone microparameters

Particle Parameters	**Bond Parameters**
E_c=30 GPa	E_{pb}=135 GPa
ρ=2680 $\frac{kg}{m^3}$	$\bar{x}_{pb}$=275 MPa
μ=0.05	s_{pb}=30 MPa
$\frac{k_n}{k_s}$=0.5	

4.4.4 Strain Rate Effects

The calibrated sandstone material was subjected to UCS tests at varying strain rates to check the behaviour of the material was consistent with that described in Section 4.2. The results of the tests, from 1 s^{-1} to 120 s^{-1}, are outlined in Figure 4.10. In the PFC^{3D} model the velocity V of the upper platen is altered according to the strain rate where $\epsilon = \frac{V}{L}$ and L is the length of the specimen. The strain rates considered here incorporate the range of strain rates used in the oedometer testing in Section 5.

As outlined in Section 4.2, various authors have presented research on laboratory based UCS tests with strain rates that range from quasi-static to dynamic. The majority of dynamic testing on sandstone appears to have been completed at a maximum of 1 s^{-1} strain rate and there appears to be no laboratory based work considering higher strain rates. Laboratory work that does consider

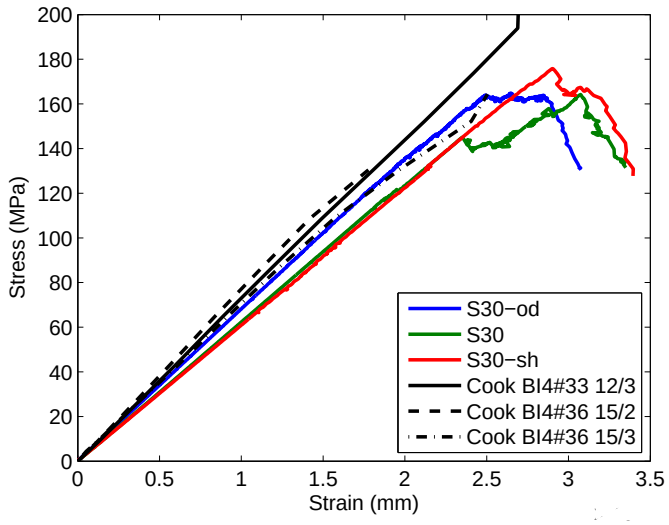

Figure 4.9: Comparison of PFC^{3D} calibrated sandstone material and Cook (2001) data.

higher strain rate tests has been completed on hard rock, such as basalt, using SHPB methods. This test method considers strain rates of 1 s^{-1} and greater.

The strain rate tests show an increase in stiffness once the strain rate is greater than 20 s^{-1} (see Figure 4.10). The lower strain rates have a consistent stiffness response with a gradual increase in peak strength from 154 to 210 MPa for this specimen. The higher strain rates of 100 s^{-1} and 120 s^{-1} along with presenting a higher stiffness, show a more ductile response with a significant post-peak region. The 50 s^{-1} strain rate results show an intermediate state as the stiffness increases and ductility begins. These results are consistent with those found by Jackson et al. (2008) and Shams Alam et al. (2015) as strain rates change from quasi-static to dynamic. It is logical to consider that the increase in stiffness and ductility should continue at higher strain rates until the material shatters. It is also clear that the synthetic sandstone material is strain-rate dependent.

In these tests the quantity of breakage increases with strain rate (see Figure 4.11) with around 50% of parallel bonds left at the end of the 120 s^{-1} test. The largest proportion of breakages occur from 0.2% to 0.6% strain, where the breakages for the slower strain rates cease once peak strength is reached. Breakages for the higher strain rate tests continue to occur through to the end of the test albeit at a slower rate than seen at the start. This stable breakage and the post-peak strength characterises the material as Class I.

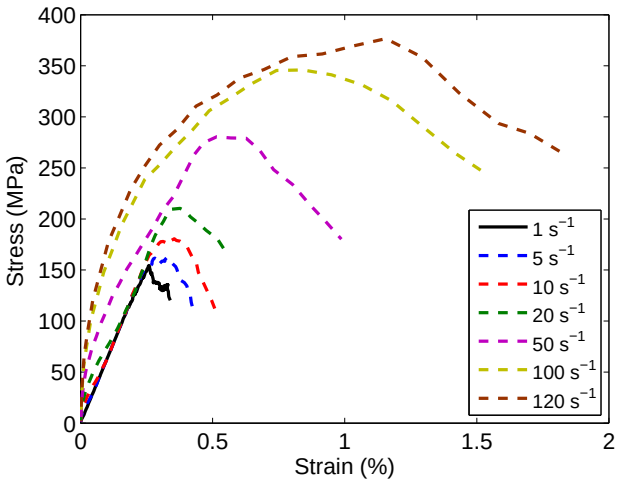

Figure 4.10: Stress-strain response of the calibrated sandstone material under varying strain rates.

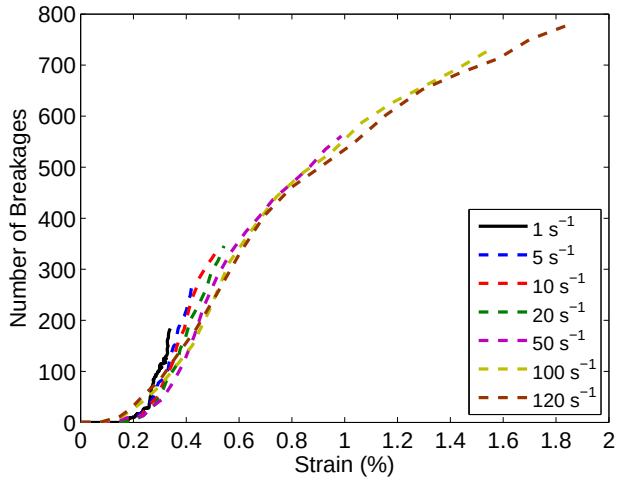

Figure 4.11: Breakage of the calibrated sandstone material under varying strain rates.

4.5 Chalk

Hutchinson (2002) states that chalk flows typically occur in weak to extremely weak and generally saturated chalk that has a porosity greater than 40%. The associated chalk cliff is normally almost vertical (60-75^o) and of a minimum height of at least 60-80m. Chalk flows occur in England and Northern Europe typically where the North and South Downs are exposed to the ocean (and equivalent areas on the French coast) and are more common in the North Downs chalks. Additional details regarding chalk flows are discussed in Chapter 2.

Chalk is a pure carbonate rock which can be considered a coccolithic limestone where a hard chalk is described as having undergone significant diagenesis to convert the coccoliths to calcium carbonate (Hutchinson, 2002). Soft chalks are characterised by grains bound together at contact points with small amounts of calcite where rigidity is attributed to the interlocking of the grains (Bell et al., 1999). The high porosity of chalk can be attributed to the high percentage of fossils as there is generally little evidence of compressional crushing during sedimentation. The strength of a chalk is significantly reduced when saturated, even minor saturation can reduce strength significantly (Bowman & Take, 2014).

4.5.1 Laboratory Tests

Bell et al. (1999) tabulates the specific material characteristics of English chalks based on laboratory tests performed by various authors. The details of an excerpt from these laboratory tests are outlined below in Table 4.4. The chalk dry density indicates the hardness of the material and from the chalks listed in Bell et al. (1999) the strongest material is also identified as the hardest. These data are used as the goal point for the calibration of chalk within PFC^{3D}.

Saturated chalk is typically weaker than dry chalk as shown by Matthews and Clayton (1993) and mentioned above. Dry chalk laboratory test data shows a positive linear relationship between a reduction in porosity and increase in unconfined compressive strength, that is strong dry chalks are the least porous. With saturated chalk however, this relationship begins to show curvature once the chalk is 40% porous or greater. The UCS is similar at around 1-2 MPa for all specimens with porosity above 40% (see Figure 4.12). Matthews and Clayton (1993) further state that regardless

Table 4.4: Excerpt of chalk characteristics as outlined by Bell et al. (1999)

Chalk Strata	**Dry Density** ($\frac{kg}{m^3}$)	**Dry UCS (MPa)**	**Sat. Density** ($\frac{kg}{m^3}$)	**Sat. UCS (MPa)**	**Young's Mod. E (GPa)**	**Porosity** η **(%)**	**Poisson's Ratio** ν
Upper Yorkshire	2060	25.6	2290	11.9	10.9	24.4	0.27
Middle Norfolk	1610	9.5	2000	3.6	8.0	35	0.31
Upper Kent	1440	5.5	1910	1.7	5.7	47	0.32

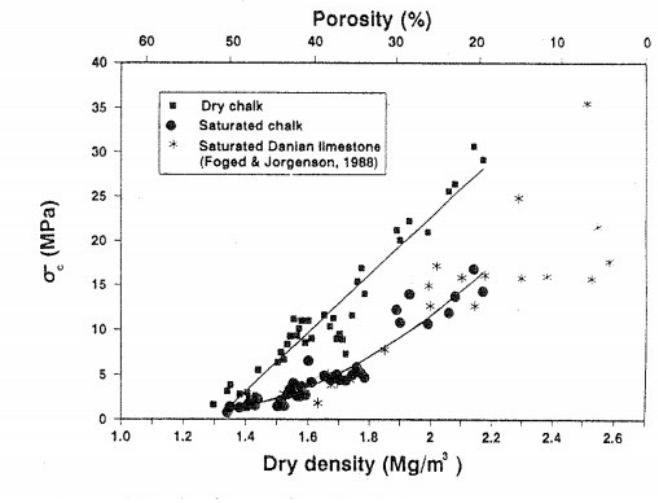

Figure 4.12: Influence of saturation on chalk strength from Matthews and Clayton (1993, Figure 2, pg 697).

of difference in specimen size and loading conditions, porosity and saturation dominate the UCS results.

4.5.2 Chalk BPM & Calibration

Although the properties of chalk are outlined by Bell et al. (1999), there are no clear indications of specimen sizes used in the laboratory tests collated. Therefore the numerical specimen radius size is set to that of the boulder in the oedometric and shear test of 0.05 m and 0.035 m, respectively. In this way the calibrated material is a synthetic representation of the chalk at the numerical specimen sizes utilised in the tests.

As stated earlier, the PSD of chalk is dominated by fines from coccoliths with a grain size of 0.5-12μm (Bell et al., 1990) with larger coccolith pieces up to 0.20 mm in size. As found earlier with the calibration of greywacke sandstone in PFC^{3D}, the number of particles can affect the efficiency of the model. Therefore, the PSD adopted for calibration is 200 times that of the actual material with a minimum particle radius of 1.0 mm and a maximum particle radius of 1.6 mm. This small range of values for the particle radii provides a fairly uniform material.

Chalk is not as brittle as sandstone and thus the friction value μ is set higher to provide a more ductile response. Otherwise the same process for calibration as followed for the sandstone is also followed for the chalk. Outlined in Table 4.5 below is an excerpt of selected calibration stages outlining microparameters, test results and calibration actions.

Table 4.5: Calibration of hard chalk

ID	Properties	Behaviour/Results	Actions
C2	Min Radius = 1.0 mm Radius Ratio = 1.6 ρ=1700 μ=0.25 $\frac{k_n}{k_s}$ = 0.4 E_c=8 GPa, E_{pb}=15 GPa $\bar{x}_{pb}$=80 MPa, s_{pb}=20 MPa	Provides a peak of 71 MPa, E=10 GPa, ν = 0.24	Peak too high - alteration of bond values required
C8	E_{pb}=14 GPa E_c=9 GPa $\bar{x}_{pb}$=60 MPa s_{pb}=30 MPa	E=9.8 GPa, peak=45 MPa is too high	Peak too high - alteration of bond values required
C10	$\bar{x}_{pb}$=30 MPa s_{pb}=10 MPa	Peak=22 MPa	Peak slightly lower than required - slight increase to $\bar{x}_{pb}$ required
C12	$\bar{x}_{pb}$=31.5 MPa	Peak=26 MPa	
C12-sat	Min particle radius = 3.5mm $\bar{x}_{pb}$=5.75 MPa s_{pb}=3.5 MPa	Peak=5.7 MPa	
C12-od	Minimum particle radius = 6mm Cylinder size equivalent to boulder of radius 45mm $\bar{x}_{pb}$=5.75 MPa s_{pb}=3.5 MPa	Peak=4.5 MPa	
C12-sh	Minimum particle radius = 6mm Cylinder size equivalent to boulder of radius 35mm $\bar{x}_{pb}$=4.3 MPa s_{pb}=2.5 MPa	Peak=4.5 MPa	

Bell et al. (1999), Hutchinson (2002) and Bowman and Take (2014) state that porosity and the percent of saturation of chalk controls the value of UCS. Table 4.4 clearly shows that there is a distinct decrease in density from the hard chalk of upper Yorkshire to the weak chalk of Kent mirrored by an increase in porosity. For calibration purposes and for this particular chalk material, weaker chalks can simply be produced by reducing the number of particles, that is reducing the volume and therefore the density of the specimen in order to increase the porosity. For example, removing 0.048 kg from C12 with a starting porosity of 35% produces a markedly reduced UCS of 6 MPa with an increased porosity of 49%.

Chalk flows occur in extremely weak to weak highly saturated chalk. Therefore C12 requires further calibration to reduce the UCS to approximately 5 MPa. The number of particles for the specimen were identified as likely to cause computational efficiency issues, thus the minimum particle radius was increased to 3.5 mm and further calibration required changes only to the parallel bond parameters. The resulting amendments to the parallel bond parameters result in the weak chalk C12-sat with η=37% and a UCS peak of approximately 5-6 MPa as required. The microparameters are outlined in Table 4.7 and results in Figure 4.13. Extremely weak chalk is found by reducing the number of particles to increase the porosity of the material with the volume removed for various porosities outlined in Table 4.6.

Table 4.6: Example of volume removal for creation of extremely weak chalk from weak chalk where the material volume of the PFC^{3D} specimen totals $0.0127m^3$.

Chalk Strength	**Porosity (%)**	**UCS (MPa)**	**Density ($\frac{kg}{m^3}$)**	**Mass (kg)**	**Reduction of Mass (kg)**
Weak	35	4.8	1700	21.658	0
	40	4	1610	20.511	1.147
	43	3	1530	19.492	2.166
	45	2	1490	18.983	2.675
Extremely Weak	47	1.5	1440	18.346	3.312

The parallel bond parameter values were recalibrated with the larger particle sizes (C12-od and C12-sh). With an increased minimum particle size to 6mm the UCS falls to 4.5 MPa, which is representative of a saturated weak chalk (see Figure 4.14). As with the sandstone material, this increase in particle size results in a minor decrease in the overall σ_t value and that of K_{1c} within PFC^{3D}.

4.5.3 Synthetic Chalk Material

The calibrated weak chalk microparameters are outlined in Table 4.7, with the stress-strain behaviour for the original C12 material and recalibrated C12-od (oedometer tests) and C12-sh (shear tests) specimens shown in Figure 4.13. This figure also outlines the associated extremely weak

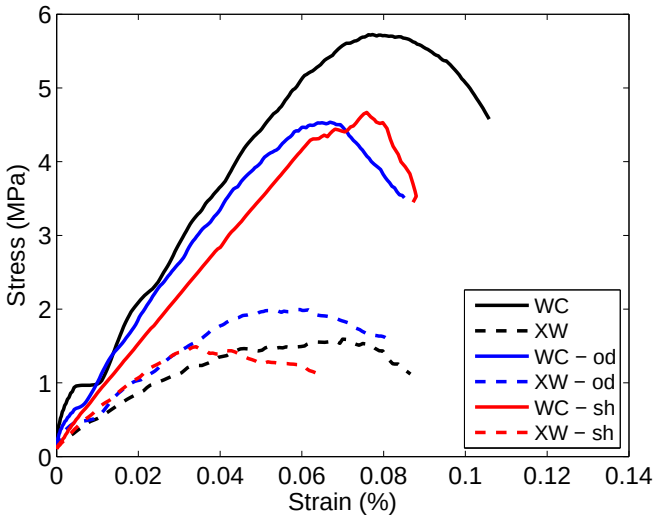

Figure 4.13: PFC^{3D} calibrated chalk materials stress-strain behaviour. Note that 'od'=oedometer specimen calibration and 'sh'=shear specimen calibration.

chalk stress-strain behaviour after material volume reduction for each of the associated weak chalks. Clearly the adjustment to the particle size reduces the peak strength of the material significantly even with the associated adjustments to the parallel bond strengths — which changes the post-peak behaviour. When the UCS peaks are plotted against those of Matthews and Clayton (1993), as shown in Figure 4.14, it can be seen that the UCS values adequately represent saturated weak chalk and saturated extremely weak chalk.

Table 4.7: Weak chalk microparameters

Particle Parameters	**Bond Parameters**
E_c=8 GPa	E_{pb}=10 GPa
ρ=1700 $\frac{kg}{m^3}$	$\bar{x}_{pb}$=5.75 MPa
μ=0.5	s_{pb}=3.5 MPa
$\frac{k_n}{k_s}$=0.4	

4.5.4 Strain Rate Effects

As for the calibrated sandstone material the calibrated weak chalk and extremely weak chalk materials are also tested at varying strain rates, to check the behaviour is consistent with that described in Section 4.2. The stress-strain results of the tests are outlined in Figure 4.15. The strain rates considered here consist of the range used in the oedometer testing in Section 5 for the chalks.

The results of the high strain rate UCS tests on the weak chalk specimen (Figure 4.15 (a)) show

a distinct increase in peak strength from 4.5 MPa to 45 MPa as strain rate increases from 1 s^{-1} to 100 s^{-1}. The stress-strain relationship also shows a jagged line at higher strain rates as seen by Zhang and Wong (2014) at their highest strain rates. The weak chalk responds more readily to the change in strain rate than the sandstone which is likely due to the higher porosity and lower strength of the chalk material. As strain rate increases, the stiffness increases and the material becomes more ductile. In the weak chalk case the 50 s^{-1} tests and above show ductility, with the 10 s^{-1} test appearing to be an intermediate situation between the brittle and ductile cases.

The bond breakage in the weak chalk specimen under varying strain rates is shown in Figure 4.16 (a). The lower strain rates cease breakage once peak strength is reached and the material becomes ductile. Under a strain rate of 50 s^{-1} the material shatters with only 1% of parallel bonds remaining at the end of the test. Under the 120 s^{-1} strain rate the weak chalk appears to explosively fragment with all parallel bonds lost almost instantaneously.

Figure 4.15 (b) plots the stress-strain results of the extremely weak chalk under varying strain rates. The extremely weak chalk also shows an increase in peak strength with increased strain rate. The material response is more ductile than that of the weak chalk with some strength increase at the 100 s^{-1} strain rate. Breakage is shown in Figure 4.16 (b) for the extremely weak chalk. The majority of breakage is complete once the peak strength is reached. Under strain rates of 50 s^{-1} and greater, the extremely weak chalk is completely shattered. As with the sandstone, both of the synthetic weak and extremely weak chalks are strain-rate dependent.

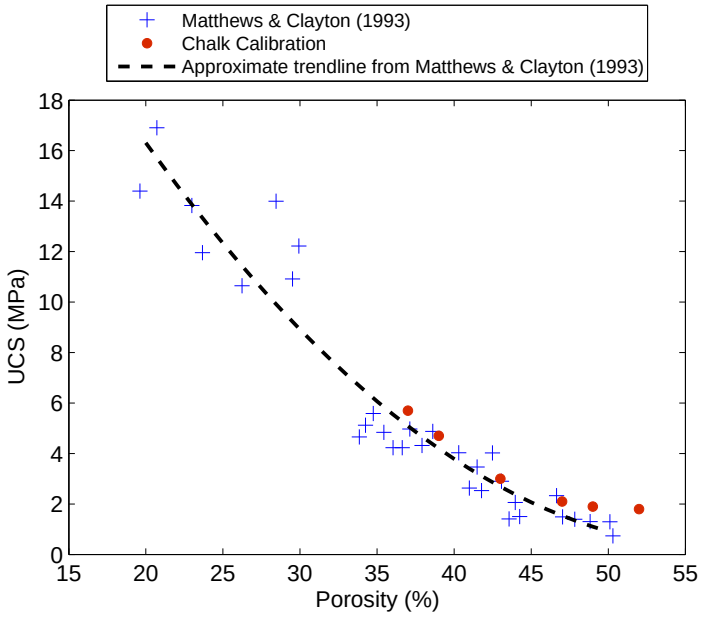

Figure 4.14: Comparison between PFC^{3D} calibrated weak (WC) and extremely weak (XW) chalk peak strengths and that of Matthews and Clayton (1993) data.

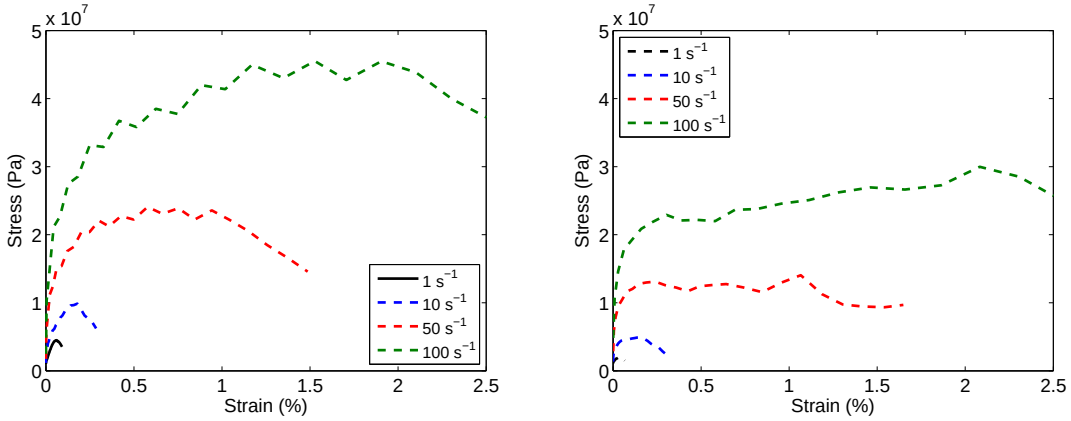

(a) Weak Chalk

(b) Extremely Weak Chalk

Figure 4.15: Stress-strain response of the calibrated chalk material under varying strain rates.

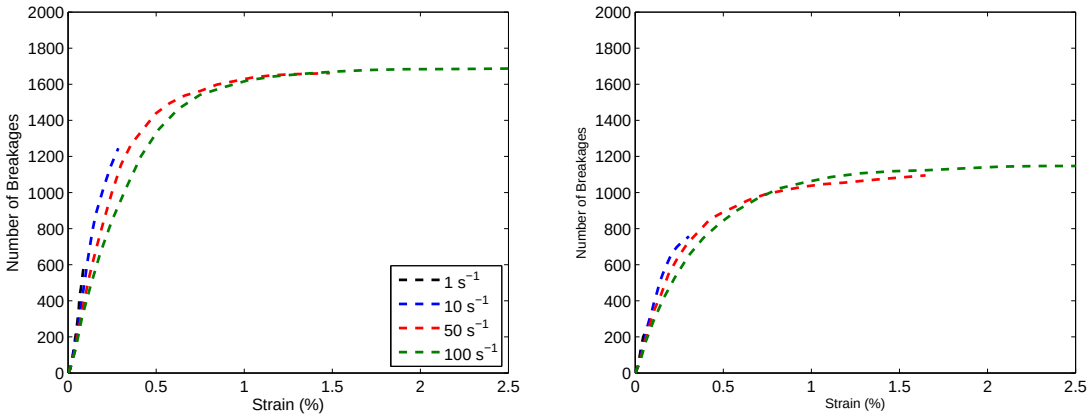

(a) Weak Chalk

(b) Extremely Weak Chalk

Figure 4.16: Breakage of the calibrated chalk material under varying strain rates.

Chapter 5

Oedometric Testing

Synthetic calibrated specimens of sandstone and chalk are tested in uniaxial compression via an oedometer in PFC^{3D}. As previously discussed in Chapter 3, the oedometer tests are designed to investigate the mechanics of rock blocks placed under fast and slow confined vertical compression. The material that becomes a sturzstrom typically falls from vertical heights above a valley floor of a few hundred metres to a kilometre or more. This material undergoes rapid compression at the transition from steep mountain side to relatively flat valley floor, at which point the pressure from the falling material is transferred through to the underlying rock blocks prior to runout beginning. For a small volume rockfall this overburden pressure is expected to be low, and for a sturzstrom the pressure is expected to be large due to the size of the initial failure.

In this series of oedometer tests, the overburden is represented by a plate (or wall) applied at varying strain rates to a cubic arrangement of rock boulders, exactly as performed in Chapter 3. The plate represents the pressure from the volume of overburden material, that may be applied at the high compression transition point from vertical fall to horizontal runout. Synthetic sandstone and chalk materials as calibrated in Chapter 4 are tested in the numerical oedometer, which allows for inferences to be made in regard to real materials under strain rates that can not be easily tested in laboratories. Comparisons can also then be made to the idealised HCP material tests of Chapter 3.

As with Chapter 3, the following oedometer tests investigate how the transition point may influence the runout of the material and in particular, the influence of energy on the system. Testing also looks at breakage of the boulder clasts, to determine if there is any enhancement to the production of energy due to the breakage, which may assist with the dispersion of material and potentially increase runout.

Table 5.1: Oedometer test platen speeds

Strain Rate (s^{-1})	Top Platen Velocity (ms^{-1})
1	0.3
5	1.5
10.0	3.0
20.0	6.0
50.0	15.2
100.0	30.4
120.0	36.5
500.0	152.0

5.1 Test Process

Following the test process outlined in Chapter 3, synthetic representations of sandstone and chalk were placed into the oedometric test arrangement with random orientation for each boulder. The calibration process for the sandstone and chalk materials and resulting material microparameters are outlined in the previous chapter. In this testing series, three random versions (in relation to particle placement) of each material were built and then tested under varying strain rates outlined in Table 5.1 below. The central boulder is built according to the material characteristics as previously calibrated, with the strength of the surrounding boulders set to higher values in order that they do not break.

As for the HCP oedometer testing in Chapter 3, rigid walls were used to represent platens and placed above and below the agglomerate system before testing began (see Figure 3.18). The speed of the top platen was adjusted to vary the strain rate as required for the testing series. The platen movement continued until 40% strain was reached, at which point gravity was turned off so that there was no additional input of energy that could influence the kinetic energy already generated by the test.

Measurement Parameters

The PFC^{3D} energy variables were tracked throughout the test process. These are outlined in more detail in Section 3.3.2 and listed below.

- Body Work
- Bond Energy
- Boundary Work
- Frictional Work
- Kinetic Energy
- Strain Energy

A measurement sphere was utilised to track additional details of the breakable central boulder. The particle items tracked closely are detailed in Section 3.3.2 and listed below.

- Coordination Number
- Porosity
- Sliding Fraction
- Stress Tensor
- Strain Rate Tensor

In addition to the variables able to be calculated via the energy and measurement logic in PFC^{3D}, information regarding the state of individual particles such as velocity, displacement and force, can be extracted using the in built FISH code. Given that particles may move outside of the measurement sphere during the test process, the FISH code was used to track each central boulder particle, and to calculate the overall central boulder microscopic stresses via summation of the mean and deviatoric stresses of each individual particle (see Section 3.3.2). System energies, breakage of the central boulder and overall wall stresses were also monitored throughout the testing process in order to determine the effect, if any, a fragmenting boulder may have on its surrounds.

5.2 Sandstone

The following section details the results obtained for oedometric tests of sandstone calibrated synthetic material in PFC^{3D}. This material has been tested with the same method and model design as outlined in Chapter 3 and above. Overall, nine boulders of 0.1m diameter are randomly rotated and placed into a cubic form within a box of dimensions 0.3 m x 0.3 m x 0.3 m, where the top platen speed is altered to create varying strain rates. The sandstone material microparameters are taken from the calibration process outlined in Chapter 4. Shown in Figure 5.1 are the orientations and values for the contact forces for the central boulder of sandstone specimen 1. On the left hand side is a plot of the direction and value of the forces across all contacts, while on the right hand side the red dots indicate the numbers of contacts in each direction. This plot indicates that the material is effectively isotropic, as are specimens 2 and 3 as shown in Appendix D.

5.2.1 Results

The oedometric test results are broken into sections so that clear inference can be drawn from the specific results, as well as considering the overall results. Overall, similar behaviour occurs across all three statistically independent specimens. The results are summarised below in the folllowing order:

- Breakage
- Energy Rates
- Stress
- Wall Stress
- Discussion

Breakage

The breakage across all specimens and selected strain rates is shown in Figure 5.2. Lower strain rates (in this figure 1 s^{-1} and 10 s^{-1}) show minor cracking occurring, with a delay until a significant breakage at around 30% strain, which leads to multiple smaller breakages across the whole material. The significant breakage is likely a key crack leading to coalescence of smaller cracks and ultimately failure of the material. The strain rate of 100 s^{-1} shows breakage occurring later (i.e. at a larger strain) than for the 500 s^{-1} strain rate and earlier than for the slowest strain rates. Again, it seems that key cracks are coalescing to cause the material to break.

It is clear that the highest strain rate of 500 s^{-1} causes breakage to occur at a lower strain than the other strain rates and that breakage is complete by 25% of strain. This suggests that the material has been compressed significantly quickly so that it has shattered or fragmented, with the coalescence of multiple cracks occurring at the same axial strain. This suggests that there is little influence of the initial fabric on breakage. The extensive breakage under the highest strain rate of 500 s^{-1} at 20% axial strain can be seen in Figure 5.3 (b) in comparison to the very minor breakages under the 10 s^{-1} strain rate (Figure 5.3 (a)).

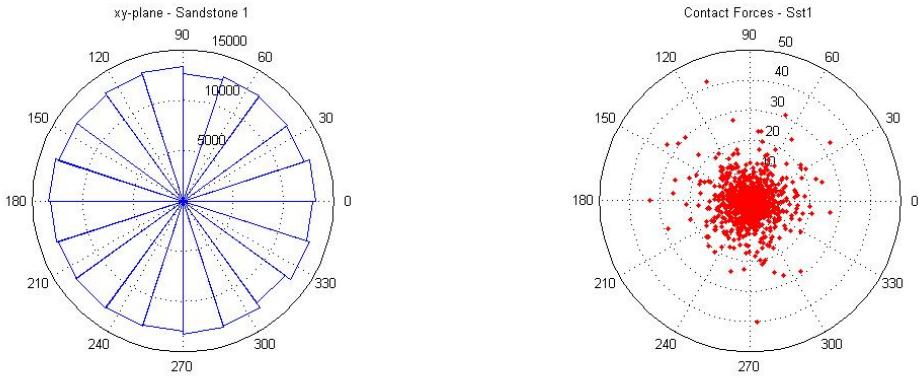

Figure 5.1: Contact orientation plots for sandstone specimen 1.

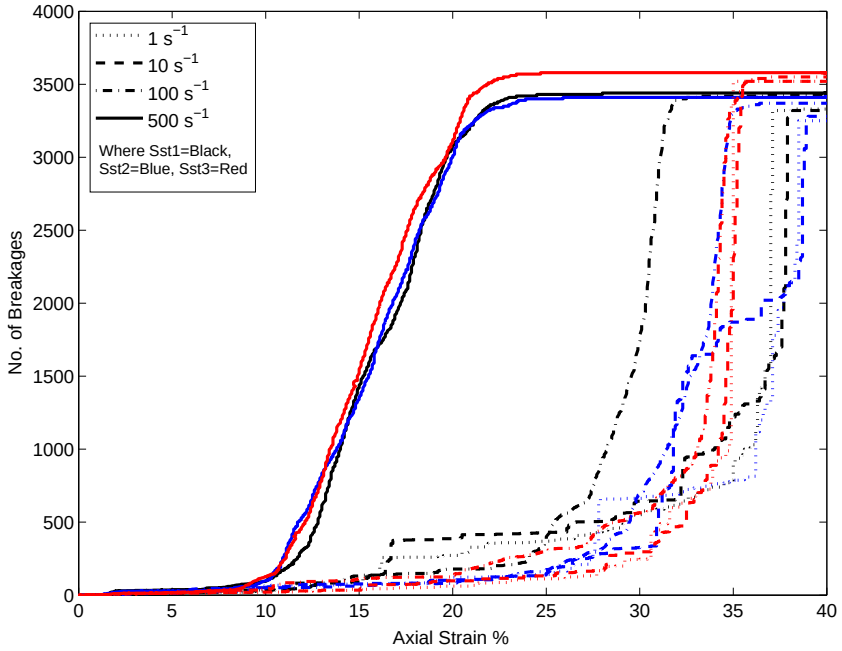

Figure 5.2: Bond breakage of three sandstone specimens (Sst1, Sst2, Sst3) with axial strain in relation to strain rate of oedometric test.

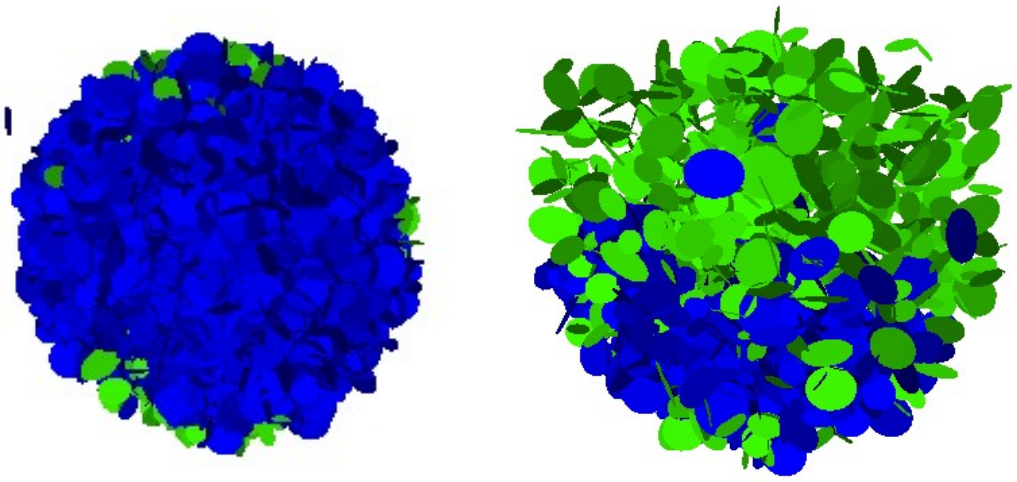

(a) 10 s^{-1} strain rate (b) 500 s^{-1} strain rate

Figure 5.3: Parallel bond breakages (green disks) for sandstone specimen 1 under slow and fast strain rates, taken at 20% axial strain.

Energy Rates

Graphs outlining the energy rate response to the oedometer tests on the sandstone material are shown in Figure 5.4. The graphs depict the energy rate (J/s^{-1}) for all tracked system energies calculated by PFC^{3D} which includes friction, bond, boundary, strain and kinetic energies, as axial strain increases.

The results indicate that the boundary work is exactly the same across strain rates $\geq$10 s^{-1} (when considered by specimen), possibly reflecting the work required to impart pressure onto the specimen. The boundary work rate increases near monotonically for all specimens. This may occur within a faster time at the higher strain rates, however the same response will occur at the same strain percentage for all specimens. Oscillations in boundary work begin after 25% strain, which represents either the beginning of breakage (for $\leq$ 50 s^{-1} strain rates) or the completion of breakage (for 500 s^{-1} strain rate). The 5 s^{-1} strain rate has a different response to that of the $\geq$10 s^{-1} strain rate tests, which occurs after 30% axial strain and directly relates to late breakage events.

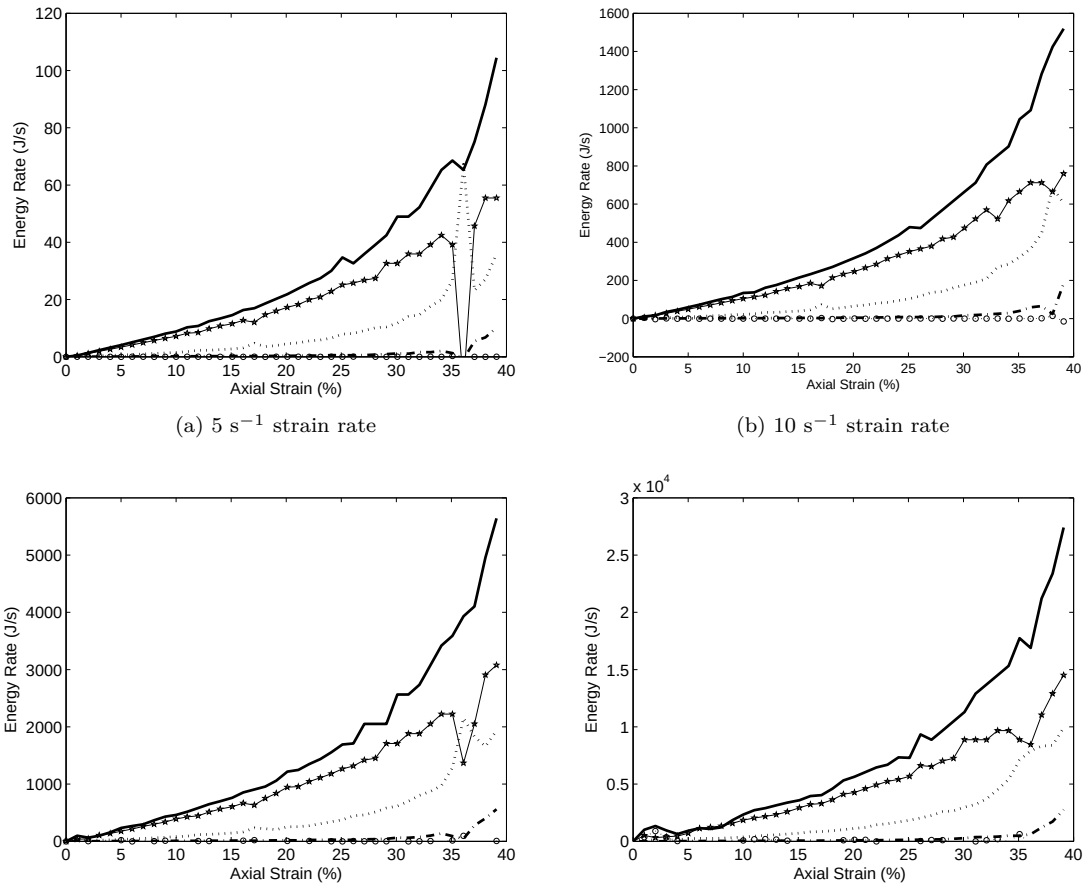

(a) 5 s^{-1} strain rate

(b) 10 s^{-1} strain rate

(c) 20 s^{-1} strain rate

(d) 50 s^{-1} strain rate

Figure 5.4: Energy rates for all tests in relation to axial strain for sandstone specimen 1.

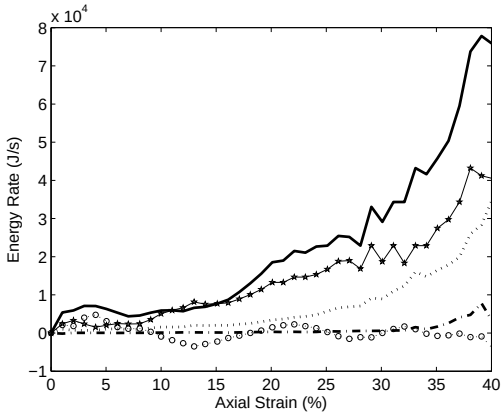

(e) 100 s^{-1} strain rate

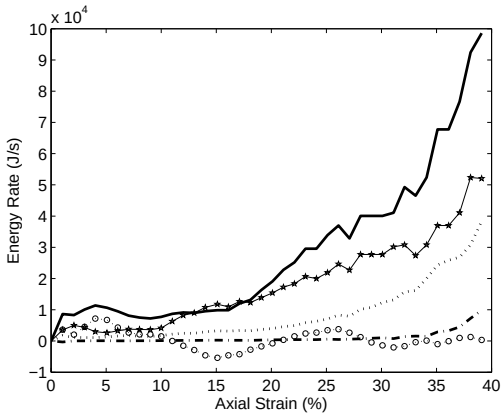

(f) 120 s^{-1} strain rate

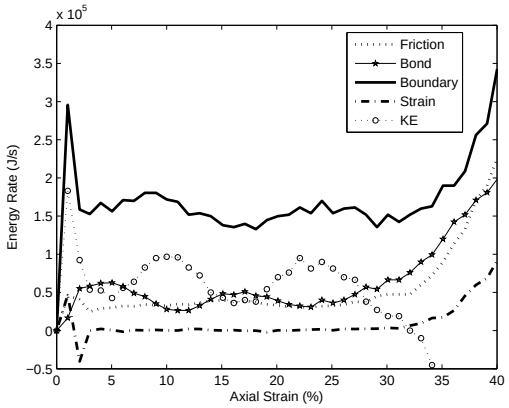

(g) 500 s^{-1} strain rate

Figure 5.4: (continued) Energy rates for all tests in relation to axial strain for sandstone specimen 1.

The bond energy rate generally increases with strain, however a decrease in bond energy is noticeable across all strain rates when substantial breakages occur. This decrease coincides with an increase in friction energy for the slow strain rates ≤ 50 s^{-1}, although the friction peak for the 50 s^{-1} strain rate is smaller and we begin to see a response from the kinetic energy. The 100 s^{-1} and 120 s^{-1} strain rate tests show a marked increase in bond energy initially above the boundary work response. Friction energy climbs at the same rate as the bond energy, with a delayed peak occurring due to the bond energy decrease that is associated with breakage.

Kinetic energy responds in a wave pattern for strain rates $\geq$100 s^{-1}, with the amplitude of the wave increasing as strain rate increases and decreasing as strain percentage increases. There is a possible inertial effect beginning to occur in these tests as kinetic energy responds with a small peak at around 1-2% axial strain. It is not directly clear from these graphs if the kinetic energy wave patterns are related to breakage. The 500 s^{-1} strain rate shows a considerable initial peak

of kinetic energy rate at 1-2% axial strain with an associated drop in bond energy rate âĂŞ– as mentioned above this is probably an inertial response, whereby after breakage the velocity in the particles is translated to kinetic energy. At this strain rate, the relationship between rates of bond energy and kinetic energy becomes more clear: bond energy rate remains low when the kinetic energy rate peaks. The kinetic energy rate peaks just prior to the beginning of breakage at 10% axial strain, drops away and then peaks again as breakage is completed between 20-25% axial strain. The kinetic energy rate then dissipates as there are no longer any bonds left to break. While breakage occurs, the rate of production of kinetic energy is higher than that of friction energy, which does not show any peaks during breakage. As soon as breakage is complete the bond, friction and strain energy rates increase to dissipate the compression forces. The energy rate graphs for sandstone specimens 2 and 3 can be found in Appendix D.

To further investigate the behaviour of kinetic energy across the varying strain rates, the kinetic energy rate was normalised by the square of the velocity of the platen and the result re-plotted. Figure 5.5 shows the behaviour of the normalised kinetic energy for each strain rate for sandstone specimen 1 (see Appendix D for the same graphs for specimens 2 and 3). For the strain rate tests below 50 s^{-1}, the greatest peaks in the normalised kinetic energy appear when breakages occur. Additional peaks occur throughout the tests, which appear to be associated with minor breakage events. As the strain rate increases, the normalised kinetic energy shows a wave response, with the highest peak occurring at around 10% axial strain when breakage begins, with other additional small peaks during later breakage events. In comparison, at the highest strain rate of 500 s^{-1}, the normalised kinetic energy climbs throughout the test reaching a maximum at around 30% axial strain, at which point breakage ceases and kinetic energy begins to reduce. Based on strain rate, the greatest normalised kinetic energy appears to occur during the slowest test, however this response is very oscillatory. The consistency of the normalised kinetic energy during the 500 s^{-1} strain rate test suggests that there is a much greater capacity for long term kinetic energy production with a fast application of load.

The kinetic energy peak values can also be considered as individual bursts of energy as breakages occur. The maximum peak values of kinetic energy for each strain rate is plotted in Figure 5.6, with the burst values compared for three strain rates of 5 s^{-1}, 50 s^{-1} and 500 s^{-1} for sandstone specimen 1 shown in Figure 5.7. In examining the maximum kinetic energy values for strain rates of 100 s^{-1} and lower, there appears to be an upper bound for the maximum kinetic energy. At these lower strain rates there is variation between the maximum kinetic energy value produced for each specimen, however as the strain rate increases, the data collapses to similar values of maximum kinetic energy regardless of specimen, and a power-law relationship appears. The arrangement of flaws is no longer governing the behaviour at high strain rates, whereas it dominates at low strain rates. This behaviour is indicative of the dynamic response of material to rapid loading as outlined

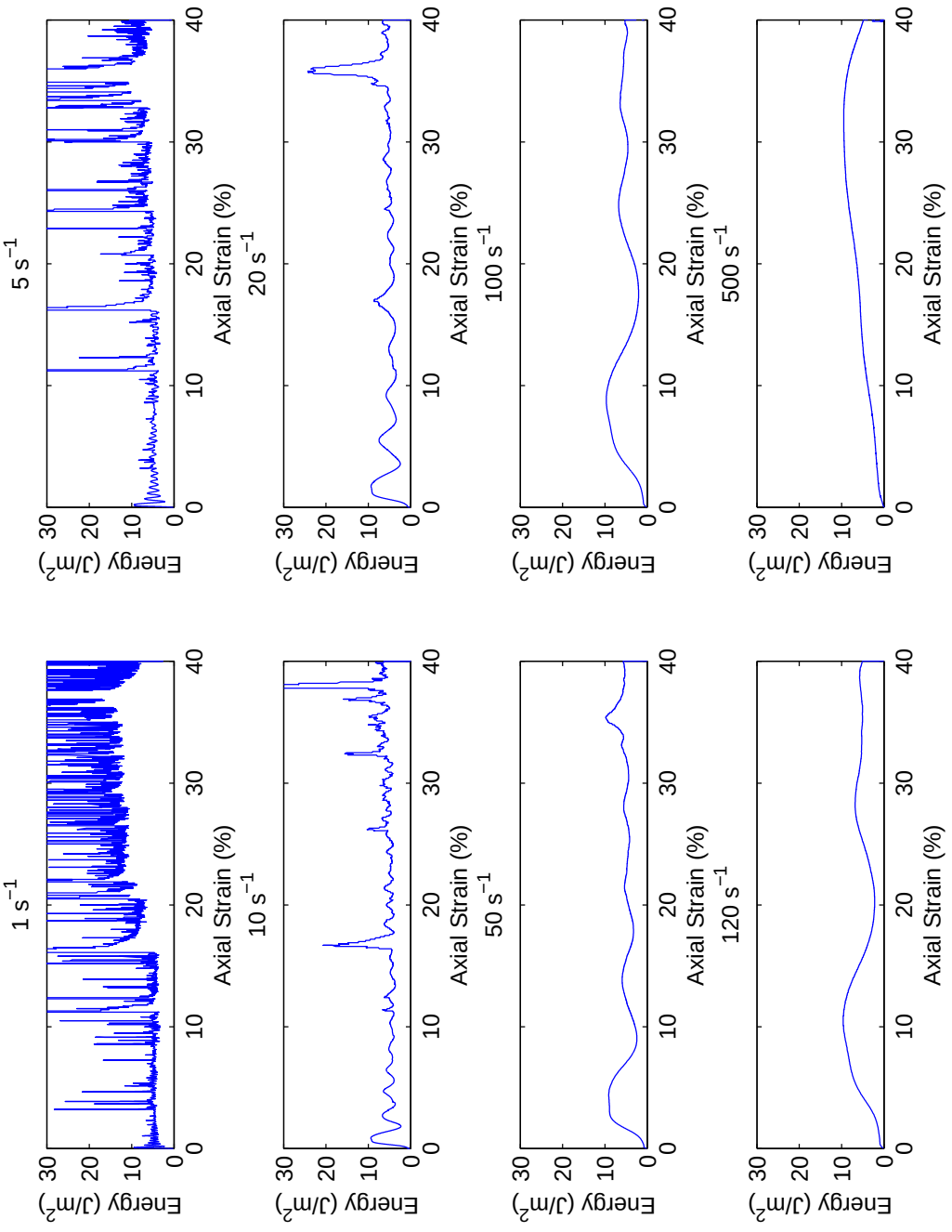

Figure 5.5: Normalised kinetic energy behaviour by strain rate for sandstone specimen 1.

by Grady and Kipp (1987).

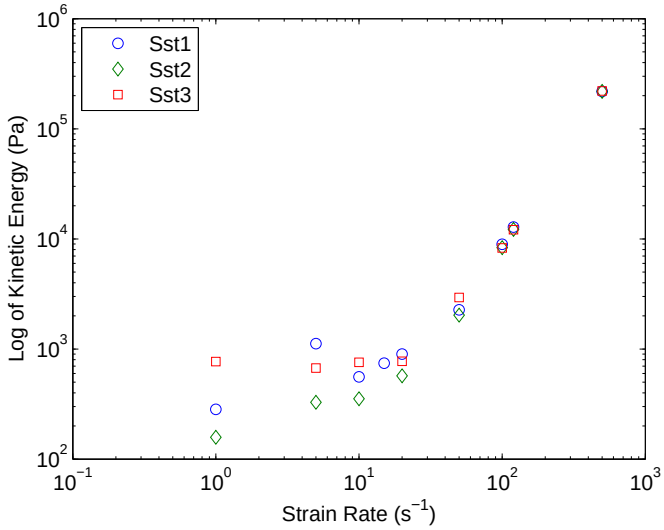

Figure 5.6: Maximum kinetic energy versus strain rate for each sandstone specimen.

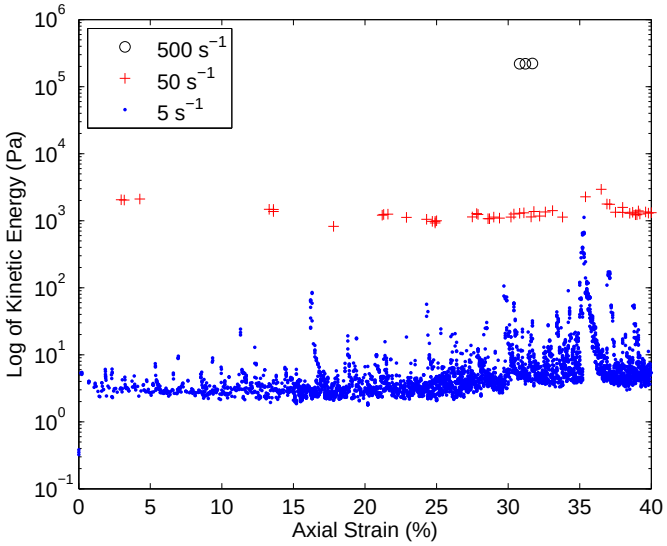

Figure 5.7: The kinetic energy peak or burst values for all sandstone specimens.

The kinetic energy burst values show clear ranges of the magnitude of kinetic energy that is available at different strain rates in these tests. At times the data may coincide when breakage occurs, for instance the 5 s^{-1} strain rate results show an increase in kinetic energy magnitude to levels seen in the 50 s^{-1} strain rate test during breakage. There is a clear increase in kinetic energy production with strain rate, although it seems that the slower strain rates may provide similar levels of kinetic energy at times of breakage.

Stress

As axial strain increases there is a direct increase in both mean and deviatoric stress for the breakable boulder, as seen in Figures 5.8 and 5.9 (see Appendix D for specimens 2 and 3). This is due to the overall increase in applied stress as the axial load increases with lateral confinement. Once the main breakage event occurs at around 25% axial strain, both micro-stresses drop substantially before beginning to climb again. For the 500 s^{-1} strain rate, breakage is spread from 10 to 25% strain and fairly consistent. The mean and deviatoric stresses plateau somewhat over this strain range, with peaks and troughs in the micro-stresses occurring just prior and at breakage, respectively (see Figure 5.10). Once breakage is complete (no further bonds are available), the mean and deviatoric stresses of the central boulder increase dramatically. At the same time it can be seen, by referring to Figure 5.4, that kinetic energy reduces and friction energy grows, which suggests that the particles may be rolling. For the slower strain rates, once the bonds of the central boulder are all broken, similar increases in micro-stresses are seen as for the 500 s^{-1} strain rate test.

During the 500 s^{-1} oedometer test, once 15% of axial strain is reached, almost half of the central boulder bonds are broken with damage to the upper two thirds of the boulder. Particles appear to begin to move sideways at this time and reach their highest velocity (see Figure 5.11 (a)). As the upper platen drops further the sideways moving particles are forced back into downward motion and velocity begins to slow (see Figure 5.11 (b)). Eventually, once the system is allowed to relax all velocity dissipates away.

Effective stress path plots (Figure 5.14) to 30% axial strain indicate a positive linear relationship, where all strain rates $\leq$500 s^{-1} reach a maximum ratio of 1.75. The stress path of the 500 s^{-1} strain rate test, however, has an unusual oscillatory behaviour. Muir Wood (1990, page 427) describes the oscillatory behaviour of a stress path plot from an undrained triaxial compression test as representing the change of loading direction in the effective stress space. Given the change in movement of the particles during the 500 s^{-1} strain rate oedometer test, changes in loading direction may explain the somewhat circuitous stress path. As outlined earlier, in DEM pore pressures do not exist (i.e. u=0), thus to have undrained behaviour would suggest that $p \neq p'$ and therefore the breakage of the material may be producing a pore pressure response.

The $\frac{q}{p'}$ stress ratio for the central breakable boulder, versus axial strain for the full 40% axial strain of the sandstone oedometer tests (Figure 5.13), provides a very different response to that seen in the HCP oedometer tests in Figure 3.16 (see Appendix D for relevant plots for sandstone specimens 2 and 3). Where the fastest strain rates in the HCP tests showed an immediate drop in $\frac{q}{p'}$ on application of load, the sandstone $\frac{q}{p'}$ instead provides an oscillatory response that settles to a consistent curve only once breakage begins. The 500 s^{-1} test shows a slightly lower value of $\frac{q}{p'}$ over the 10-25% axial strain period when breakage is occurring. So there is some, albeit slight, reduction in friction suggested by this response to fast loading.

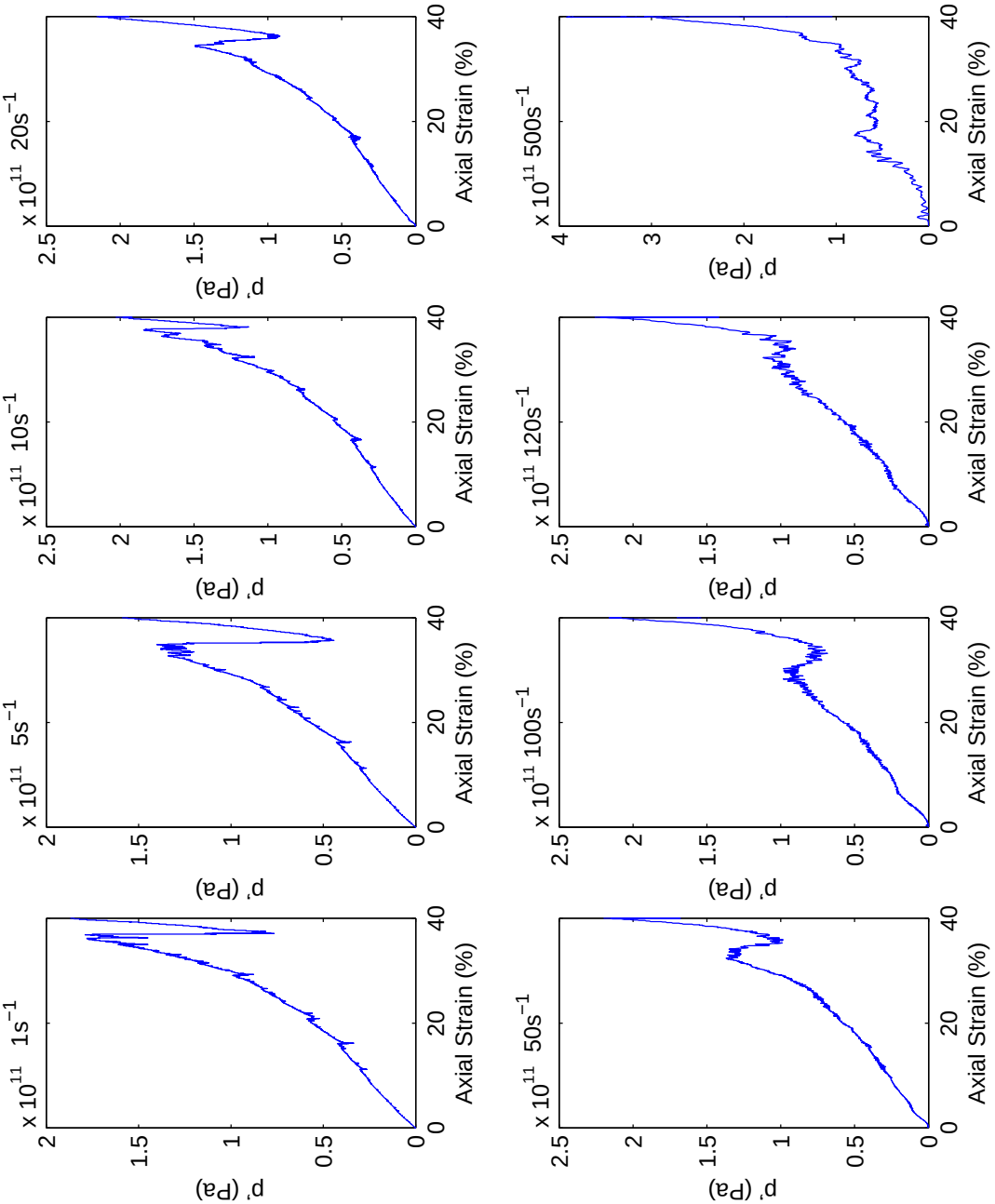

Figure 5.8: Mean stress for sandstone specimen 1.

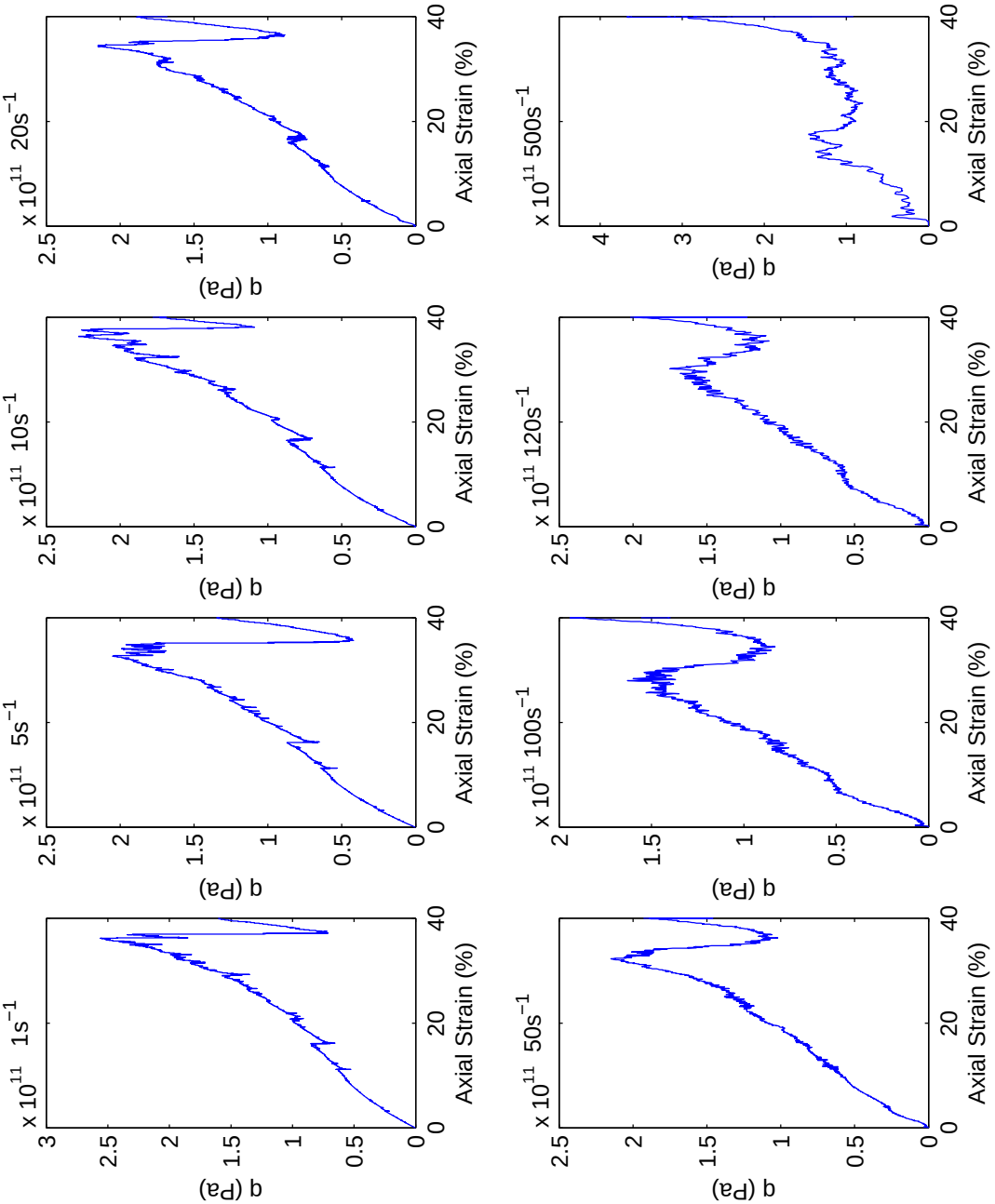

Figure 5.9: Deviatoric stress for sandstone specimen 1.

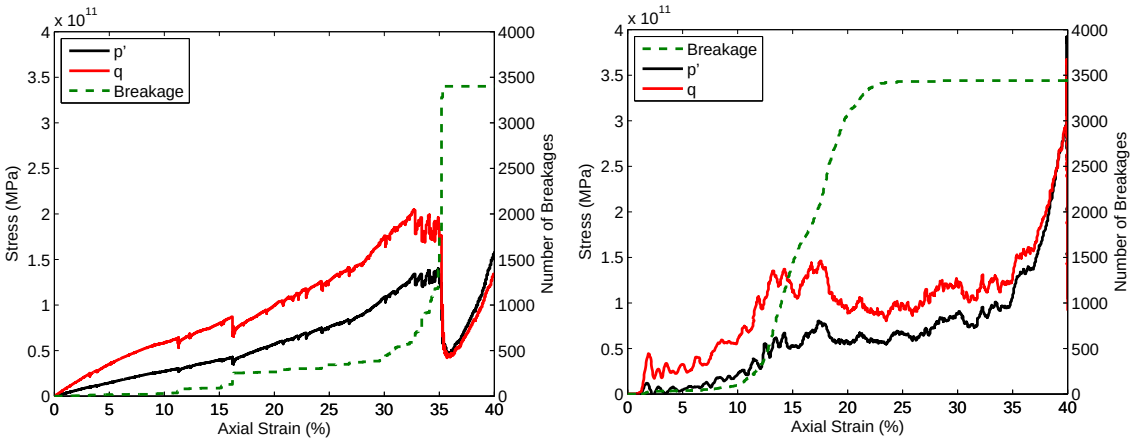

(a) 5 s^{-1} strain rate

(b) 500 s^{-1} strain rate

Figure 5.10: Breakage of central boulder bonds in comparison to q and p' microstresses for sandstone specimen 1 at 5 s^{-1} and 500 s^{-1} strain rates.

(a) 15% strain

(b) 20% strain

Figure 5.11: Velocity direction of particles, represented by arrows, for sandstone specimen 1 at 15% and 20% axial strain.

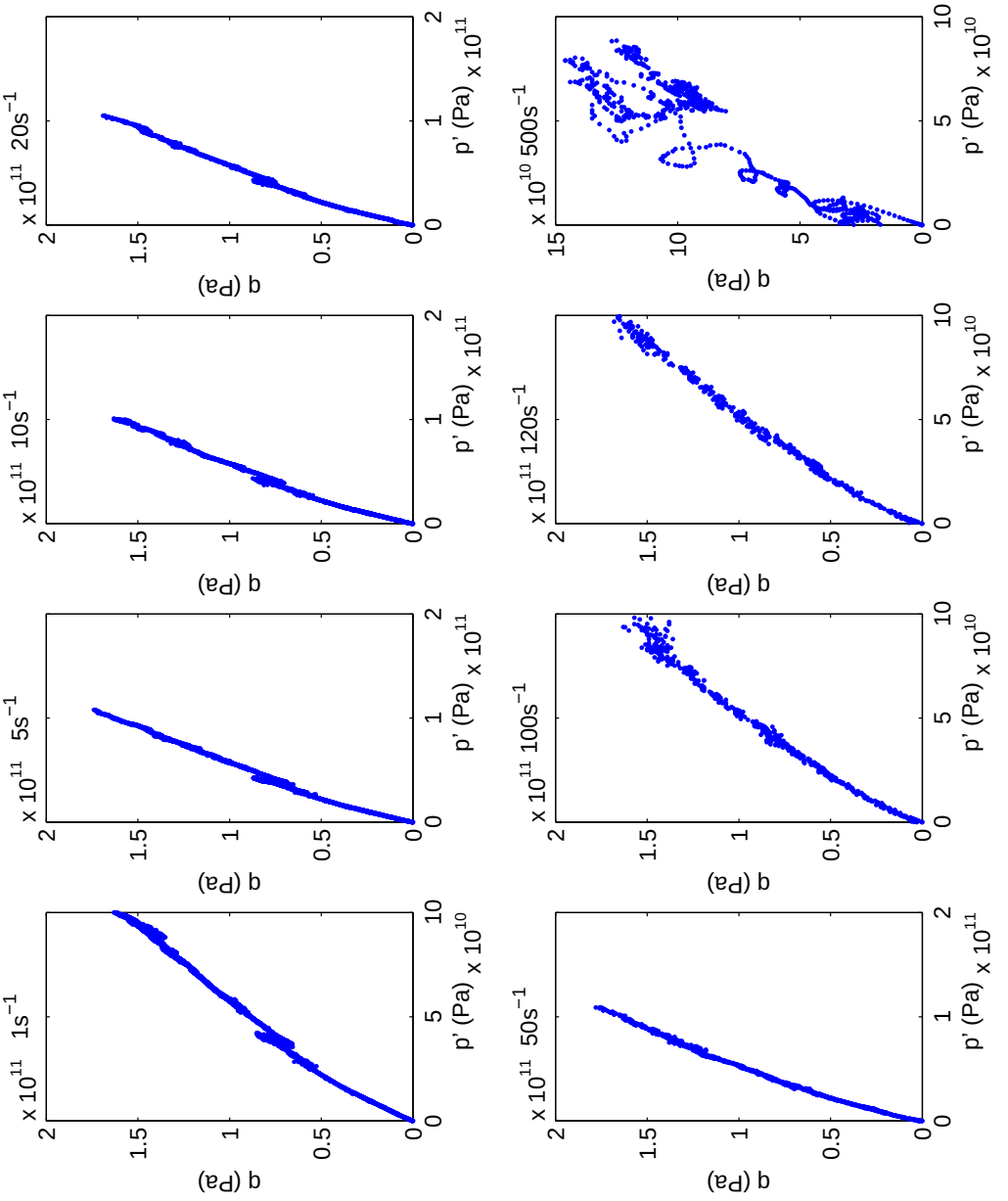

Figure 5.12: Stress path to 30% shear for sandstone specimen 1 - see Appendix D for results for other specimens.

The $\frac{q}{p'}$ stress ratio for the 10 s^{-1} and 100 s^{-1} strain rate oedometer tests shows far less oscillation, before settling into a slow decrease from around 5% axial strain until reaching a critical stress ratio of 1.0 at around 40% axial strain. Interestingly, there appears to be no substantial reduction in $\frac{q}{p'}$ when breakage occurs for the 100 s^{-1} (25-35% axial strain) and 10 s^{-1} (35-40% axial strain) tests. Once axial strain reaches 40% there is little separation in value between the resulting $\frac{q}{p'}$ for the three strain rates mentioned.

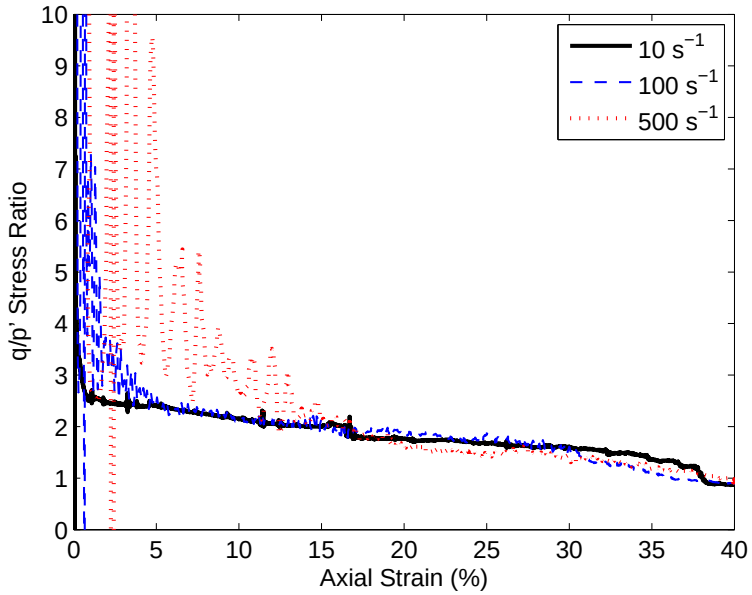

Figure 5.13: $\frac{q}{p'}$ stress ratio for sandstone specimen 1.

A comparison of the maximum values obtained by the stress paths at 15% axial strain gives a very linear relationship. When the relationship is estimated by a straight line, this line passes close to the origin suggesting a Mohr-Coulomb failure criterion may be appropriate for this material. This is perhaps not surprising, given that the PFC^{3D} contact model default is linear, and that the parallel bonds behave elastically until they break, when friction between particles takes over.

Wall Stress

As outlined above the initial contact forces in the specimens are isotropic, thus the wall stresses are similar at the start of each test. The wall stress average value is determined from the data of the three specimens where error bars show the minimum and maximum values with a cross or open circle for the average. The result is shown in Figure 5.14.

Results from all strain rate tests show that the X and Y wall stresses (refer Figure 3.20 for specimen orientation) deviate from one another, with the Y direction stress in particular growing. The maximum difference between wall stresses is within 0.1 MPa in most cases to 0.5 MPa at 40% axial strain. Interestingly, the 1 s^{-1} strain rate test has quite different wall stresses to those

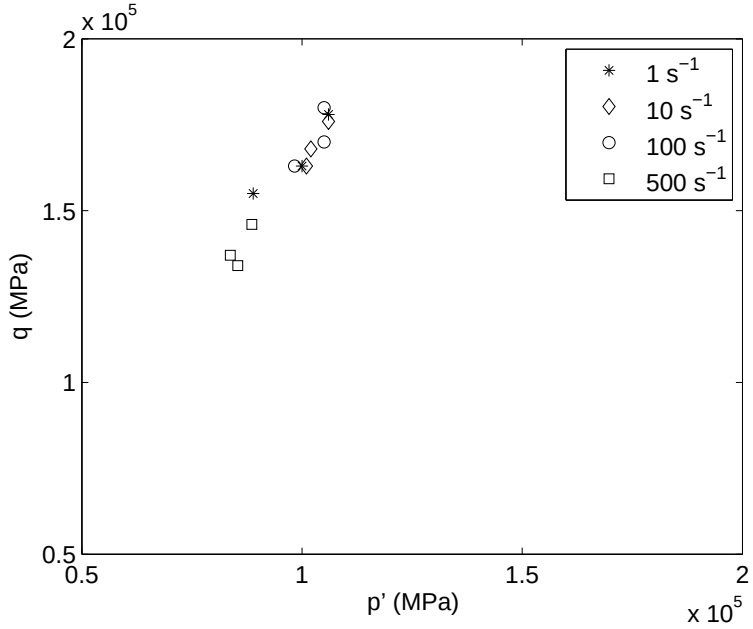

Figure 5.14: Maximum stress path values for selected strain rates and all sandstone specimens at 30% strain.

shown by all other tests. The Y wall stress remains below 0.3 MPa and does not undergo the rapid increase seen in all other tests. In fact, on average the Y wall stress is around 50 kPa and the X wall stress much less. This suggests that as the boulder is loaded there is some anisotropy occurring in response to the expansion of the boulder, however, substantial breakage does not take place until around 30% axial strain (Figure 5.2) at which point the Y wall stress begins to increase. Rapid breakage from 35-40% axial strain does little to increase this stress value. In comparison, the other strain rate tests show an increase in the Y wall stress during breakage, however. the main increase in stress appears to be related to the highest level of strain.

Once compression is completed, the material is left to relax with no gravity to influence any further movement. Under 5 s^{-1} strain rate, the wall stresses rise gradually throughout the test (see Figure 5.15 (a)). The introduction of relaxation sees the wall stress stabilise to a consistent value, however the X and Y stresses do not equalise or return to their initial values. Long term, as relaxation occurs, the wall stresses for the 500 s^{-1} test return toward their initial values (see Figure 5.15 (b)) prior to the commencement of the compression with X and Y values becoming similar again. This shows that the behaviour of the wall stresses is very reliant on the rate of compression, as to be expected.

5.2.2 Summary

Three independent synthetic sandstone materials have been placed under varying strain rates via an oedometer. The results show that under lower strain rates $\leq$100 s^{-1}, breakage is slow to begin

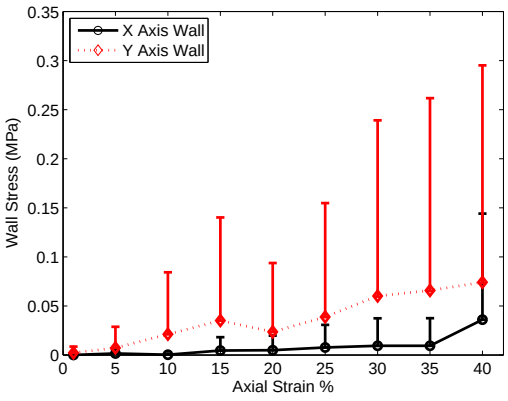

(a) 1 s^{-1} strain rate

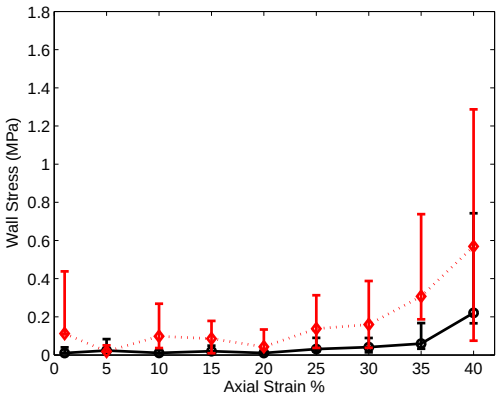

(b) 5 s^{-1} strain rate

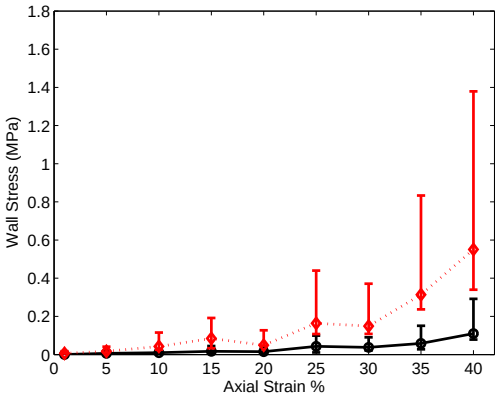

(c) 20 s^{-1} strain rate

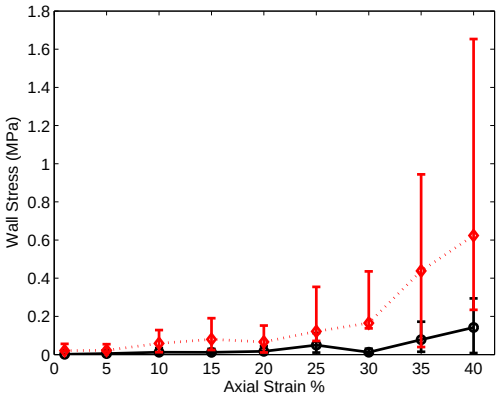

(d) 50 s^{-1} strain rate

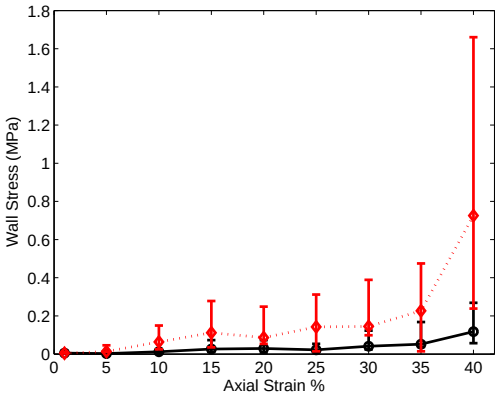

(e) 100 s^{-1} strain rate

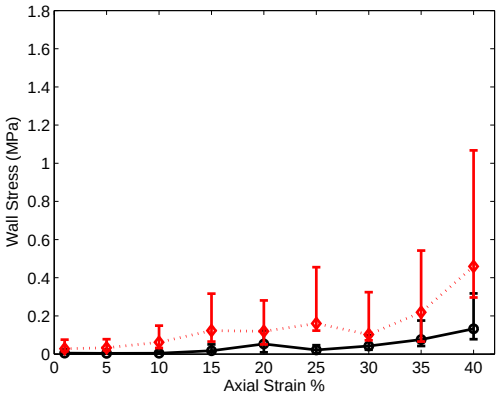

(f) 120 s^{-1} strain rate

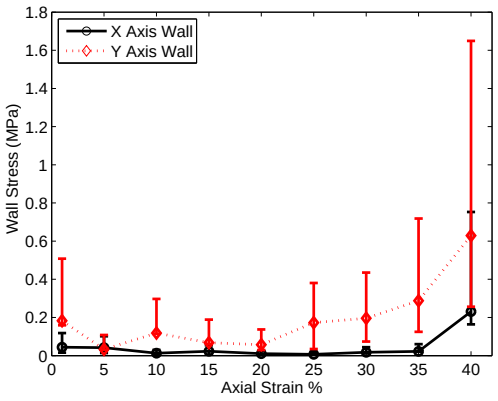

(g) 500 s^{-1} strain rate

Figure 5.14: (continued) Wall stress averages determined from all sandstone specimens.

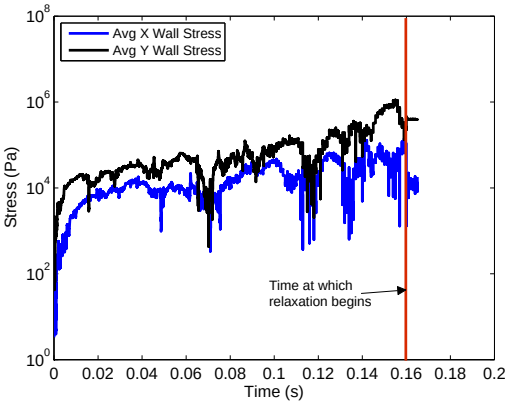

(a) 5 s^{-1} strain rate

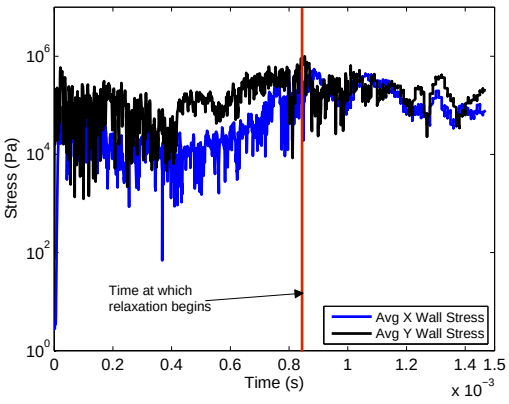

(b) 500 s^{-1} strain rate

Figure 5.15: X and Y wall stress averages against time for 5 s^{-1} and 500 s^{-1} strain rate tests.

and completed by 40% strain. The energy in the system under these lower strain rates is dominated by boundary and bond energy with little kinetic energy occurring in response to the breakages. The 500 s^{-1} strain rate, however, produces significant early breakage in the central breakable boulder with associated influences on kinetic energy production. The bond energy rate from all strain rate tests decreases during breakage with friction increasing for low strain rates and kinetic energy increasing for high strain rates. There is a possible kinetic energy inertial effect at high strain rates.

High strain rates produce larger kinetic energy peaks than those of the lower strain rates, with a consistent growth in kinetic energy throughout the tests. Overall, the maximum kinetic energy points for the oedometer tests produce a power-law relationship. The slow strain rate tests provide a static response with an upper bound of kinetic energy. Once the strain rate reaches 50 s^{-1} and higher, the relationship moves into a dynamic regime.

Once breakage occurs the micro-stresses in the central boulder drop with an overall reduction in the $\frac{q}{p'}$ stress ratio, suggesting a slight reduction in friction as a result of breakage under all strain rates. The X and Y wall stresses are reliant on the rate of compression and show anisotropy as axial strain increases. Once the grains are relaxed the wall stresses return to pre-test and equal values under high strain rates. This suggests that there is some influence from the boulders on the wall stresses during the oedometer test, however it is not clear if this is directly related to breakage.

5.3 Chalk

5.3.1 Results – Weak Chalk

Parameters & Calibration

Initial testing of the weak chalk material followed the methodology described for the sandstone above. Tests were performed using the oedometer strain rates as outlined in Table 5.1 where for a cubic specimen of 0.3 m x 0.3 m x 0.3 m the top platen velocity is 152 ms^{-1}. Results suggested that the strain rates as utilised for the sandstone were too high for the weak chalk, as the results produced a linear relationship between the log of kinetic energy and log of strain rate. This result suggests that these tests were performed within the dynamic regime of weak chalk.

If the fall height of a chalk cliff is compared to that of the fall height of a sandstone sturzstrom, then it would be expected that the chalk would fall a maximum of around 100m to the sandstone's 1000m (10%). Chalk would therefore be expected to experience a lower strain rate than that of the sandstone at the transition point. For example, consider a sandstone sturzstrom travelling at 80 ms^{-1} velocity, then it could be considered that a chalk flow may travel at 8 ms^{-1} velocity (10%). Thus, the strain rates for a cubic specimen of 0.3 m height would be approximately 260 s^{-1} for the sandstone, and 26 s^{-1} for the weak chalk.

To produce results in the static regime would require much slower strain rates, resulting in time consuming numerical runs due to the number of particles and resulting calculations per time step. As the strain rate is equivalent to the ratio of the platen velocity and height of the specimen, it was decided to reduce the size of the boulders, and therefore the cube, in order to reduce the strain rate and the overall number of particles. The resulting weak chalk cubic specimen was set to 0.225 m x 0.225 m x 0.225 m, with the diameter of each boulder reduced to 0.075 m each. The strain rates for the chalk tests are outlined in Table 5.2.

While the fastest strain rate of 500 s^{-1} appears extreme for chalk material it is worth considering the potential strain rates that may be experienced in the field. For example, a chalk block of 100mm diameter that falls from 100m height will attract a free fall velocity of $v^2 = u^2 + 2as = 0 + 2x10x100 = 2000$ or a maximum velocity of 45 ms^{-1}. Given the diameter of the boulder falling from the cliff, this results in a strain rate of 450 s^{-1}. Therefore, a strain rate of 500 s^{-1} is realistic for this material.

Table 5.2: Oedometer test platen speeds — chalk

Strain Rate (s^{-1})	Top Platen Velocity (ms^{-1})
1	0.225
10.0	2.25
50.0	11.25
100.0	22.50
500.0	112.50

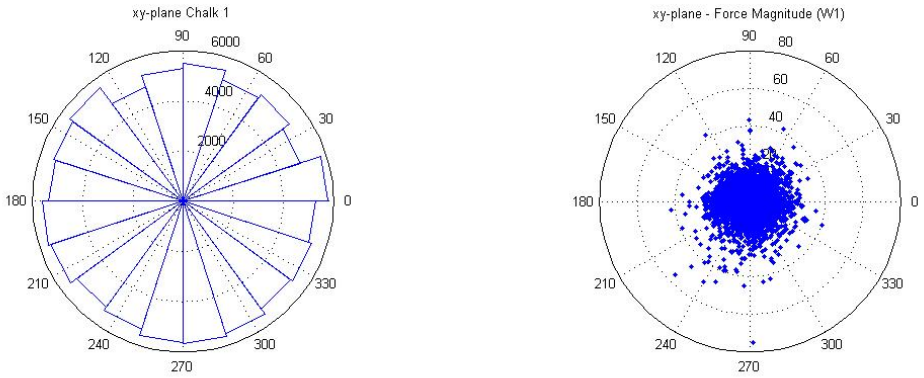

Figure 5.16: Contact orientation plots for weak chalk specimen 1.

The parameters for the recalibrated weak chalk material are outlined in Chapter 4 (C12-od) and are used here to build three weak chalk specimens for oedometer testing. As with the HCP testing in Chapter 3 and the testing on the sandstone material outlined above, the central boulder of the cubic arrangement of 27 rock boulders is breakable, with the surrounding boulders not breakable. Contact orientation and values for weak chalk specimen 1 are shown in Figure 5.16.

As with the sandstone oedometer testing, the results are outlined below under sub-headings relevant to the areas of interest before being summarised.

Breakage

The slower tests of 1 s^{-1} and 10 s^{-1} strain show a substantial breakage (35-70% of bonds) from 0-5% axial strain, followed by additional periods of breakage throughout the remainder of the compression to 40% axial strain. The 50-500 s^{-1} strain rate weak chalk oedometer tests indicate that breakage is almost complete within 5% axial strain. The results for weak chalk specimen 1 are outlined in Figure 5.17 with specimens 2 and 3 in Appendix E. For the slower tests it takes greater strain to break the bonds, in contrast to the dynamic regime where the breakage is almost instantaneous. An increase in strain rate from 10 s^{-1} to 50 s^{-1} results in near instantaneous breakage, which is perhaps explained by the inertial effect.

Energy Rates

The energy rate results of the weak chalk strain rate tests up to 100 s^{-1} indicate that boundary work, accumulated work done by the walls on the system, dominates the energies monitored (see Figure 5.18). Bond energy and strain energy show signs of being interrelated and mimic each other closely. Kinetic energy and friction energy are low, with kinetic energy at times appearing to be negligible. The energy rates are plotted in Figure 5.19 to 5% axial strain. These plots show that little is happening with the energies in the system below a strain rate of 100 s^{-1}.

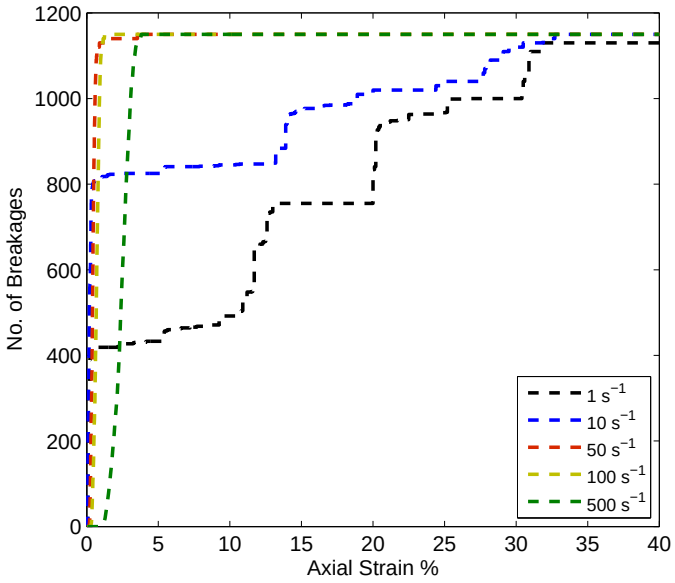

(a) Breakage

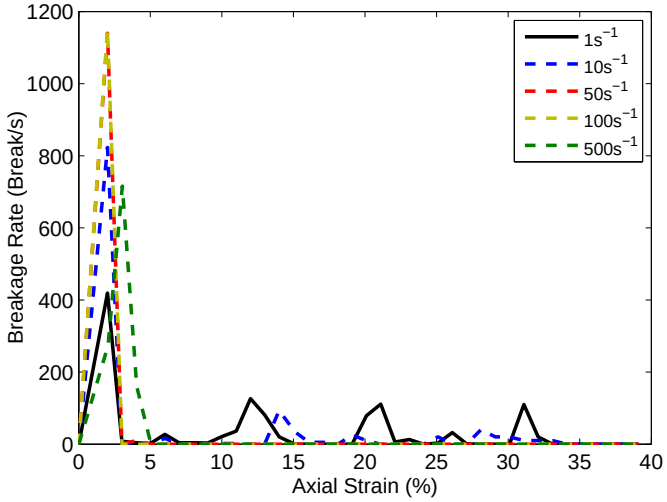

(b) Breakage rate

Figure 5.17: Breakage and breakage rate for weak chalk specimen 1 across all strain rates tested.

Once the strain rate is increased to 500 s^{-1} energy rate changes occur. At the completion of breakage it can be seen that bond energy increases above that of boundary work. Strain energy follows the bond energy, as also seen in the slower strain rate tests, and friction energy remains low. A peak occurs in the kinetic energy at the time of breakage and it seems that the kinetic energy then oscillates, which may be a result of loose particles rolling. The energy rate graphs for weak chalk specimens 2 and 3 are located in Appendix E.

The normalised kinetic energy at the 1 s^{-1} and 10 s^{-1} strain rates shows sharp peaks that appear to be coincident with breakage events (Figure 5.20 for specimen 1, Appendix E for specimens 2 and 3). For the 50 s^{-1} strain rates and upward, the normalised kinetic energy shows oscillatory behaviour. The 50 s^{-1} and 100 s^{-1} graphs also show a damping of this oscillation after reaching 10% axial strain. This damping may relate to the fact that the main breakage events are complete for these tests after only 5% axial strain, and thus there is no further introduction of energy to the system. The continued oscillation of the 500 s^{-1} normalised kinetic energy is directly related to the pulsing of the kinetic energy rate as outlined above.

The maximum kinetic energy values for the weak chalk specimens is shown in Figure 5.21 and as with the sandstone material, also produces a power-law relationship of order 2. The regime changes from quasi-static to dynamic at the 10 s^{-1} strain rate. In this plot it can be seen that all specimens have very similar values for each strain rate. In Figure 5.22, the kinetic energy peak values across the axial strain of the tests show a clear distinction between strain rates. Although less peaks or bursts occur for the 500 s^{-1} strain rate test, the order of magnitude is much greater than that for the lower strain rate tests.

Stress

While breakage is occurring the mean and deviatoric stresses remain low for the 1 s^{-1} and 10 s^{-1} strain rates. From 20% axial strain both stresses begin to increase with this becoming more rapid from around 30% axial strain, as can be seen in Figures 5.23 and 5.24. As with the sandstone, this sudden increase in mean and deviatoric stresses could be attributed to the rolling of individual particles once breakage has ceased. The 1 s^{-1} strain rate micro-stresses show very small peaks that are coincident to additional breakage events, which occur after the main breakage event of 0-5% axial strain. The 100-500 s^{-1} strain rate tests show small and large (respectively) peaks in both the mean and deviatoric stresses that occur at the same time as the initial breakage event. As with the lower speed tests, both micro-stresses increase rapidly from 30% axial strain onward for the higher strain rates.

Given that the majority of breakage is complete by 5% axial strain, the effective mean p' and deviatoric q stresses are considered in comparison to breakage to 5% axial strain in Figure 5.27. It is clearly shown in this figure that increases in both p' and q occur just prior to breakages. The largest increases are directly related to the largest number of breakages to follow, with both

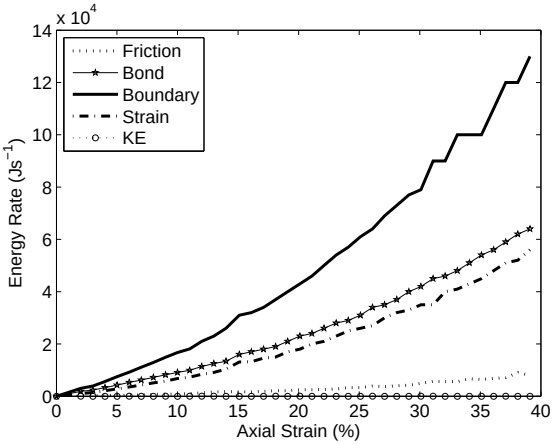

(a) 1 s^{-1} strain rate

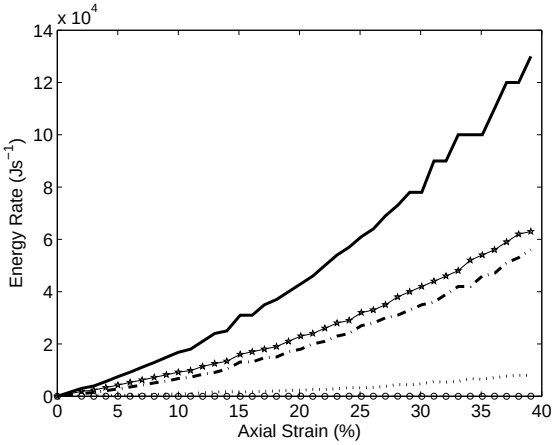

(b) 10 s^{-1} strain rate

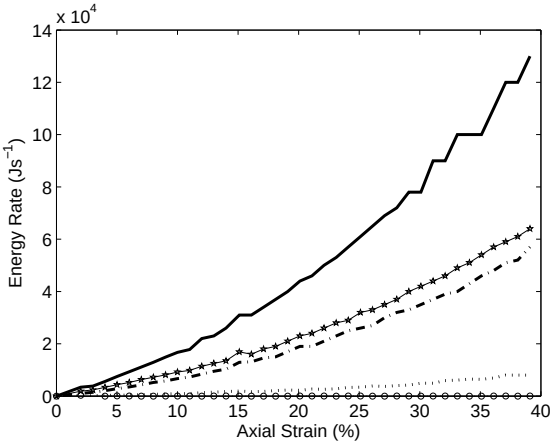

(c) 50 s^{-1} strain rate

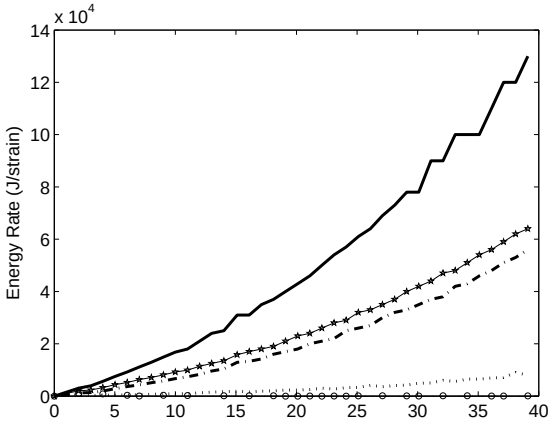

(d) 100 s^{-1} strain rate

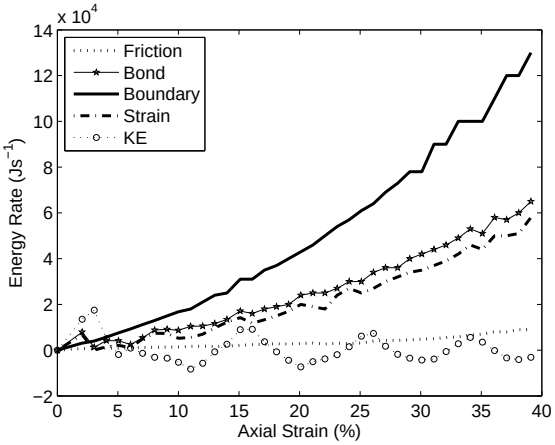

(e) 500 s^{-1} strain rate

Figure 5.18: Energy rates from 1 s^{-1}, 10 s^{-1}, 50 s^{-1}, 100 s^{-1} and 500 s^{-1} strain rates to 40% axial strain- weak chalk specimen 1.

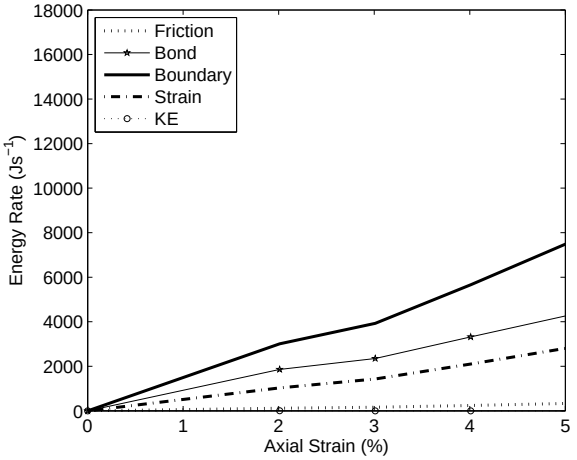

(a) 1 s^{-1} strain rate

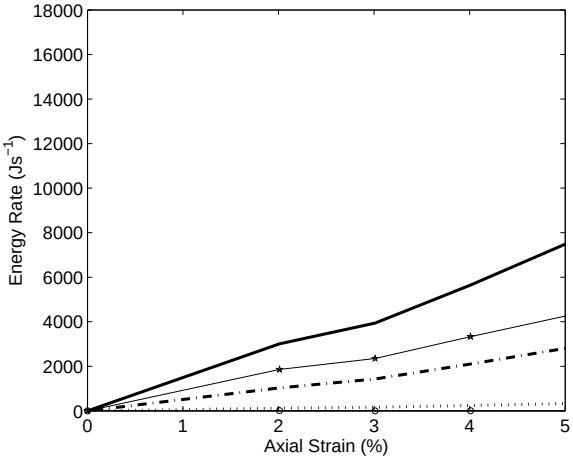

(b) 10 s^{-1} strain rate

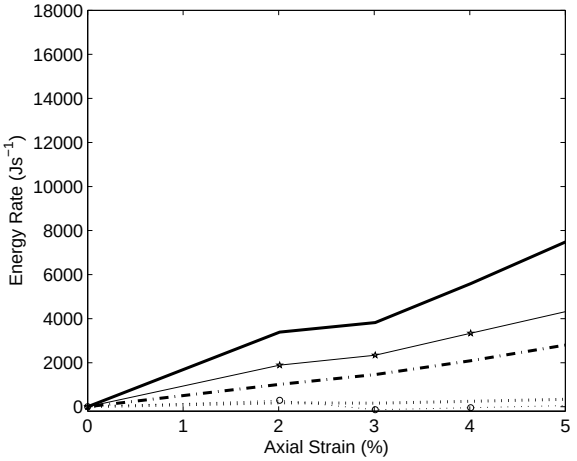

(c) 50 s^{-1} strain rate

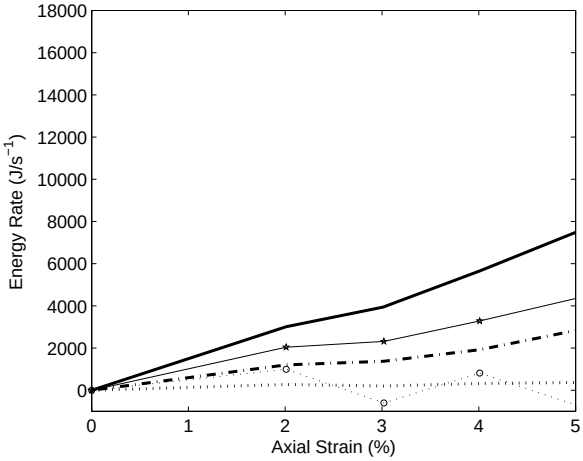

(d) 100 s^{-1} strain rate

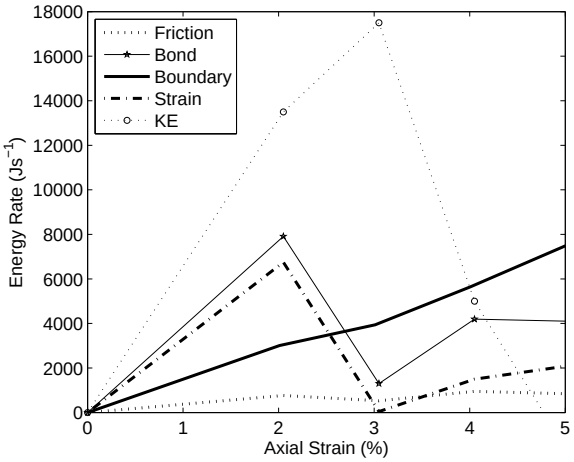

(e) 500 s^{-1} strain rate

Figure 5.19: Energy rates from 1 s^{-1}, 10 s^{-1}, 50 s^{-1}, 100 s^{-1} and 500 s^{-1} strain rates to 5% axial strain- weak chalk specimen 1.

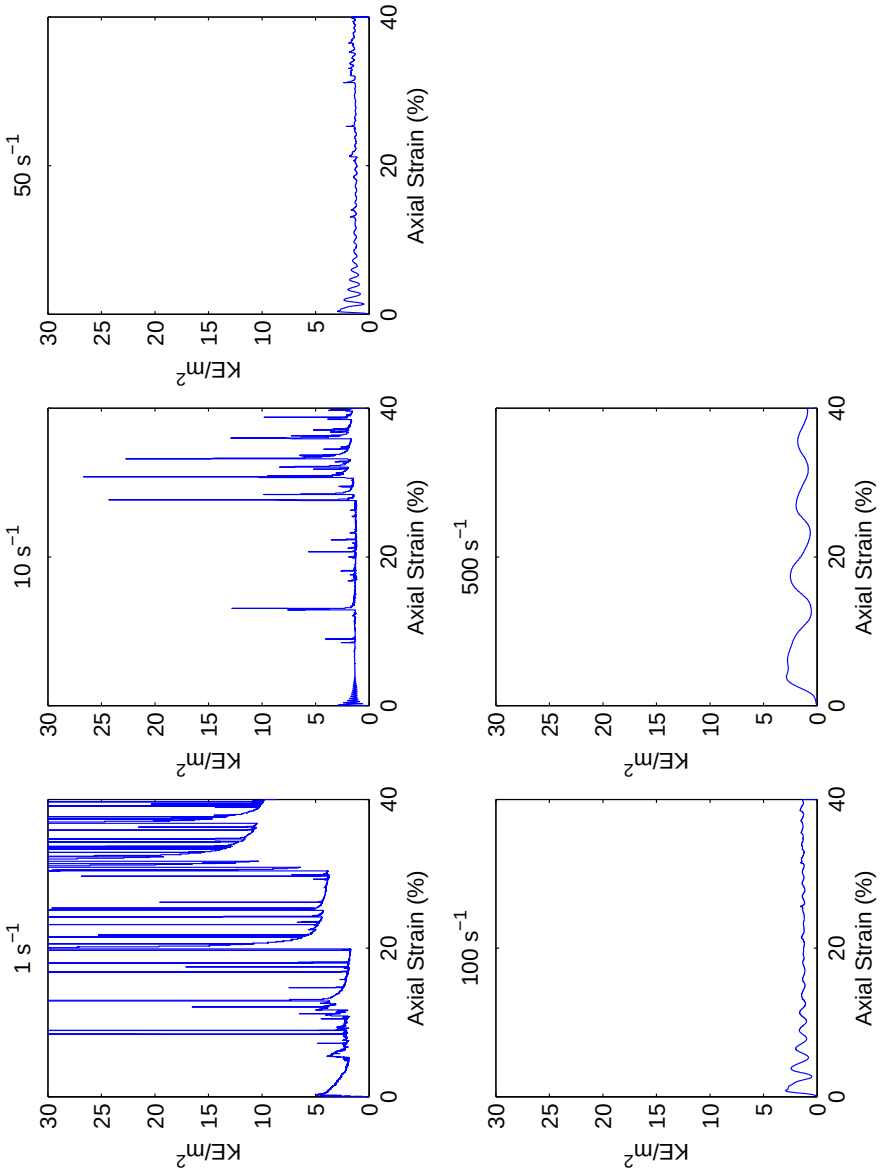

Figure 5.20: Normalised kinetic energy behaviour by strain rate for weak chalk specimen 1.

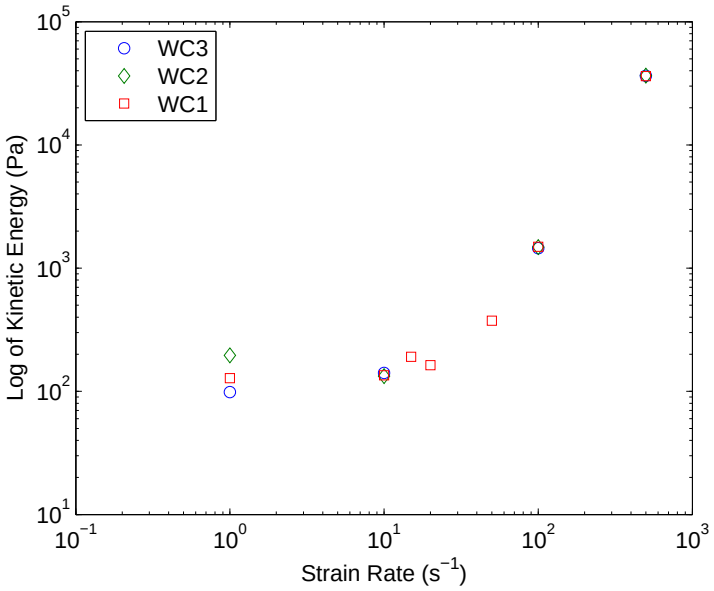

Figure 5.21: Maximum kinetic energy versus strain rate for all weak chalk specimens.

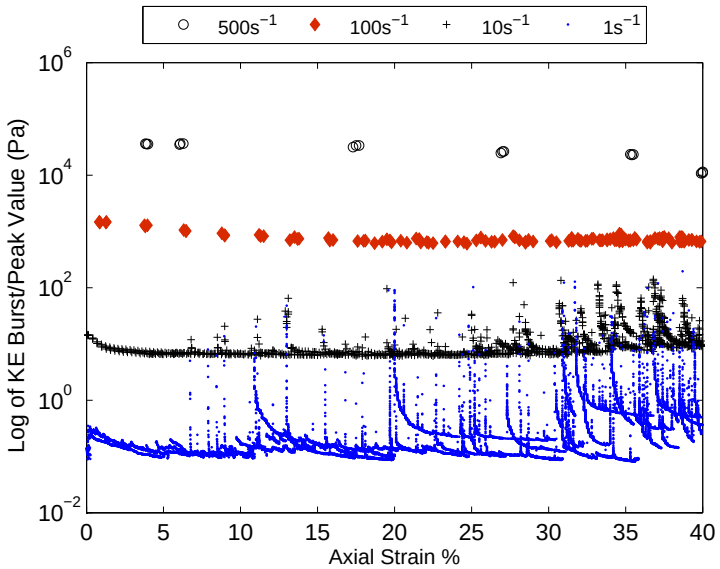

Figure 5.22: The kinetic energy peak or burst values for all weak chalk specimens.

micro-stresses quickly dissipating after breakage has occurred.

The effective stress path plots in Figure 5.26 for the weak chalk oedometer tests are generally positive and linear, with the maximum ratio values reaching around 1 for all strain rates. All stress paths appear to reach a local maximum at 15% axial strain before oscillating, which is most noticeable for the faster strain rate tests. For example, the stress path for 500 s^{-1} increases linearly until around 4% axial strain when it begins to decrease and then oscillate. This 4% axial strain value coincides with the strain at which the majority of bonds are broken, thus suggesting that the unbonded particles may be influencing the stress (and energy) response. This could be due to the spherical shape of the particles allowing them to roll as already noted with the sandstone tests.

The graph of the maximum values reached by the stress paths at 15% axial strain is given in Figure 5.27, and shows that the values collapse to an approximate linear relationship, where a best-fit line travels approximately through zero. This suggests that a Mohr-Coulomb failure criterion is appropriate for this material, which as already noted for the sandstone material is likely to be related to the default linear contact model — where the parallel bonds behave elastically until they break, at which point friction between particles controls the contact.

The $\frac{q}{p'}$ stress ratio plot of the 1 s^{-1}, 50 s^{-1} and 500 s^{-1} strain rates shows interesting behaviour, as can be seen in Figure 5.28. The 1 s^{-1} stress ratio plot shows substantial oscillations coinciding with breakage events until approximately 10% axial strain, before decreasing toward a final critical value of 1.5. Additional peaks occur throughout the 10-40% axial strain period, where each coincides directly with a breakage event. It can be seen from Figure 5.28 that at around 12% axial strain 50% of the total bonds have broken and the stress ratio begins to decrease.

In comparison the 50 s^{-1} stress ratio plot shows a small decrease at the start coinciding with breakage events. As soon as breakage has ceased at approximately 1% axial strain, oscillations begin and become larger, before decreasing toward a final critical value of 1.5.

Finally, the 500 s^{-1} strain rate test shows an initial decrease that occurs at the same time as the first breakage event. The $\frac{q}{p'}$ stress ratio remains at this level until the breakage ceases at around 4% axial strain (as marked on Figure 5.28) before gradually increasing. All strain rates settle to a critical value at a similar level (close to 1.0). This suggests that there is a reduction in friction in chalk during the fast application of load when and while breakage is occurring, and not once breakage has ceased.

Wall Stresses

The contact force orientation plot (Figure 5.16) shows that the weak chalk specimens are largely isotropic. This is supported by the initial wall stresses also being equal, as was the case with the sandstone specimen in Section 5.2. By 10% axial strain the majority of breakage has been completed (see Figure 5.29). From this point onward the X and Y wall stresses diverge greatly from one another, which is likely a result of the increasing strain on the specimen. It is interesting

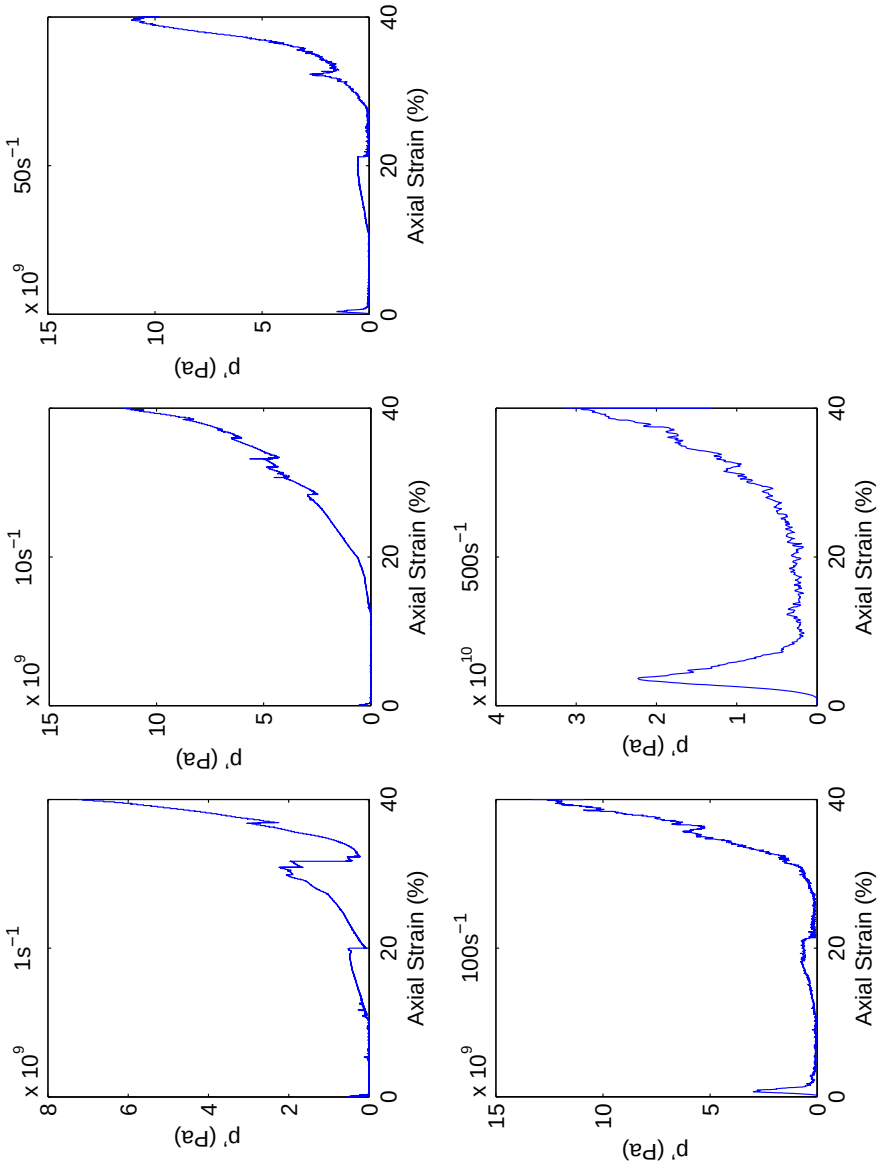

Figure 5.23: Mean stress for weak chalk specimen 1.

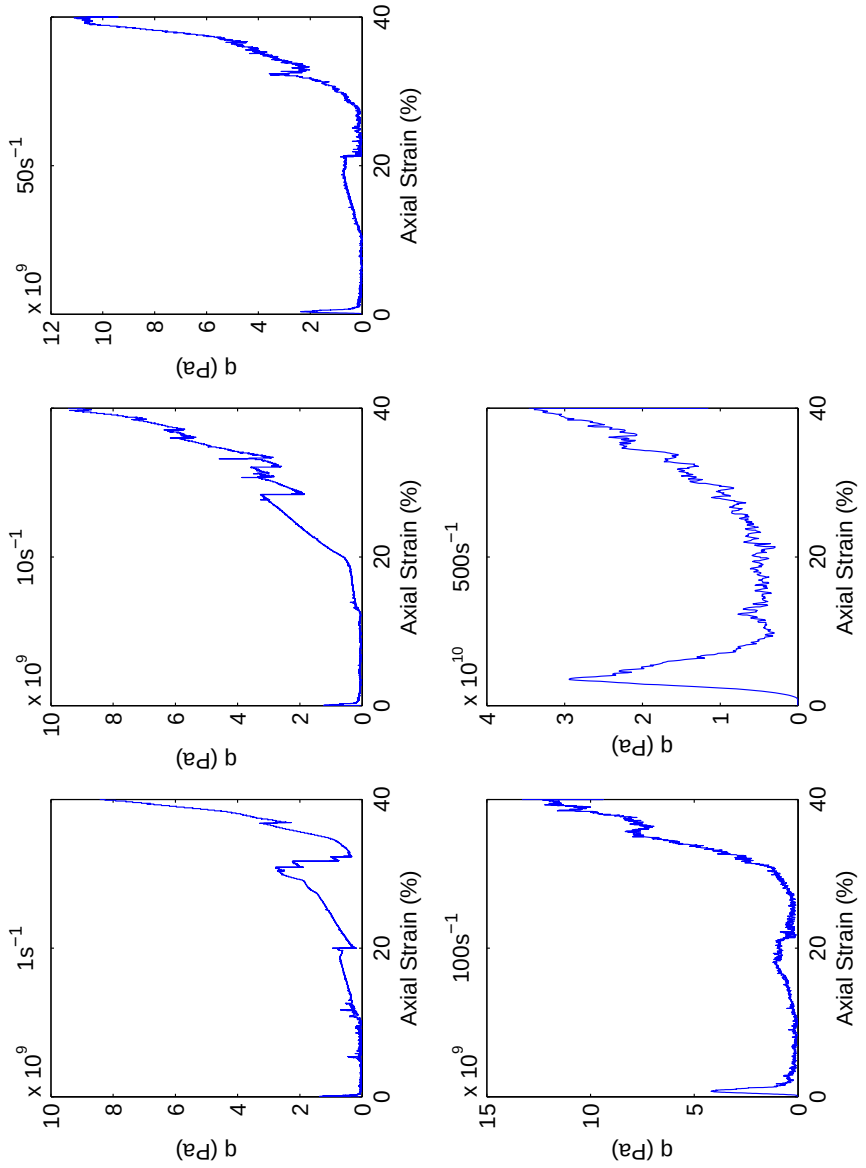

Figure 5.24: Deviatoric stress for weak chalk specimen 1.

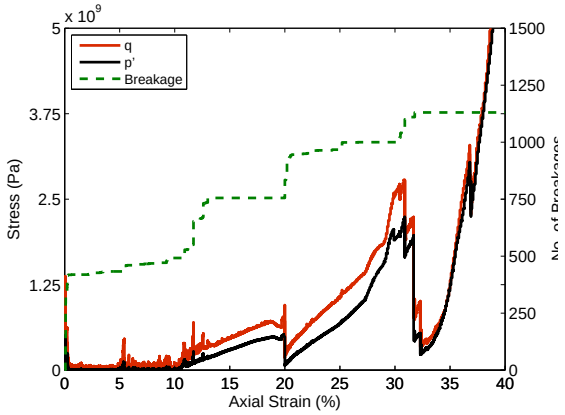

(a) 1 s^{-1} strain rate

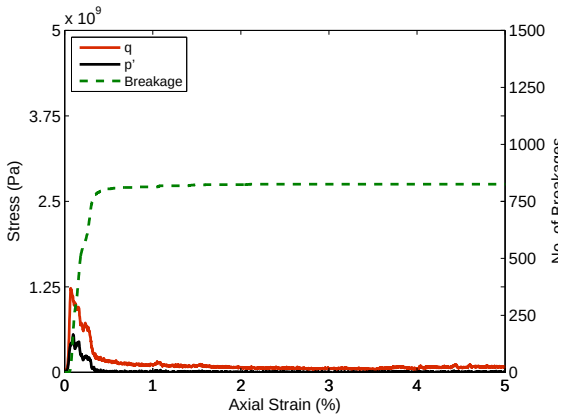

(b) 10 s^{-1} strain rate

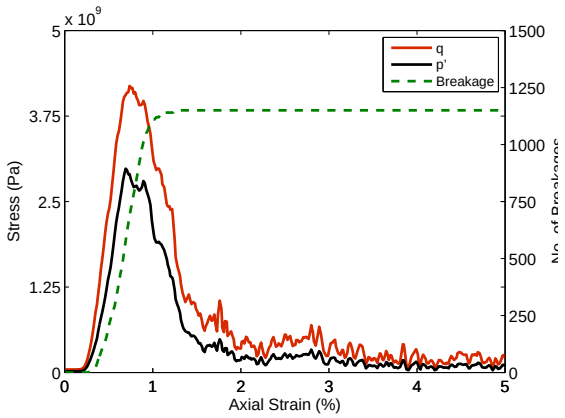

(c) 100 s^{-1} strain rate

Figure 5.25: Breakage of central boulder bonds in comparison to q and p′ microstresses for weak chalk specimen 1 at 1 s^{-1}, 10 s^{-1} and 100 s^{-1} strain rates through to 5% axial strain.

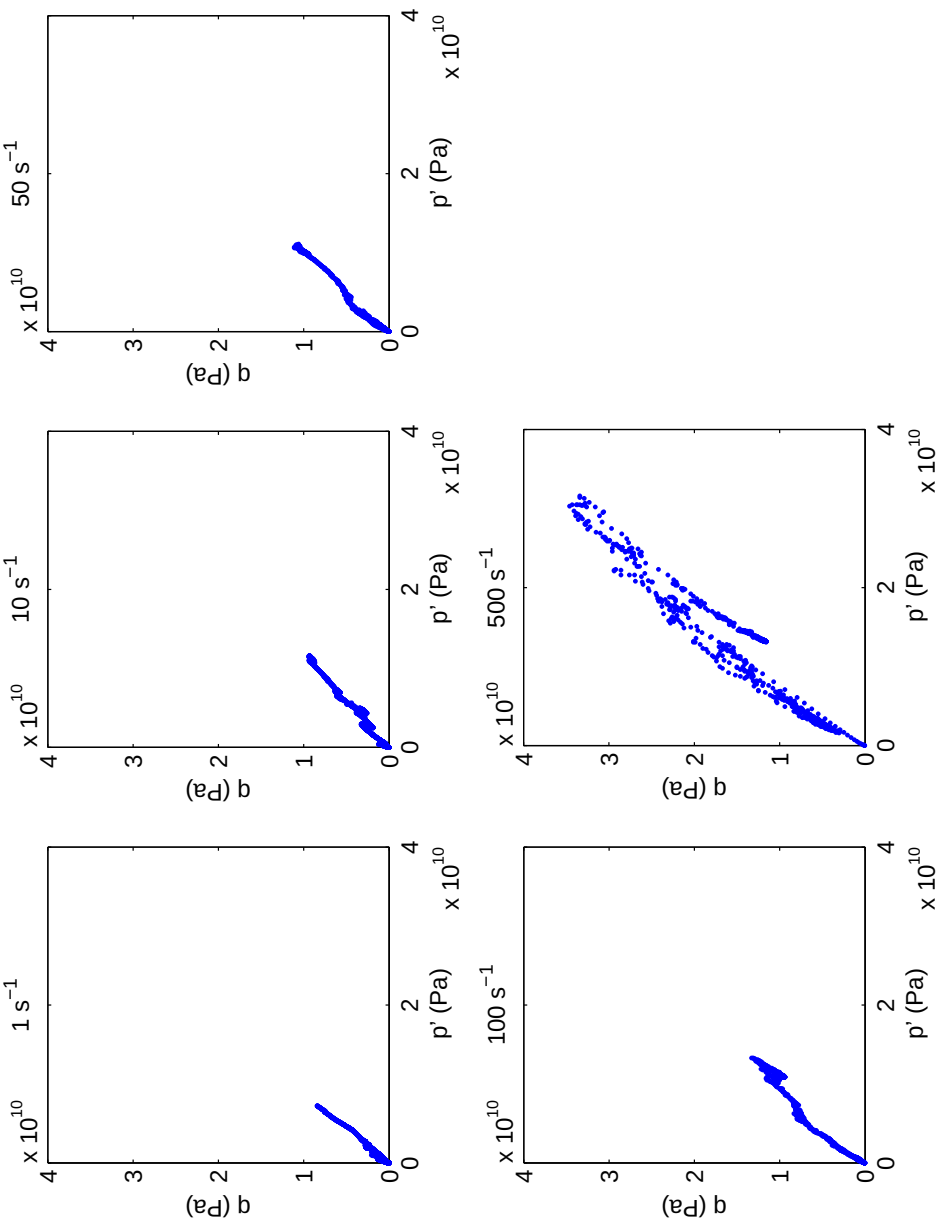

Figure 5.26: Stress path to 40% axial strain for weak chalk specimen 1 – see Appendix E for results for other specimens.

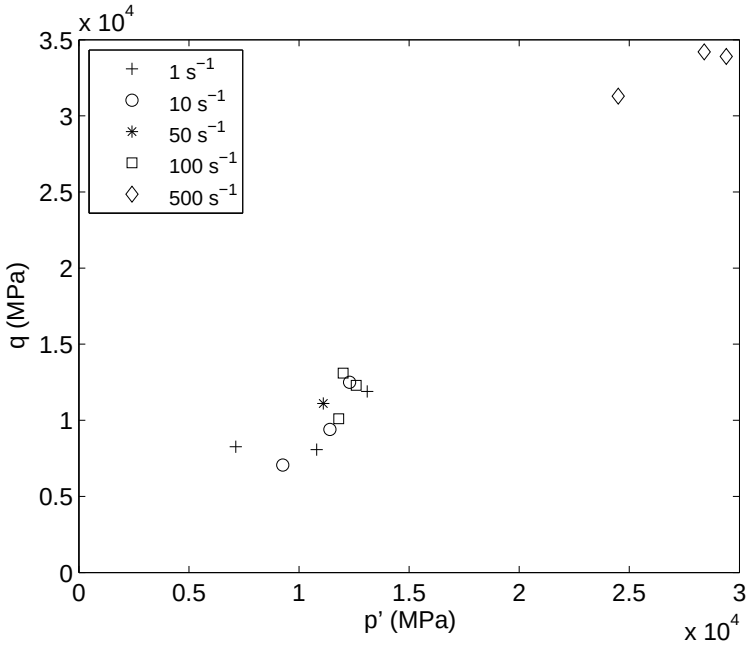

Figure 5.27: Maximum stress path value relationship for all weak chalk specimens at 40% strain.

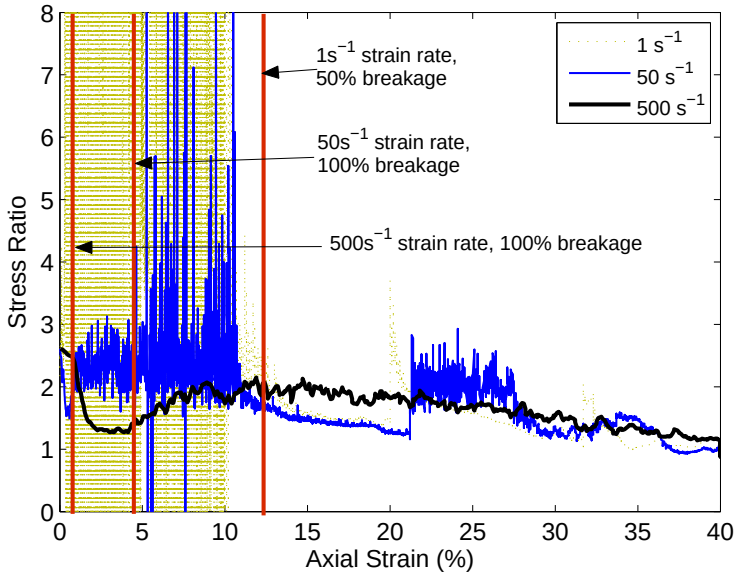

Figure 5.28: $\frac{q}{p'}$ stress ratio for weak chalk specimen 1 – see Appendix E for results for other specimens.

to note, however, that the y-axis wall stresses appear to be significantly different from those of the x-axis. This may be a result of the overall specimen becoming anisotropic with respect to stress transfer through the specimen, as breakage occurs and force chains rearrange as a result of particle movement.

As axial strain increases wall stress increases (Figure 5.30) with a sharp decrease occurring during the key breakage period at around 0.1s. Momentary decreases in the X wall stress occur due to breakages in the 1 s^{-1} test, with slight dips occurring in the Y wall stress. Oscillations in wall stress occur throughout the 500 s^{-1} test, until the final axial strain of 40% when relaxation begins. At this point the Y wall stress ceases to oscillate and maintains a consistent stress level, whereas the X wall stress continues to oscillate prior to also settling to a consistent level. This difference between the X and Y wall stress responses and continued oscillations in the X wall stress suggests that the particles are continuing to rearrange and/or move during the period of relaxation. The wall stresses cease to grow once the material is allowed to relax and do not return toward their initial values.

Summary

Statistically independent weak chalk specimens have been tested under varying strain rates in an oedometer, to investigate the roles of breakage and rate of loading in long runout chalk cliff collapses. Oedometer tests on weak chalk give an insight into the differences between weak and strong rock behaviour in similar conditions. The slower strain rates show a very low kinetic energy response when breakage events occur. Breakages do influence the p′ and q micro-stresses and only once over 50% of the bonds are broken does the $\frac{q}{p'}$ stress ratio cease oscillating. For the 500 s^{-1} strain rate, breakage leads to a peak in kinetic energy and bond energy while friction energy remains low. At the same time the $\frac{q}{p'}$ stress ratio drops reflecting the low levels of friction in the system. The kinetic energy at the 500 s^{-1} strain rate is more continuous and of a greater magnitude than that from the slower tests. Wall stresses appear to be reliant on the rate of compression as also seen in the sandstone tests above. There appears to be an element of anistropy within the wall stresses during the test which could be a result of material movement during and after breakage.

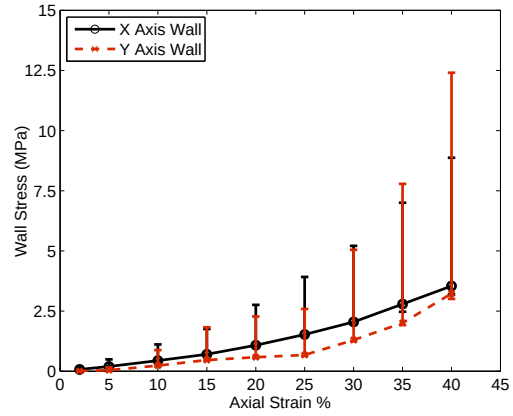

(a) 1 s^{-1} strain rate

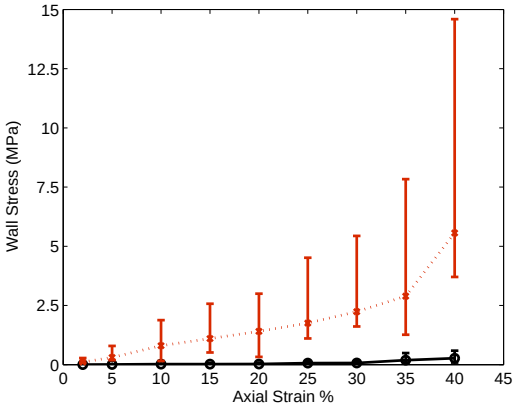

(b) 10 s^{-1} strain rate

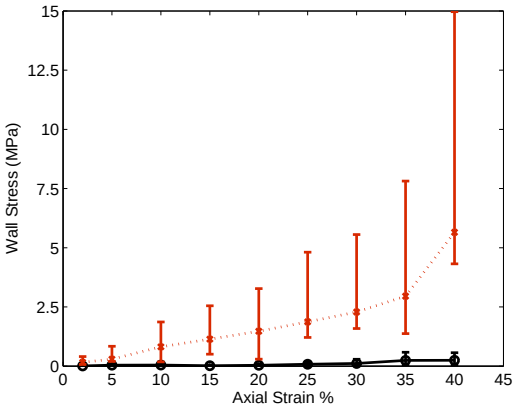

(c) 100 s^{-1} strain rate

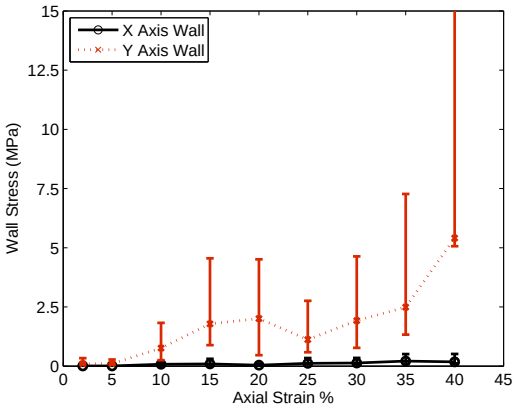

(d) 500 s^{-1} strain rate

Figure 5.29: Wall stress averages determined from all weak chalk specimens.

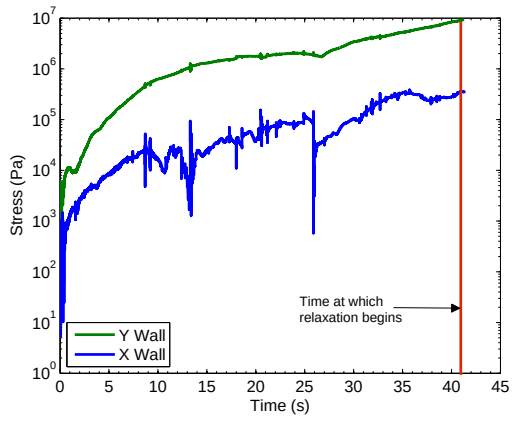

(a) 1 s^{-1} strain rate

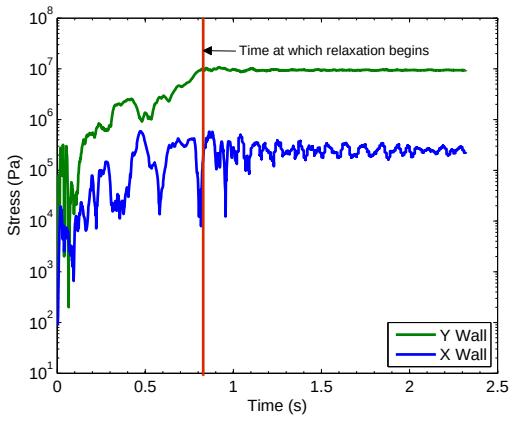

(b) 500 s^{-1} strain rate

Figure 5.30: Wall stress behaviour over time for weak chalk 1 at 1 s^{-1} and 500 s^{-1} strain rates.

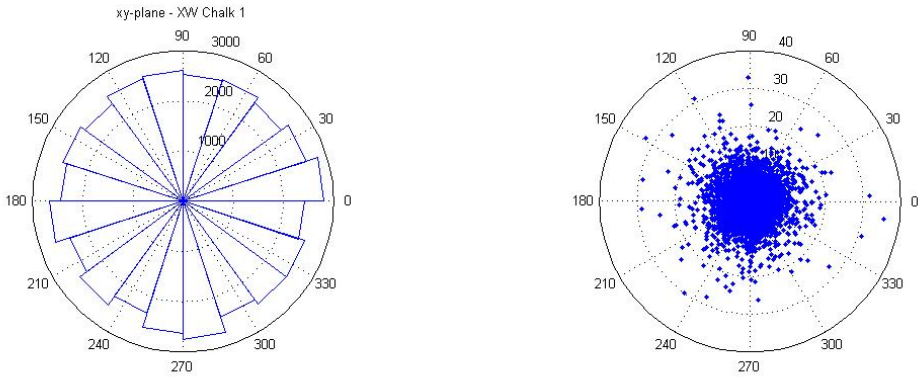

Figure 5.31: Contact orientation plots for extremely weak chalk specimen 1.

5.3.2 Results – Extremely Weak Chalk

The extremely weak chalk material is built as outlined in Chapter 4 by the removal of a volume of material from the calibrated weak chalk material. As with the sandstone and weak chalk, three specimens are built for oedometer testing where the central boulder of the cubic arrangement of 27 rock boulders is breakable, and the surrounding boulders not breakable. Contact orientation and values for extremely weak chalk specimen 1 are shown in Figure 5.31 above, which suggest that the material is isotropic.

The results from the extremely weak chalk oedometer tests are outlined below under the same sub-headings as used to discuss the weak chalk and sandstone test results.

Breakage

Breakage of the extremely weak chalk (see Figure 5.32) is similar to that found for the weak chalk under the high strain rates of 100-500 s^{-1}. All breakage is completed by 5-6% axial strain. For the lower strain rates of 1 s^{-1} and 10 s^{-1} breakage is quite different than that seen in the weak chalk. Rather than a large initial breakage followed by 3-4 consistent breakage events, the extremely weak chalk has a small initial breakage event followed by consistent breakages, forming a step-wise response and 1-2 large breakage events at 10% and 20% axial strain. For the 10 s^{-1} strain rate test on extremely weak chalk, breakage is virtually complete by 22% axial strain, whereas for the weak chalk breakage is completed at 32% axial strain. It is possible that the additional voids introduced into the system, due to the removal of material to create the extremely weak chalk, causes the oedometer test to take longer to place pressure on the key force chains. However, once this pressure is realised the bonds forming the chains break quickly, and given that there are fewer bonds overall in the extremely weak material, complete breakage is reached much more quickly than for the weak chalk.

The breakage rate of the extremely weak chalk during all strain rate tests is also very similar to the breakage rate result for the weak chalk, as can be seen in Figure 5.32. The main breakage events are complete by 8% axial strain. The 10 s^{-1} strain rate test has some breakage events occurring after this 8% strain value, with all breakage largely complete by approximately 25% axial strain.

Energy Rates

Boundary work is again the dominant measured energy response for all tests where the strain rate is $\leq$ 500 s^{-1} (see Figure 5.33). Unlike the weak chalk, it appears that bond energy has no relationship with strain energy. Instead the slower tests suggest that the strain energy and friction energy appear related, in regard to dips in strain energy resulting in peaks in friction energy, especially for the 10 s^{-1} strain rate test, but also noticeable in the 100 s^{-1} strain rate test. As strain rate increases, the bond energy increases and surpasses boundary work quickly for the 500 s^{-1} strain rate test. This is likely to be due to the work required by the unbreakable bonds under the high strain rate.

Kinetic energy appears to be negligible at the 10 s^{-1} strain rate. Very small peaks occur that appear to relate to dips in strain energy, and an increase in friction energy is mirrored with an increase in kinetic energy. At the 100 s^{-1} strain rate, kinetic energy shows a small peak at 1% axial strain that is associated with a breakage event, where later additional small peaks appear associated with dips in strain energy.

At the 500 s^{-1} strain rate, the measured energy produces very different behaviour to that of the slower strain rates. Initially, bond energy increases as the top platen lowers and then dips as breakage occurs. During this same breakage event kinetic energy peaks before dissipating. Once all breakage is complete at approximately 8% axial strain, all energies excluding kinetic energy increase. From 10% axial strain onwards, kinetic energy oscillates in a similar way to that described above for weak chalk at this same strain rate. It is possible that kinetic energy is oscillating as the now unbonded central particles move around within the system, however the effects of this are likely negligible given the associated rise in friction energy.

The normalised kinetic energy (Figure 5.34) from the 10 s^{-1} strain rate test is very similar to that shown prior for the weak chalk. During the first main breakage event little change is noticeable in kinetic energy. Further peaks in kinetic energy from 10-25% axial strain occur in tandem with breakage events, however these peaks quickly dissipate. After 25% axial strain, peaks of kinetic energy occur, however there is no breakage occurring at this time, suggesting that the peaks could well be occurring due to the movement of unbonded particles as mentioned above.

An initial peak in the normalised kinetic energy for the 100 s^{-1} strain rate test coincides with the only breakage event. Here the kinetic energy does not completely dissipate to initial values, and instead retains around half of the initial peak height. Additional peaks of kinetic energy occur

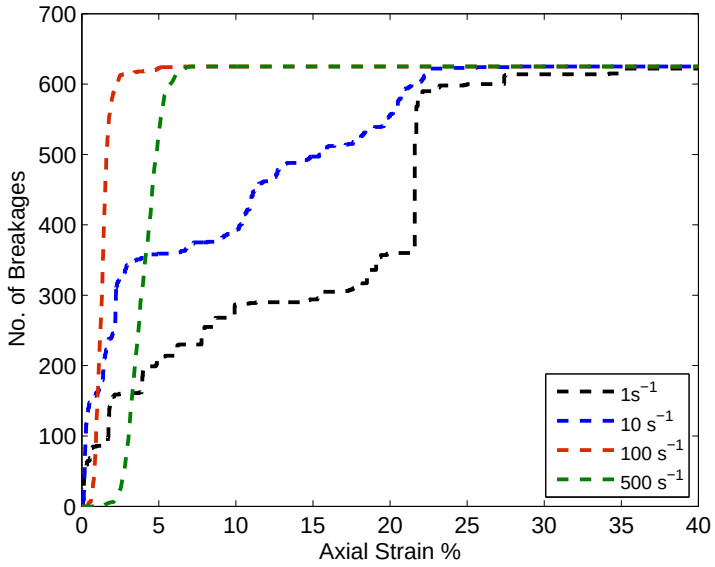

(a) Breakage

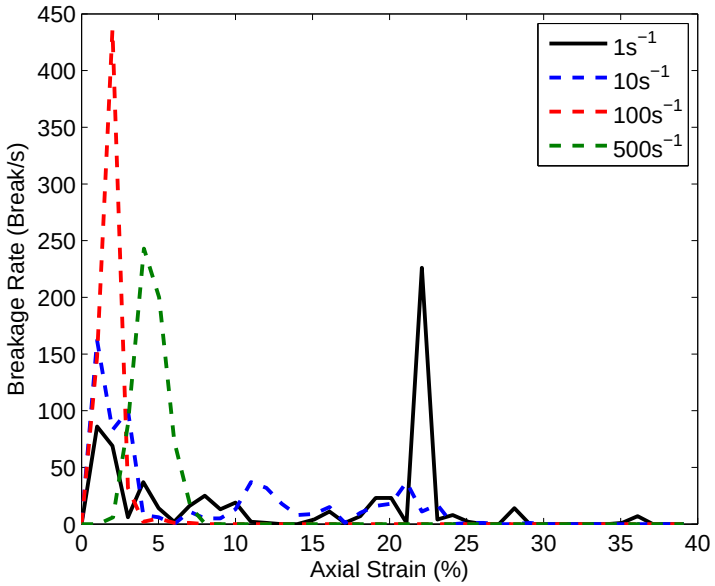

(b) Breakage Rate

Figure 5.32: Breakage and breakage rate for extremely weak chalk specimen 1 across all strain rates tested.

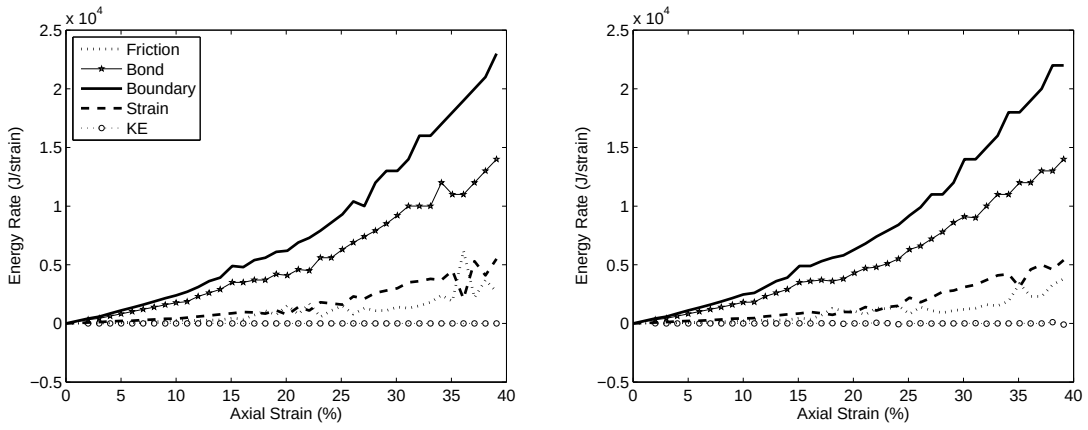

(a) 1 s^{-1} strain rate

(b) 10 s^{-1} strain rate

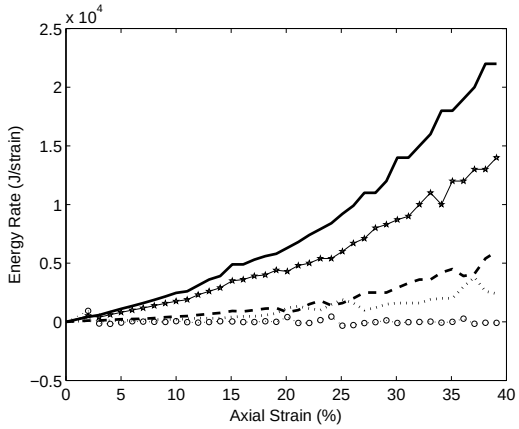

(c) 100 s^{-1} strain rate

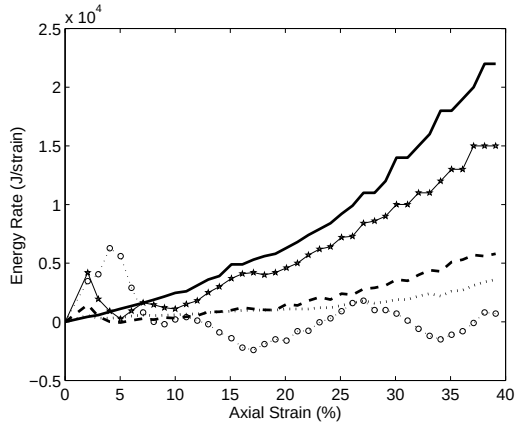

(d) 500 s^{-1} strain rate

Figure 5.33: Energy rates of 1 s^{-1}, 10 s^{-1}, 100 s^{-1} and 500 s^{-1} to 40% axial strain — extremely weak chalk specimen 1.

at 21%, 25% and 36% axial strain which are not correlated with breakage events. These peaks do however coincide with increases in friction energy and decreases in strain energy as mentioned above, where the increased friction could again be explained by the contact of unbonded particles with the unbreakable boulders or other particles.

The normalised kinetic energy from the 500 s^{-1} strain rate test peaks as breakage is completed with the level maintained for almost 10% of axial strain, before dropping below the normalised kinetic energy value produced at that time by the 100 s^{-1} strain rate test. The additional peak and troughs that occur later in the test are likely to be related to the movement of unbonded particles as discussed earlier.

The log maximum kinetic energy values are plotted against strain rate in Figure 5.35. These results are similar to those already found for the sandstone and weak chalk materials; a semi-static regime at low strain rates with a distinct change to a dynamic regime once the strain rates become sufficiently fast. There are some differences between the specimens however, at high strain rates the values collapse together and produce a power-law relationship. As with the sandstone and weak chalk materials, the kinetic energy burst plot shows distinct layering with the higher strain rate tests consistently producing the largest kinetic energy bursts (Figure 5.36).

Stress

For the strain rate tests <500 s^{-1} the mean and deviatoric stresses, as shown in Figures 5.37 and 5.38, begin to increase well after the completion of breakage with only a very minor peak occurring when breakage actually happens. In comparison, the 500 s^{-1} strain rate tests show a clear peak in the mean and deviatoric stresses when breakage occurs. This is similar to the behaviour seen in the weak chalk. The rapid increase and oscillation in micro-stresses toward the end of the tests could again be attributed to the rolling of the central boulder's spherical particles, once the majority of bonds are broken.

Figure 5.39 plots the p' and q micro-stresses with the number of breakages for the first 5% axial strain. Under the 5 s^{-1} strain rate, small peaks can be seen in the micro-stresses at each period of breakage. These peaks dissipate away quickly once breakage has ceased at that axial strain. Under the highest strain rate of 500 s^{-1}, the micro-stresses begin to increase just prior to the start of a period of consistent breakage. The stresses continue to climb as breakage occurs.

The effective stress path plots of all strain rate tests maintain a positive linear relationship, reaching a maximum $\frac{q}{p'}$ stress ratio value of approximately 1.0 (see Figure 5.40). A substantial amount of oscillation is present in the lower strain rate test results ($\leq$10 s^{-1}), and this is more noticeable for the extremely weak chalk than for the weak chalk. There is also a noticeable oscillation in the stress path for the 500 s^{-1} strain rate test however the ratio between the q and p' stresses remains similar. The oscillatory response suggests that there may be some material strength related influence on the micro-stress behaviour.

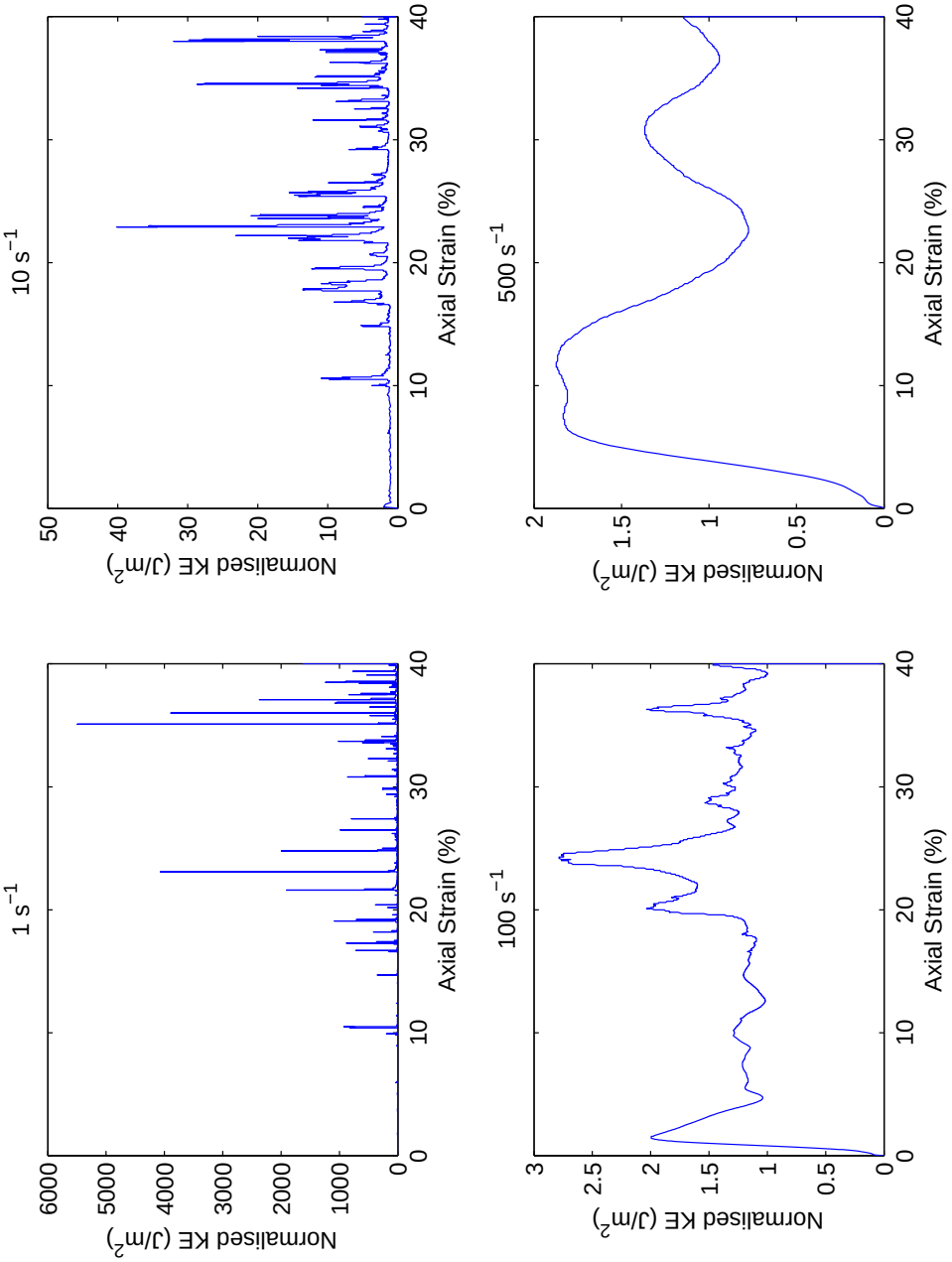

Figure 5.34: Normalised kinetic energy behaviour by strain rate for Extremely Weak Chalk Specimen 1 – see Appendix F for specimens 2 and 3.

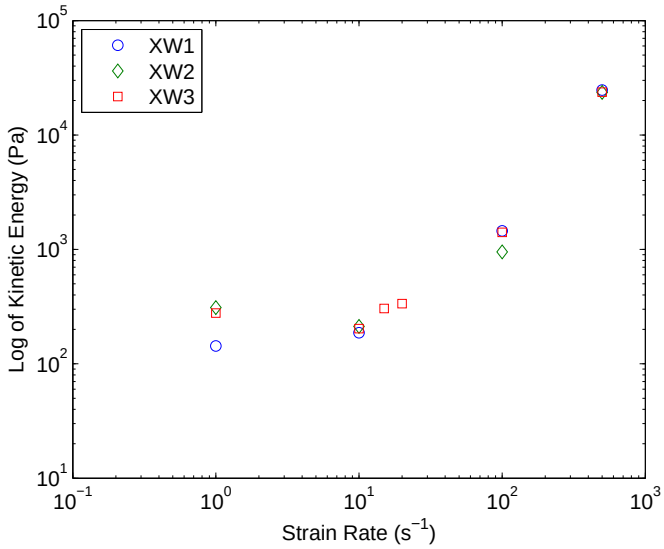

Figure 5.35: Maximum kinetic energy versus strain rate for all extremely weak chalk specimens.

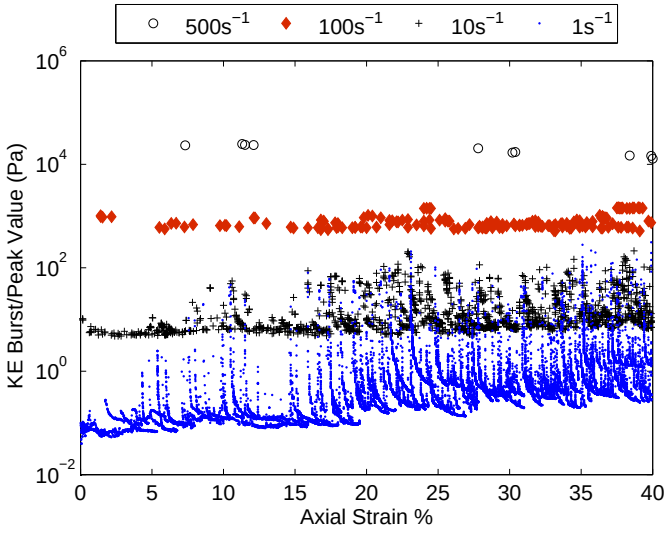

Figure 5.36: The kinetic energy peak or burst values for all extremely weak chalk specimens.

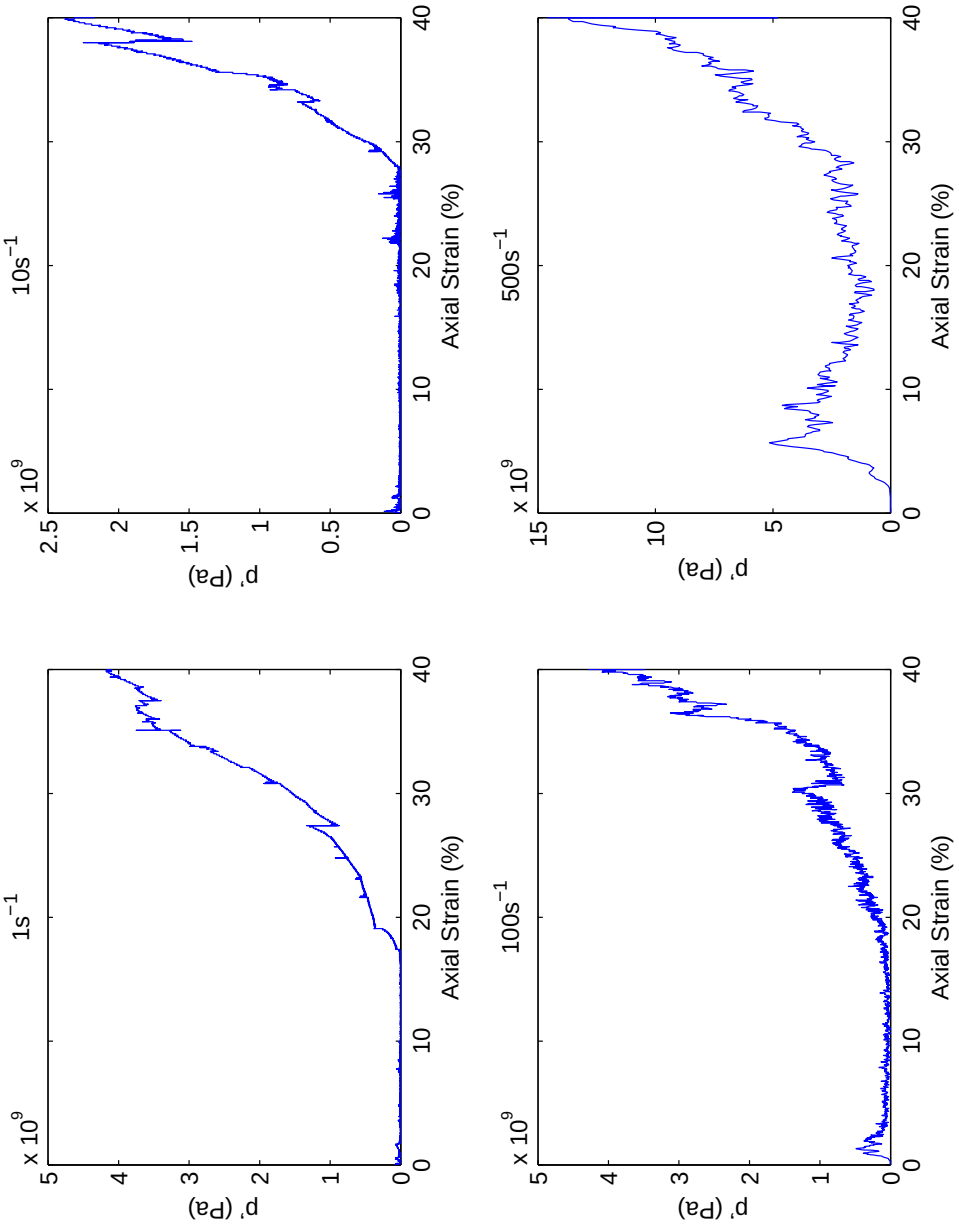

Figure 5.37: Mean stress for extremely weak chalk specimen 1.

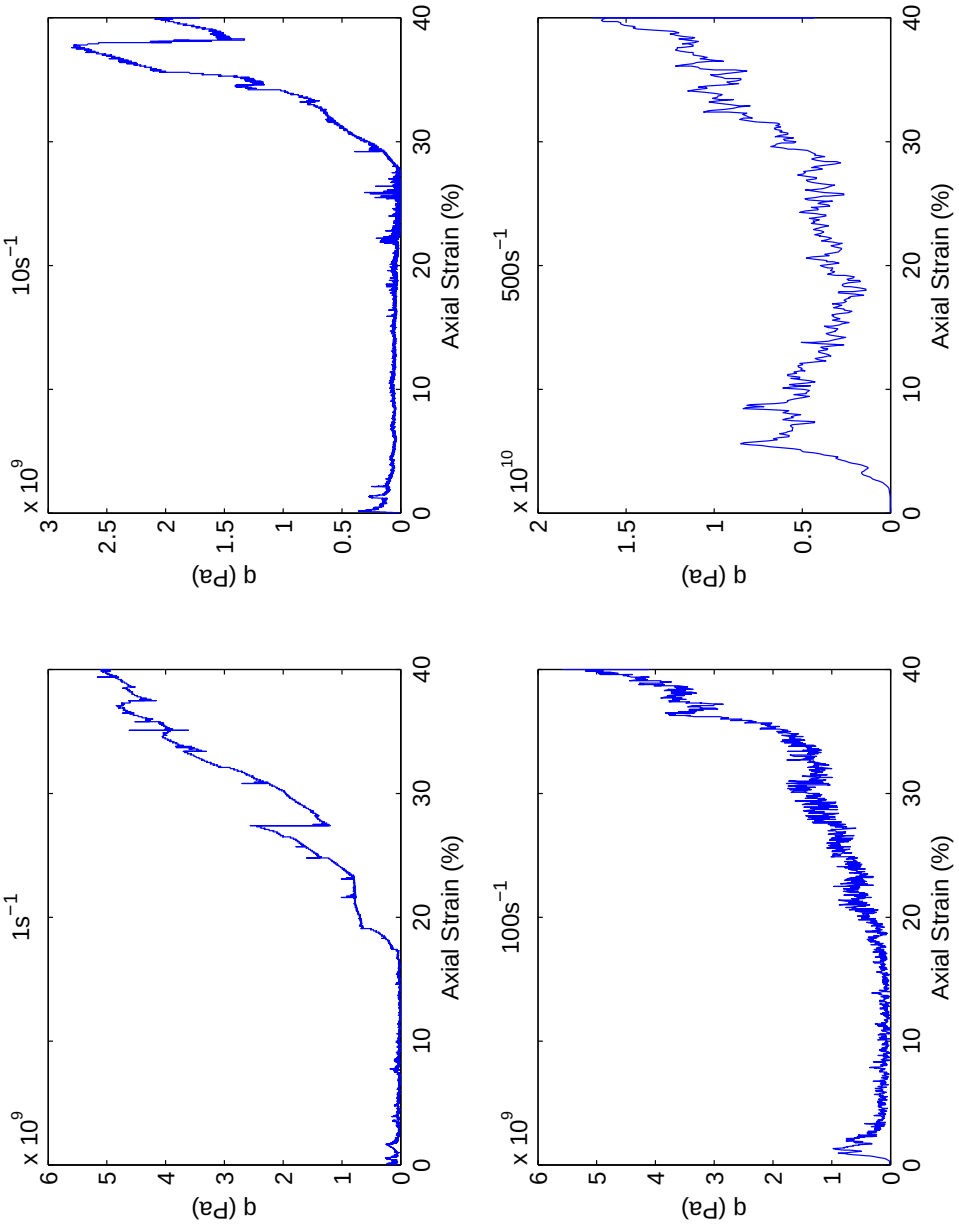

Figure 5.38: Deviatoric stress for extremely weak chalk specimen 1.

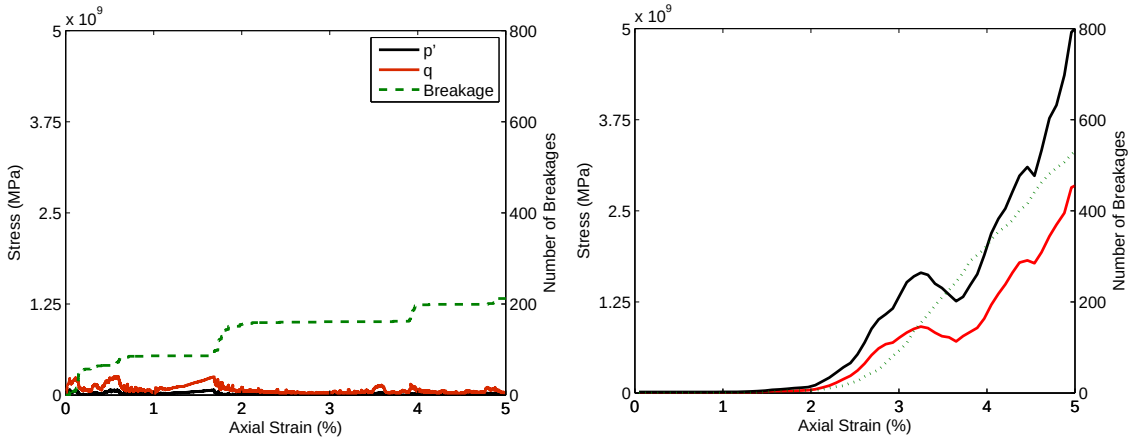

(a) 1 s^{-1} strain rate

(b) 500 s^{-1} strain rate

Figure 5.39: Breakage of central boulder bonds in comparison to q and p' microstresses for extremely weak chalk specimen 1 at 1 s^{-1} and 500 s^{-1} strain rates up to 5% axial strain.

The 500 s^{-1} strain rate test was again closely monitored to investigate the oscillatory behaviour. As noticed for the sandstone specimens, particles move downwards due to platen pressure before beginning to move sideways after the main breakage event (see Figure 5.41). By 30% axial strain the velocity of the unbonded particles is slower than that of the upper platen, and as the platen compresses further the particles are forced down and between the faster moving unbreakable boulders. These changes in velocity are likely to be responsible for the stress path oscillations.

The maximum values attained by the stress paths to 40% axial strain are shown in Figure 5.42. The values clearly lie along a linear line centred through the origin as also seen with the weak chalk and sandstone. As mentioned earlier, this is likely due to the contact and bond models utilised in PFC^{3D}.

The $\frac{q}{p'}$ stress ratio plot in Figure 5.43, indicates an immediate drop in both of the $\frac{q}{p'}$ stress ratios for the 100 s^{-1} and 500 s^{-1} strain rates that coincide directly with breakage. The 500 s^{-1} strain rate stress ratio drops just slightly further than that for the 100 s^{-1} test. In comparison, the $\frac{q}{p'}$ stress ratio from the 10 s^{-1} strain rate test oscillates continuously until breakage is complete at which point it follows a similar gentle decrease as the ratios from the other strain rate tests.

Wall Stresses

At the start of the oedometer tests the material is initially isotropic and the measured wall stresses are equal in all three dimensions. Figure 5.44 shows the x- and y-axis wall stresses for each test to 40% axial strain. The minimum, maximum and average values across all specimens are plotted as error bars. The figure shows that as the compression increases in the z-direction the x- and y-axis wall stresses diverge from one another, with the x-axis wall stresses showing a substantial increase as axial strain increases. The average values of the x- and y-axis wall stresses can differ by up to

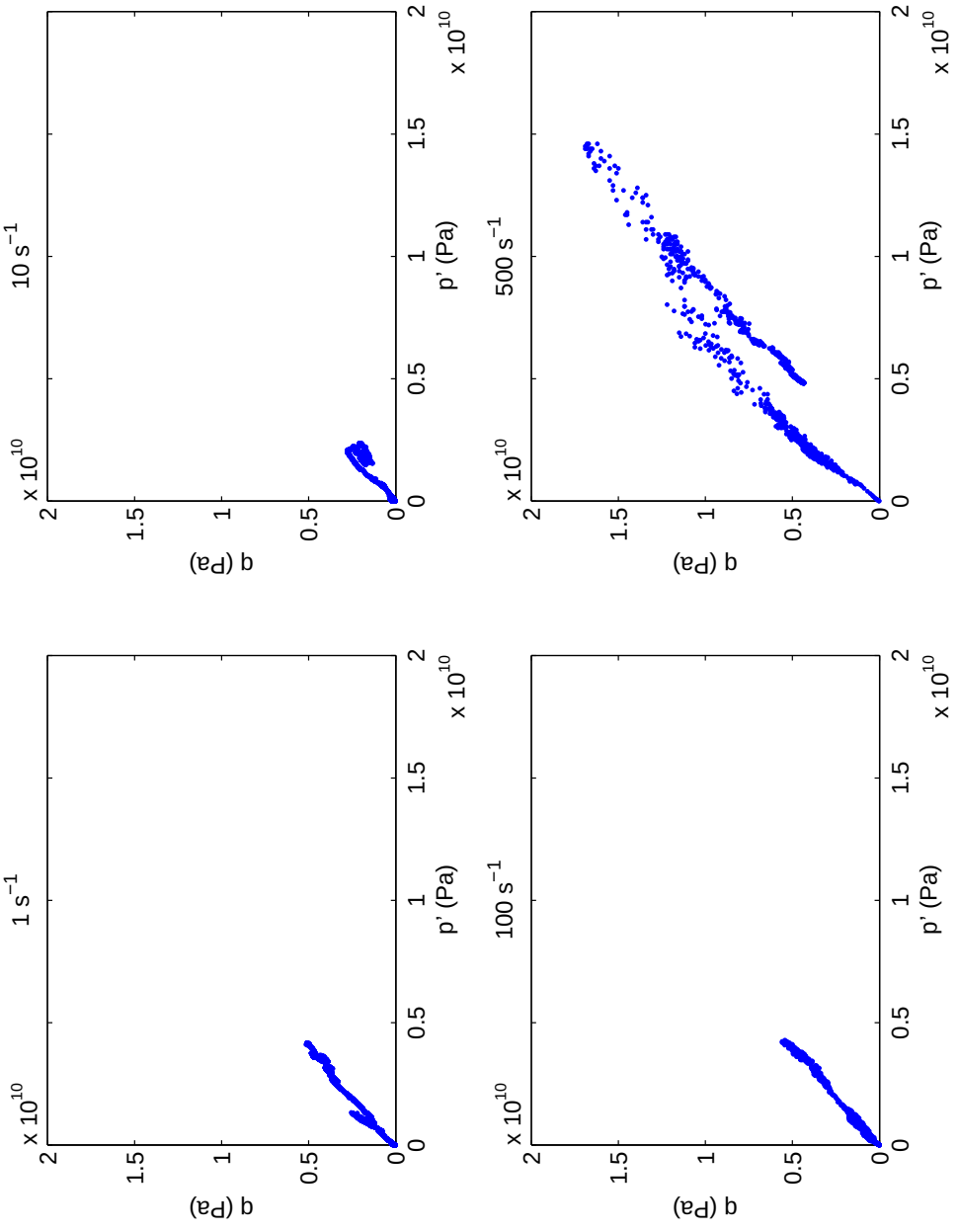

Figure 5.40: Stress path to 40% axial strain for extremely weak chalk specimen 1 — see Appendix F for results for other specimens.

Figure 5.41: Relative velocity of particles in central boulder of extremely weak chalk specimen, represented by arrows, at 6% axial strain.

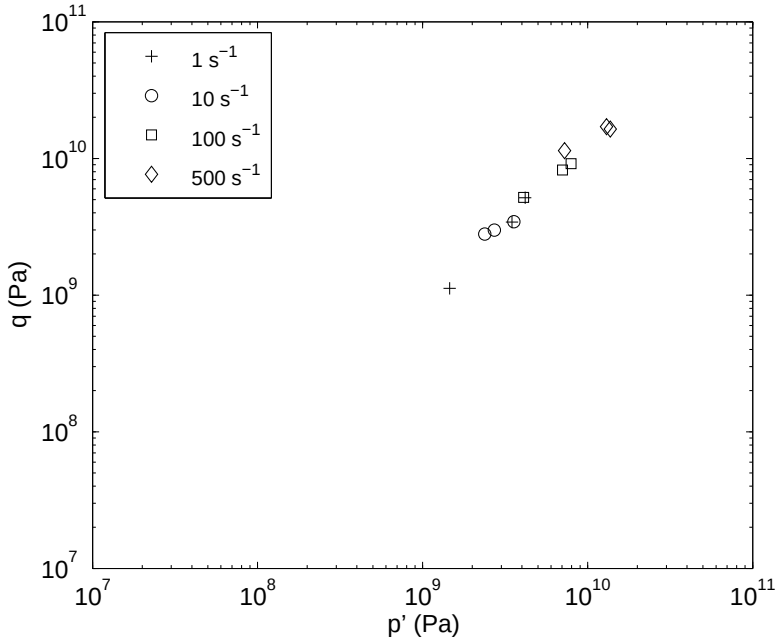

Figure 5.42: Maximum stress path values to 40% axial strain for extremely weak chalk specimens – see Appendix E for results for other specimens.

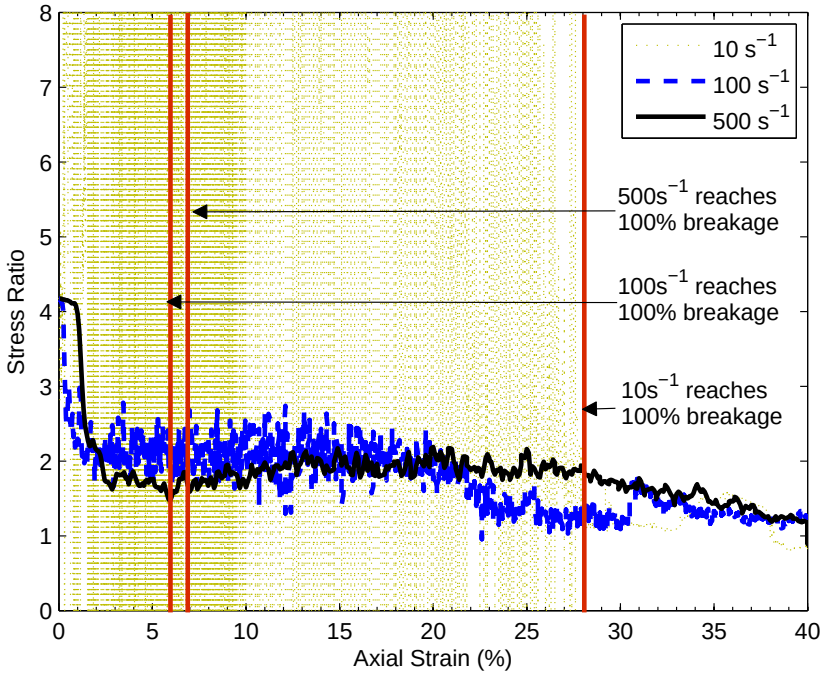

Figure 5.43: $\frac{q}{p'}$ stress ratio for extremely weak chalk specimen 1 — see Appendix E for results for other specimens.

0.7 MPa. This is the reverse of that seen in the weak chalk and sandstone materials where the y-axis wall stresses were substantially higher.

Figure 5.45 plots the x- and y-axis wall stresses for the full time period of the test, rather than just to 40% strain. The wall stresses increase with compression, as expected. Interestingly, the slow test of 5 s^{-1} reaches the same order of magnitude of stress as that of the 500 s^{-1} test, however takes much more time to reach this point. It can also be seen that once the grains are left to relax at the end of 500 s^{-1} test, the X and Y wall stress responses gradually reduce in oscillation and settle to a relatively consistent value. This suggests that there is a definite relationship between wall stress and compression rate as also found earlier for the sandstone and weak chalk materials. This is a logical response given that the material is isotropic and at rest prior to the oedometer tests beginning.

5.3.3 Summary

The results of oedometer tests on three independent extremely weak chalk specimens are very similar to those of the weak chalk. Breakage occurs throughout the quasi-static tests and is complete by 8% axial strain for the dynamic regime. Kinetic energy is negligible at low strain rates and peaking at high strain rates when breakage occurs. Once all breakage is complete, friction energy grows as the individual spherical particles, now unbonded, are able to roll and slide

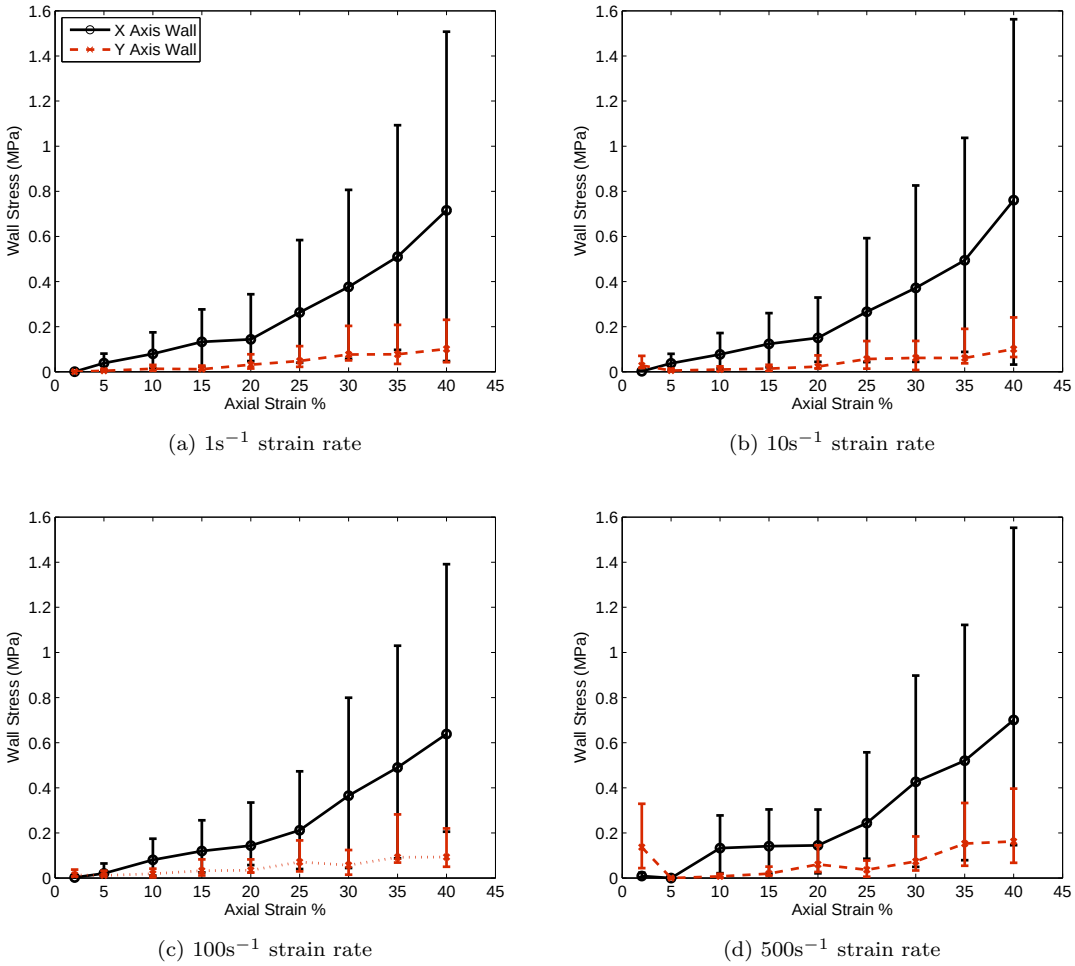

(a) $1s^{-1}$ strain rate

(b) $10s^{-1}$ strain rate

(c) $100s^{-1}$ strain rate

(d) $500s^{-1}$ strain rate

Figure 5.44: Wall stress averages determined from all extremely weak chalk specimens.

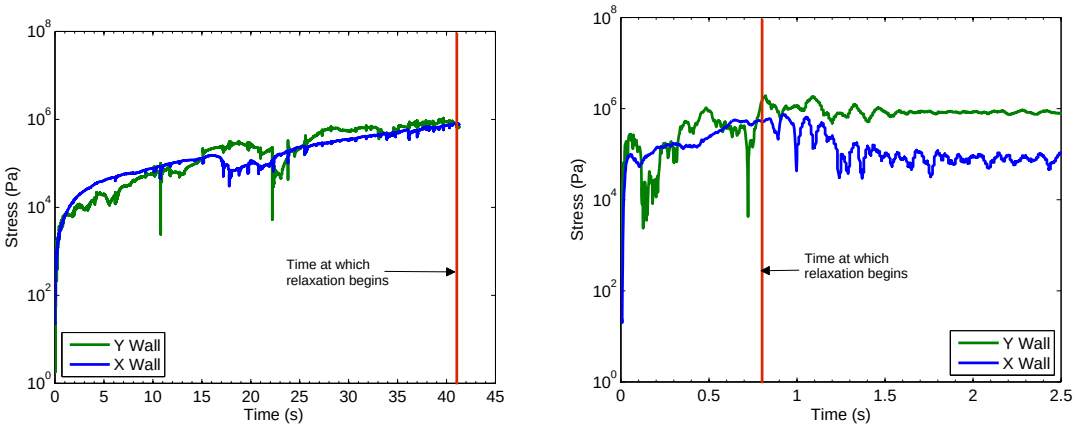

(a) 1 s^{-1} strain rate

(b) 500 s^{-1} strain rate

Figure 5.45: Wall stresses plotted against time for extremely weak chalk specimen 1 at 1 s^{-1} and 500 s^{-1} strain rates with onset of relaxation showing reduction in oscillations of stress.

which results in a subsequent and almost equal increase in q and p′ values.

Breakage also results in an immediate drop in the $\frac{q}{p'}$ stress ratio for high strain rates before slightly decreasing to a final critical value. The $\frac{q}{p'}$ stress ratio for the quasi-static strain rates oscillate until breakage is complete. As for all other tests the wall stresses appear to be related to strain rate with anisotropy in the wall stresses occurring likely due to the force chain response of the system as the strain rate increases.

Figure 5.46 charts the log-log relationship of the overall maximum kinetic energy reached by all chalk materials. This figure shows a power-law relationship occurs as is also seen in the sandstone and HCP tests. It seems that the extremely weak chalk produces more kinetic energy at lower strain rates than the weak chalk, which produces more kinetic energy at higher strain rates –âĂŞ although there are not order of magnitude differences in values.

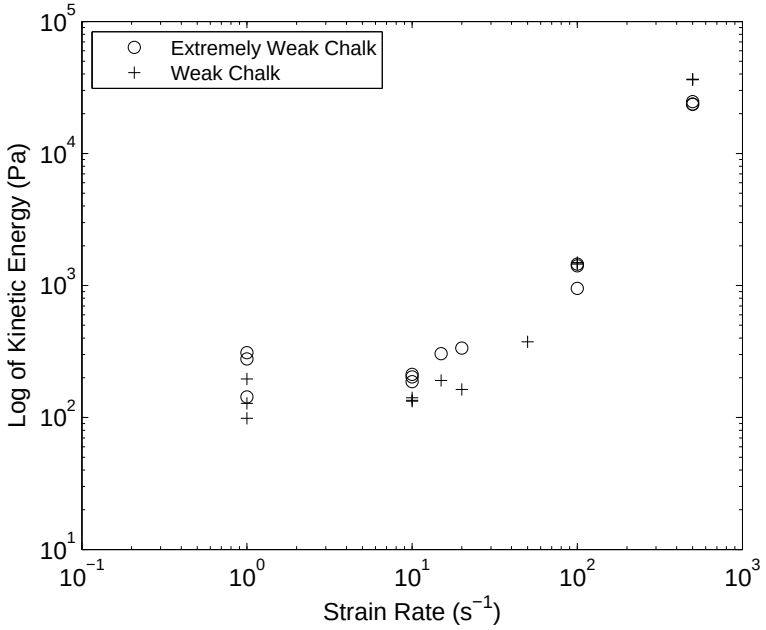

Figure 5.46: Maximum kinetic energy values obtained for all chalk oedometer tests.

5.4 Chapter Summary

Numerical oedometric tests with varying strain rates were performed on three synthetic materials calibrated in PFC^{3D}, to investigate the possible influences of loading rate or weight of material overburden, at the high impact transition point from vertical fall to horizontal runout in sturzstroms and long runout chalk flows. Three specimens each of strong sandstone (Falling Mountain sturzstrom material), weak chalk and extremely weak chalk (for chalk flows or miniature sturzstroms) were tested. The results as summarised above suggest similar behaviour occurs across all materials with increasing strain rate.

A key finding from the numerical oedometer tests is that the fast application of load causes fast and significant breakage of material. This material breakage is directly related to kinetic energy, where a fast rate of loading provides a longer term influence on kinetic energy production when compared to slow rates of loading. The stronger sandstone material may show an inertial kinetic energy response, however at high strain rates kinetic energy peaks still occur at the same time as breakage events.

A decrease in the $\frac{q}{p'}$ stress ratio is coincident with breakage events. The low strain rate oedometer tests for the chalk materials show an oscillatory response while breakage is occurring, before settling toward a critical level once breakage has ceased. The strong sandstone material has a slightly different response. The low strain rates show no decrease in $\frac{q}{p'}$ stress ratio in response to breakage, instead oscillating briefly before gradually declining to the same critical value as the 500 s^{-1} strain rate test. At the 500 s^{-1} strain rate there is a small drop in the $\frac{q}{p'}$ stress ratio for the test when breakage occurs, with oscillations following until breakage ceases. The $\frac{q}{p'}$ stress ratio for the materials indicates a reduction in mobilised friction occurs during fast loading that directly relates to breakage.

The oedometer testing has also highlighted that the loss of all material bonds may cause artificial behaviour due to rolling of the spherical particles. This is represented by oscillations in the stress paths. The close inspection of the 500 s^{-1} tests indicates that the particles change their direction of movement and velocity multiple times throughout the test. After breakage, the unbonded particles begin to move sideways until their velocity reduces to a level below that of the upper platen. The particles are then forced back into downward movement. It is likely that the fluctuations in the micro-stresses are a direct result of these changing force and velocity directions, which may cause a rolling behaviour in the spherical particles.

Figure 5.47 outlines the maximum kinetic energy for all materials tested versus strain rate. The maximum kinetic energy values obtained for both the sandstone and chalk oedometer tests show a power-law relationship, with a distinct change from a static to dynamic regime at a strain rate of 20 s^{-1}. Under quasi-static strain rates, the extremely weak chalk produces a higher kinetic energy peak than the weak chalk. The sandstones specimens produce similar or slightly higher kinetic

energy peaks than the chalks for all strain rates. The order of magnitude of the maximum kinetic energy value under quasi-static strain rates is the same as that for both chalks. At high strain rates, and in the dynamic regime, the strong sandstone produces a much higher kinetic energy peak than that of the chalks. This indicates that a stronger material produces a greater maximum kinetic energy under dynamic strain rates. A stronger material will contain greater bond strengths which when overcome produces more kinetic energy than that obtained for weaker materials.

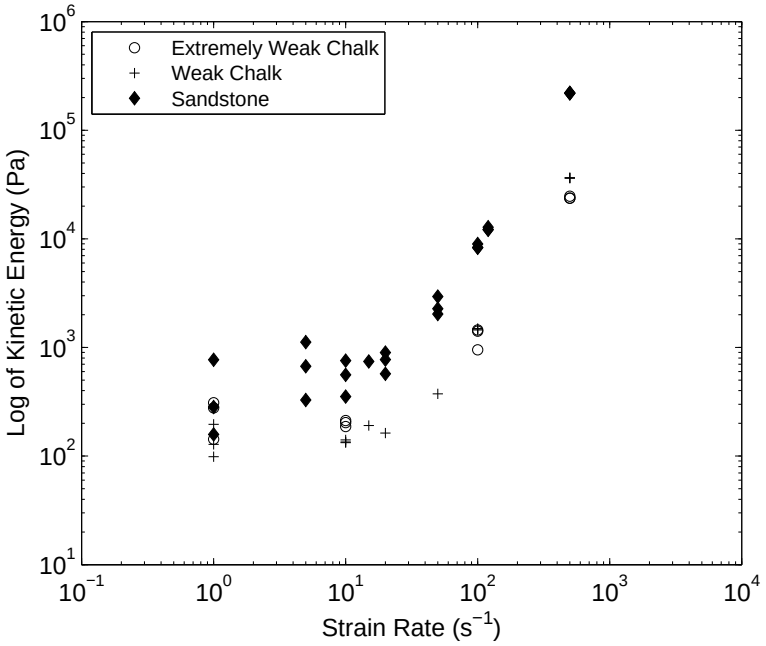

Figure 5.47: Maximum kinetic energy values obtained for all chalk and sandstone oedometer tests.

Chapter 6

Shear Testing

6.1 Introduction

The results of the oedometric testing outlined in Chapters 3 and 5 show that the high strain rate loading of quasi-brittle rock can produce substantial breakage. This can lead to a local increase in kinetic energy and a reduction in friction if the breakage is via explosive fragmentation. This oedometric test relates largely to the high impact point during a sturzstrom at the change from vertical fall to horizontal runout. To consider the potential for further influence of fragmentation within sturzstrom it is necessary to also examine the horizontal runout phase. This runout phase of the avalanche typically contains partially fragmented material from rock flour through to rock blocks. The debris is likely to be inversely graded and in stratigraphic sequence as shown by deposits of sturzstroms.

To synthesise the horizontal runout of a sturzstrom, a very small portion of the runout debris is considered where there are small rock blocks surrounded by partially broken material and fines. This specimen would likely be found within the central area of the material with respect to depth during runout, as shown in Figure 2.38, and as shown by the Falling Mountain debris (see Figure 2.8, section 2.1). Therefore a material overburden will exist above the specimen and, given the deposit characteristics of a sturzstrom, a layer of fines is likely to exist below. The quantity of overburden above the specimen will change throughout the runout. For example the depth of a sturzstrom runout occurring from a typical rock avalanche in sandstone may begin at, say, 40m decreasing to 4m as runout ceases. In this case (where $\gamma \approx 25$ kN/m^3 for sandstone) this equates to around 1 MPa of pressure at the start of horizontal runout to around 100 kPa of pressure at the end of runout. For chalk flows, these depths are estimated at 5-6 m as horizontal runout begins, to around 0.5 m as runout ceases, or around 100 kPa reducing to 10 kPa for a unit weight of $\gamma \approx 15$ kN/m^3.

Horizontal runout is considered to be a shearing event in this Chapter, with the representative sturzstrom specimen outlined above undergoing bi-directional shear. Runout material travelling over the existing ground creates friction from contact between the ground and the debris base.

This friction opposes the runout movement but does not stop the debris. Shearing behaviour can be represented in the laboratory via 'shear box tests' which can be synthesised in PFC^{3D}.

In this chapter the synthetic sandstone, weak chalk and extremely weak chalk materials are prepared as sturzstrom runout specimens and subjected to bi-directional shear. The process for preparing the specimen and arrangement of the shear test along with the associated results are outlined below.

6.2 Specimen Preparation

A small rock specimen is built (following the BPM process of Potyondy and Cundall (2004)) into a rectangular block of 0.3m width by 0.2m depth by 0.2m height in the x, y and z directions respectively. The micro-parameters of the sandstone and chalk calibrated in Chapter 4 specifically for the shear testing are applied to the materials in this Chapter.

To produce the sturzstrom runout specimen as outlined above, with rock blocks surrounded by fines or partially broken rock, the small rectangular block is refined into two types of material. The first part of the specimen considered is that of the rock blocks or boulders. Three boulders are formed from particles identified as being, at most, of vector length $\frac{d}{2}$ from a designated central point for each boulder in the specimen. The boulders are each approximately 75mm in diameter and placed in a line across the centre of the rock specimen to allow for boulder interaction during breakage. These boulders (and the particles that they consist of) are isolated from the rest of the material by assigning parallel bonds between the contacting particles that form each boulder.

The specimen then requires fine materials and partially broken material to surround the rock blocks. To simulate this in PFC^{3D}, the remaining particles surrounding the boulders are refined, that is, each particle is replaced by two particles smaller in size with the same joint volume as the original particle. In this way, the rock boulders are separated from one another. Parallel bonds are then assigned to randomly chosen particles to produce a fragmented matrix with unbonded particles acting as fines. An example of the material is shown in Figure 6.1.

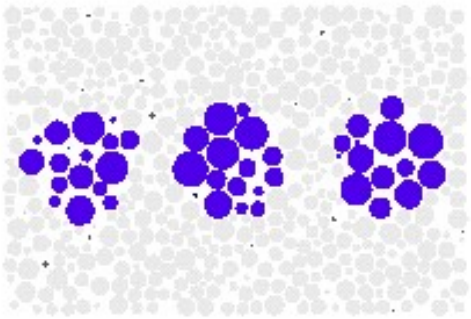

Figure 6.1: Example of shear test specimen from PFC^{3D}.

To determine the proportion of matrix particles that should be assigned parallel bonds, a PSD plot was formed from specimens of each material with varying percentages of matrix particles bonded. Figure 6.2 outlines the change in the PSD as parallel bonds are installed at varying percentages of the matrix contacts for the sandstone and extremely weak chalk materials. There is a clear reduction in individual particles as more parallel bonds are assigned, with around 10% of the material measured at the chosen boulder size of 75 mm (or 0.075 m) diameter. Clearly a 0% or 100% parallel bonded matrix is not appropriate for a sturzstrom runout material. Instead all materials were chosen to have 30% of particles in the matrix bonded so that at least 50% of the matrix particles could then be free to move individually to simulate small fragments, fines and rock flour during shear.

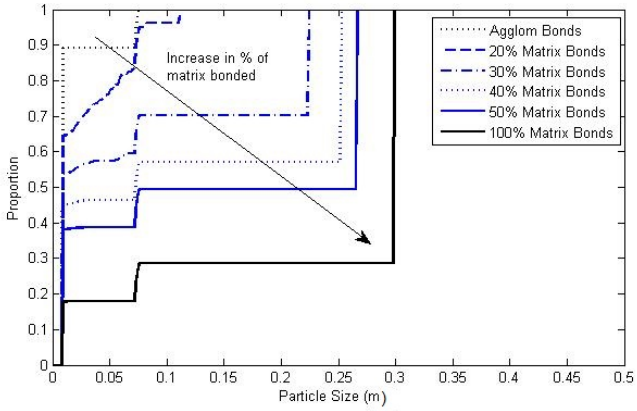

(a) Sandstone PSD

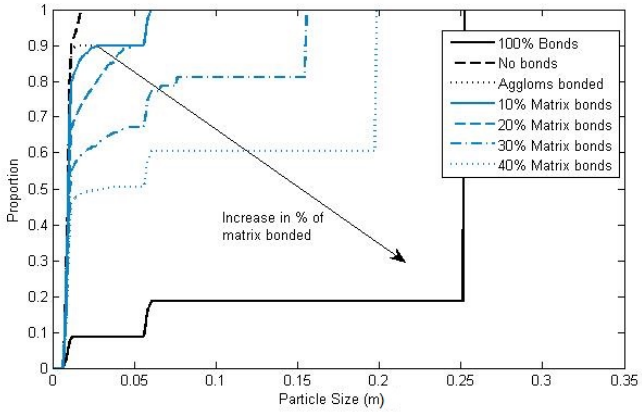

(b) Extremely Weak Chalk PSD

Figure 6.2: Sturzstrom runout specimen PSD plots with varying percentages of matrix particles assigned parallel bonds.

Following Mars Ivars et al. (2011) the overburden loads, as outlined above, were applied incrementally through an applied force in the negative z-direction. This force was introduced to a

selection of upper matrix particles of total thickness of 4d, where d is the diameter of the average particle. The upper matrix particles were then assigned extremely strong parallel bonds in order to ensure that material below did not move away from the specimen during loading. The total load in each test case was applied in five equal applications with substantial periods of equilibration between each. This process was required in order to remove any likelihood of breakage occurring in the boulders, to retain equilibrium in the overall specimen and to correctly transfer the overburden stress state throughout the system prior to the application of shear. The applied vertical forces were maintained throughout the shear test process.

6.3 Test Process

As outlined above, the test process involves simulating a small portion of rock material within the horizontal runout of a sturzstrom. This shearing process can be represented by the numerical modelling of a laboratory simple shear device albeit under high speed and high stress. The x-direction walls of the specimen are set as periodic to allow for continuous shear to occur and the y-direction walls are fixed to ensure a plane strain condition — similar to how a valley may confine the runout of a sturzstrom.

In addition to the overburden loads applied as outlined above, for a sturzstrom horizontal runout test, the specimens must also have shearing speeds assigned to the particles as may be found in a moving avalanche. The relevant velocity was incorporated into the shear test via the assignment of particle velocities to the matrix material. The velocity was set as a constant velocity field where the z-position of the particle determined the velocity assigned. The velocity of each matrix particle was fixed so that it could not increase or decrease during the shear test. At the top and base of the specimen, the velocity values were set as opposite signs so that at the centre of the material the velocity was zero, as shown in Figure 6.3. Quasi-static and dynamic shear speeds were considered in the shear tests for all materials.

Typical speeds of sturzstroms have been estimated from witness accounts, valley wall runup and elevation of gouging, with a range of speeds from 20-180 ms^{-1}. For the sandstone shear tests, a speed of ± 16 ms^{-1} was chosen which can be considered as representing a sturzstrom that is globally traveling at 32 ms^{-1} when the variation in velocity is considered from the top to the base of the specimen. This speed could be considered to be slow for a sturzstrom, however extreme speeds produce difficulties with convergence in PFC^{3D} under the default time step. Smaller time steps in turn increase computational time significantly. For sandstone, the quasi-static speed was chosen as ± 0.016 ms^{-1}. This speed would be equivalent to movement of approximately 1m in 60s, which is significantly slower than that of a typical sturzstrom.

Chalk flow speeds are more difficult to estimate, however it is understood that a flow would be complete well before that of the much larger sturzstroms ($\sim$60 s). Runout distances of chalk

flows can reach up to 160 m, within say 20 s, thus shear speed for the chalk materials was chosen as ± 2 ms^{-1} or 4 ms^{-1} globally. The quasi-static speed was chosen as ± 0.005 ms^{-1} for the chalk materials which represents movement of 1 m over 200 s and could be considered as the speed of a small slump.

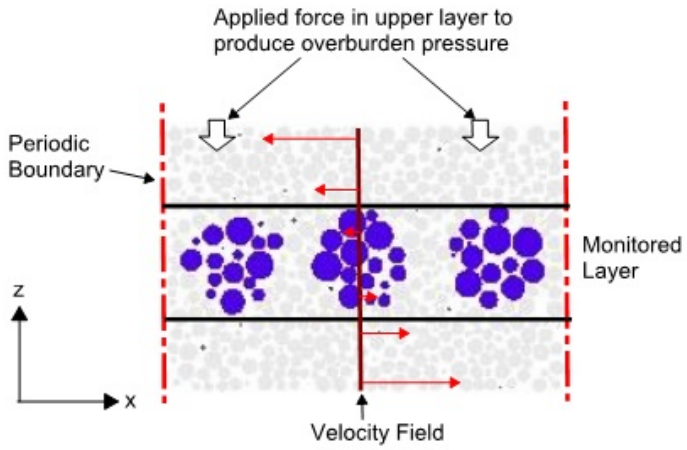

(a) Applied velocity field

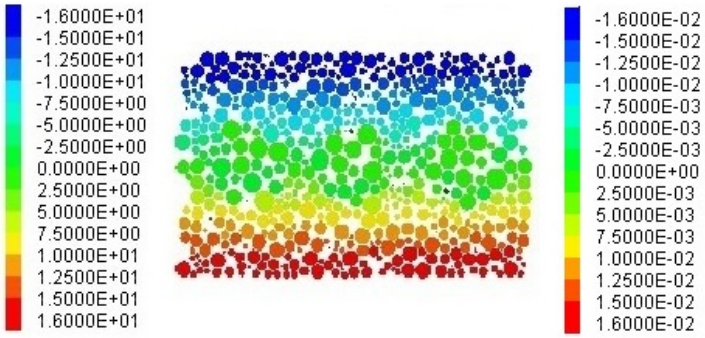

(b) Sandstone specimen example

Figure 6.3: The method for applying the velocity field for shear testing is shown in (a). In (b) is shown an example of the resulting application of the velocity field in PFC^{3D} for a sandstone shear specimen with two legends outlining the velocity applied to the relevant coloured particles. The legend to the left of (b) relates to the dynamic shear speed (ms^{-1}) and the legend on the right of (b) to quasi-static shear speed (ms^{-1}).

In this model, it is considered that, during horizontal runout, a small area of debris (similar to that built here) will undergo a large amount of shear given the extent of runout. Given the amount of computational time a large amount of shear would take to complete in PFC^{3D}, particularly at quasi-static shear velocities, in this model the amount of horizontal shear strain is limited directly

to the behaviour of the material. Once it is clear from the stress ratio, $\frac{q}{p'}$, for the boulder that the test has reached a critical state, the test is stopped. At this point the material is deemed to have reached a low level of frictional resistance with no further significant changes likely to occur to the material that could influence further large breakage events or contribute to an additional reduction in frictional resistance.

6.4 Monitoring and Measurement

As outlined in Chapters 3 and 5, PFC^{3D} energy variables were tracked throughout each test process with each variable explained in Section 3.3.1. Because periodic boundaries were used in this test, it was not possible to monitor the boundary work energy. The remaining energy variables tracked are listed below.

- Frictional Work
- Kinetic Energy
- Strain Energy

Bond energy has not been considered in the shear tests as it incorporates all parallel bonds within the system. In this case, a proportion of the parallel bonds are set to be unbreakable to contain the material. The inclusion of this energy would therefore incorrectly estimate the real energy occurring within the matrix and boulders.

Each boulder was monitored for micro-stresses through the use of multiple measurement spheres. Additional measurement spheres were introduced in the matrix directly above and below the boulder layer to monitor the matrix behaviour around the boulders. Measurement sphere items monitored are listed below and detailed in Chapter 3. In addition, breakage within the matrix and boulders were also monitored.

- Coordination Number
- Porosity
- Sliding Fraction
- Stress
- Strain

To determine displacement of the material, gauge particles were chosen and their coordinates monitored throughout the test. Eighteen particles were identified in a grid pattern with 6 layers of 3 particles closely monitored to determine, in particular, axial shear and dilation responses of the layers during the test. An example of the positions of these gauge particles is shown in Figure 6.4.

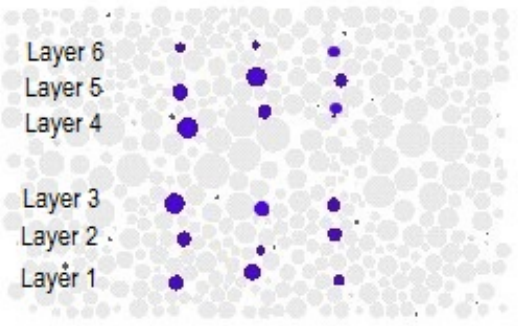

Figure 6.4: Example of gauge particle positions across a y-axis plane cut through a shear specimen.

6.5 Sandstone Results

6.5.1 Bonds and Force Chains

The initial and final state of the shear test specimen can be examined visually by taking a snapshot of a plane (or of several planes) through the material. The parallel bond and force chain structures can be viewed in this manner, as shown in Figures 6.5 and 6.6. Here the cutting plane is set in the y-direction and placed through the row of boulders along the origin. The contact points between particles where parallel bonds exist are represented by blue disks, and contact points where there are no bonds by gray disks. Force chains are shown as black lines or areas and are thickest at the strongest points.

Figure 6.5 shows the parallel bond and force chain planes at the centre of sandstone specimen 1 under both loading cases of 100 kPa and 1 MPa prior to shearing. Figure 6.5 (a) and (b) show that there is very little difference between the initial parallel bond state of the specimen, as to be expected. Figure 6.5 (c) and (d) do, however, show a clear difference between the strength of the force chains for the two loading cases. The overall increase in force chains clearly indicates that the overburden pressures have travelled through the system, and that the load is carried more strongly via some force chains than others.

At the end of the quasi-static shear test at approximately 10% shear strain (Figure 6.6) the difference in force chain magnitude is maintained between the two loading cases with some alignment in force chains particularly notable in the 1 MPa case in Figure 6.6 (d), from the shearing of the material (Figure 6.6 (c) and (d)). The parallel bond figures show a minor dilation in the material for both loading cases under quasi-static shear with perhaps more movement within the 1 MPa loaded specimen. For the dynamic shear test (Figure 6.6 (e) to (h)) there is some difference between both the parallel bonds in the boulders and force chains under the two loading cases. Bond breakages have occurred and it appears that the boulders have fragmented and partially separated during shear. Both loading rates have undergone dilation during shear with the force

chains suggesting that the majority of the material is not in close contact except for at the periodic boundary edges.

The force chains of the quasi-static and dynamic shear tests under the same overburden load are very different at the end of the tests. Where the quasi-static tests show some alignment of force chains after shear, as mentioned above, the dynamic tests show no alignment and substantial separation of force chains due to dilation. This suggests that there may be differences in the response to shear between the quasi-static and dynamic tests.

The force chains throughout the quasi-static test are shown in Figures 6.7 and 6.8 for the 100 kPa and 1 MPa overburden loads, respectively. The figures are shown with the force chains at the same scale, which clearly indicates the influence of the overburden load in developing strong vertical force chains from the top to the base of the specimen. During shear, the major central force chain is partially interrupted before reappearing on an angle consistent with the shearing direction. This is more noticeable in the force chains of the 1 MPa test (Figure 6.8).

The evolution of the force chains under dynamic shear can be seen in Figures 6.9 and 6.10 for the 100 kPa and 1 MPa overburden loads, respectively. The images are taken at similar shear strains and using the same viewing scale in PFC^{3D}. In both cases, as shear begins the force chains become strongest at the base of the specimen. As breakage occurs and the material begins to dilate it can be seen that the force chains weaken. The strongest force chains remain at the periodic boundaries.

6.5.2 Translational Velocity

As with the parallel bonds and force chains, the translational velocity colour contour of the two shear speeds and loading cases can be examined after shear (Figure 6.11). The shear velocities are fixed throughout the specimen once applied, however, these can change during shearing as can be seen when comparing the typical starting contours in Figures 6.3 and 6.11. It is clear that there are discrete particles that have increased their velocity within the specimen and it is likely also that some smaller particles have moved within the system as the material has dilated. These changes are more notable in the quasi-static shear tests, which is likely to be due to the greater ability of the particles to move under the lower shear speed.

Further data from the shear tests is presented below, with focus on the breakage, micro-stress and energy rate responses. As identified from the images of the parallel bonds and force chains in Figures 6.5 to 6.10, the 100 kPa and 1 MPa loading cases have produced similar results under dynamic shear speeds. This is confirmed with a more detailed analysis of the resulting data for the two sandstone specimens in Sections 6.5.3 onward.

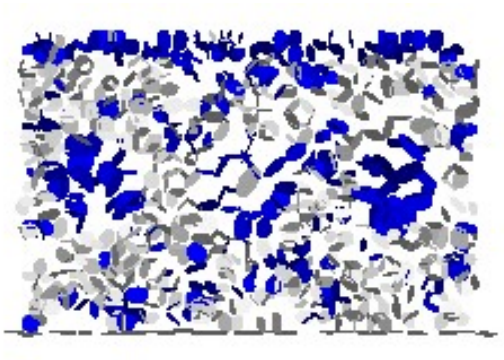

(a) 100 kPa parallel bonds at start

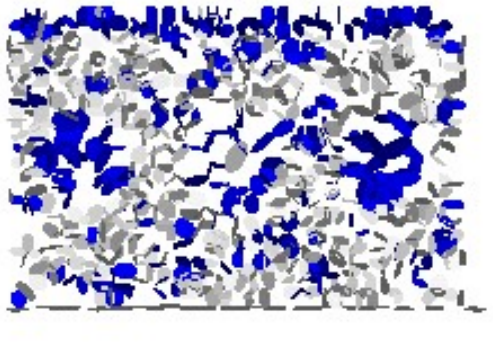

(b) 1 MPa parallel bonds at start

(c) 100 kPa force chains at start

(d) 1 MPa force chains at start

Figure 6.5: Parallel bonds (plane through y-axis) and system force chains of sandstone specimen at beginning of shear.

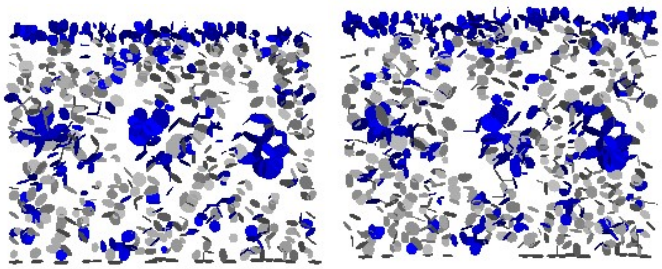

(a) Quasi-static 100 kPa (b) Quasi-static 1 MPa

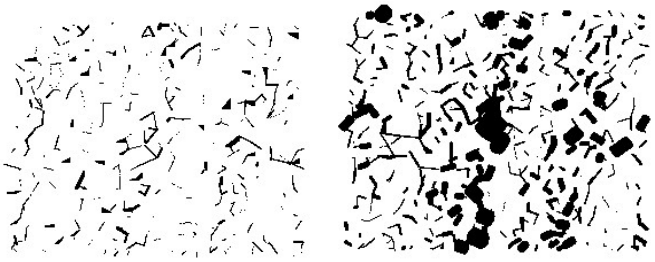

(c) Quasi-static 100 kPa (d) Quasi-static 1 MPa

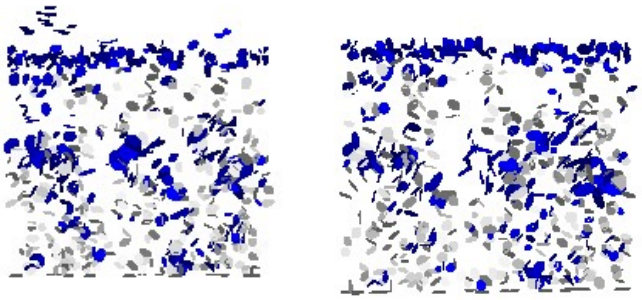

(e) Dynamic100 kPa (f) Dynamic 1 MPa

(g) Dynamic 100 kPa (h) Dynamic 1 MPa

Figure 6.6: Parallel bonds (plane through y-axis) (a, b, e, f) and system force chains (c, d, g, h) of sandstone specimen 1 at the end of shear. Note that there is a scale difference of approximately 2.5 orders of magnitude between the initial state at the beginning of shear and the end state for the dynamic force chain plots. This scaling of force chains allows for them to be visualised in PFC^{3D} to check on patterns of loading.

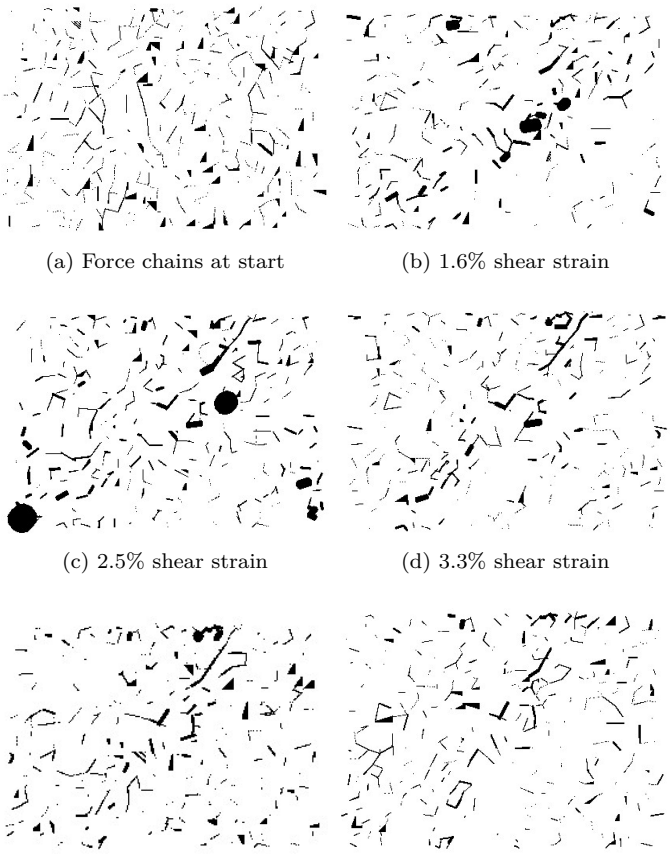

(a) Force chains at start (b) 1.6% shear strain

(c) 2.5% shear strain (d) 3.3% shear strain

(e) 5% shear strain (f) 7.1% shear strain

Figure 6.7: Evolution of force chains throughout quasi-static shear test under 100 kPa overburden load on sandstone specimen 1.

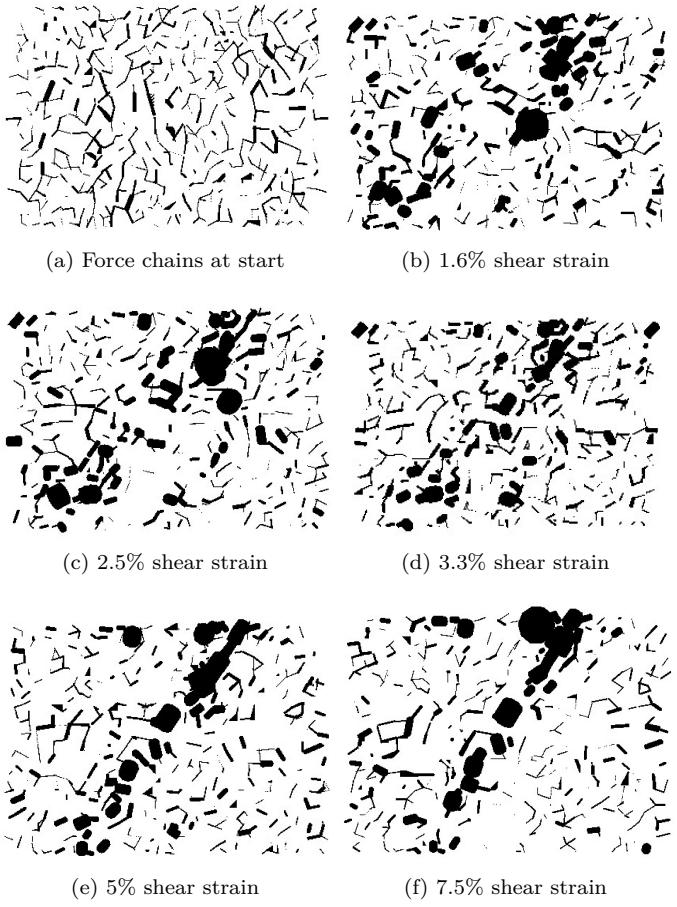

(a) Force chains at start (b) 1.6% shear strain

(c) 2.5% shear strain (d) 3.3% shear strain

(e) 5% shear strain (f) 7.5% shear strain

Figure 6.8: Evolution of force chains throughout quasi-static shear test under 1 MPa overburden load on sandstone specimen 1.

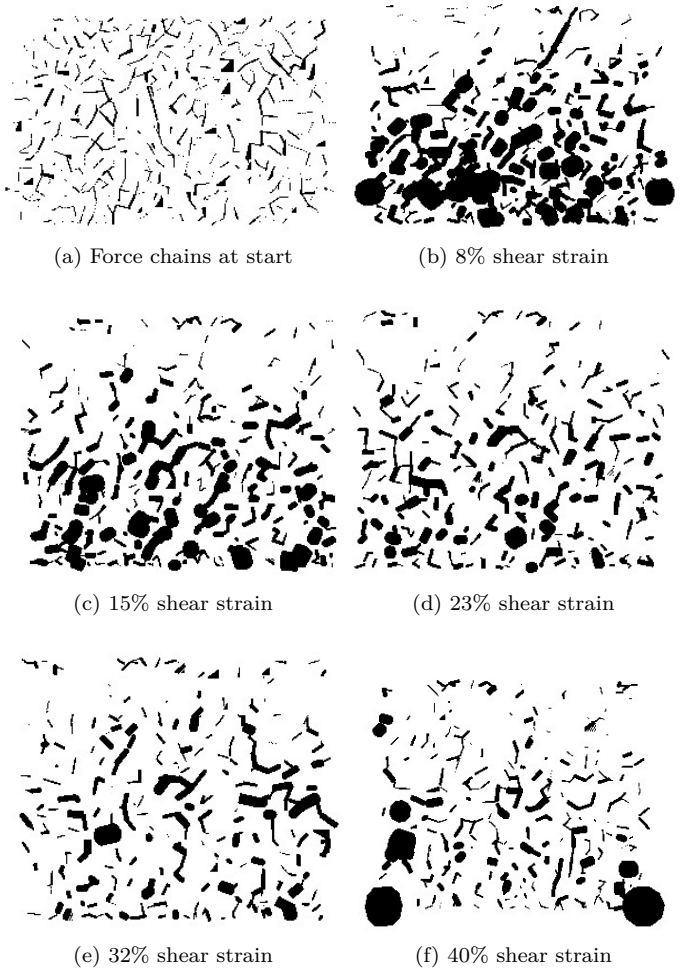

(a) Force chains at start (b) 8% shear strain

(c) 15% shear strain (d) 23% shear strain

(e) 32% shear strain (f) 40% shear strain

Figure 6.9: Evolution of force chains throughout dynamic shear test under 100 kPa overburden load on sandstone specimen 1.

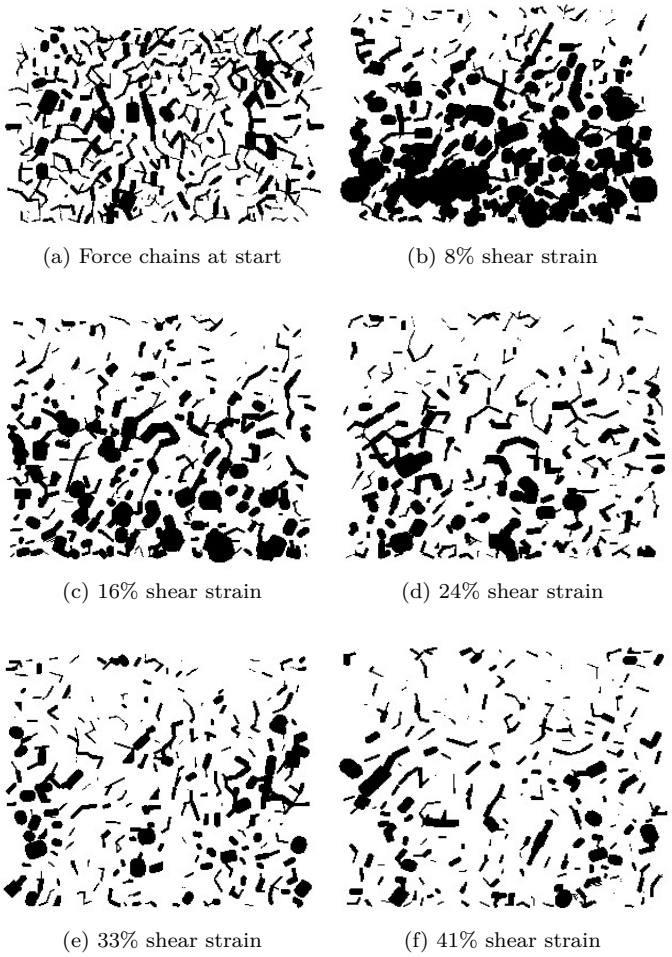

(a) Force chains at start (b) 8% shear strain

(c) 16% shear strain (d) 24% shear strain

(e) 33% shear strain (f) 41% shear strain

Figure 6.10: Evolution of force chains throughout dynamic shear test under 1 MPa overburden load on sandstone specimen 1.

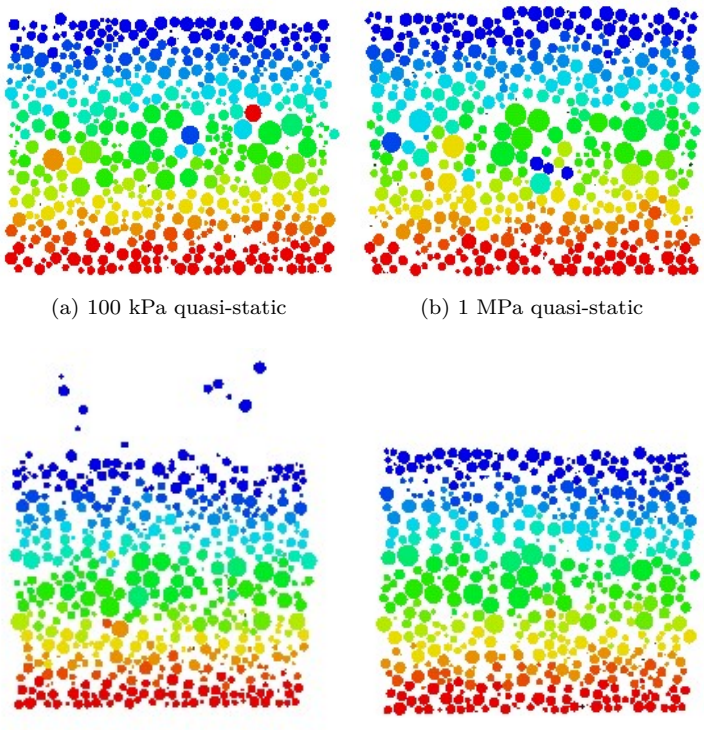

(a) 100 kPa quasi-static (b) 1 MPa quasi-static

(c) 100 kPa dynamic (d) 1 MPa dynamic

Figure 6.11: Translational velocity with coloured contour to represent particle direction and magnitude of velocity at the end of the shear test — compare with the typical contour provided at the start of the shear test in Figure 6.3.

6.5.3 Breakage

Breakage from quasi-static and dynamic shear under both overburden loads grows reasonably quickly (see Figure 6.12 showing the number of breakages against shear strain for each case) as the material moves under shear, before reaching a point at around 2% shear strain, when the frequency of breakages reduces. This point coincides with the completion of the majority of boulder breakages for the dynamic shear tests, as seen in Figure 6.13. The greatest quantity of breakage in all cases occurs within 0-3% shear strain with minor additional breakage events occurring throughout the test, as shown by the breakage rate in Figure 6.13 (c) and (d). The initial breakage event under dynamic shear, as indicated by the large peak in (d), includes the majority of the boulder breakages and is approximately 90% matrix breakages (or around 650 of the 730 breakages within the first 1-2% shear strain). This may also be an inertial response as shear begins. In the quasi-static shear test there are no boulder breakages, (except for the 1 MPa loading of specimen 1 where there are a total of 8), which suggests that the peak in (c) is related to the breakage of matrix material to allow shear to occur.

The breakages of parallel bonds within the boulders under dynamic shear can be separated out from the overall breakage count, resulting in around only 20% of the boulder bonds broken (or breakages of 80-100 bonds from a total of 424 bonds) during the dynamic shear test. The majority of breakages occur within the matrix material. The 20% of boulder bonds broken are likely to be key bonds within the larger force chains. This suggests that once the boulders are broken into fragments, the material is able to shear more freely with additional breakages occurring in other fragments within the matrix.

6.5.4 Micro-stress

Figure 6.14 show microstress parameters p′ and q against shear strain for the quasi-static and dynamic shear speeds. In the quasi-static shear tests, p′ and q rise slightly from the initial loading conditions and remain fairly consistent as they gradually drop back toward the initial loading state values with an order of magnitude difference between the 100 kPa and 1 MPa cases, as expected. Both the mean effective stress p′ and deviatoric stress q of the boulders climb quickly from their initial values of approximately 70-80 kPa (100 kPa case) and 600-700 kPa (1 MPa case) in the first 1-2% shear of the dynamic tests as seen in Figure 6.14. The initial major increase occurs at the same strain as the majority of the breakage, with minor fluctuations occurring after later breakage events.

Stress ratio $\frac{q}{p'}$ plots are shown in Figure 6.15. The quasi-static $\frac{q}{p'}$ stress ratio of the boulders shows a rise within the first 0-3% shear in the 100 kPa loading case with an increase in the ratio for the 1 MPa loading case towards 1.7, which is maintained relatively consistently until around 8% shear. At this time the $\frac{q}{p'}$ stress ratio gradually begins to decline towards critical state. For

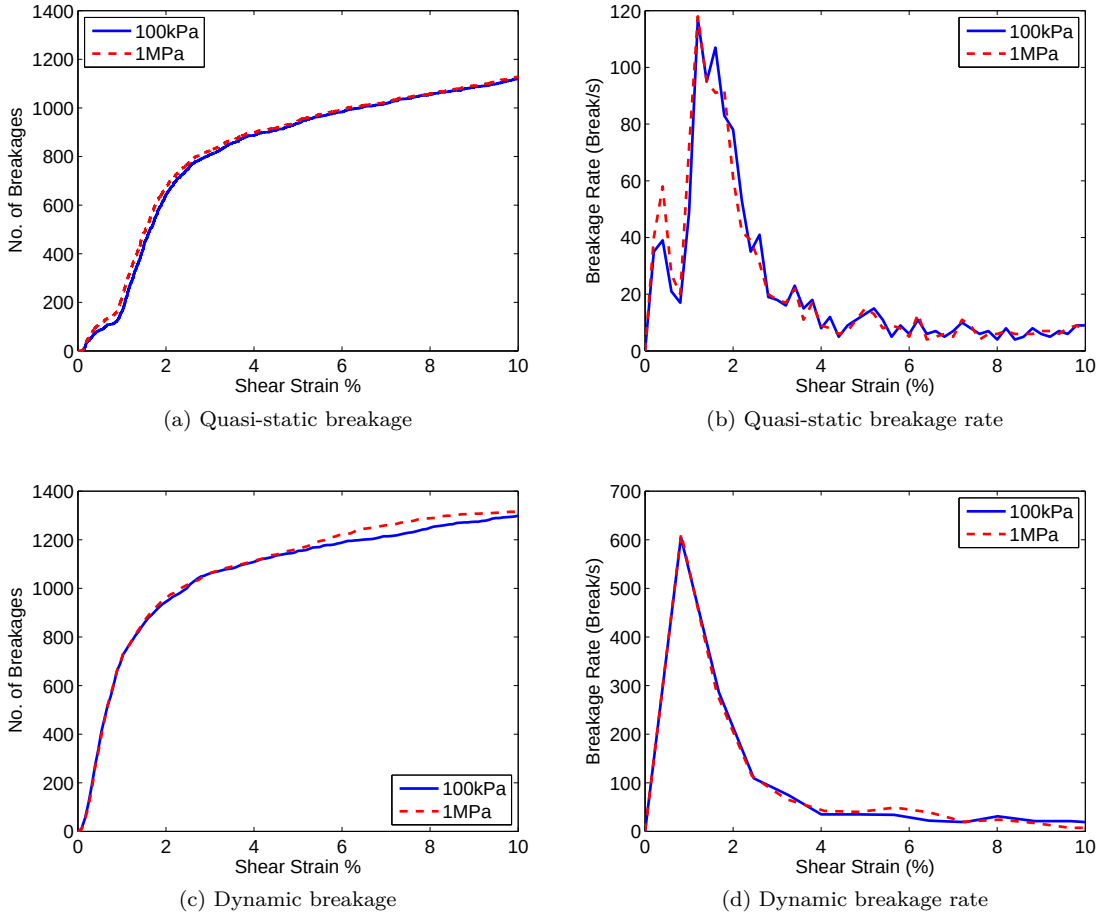

(a) Quasi-static breakage

(b) Quasi-static breakage rate

(c) Dynamic breakage

(d) Dynamic breakage rate

Figure 6.12: Total breakage under shear testing for sandstone specimen 1. (a, c) total bond breakage against shear strain; (b, d) breakage rate; for quasi-static and dynamic cases, respectively.

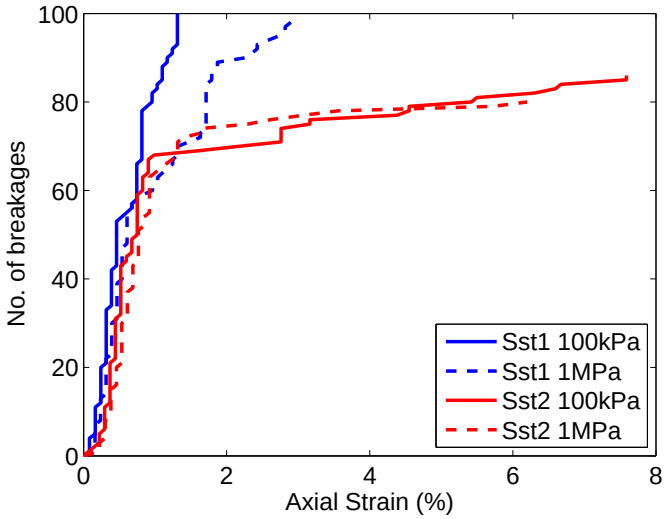

Figure 6.13: Boulder breakages (alone) under dynamic shear testing for sandstone specimens. Note that under quasi-static shear speeds boulder breakages in general do not occur.

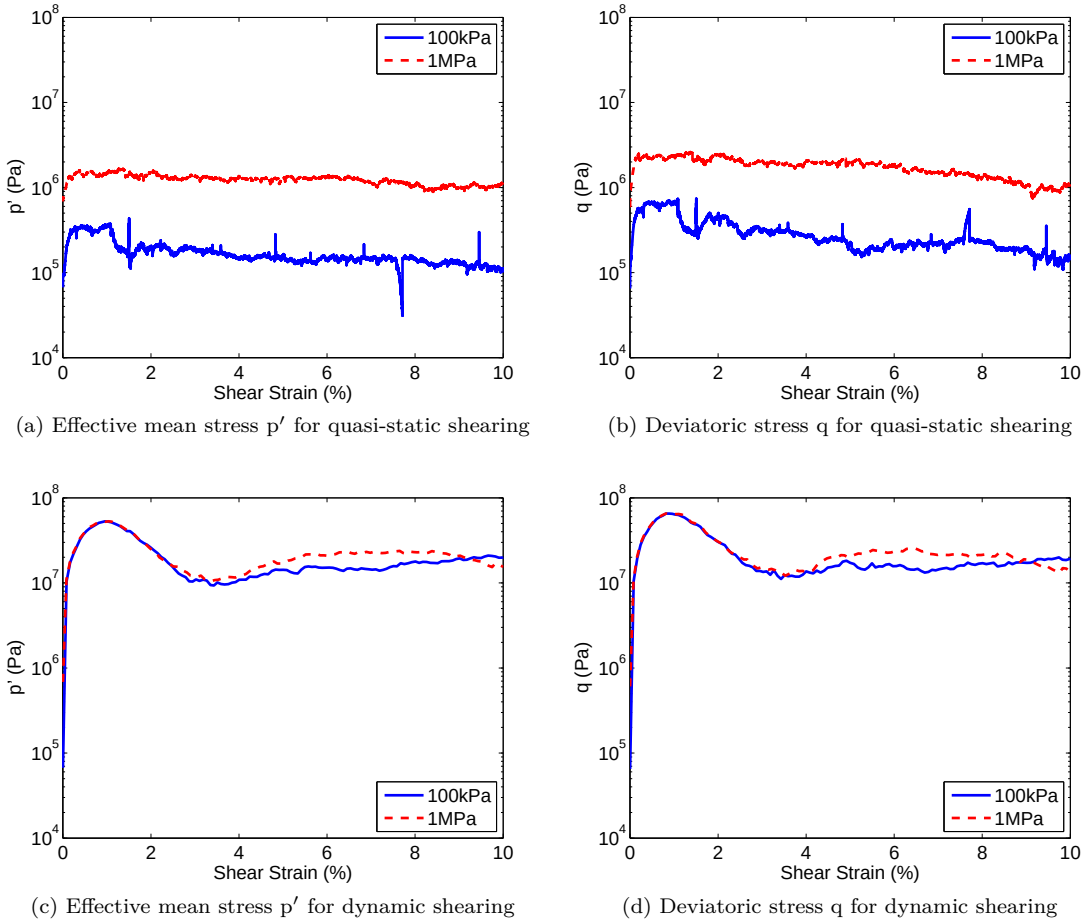

(a) Effective mean stress p′ for quasi-static shearing

(b) Deviatoric stress q for quasi-static shearing

(c) Effective mean stress p′ for dynamic shearing

(d) Deviatoric stress q for dynamic shearing

Figure 6.14: Mean effective and deviatoric stress responses within the boulders under shear testing for sandstone specimen 1. (a, c) show the effective mean stress p′ against shear strain; (b, d) show the deviatoric stress q against shear strain; for quasi-static and dynamic cases, respectively.

the 100kPa loading case, there are minor oscillations before this $\frac{q}{p'}$ stress ratio becomes consistent, with small oscillations around 1.5. The stress paths for the quasi-static shear tests show a linear relationship, with the 100 kPa and 1 MPa loading cases showing clear differences in the internal boulder stresses during the test (Figure 6.15 (b)).

The similarity in data between the loading rates under dynamic shear is also seen in the $\frac{q}{p'}$ stress ratio of the boulders (Figure 6.15 (c)) with an initial rise in the ratio, over the 1-2% shear strain of substantial breakage, followed by a gradual fall toward critical state. The stress ratio oscillates throughout the shear test, which is likely to be due to the movements of the boulder particles. The associated stress path in Figure 6.15 follows a linear response again during the 1-2% shear strain of substantial breakage, before dropping in value and oscillating around 10-20 MPa. Although the loading cases start at different values, 100 kPa and 1 MPa, the overall behaviour is very similar.

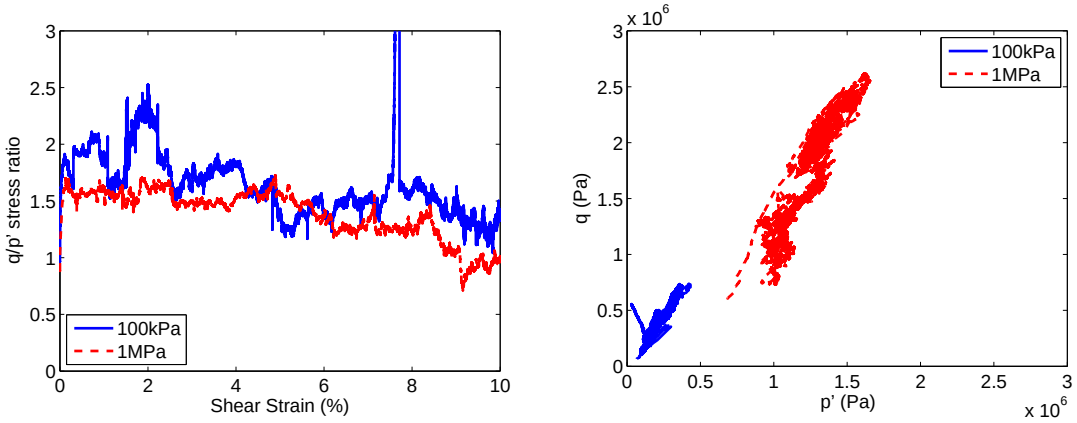

(a) Quasi-static $\frac{q}{p'}$ stress ratio

(b) Quasi-static stress path

(c) Dynamic $\frac{q}{p'}$ stress ratio

(d) Dynamic stress path

Figure 6.15: $\frac{q}{p'}$ stress ratio of the boulders against shear strain (a, c) and stress path response (b, d) under shear testing for sandstone specimen 1 for quasi-static and dynamic shear cases.

6.5.5 Energy Rates

Under quasi-static shear speeds, the energy rates (Figure 6.16 (a)) are very small and dominated by friction. Kinetic energy is virtually zero throughout the test and strain energy shows minor increases during the major breakage events. Friction energy spikes at around 3% once the major breakage events have finished, suggesting that friction increases as broken fragments move past one another.

The energy rates of the system for the dynamic shear speeds (Figure 6.16 (b)) show an increase in all energies over 1-2% shear strain associated with the substantial breakage occurring at the same time. Strain energy reaches the highest peak and then falls relatively quickly whereas the kinetic energy falls away a little slower. This initial reaction can be considered as a partial inertial response as the shear test begins. All energies appear to reach a steady state after around 10% shear strain.

Strain energy climbs just prior to that of kinetic energy — falling just as kinetic energy is climbing, which in turn falls as friction energy reaches a peak. The strain energy rate represents the total strain energy stored at the contacts within the system — a whole system energy. It can be considered that when breakage events occur in the system, the number of contacts reduces as particles separate and so the strain energy dips. In turn, kinetic energy is formed from the breakages and as the particles move away from one another and contact other particles friction energy rises, dissipating the kinetic energy. The rise and fall of energy in the first 5% shear strain can be directly attributed to the substantial breakage event that occurs during the first 0-2% shear strain.

The changes in kinetic energy are best viewed by considering the behaviour of the kinetic energy separately, as shown in Figure 6.17. For the quasi-static shear tests, as noted above, there is little kinetic energy created in the system. Under 1MPa loading there is a small spike associated with the final major breakages at 2-3% strain. For the dynamic tests the kinetic energy peaks are more noticeable and match reasonably well to the peaks in the breakage rate, although there is a slight delay in kinetic energy response after breakage occurs. Interestingly, the mean effective and deviatoric stresses (Figure 6.14 (c) and (d)) both climb when the kinetic energy climbs, so that there is little reduction in mobilised friction due to breakage. Reductions in the kinetic energy shown by the downward trend of the kinetic energy response (Figure 6.17) in the system suggests that, in general, kinetic energy produced within the system is dissipated fairly quickly. This figure also highlights that small breakage events appear to have very little influence on the kinetic energy of the system.

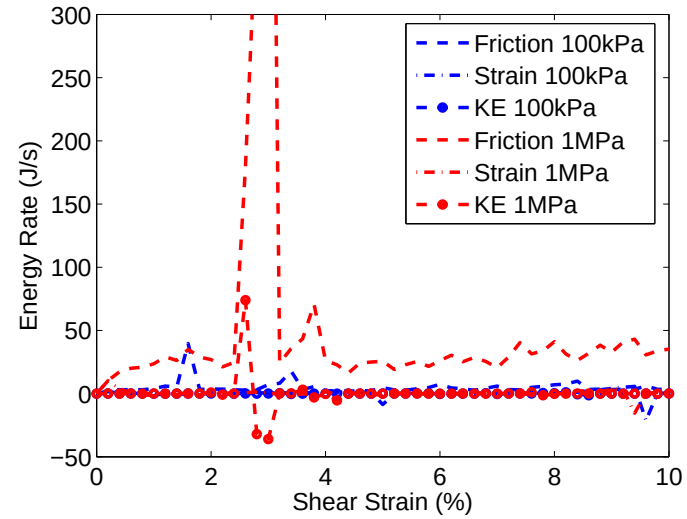

(a) Quasi-static

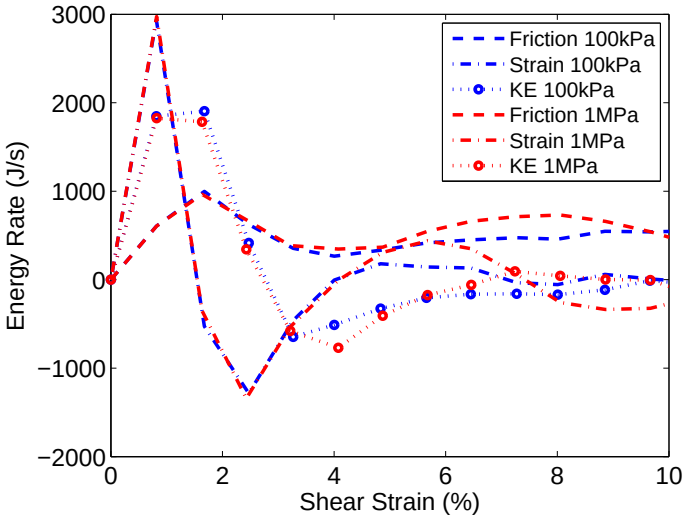

(b) Dynamic

Figure 6.16: System energy rates against shear strain from shear testing of sandstone specimen 1 for quasi-static (a) and dynamic (b) cases.

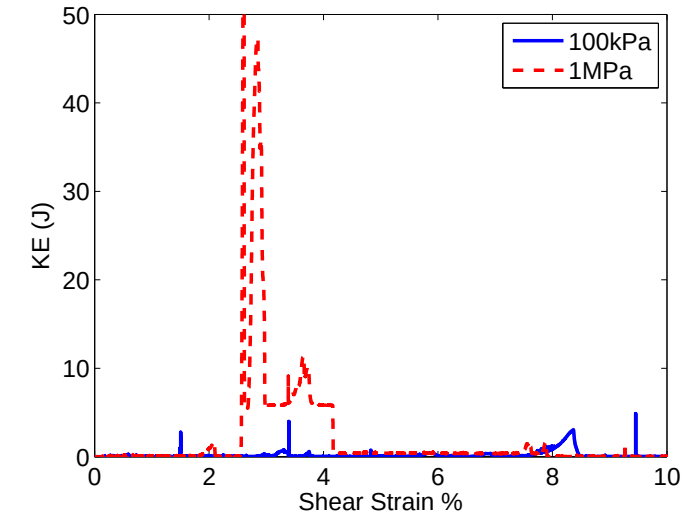

(a) Quasi-static

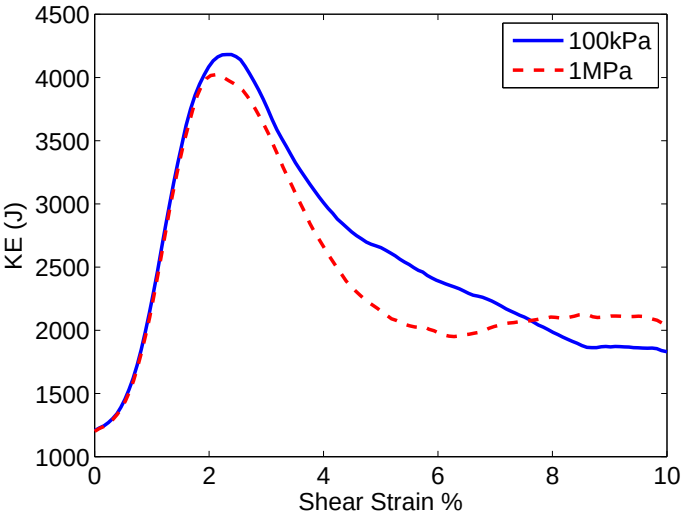

(b) Dynamic

Figure 6.17: System kinetic energy against shear strain from shear testing of sandstone specimen 1 for quasi-static (a) and dynamic (b) cases.

6.5.6 Particle Movement

The movement of the gauge particles against shear strain is shown in Figure 6.18. There is a clear difference in dilation between the material above the boulders and that below the boulders. The upper gauge particles in the layers above the boulders dilate at 25 mm to 40 mm with the greater movement seen in the quasi-static case. This is likely due to the material having greater time to rearrange during quasi-static shear.

The additional confinement of the lower parts of the specimen beneath the boulders reduces the dilation of the lower gauge layers to a maximum of 12 mm to 17 mm, for the dynamic and quasi-static shear speeds respectively. Dilation begins as shearing and breakage occurs, with a majority of the dilation likely in response to the initial main breakages for both speeds. There are further minor increases in dilation as small breakage events occur, most noticeable in the response to the quasi-static shear speed.

Dilation in the quasi-static tests is slightly higher (39 mm) than the dynamic tests (30-32 mm), irrespective of overburden. The inertial response from dynamic loading results in the mean stress being higher than the overburden stress, likely masking the influence of the overburden. This suggests that a significant stress would be required to restrain dilation under dynamic shear speeds. Figure 6.18 also shows that each gauge particle moves in a slightly different manner for each test.

In the dynamic case, additional shear to 40% strain suggests that dilation continues, even though there is little in the way of additional breakages and no substantial kinetic energy created. This suggests that the spherical nature of the particles may be influencing the behaviour; the particles riding over one another during shear. This is supported by the friction energy dominating the systems.

6.5.7 Wall Pressures

Figure 6.19 shows the confining wall and base pressures against shear strain for the quasi-static and dynamic shear tests. For the quasi-static case ((a) and (b)), the wall pressures show a distinct difference for the 100 kPa and 1 MPa overburden loads, with the 100 kPa overburden resulting in pressures around 100-400 kPa and the 1 MPa overburden resulting in pressures around 1-1.85 MPa. The wall pressures show a minor increase under quasi-static loading occurring during the main period of breakage from 0-3% shear strain before a slight reduction back toward the initial state. The 100 kPa graph has two vertical spikes in wall pressure that occur at the same time as breakage events. The base pressures increase slightly from the initial overburden state with peaks during breakage.

Figure 6.19 (c) and (d) shows a very different behaviour to that of the static case. Under dynamic shear the wall and base pressures produce a wave-like behaviour. As with the other

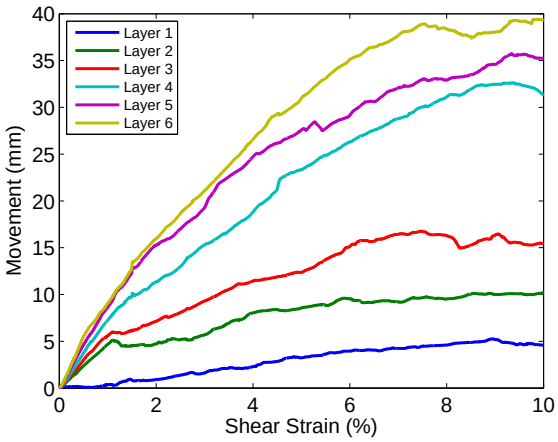

(a) Quasi-static 100kPa

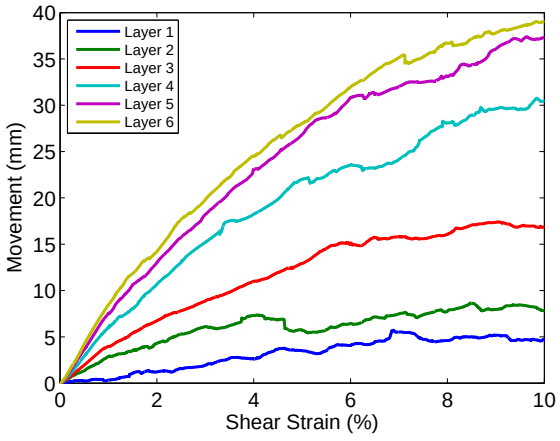

(b) Quasi-static 1MPa

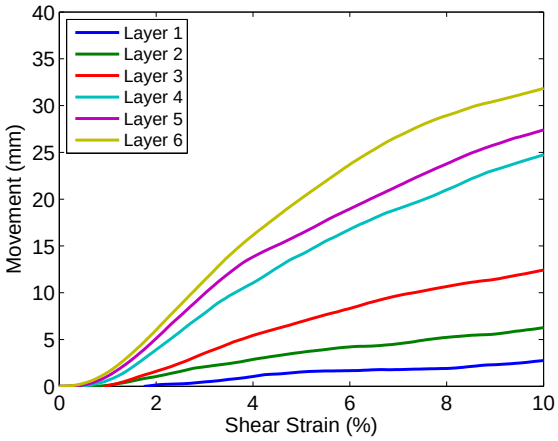

(c) Dynamic 100kPa

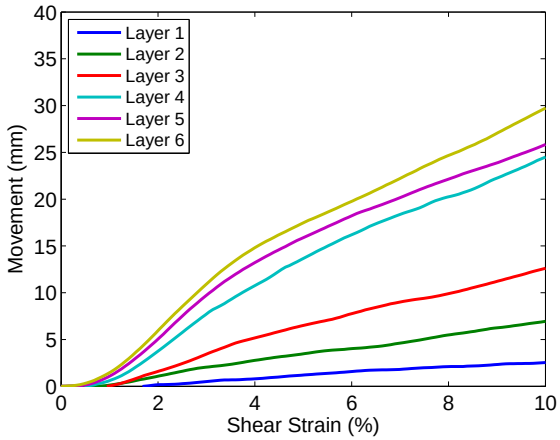

(d) Dynamic 1MPa

Figure 6.18: Dilation of sandstone specimen 1 as measured by gauge particles for quasi-static (a, b) and dynamic (c, d) shear speeds.

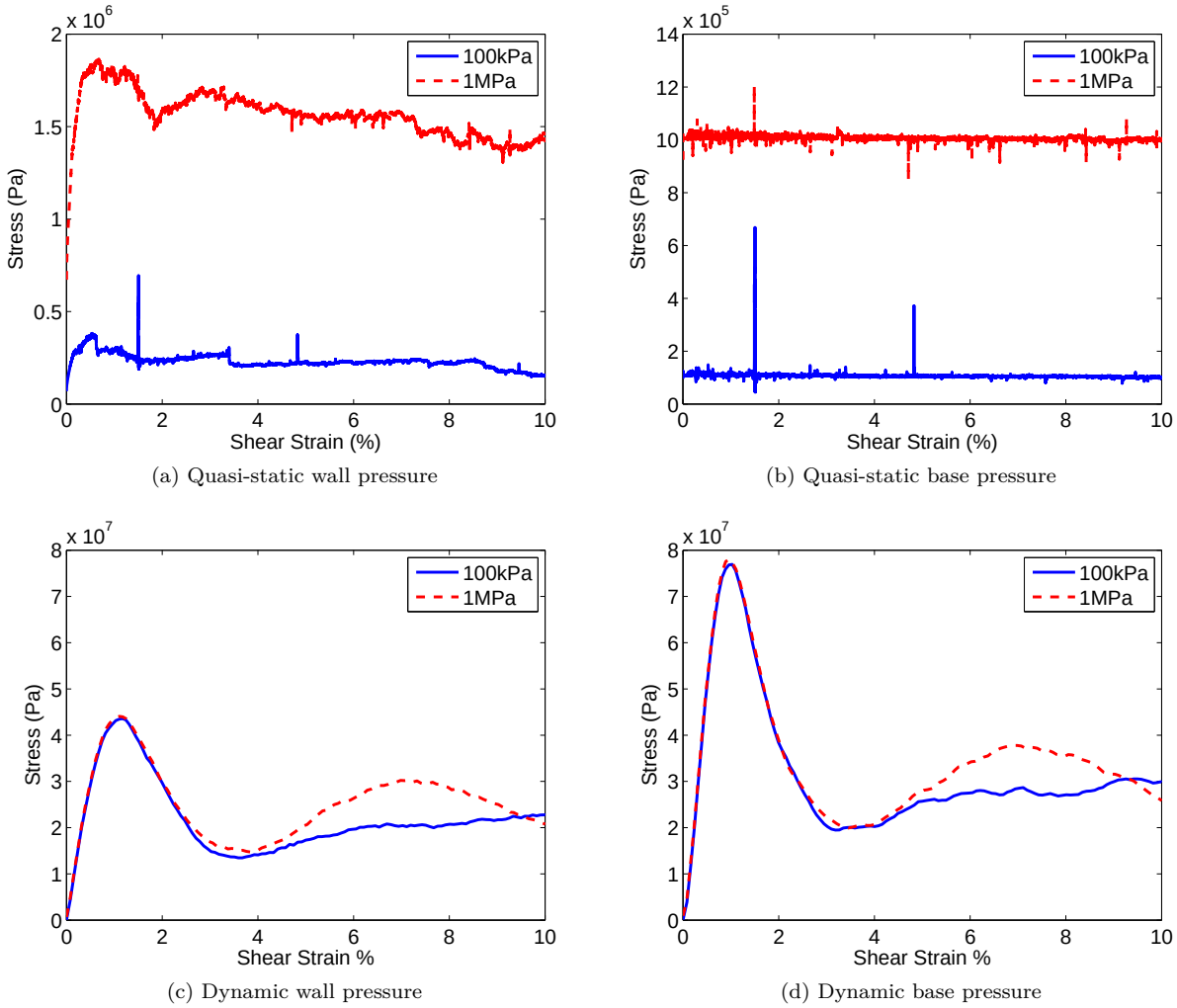

(a) Quasi-static wall pressure

(b) Quasi-static base pressure

(c) Dynamic wall pressure

(d) Dynamic base pressure

Figure 6.19: Plane strain confining wall pressures and base wall pressures for sandstone specimen 1 for quasi-static (a, b) and dynamic (c, d) shear speeds.

parameters measured during the dynamic shear testing, the side wall and base wall pressures show similarity in values between the two overburden loading cases. Wall pressure increases and decreases occur at the same shear strain as the changes in strain energy. The wall forces are measured directly using the PFC^{3D} in built wall logic and thus it seems reasonable that a global measure of ball-to-ball contact energy shows similarity to a measure of ball-to-wall contacts. This also suggests that the pressures exerted on the walls are affected by events occurring away from them such as breakage, or surrounding material in the case of sturzstroms.

6.5.8 Summary

The two sandstone specimens results for the quasi-static shear testing show differences in micro-stresses and wall pressures under the two loading rates of 100 kPa and 1 MPa, whereas for the dynamic shear test the specimens show close similarity in results. The images taken of the parallel

bonds and force chains from the start and end of the shear test in Figures 6.5 and 6.6 suggest that the overburden load appears to have little influence on the micro-mechanical results of the dynamic shear tests.

The initial period of breakage (0-3% shear strain) is the largest for all of the quasi-static and dynamic shear speed tests, followed by several much smaller events throughout the tests. Boulder bonds failed to break under quasi-static shear speeds and only 20% of the boulder bonds break under the dynamic shear speeds. The majority of bond breakages occur within the matrix. Even though a minimal number of bonds break within the boulder, these breakage events still affect the overall response under dynamic shear as they occur during the initial major breakage period. This suggests that the disruption of force chains due to breakages under dynamic shear, whether in the matrix or boulders, is more important than the area of the specimen that is breaking. Under quasi-static shear, breakages cause a change to pressures on the walls, however, these do not produce substantial amounts of kinetic energy within a friction dominated system.

Micro-stresses, in general, rise initially as shear begins and then fall away toward a critical state. The rise for the dynamic shear speed is at least $\mathcal{O}(1)$ bigger in comparison to that for the quasi-static shear speed. An initial rise in kinetic energy under dynamic shear is quickly dissipated with friction energy dominating the majority of the test. It would appear that the initial changes in stress and energy during the dynamic shear test are due to a combined affect of inertia and breakage. Overall, the gauge particles indicate that the material dilates under shear with greater movement occurring for the layers situated above the boulders.

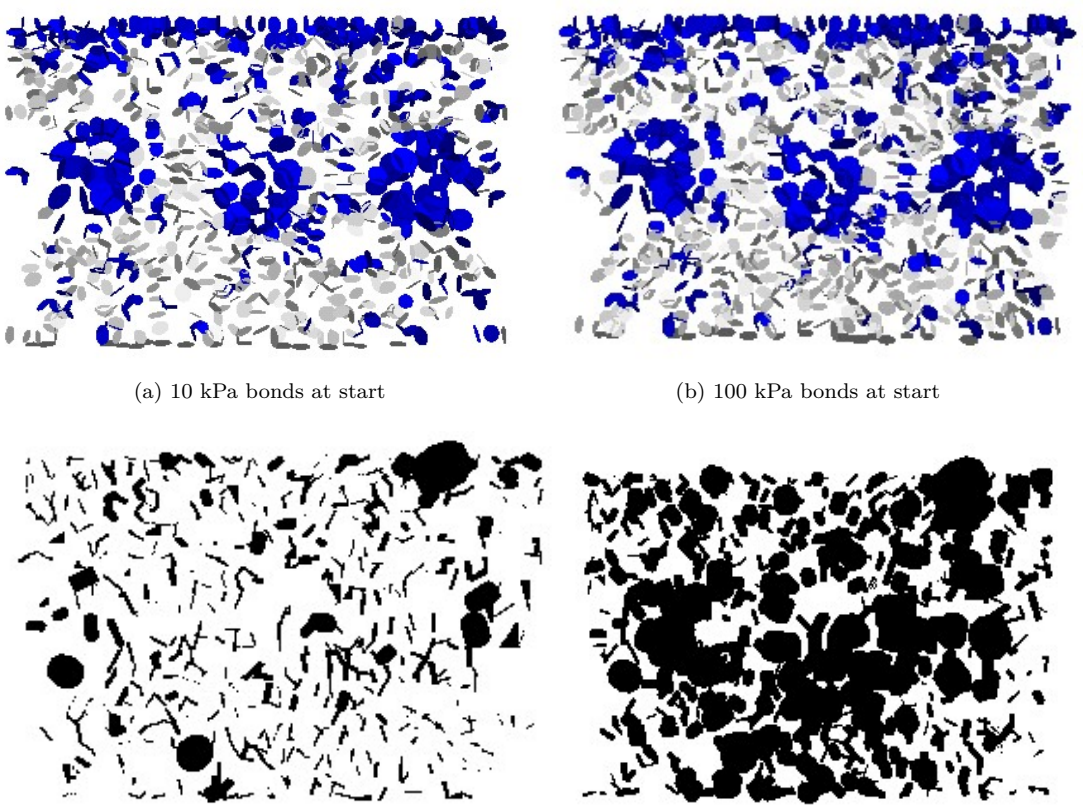

(a) 10 kPa bonds at start

(b) 100 kPa bonds at start

(c) 10 kPa force chains at start

(d) 100 kPa force chains at start

Figure 6.20: Parallel bonds and system force chains (plane through y-axis) of weak chalk specimen at the beginning of shear.

6.6 Weak Chalk Results

6.6.1 Bonds and Force Chains

Following the sandstone shear tests, two weak chalk materials were prepared following the calibration process outlined in Chapter 4. The two specimens were arranged into shear test format, and two loading cases for each specimen were created by incrementally loading the specimens with 10 kPa and 100 kPa of overburden pressure as described in Section 6.2. The initial parallel bond starting state of both overburden cases for weak chalk 1 are shown in Figure 6.20 (a) and (b), along with the associated force chains ((c) and (d)) for a plane through the y-axis of the specimen at the origin. The figures show that the 100 kPa load case has larger force chains than the 10 kPa case, as expected, with the parallel bond arrangement for the two cases the same. All specimens are tested under a quasi-static and dynamic shear speed in a similar manner to that of the sandstone material above and at the shear speeds outlined earlier in Section 6.3.

Figure 6.21 outlines the parallel bond and force chains for a plane through the y-axis of weak chalk specimen 1 at the end of the shear tests (5% shear strain for the quasi-static tests and 10%

shear strain for the dynamic tests). Under quasi-static shear, it can be seen that there is some minor movement in the boulder particles resulting in a slight elongation of the boulders (Figure 6.21 (a) and (b)). The force chain strengths in Figure 6.21 (c) and (d) are very similar across the two loading cases, with the strongest chains appearing to travel through the boulders. From the dynamic shear tests the parallel bond images ((e) and (f)) outline the large extent of shear that has occurred, and suggest that the boulders have separated into fragments rather than undergoing explosive fragmentation. The force chains of the 100 kPa load case are slightly larger in magnitude than those of the 10 kPa case ((g) and (h)), and in both overburden tests the force chain lengths have shortened and magnitudes reduced, due to the effects of shear on the boulders.

Figures 6.22 and 6.23 show the force chain evolution for the quasi-static shear tests. The 100 kPa overburden can be seen to produce more force chains in the specimen than that of the 10 kPa overburden load. The force chains, under both overburden loads, respond to the shear by lining up into a preferential diagonal direction, which is aligned with the shearing direction. As shearing continues this diagonal area becomes more dominant until ultimately the entire specimen is overtaken with force chains.

The force chain evolution for the dynamic shear tests can be seen in Figures 6.24 and 6.25. A similar progression of force chain behaviour is seen here as was seen in the sandstone specimens (see Figures 6.9 and 6.10). Large magnitude force chains in the weak chalk become concentrated at the base of the specimen, until enough breakage has occurred to allow shear to continue, at which point the material begins to dilate and the force chains weaken as they separate. It is possible that the dynamic shear speed is so fast for this material that the force chains are not able to form into a strong preferential direction.

6.6.2 Translational Velocity

The shear velocity profile at the start of the tests is shown in Figure 6.26 via a coloured contour. The maximum starting shear velocity in the x-direction is 0.005 ms^{-1} for the quasi-static shear tests, and 2 ms^{-1} for the dynamic shear tests, represented by the blue and red particles in the figure (where these colours indicate the movement of particles in the negative and positive x-directions respectively). The particles are able to increase or decrease their respective velocities as shearing advances, resulting in the final translational velocity colour contours shown in Figure 6.27. In some cases particle velocities have increased, as can be seen by the change in particle colour from the starting state. In particular, several of the boulder particles that had near zero velocity at the start of the shear test appear to have increased or attracted a velocity during the shearing process. The translational velocity colour contour of the dynamic tests shows the extent of dilation and space around the particles, whereas the quasi-static colour contour shows a more tightly packed material at the end of shear.

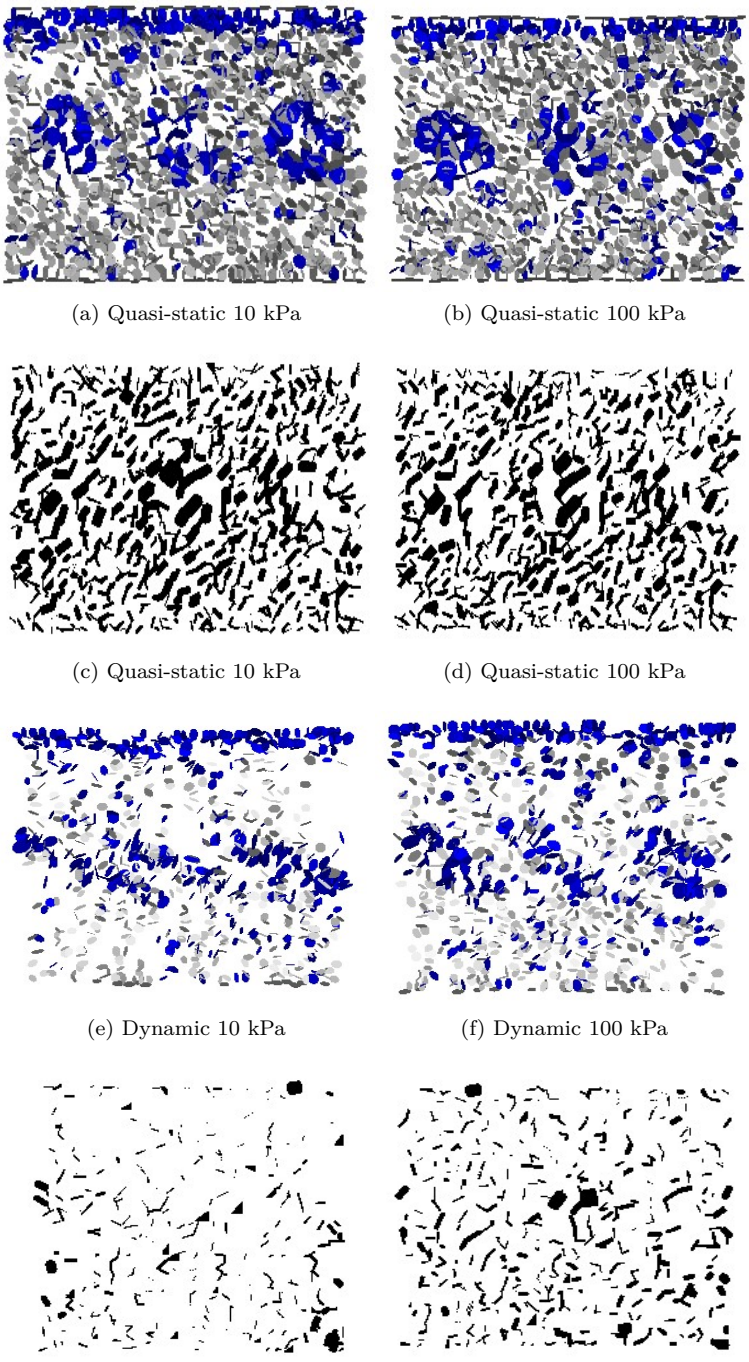

(a) Quasi-static 10 kPa (b) Quasi-static 100 kPa

(c) Quasi-static 10 kPa (d) Quasi-static 100 kPa

(e) Dynamic 10 kPa (f) Dynamic 100 kPa

(g) Dynamic 10 kPa (h) Dynamic 100 kPa

Figure 6.21: Parallel bonds (plane through y-axis) (a, b, e, f) and system force chains (c, d, g, h) of weak chalk specimen 1 at the end of shear. Note that in order to view the force chains within PFC^{3D} there is a scale difference of 2 orders of magnitude between the quasi-static (larger scale) and dynamic (smaller scale) force chains. There is also a significant scale difference of 2-4 orders of magnitude (quasi-static to dynamic respectively) between the initial force chains in Figure 6.20 (c) and (d) and the end states represented here.

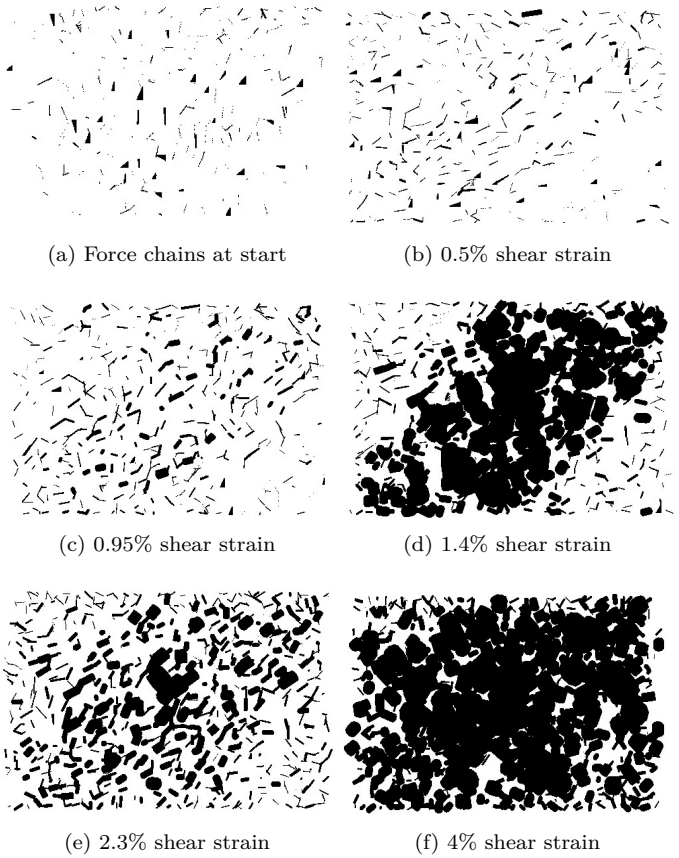

(a) Force chains at start (b) 0.5% shear strain

(c) 0.95% shear strain (d) 1.4% shear strain

(e) 2.3% shear strain (f) 4% shear strain

Figure 6.22: Evolution of the force chains throughout the quasi-static shear test under 10 kPa overburden load on weak chalk specimen 1. Note that the viewing scale of the force chains is consistent for figures (a) to (d) and is reduced to obtain a clear indication of the force chains up to 4% shear strain in (e) and (f). The force chain scale is at least $\mathcal{O}(2)$ smaller than that shown for the starting state in Figure 6.20.

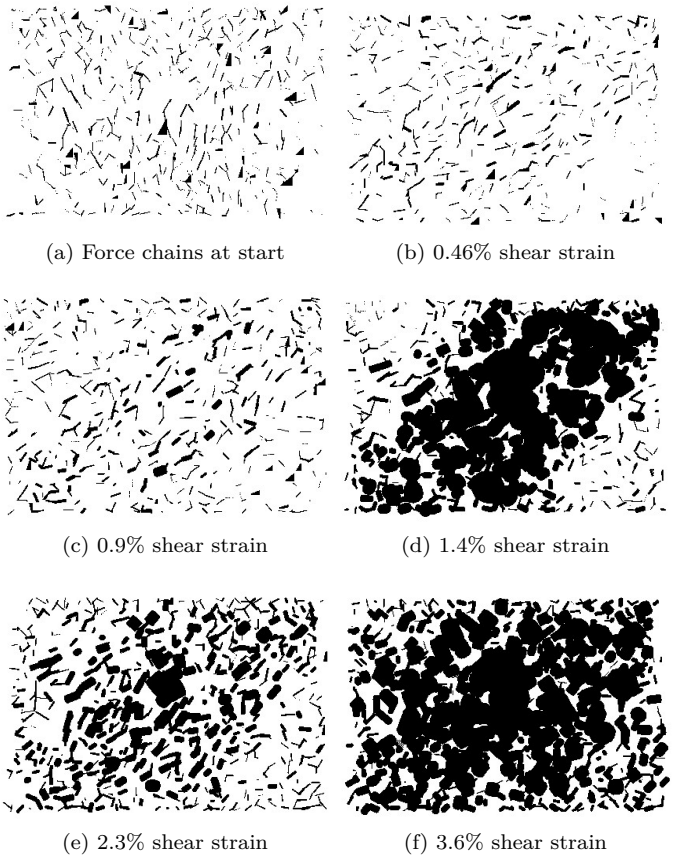

(a) Force chains at start (b) 0.46% shear strain

(c) 0.9% shear strain (d) 1.4% shear strain

(e) 2.3% shear strain (f) 3.6% shear strain

Figure 6.23: Evolution of the force chains throughout the quasi-static shear test under 100 kPa overburden load on weak chalk specimen 1. Note that the viewing scale of the force chains is consistent for figures (a) to (d) and is reduced to obtain a clear indication of the force chains up to 4% shear strain in (e) and (f). The force chain scale is at least $\mathcal{O}(2)$ smaller than that shown for the starting state in Figure 6.20.

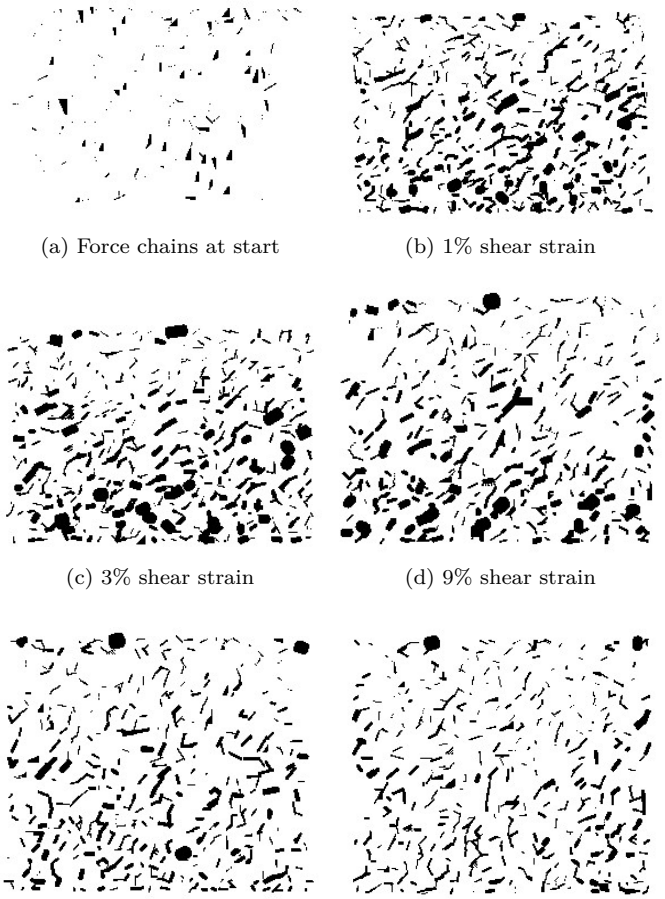

(a) Force chains at start (b) 1% shear strain

(c) 3% shear strain (d) 9% shear strain

(e) 19% shear strain (f) 28% shear strain

Figure 6.24: Evolution of the force chains throughout the dynamic shear test under 10 kPa overburden load on weak chalk specimen 1. Note that the viewing scale of the force chains is consistent throughout this figure and is at least $\mathcal{O}(2)$ smaller than that shown for the starting state in Figure 6.20.

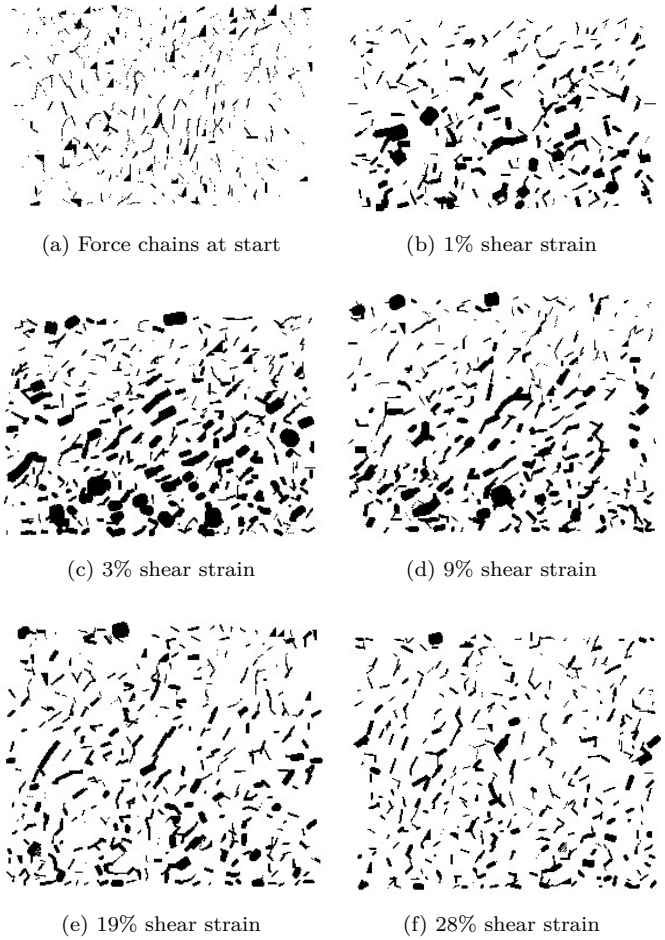

(a) Force chains at start (b) 1% shear strain

(c) 3% shear strain (d) 9% shear strain

(e) 19% shear strain (f) 28% shear strain

Figure 6.25: Evolution of the force chains throughout the dynamic shear test under 100 kPa overburden load on weak chalk specimen 1. Note that the viewing scale of the force chains is consistent throughout this figure and is at least $\mathcal{O}(2)$ smaller than that shown for the starting state in Figure 6.20.

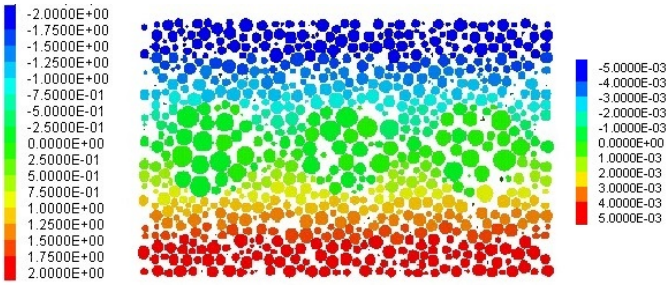

Figure 6.26: Translational velocity starting state for weak chalk and extremely weak chalk specimens represented as a coloured contour with two legends outlining the velocity applied to the relevant coloured particles. The legend to the left relates to the dynamic shear speed (ms^{-1}) and the legend on the right to quasi-static shear speed (ms^{-1}).

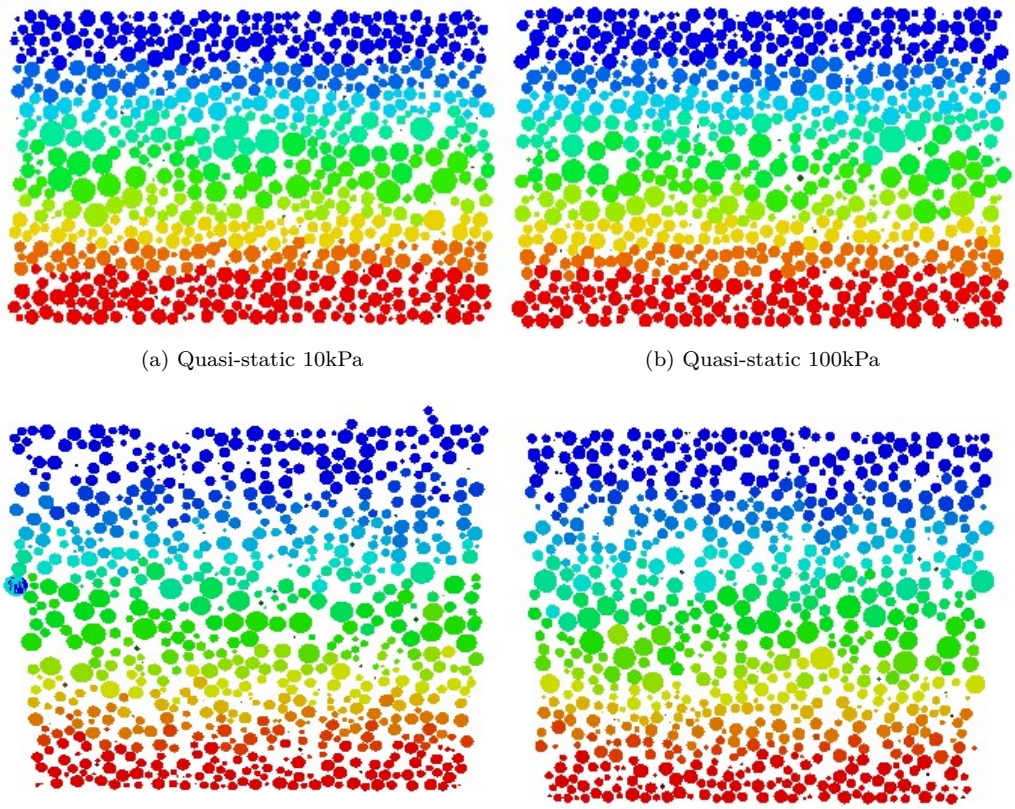

(a) Quasi-static 10kPa

(b) Quasi-static 100kPa

(c) Dynamic 10kPa

(d) Dynamic 100kPa

Figure 6.27: Translational velocity with coloured contour to represent particle direction and magnitude of velocity at the end of the shear test for weak chalk specimen 1 — compare with the typical contour provided at the start of the shear test in Figure 6.26.

6.6.3 Breakage

Figure 6.28 shows the number of breakages of parallel bonds and the breakage rate (breaks/s) under quasi-static and dynamic shear speeds. The breakage results from the test data (Figure 6.28 (a) and (c)) support the visual results from PFC^{3D}, by showing that there is very little difference in bond breakage between the two loading states of 10 kPa and 100 kPa, during either the quasi-static or dynamic shear tests. In both loading cases, significant breakage occurs within the first 1-2% of shear strain (Figure 6.28 (b) and (d)). Additional breakage events occur throughout the dynamic test, however all are relatively small in number and do not appear to cause a significant increase in the overall breakage. The quasi-static test appears to reach a localised breakage limit after the first 2% shear strain which suggests the breakages were required in order for shear to occur.

The boulder breakages are considered separately from the matrix breakages in Figure 6.29. It can be seen when this is compared with Figure 6.28, that the boulders are a source for only a small proportion of the overall number of breakages. Around 20-25% of the boulder bonds break (140-170 parallel bonds of a total of 676) during the quasi-static and dynamic tests, with the majority of these occurring within the first 1% shear strain for quasi-static shear and 0.5% shear strain for dynamic shear. Little additional breakage occurs in the boulders throughout the remainder of the shear tests. It can also be seen that more boulder breakages occur in the quasi-static shear case than the dynamic shear case to 5% axial strain.

6.6.4 Micro-stress

When the main breakage events occur in weak chalk 1 (see Figure 6.28 at around 0.5% to 1% shear strain), the mean effective stress p' and deviatoric stress q measured in the boulders (see Figure 6.30) begins growing for the quasi-static tests ((a) and (b)), and causes a sharp spike in those from the dynamic tests ((c) and (d)). For the quasi-static shear tests both micro-stresses continue to climb linearly throughout the test. The dynamic tests, however, show both micro-stresses falling quickly back to around 500 kPa-1 MPa with minor fluctuations during small breakage events.

The stress ratio of the deviatoric stress against the mean effective stress p$'$, and q-p$'$ stress paths, are shown in Figure 6.31. The response of the 100 kPa loaded specimen under quasi-static shear results in an increase and immediate drop in the $\frac{q}{p'}$ stress ratio during breakage (Figure 6.31 (a)). The 10 kPa loaded specimen also produces a drop in the $\frac{q}{p'}$ stress ratio under quasi-static shear during breakage at 0.5% shear strain. Both ratios recover before gradually declining once all initial breakages are complete. The stress paths in Figure 6.31 (b), for both loading cases under quasi-static shear, are fairly similar and linearly increasing.

It can be seen that the $\frac{q}{p'}$ stress ratio from the dynamic shear tests (Figure 6.31 (c)) has an initial sharp drop in value during the main breakage event, followed by a gradual decline over the remainder of the test. The stress ratios for the two load cases under dynamic shear (Figure 6.31 (d))

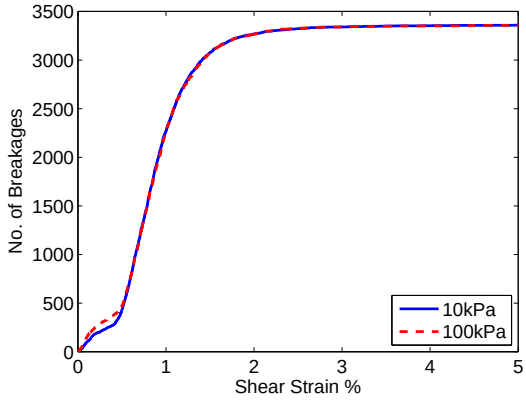

(a) Quasi-static breakage

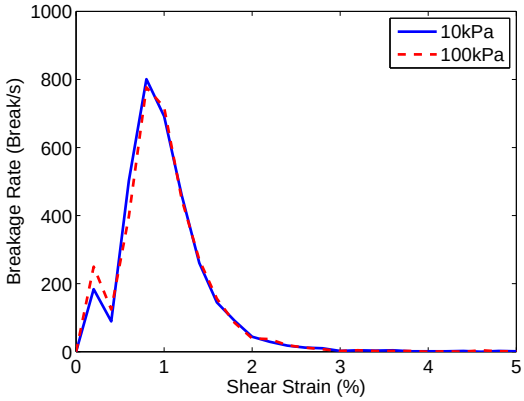

(b) Quasi-static breakage rate

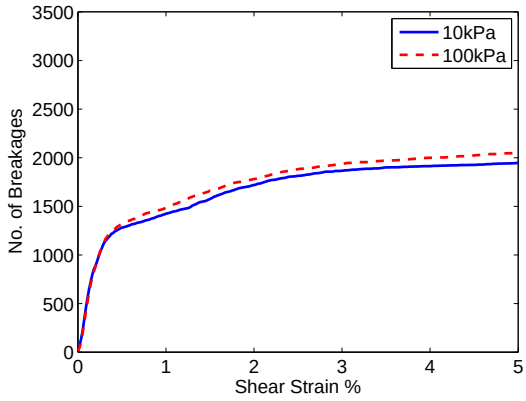

(c) Dynamic breakage

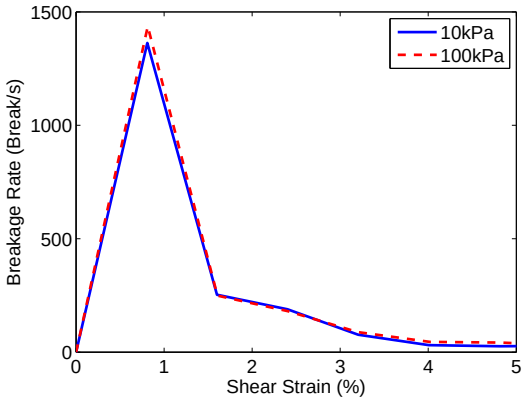

(d) Dynamic breakage rate

Figure 6.28: The number of breakages and the breakage rate (breaks/s) for quasi-static (a, b) and dynamic (c, d) shear speeds for weak chalk specimen 1.

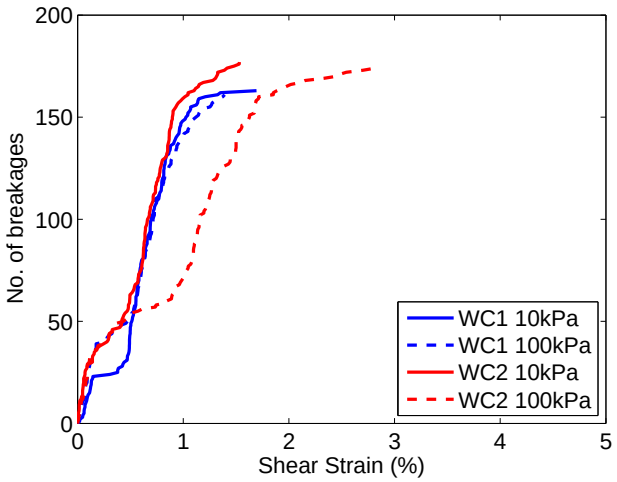

(a) Quasi-static

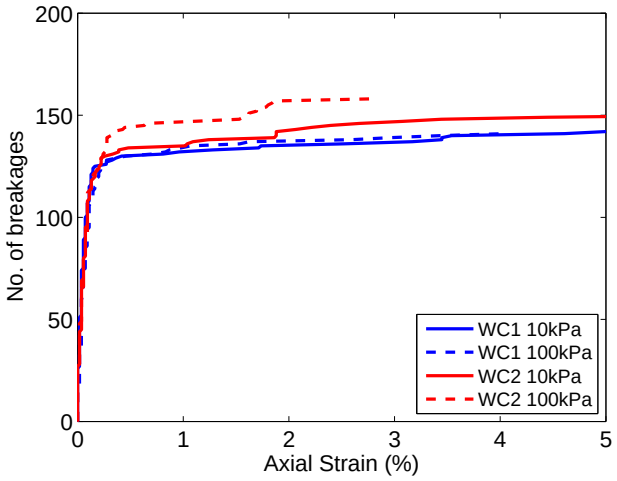

(b) Dynamic

Figure 6.29: Number of boulder breakages under shear testing for weak chalk specimens for quasi-static (a) and dynamic (b) shear speeds.

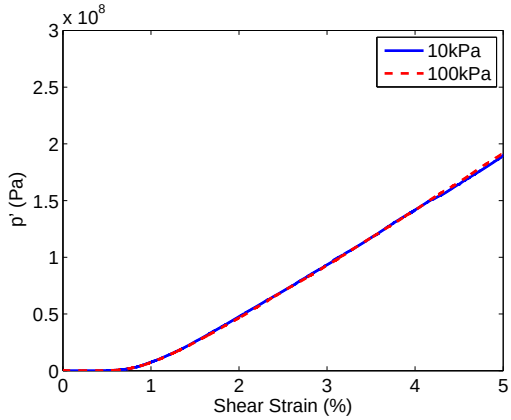

(a) Mean effective stress p′ under quasi-static shear

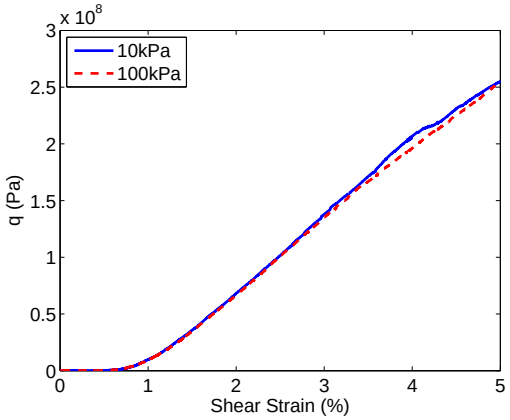

(b) Deviatoric stress q under quasi-static shear

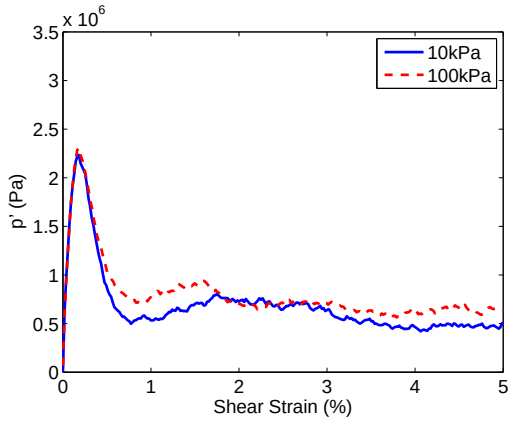

(c) Mean effective stress p′ under dynamic shear

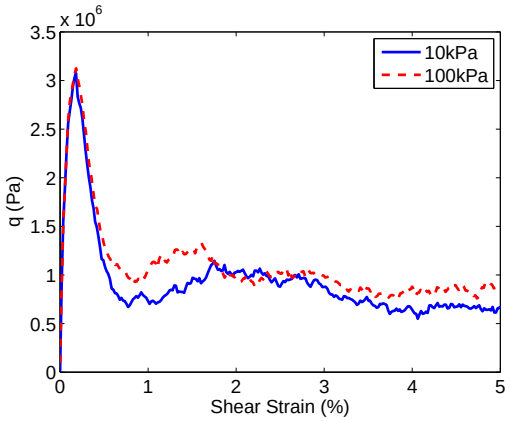

(d) Deviatoric stress q under dynamic shear

Figure 6.30: Mean effective and deviatoric stress responses under shear strain for quasi-static (a) and (b), and dynamic (c) and (d) shear speeds for weak chalk specimen 1.

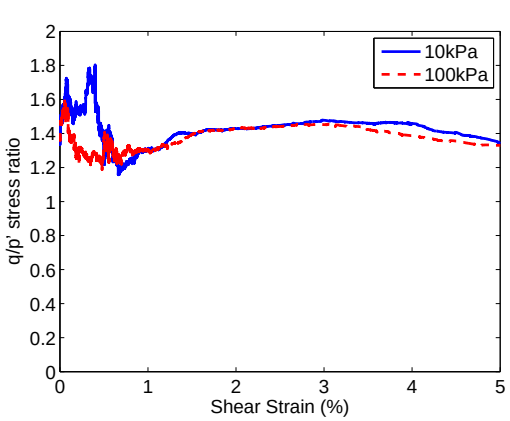

(a) $\frac{q}{p'}$ stress ratio under quasi-static shear

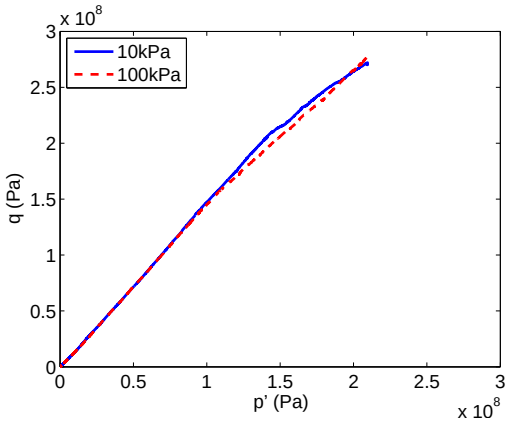

(b) Stress path due to quasi-static shear

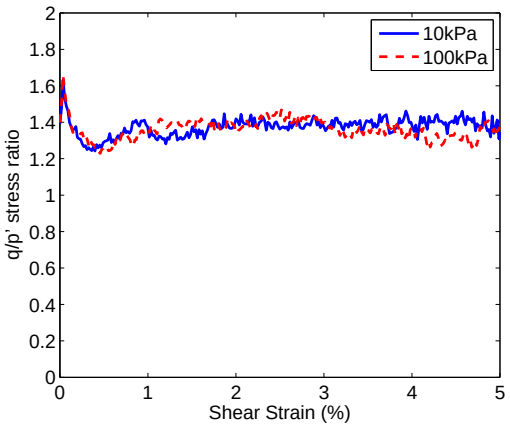

(c) $\frac{q}{p'}$ stress ratio under dynamic shear

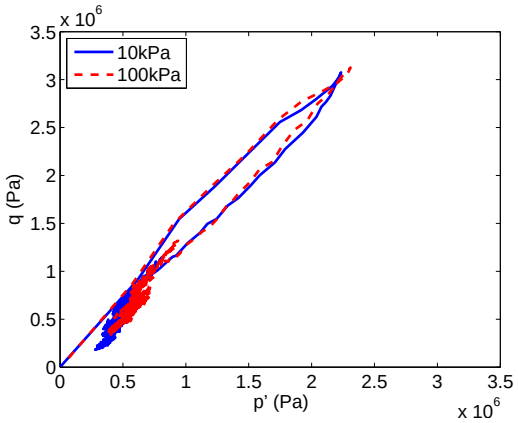

(d) Stress path due to dynamic shear

Figure 6.31: $\frac{q}{p'}$ stress ratio and q-p′ stress path response under shear testing for quasi-static (a) and (b), and dynamic (c) and (d) shear speeds for weak chalk specimen 1.

oscillate, with the curves crossing one another several times before the critical state is reached. The oscillatory response of the stress path is most likely related to the rotation of individual particles within the boulders, which becomes more dominant once the majority of breakage has occurred in the boulders, or the fragments separated. This oscillatory response may also become a future source of numerical convergence issues in the model, hence the test was stopped as soon as a critical state appeared to have been achieved.

6.6.5 Energy Rates

Figure 6.32 shows the friction, strain and kinetic energy rates against shear strain for the quasi-static and dynamic shear tests. The energy rates of the quasi-static shear tests shown in (a) are virtually identical for the two loading cases. Strain energy (stored within the contacts in the system) dominates with both strain energy and friction energy growing once the majority of

breakage has occurred. The strain energy is likely to decrease if a major breakage event was to occur. Kinetic energy is very small in comparison to the strain and friction energies, and so the system is considered to be dominated by strain energy until such time as another major breakage event occurs.

In the dynamic shear test, there is an immediate rise in all energies as shear begins and this coincides with the main breakage event. Friction energy rises during breakage and drops away once substantial breakage has finished. The friction energy remains substantially higher than all other energies suggesting that the system is friction dominated. After the main breakage event is complete, both the strain energy and kinetic energy remain very low with only very minor peaks occurring throughout the rest of the shear.

The kinetic energy against shear strain is shown separately in Figure 6.33. The kinetic energy in the quasi-static shear test is very small and nonlinear, with discrete peaks starting to occur after around 60% of breakage is complete or around 1.25% shear strain. Later peaks around 4-5% strain are likely to be from the movement of particles as the material is overcome by the shear forces. Under quasi-static shear speeds, kinetic energy is most likely forming from discrete breakage events rather than from large breakage events.

In the dynamic shear test, over the shear strain period of 0-2% when the majority of breakage is occurring (see Figure 6.28 (d)), it appears from Figure 6.33 that there is an instantaneous kinetic energy response, although a proportion of this could be attributed to inertia. The kinetic energy dissipates throughout the remainder of the shear test to lower levels.

6.6.6 Particle Movement

The movement of the gauge particles against shear strain is shown in Figure 6.34. The gauge particle layers move very similarly under the 10 kPa and 100 kPa overburden loads for the quasi-static and dynamic shear tests, which suggests that the overburden load is having little effect on the behaviour of these particles. As outlined earlier, it is likely that the position and possible bonds associated with the gauge particles influence movement.

As the main breakage event begins at the start of shearing, the material undergoes the largest dilation with layer 6 moving up to 4.5 mm at 0.5% strain. The more confined material toward the base of the specimen is restricted to 0.5-1.5 mm of movement. As the shear progresses to 5% strain the particles continue to gradually dilate up to 1 mm further. In contrast, layers 1 and 2 show a gradual decline in position suggesting that these particles or layers are contracting.

During the dynamic shear test the gauge particle layers indicate that the material above the boulders dilates further than that below, showing the effect of confinement on the basal material. The dilation is gradual and consistently increasing throughout the dynamic test, and far larger at 20 mm in total at the top of the specimen than seen in the quasi-static cases. Under further shear,

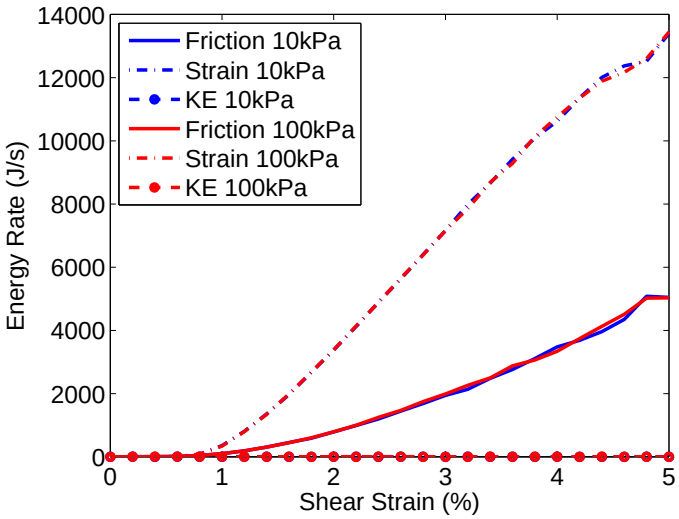

(a) Quasi-static shear

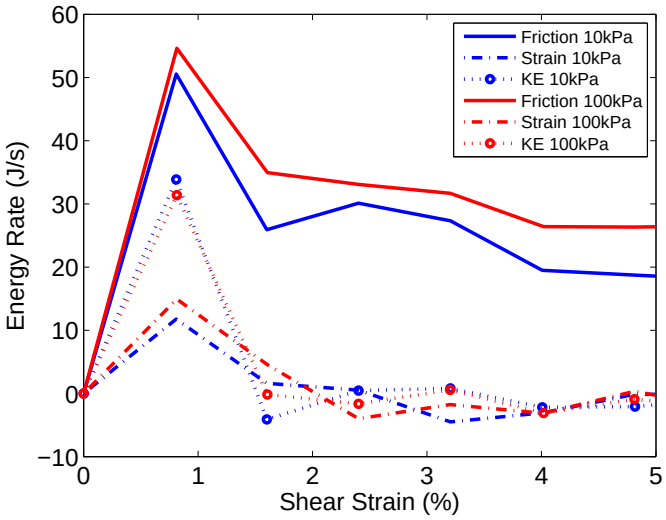

(b) Dynamic shear

Figure 6.32: System energy rates from shear testing of weak chalk specimen 1 for quasi-static (a) and dynamic (b) shear speeds.

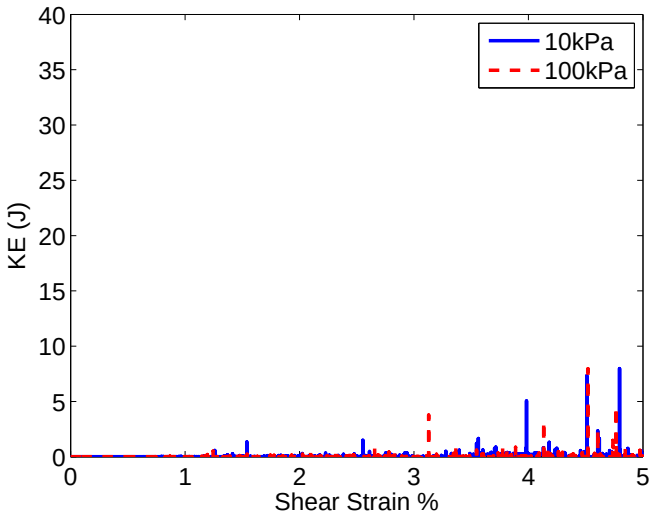

(a) Quasi-static shear

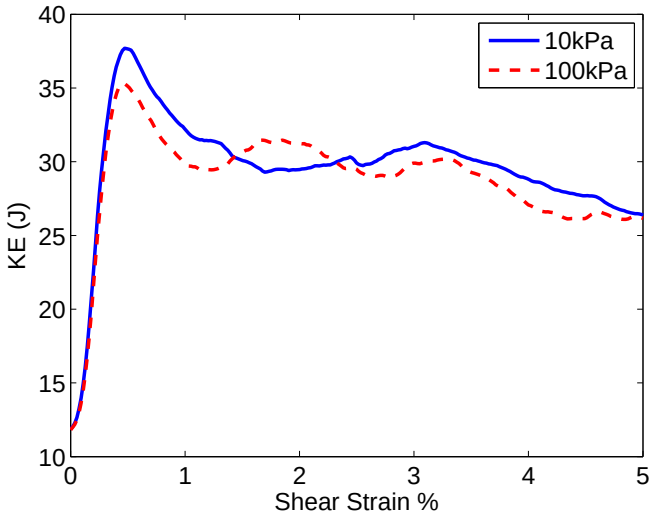

(b) Dynamic shear

Figure 6.33: System kinetic energy response from shear testing of weak chalk specimen 1 for quasi-static (a) and dynamic (b) shear speeds.

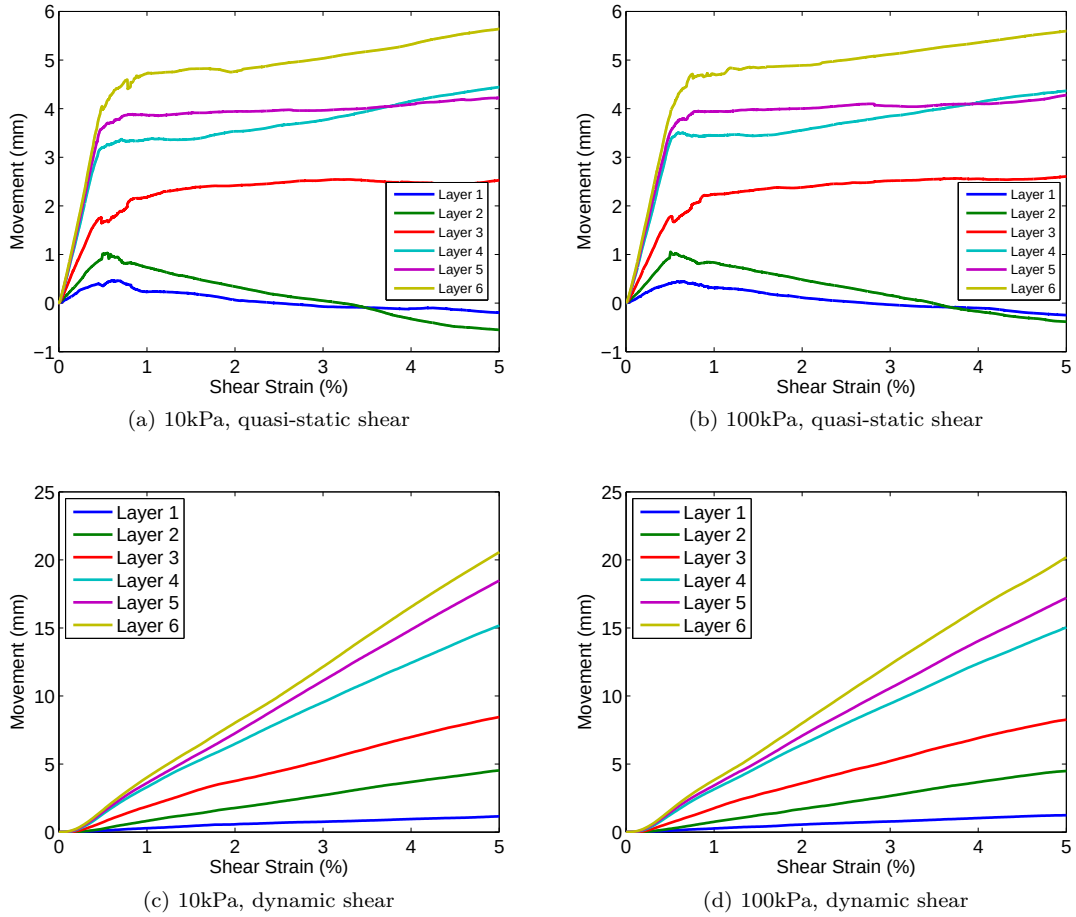

(a) 10kPa, quasi-static shear

(b) 100kPa, quasi-static shear

(c) 10kPa, dynamic shear

(d) 100kPa, dynamic shear

Figure 6.34: Dilation of gauge particles against shear strain for weak chalk specimen 1 for quasi-static (a, b), and dynamic (c, d) shear speeds.

as seen in the sandstone case, dilation continues even with little else happening within the system. It is likely that the spherical shape of the particles influences the ability of the material to dilate.

6.6.7 Wall Stresses

The wall and base pressures for the quasi-static shear tests (Figure 6.35 (a) and (b)), begin increasing once the major breakage event occurs at around 0.5% strain, and continue to climb until the end of the test. This increase is also seen in p′ and q (Figure 6.30) under quasi-static shear, which suggests that the particles are locking together rather than breaking parallel bonds, increasing the amount of stress in the system. This is supported by the increase in the magnitude of the force chains. The stress is anticipated to reduce once additional shear or breakages occur so that the forces can be redistributed throughout the specimen.

The wall and base pressures for the dynamic shear test (Figure 6.35 (c) and (d)) produce an initial substantial peak under both loading cases, which coincides with the main breakage event

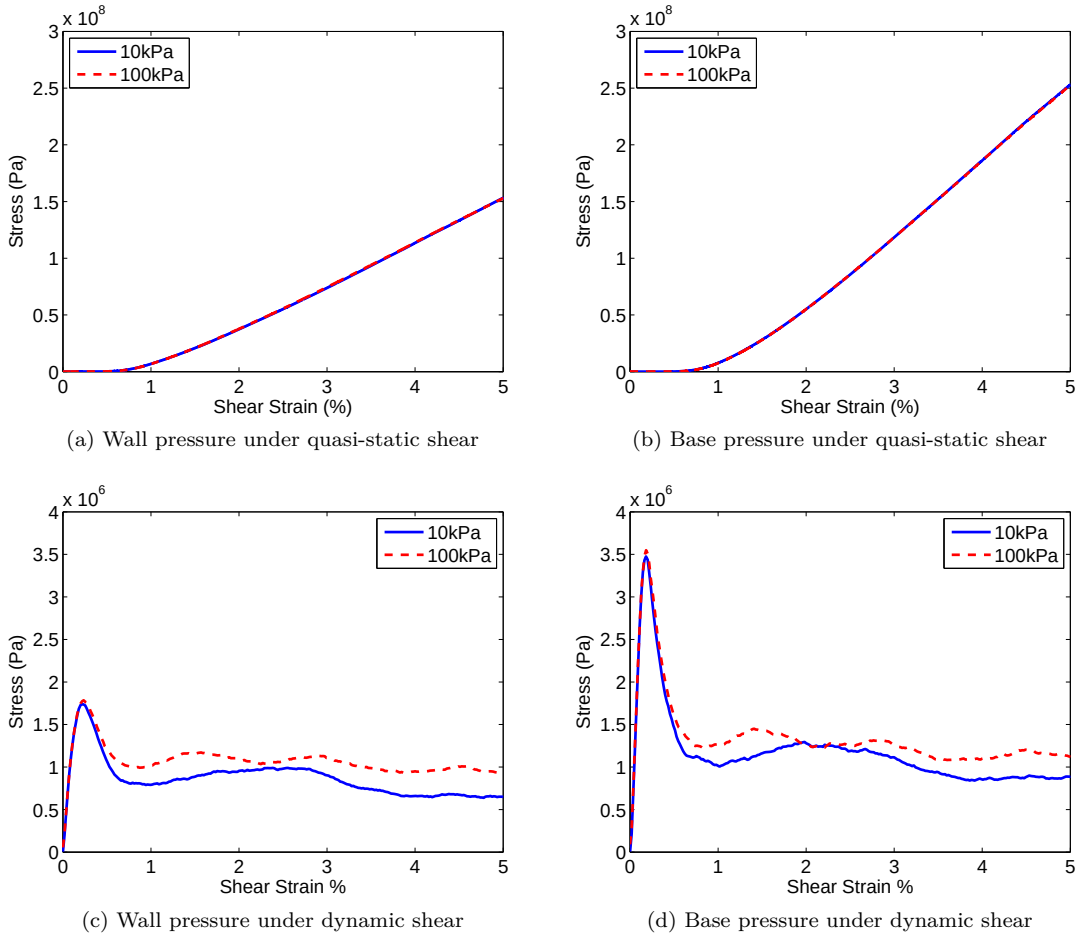

(a) Wall pressure under quasi-static shear

(b) Base pressure under quasi-static shear

(c) Wall pressure under dynamic shear

(d) Base pressure under dynamic shear

Figure 6.35: Plane strain confining wall pressures and base wall pressures for weak chalk specimen 1 under quasi-static (a, b), and dynamic (c, d) shear speeds.

(Figure 6.28 (d)). This initial peak drops away as quickly as it occurs however, and this suggests that it may be caused by an inertial response to the start of shear, rather than by the effects of breakage. Following this peak, the wall and base pressures continue to fall gently throughout the remainder of the shear test, with the 100 kPa load case remaining slightly higher overall. The movements in the wall and base pressures bear some resemblance to the movements in the mean effective and deviatoric stresses of the boulders (Figure 6.30 (c) and (d)). These increases and decreases in wall pressures are likely a direct result of the movements of the particles during shear and associated collisions with surrounding particles.

6.6.8 Summary

Two overburden loading cases of 10 kPa and 100 kPa are applied to weak chalk and examined under quasi-static and dynamic shear speeds. The 10 kPa and 100 kPa loads create clear force chain differences prior to shearing. Throughout shearing, the force chains increase in magnitude

until resistance to shearing decreases, or the material dilates allowing the force chain magnitudes to reduce. Once shearing ceases, the force chains in the quasi-static tests show clearly defined paths through the material. In comparison, the dynamic tests undergo significant dilation which causes the force chains to separate under the 10 kPa overburden load, while the larger force chains are still evident under the 100 kPa overburden load.

The slice through the parallel bonds at the end of the dynamic shear tests suggests that the boulders are fracturing into multiple fragments, rather than undergoing dynamic fragmentation. One significant breakage event occurs under both shear speeds at low strains with minor events following throughout the remainder of the tests. Around 20-25% of the total breakages occur within the boulders during the initial major breakage event within the first 2% of shear strain, which is consistent across the shear speeds. The remainder of the breakages occur within the matrix.

The micro-stresses of the boulders increase sharply during the first initial breakage, however, it is likely that a proportion of this increase can be attributed to inertia as shear begins. The $\frac{q}{p'}$ stress ratios show a sharp decline during breakage for the quasi-static shear test followed by a gradual settling of the ratio as shear continues. The $\frac{q}{p'}$ stress ratio response under dynamic shear is one of gradual decline following an initial peak.

The quasi-static and dynamic system energy rates are dramatically different. The quasi-static test is dominated by high levels of strain and friction energy with minimal influence of kinetic energy. The dynamic energy response shows increases of all energies during the initial breakage and inertia period, however, friction energy remains dominant throughout the remainder of these tests regardless of breakages that may occur. This suggests that the breakages under quasi-static speeds are not substantial enough to increase kinetic energy and reduce friction energy within the system. The dynamic shear speed is capable of producing breakages that increase kinetic energy in the system, however the energy produced is not substantial enough to reduce the friction within the system.

The start of shear at any speed causes the specimen to dilate. Under quasi-static shear speeds the dilation is less than 6mm to 5% shear strain after the initial breakage with minor movements following. The dynamic shear speed causes dilation of up to 30 mm to 5% shear strain, with a consistent increase throughout the test. The layers beneath the boulders dilate the least due to confinement effects.

6.7 Extremely Weak Chalk Results

6.7.1 Bonds and Force Chains

Figure 6.36 depicts the parallel bond and force chain arrangements prior to shearing. The figures represent a plane cut through the origin of the specimen. Due to the high porosity of the extremely weak chalk, substantial voids can be seen in the material as seen in Figure 6.36 (a) and (b). There are also voids apparent within the boulders which appears to interrupt the formation of large parallel bond groups which are seen in the sandstone and weak chalk materials (Figures 6.5 and 6.20).

The parallel bond and force chain graphics shown in Figure 6.41 represent the state of the specimen at the origin after shearing has ceased. At the end of the quasi-static tests, strong diagonal force chains can be seen ((c) and (d)) that appear to coincide with the boulders, which are largely intact. Dynamic shear causes the force chains to decrease in magnitude as the particles separate due to dilation ((g) and (h)), which reduces the capacity of the forces to travel throughout the specimen. Figure 6.41 (e) and (f) show minor differences between the response of the parallel bonds of the boulders to dynamic shear. The figures suggest that the boulders have rotated while shearing with large void spaces above the boulders suggesting dilation has occurred.

Quasi-static force chain evolution for the extremely weak chalk is shown in Figures 6.37 and 6.38. It can be seen that in the slice of the chains shown, the voids impact the creation of strong linear force chains, like those seen in the sandstone (Figures 6.7 and 6.8). As shear begins, the force chains quickly align to the shear direction and increase in strength as the particles are forced into contact with one another.

The evolution of the force chains under dynamic shear is shown in Figures 6.39 and 6.40. The force chains for both the 10 kPa and 100 kPa overburden cases show an increase in strength toward the base of the specimen as shear begins ((b) to (d) in both figures). In the 100 kPa overburden case the effect of the overburden appears to be lost as soon as shear begins, with a large reduction in the size of the force chains from 0% to 1% shear strain. As shear continues and the material dilates, the force chains weaken.

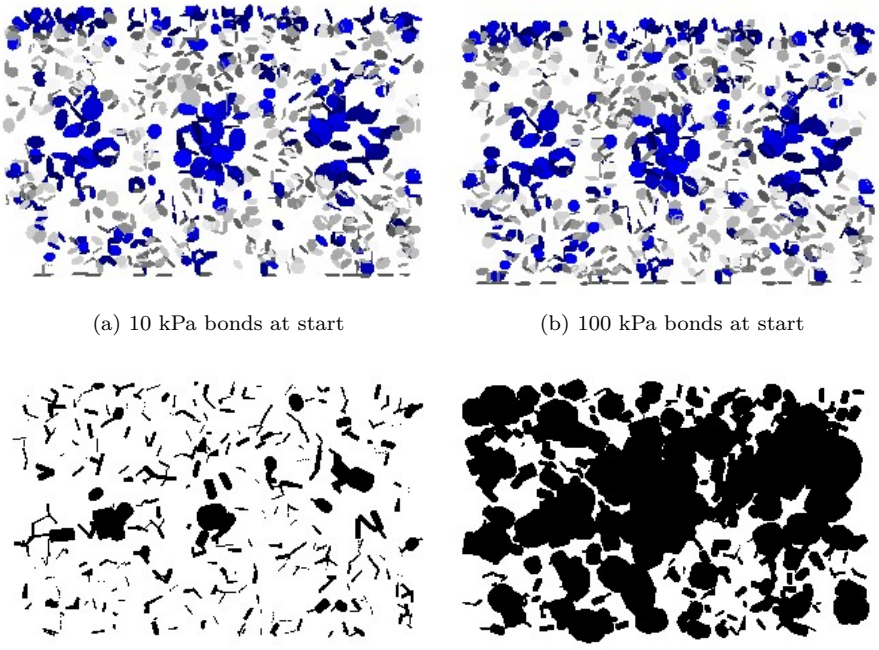

(a) 10 kPa bonds at start

(b) 100 kPa bonds at start

(c) 10 kPa force chains at start

(d) 100 kPa force chains at start

Figure 6.36: Parallel bonds (typical plane through boulders parallel to the y-axis) and system force chains of extremely weak chalk specimen 2 prior to shear.

6.7.2 Translational Velocity

The translational velocity colour contours of the quasi-static and dynamic shear tests are shown in Figure 6.42. The colour contours from the quasi-static tests ((a) and (b)) indicate that the velocity layers may be mixing, or particle velocities changing during shear. This change in velocity is likely to be related to the voids in the material allowing particles to travel throughout the system. In the quasi-static shear test, under a 10 kPa overburden load the mixing between the velocity contour layers is more noticeable as more particles appear to have moved from the upper layer in the system down toward the boulders. This mixing is less apparent in the dynamic shear results, likely due to the higher shear speed reducing the ability of the material to fill and remain in voids.

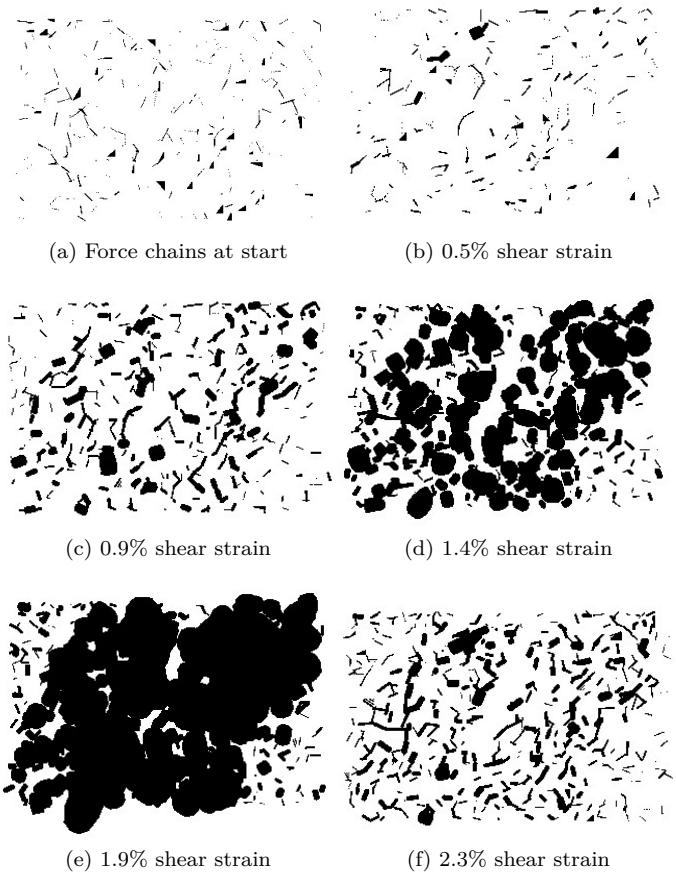

(a) Force chains at start (b) 0.5% shear strain

(c) 0.9% shear strain (d) 1.4% shear strain

(e) 1.9% shear strain (f) 2.3% shear strain

Figure 6.37: Evolution of the force chains throughout the quasi-static shear test under 10 kPa overburden load on extremely weak chalk specimen 2. Note that the viewing scale of the force chains is consistent for figures (a) to (e) and is reduced to obtain a clear indication of the force chains up to 2.3% shear strain in (f). The force chain scale is at least $\mathcal{O}(2)$ smaller than that shown for the starting state in Figure 6.36.

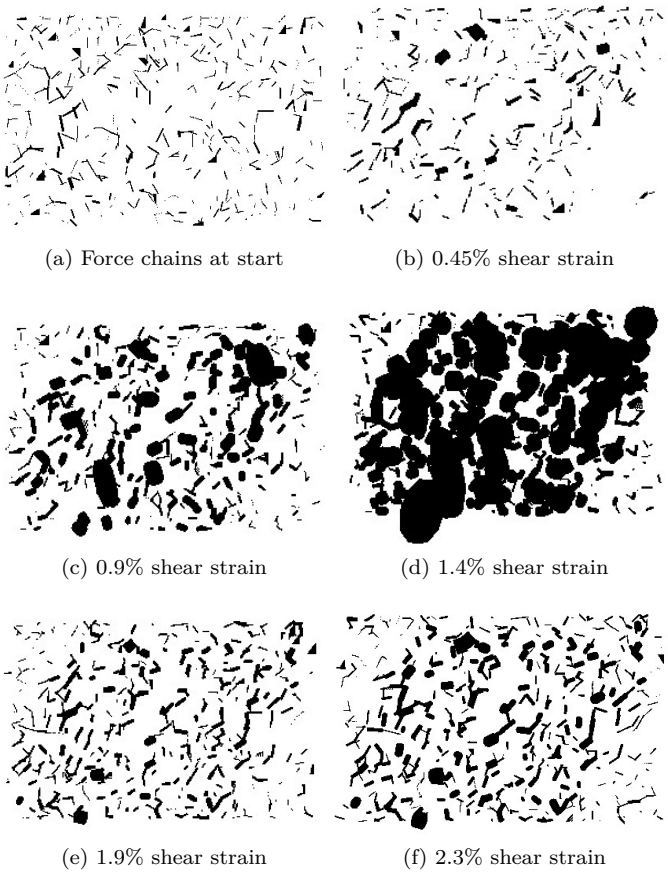

(a) Force chains at start (b) 0.45% shear strain

(c) 0.9% shear strain (d) 1.4% shear strain

(e) 1.9% shear strain (f) 2.3% shear strain

Figure 6.38: Evolution of the force chains throughout the quasi-static shear test under 100 kPa overburden load on extremely weak chalk specimen 2. Note that the viewing scale of the force chains is consistent for figures (a) to (d) and is reduced to obtain a clear indication of the force chains up to 2.3% shear strain in (e) and (f). The force chain scale is at least $\mathcal{O}(2)$ smaller than that shown for the starting state in Figure 6.36.

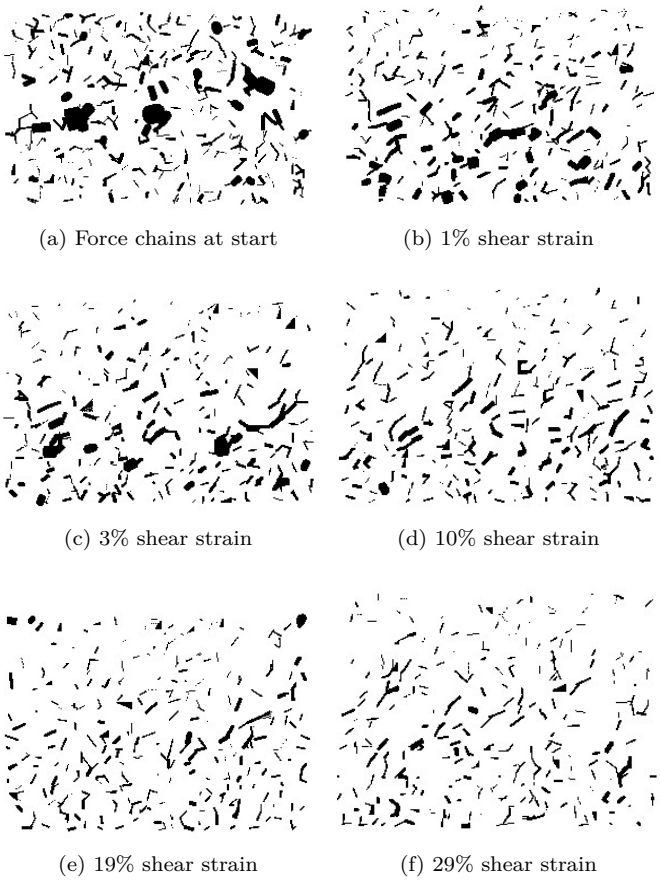

(a) Force chains at start (b) 1% shear strain

(c) 3% shear strain (d) 10% shear strain

(e) 19% shear strain (f) 29% shear strain

Figure 6.39: Evolution of the force chains throughout the dynamic shear test under10 kPa overburden load on extremely weak chalk specimen 2.

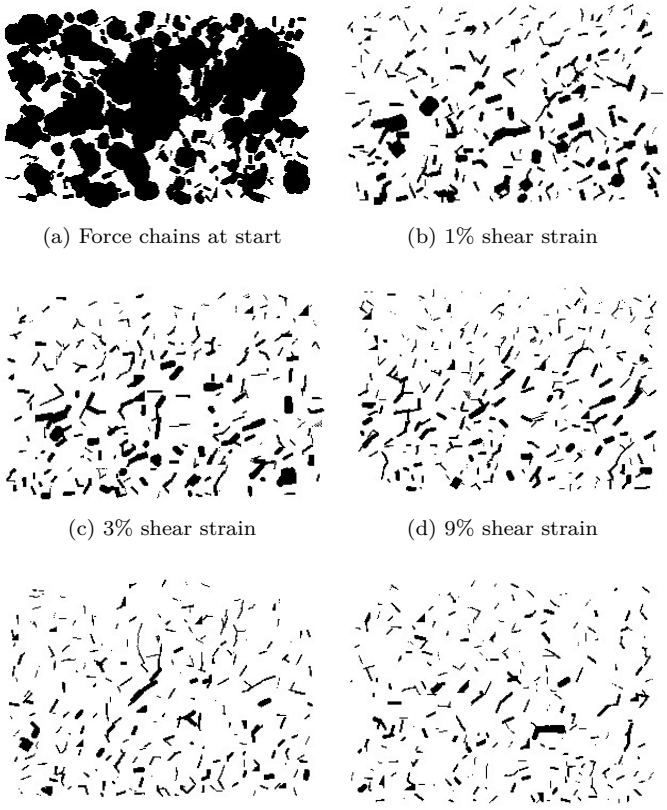

(a) Force chains at start (b) 1% shear strain

(c) 3% shear strain (d) 9% shear strain

(e) 19% shear strain (f) 28% shear strain

Figure 6.40: Evolution of the force chains throughout the dynamic shear test under100 kPa overburden load on extremely weak chalk specimen 2.

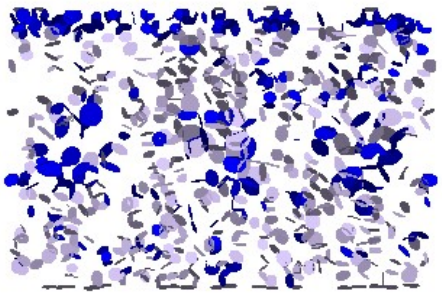

(a) Quasi-static 10 kPa bonds

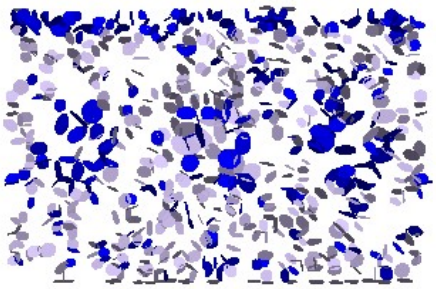

(b) Quasi-static 100 kPa bonds

(c) Quasi-static 10 kPa force chains

(d) Quasi-static 100 kPa force chains

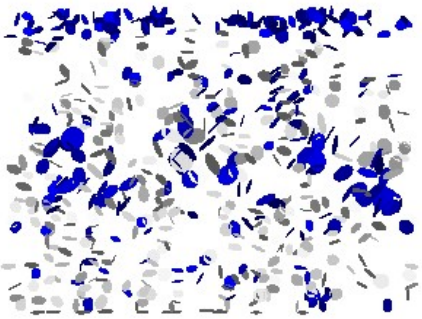

(e) Dynamic 10 kPa bonds

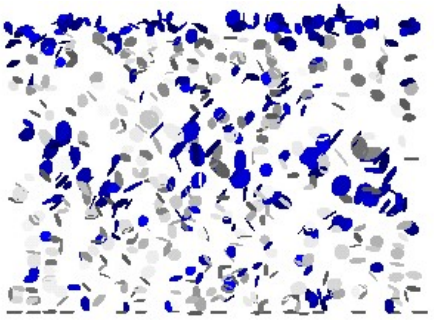

(f) Dynamic 100 kPa bonds

(g) Dynamic 10 kPa force chains

(h) Dynamic 100 kPa force chains

Figure 6.41: Parallel bonds (typical plane through boulders parallel to the y-axis) and system force chains of extremely weak chalk specimen 2 at the end of shear (2% shear strain for the quasi-static shear tests and 5% shear strain for the dynamic shear tests). Note that the scale of force chains for the dynamic tests is half that of the quasi-static test for visualisation in PFC^{3D}.

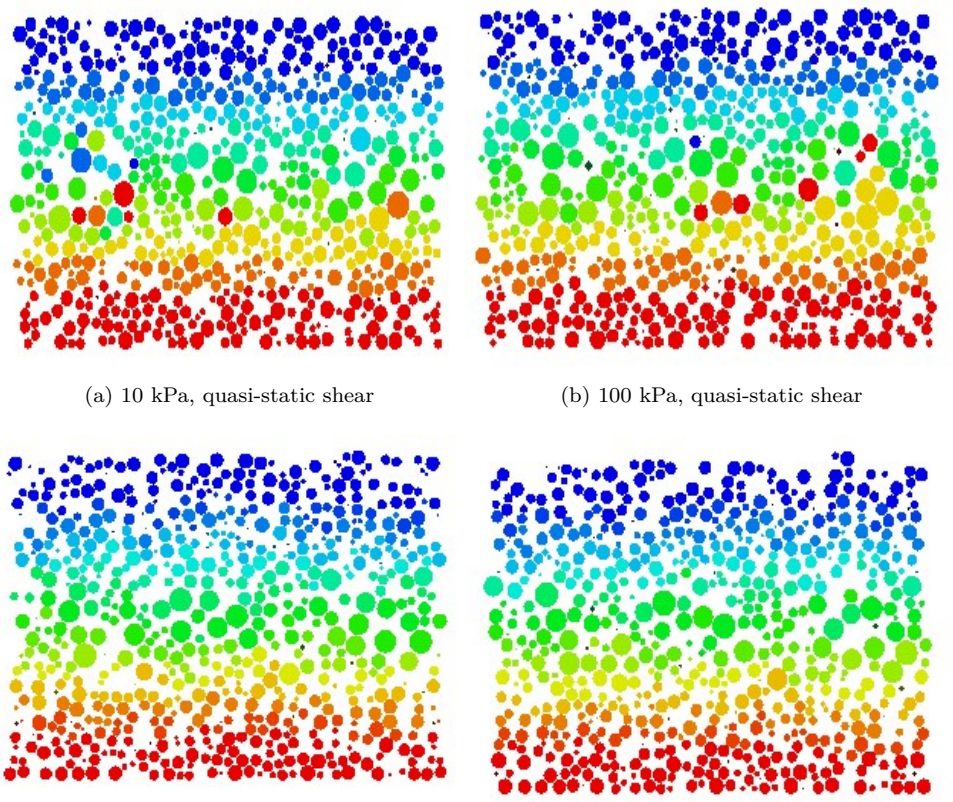

(a) 10 kPa, quasi-static shear

(b) 100 kPa, quasi-static shear

(c) 10 kPa, dynamic shear

(d) 100 kPa, dynamic shear

Figure 6.42: Translational velocity with coloured contour to represent particle direction and magnitude of velocity at the end of the quasi-static (a), (b) and dynamic (c), (d) shear tests. Compare these with the typical contour provided at the start of the shear test (see Figure 6.26), which is the same for the extremely weak and weak chalk material.

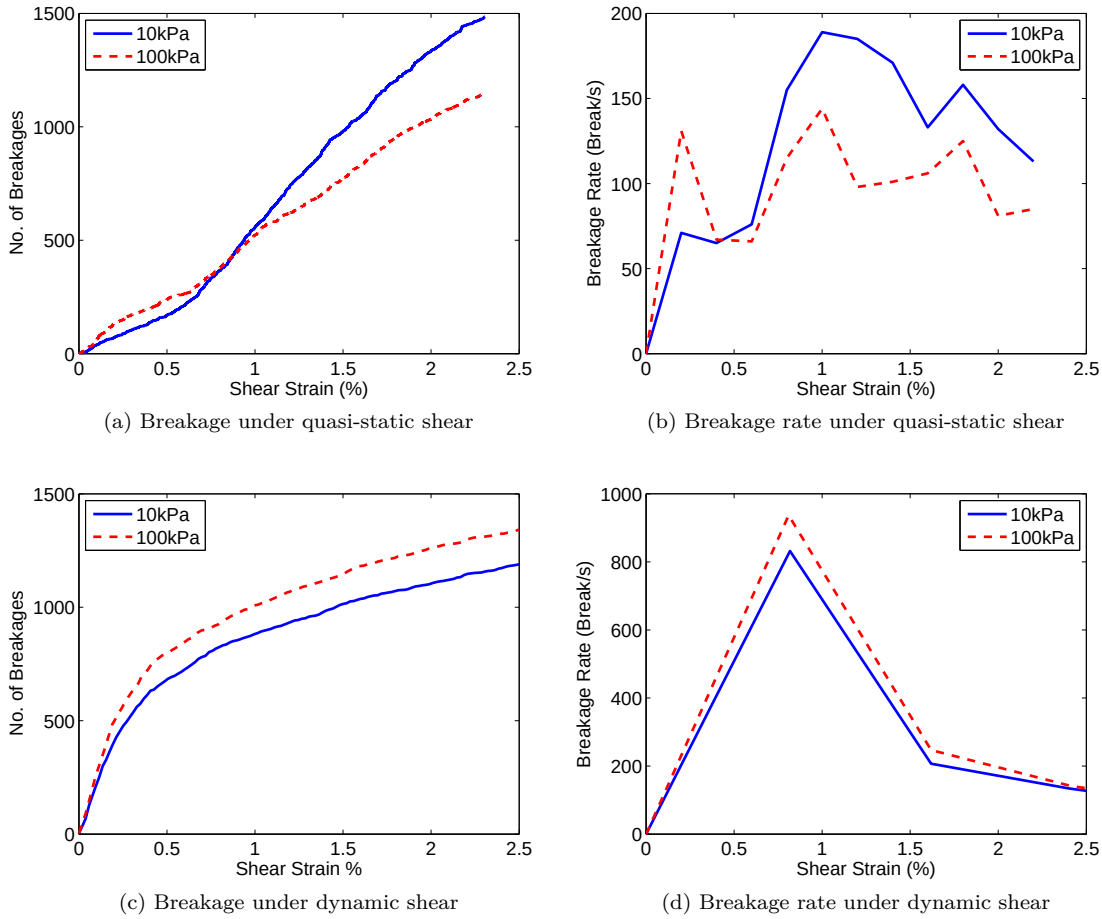

(a) Breakage under quasi-static shear

(b) Breakage rate under quasi-static shear

(c) Breakage under dynamic shear

(d) Breakage rate under dynamic shear

Figure 6.43: Total breakage during shear testing for extremely weak chalk specimen 2 under quasi-static shear (a, b) and dynamic shear (c, d).

6.7.3 Breakage

Figure 6.43 shows the number of breakages and rate of breakage of parallel bonds within the specimen under quasi-static and dynamic shear. A slightly larger quantity of breakage occurs for the 10 kPa load case than the 100 kPa load for the quasi-static shear speed, as seen in (a) and (b), with the opposite situation for the dynamic shear speed. In all cases, the major breakage events are complete by around 3% shear strain, with additional minor breakages occurring throughout the remainder of the dynamic test. The rate of breakage and quantity of breakages are fairly similar between the quasi-static and dynamic shear speeds.

A major difference between extremely weak chalk specimens 1 and 2 are the quantity of boulder bonds, with 20% less bonds created in the boulders of specimen 1. This is likely due to the use of the random removal of particles to increase porosity. Figure 6.44 shows the number of breakages of parallel bonds within the boulders against shear strain for the two specimens. Under quasi-static shear, Figure 6.44 (a), it can be seen that the breakage of the boulder bonds within the two

specimens are quite different under the 100 kPa overburden load. This suggests that the additional boulder bonds in weak chalk specimen 2 provide a resistance to shear that is not seen in specimen 1. Boulder breakage is almost instantaneous under dynamic shear Figure 6.44 (b), and is slightly delayed for the quasi-static tests. It seems from Figure 6.41 (a, b, e, f) that the boulders break into large fragments along the shear axis. From the data, boulder breakages are also more likely under the lower overburden load of 10 kPa due to a greater ability of the material to shear further and break with less confinement.

For both specimens around 25-40% of the total boulder bonds are broken (Figure 6.44 (b); breakages of 90-170 parallel bonds from a total of 407 bonds) during dynamic shear, the majority almost as soon as shear begins. When these boulder breakages are compared to the final parallel bond images in Figure 6.41 (e) and (f), it can be considered that the boulders are likely to be fracturing into multiple fragments during shear rather than undergoing dynamic fragmentation.

6.7.4 Micro-stress

The mean effective p′ and deviatoric q micro-stresses local to the boulders are plotted against shear strain in Figure 6.45. Under quasi-static shear the p′ and q stresses (a, b) are consistent in value with the initial overburden load for approximately the first 1% of shear strain. As boulder breakage begins during the main breakage event, the p′ and q stresses increase sharply for the 10 kPa overburden load. The 100 kPa overburden case shows a more gradual increase in local boulder stresses once the boulders have fragmented.

Under dynamic shear speeds (Figure 6.45 (c) and (d)) the 10 kPa and 100 kPa overburden load cases show similar behaviour, with the 100 kPa response largely greater than that of the 10 kPa case. Both dynamic micro-stresses increase within the first 0.5% of shear strain coinciding with the main breakage events, although, as discussed earlier, it is likely that this response is largely due to inertia. Following the initial rise in p′ and q both micro-stresses drop away toward a more consistent value. This result is comparable to that obtained for both the weak chalk and sandstone materials under the higher overburden load.

Figure 6.46 compares the $\frac{q}{p'}$ stress ratios of the 10 kPa and 100 kPa overburden loads for the quasi-static and dynamic shear speeds. In general the $\frac{q}{p'}$ stress ratio rises as shear begins, and slowly decreases as breakage occurs, before settling to a critical value of approximately 1.0-1.2 once the majority of boulder breakages are complete (2% shear strain for the quasi-static shear and 2-5% shear strain for the dynamic shear). Under dynamic shear, Figure 6.46 (c), there is an immediate decrease at the very start of shearing, followed by a gentle decrease toward a critical state value of approximately 1.0 at 20% shear strain. There is a slight fluctuation in the $\frac{q}{p'}$ stress ratio at around 10% shear strain with no major breakage events or system energy changes occurring. This behaviour may be the result of rotation of the boulder particles during shear, creating changing

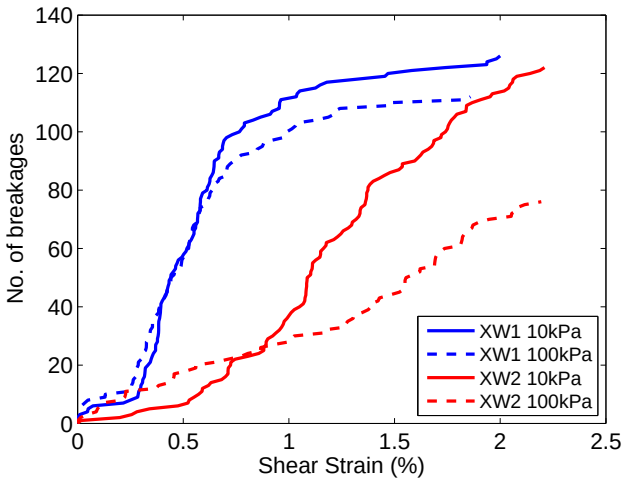

(a) Quasi-static shear

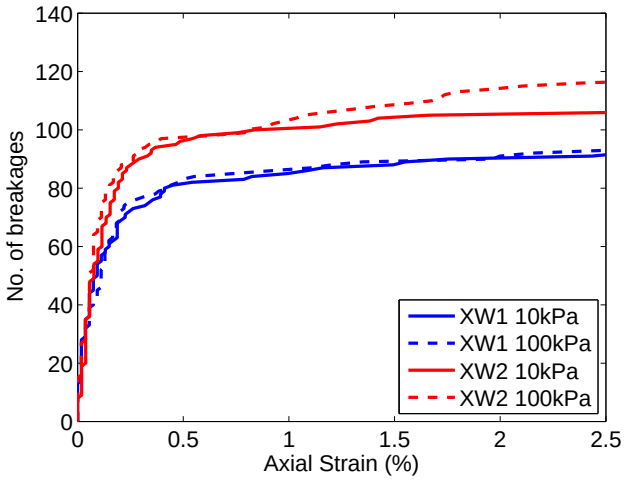

(b) Dynamic shear

Figure 6.44: Boulder breakages under shear testing for extremely weak chalk specimens under quasi-static (a) and dynamic (b) shear.

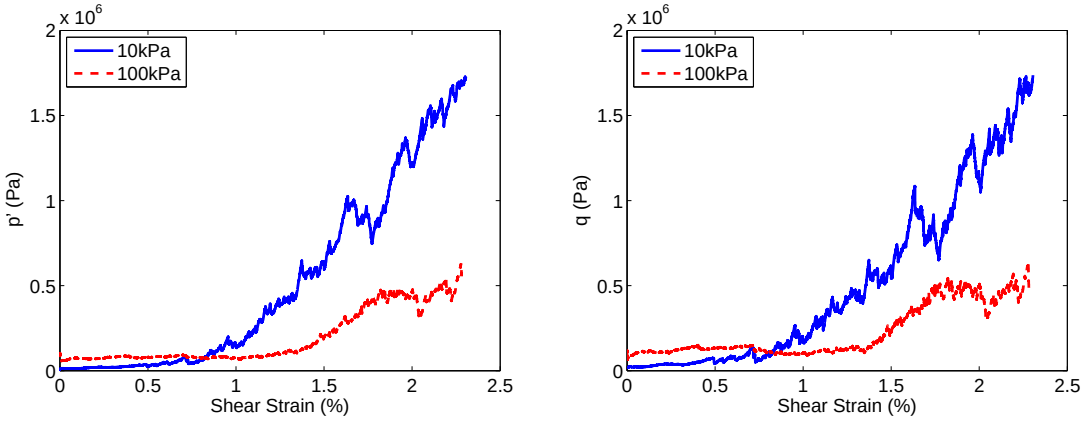

(a) Quasi-static mean stress p′

(b) Quasi-static deviatoric stress q

(c) Dynamic mean stress p′

(d) Dynamic deviatoric stress q

Figure 6.45: Mean effective and deviatoric stress response for extremely weak chalk specimen 2 under quasi-static (a, b) and dynamic (c, d) shear.

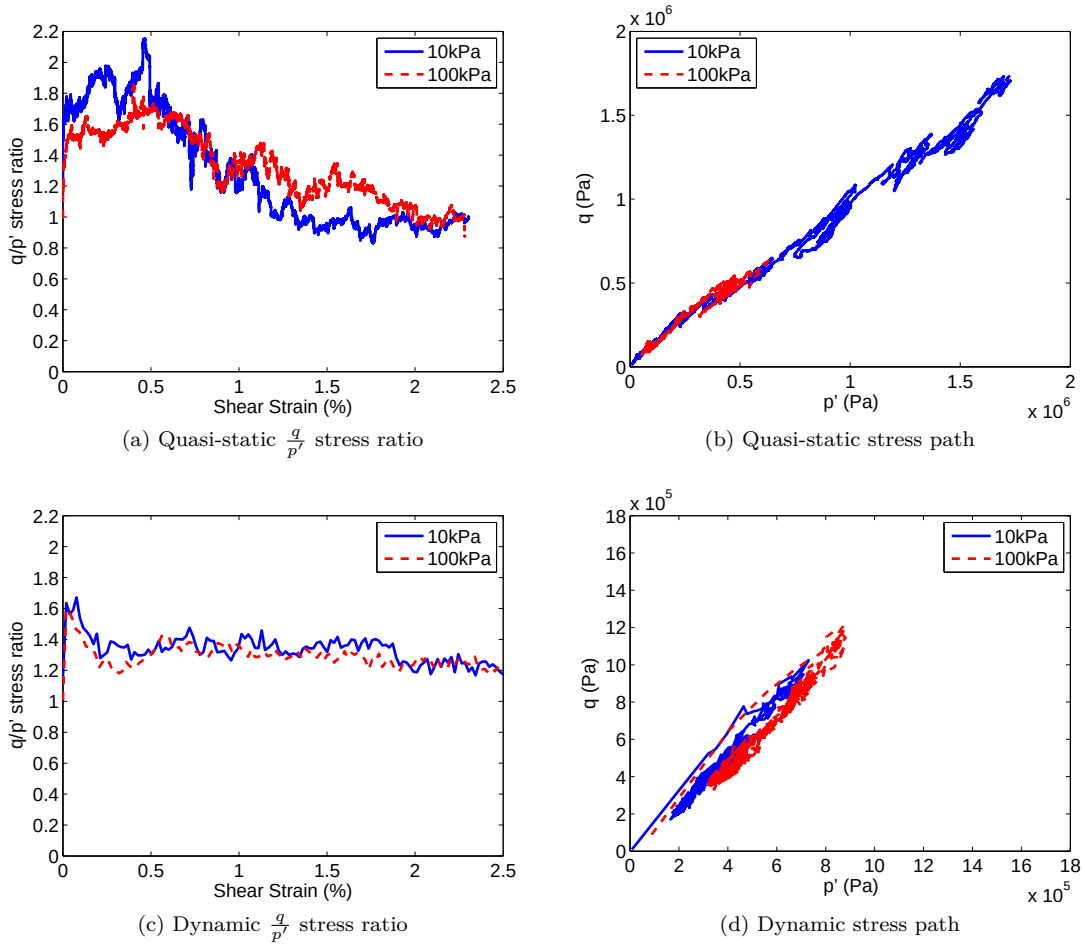

(a) Quasi-static $\frac{q}{p'}$ stress ratio

(b) Quasi-static stress path

(c) Dynamic $\frac{q}{p'}$ stress ratio

(d) Dynamic stress path

Figure 6.46: $\frac{q}{p'}$ stress ratio and stress path response for extremely weak chalk specimen 2 under quasi-static (a, b) and dynamic (c, d) shear.

stress states within the boulder fragments.

The stress paths (Figure 6.46 (b) and (d)) rise in a linear manner from the 10 kPa and 100 kPa initial loading states. The quasi-static stress paths (b) remain linear throughout shear with some oscillations. Under dynamic shear (d), once the initial breakage event has occurred (and inertia effects have cleared), the stress paths drop back along a linear line and oscillate for the remainder of the shear test. These oscillations are likely a response to the rotation of the boulders or fragments as indicated above.

6.7.5 Energy Rate

The energy rate graphs in Figure 6.47 shows the friction, strain and kinetic energy rates against shear strain, for the quasi-static and dynamic shear speeds. Figure 6.47 shows that both loading rates and shearing speeds are dominated by friction energy for the extremely weak chalks. In the quasi-static case friction energy reflects the behaviour of the p′ and q micro-stresses, remaining low

until approximately 1% shear strain until the main breakage event has finished, then increasing sharply in the 10 kPa case and gradually in the 100 kPa case. The quasi-static shear system is dominated by friction with little kinetic energy apparent, with increases in strain energy occurring once boulder breakages begin.

Under dynamic shear, all system energies increase rapidly within the first 1% shear strain coinciding with the main breakage event, and likely also an inertial response to the start of shear. Strain energy and kinetic energy rapidly decrease to remain low for the remainder of the test. The exception is the kinetic energy under the 10 kPa loading case at later stages of shear (refer Figure 6.47). Although there is a peak in the kinetic energy at around 6% shear strain there are no associated major breakages or changes in micro-stresses. It is possible that this energy is associated with breakages in the matrix that form a major force chain, so that when minor breakages occur large amounts of energy are released. The same test also produces peaks in the strain and friction energies at 18% shear strain, again with little else happening among the monitored parameters.

As with the sandstone and weak chalk materials, the kinetic energy for the extremely weak chalk increases during the initial breakage and inertia periods of the tests, as seen in Figure 6.48. Kinetic energy is very low under quasi-static shear and increases in the 10 kPa overburden case as boulder breakage occurs. The two loading cases under dynamic shear produce similar kinetic energy responses. The kinetic energy of the 10 kPa load case for extremely weak chalk 2 produces an unusual response at around 6% shear strain (refer Figure 6.48), and a slightly elevated level at 8-10% shear. As indicated earlier, this may be due to a breakage occurring in a major force chain, which suggests that the quantity of breakage may not be the most important factor in producing kinetic energy. Rather the position of the breakage within the material may be more important for producing kinetic energy.

6.7.6 Particle Movement

The movement of the gauge particles within the specimen against shear strain is shown in Figure 6.49. After 1% shear strain, under quasi-static shear speeds ((a) and (b)), the extremely weak chalk specimen shows greater dilation in the upper gauge layers, with the lower gauge layers confined within or beneath the boulders. The 10 kPa and 100 kPa overburden loads produce quite different behaviour. The 100 kPa overburden load appears to influence the gauge particle behaviour, as they move upward faster than the same gauge particles under 10 kPa of overburden load. The upper most gauge particle layer achieves 1 mm extra dilation under 100 kPa overburden than the 10 kPa overburden. This appears to contradict the expected behaviour of the 10 kPa overburden load showing greater dilation. However, from the breakages (refer Figure 6.43 (a)) for the extremely weak chalk specimen 2, it can be seen that the 100 kPa overburden case does not undergo as much breakage as that of the 10 kPa overburden case. It is possible that the lack of breakage forces the

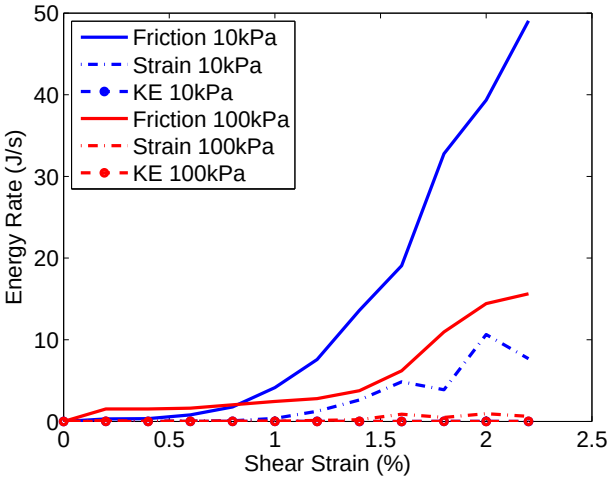

(a) Quasi-static energy rates

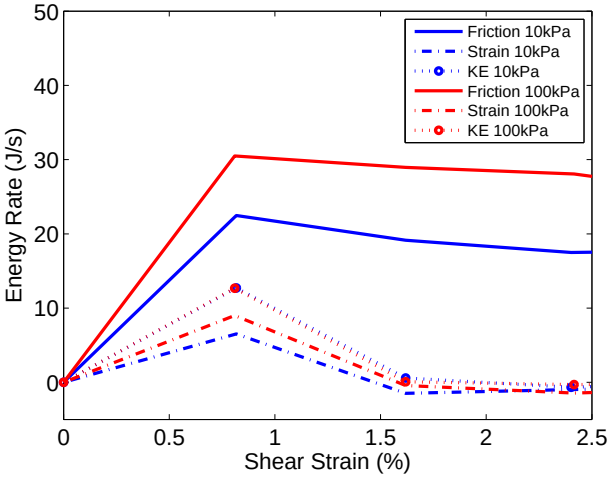

(b) Dynamic energy rates

Figure 6.47: System energy rates from extremely weak chalk specimen 2 under quasi-static (a) and dynamic (b) shear.

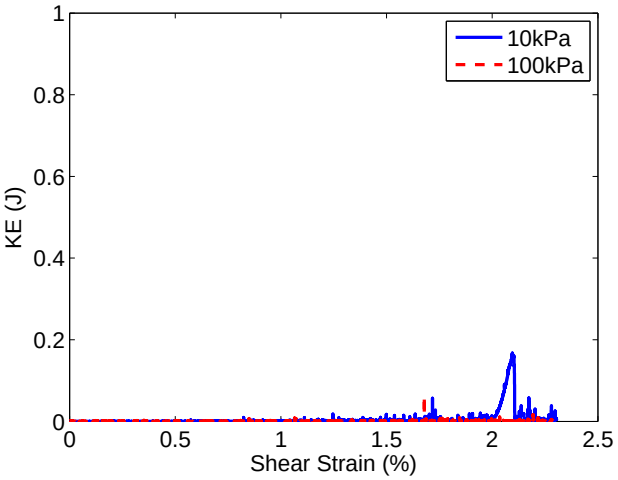

(a) Quasi-static

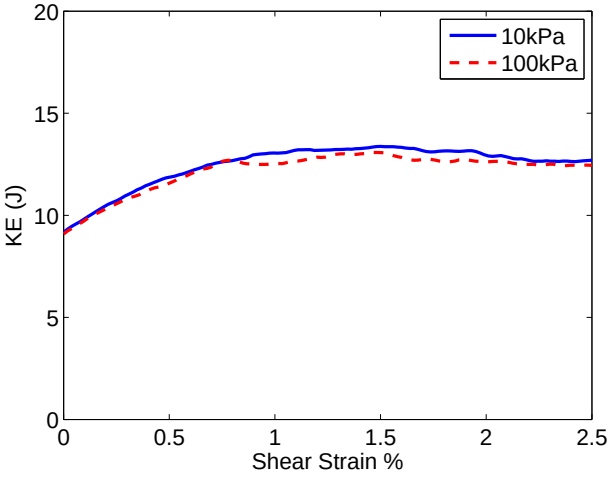

(b) Dynamic

Figure 6.48: System kinetic energy response from extremely weak chalk specimen 2 under quasi-static (a) and dynamic (b) shear.

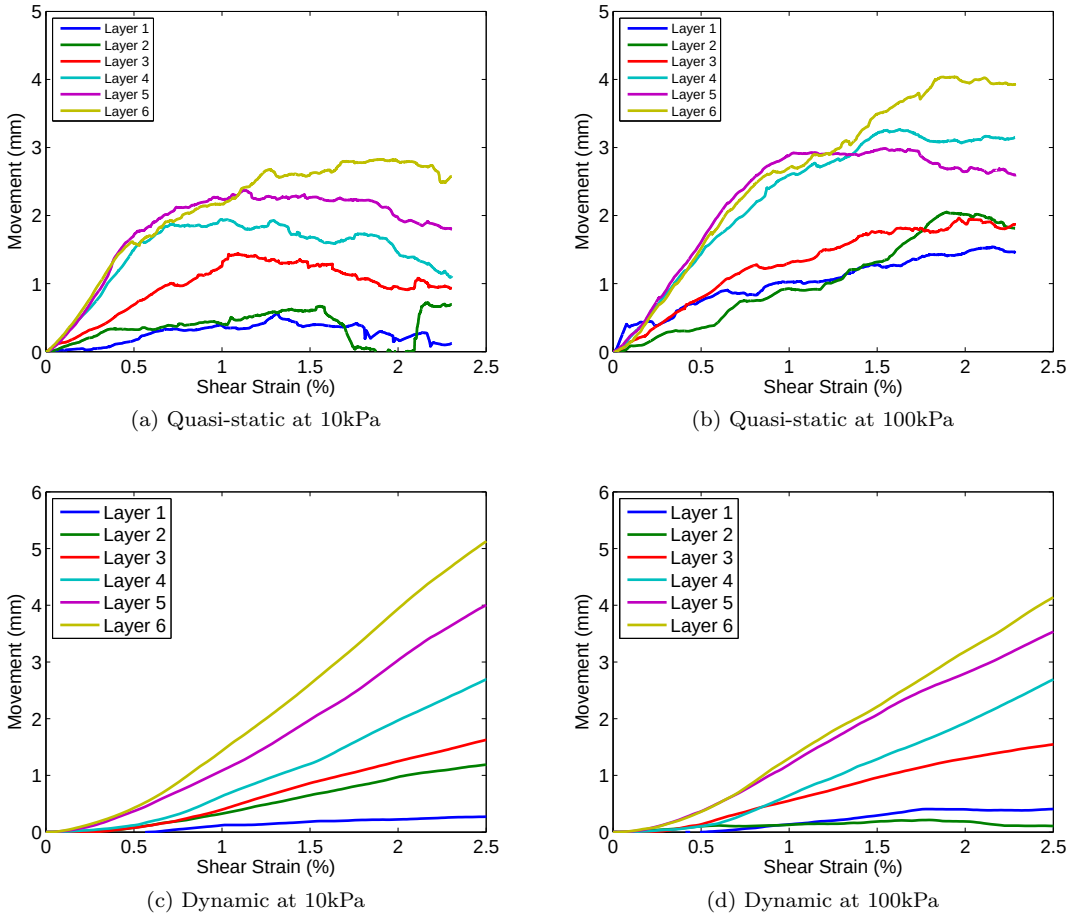

(a) Quasi-static at 10kPa

(b) Quasi-static at 100kPa

(c) Dynamic at 10kPa

(d) Dynamic at 100kPa

Figure 6.49: Vertical movement of the gauge particles within the extremely weak chalk specimen 2 under quasi-static (a, b) and dynamic (c, d) shear.

material to dilate in order to continue to shear.

In the dynamic shear case (Figure 6.49 (c) and (d)), the initial dilation is delayed in comparison to that of the quasi-static cases. The gauge layers move relatively consistently, with the lower layers moving less due to the greater confinement of the boulders and matrix above. In contrast to the quasi-static cases, the 10 kPa overburden loading produces greater dilation than that of the 100 kPa loading which is expected.

6.7.7 Wall Pressures

Figure 6.50 shows graphs of the side and base wall pressures against shear strain. The side and base wall pressures under quasi-static shear speeds reflect the behaviour seen from the p' and q boulder micro-stresses, total breakage and system energy rates ((a) and (b)). The stresses remain close to their initial values until approximately 1% shear strain, when breakage ceases, at which point the 10 kPa stresses rise sharply and the 100 kPa stresses rise gently. With further shear, it

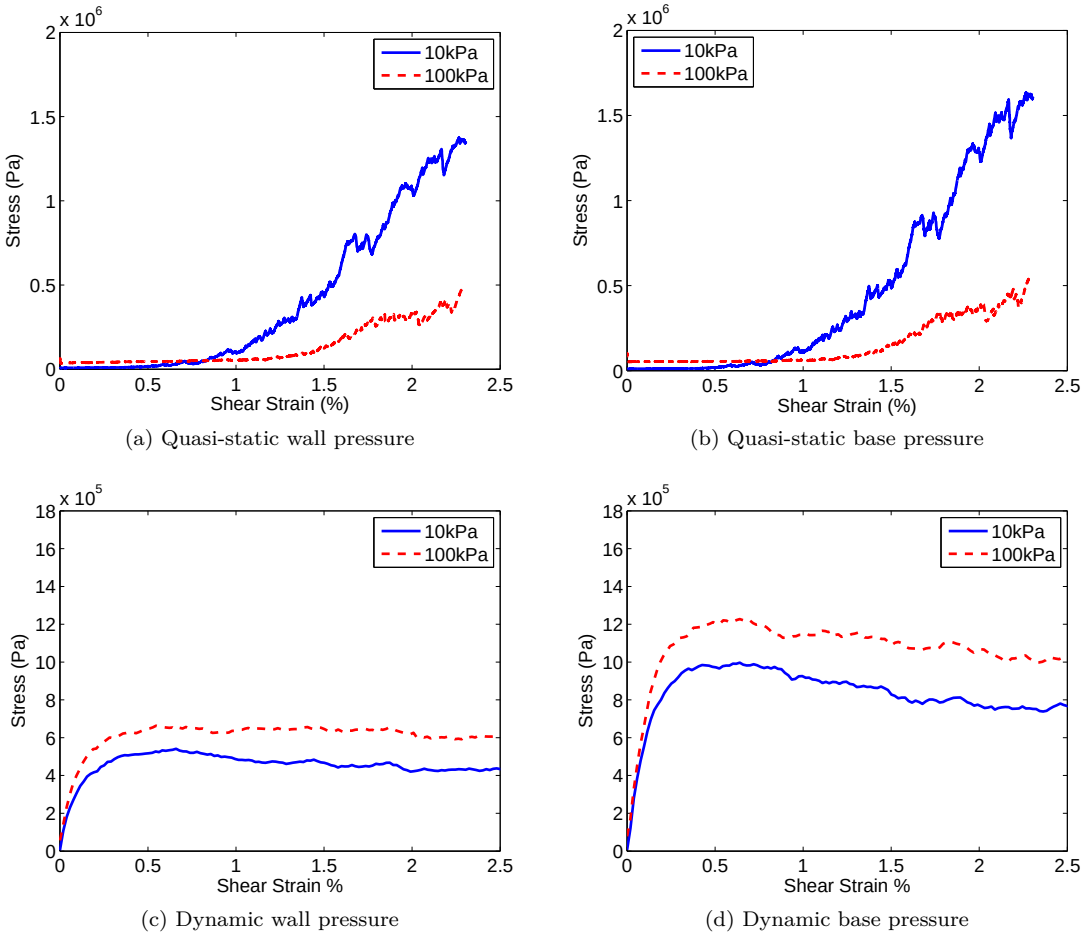

(a) Quasi-static wall pressure

(b) Quasi-static base pressure

(c) Dynamic wall pressure

(d) Dynamic base pressure

Figure 6.50: Plane strain confining wall pressures and base wall pressures for extremely weak chalk specimen 2 under quasi-static (a, b) and dynamic (c, d) shear.

would be expected that these stresses would eventually drop again and reach a consistent value close to the initial overburden state.

As with the other monitored parameters, under dynamic shear ((c) and (d)) the wall and base pressures rise sharply within the first 0.5% shear strain, and then gradually drop away throughout the remainder of the test. In all cases, the 100 kPa load case produces the larger wall and base pressures, as expected. The wall pressures drop toward a fairly consistent value of 250-300 kPa and 400 kPa for the 10 kPa and 100 kPa load cases respectively. It is possible with further shear that these pressures may drop further.

6.7.8 Summary

The extremely weak chalk is highly porous with voids clearly seen in the cross-sections of the parallel bonds and force chains. During quasi-static shear, the force chains are able to align under low overburden loads with the voids allowing for the migration of material. Under dynamic shear,

the material dilates and the force chains become less well linked. The boulders appear to rotate during dynamic shear and the particles forming the boulders increase velocity in some places, due to the effects of the shearing system. The material above the boulders shows the greatest dilation during the test, while material beneath the boulders is more confined and dilates less.

As with the weak chalk and sandstone materials there is a major breakage event in the early part of the shear tests, followed by minor breakages throughout the remainder of the test. Around 25-30% of the boulder bonds break during shear with little effect on kinetic or strain energy, suggesting that the boulders are fracturing into fragments rather than undergoing dynamic fragmentation. Very little energy is created under quasi-static shear until breakage reaches a maximum, at which point friction energy dominates. Under dynamic shear, all energies climb initially during the main breakage event before becoming dominated by friction. The largest effect on the system appears to come from inertia as the dynamic shear test begins.

Micro-stresses within the system under both shear speeds gradually drop away after the initial breakages, with the $\frac{q}{p'}$ stress ratios reaching a critical state value of 1.0. This occurs within the first 2% of shear strain for the quasi-static tests and takes at least 10% shear strain for the dynamic tests, suggesting that the quasi-static system produces more friction. Oscillations in the stress path suggest that particles or fragments within the system are rotating, and this also contributes to the quantity of friction energy in the system.

6.8 Chapter Summary

Three materials have been formed into a parallelepiped shape, with three boulders in a row through the middle of the specimen surrounded by finer material and fragments. A shear box test has been simulated at quasi-static and dynamic shear speeds, to compare the speed hypothesised to be encountered in sturzstroms or chalk flows with a more typical static failure situation. The velocity is applied in a linear fashion, and the system monitored for localised and overall responses to breakages under shear.

The largest breakage events occur within the first 1-5% shear strain for all specimens and loading cases. Around 20-45% of the parallel bonds located within the boulders break, with the majority of the breakages occurring within the matrix. The before and after images of the specimens suggest that although there are clear loading differences prior to the testing beginning, these differences are greatly lessened under shear. This suggests that the quantity of overburden load applied to the material has little influence on the behaviour of the system under forced shear.

All specimens dilate due to the shearing process, with the layers directly above the boulders generally dilating more than those confined below. Results from extremely weak chalk 2 suggest that breakages in the matrix can interrupt major force chains, and produce kinetic energy that coincides with additional movements in the gauge particles.

In general, the shear tests at high velocity produce small differences in energy to that of the quasi-static tests. The quasi-static tests are dominated by friction once breakage begins with little fluctuation in kinetic energy during breakages. Inertial responses to the dynamic shear speed cause all energies to respond across the three materials with minor fluctuations in kinetic energy observed during breakage events. All specimens are dominated by friction throughout the test regardless of shear speed and overburden load.

As the material tested becomes weaker, the system becomes more friction dominated under dynamic shear speed, with the sandstone tests showing that the initial breakages may be capable of producing enough kinetic energy to surpass the friction energy for a very short period of strain. This kinetic energy is however dissipated relatively quickly so that the effects of any reduction in friction are very short-term.

The higher the speed of shearing the more prevalent the initial inertial effects. As shearing begins, the confinement and bonding of the material leads to a sharp increase in the mean stress within the system that overrides the effect of the overburden stress. Intense crushing and dilation follows to allow the material to move under shear. Once enough breakage has occurred the material can freely shear and the stress responses in the system reflect the initial differences in overburden pressures.

In comparing the quasi-static and dynamic test results, it is clear that breakages interrupt the friction energy under dynamic shear speeds, converting this to kinetic energy for a very short

period of time. It is possible that multiple breakages occurring simultaneously may produce enough kinetic energy to cause a minor influence on the behaviour of the system, however, this kinetic energy appears to dissipate very quickly suggesting that dynamic fragmentation is not occurring. The fast dissipation of kinetic energy, and lack of dynamic fragmentation under high speed shearing, suggests that the shearing action is of less importance in the internal processes of a sturzstrom in terms of mobility. The lack of mixing of layers perhaps explains why stratigraphy is preserved under such extreme conditions, with fragments remaining contained within a fines matrix likely created from the intense crushing under shear coupled with normal loading. Globally, it is likely that high strain rate normal loading is of more importance in the overall mobility of sturzstroms.

Chapter 7

Discussion

7.1 Introduction

Landslides of substantial volume such as sturzstroms can often exhibit extremely long runout that appears to violate the simple frictional rules of a block mass sliding downslope. Long runout applies when the material in the distal part of the deposit travels further than would normally be expected based on an energy line concept (Scheidegger, 1973; McSaveney and Davies, 1999; Crosta et al., 2007; Davies et al., 2010). A short runout in large volume rock avalanches tends to occur where the avalanche has been confined by topography, the runout path is very rough or there is a reduced fall height (Hsu, 1978). Sturzstroms produce long runout along flat or gently inclined valley floors, often for several kilometres and for larger distances than the initial fall height. This unusual behaviour of sturzstroms is termed the 'long runout problem'.

Many theories advanced to explain the mobility and mechanisms of long runout discuss characteristics that are specific to the avalanche examples considered, and do not fully explain the behaviours typical across all sturzstrom events. However, a theory put forward by McSaveney and Davies (1999) considers the influence of dynamic fragmentation on both the propulsion of a sturzstrom and the resulting deposit. Initially, McSaveney (1978) considered a possible theory of a collisional flow where internal friction is lowered through the rebound of clasts from multiple collisions. Davies and McSaveney (1999) later extended this concept to consider the fragmentation of rock under an overburden stress that exceeds the rock strength, whereby the fragments travel at high velocity in all directions dilating the debris. The concept is extended further still by Davies and McSaveney (2008) who suggest that rapid brittle failure under high direct stress produces internal pressures on the surrounding clasts reducing effective stress in the shear layer, and therefore reducing the overall frictional resistance to shear.

This thesis has considered the fragmentation theory from a conventional soil mechanics perspective, to investigate the micro mechanical behaviour within a sturzstrom during breakage and how this may contribute to the mobility of the debris.

A sturzstrom can be separated into two events in an idealised framework: the fall and the

runout. Oedometric and shear testing has been performed on various materials to replicate these two key events during a sturzstrom. The oedometer testing focuses on normal compression at varying loading rates with no lateral strain allowed. The shear testing allows for shear in one direction under plane strain conditions and varying strain rates, with pressure added at the surface of the specimen to represent overlying material. In this manner, the compression inducing impact phase of the fall event can be modelled using the oedometer tests and the shear dominated runout phase can be modelled using the shear tests. In both cases, the micromechanical behaviour of breakable synthetic rock material has been investigated to ascertain the effects of fragmentation on the movement of surrounding particles, and overall potential effects of fragmentation on a sturzstrom event.

Materials such as HCP boulders and synthetic rock materials can be utilised in PFC^{3D} and calibrated to laboratory tests. Table 2.1 outlines some examples of sturzstrom events and indicates the geological material involved in each failure. In New Zealand, the Southern Alps are dominated by greywacke material which is strongly indurated and heavily fractured. Sturzstrom, rock falls and other landslides have occurred in this material. For this thesis it is considered a useful material to calibrate and test. The unusual behaviour of chalk flows and the hypothesis from Bowman and Take (2014) that these may be miniature sturzstroms, suggests that there may be a material strength versus fall height relationship to produce sturzstrom-like behaviour. Therefore chalk of varying strengths is also considered.

This chapter discusses the results of the oedometer and shear testing with specific reference to the materials used. Discussion focuses on the relationship between the results obtained and those obtained by other authors in relation to the behaviour of sturzstroms and dynamic fragmentation of materials. The sections follow the order of the results outlined in the prior chapters, with the final sections relating this information back to the original research objectives (Section 1.4).

7.2 Oedometer Testing

Oedometer testing under rapid loading rates represents the fast application of overburden as the volume of failed material comprising the sturzstrom compresses onto a relatively flat surface. The resulting breakage of material from this rapid loading of debris is considered to be the first significant propulsion during a sturzstrom. The purpose of the numerical oedometer testing is firstly to perform tests that could not otherwise be easily conducted in laboratories and secondly to investigate the micromechanical response of confined boulders under rapid loading.

In the series of oedometer tests reported in Chapters 3 and 5, the overburden pressure is represented by a plate (or wall) applied at varying strain rates to a cubic arrangement of rock boulders. An idealised HCP material is first tested to consider whether PFC^{3D} is an appropriate tool for testing the hypotheses, by considering how a generalised rock material may respond to

these conditions. Synthetic sandstone and chalk materials as calibrated in Chapter 4 are also tested in the numerical oedometer which allows for inferences to be made in regard to real materials and comparisons drawn to the idealised HCP material tests. The results and implications of the oedometer tests are discussed below.

7.2.1 HCP Material

Single HCP Agglomerates

When single HCP agglomerates are compressed between two rigid platens, a clear power law relationship (with a gradient of 2) occurs between the strain rate and the maximum kinetic energy produced once a dynamic regime is reached (Figure 3.18), in line with the results of Grady and Kipp (1987). This power law relationship suggests that in the dynamic regime, material is failing through dynamic fragmentation whereas in the static regime, material is simply breaking along preferred flaws. This is further supported via visual inspection of the results (Figures 3.6 and 3.7) where the slower strain rate results indicate that the material fractures and separates into large pieces, while the higher strain rate results indicate that the material undergoes fragmentation into small pieces or single particles. These compression tests show similarity to those performed by Cheng et al. (2004).

The kinetic energy is found to be related to the rate of breakage and is also dependent on strain rate and material strength. This is further supported by the large bursts of kinetic energy occurring coincident with breakage (Figures 3.9, 3.10 and 3.11) when the strain rate is in the dynamic region. High strain rates are able to obtain peak kinetic energy almost instantaneously suggesting that explosive or dynamic fragmentation may occur. These kinetic energy peaks also relate to a reduced $\frac{q}{p'}$ stress ratio (Figure 3.16) indicating a reduction in mobilised friction, so for a rapid application of overburden stress there is an associated rapid reduction in mobilised friction.

Compression tests of a single HCP agglomerate clearly show that the application of a high strain rate produces dynamic behaviour. This suggests that under rapid overburden loading, energy dominated behaviour occurs as described by Grady and Kipp (1987) where energy governs fragmentation and not inherent flaws. The speed of the platens overrides the structure of the material due to nucleation of failure at multiple points. This causes the bond strengths to become irrelevant at high strain rates and leads to similar peak levels of kinetic energy being developed for the two bond strengths tested. For the weaker material, the bonds fail to last long enough to have any substantial effect on the $\frac{q}{p'}$ stress ratio. The stronger material shows that additional rotational resistance is provided by material that retains bonds, and this reduces the rate of the decrease of the $\frac{q}{p'}$ stress ratio toward critical state and the reduction in friction. Bond strength therefore plays a role in determining the threshold for dynamic behaviour. This is consistent with the suggestion of Kipp et al. (1980) that the inherent flaws in material are responsible for strain-rate dependent

behaviour.

HCP Agglomerate System

The addition of the surrounding unbreakable HCP agglomerates provides confinement to the breakable agglomerate in the centre and can be considered to represent a group of boulders within a sturzstrom. The results of the oedometer testing on the agglomerate system provides similarities and differences to the results of the single HCP compression tests.

At slower strain rates, the maximum kinetic energy (Figure 3.27) is dependent on the initial state of the agglomerate, which is based on the way the material was built through the use of random flaws and rotation of axes. The breakage associated with the maximum kinetic energy suggests that only the weakest bonds are breaking from which it appears little energy is released and frictional dissipation dominates.

At high strain rates the central breakable boulder completely fragments allowing individual spherical particles to travel between the other agglomerates or to rebound from them, as shown in Figure 3.21. This more closely replicates the expected situation in a sturzstrom than the singular crush tests. The high strain rate results also show a greater reduction in mobilised friction as measured for the breakable boulder than seen for the slow strain rate tests (Figure 3.23) with an almost instantaneous reduction in the $\frac{q}{p'}$ stress ratio concurrent with breakage and sporadic or burst peaks in kinetic energy. The maximum kinetic energy achieved is similar for all agglomerate system tests $\geq 1s^{-1}$, suggesting that kinetic energy is influenced directly by the strain rate.

A rapid application of overburden load causes a large amount of damage to occur with little strain developed so long as the strength of the material can be overcome. The breakage behaviour combined with the kinetic energy burst response to the boundary work and the wave-like wall stresses suggest that at the highest strain rate the central cluster has failed through dynamic fragmentation. This assumption of dynamic fragmentation is also supported by the fast reduction in $\frac{q}{p'}$ stress ratio under high strain rates to a very low critical value at low strains, suggesting a reduction in mobilised friction.

The work of Grady and Kipp (1987), associated with the expansion of a fracturing body, suggests that kinetic energy fuels the breakage process. If, as Grady and Kipp (1987) suggest, kinetic energy and not inherent flaws governs fragmentation then the rate of loading is crucial to the overall behaviour of material. In the oedometer test results, the kinetic energy response was found to be dependent on the rate of loading (resulting in a power law relationship with a gradient of 2 as shown in Figure 3.27) and is also influenced by major breakage events with the resulting expansion in the material influencing the pressure felt on the wall plates surrounding the specimen. This can be seen at high strain rates, where the oedometer tests produce a divergent wall stress response (Y>>X, see Figure 3.26). Inherent flaws, or easily broken bonds in the PFC^{3D} model, control the response of the material under low strain rates and become less important at high

strain rates due to the rate of application of the load activating multiple force chains. Thus the oedometer test results are in agreement with the suggestions of Grady and Kipp (1987).

Due to the spherical nature of the PFC^{3D} discrete particles, once all bonds around a particle are broken, it is likely to roll to reduce the stress placed on it. In so doing the particle increases frictional contact with other particles in the system and thus the system friction response also increases, influencing the stress path response of the material.

7.2.2 Sandstone

Following on from synthetic boulder testing utilising HCP formed clusters, synthetic greywacke sandstone boulders were formed from agglomerates with diameter of 0.1m calibrated to the parameters in Chapter 4. As with the oedometer tests on the HCP material, a breakable boulder of sandstone is placed within a cubic arrangement of unbreakable sandstone boulders and placed under rapid loading. Three independent specimens were placed under varying strain rates utilising the top platen to produce the required compression. These tests are used to investigate how a more realistic material may respond to rapid loading to represent a group of typical greywacke sandstone boulders within a sturzstrom.

As seen for the HCP agglomerate system, a power law relationship develops between strain rate and maximum kinetic energy (with a gradient of 2). Where the relationship becomes a power-law is considered the change from a static to a dynamic regime. Whereas the dynamic regime begins from a strain rate of 1 s^{-1} for the HCP agglomerate system tests, Figure 5.6 shows that, for the sandstone agglomerate specimens, the dynamic regime begins at a higher strain rate of approximately 20 s^{-1}.

As discussed earlier, the power law relationship suggests that in the dynamic regime material is failing through dynamic fragmentation. The highest strain rates cause breakage to occur earlier than the slower strain rates with cracks likely coalescing to cause failure. 'Inertial confinement' effects (as described by Cheng et al. (2004) and discussed in Chapter 2) appear to occur at high strain rates with kinetic energy peaking almost instantaneously. After this burst of energy dissipates additional kinetic energy peaks can be seen to occur in association with significant breakage. Kinetic energy consistently grows under rapid loading with greater peaks than seen in the low strain rate tests (Figure 5.4).

Complimenting the kinetic energy response due to breakage, the micro-stresses in the central boulder drop during breakage with an overall reduction in the $\frac{q}{p'}$ stress ratio suggesting a slight reduction in friction (Figures 5.13). Similarity to the HCP agglomerate results continues with anisotropy in the X and Y wall stress response, however in the sandstone oedometer testing it is not clear if the wall stress response is related to breakage. The largest period of breakage coincides with a minor increase in wall stresses which appear to dissipate slightly as breakage continues.

7.2.3 Chalk

Synthetic weak and extremely weak chalk specimens are calibrated to known material characteristics that are typical of chalk in areas susceptible to chalk flows. Both weak and extremely weak chalk are considered as both can result in chalk flows. However, only extremely weak saturated chalk results in flows that could be considered miniature sturzstroms (Hutchinson (2002)). It is of interest to consider the material difference between chalk and greywacke for micro-mechanical behaviours that may shed light on larger sturzstrom behaviour.

The chalk specimens are placed under varying strain rates following the same method as for the HCP agglomerate and greywacke sandstone. The results of these tests is used to consider strength dependency of material in relation to sturzstroms or chalk falls and if the results found in the prior testing can be replicated.

Given that chalk as a material is significantly weaker than sandstone it is not surprising to find that breakage is complete within 5-10% axial strain (Figures 5.17 and 5.32). A typical sturzstrom may fall up to 1000m prior to transition to runout with a chalk flow falling a maximum of 100m prior to runout. It is reasonable to assume that less strain is required to provide substantial breakage for a weak material. It can also be assumed therefore that the kinetic energy production will be lower, overall.

The results from both the weak and extremely weak chalk oedometer testing are similar to the sandstone and HCP results. Again, breakages result in peaks in the kinetic energy (Figure 5.18 and 5.33) combined with a drop in the $\frac{q}{p'}$ stress ratio (Figure 5.28) reflecting the low levels of friction in the system. Under rapid loading, kinetic energy is of greater magnitude and more consistent. Material movement after breakage results in rolling and/or sliding behaviour, resulting in stress path oscillations and growth in friction energy. Anisotropy in the wall stress response suggests impacts due to explosive fragmentation could be occurring.

A power-law relationship is again formed between strain and maximum kinetic energy (Figure 5.21 and 5.35) however it appears that material strength may have an influence. The extremely weak chalk produces more kinetic energy at lower strain rates than the weak chalk although the differences are not large they are potentially significant when the material strength differences are considered. Given the greater porosity of the extremely weak chalk, particles have an ability to travel before impacting other particles suggesting that kinetic energy may be available for longer in the system than for weak chalk. It is also not unreasonable to consider that the extremely weak chalk produces more kinetic energy due to pore collapse mechanisms associated with the loss of critical force chains due to breakages. In general, a weaker material appears to require far less loading in order to produce fragmentation thus a smaller overburden during a chalk flow may well produce similar behaviour to that seen in sturzstrom.

7.2.4 Summary

Numerical oedometer tests of varying strains have been performed on three synthetic materials to investigate the influences of rapid loading representing the compression of material due to substantial overburden at the sturzstrom transition point between fall and runout. All materials tested indicate similar behaviours at high strain rates.

Key findings from the oedometer testing are:

- Rapid application of load causes fast and significant breakage of material. This is consistent with the findings of Janach (1976) that increasing the compressive load leads to greater breakage and separation of the fragments.
- Breakage events due to rapid loading cause a positive and noticeable response in the system kinetic energy. Thus more kinetic energy is available due to breakage.
- Under the rapid application of load the material strength becomes less relevant as the strain rate overrides the response of the system. This suggests that strain rate effects (see Section 2.2.3, the increase of peak strength under rapid loads) are not influencing the system response.
- More kinetic energy is available from breakages that occur under rapid loading than static loading with the energy remaining available in the system for longer.
- When breakages occur there is an associated decrease in the $\frac{q}{p'}$ stress ratio thus a reduction in mobilised friction.
- Artificial behaviour of material may occur in PFC^{3D} due to rolling/sliding of the discrete spherical particles once all bonds are broken.
- Maximum kinetic energy vs strain rate graphs show a power-law relationship (generally of 2) with a distinct change from the static to dynamic regimes.
- Stronger materials require a greater impact (i.e. high loading rate) force to retrieve the maximum kinetic energy available - a material strength effect. Grady et al. (1977) state that brittle failure under dynamic loads may lead to stress paths that are controlled by the strength of the internal structure of the material.

The theory of dynamic fragmentation in sturzstrom as suggested by Davies and McSaveney (2008) is reliant on the reduction of friction within a sturzstrom during runout. The high strain rate oedometric tests suggest that dynamic fragmentation occurs under fast loading rates. The dynamic fragmentation in the oedometer tests is associated with an increase in kinetic energy and decrease in mobilised friction. This agrees with the analysis of Grady and Kipp (1987) that shows kinetic energy governs fragmentation, and also with the hypothesis of Davies and McSaveney

(2008) that dynamic fragmentation causes a reduction in friction. However this also results in a caveat to the original Davies and McSaveney (2008) hypothesis as high stresses alone are not sufficient to cause fragmentation, there must also be high loading rates. This is not proposed as part of the original theory. The oedometer tests therefore indicate that it is plausible that dynamic fragmentation in a sturzstrom due to rapid loading at the transition point from fall to runout is likely to reduce friction, increase kinetic energy and therefore enhance mobility.

7.3 Shear Testing

Shear box testing of synthetic rock materials is used to investigate the response of an idealised sturzstrom specimen found in the runout zone when placed under fast shear. The idealised sturzstrom specimen is formed as a representation of the runout portion of the sturzstrom event where material has already fragmented, providing a matrix of fines and fragments surrounding rock boulders that are yet to break. The specimen is placed under a bi-directional shear with an applied shearing velocity as would be experienced in a typical (and material relevant) runout, as the debris travels. The purpose of the shear testing is similar to that for the oedometer testing: to perform tests that could not otherwise be easily conducted in laboratories and to investigate the micromechanical response of boulders confined within a shearing matrix.

In the series of shear tests reported in Chapter 6, small parallelepiped specimens, 0.3m length by 0.2m width by 0.2m height, are formed with three boulders of diameter 75mm placed in a row in the middle (see Figure 6.2). Periodic boundaries are installed in the x-direction to allow the material to undergo continuous shear. Two overburden loads are incrementally applied to the material prior to testing following from the oedometer testing results and the shearing velocity is applied in a linear manner to the matrix material. The loads represent likely quantities of debris that may overlie the representative specimen during runout. In this series of testing, the same synthetic sandstone and chalk materials as used for the oedometer tests are used to consider how real materials may react under a fast shearing process. Quasi-static and dynamic shear speeds relevant to the scale of sturzstroms are considered for all materials. Local and global parameters are monitored throughout the test process to consider the effects of breakage of the boulders on the overall system.

The results and implications of the shear tests are discussed below.

7.3.1 Sandstone

Two synthetic greywacke sandstone specimens are formed into an idealised shear test specimen to replicate the debris likely to be encountered in the runout phase of a sturzstrom. The specimens are placed under a low (100kPa) and high (1MPa) level of overburden to represent the upper and lower quantities of debris above the specimen that may be found during different periods of runout.

Images from planes cut through the material (Figure 6.6) indicate that although there are clear differences in force chain strength due to the applied overburden loading prior to shearing, at the end of the shear tests the force chains and overall state of the specimens are quite similar. The evolution of the force chains is similar under dynamic shear and under both overburden loads. This suggests that the overburden loads have little influence on the outcome of the shear tests.

Although significant breakages occur early within the quasi-static shear test there is no corresponding response within the system energies or wall stresses to suggest any inertial issues. In comparison, an inertial response to the onset of dynamic shear occurs with almost instantaneous peaks in system energies and wall stresses for all four tests. Overall, breakage begins with the initial large events followed by several small minor events throughout the remainder of the tests. For the quasi-static shear tests, the early breakages occur within the matrix, however for the dynamic shear tests the majority of these early breakages are within the boulders. The majority of breakage occurs over 0-2% shear strain for both the quasi-static and dynamic shear events as the material gives way to shearing forces.

Quasi-static shear results in very low energy that is dominated by friction. Kinetic energy peaks occur simultaneously to the large initial breakage events under dynamic shear, however all other kinetic energy peaks fail to surpass the value of the friction energy which remains relatively high and dominates the other system energies, as measured in the numerical tests. The normalised kinetic energy response indicates that the energy dissipates as shear continues. The kinetic energy produced under dynamic shear does not provide a major influence on the mobilised friction of the system therefore it appears that dynamic fragmentation is not occurring in this shear situation.

As shear is forced onto the specimens the matrix layer breaks to reduce stress and allow movement. Up to 20% of the total parallel bonds contained within the boulders break under dynamic shear with the remainder of the breakages occurring within the matrix (Figures 6.12 and 6.13). There is a minor amount of mixing between the boulders and matrix which is more obvious under quasi-static shear as shown in the translational velocity profiles (Figure 6.11). Under dynamic shear it appears that the boulders rotate slightly with some of the boulder particles attracting a slightly higher velocity from the surrounding matrix particles. The low percentage of breakages in the boulders during dynamic shear and rotation of the remaining fragments support the comment above that dynamic fragmentation is not occurring.

The trace of the gauge particles indicates that dilation occurs within the specimen as shear progresses regardless of shear speed. This suggests that there is a kinematic constraint in these model tests, such that particles must move over each other to enable shearing to occur. This in turn probably results in the very high stresses experienced within the samples, irrespective of the overburden applied. The greatest amount of dilation of the gauge particles occurs above the boulders. The boulders appear to produce a barrier which suppresses movement in the lower layers

as the specimen dilates, whereas layers 4-6 above the boulders freely dilate during shear.

7.3.2 Chalk

Following the sandstone shear testing, chalk materials were also considered. Weak chalk and extremely weak chalk materials were prepared for shear testing to investigate how these weak and more porous materials may behave in the runout phase of a chalk flow. The chalk specimens were prepared in the same manner as those for the sandstone material with loading levels of 10 kPa and 100 kPa — lower than the sandstone to represent the lesser volume of material likely to be acting as overburden.

The initial states of the weak and extremely weak chalk specimens (Figures 6.20 and 6.36) show differences in force chain strength due to the overburden loads. The extremely weak chalk specimen has high porosity and the cross-sections of the material contains substantial voids that may interrupt the ability of force chains to form strong groups throughout the material. In both chalk materials and load cases the force chains strengthen due to shear as the central boulders rotate. It also appears that the voids in the extremely weak chalk boulders allow fine material to move more easily with mixing of layers apparent (Figure 6.42) under quasi-static shear. As with the sandstone results, the weak chalk and extremely weak chalk boulders appear to fracture into fragments under dynamic shear rather than undergoing dynamic fragmentation.

As dynamic shear begins, an inertial response can be seen in the system energies and wall stresses for both chalk materials and load cases with no similar response under quasi-static shear. The majority of breakage occurs during this time (0-3% shear) and at a slightly faster rate than when compared to the sandstone — there is little resistance to shearing. Less than 40% of the boulder bonds are broken with the majority of these occurring during the first major breakage event (Figures 6.28 and 6.43). Minor breakages that occur after the initial main breakage event appear to have little influence on any of the other monitored parameters.

Throughout all of the chalk tests, friction energy dominates all other system energies. The mean effective and deviatoric stresses climb under quasi-static shear speeds and, after the inertial response, remain fairly consistent for the dynamic shear test on weak chalk, while decreasing for the extremely weak chalk. The associated $\frac{q}{p'}$ stress ratio gradually decreases for the weak chalk under both shear speeds. Under quasi-static shear the $\frac{q}{p'}$ stress ratio decreases for extremely weak chalk, and under dynamic shear remains relatively consistent.

Dilation occurs in both the weak and extremely weak chalk specimens with the boulders providing some confinement of the lower 1-3 gauge layers (Figure 6.34 and 6.49). The quasi-static shear tests produce substantially less dilation than those at the dynamic shear speed, indicating the influence of the shear speed on the movement of the particles within the specimen. The weak chalk dilates up to two times as much as the extremely weak chalk and dilates earlier at the same

velocity. This suggests that the material strength and initial porosity are important under fast shear conditions and that the voids within the extremely weak chalk may be collapsing. This is also seen in the creation of putty chalk in the field due to earthworks in highly porous and highly saturated chalk (Mortimore et al., 2004).

7.3.3 Summary

Shear tests at velocities consistent with that of sturzstrom in sandstone, and chalk flows in weak chalk and extremely weak chalk, have been performed to investigate the influences of rapid shear during runout. As a comparison, quasi-static shear speed tests have also been completed. The results show that the overburden loads, or runout debris, above the representative specimen have little influence on the overall behaviour of the system, regardless of shear speed. Inertia occurs as dynamic shear begins and the main breakage events occur at the same time. Breakages within the boulders are minimal and allow for the boulders to fracture into fragments which can then rotate as shearing continues. Breakage appears to have little effect on the overall behaviour of the specimens.

Key findings from the shear testing are:

- The main breakages within the boulders typically occur during the first major breakage event with the majority of breakages overall occurring within the matrix.
- Major breakage events coincide with an inertial response under dynamic shear only which sees all system energies, micro-stresses and wall stresses rapidly climb. These responses are not all likely to be due to inertia and thus it is possible that a proportion of these increases are due to the additional kinetic energy in the system.
- The amounts of kinetic energy produced during shearing are less than the underlying friction energy throughout the process. Kinetic energy produced is quickly dissipated through particle movement and does not survive in the system long enough to influence further breakage. All tests are dominated by friction.
- Micro-stresses rise throughout the quasi-static shear tests, and under dynamic shear gently decline after the initial major breakage/inertia event. Quasi-static $\frac{q}{p'}$ stress ratios behave similarly to a typical laboratory shear box test with a rise as shear begins and then gentle decline toward critical state as shear strain accumulates. The dynamic $\frac{q}{p'}$ stress ratios either gently decline (sandstone and weak chalk) or remain consistent (extremely weak chalk). There is no distinct reduction in mobilised friction from breakage; the decline in the stress ratios appears to occur from the act of shearing itself.
- All material specimens dilate under shear, with the boulders generally assisting with the confinement of the lower layers of material, and the layers above the boulders dilating further.

The sandstone and weak chalk dilate around twice that of the extremely weak chalk which is clearly influenced by its high porosity. Quasi-static shear tests typically result in much less dilation.

Work by Carolan and O'Sullivan (2006) found that a DEM model of the direct shear test produced contractant behaviour when the parallel bonds were weak and dilatant behaviour when the bonds were strong. The DEM model produced shear banding as shear progressed, as was also seen in the quasi-static shear tests in this chapter. Carolan and O'Sullivan (2006) also found that the collapse of force chains caused fluctuations in the stress-strain curve, and that breakage during shear interrupted the force chains, which impacted on the development of shear stress as also found by Cheng et al. (2008). Breakages in the shear tests performed here appear to have had little impact on the micro-stresses, outside of the inertial response during dynamic shear. Guo and Morgan (2006) found that shear testing in DEM resulted in dilation at the onset of shear with an associated reduction in friction. They suggested that the dilation may have been a transitional response as the interlocked grains began to move, a behaviour seen in the shear tests here under both shearing speeds.

Quasi-static shear test results bear similarity to those of the dynamic shear tests in quantities and timing of breakages. Otherwise the micro-stresses, energies and dilation are different. There is obviously an influence of shear speed on particle movement which in turn affects all measurements of system energies and stresses. This suggests that faster moving particles lead to more disruption to the system with dynamic fragmentation not apparent under high shearing speeds.

Grady and Kipp (1987) suggest that kinetic energy is responsible for fueling the breakage process where during dynamic fragmentation, the kinetic energy from moving fragments becomes responsible for fracturing forces. From the testing here, large breakage events under dynamic shear produce kinetic energy, however it appears that the quantity of energy is not enough to remain in the system and fuel further breakages. This suggests that there is little likelihood of the fast shearing of this representative specimen reaching a dynamic regime. Therefore it appears unlikely that dynamic fragmentation can occur in this type of specimen under fast shear even with constant high levels of stress applied as an overburden.

7.4 Sturzstroms

As previously outlined in Chapter 2, a sturzstrom results in a highly mobile landslide that can travel at excessive speeds for a distance far greater than the fall height. Deposits formed from sturzstrom events indicate that little mixing between stratigraphic layers has occurred, and that rock clasts, fragments and/or boulders can be found buried within rock flour of the same strata. A reasonable amount of macroscopic data has been collected for various sturzstrom events around the globe including estimations of initial fall volume. This data is not exhaustive, however, in

combination with prior research provides a good basis for further work including consideration of the mechanical behaviours leading to long runout.

7.4.1 The Long Runout Problem

There is a notable relationship between the runout distance of a sturzstrom and the source volume as outlined in Section 2.1.5 (Hsu, 1978; Melosh, 1986; Staron, 2008; McSaveney et al., 2000; McSaveney and Davies, 1999). The long runout problem, as described earlier and above, has been considered in this thesis through the numerical modelling of the impact transition zone (oedometer tests) and runout shear (shear tests) behaviour of synthetic rock materials.

The key mechanical fluidisation theory considered for the excessive travel distance of sturzstrom debris in this thesis is that postulated by Davies and McSaveney (1999) — the concept of explosive fragmentation of rock during a sturzstrom. Fragmentation requires the rapid application of load that exceeds that of the strength of the rock involved; in a sturzstrom the large volume of the failure debris is capable of producing a substantial overburden stress. McSaveney et al. (2000) propose that multiple fragmentation events within a sturzstrom can assist with enhancing mobility through the production of an isotropic dispersive stress as fragments separate at high velocity.

In this thesis it is proposed that the fragmentation behaviour postulated to occur within sturzstroms can be described from a micro- mechanical perspective. Multiple catastrophic breakages in a system from rapid loading or fast shear may cause an increase in kinetic energy. The catastrophic breakages cause a brief separation of particles due to the increased kinetic energy as the particle fragments. The temporary unloading and redistribution of normal stress (perhaps leading to the wholesale separation of the particles in some cases), reduces the mobilised friction which assists with enhancing the runout. That is, the system requires both an increase in kinetic energy from catastrophic breakages and a reduction in mobilised friction for the mobility to increase.

The explosive or dynamic fragmentation of a material can occur through the rapid application of forces through a dynamic tensile stress (Grady, 1982). Grady (1982) states that kinetic energy is associated with fracturing forces and that a large proportion of kinetic energy remains after fragmentation. The most likely situation within a sturzstrom for the rapid application of forces is at the transition point from the fall of the debris to the horizontal runout. Numerical oedometer testing of sandstone and chalk materials shows a close relationship exists between breakage, an increase in kinetic energy, a decrease in mobiliised friction and the dispersion of particles under high strain rates. The numerical oedometer tests provide evidence of longer term residual kinetic energy, the levels of which are also influenced by the strain rate.

Consideration has also been given to the runout stage of a sturzstrom. By utilising quasi-static and dynamic shear speeds, the shear tests performed in Chapter 6 were used to consider

how the breakage of boulders suspended within a matrix of fines and fragments may influence the overall behaviour of the specimen. It appears from the dynamic shear tests that although breakages increase kinetic energy, the effects do not last long enough to fuel further breakage or to greatly affect the overall behaviour of the specimen under shear. The material behaviour is dominated by friction under quasi-static and dynamic shear and the boulders fracture into fragments. This suggests that although material in the runout portion of a sturzstrom may be under high overburden stress, dynamic fragmentation cannot occur as there is no rapid loading taking place. Fragmentation may occur due to the shear speed, which will increase kinetic energy and reduce mobilised friction, however these events may not be substantial enough, or last for long enough, to be solely responsible for the continued propagation of the debris for such long distances as recorded for sturzstroms.

If the rapid application of forces is considered to occur at the same time as dynamic shearing, perhaps through a minor change in topography or impact with an obstruction, it is possible that the combination of multiple dynamic fragmentation events from this rapid loading combined with small increases in kinetic energy from shear, could result in propulsion to disperse the system. The size of the obstructions or topographical changes required to cause this response could be considered in both further numerical and laboratory based flume or centrifuge tests. This suggests also that dynamic fragmentation events may occur within landslides of shorter runouts or a less inclined fall, if rapid loading is able to be achieved.

7.5 Recent Numerical Modelling Work in DEM

As outlined in Chapter 2, Section 2.3.3, recently many authors have utilised DEM to model the runout of landslides. A small selection of this work is briefly revisited to consider the results of this thesis in comparison to the results already available in the literature.

Tommasi et al. (2008) modelled potential rock avalanches in the Lavini di Marco area using PFC^{2D}. The limestone material that has previously failed in the area was tested both in the field and in the laboratory. The PFC^{2D} material parameters were calibrated to these results and aggregates used to represent rock blocks, although the authors do not stipulate the associated rock block size. In order to consider the application of the model to potential failure zones, Tommasi et al. (2008) back analysed a planar rockslide event that occurred in the area from the same material. This back analysis resulted in a realistic runout distance with bonded aggregates (rock blocks) intact at the surface and significant breakage at the base of the runout. A smooth basal failure surface was prepared with debris (bonded blocks) placed on a saddle and valley floor. The slide body was divided into blocks consistent with the joint spacing observed in the field. The results discussed by the authors focused solely on the velocity output, breakages and visual inspection of the overall avalanche. They note that velocity peaked at the transition point from

vertical fall to horizontal runout, with an additional peak occurring when the rear of the avalanche pushed the material further into the valley. The upper layers of the debris appeared to acquire a higher velocity than the basal layers. Visual inspection of the debris indicated that the basal area showed greater fragmentation than the surface.

Although Tommasi et al. (2008) have utilised DEM modelling, they focused specifically on the macroscale behaviour rather than utilising the ability of PFC to interrogate the microscale behaviour. However, the particle size utilised would be relatively large to represent rock blocks as they were specifically interested in predicting the runout. This means that the microscale behaviour evident within their model is unlikely to be accurate enough to represent the microscale behaviour occurring within a rock avalanche.

Cagnoli and Piersanti (2015) model flows of angular rock fragments travelling down a curved chute to consider the effects of grain size and volume found in separate laboratory experiments. They state that they utilise 3D DEM to investigate the relative mobility, rather than actual mobility observed in the laboratory, and therefore do not calibrate their material. Instead they define their parameters for general igneous rock fragments flowing down a soil chute. The rock fragments are represented by three different cubic polyhedrons and randomly placed behind a gate, prior to release down the chute. Cagnoli and Piersanti (2015) find that their numerical simulations represent the laboratory chute tests well, even though parameter calibration was not undertaken. The numerical tests indicate that particle agitation increases downward within the flow. As the grain size decreases any agitation due to interaction with the ground surface penetrates far less distance inside the flow. A decrease in the agitation of the flow was found to lead to a decrease in the dissipation of kinetic energy. An increase in volume resulted in greater accumulation of material at the back of the flow, with the front of the flow acting as a barrier.

As with the Tommasi et al. (2008) work, Cagnoli and Piersanti (2015) use a DEM model to investigate macroscale behaviour and this provides little insight into the microscale behaviour of the flow of rock fragments. The results regarding agitation are however useful to consider, as they indicate that reduced agitation results in increased energy. This could be considered in two ways, firstly, that any breakage could be regarded as agitation and thus dissipate energy; or secondly, that a loose flow with low overburden may travel less distance, due to the ability of particles to move more readily and dissipate energy. Thus a sturzstrom could be categorised as a flow with reduced agitation due to the large volume of overburden and stratigraphic sequencing of the deposit (i.e. little mixing).

Recent work by Johnson et al. (2016) involves the use of a 2D DEM code to model a simple landslide. This numerical model follows directly from the work by Campbell et al. (1995) and is used to consider the mechanism that reduced friction in the earlier models. In Campbell et al. (1995), the number of particles contained within their DEM landslide had an affect on the stress

ratio through the centre of the sliding mass. An increase in the number of particles resulted in a decrease in the stress ratio or mobilised friction. However, the shape of the final deposits presented by Campbell et al. (1995) are somewhat unusual, as the majority of the debris is shunted toward the toe with less particles in the model, and remains toward the rear of the deposit with more particles in the model. These shapes are not typical of the deposits found in the field or in general by other researchers.

Johnson et al. (2016) follow a similar method by considering the comparison of the effective normal stress felt at a point on the ground through the centre of mass of the landslide, versus the overburden pressure. Johnson et al. (2016) state that when the effective normal stress is less than the overburden pressure, that friction is reduced and sliding will occur. The authors go on to note that the reduction in normal stress is consistent with the theory of acoustic fluidisation. Johnson et al. (2016) conclude that the pressure variations from their model produce low-frequency vibrations which if large enough may break particle contacts. This is in contrast to the discussion of Campbell et al. (1995) where they state that the frequencies seen in their models are much lower than those required to represent acoustic fluidisation.

The DEM modelling of Johnson et al. (2016) is utilised to consider macroscale behaviour. The modelling work discusses vibrations due to pressure variations that may disrupt particle contacts, which is similar to the concept of agitation raised by Cagnoli and Piersanti (2015). In effect, the microscale behaviour is critical to understanding how the particle force chains and bonds may be disrupted, in order to allow for vibrations or agitation to affect the runout of the debris.

The macroscopic behaviour of sturzstroms has been numerically modelled using DEM by various authors. In general, the results of these models match relatively well with the runout extent and overall macroscopic response seen in most sturzstrom cases. Very few authors have considered the ability of DEM models to consider the microscale behaviour of sturzstroms to assist with determining a mechanism for the enhanced mobility of these failures.

This thesis has considered the microscale behaviour that may occur at both the transition point from vertical fall to runout and during high speed shearing. The results of the oedometer testing indicate that a large volume of source material falling vertically onto a horizontal surface is capable of producing multiple dynamic fragmentation events, which increase kinetic energy and reduce the mobilised friction of the system. High speed shearing was found to have little overall influence on the reduction in friction within the system, even though significant breakages can momentarily reduce friction. These microscale results do however provide insight into the behaviours that may be occurring within a sturzstrom. The dynamic fragmentation of rock under rapid loading may cause a vibrational or dispersive response within the system, as energy waves travel away from the fragmentation source. This microscale behaviour could explain the agitation and/or vibrations within the macroscale system that results in additional breakages and enhanced mobility of the

debris.

7.6 Chapter Summary

Many discussions have occurred within the landslides research community regarding the underlying behaviour of sturzstroms. The collision of grains is suggested as a possible explanation for long runout (Hsu, 1978), with the presence of interstitial dust and small debris reducing friction or effective normal pressure to allow for the extensive movement. Turbulence, however, cannot occur during runout or else stratigraphy would not be preserved due to material mixing, and jigsaw boulders would not be so prevalent (McSaveney and Davies, 1999). The suggestion is that turbulence occurs only within the basal layer of the avalanche, producing a dilative energy and little dissipation. More recent discussions have resulted in the suggestion that fragmentation of rock under high overburden stresses produces high velocity fragments that dilate the debris resulting in an isotropic dispersive stress (Davies and McSaveney, 2008).The dynamic fragmentation of material during two key phases of a sturzstrom, the fall and the runout, is likely to produce the angular material seen throughout the deposit. The significant question here is whether dynamic fragmentation can be responsible for both the angularity of the deposit and the long runout.

In this thesis, oedometer and shear tests are performed to consider the fall and runout of a sturzstrom. The results of the oedometer and shear tests presented in Chapters 3 to 6 of this thesis are outlined in this chapter. The implication of the results is considered in relation to the initial research question around the long runout behaviour of sturzstroms. The numerical modelling in PFC^{3D} has focused on HCP formed boulders and synthetic rock materials to consider the theoretical material response and a more realistic material response, respectively, that can be compared to examples of sturzstroms and chalk flows.

The results agree with that of Grady and Kipp (1987), whereby kinetic energy governs fragmentation and that dynamic fragmentation causes a reduction in friction. The theory of fragmentation as described by Davies and McSaveney (2008) states that dynamic fragmentation, under an overburden stress significant enough to break the rock, will cause apparent pressures on the surrounding material and reduce effective stress and friction. The oedometer results suggest that high overburden stresses alone are not sufficient to cause dynamic fragmentation but that the rapid loading of material is required. Dynamic fragmentation in these conditions is likely to reduce the mobilised friction, increase kinetic energy and assist with mobility of the debris.

Kinetic energy produced during shearing is minimal and dissipates quickly as particles impact and roll, with all tests dominated by friction. This means that any kinetic energy produced, regardless of shear speed, does not survive long enough in the system to influence further breakage. The fast dissipation of kinetic energy for a small specimen, such as that tested, is likely to occur even if simultaneous large breakage events were to occur near the basal area of a sturzstrom.

Although there may be an instantaneous response to a simultaneous event, such as momentary propulsion, it is unlikely that the kinetic energy will remain for long enough to influence further breakage. The results of the shear testing suggest that it is unlikely that a specimen in this form will reach a dynamic regime under high velocity shearing, and therefore that dynamic fragmentation will occur.

Chapter 8

Conclusions

8.1 Introduction

Sturzstroms are catastrophic long runout rock avalanches that are typically dry, pervasively fragmented and involve large volumes of source material. These events are difficult to predict and occur quickly, thus there is a degree of difficulty in physically applying instrumentation in the correct area to obtain real time information. The macroscale characteristics of sturzstroms can be postulated reasonably accurately from deposits and witness accounts. However the microscale characteristics, that would assist with explaining the long runout, are difficult to obtain from these same sources and unable to be fully replicated using laboratory techniques. The application of numerical modelling is of benefit in this situation. Continuum modelling approaches provide useful information regarding the macroscopic behaviour, however, it is difficult to consider a small section of material within the overall avalanche using this method. Discrete element methods allow for microscale behaviour to be considered and investigated in detail.

This research has considered two key phases of a sturzstrom, namely the transition or impact point between the vertical fall and horizontal runout, and the shearing of debris during runout. These two phases have been investigated via a discrete element model PFC^{3D} with oedometer and shear box tests respectively. Chapter 3 considered HCP formed material as a singular boulder and as a cubic arrangement of agglomerates, with both specimen types placed under rapid vertical loading in a simulated oedometer. Chapter 4 discussed the calibration process of the sandstone, weak chalk and extremely weak chalk materials for use in Chapters 5-6. Following on from the HCP oedometer testing, Chapter 5 outlined the oedometer tests of the synthetic rock materials also formed into cubic arrangements of agglomerates. Chapter 6 then considered the high speed shearing of sturzstrom debris, utilising the same synthetic rock materials as used in the oedometer tests. The results from Chapters 3-6 are summarised in the discussion in Chapter 7.

In conclusion to this thesis the applicability of the research, key developments, limitations and recommendations for future work are outlined below.

8.2 Applicability of the Research

The Fall

As a sturzstrom begins, a large volume of debris reaches a topographic change, resulting in a sudden transition in the movement of the material from sub-vertical to sub-horizontal. Oedometer testing has shown that the rapid loading of the material will result in dynamic fragmentation occurring. This results in an increased quantity of kinetic energy within the material during fragmentation and a reduction in mobilised friction, and therefore will enhance the mobility of the material. The results support the postulated theory of fragmentation as a mechanism to increase runout.

The Runout

The high speed shearing of a representative specimen from the bulk of the sturzstrom debris will produce intensely crushed and fractured material. Crushing of the debris results in a minimal amount of kinetic energy which is dissipated quickly as the material dilates. The system is dominated by friction and does not reach a dynamic breakage regime. Rapid loading during shearing may produce the effects described above, as found in the oedometer testing, and this is likely to occur when the sturzstrom comes into contact with small topographic changes or obstacles. The results suggest that shearing is not as important to the overall mechanism involved in the long runout of sturzstroms as that of rapid normal loading.

Field Geology

The microscale numerical modelling conducted within this thesis is applicable to the work of field researchers. As outlined in Section 2.1.2 key small scale markers of rock avalanche deposits are noticeable in the field, mainly the angularity and variation in size of the debris, and jigsaw-fractured clasts. The oedometer testing has shown that the dynamic fragmentation of material is likely during rapid loading resulting in fines and small angular fragments. In comparison the shear testing has indicated that although material fractures, it does not dynamically fragment. Collectively the two tests can be considered in regard to the phase of the sturzstrom and physical behaviour occurring at that point.

In the field the intensely crushed basal zone is representative of an area of rapid loading, where the overburden is reasonably large. Toward the distal edges of the deposit where the overburden is less, it is anticipated that the basal zone will contain more fragmented clasts. The quantity of overburden load, as shown by the varying strain rates in the oedometer tests, will influence the resulting degrees of fragmentation or fracture throughout the debris. This supports the delineation of facies outlined by Dufresne et al. (2016) both vertically within the sturzstrom deposit and spatially. As the quantity of overburden reduces the likelihood of dynamic fragmentation and intense crushing decreases.

Jigsaw fractured clasts and boulders within the debris are consistent with the results from the high speed shear tests in this thesis. Shearing events, in situations where rapid loading has not occurred, are shown by the numerical modelling to produce minimal mixing, small fragments within a matrix of fines and fragmented boulders. The fragments of the boulders do not separate in the numerical model resulting in jigsaw fractured clasts. Thus, areas of high shear and minimal rapid loading in real events will likely result in jigsaw fractured clasts in the deposit. The variation throughout the sturzstrom deposit can be explained through the combined and isolated effects of rapid loading and shear.

8.3 Key Developments

Dynamic fragmentation is an intense impulsive process that can occur due to a rapid transfer of energy through contact forces:

Under slow strain rates, quasi-brittle material like Class I rock simply fractures and separates whereas under dynamic strain rates the material dynamically fragments. Rapid loading causes critical cracks to extend quickly in comparison to the time taken to apply the load and causes a high stress state to be achieved before the material flaws coalesce. There is a clear strain-rate dependency for rock-like materials to reach a dynamic regime and this directly relates to the material strength.

Breakage events due to rapid normal loading cause a noticeable response in the system kinetic energy:

Fast and significant breakage as a result of the extension of critical cracks under rapid loading, causes a noticeable response in the system kinetic energy, providing more energy for further breakages. This kinetic energy under dynamic normal loading, also remains within the system for a longer period of time than that produced by static breakage.

Breakage events due to rapid normal loading cause a reduction in mobilised friction:

A key interrelationship from the oedometer testing is that rapid loading causes fast and intense breakage, which increases kinetic energy in the system and decreases the $\frac{q}{p'}$ stress ratio response. Thus in a dynamic regime, breakages are capable of reducing the mobilised friction in the system, which will allow for an increased mobility of the debris until the kinetic energy is dissipated.

High stresses alone are not sufficient to cause dynamic fragmentation:

Dynamic fragmentation in the oedometer testing is associated with an increase in kinetic energy and a decrease in mobilised friction. In order to reach the dynamic regime rapid loading must occur. Therefore in order for dynamic fragmentation to occur and enhance mobility, high stresses must be applied through rapid loading.

Material strength influences whether a material can produce a sturzstrom at given fall heights:

Stronger materials require a greater impact force to produce the maximum kinetic energy available. This directly translates to the fall height of the material. For instance, an extremely weak chalk may only need to fall say 50-100 m in order to reach the dynamic regime for that material, and thus intense breakage (and void collapses) will assist propagation of the runout. As the material strength increases so too does the vertical fall height of the material in order to reach a dynamic regime. Therefore to some extent, the material strength, when compared to the potential energy, can be used to consider whether the material in question is capable of producing a sturzstrom i.e. long runout.

Shearing at high velocities under a continuous overburden pressure fails to produce dynamic fragmentation:

An overburden pressure consistent with the likely depths of sturzstrom debris has little influence on the behaviour of debris under kinematically constrained high speed shearing. Inertial responses due to the commencement of shearing likely mask the response of the system to the main breakage event. Regardless, breakage events have little influence on the overall system responses, and in particular, the boulders of the shear specimen form fragments rather than shattering.

High speed shearing results in a friction dominated system:

Kinetic energy produced from breakages is quickly dissipated from the system. As with a standard laboratory shear box test, the high speed shear tests result in material dilation and this utilises all kinetic energy available. The system is dominated by friction energy and so it appears unlikely that high speed shearing will reach a dynamic regime and induce dynamic fragmentation.

Rapid loading during high speed shearing may result in dynamic fragmentation events:

Given that rapid loading initiates dynamic fragmentation, it is possible that, during high speed shearing, minor changes in topography may result in the occurrence of short rapid compressive loading events. These short events could cause dynamic fragmentation and bursts of kinetic energy that may assist with propulsion of the debris during runout. It is therefore sensible to consider that similar rapid loading events may also occur during short runout landslides, if there is significant landslide debris.

8.4 Limitations

As with all numerical models, limitations in the use of the model and interpretation of the resulting data exist. The most obvious limitation with the use of PFC^{3D} relates to the discrete element employed by the model — a spherical particle. This sphericity is typically dealt with by utilising

contact bonds or parallel bonds. In particular, the use of the BPM as described by Potyondy and Cundall (2004), helps to reduce this issue by providing the ability to produce synthetic versions of real rock materials. As shown in the results however, unbonded spherical particles can produce arbitrary results once they are free to roll. If enough particles begin to do so the effects are noticeable across the system, in particular through the micro-stresses calculated from the measurement circle logic.

Computational limitations have caused additional iterations of models in order to find an appropriate real run time, without compromising the ability of the resulting model to represent the intended process and behaviours. These limitations are directly related to the number of particles in the system, and reliance of the time step on material stiffness. Due to the limitations of particle numbers, a discrete element cannot represent an individual particle within a material. As indicated by Cheng et al. (2003), this results in the material parameters and particle size distribution becoming crucial for the production of a reasonable model. In this study, the size of the particle constrains the size of fragments possible when in reality they could be much smaller.

As with a large number of geotechnical software programmes, PFC^{3D} effectively relies on a constitutive model to represent material which is created from a contact model and material bonds. The contacts in PFC^{3D} are controlled by a force-displacement law dependent on a contact stiffness. The contact model can be joined by a dashpot from the application of damping in the model and a bond represented by springs. Overall, there is a substantial quantity of parameters that must be calibrated in order to represent a particular material, with the calibration process performed by the trial-and-error method. The number of parameters and method of calibration lead to limitations in the behaviour of the material. Thus the results of all testing must be considered with care and robustly analysed to ensure that they are realistic.

8.5 Recommendations for Future Work

The representative specimens chosen for the oedometer and shear testing are simplified, and perhaps crude, for making generalised assumptions in regard to the micro-mechanical behaviour of sturzstroms. Several other approaches could be considered for future numerical work, to either support the findings of this thesis or provide additional insight into the behaviour of sturzstroms. Examples of future work that could be considered are outlined below.

Oedometer Testing:

The numerical investigations here focused on one breakable boulder placed in the centre of a cubic arrangement of agglomerates. Oedometer testing at varying strain rates on variations of this representative specimen would be useful to confirm if the behaviours reported here are consistent for different configurations. The specimen may be larger, with a greater number of breakable boulders

or could contain fines or fragments between the boulders to investigate multiple breakages or the effect of fines on the system.

Shear Testing:

High speed shear testing as undertaken in this thesis, although not producing dynamic fragmentation, may be occurring within the dynamic regime for the materials tested. It would be of interest to perform an additional series of shear tests at varying speeds to determine a realistic static shearing speed, and to ascertain the approximate velocity at which the static regime becomes dynamic. This process may also help with the understanding of the inertial effects found in the series of shear tests conducted here.

As with the oedometer testing, the representative specimen is fairly particular, and perhaps only relevant to the latter runout of a sturzstrom. A sensitivity analysis of the specimen design should be considered in order to confirm the likelihood, or otherwise, of dynamic fragmentation occurring under shear. Variations to the specimen design could include more (or less) boulders, geometry and random placement of boulders, or in fact a grouping of rock fragments. The position in the runout is also of importance. For instance, just after the transition zone there are likely to be greater quantities, and larger, boulders that are likely quite angular. The breakage of this type of material could be of great interest in considering the areas of the runout which may be most important during shearing.

Extended Model:

The testing here has considered two specific and isolated events — the fall and the runout. It would be of interest to consider the entire process with a DEM model such as PFC^{3D}. A fully bonded and jointed synthetic rock material could be released from a numerically defined mountain side where topography is carefully mapped with the use of walls. In this way the entire behaviour of a sturzstrom — macroscopic and microscopic — could be monitored and analysed although the model may require substantial amounts of computational time. Column collapse models have been produced by Lo et al. (2009) and Langlois et al. (2015) in DEM, and there are several pieces of research considering 2D granular flow or avalanche behaviour (for example, Tommasi et al. (2008), Banton et al. (2009) and Thompson et al. (2009)). However, the majority of the DEM modelling of landslides focuses on the macroscopic behaviour and so utilise a minimum particle size equivalent to rock blocks.

Numerical Model:

An alternative approach toward the problem could also be undertaken by using continuum modelling methods coupled with DEM. In this way discrete localised behaviours could be fed back into

a global model, and vice versa, throughout the full runout of a sturzstrom. This would provide a clearer understanding of how the micro-mechanical behaviours affect the global behaviour.

Field Geology

A database of sturzstrom events and the relevant geological material they have occurred in would be useful, to consider whether there is a true material strength effect. It is not clear from the work already completed for instance, if sturzstrom are more likely to occur in sedimentary materials as opposed to metamorphic or igneous materials. The characterisation of the climatic conditions and geologic characteristics and structure of materials in relation to events would be useful for indicating areas more at risk of sturzstrom.

8.6 Summary

PFC^{3D} has been utilised to study two idealised events during a sturzstrom: the transition between vertical fall and horizontal runout, and the high speed shearing during runout. The two events have been characterised by oedometer and shear box tests, respectively. The majoirty of other work completed using DEM on rock avalanche or landslide issues has focused on the macroscale behaviour. In comparison, this thesis has attempted to focus solely on the microscale behaviour to consider the effect of material fragmentation on two small specimens and then extrapolate this behaviour to postulate the global behaviour.

Key findings from this research include that dynamic fragmentation is a plausible explanation for the enhanced mobility of sturzstroms under rapid normal loading. Conversely the shear testing has shown that intense crushing during the initial start of shearing is not sufficient to produce kinetic energy that remains in the system for extended periods of time. It has been noted that rapid normal loading due to small topographical changes during runout may cause dynamic fragmentation that maintains a low effective stress and reduces frictional resistance, even in much smaller avalanche or landslide events.

Future work on this topic is recommended to include variations on the specimen design for both the oedometer and shear tests. The idealised specimens used in this research have focused on boulders placed within fines, however a specimen of small rock fragments could be considered, among others. Variations in testing speeds could also be considered. An extended DEM or alternative numerical model could also be considered to model a sturzstrom. This could involve extending the DEM model to encompass the entire avalanche or the coupling of FEM and DEM models to consider macroscopic and microscopic behaviours.

Appendix A

Rait & Bowman (2010)

Numerical Methods in Geotechnical Engineering – Benz & Nordal (eds)
© 2010 Taylor & Francis Group, London, ISBN 978-0-415-59239-0

Dynamic fragmentation in rock avalanches: A numerical model of micromechanical behaviour

K.L. Rait & E.T. Bowman
Department of Civil and Natural Resources Engineering, University of Canterbury, Christchurch, New Zealand

ABSTRACT: It is hypothesized that the dynamic fragmentation of rock clasts is a key mechanism to the long run out of rock avalanches. That is, large rock avalanches tend to travel further than expected in comparison with scaled-up grain flows and this so-called "size effect" is a function of the avalanche size. It is thought that the overburden pressure due to the avalanche size in a large rock avalanche promotes fragmentation of rock clasts and therefore influences run out. The discrete element method is used to investigate this micromechanical behaviour by placing a single brittle fragmenting cluster of particles within a group of non-fragmenting clusters. Using PFC3D this system is placed under a high strain rate to determine the effect of fragmentation on the behaviour of near particles. This paper shows that the overburden strain-rate is directly related to the fragmentation process and that so long as load is applied sufficiently quickly, particles will dynamically fragment rather than simply split or crush; the associated fragments will possess a kinetic energy and therefore collide with near particles. This force of collision can influence the behaviour of the near particles, and under dynamic fragmentation, kinetic energy is dispersed through the system as the near particles fragment. It is postulated that this energy movement produces an isotropic dispersive stress that could explain the long run-out of rock avalanches via the decrease in effective stress within the system.

1 INTRODUCTION

1.1 *Rock avalanches*

Sturzstrom or giant rock avalanches are known to behave significantly differently to other avalanche and landslide phenomena. For mountainous areas around the world these catastrophic hazards are a threat to populations and their lifelines.

A pre-fractured ground mass and a tectonically active region in a steep mountainous area are recognised as an initial condition for many events (Friedmann et al., 2003). A sturzstrom generally begins as a rock fall or rock slide and changes into a dynamically disintegrating rock mass that appears to behave as a granular flow. It can also entrain and/or deposit material as it falls.

Sturzstrom are understood to travel upwards of 30 times in horizontal distance compared to the initial fall height and the momentum of the flow may cause the debris to surge upward especially in valleys where there are confining walls (e.g. Elm and Falling Mountain events, Hsu 1978, Davies and McSaveney 2002). These flows travel for 30–100 seconds and characteristically stop suddenly (Hsu 1975, 1978). The deposit from a sturzstrom can cover tens of square kilometres and can be only a few metres thick at the distal regions which are often deposited as a levee (Friedman et al., 2006). Typically a sturzstrom deposit shows a preserved stratigraphy and inverse grading – silt is present at the base and as a matrix material, with angular blocks supported within the matrix and large boulders sitting on the top. The inverse grading of sturzstrom deposits is perhaps partly explained by the higher probability of fine particles or powder filling small voids as the sturzstrom flows – a sieving process (Friedmann et al., 2006). It may also be explained through greater crushing of rock deeper in the deposit, as discussed later.

Many mechanical theories to describe the behaviour of sturzstrom have been advanced by researchers over the last century. The first of these theories involved mechanical fluidisation which was suggested by Albert Heim in 1882 after his investigation of the famous Elm sturzstrom (Hsu, 1978). This was later supported to some degree by Hsu (1975) who suggested that sturzstrom are likely to follow Bagnoldian (i.e. collisional) grain flow behaviour. Further theories advanced since 1882 include air cushioning (Kent, 1966), air fluidization (Shreve, 1968), the development of frictionite (Erismann, 1979) and acoustic fluidization (Melosh, 1983).

Each of these theories appear relevant to specific sturzstrom events, however they do not appear able to fully explain the behaviours and deposits that are common to all sturzstrom. In particular, these theories are collectively unable to explain the flow of the rock debris as a dry granular mass, the angularity of the blocks and fine silt found in the deposits, and the inverse grading.

McSaveney and co-authors have suggested that fragmentation of rock during a sturzstrom is responsible for producing the very fractured and angular rubble

that commonly occurs in the deposit area (McSaveney 1978; Davies and McSaveney, 2002; Davies et al., 1999). Fragmentation according to Davies et al. (1999), occurs in a sturzstrom as the overburden stress, or pressure from the high volume of material from these events, exceeds the strength of unjointed rock. Therefore the rock material at the base of a sturzstrom is more likely to undergo fragmentation. The fragmentation of a rock in this situation is thought to result in an isotropic dispersive stress that dilates the debris – an effect that is additional to mechanical fluidisation for long run-out in sturzstrom. Davies et al. (1999) state that the process responsible for fragmentation is more likely to involve a crushing or grinding behaviour than grain collisions thus producing substantial silt. As rock clasts undergo fragmentation at the base of a sturzstrom, larger material will be found at the top of the flow, as it is under less pressure, with the finer material at the base – thus inverse grading.

We suggest that the fragmentation of multiple grains occurring under this high overburden stress produces high velocity fragments of rock that impulsively load surrounding grains. As the fragmentation becomes more violent, these impacts produce an internal isotropic pressure that causes the fine rock material to act like a pressurised fluid, reducing effective stress and therefore reducing friction (i.e. following Terzaghi's theory of effective stress and Coulomb-type friction) (Terzaghi and Peck, 1967). The reduction in friction allows the granular material to flow rapidly across terrain and produce long run out.

1.2 *Discrete Element Modelling (DEM)*

The Discrete Element Method utilizes discrete particles that only interact at contact points (Cundall and Strack, 1979). Calculations of contact forces and for the displacements of particles alternate between Newton's second law and a force-displacement law. This is the basis for the software Particle Flow Code in Three Dimensions (PFC^{3D}) built by Itasca Consulting Group.

PFC^{3D} utilises spherical discrete particles that can be arranged and bonded as agglomerates to represent angular and breakable rock or grains, or retained as individuals to represent a granular medium such as sand at low stress. The PFC^{3D} numerical code can show the effect of the applied macroscopic stress and strain on the micro mechanisms within the medium being tested, and give numerical and graphical results relating to particle-level behaviour, such as the number of bonds broken, kinetic energy of the system or individual particles and so on.

Using the DEM method, numerical agglomerates can be impacted against a wall at high velocity or crushed between two platens to investigate comminution in a particle of sand or piece of rock (Thornton et al., 1996; McDowell and Harireche 2002). The strength of the agglomerate is represented by bonding the particles at their contact points. As these bonds break the agglomerate is said to fracture, and fragments occur once groups of bonded particles move away from the original agglomerate being tested.

At sufficiently high impact, there are generally no large fragments remaining due to the extensive shattering that occurs (Kafui and Thornton 2000). Dense agglomerates during high velocity impact will fracture or shatter, whereas loose or highly porous agglomerates simply disintegrate (Mishra and Thornton 2001). Thornton et al., (1996) found through their DEM experiments that a compressive wave propagates from the point of contact through the agglomerate when it impacts a wall at high velocity. If the rate of loading an agglomerate is rapid in comparison to crack growth many flaws will be activated to accommodate the unloading of the stress (Thornton et al., 1996), a conclusion supported by the earlier experimental and analytical work of Grady (1981) and Lundberg (1976).

There are several methods of packing spherical particles to represent a grain or rock clast. The most strongly supported type of packing for crystalline structures is hexagonal close packing (HCP) where every other layer is the same. Random percentages of particles can then be removed to represent flaws and create the correct porosity required to simulate the targeted material. The removal of particles in this random manner from agglomerates produces a Weibull distribution of strengths (McDowell and Harireche 2002).

Under slow isotropic compression agglomerates will undergo deformation through the contact bonds initially being broken by shear. At a critical point unstable fracture begins and the bonds are then broken rapidly through tensile stresses (Bolton, et al., 2008). In agglomerates there are critical bonds that once broken lead to the splitting or disintegration of the agglomerates (Cheng et al., 2003). Under triaxial compression, the frequency of breakage was found to increase as confining pressure increased with around 15% of energy dissipated through bond breakage (Bolton et al., 2008). This suggests that high overburden pressure may cause multiple fragmentation events which in turn could provide a mechanism towards the high mobility of sturzstrom.

In this work we attempt to represent the behaviour that might be seen within a microscopic area of the basal region of a sturzstrom during the fragmentation of rock clasts. We utilize PFC^{3D} to model the resultant influence a fragmenting clast has on surrounding clasts and compare this to the behaviour seen by Cheng et al (2003) and Robertson (2000) in single agglomerate testing.

2 SINGLE AGGLOMERATE TEST

2.1 *Agglomerate creation*

HCP agglomerates built from discrete spherical particles in PFC^{3D} are created following the method outlined by Robertson (2000) and Cheng et al (2003). In Table 1 are listed the properties assigned to the discrete particles.

An agglomerate is built from a maximum of 1150 particles and brought together into an HCP form. This minimizes the space between spheres and eliminates

Table 1. Numerical model details of agglomerate.

Parameter	Dimensions	Numerical Value
Agglomerate radius	m	0.25
Particle radius	m	0.002
Particle density	kgm^{-3}	2650
Normal and shear bond strength	N	4 and 4×10^3
Particle normal and shear stiffness	Nm^{-1}	4×10^6
Particle friction coefficient		0.5
Percentage removed for flaws		20%

overlapping which can cause locked-in forces to occur (Cheng et al., 2003). Statistical variability of strength and shape is introduced by randomly removing particles. In these tests 20% of the particles were removed to reduce the regularity of the packing and introduce flaws (Cheng et al., 2003). Following Robertson (2000) only contact bonds were used. The high coordination number from the use of contact bonds in an HCP packed agglomerate allows the generation of resistance to moment without mechanical complexity. The use of contact bonds only is also supported by the 'Block Caving' example in the Itasca manuals (Itasca, 2008) which states that contact bond values control fragmentation. The agglomerate is then brought to equilibrium such that the mean unbalanced forces acting on the agglomerate are virtually zero.

Single ball drop experiments similar to those in the Itasca Verification Problems manual (Itasca, 2008) were performed to obtain a critical damping factor of 0.2 which corresponds to a coefficient of restitution of approximately 0.55. Platens (represented by smooth and stiff walls in PFC^{3D}) are placed at the base and top of the agglomerate and testing is undertaken by altering the speed of descent of the top platen to reach 40% strain. The intention behind this method is to represent the degree to which rock avalanche material may be crushed via the overburden pressure due to the velocity of loading as the sturzstrom moves at high speed over a changing terrain.

2.2 *Results of single agglomerate testing*

Bond strengths of 4 N and 4 kN were tested to determine what differences may occur with weaker or stronger materials. A randomly chosen agglomerate was crushed under varying platen speeds with only the bond strength changed between tests. Once the prescribed strain was met gravity was turned off so that there was no increase in kinetic energy from the relaxing of grains under the effects of gravity.

From Figure 1A it can be seen that at high strain rates "inertia-induced dynamic impact effects" have an effect on crushing behaviour as also found by Cheng et al (2003). This dynamic regime is suggested as being of the dominant influence on the run out of sturzstrom.

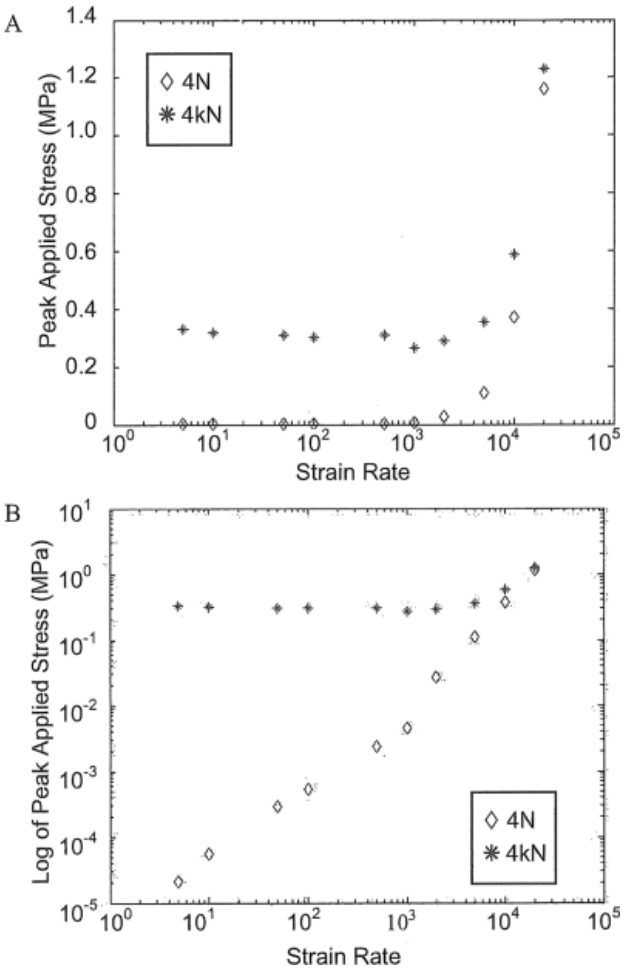

Figure 1. A – Peak applied stress by strain rate for bond strengths; B – Power law relationship for bond strengths.

Both the 4 N and 4 kN data collapse to power law relationships (see Figure 1B) as also reported by Grady (2008) in highly brittle material. The power law relationship for the stronger material appears to begin under a greater strain rate compared to that for the weaker material. Curiously the data from both bond strengths converge to a similar peak stress at high strain.

We find that at low strain rates, after the peak stress is reached and the agglomerate is fractured, the platens continue to approach one another until another contact is found on the agglomerate where another fracture may occur. This behaviour was also reported by Cheng et al (2003). Under high strain rates the material in contact with the load applying platen is crushed quickly into individual particles or fines, with the base of the agglomerate showing multiple fractures. Once the full strain is reached and gravity removed, the base of the agglomerate separates quickly into small fragments and all material disperses quickly.

The stronger material was chosen as the most realistic representation of rock, given that tests on this stronger agglomerate revealed a more brittle nature similar to that seen in real rock. The peak kinetic energy produced from crushing a randomly oriented and flawed agglomerate with 4 kN bond strengths at

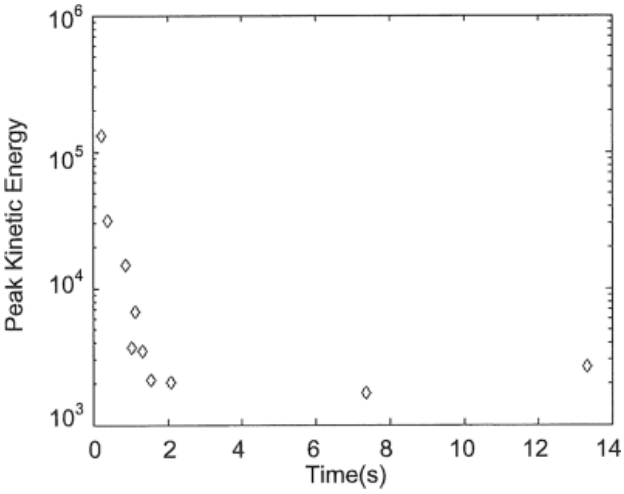

Figure 2. Peak kinetic energy by approximate real time for bond strength of 4 kN by strain rate.

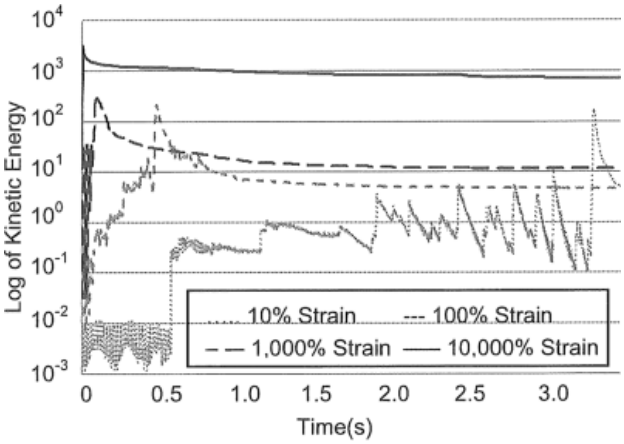

Figure 3. Kinetic energy histories of a 4 kN bond strength HCP agglomerate model.

varying strain rates is plotted against approximate real time in Figure 2. The peak kinetic energies indicate a logarithmic relationship. This suggests fairly sensibly that a low strain rate will take longer to cause fracturing and therefore peak kinetic energy in this synthetic rock sample. Conversely high strain rates appear to obtain peak kinetic energy almost instantaneously suggesting that explosive fragmentation may occur as discussed by Grady (1981).

The kinetic energy history of four of the strain rates tested with the 4 kN model is shown in Figure 3. The residual kinetic energy declines in all cases however remains the highest where the original agglomerate was crushed with high strain rate. We suggest that a very high strain rate, arising from a voluminous load progressing at high speed over a rough terrain, can cause high values of residual internal kinetic energy leading to high numbers of particle impacts within the sturzstrom body. This leads to a high internal pressure, analogous to a pore pressure, and an associated reduction in effective stress which reduces the resistance to sturzstrom motion.

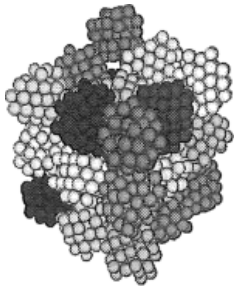

Figure 4. The agglomerate system.

3 AGGLOMERATE SYSTEM TESTING

3.1 *Agglomerate system creation*

The stronger synthetic material was also chosen for the agglomerate system testing. Due to hardware limitations however, the particle radius size was increased to 0.09 m in order to reduce the total number of particles in the system. At a maximum of 69 particles and 282 contact bonds per agglomerate with 27 agglomerates overall in the system, the maximum total number of particles was 1863 with a maximum of 7614 contact bonds of which a maximum of 282 can break.

Pre-determined central coordinates were chosen for the 27 agglomerates. At each set of coordinates an HCP agglomerate was created following Robertson (2000), randomly rotated and flawed by removing 20% of the particles. A cubical arrangement of walls set at low velocity was then used in order to bring the agglomerates into close contact (see Figure 4). All contact bonds were set to extremely high levels initially so that the agglomerates would not unduly break during this compression and subsequent cycling to equilibrium under gravity. The close contact of the agglomerates was used to represent the assumed close contact of rock clasts at the base of a sturzstrom.

Once brought to equilibrium, a top platen was placed above the system and this platen set to descend at varying velocities to compress the system to 40% strain. For these tests, all other confining walls were kept stationary in order to test the system behaviour under one dimensional loading at varying strain rates. Once 40% strain had been achieved in these tests, as with the single agglomerate tests, gravity was turned off so as to remove any effects on the kinetic energy of the system relaxing.

The stress on each wall and kinetic energy of the system was logged and analysed. Stress is calculated as the ratio of the force on the wall (or platen) by the cross-sectional area of agglomerates that are in contact – $9\pi r^2$ (9 agglomerates in contact with each platen). The peak applied stress is then defined as the maximum stress that occurs on the top platen as it descends.

3.2 *Results of agglomerate system testing*

At high strain rate the central agglomerate quickly separates into individual particles or fines – all bonds are broken. As the system relaxes the fine particles move throughout the system settling into the spaces between

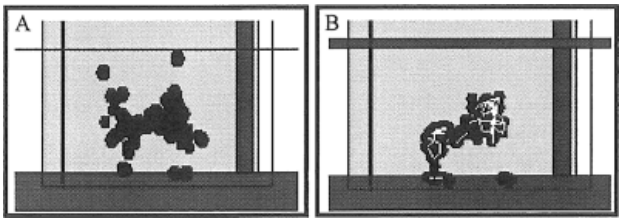

Figure 5. Resulting graphic of the central agglomerate behaviour at 40% strain after compression under high strain rate (A) and low strain rate (B) of the agglomerate system.

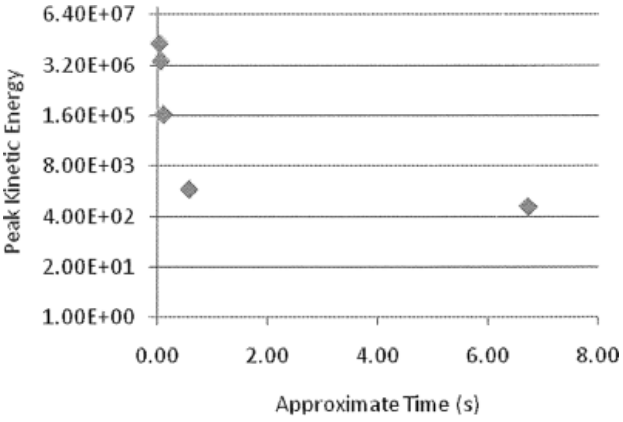

Figure 6. Peak kinetic energy by strain rate versus time.

the surrounding agglomerates. These fines move both horizontally and vertically as the surrounding agglomerates push into the space left void from the dynamic breakage of the central agglomerate (see Figure 5A).

In comparison, at low strain rate, the central agglomerate slowly fractures into a few fragments surrounded by fines (around 90% of the bonds are broken at 40% strain). As the system relaxes, the fines drift to the base of the system and the fragments are held in the central void of the system by the surrounding agglomerates (see Figure 5B).

As seen in the single agglomerate testing and in the work completed by Cheng et al (2003), the value of the peak applied stress grows exponentially as strain rate increases. As discussed in the single agglomerate testing above this collapses to a power law relationship where the power law begins at a higher value of strain rate due to the use of the stronger material in the breakable agglomerate. Similarly the peak kinetic energy follows the same logarithmic trend indicated in the single agglomerate testing. The highest peak kinetic energy occurs almost instantaneously at high strain rate and the lowest peak kinetic energy occurs after approximately 6.5 seconds for the lowest strain rate of 10% (see Figure 6).

From Figure 7 it can be seen that the higher strain rates produce higher kinetic energy. Over time all kinetic energy histories dissipate towards zero after gravity is removed and the particles and agglomerates settle. These tests on a system of agglomerates show the kinetic energy from a higher strain rate dissipating faster than that of a low strain rate. This is likely to be due to a higher frequency of impacts with adjacent

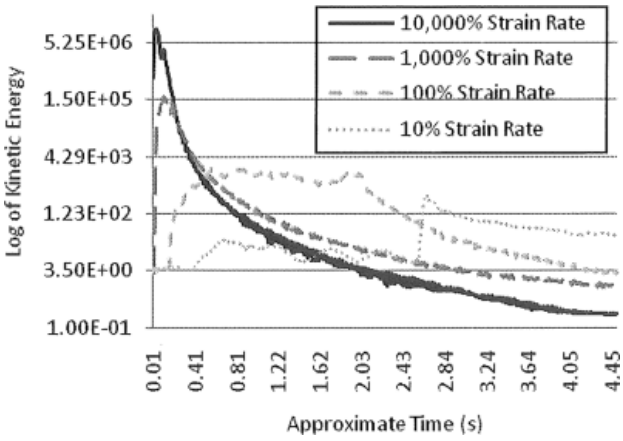

Figure 7. Kinetic energy of agglomerate system.

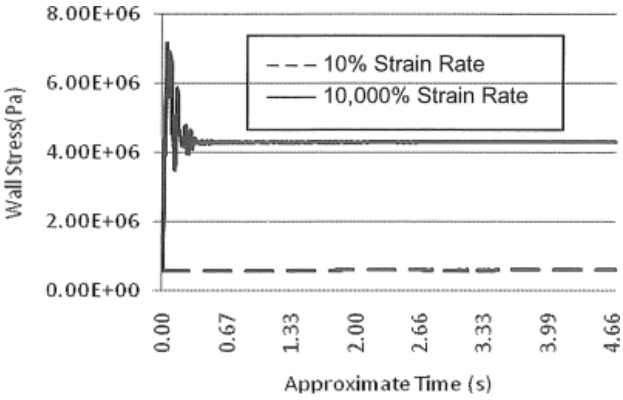

Figure 8. Average horizontal wall stress.

particles, leading to faster energy dissipation in the particle system overall.

Compare this graph with Figure 8 of the average wall stress in the horizontal directions. The high strain rate case shown here retains a much greater proportion of wall stress after the particles have settled than is seen for the low strain rate. Although the high strain rate may lose kinetic energy at a faster rate after a fragmentation event, the high average stress on the horizontal walls (in comparison to the test at low strain rate) suggests that there is substantial internal pressure applied to the surrounding agglomerates from both the strain and impulsive loading of the fragmented grains from the central agglomerate.

4 DISCUSSION

The complex nature of sturzstrom – for example their temporal unpredictability, high speed, large volume of material and short duration – means that it is virtually impossible to study these phenomena in situ. This paper presents a study utilizing discrete numerical modelling in PFC^{3D} to investigate the micromechanical behaviour postulated to occur during a sturzstrom which may influence both run out and deposit type. From the results presented above it is clear that modelling in PFC^{3D} is capable of providing useful information about the likely internal mechanisms involved in sturzstrom.

From the results shown of the single agglomerate and multi agglomerate system tests it is found that a high strain rate modelled by the high velocity of a top loading platen produces high peak kinetic energy levels in the material tested. This high strain rate also represents the fast application of a load which results in explosive fragmentation which separates the material into fines. At low strain rate (or low platen velocity), the material separates into fragments with fines drifting toward the base platen. Similar results have been reported by Mishra and Thornton (2001) when impacting single agglomerates at varying velocities into a stiff platen.

The agglomerate system results indicate that pressure increases on surrounding agglomerates when a neighbouring agglomerate explosively fragments. The fines from a fragmented particle appear to travel throughout the available spaces between other agglomerates with the resultant void being filled by these other agglomerates. This behaviour suggests that towards the base of a sturzstrom, rock clasts may fragment explosively causing fine rock powder and dilation of the flow and as the effective stress of the whole system is reduced, produce long run out.

5 FURTHER WORK

In future work to further investigate the micromechanical behaviour of sturzstrom, it is intended to continue discrete numerical testing examining the impact of an explosively fragmenting agglomerate on its neighbours where the neighbouring agglomerates are also able to fragment. This work will utilise a larger particle system and more highly powered computational hardware.

ACKNOWLEDGEMENTS

Funding for this work has been provided by the Department of Civil and Natural Resources Engineering at the University of Canterbury.

REFERENCES

Bolton, M. D., Nakata, Y., Cheng, Y. P. (2008). Micro- and macro-mechanical behaviour of DEM crushable materials. *Geotechnique* 58(6): 471–480.

Cheng, Y. P., Bolton, M. D., Nakata, Y. (2003). Crushing and plastic deformation of soils simulated using DEM. *Geotechnique* 54(2): 131–141.

Cundall, P. A. and Strack O. D. L. (1979). Discrete numerical model for granular assemblies. *Geotechnique* 29(1): 47–65.

Davies, T. R., McSaveney, M. J., Hodgson, K. A. (1999). A fragmentation-spreading model for long-runout rock avalanches. *Canadian Geotechnical Journal* 36(6): 1096–1110.

Davies, T. R. and McSaveney M. J. (2002). Dynamic simulation of the motion of fragmenting rock avalanches. *Canadian Geotechnical Journal* 39(4): 789–798.

Erismann, T. H. (1979). Mechanisms of large landslides. *Rock Mechanics* 12: 15–46.

Friedmann, S. J., Kwon, G., Losert, W. (2003). Granular memory and its effect on the triggering and distribution of rock avalanche events. *Journal of Geophysical Research-Solid Earth* 108(B8).

Friedmann, S. J., Taberlet, N., Losert, W. (2006). Rock-avalanche dynamics: insights from granular physics experiments. *International Journal of Earth Sciences* 95(5): 911–919.

Grady, D. E. (1981). Fragmentation of solids under impulsive stress loading. *Journal of Geophysical Research* 86(NB2): 1047–1054.

Grady, D. E. (2008). Fragment size distributions from the dynamic fragmentation of brittle solids. *10th Hypervelocity Impact Symposium (HVIS 2007)*, Williamsburg, VA.

Hsu, K. J. (1975). Catastrophic debris streams (sturzstroms) generated by rockfalls. *Geological Society of America Bulletin* 86(1): 129–140.

Hsu, K. J. (1978). Albert Heim: Observations on Landslides and Relevance to Modern Interpretations. *Rockslides and Avalanches I.* B. Voight (ed).

Itasca (2008). *Particle flow code in three dimensions*, Itasca Consulting Group Inc.

Kafui, K. D. and Thornton C. (2000). Numerical simulations of impact breakage of a spherical crystalline agglomerate. *Powder Technology* 109(1–3): 113–132.

Kent, P. E. (1966). Transport mechanism in catastrophic rock falls. *Journal of Geology* 74(1): 79–83.

Lundberg, B. (1976). Split Hopkinson bar study of energy absorption in dynamic rock fragmentation. *International Journal of Rock Mechanics and Mining Sciences* 13(6): 187–197.

McDowell, G. R. and Harireche O. (2002). Discrete element modelling of soil particle fracture. *Geotechnique* 52(2): 131–135.

McSaveney, M. J. (1978). Sherman Glacier Rock Avalanche, Alaska, U.S.A. *Rockslides and Avalanches I.* B. Voight (ed).

Melosh, H. J. (1983). Acoustic fluidization. *American Scientist* 71(2): 158–165.

Mishra, B. K. and Thornton C. (2001). Impact breakage of particle agglomerates. *International Journal of Mineral Processing* 61(4): 225–239.

Robertson, D. (2000). *Computer simulations of crushable aggregates.* PhD Dissertation. University of Cambridge.

Shreve, R. L. (1968). Leakage and fluidization in air-layer lubricated avalanches. *Geological Society of America Bulletin* 79(5): 653–657.

Terzaghi, K. and R. B. Peck (1967). *Soil Mechanics in Engineering Practice.* New York, John Wiley & Sons, Inc.

Thornton, C., Yin, K. K., Adams, M. J. (1996). Numerical simulation of the impact fracture and fragmentation of agglomerates. *Journal of Physics D-Applied Physics* 29(2): 424–435.

Appendix B

Rait, Bowman & Lambert (2012)

Rait, K. *et al*. (2012) ***Géotechnique Letters* 2**, 167–172, http://dx.doi.org/10.1680/geolett.12.00038

Dynamic fragmentation of rock clasts under normal compression in sturzstrom

K. L. RAIT*, E. T. BOWMAN* and C. LAMBERT*

Sturzstrom are massive and catastrophic long run-out rock avalanches that occur in mountainous areas around the world. The dynamic fragmentation of rock clasts is considered by some to be a key mechanism leading to long run-out behaviour in sturzstrom, but details on the micromechanics of the process are lacking. It is hypothesised here that the high strain rates applied to rock clasts at depth within a sturzstrom in motion promote dynamic fragmentation. The kinetic energy of the fine material generated during fragmentation is postulated to decrease effective stress in the system via a disruption of load transfer between heavily loaded particles (i.e. the strong force network). This results in a reduction in effective friction within the system, leading to longer run-out or greater clast spreading than would otherwise occur. The discrete element method is utilised via PFC^{3D} to investigate this behaviour by placing a single brittle cluster of particles within a cubic arrangement of non-breakable clusters, each of which is hexagonally close packed. This system is placed under varying normally applied strain rates while determining the effect of fragmentation rate on the behaviour of near particles. It was found that strain rate is directly related to the fragmentation process where, so long as a load is applied sufficiently quickly, particles will dynamically fragment rather than simply split or crush. The strain rate tests indicate an abrupt change from a static to dynamic regime where the process of bond breakage changes from fracture to explosive fragmentation and kinetic energy dominates frictional dissipation of energy.

KEYWORDS: discrete-element modelling; landslides; particle-scale behaviour

INTRODUCTION

In steep mountainous areas around the world, pre-fractured ground masses and tectonic activity can be a precursor to long run-out rock avalanches or sturzstrom (Friedmann *et al.*, 2003). Sturzstrom are catastrophic dry rock avalanches that travel substantially further horizontally than vertically (Hsu, 1975). A sturzstrom generally begins as a rock fall or rock slide before the debris material completely disintegrates during the high-speed run-out. Typically, the debris will be deposited with fine rock silt dominating the base, the central part consisting of disaggregated or jigsaw fractured rocks suspended within a silt-sized matrix and, near the surface, large angular boulders forming a 'carapace' (Dunning & Armitage, 2010). Throughout the deposit, the stratigraphy from the original failure site is retained (McSaveney *et al.*, 2000).

The behaviour of sturzstrom has been investigated by several researchers. Albert Heim was the first to suggest that the jostling flow of a sturzstrom was one of rearward blocks impacting forward blocks (Hsu, 1978). Hsu (1978) describes the possibility of Bagnoldian grain flow involvement where the flow behaviour is caused by impacts between grain layers as upper layers attempt to overtake lower layers in a sheared system (Bagnold, 1954). Other mechanical theories that have been suggested include air cushioning (Shreve, 1968) (since refuted by most researchers due to the occurrence of sturzstrom on the Moon and Mars), the formation of frictionite (Erismann, 1979), acoustic fluidisation (Melosh, 1983) and dynamic fragmentation (Davies *et al.*, 1999). Frictionite is not seen across all sturzstrom deposits and acoustic fluidisation may be related to fragmentation as acoustic waves are likely to be transmitted by boulder impacts (Melosh, 1983).

There are fundamental geomechanics questions regarding the ability of dynamic fragmentation to reduce friction between particles. Dynamic fragmentation can be described as a rock rupture event that occurs so rapidly under loading that multiple sites of failure appear simultaneously within the material and cause it to break apart into fragments. Davies & McSaveney (2008) suggest that, on a large scale, multiple fragmentation events in the basal area of a sturzstrom could create an isotropic dispersive pressure, like a pore pressure reducing effective stress and therefore friction. On a microscale, this dynamic behaviour may disrupt the strong force chains in the system as newly created fines disperse violently during a fragmentation event.

Both the effects of overburden load and shear are likely to influence the behaviour of a sturzstrom. The focus of this paper is specifically on the influence of overburden load on fragmentation. Dynamic fragmentation requires the rapid deposition of material in order to produce enough stress to overcome the strength of the underlying material (Grady, 1981). Beneath the carapace of a sturzstrom in motion, the combined impulsively applied load from multiple large boulders and surrounding material may provide enough pressure to fragment material towards the basal layer.

Using the discrete element method via PFC^{3D}(Itasca, 2008), this paper presents a model of the fragmentation behaviour of a synthetic hexagonally close packed (HCP) material under different strain rates. Preliminary work performed by Rait & Bowman (2010) is followed and associated forces and stresses in the synthetic sturzstrom material are measured as the strain rate is varied.

Manuscript received 7 June 2012; first decision 24 July 2012; accepted 30 August 2012.
Published online at www.geotechniqueletters.com on 28 September 2012.
*University of Canterbury, Christchurch, New Zealand

SYNTHETIC MATERIAL TESTING

The initial failure phase of a sturzstrom is suggested as a rock fall or rock slide that then dynamically disintegrates as the material is compressed and sheared. Only the compressive process is examined here. The oedometric strain rate test is designed to investigate the breakage behaviour of a rock when confined between other boulders as disintegration takes place. To explore this phenomenon, oedometric tests in PFC^{3D} were performed on five different but statistically similar HCP specimens (HCP1–HCP5); all specimens contain cubically arranged clusters with only the central cluster of each cube being breakable (as indicated in Fig. 1). Each cluster, of radius 0·5 m, was created at a designated central coordinate with all particles of radius 0·09 m (see material values in Table 1), following the process for HCP packing outlined by Robertson (2000) and randomly rotating each cluster. Flaws were introduced into each cluster by removing 20% of the particles as suggested by Cheng *et al.* (2003) and the particles were then bound together using contact bonds. The cubic arrangement of clusters was gently brought together using the confining walls until just in contact and the whole system was settled to equilibrium.

As the clusters were arranged using the same particle size, the difference between specimens rests solely on the random rotation of each cluster and the random placement of flaws. A suite of oedometric strain rate tests was performed on each specimen, ranging from quasi-static compression at 0·001 s^{-1} up to fast compression at 10 s^{-1}.

The microscopic stresses and bond breakages in the breakable cluster were measured, along with system energies (kinetic, frictional, boundary and so forth) and overall wall stresses, to determine what effect, if any, a fragmenting boulder may have on a group of surrounding confined boulders. The microscopic stresses of the breakable cluster were measured via the summation of the mean and deviatoric stresses on each individual particle identified as belonging to the central cluster.

Table 1. HCP material details

Parameter	Value
Cluster radius: m	0·5
Particle radius: m	0·09
Particle density: kg/m^3	2650
Particle friction coefficient	0·50
Particle normal and shear stiffness (central cluster): N/m	4×10^6
Normal and shear bond strength (central cluster): N	4×10^3
Proportion removed for flaws: %	20

RESULTS AND DISCUSSION

Figure 2 shows the microscopic deviatoric stress q plotted against microscopic mean stress p for HCP3 (with Fig. 3 indicating the maximum values reached for all specimens at 15% axial strain), while Fig. 4 shows the microscopic stress ratio (q/p) plotted against axial strain. The stress paths are similar in the early stages of the compression tests up to 6% strain. For the lower strain rates, however, deviatoric stress q reaches a peak of 12 MPa at an axial strain of 15% whereas for the 10 s^{-1} strain rate, q rises to 46 MPa at the same strain. Figure 3 shows that this difference of maximum q at 15% axial strain occurs across all specimens, following the same behaviour as that of HCP3.

Figure 4 shows that, with an increase in axial strain, the stress ratio varies erratically for the 0·001 s^{-1} strain rate tests, with peaks occurring throughout associated with large numbers of bonds being broken (Fig. 5). The first large breakage event at around 5% axial strain produces a drop in the stress ratio once the material settles during the next phase of overburden pressure increase. For the test at 1 s^{-1}, in which bond breakage occurs more gradually with axial strain from around 5%, breakage produces positive spikes in stress ratio, albeit less abrupt ones. In the 10 s^{-1} strain rate tests though, we see a decrease in the stress ratio at around 6% axial strain, as breakage commences. The stress ratio then continues to decrease, remaining below that of the lower strain rate values until towards the end of the test where the stress ratios generally meet (Fig. 4). This suggests that the higher strain rate is producing a reduction in interparticle friction during the main breakage period, after which both lower and high strain rate tests become nearly equal. The axial strain point at which the behaviour becomes similar is a result of breakage occurring to the extent that rolling between particles may take place.

The wall stress response provides an interesting comparison between the 0·001, 1 and 10 s^{-1} strain rates. Figures 6(a)–(c) show that the average wall stress taken across all tests for the X- and Y-directions (see Fig. 1) increases smoothly with strain and that there is little

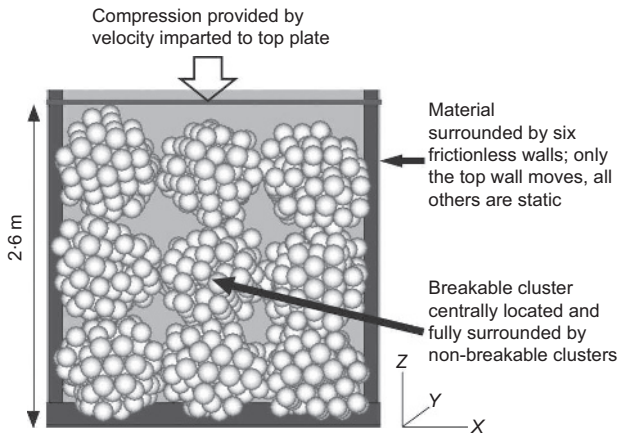

Fig. 1. Testing process of the cubic arrangement of HCP clusters under oedometric compression

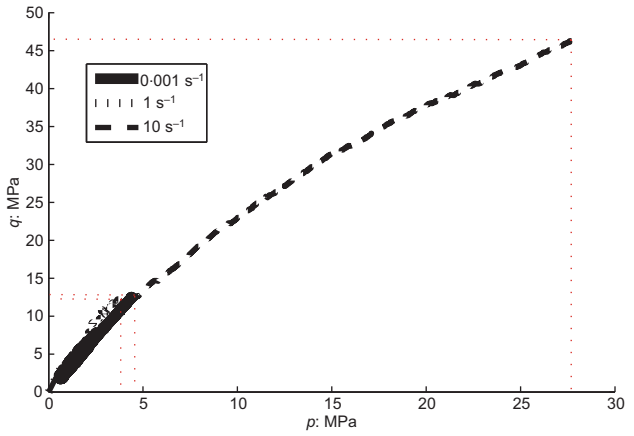

Fig. 2. Stress path plot for HCP3 for 0·001, 1 and 10 s^{-1} strain rates to 15% axial strain

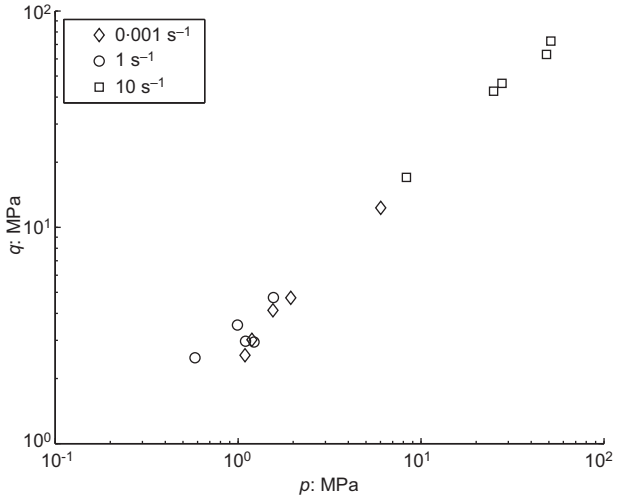

Fig. 3. Stress path maximum values for all HCP specimens for 0·001, 1 and 10 s^{-1} strain rates to 15% axial strain

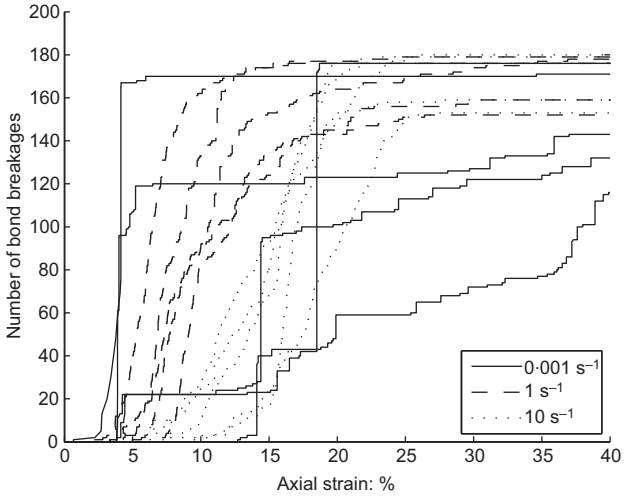

Fig. 5. Plot of bond breakage throughout the test for 0·001, 1 and 10 s^{-1} strain rates for all HCP specimens

variability when comparing the averages of *X*- and *Y*-directions across all HCP specimens. The bars in Figs 6(a)–(c) show the range of wall stresses observed from specimen to specimen. As shown in Fig. 6(d) for an individual specimen, once breakage begins, the material becomes non-isotropic and therefore the wall stresses in the *X*- and *Y*-directions differ. This is also indicated by the lengthening of the range bars in Figs 6(a)–(c) at higher axial strain values. Figure 6(d) also shows that the 1 s^{-1} and 10 s^{-1} tests have the same general increase in wall stresses as the 0·001 s^{-1} test, but they now exhibit distinctive 'wave-like' patterns with strain. It appears that the wave-like patterns occur due to an interaction between the compression effect and the response of kinetic energy associated with the rate of compression. A damped wall stress response occurs as a result, slightly delayed relative to the kinetic energy peaks; the wider implications of this are yet to be confirmed.

Figure 7 plots the logarithm of peak kinetic energy against applied strain rate for all five specimens tested at all the strain rates considered. As strain rate increases, the peak kinetic energy does not begin to increase until a threshold of 1 s^{-1} is reached, beyond which a dramatic increase emerges with increasing strain rate. Below a strain rate of 1 s^{-1}, a similar and near-constant difference in peak kinetic energy develops between the specimens at increasing strain rates. By 10 s^{-1} strain rate, it is difficult to discern the different data on the log plot. These results indicate that, at lower loading rates, the peak kinetic energy developed is dependent only on the initial state of the cluster (flaws and loading direction) and not on the loading rate, whereas beyond a rate of 1 s^{-1}, the peak kinetic energy is less influenced by the initial state and instead becomes a function of the loading rate.

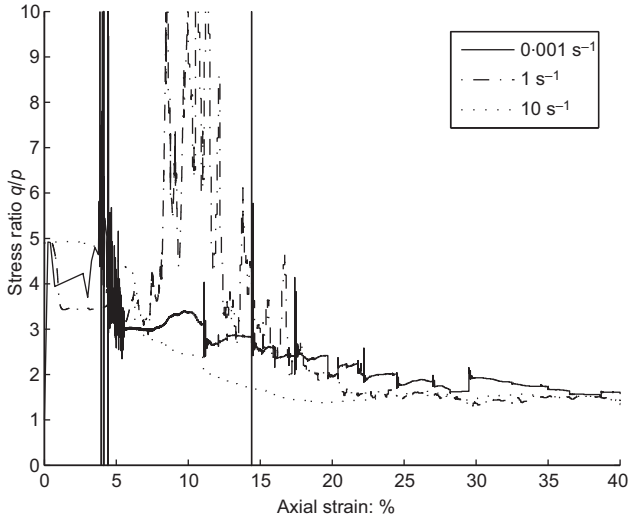

Fig. 4. Plot of stress ratio behaviour throughout the test for 0·001, 1 and 10 s^{-1} strain rates for HCP3

The relationships between the varying energies that can be traced in PFC^{3D} can be clearly seen in Fig. 8 for the 0·001 s^{-1} and 10 s^{-1} tests for HCP3. For the 0·001 s^{-1} test, the increasing boundary work is converted into strain energy and frictional dissipation, with kinetic energy remaining very low (the 1 s^{-1} strain rate and other tests are similar). At the 10 s^{-1} strain rate, a very different behaviour emerges, with three distinct peaks in boundary work replicated in the kinetic energy and strain energy. At this high strain rate there is an abrupt change where the boundary work is now converted into strain energy and kinetic energy while frictional dissipation remains very low. The sudden 'bursts' of kinetic energy are not seen in any of the lower strain rates and appear to indicate the reaching of a dynamic or explosive regime. This is further clarified in Fig. 8(c), which shows similar initial bursts of kinetic energy from all specimens across all strain rates up to around 1% axial strain, followed by clearly differentiated kinetic energy maxima that are dependent on the strain rate of the test.

A comparison of breakage rate over axial stress for different strain rates is shown in Fig. 9 for three specimens. This indicates that the 10 s^{-1} strain rate test produced the most consistent breakage across the test, with the majority of breakage occurring between 5 and 25% strain (see also Fig. 5). The remainder of the test resulted in a few remaining breakages and movement of the particles to their final resting positions. In contrast, the 0·001 s^{-1} strain rate test shows a few distinct peaks of high breakage rate as the material cleaves into fragments, but otherwise far less breakage by the test end at 40% strain. During these significant fragmentation events the released strain energy is dissipated by friction (see Fig. 8).

For low strain rates, Fig. 7 shows that the maximum kinetic energy produced is around two orders of magnitude less than that for the highest strain rate test. This suggests

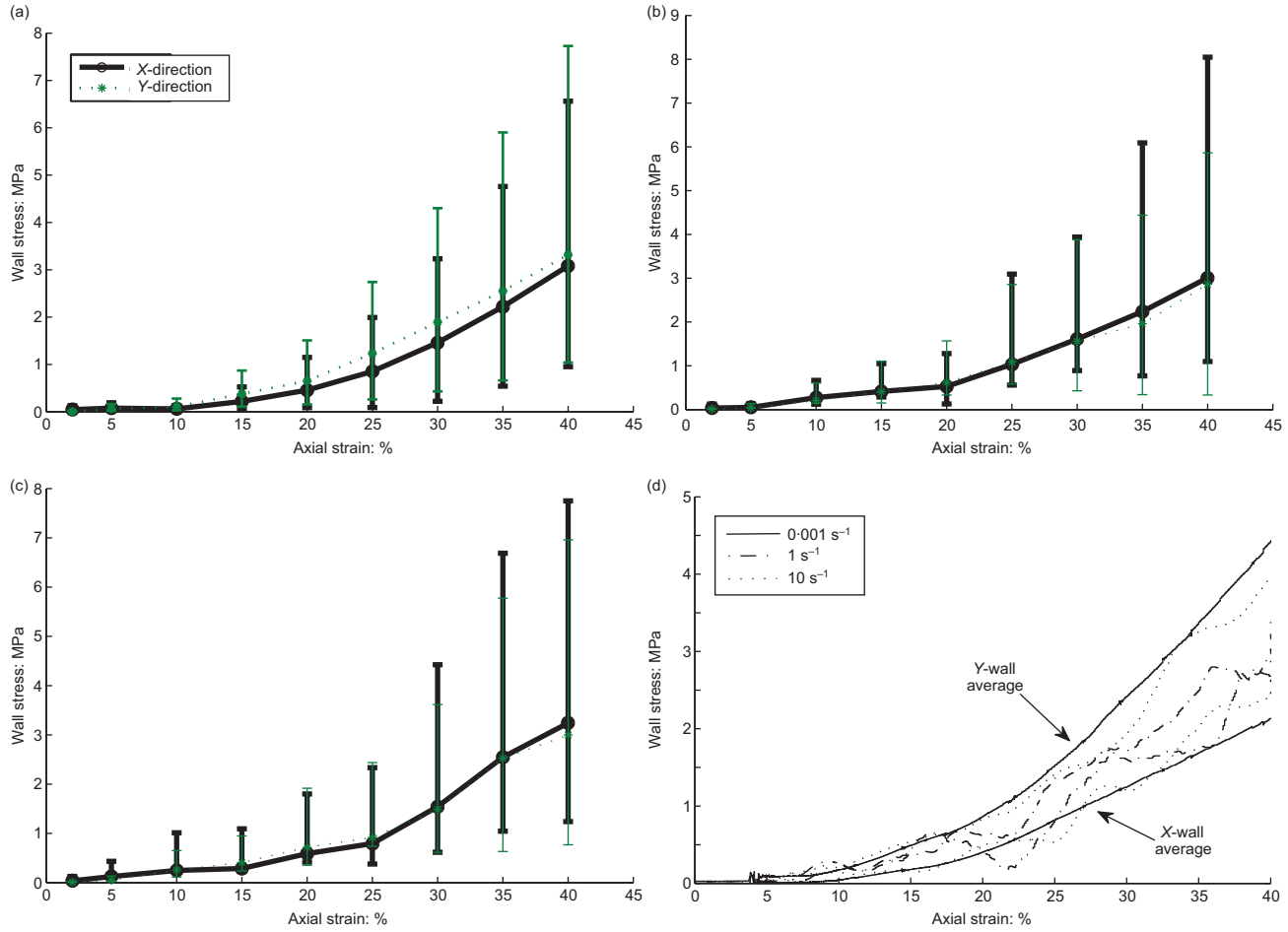

Fig. 6. *X*- and *Y*- direction average wall stresses for strain rates of (a) 0·001 s^{-1}, (b) 1 s^{-1} and (c) 10 s^{-1} across all HCP specimens; range bars indicate minimum to maximum values observed. (d) Behaviour of *X*- and *Y*- direction average wall stresses for HCP3

that, although applying a low strain rate can cause breakage in this particular synthetic specimen, the slow transfer of the forces allows for only the weakest bonds to break in the central cluster and these are represented by the large breakage events. The 1 s^{-1} strain rate test shows the majority of breakage occurring relatively early (with the greatest rate of breakage occurring at 7% strain, albeit at a lower rate than for the 0·001 s^{-1} strain rate) with few bonds left by 20% strain. The maximum kinetic energy is beginning to climb past that of the pseudo-static tests from 0·001 s^{-1} to 0·1 s^{-1}. Together, these results suggest that rapid application of an overburden load can cause a large amount of damage to occur to a rock-type material with relatively little strain developed so long as it can overcome the strength of the material. The breakage behaviour combined with the impulsive kinetic energy in response to the boundary work and the oscillating wall stresses at higher strain rate suggest that, for the highest rate of strain, the central cluster has disintegrated via dynamic fragmentation.

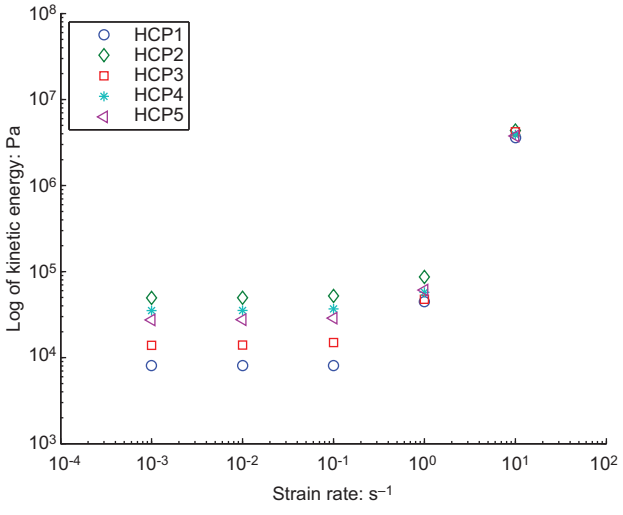

Fig. 7. Maximum kinetic energy results across all HCP specimens by strain rate value

CONCLUSIONS

One mechanism that may cause fragmentation in sturzstrom is the high-speed application of overburden load. The results of tests on an HCP agglomerate system under varying strain rates support the suggestion that dynamic fragmentation can reduce the mobilised friction q/p during breakage. A high loading rate is seen to cause sustained breakage, which produces a much higher peak in kinetic energy compared with a low loading rate. For rapid loading, the stress ratio decreases quickly at the onset of breakage, suggesting that the explosive dispersion of the rapidly created fines reduces the effective stress and therefore friction when fragmentation occurs. Comparison between the test results at strain rates

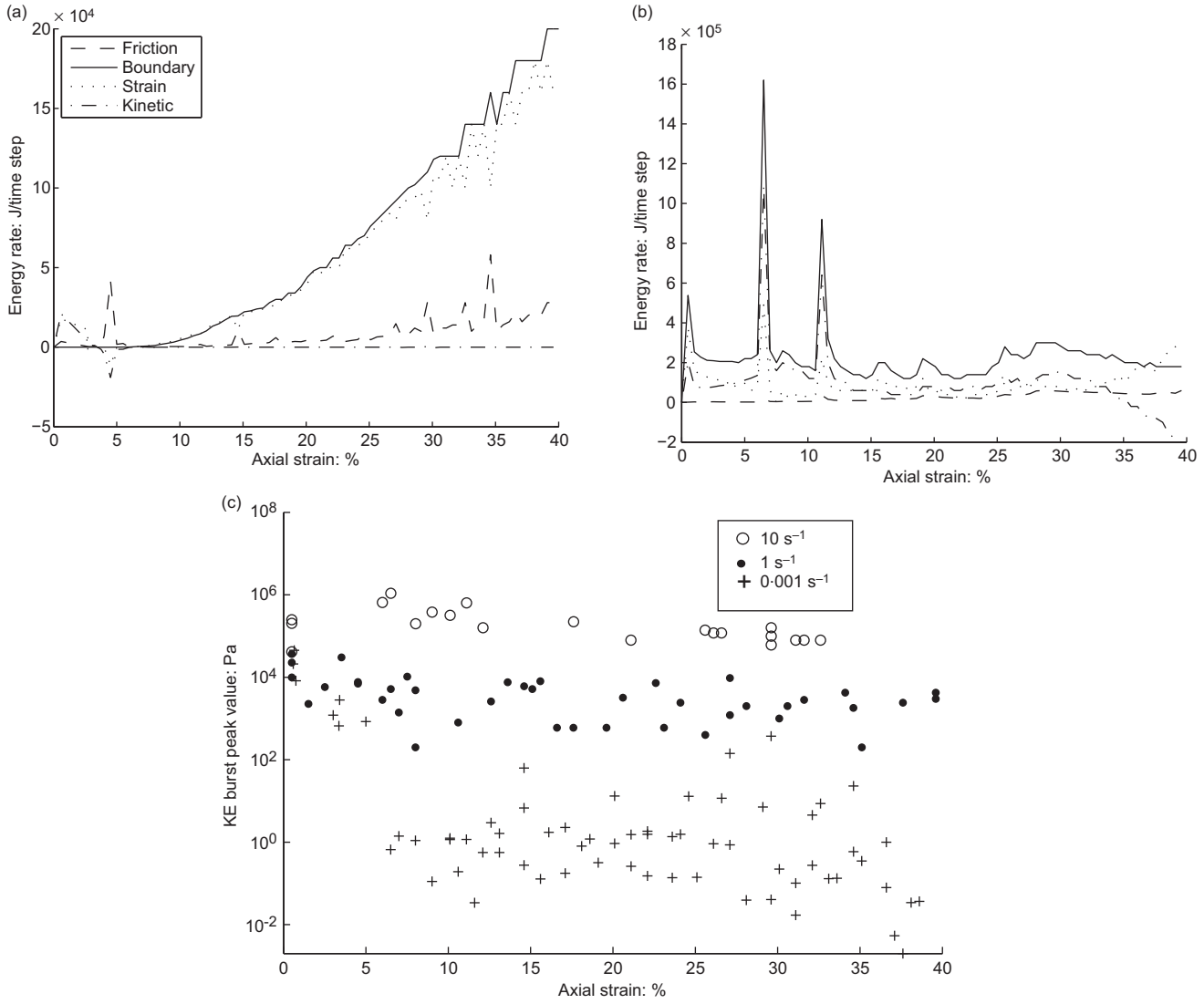

Fig. 8. Energy behaviour for strain rates of (a) 0·001 s^{-1} and (b) 10 s^{-1} for HCP3. (c) Kinetic energy (KE) burst maxima across all HCP specimens for all strain rates

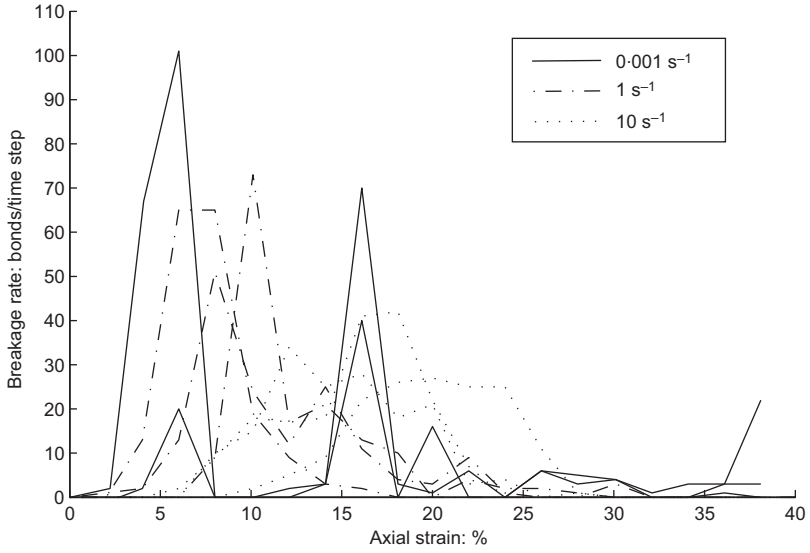

Fig. 9. Breakage rate comparison for 0·001 s^{-1}, 1 s^{-1} and 10 s^{-1} strain rates for HCP1, HCP3 and HCP5

from 0·001 s^{-1} to 10 s^{-1} shows the progression from static to dynamic loading and suggests that overburden rate is indeed important to the behaviour of sturzstrom. Future work will examine the influence of shearing rate within sturzstrom and will examine materials modelled on specific rock types.

Acknowledgements

The authors wish to acknowledge the support of the Department of Civil and Natural Resources Engineering at the University of Canterbury, and the New Zealand Earthquake Commission, as well as and the reviewers for their helpful comments.

REFERENCES

Bagnold, R. A. (1954). Experiments on a gravity-free dispersion of large solid spheres in a Newtonian fluid under shear. *Proc. Royal Soc. London A Math. Phys. Sci.* **225**, No. 1160, 49–63.

Cheng, Y. P., Nakata, Y. & Bolton, M. D. (2003). Discrete element simulation of crushable soil. *Géotechnique* **53**, No. 7, 633–641.

Davies, T. R. & McSaveney, M. J. (2008). The role of rock fragmentation in the motion of large landslides. *Engng Geol.* **109**, No. 1–2, 67–79.

Davies, T. R., McSaveney, M. J. & Hodgson, K. A. (1999). A fragmentation-spreading model for long-runout rock avalanches. *Can. Geotech. J.* **36**, No. 6, 1096–1110.

Dunning, S. A. & Armitage, P. J. (2010). The grain-size distribution of rock-avalanche deposits: implications for natural dam stability. In *Natural and artificial rockslide dams* (Evans, S. G. *et al*. (eds)). Berlin: Springer, pp. 479–498.

Erismann, T. H. (1979). Mechanisms of large landslides. *Rock Mech.* **12**, No. 1, 15–46.

Friedmann, S. J., Kwon, G. & Losert, W. (2003). Granular memory and its effect on the triggering and distribution of rock avalanche events. *J. Geophys. Res. Solid Earth* **108**, No. B8, 2380–2391.

Grady, D. E. (1981). Fragmentation of solids under impulsive stress loading. *J. Geophys. Res.* **86**, No. NB2, 1047–1054.

Hsu, K. J. (1975). Catastrophic debris streams (sturzstroms) generated by rockfalls. *Geol. Soc. Am. Bull.* **86**, No. 1, 129–140.

Hsu, K. J. (1978). Albert Heim: observations on landslides and relevance to modern interpretations. In *Rockslides and avalanches,* Vol. I (Voight, B. (ed.)). Amsterdam: Elsevier, pp. 71–93.

Itasca (2008). *Particle flow code in three dimensions*. Minneapolis, MN: Itasca Consulting Group Inc.

McSaveney, M. J., Davies, T. R. & Hodgson, K. (2000). A contrast in deposit style and process between large and small rock avalanches. Paper presented at the *8th International Symposium on Landslides, Cardiff*.

Melosh, H. J. (1983). Acoustic fluidization. *Am. Sci.* **71**, No. 2, 158–165.

Rait, K. L. & Bowman, E. T. (2010). Dynamic fragmentation in rock avalanches: A numerical model of micromechanical behaviour. Paper presented at the *7th European Conference on Numerical Methods in Geotechnical Engineering, Trondheim*.

Robertson, D. (2000). *Computer simulations of crushable aggregates*. PhD thesis, University of Cambridge, Cambridge, UK.

Shreve, R. L. (1968). Leakage and fluidization in air-layer lubricated avalanches. *Geol. Soc. Am. Bull.* **79**, No. 5, 653–657.

Appendix C

Oedometric HCP Testing

C.1 Single Agglomerate

C.1.1 4N Bond Strength

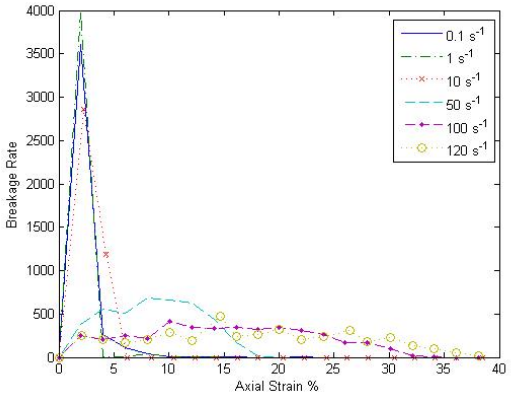

(a) Specimen 2

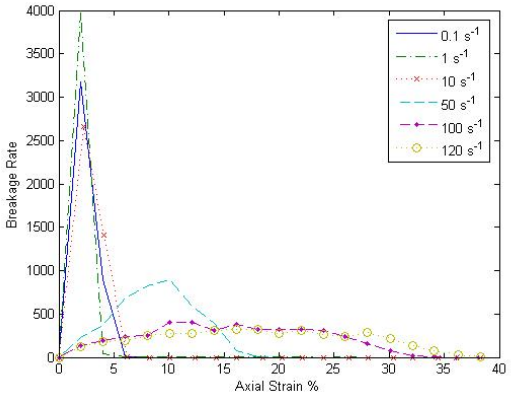

(b) Specimen 3

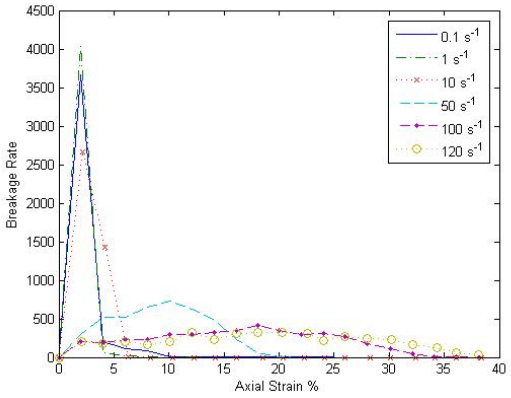

(c) Specimen 4

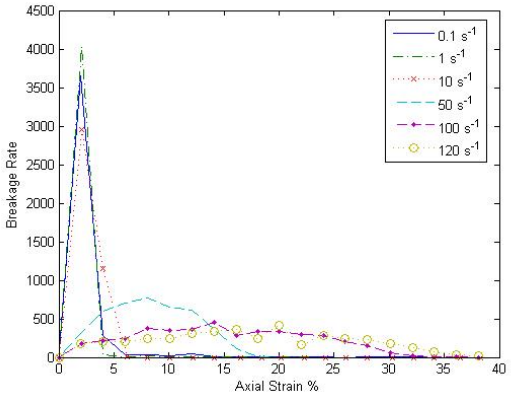

(d) Specimen 5

Figure C.1: Breakage rate

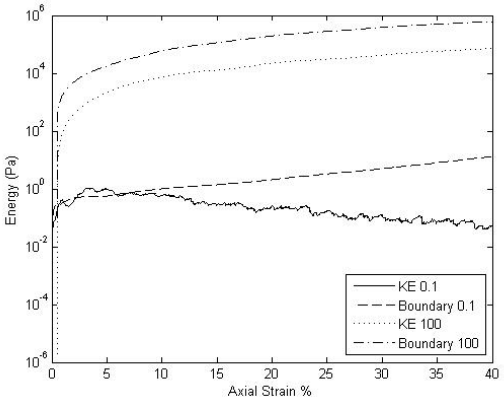

(a) Specimen 2

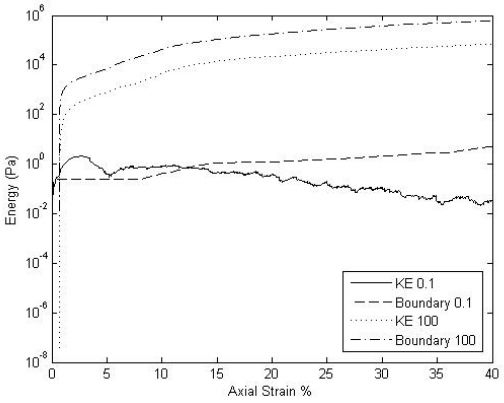

(b) Specimen 3

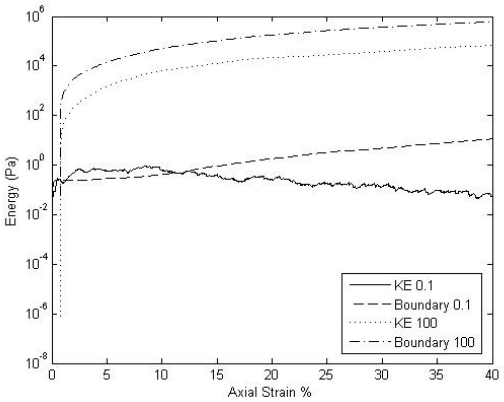

(c) Specimen 4

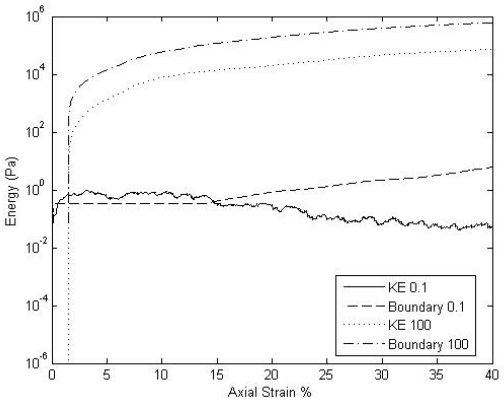

(d) Specimen 5

Figure C.2: Kinetic and boundary energy comparison

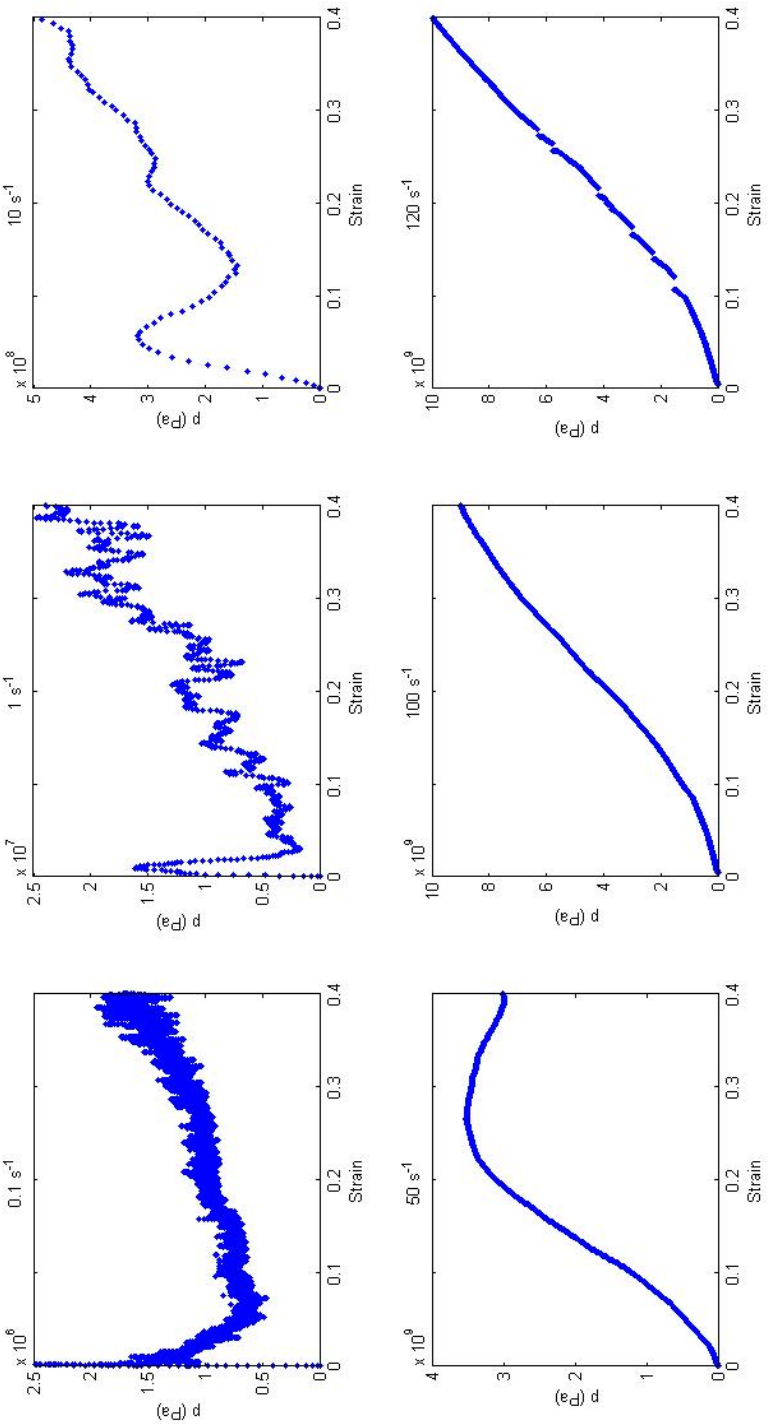

Figure C.3: Mean stress response for specimen 2 at 4N bond strength

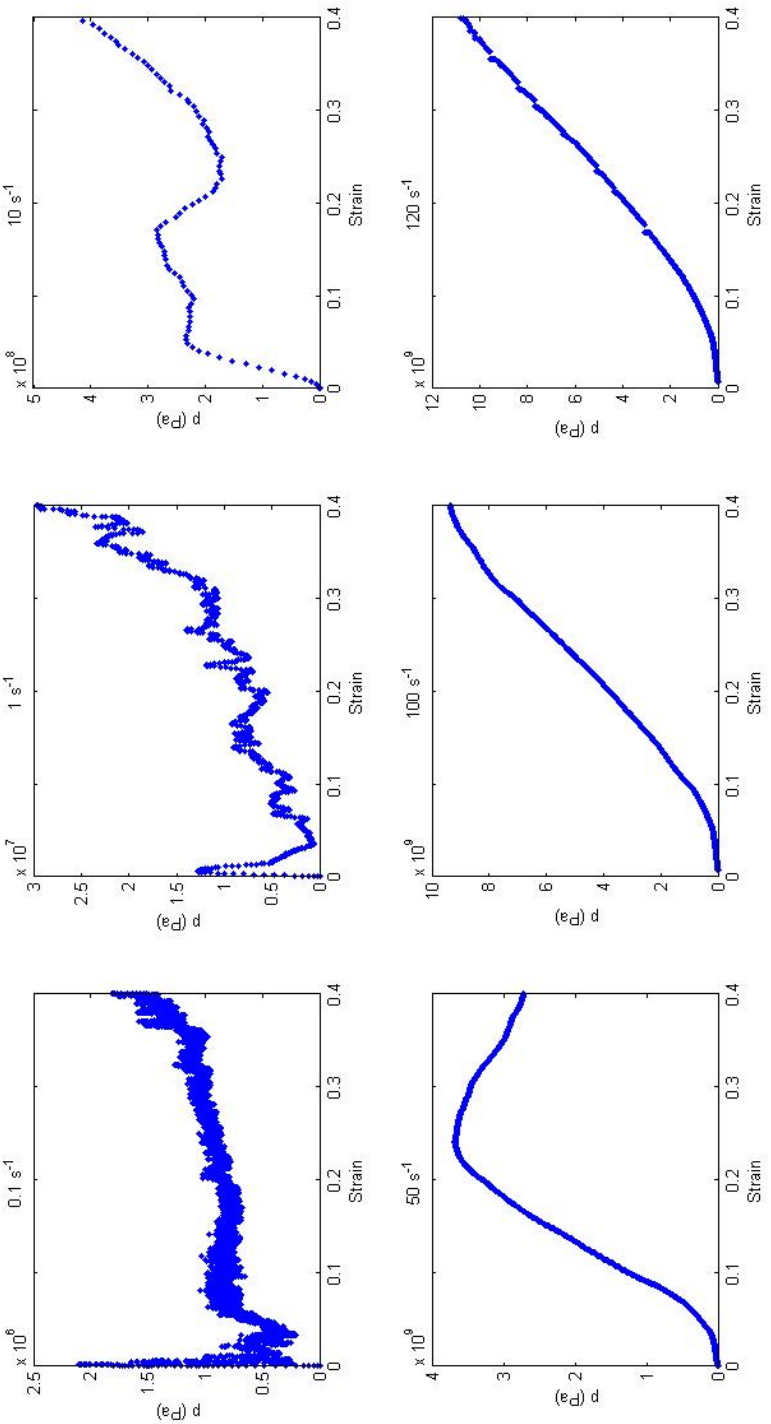

Figure C.4: Mean stress response for specimen 3 at 4N bond strength

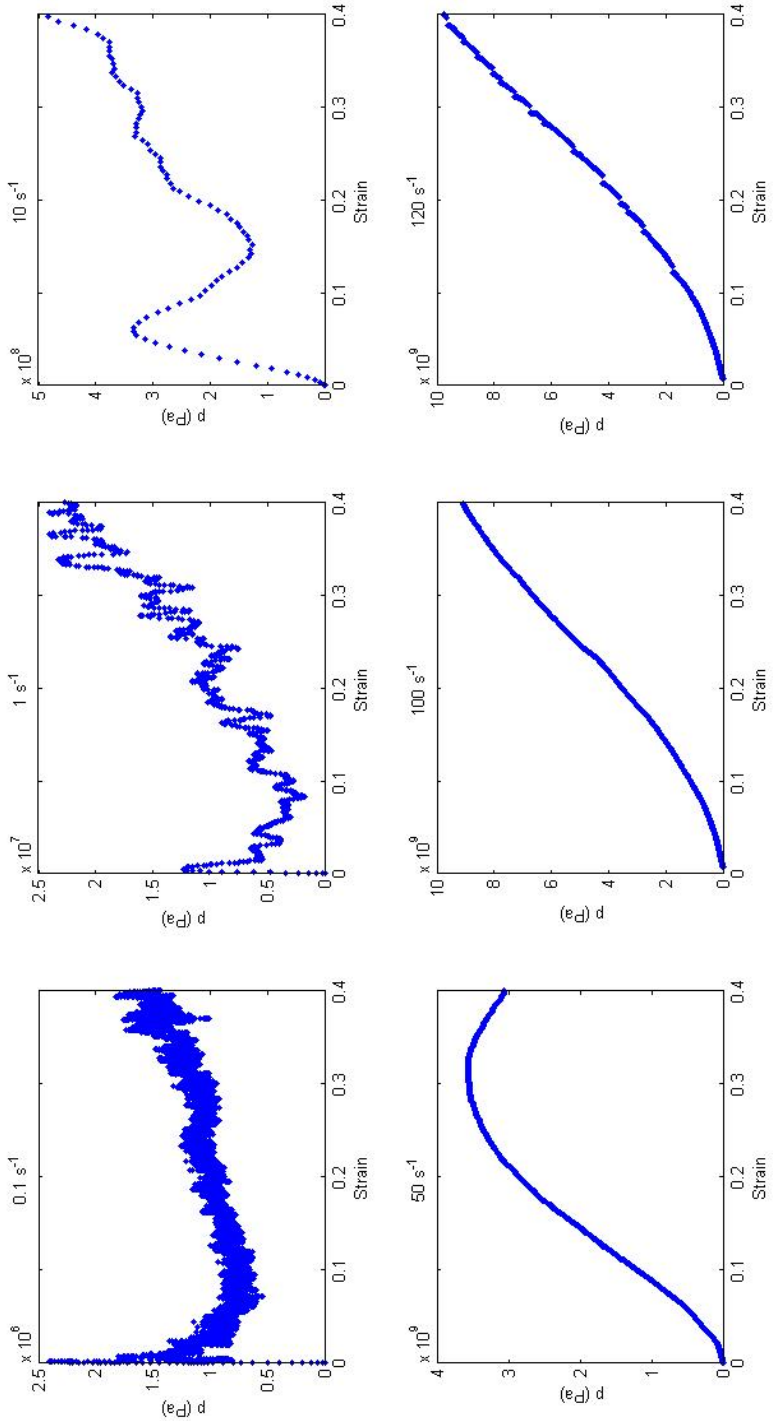

Figure C.5: Mean stress response for specimen 4 at 4N bond strength

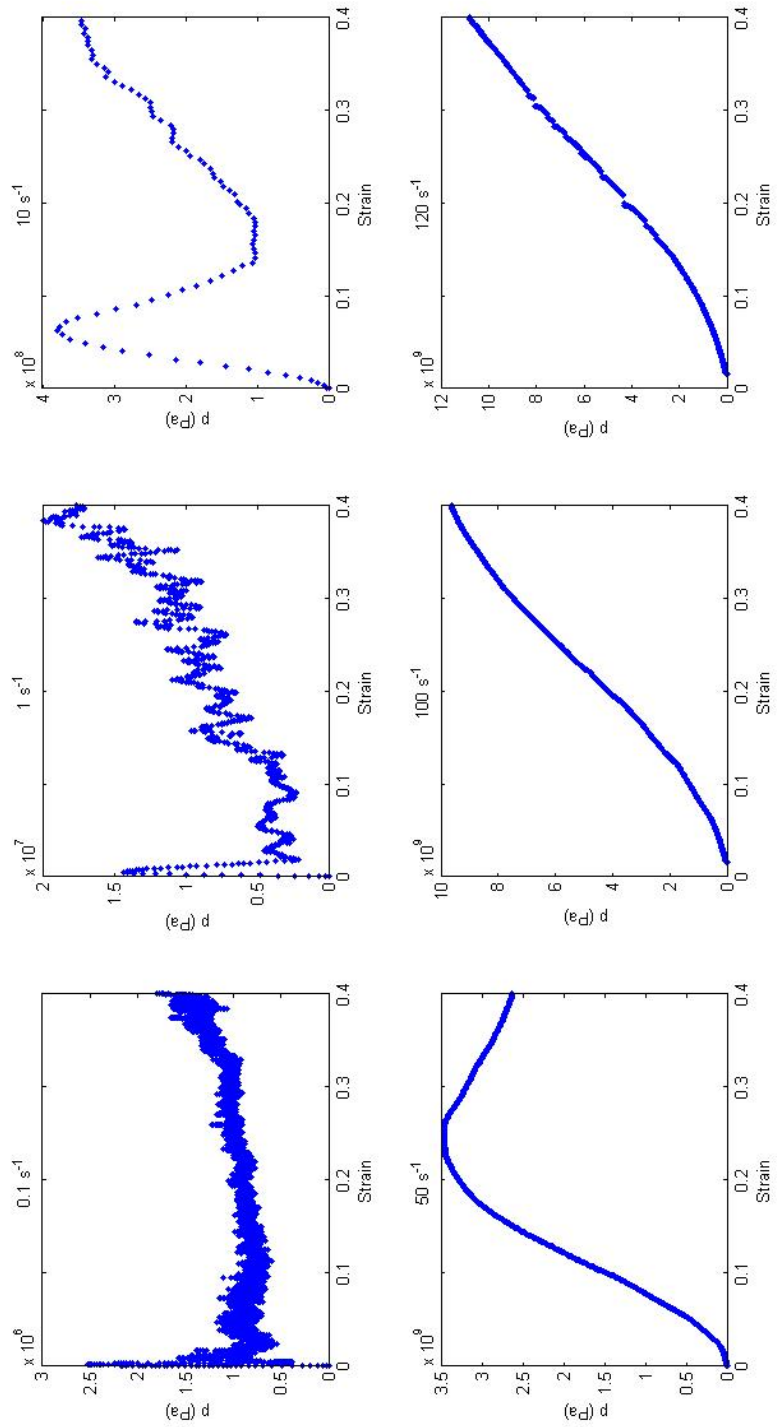

Figure C.6: Mean stress response for specimen 5 at 4N bond strength

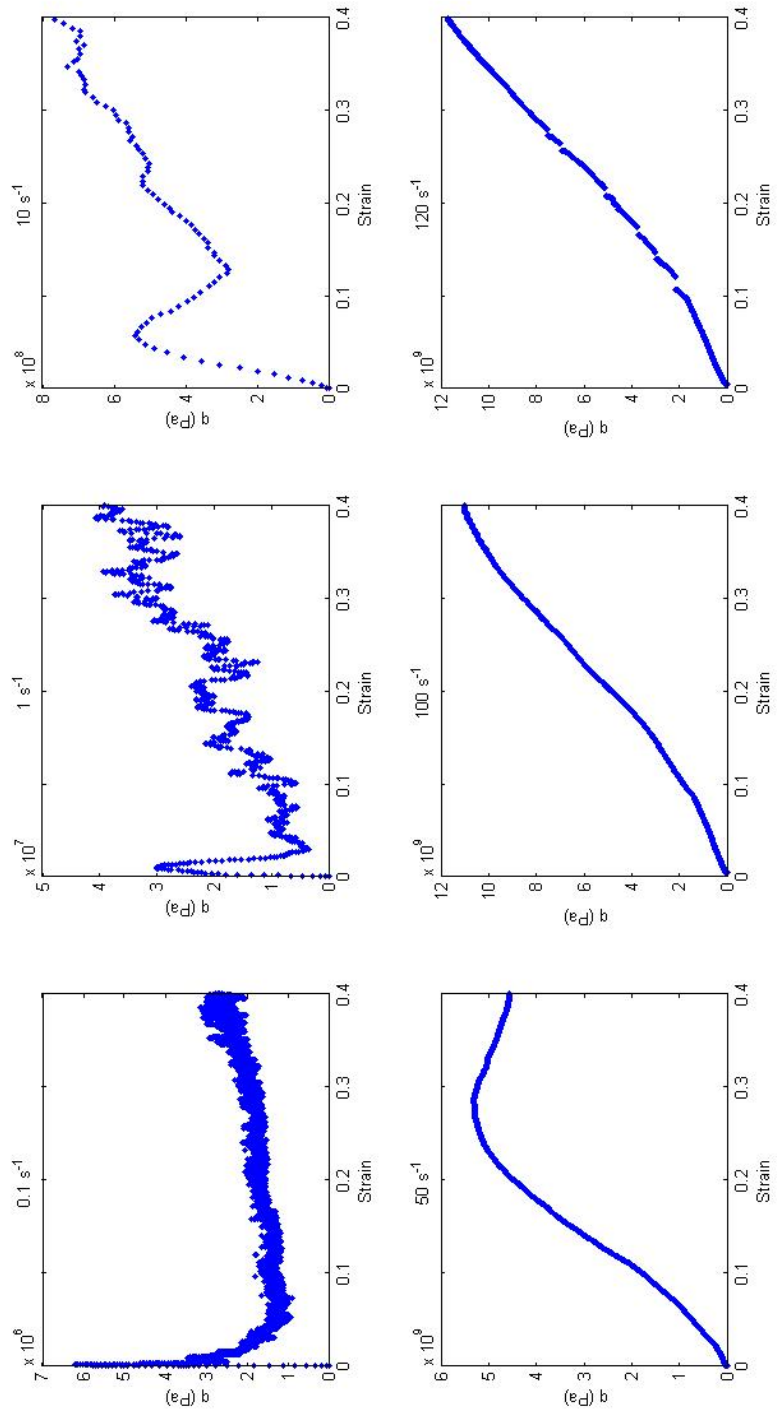

Figure C.7: Deviatoric stress response for specimen 2 at 4N bond strength

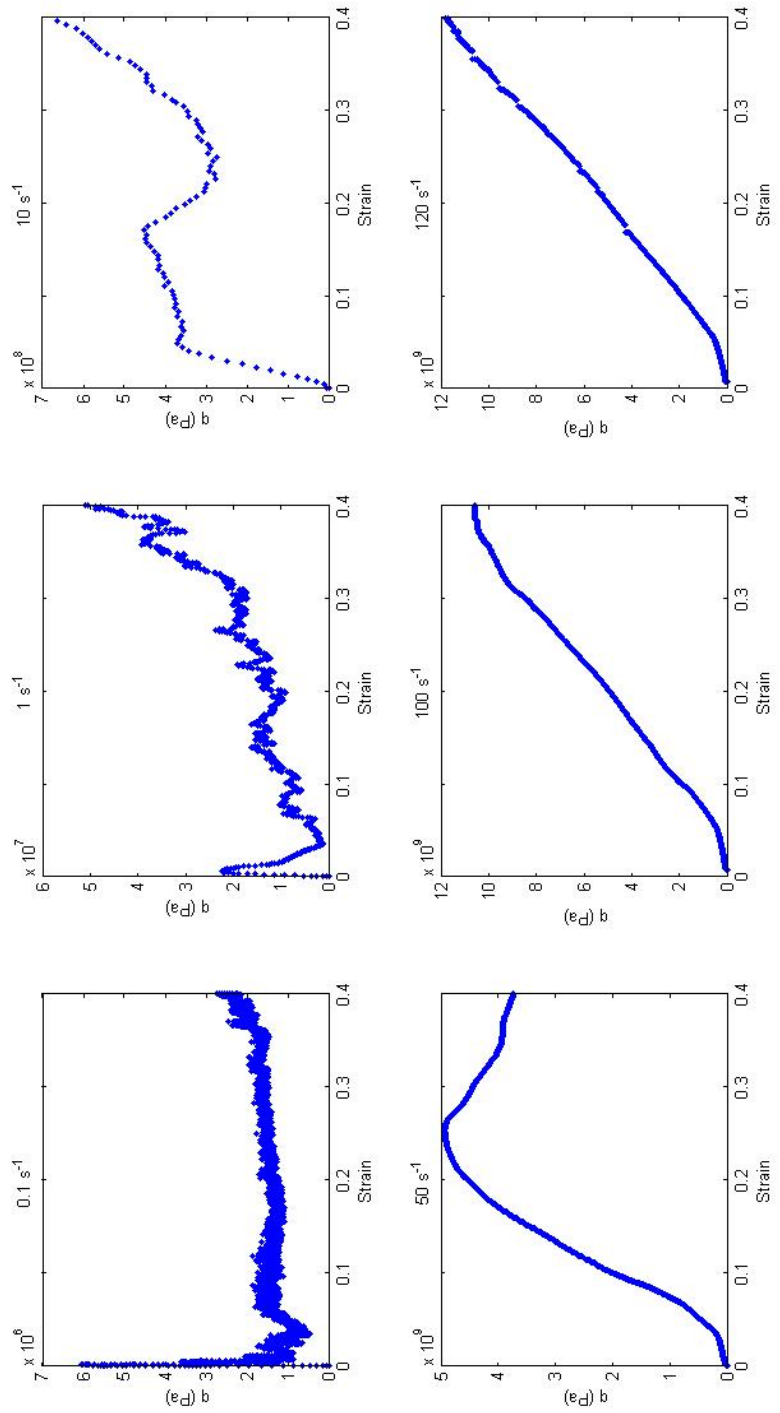

Figure C.8: Deviatoric stress response for specimen 3 at 4N bond strength

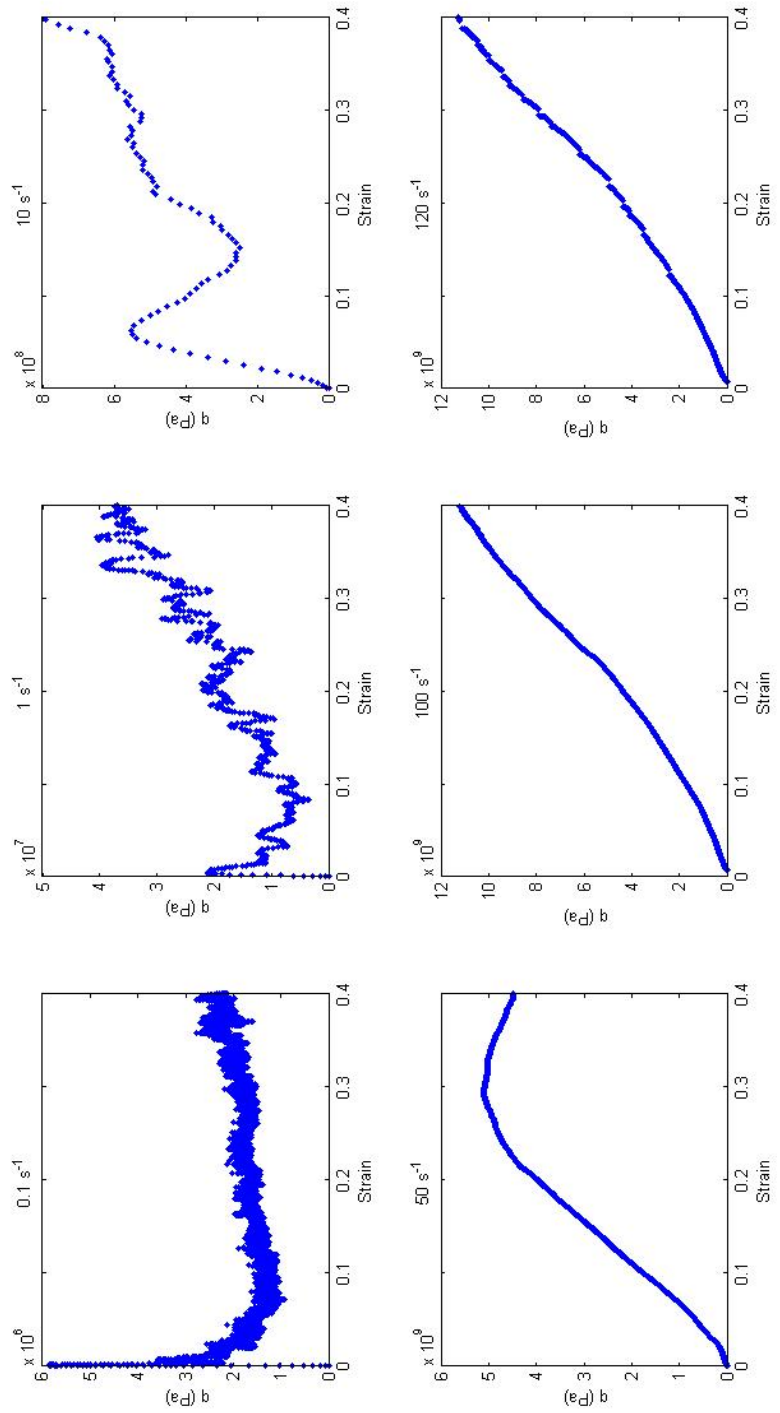

Figure C.9: Deviatoric stress response for specimen 4 at 4N bond strength

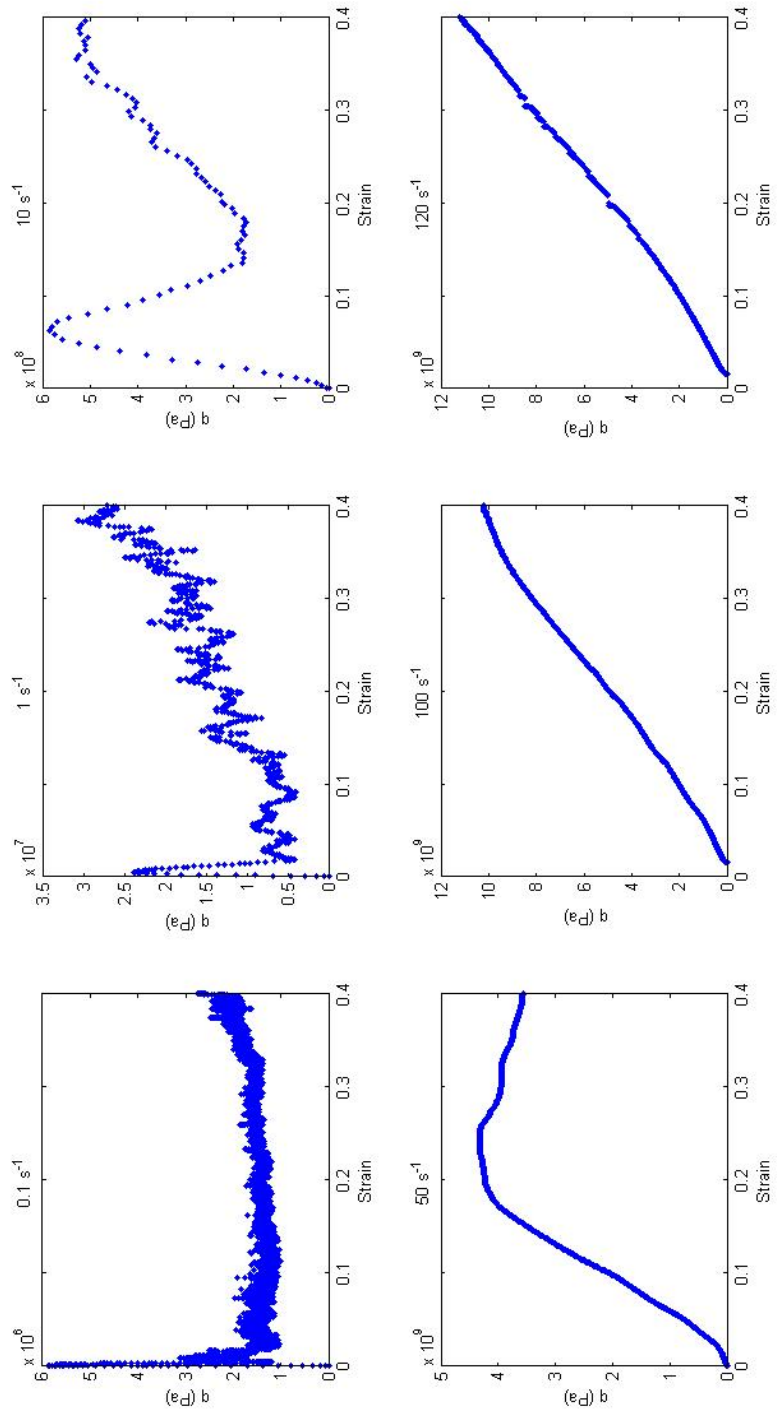

Figure C.10: Deviatoric stress response for specimen 5 at 4N bond strength

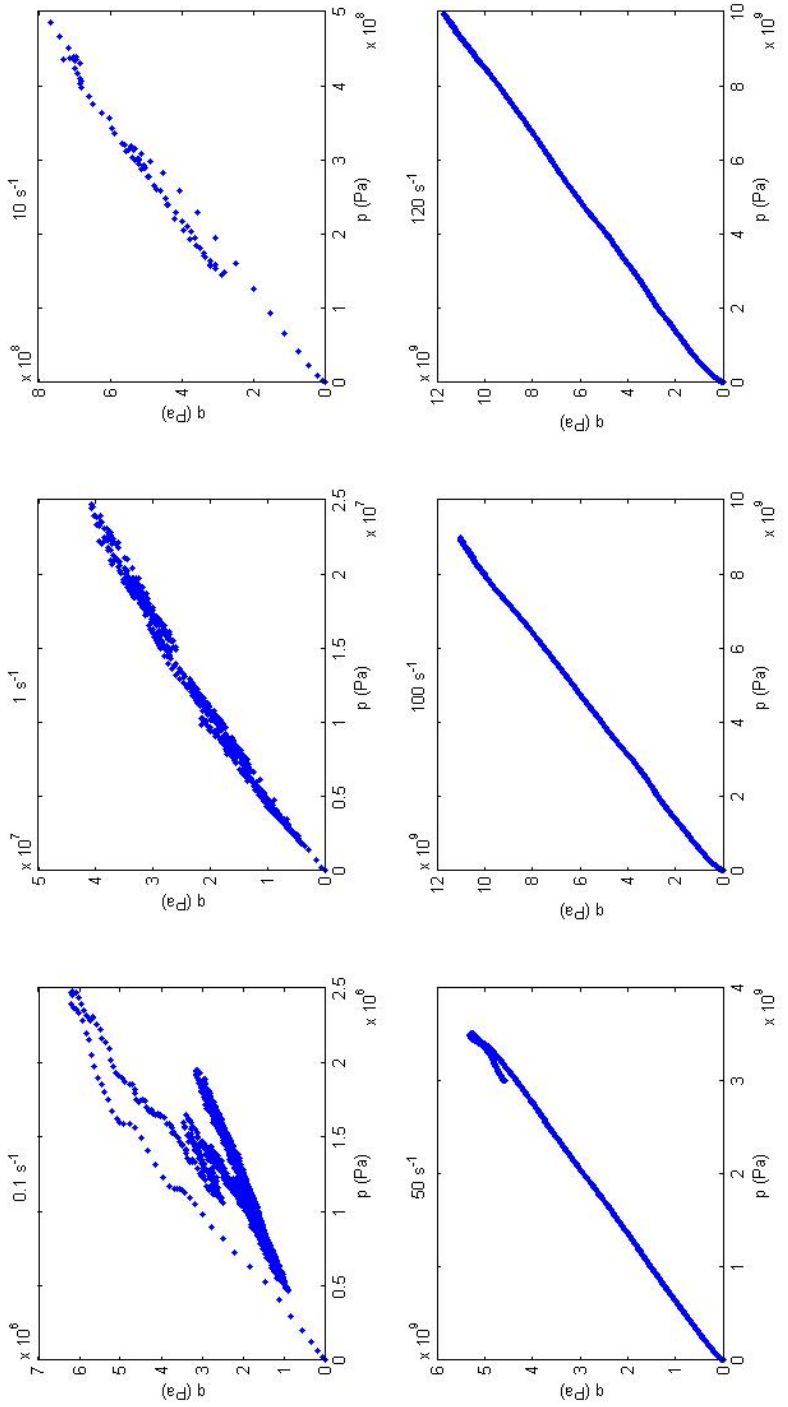

Figure C.11: Stress path for specimen 2 at 4N bond strength

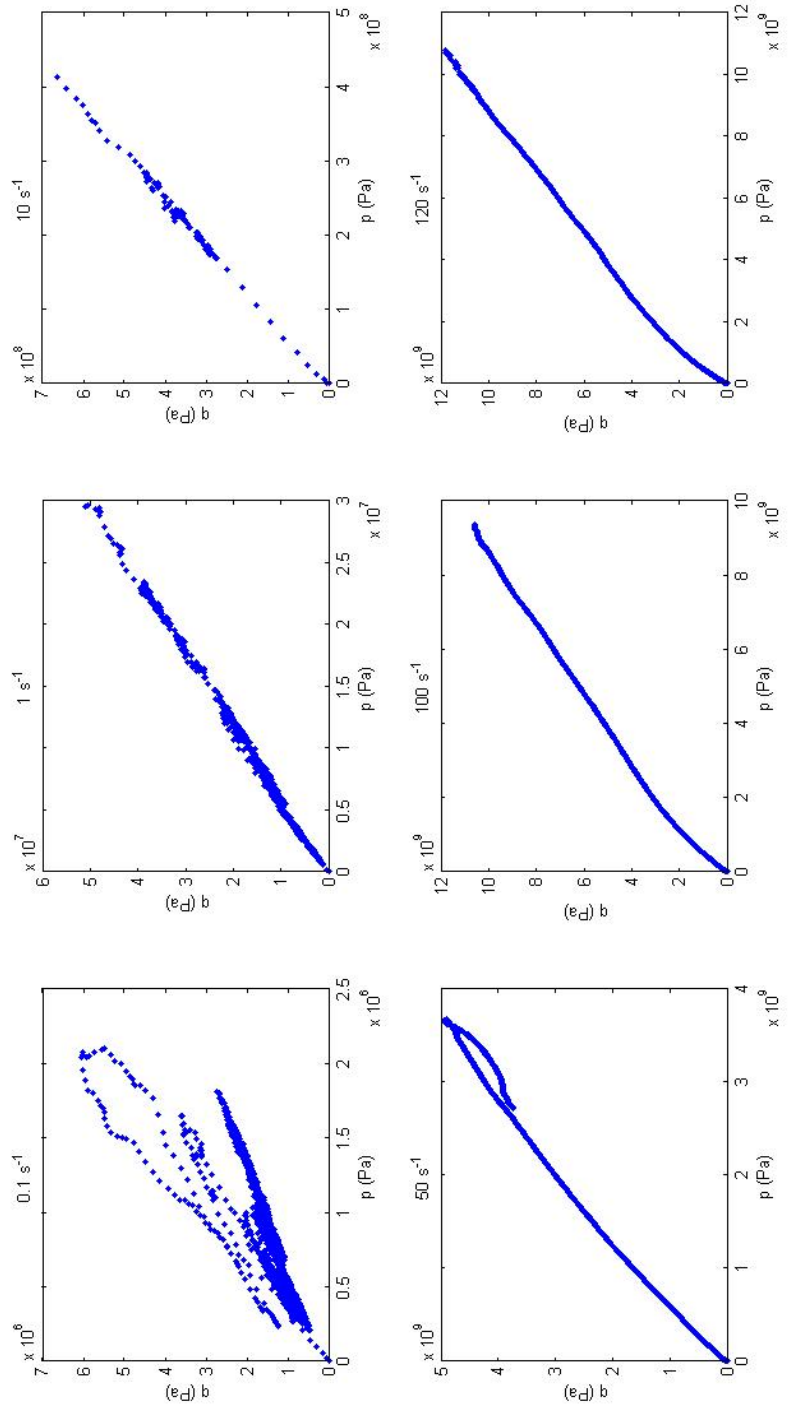

Figure C.12: Stress path for specimen 3 at 4N bond strength

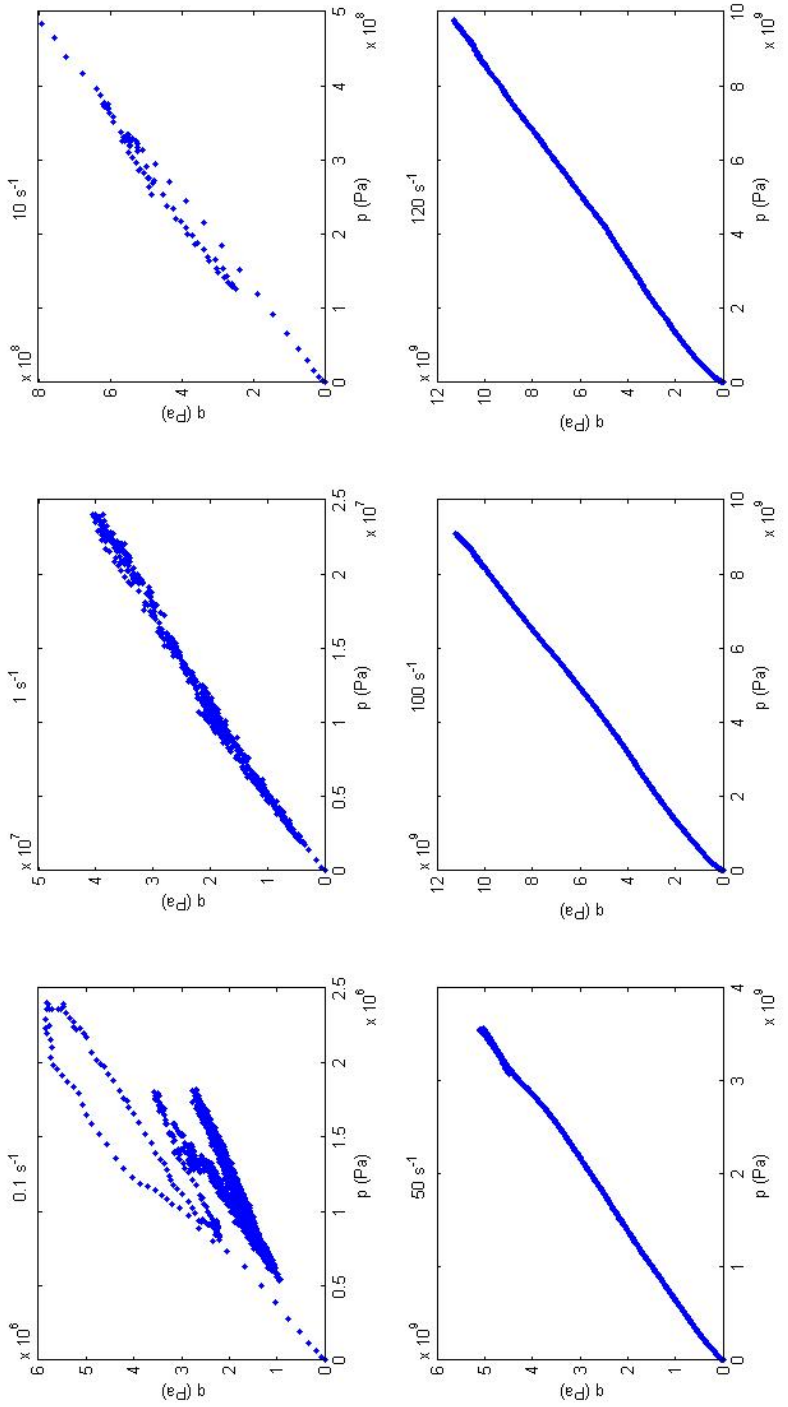

Figure C.13: Stress path for specimen 4 at 4N bond strength

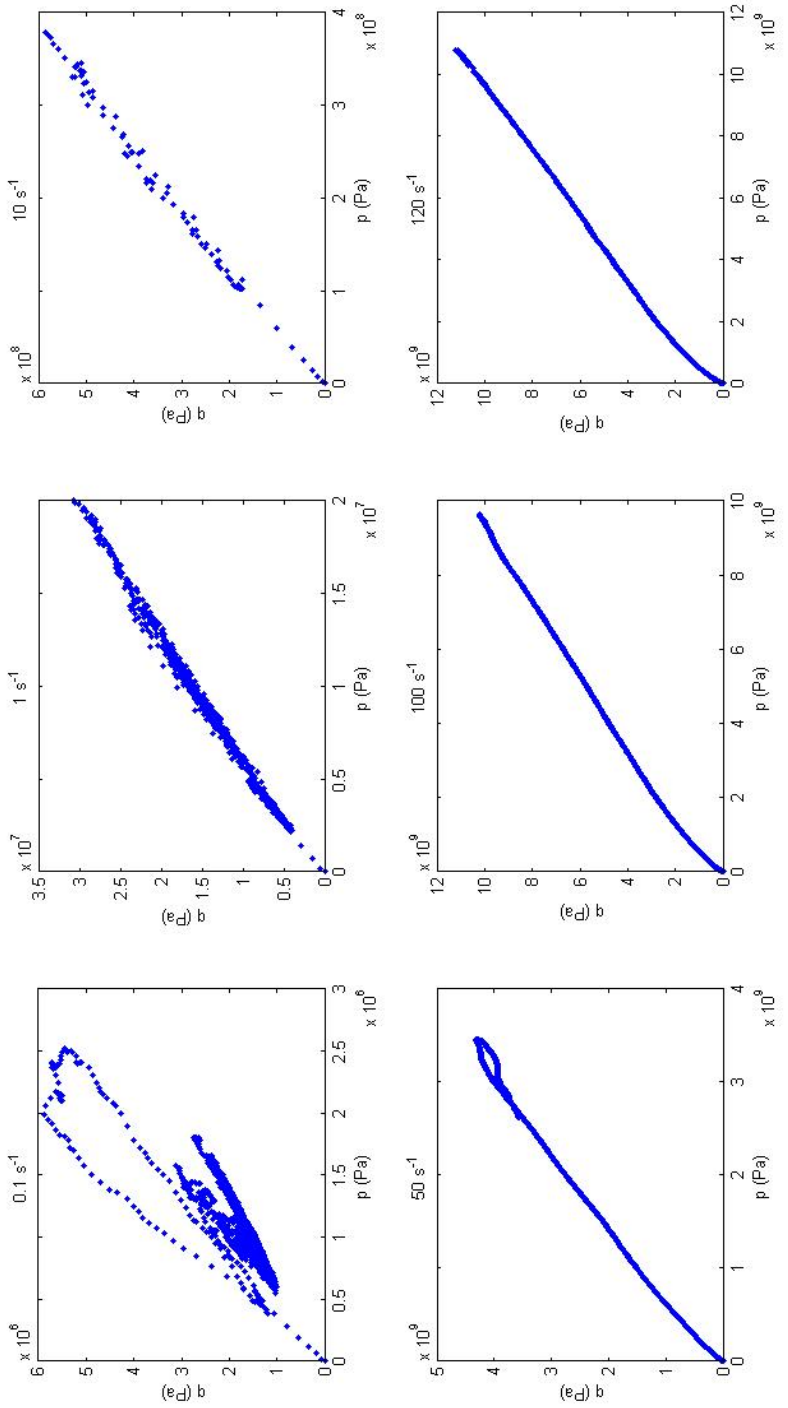

Figure C.14: Stress path for specimen 5 at 4N bond strength

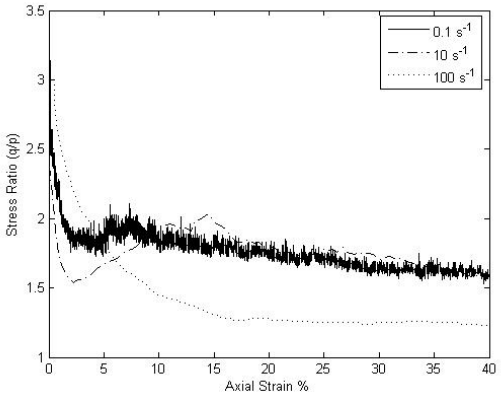

(a) Specimen 2

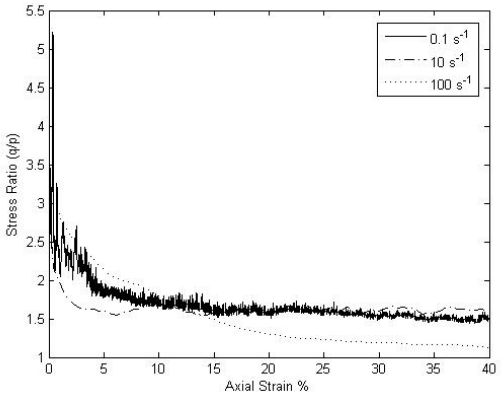

(b) Specimen 3

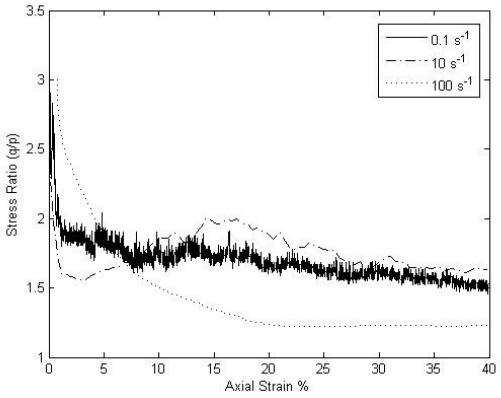

(c) Specimen 4

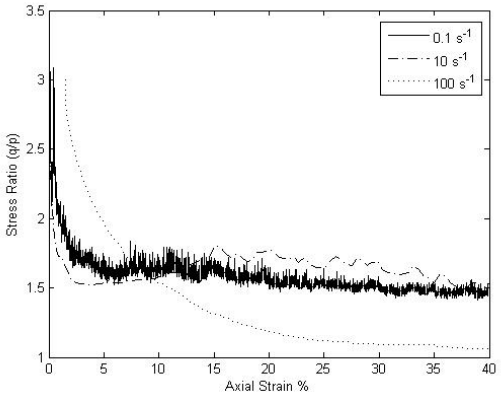

(d) Specimen 5

Figure C.15: $\frac{q}{p'}$ stress ratio

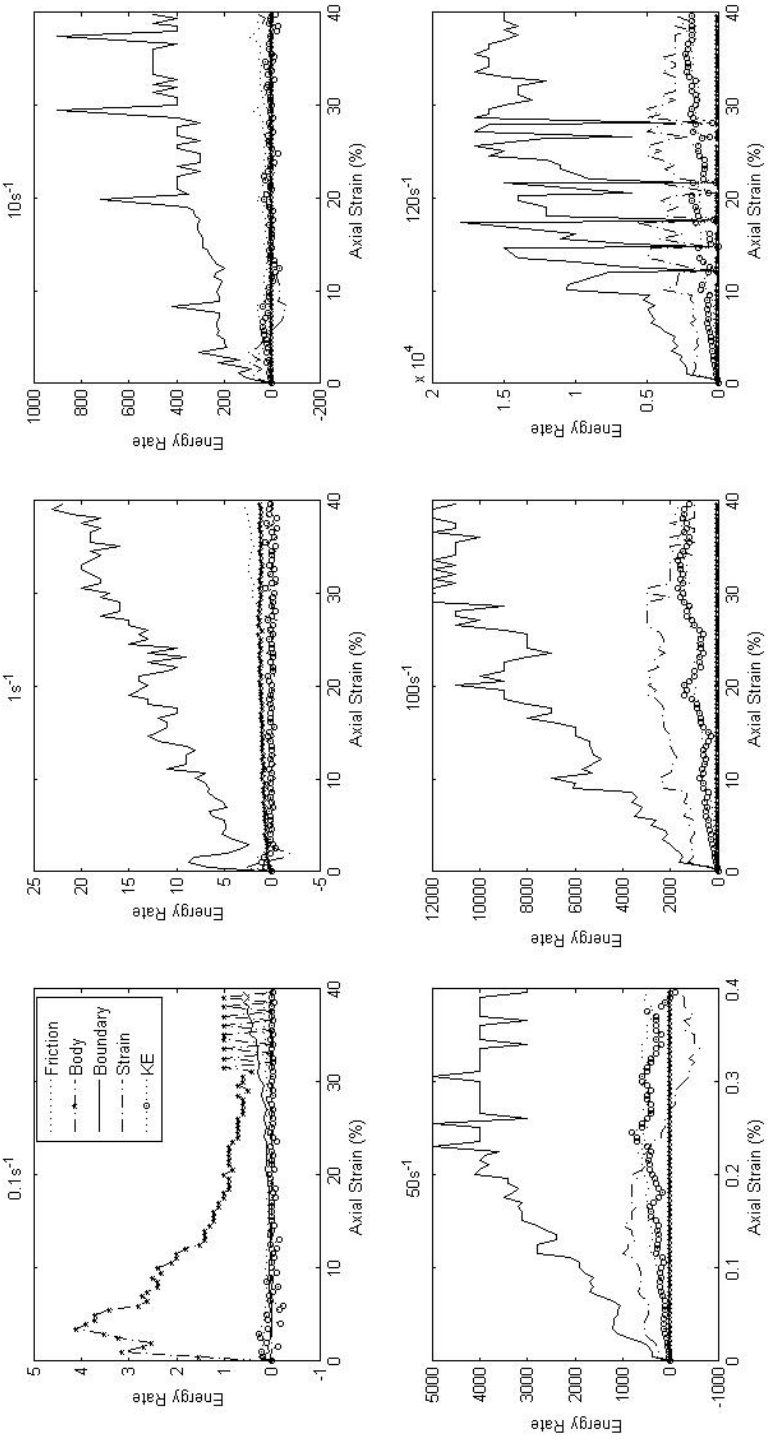

Figure C.16: Energy rate responses for specimen 2 at 4N bond strength

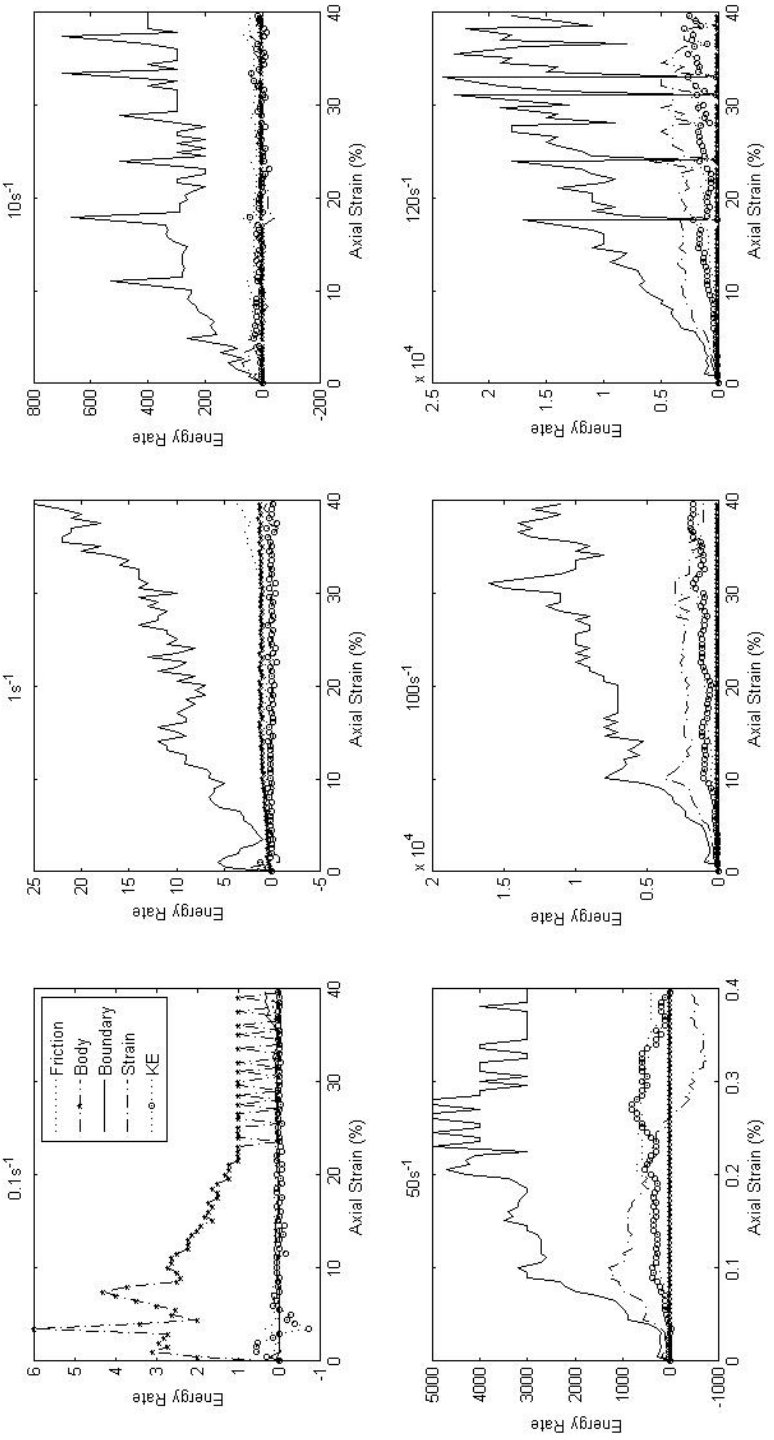

Figure C.17: Energy rate responses for specimen 3 at 4N bond strength

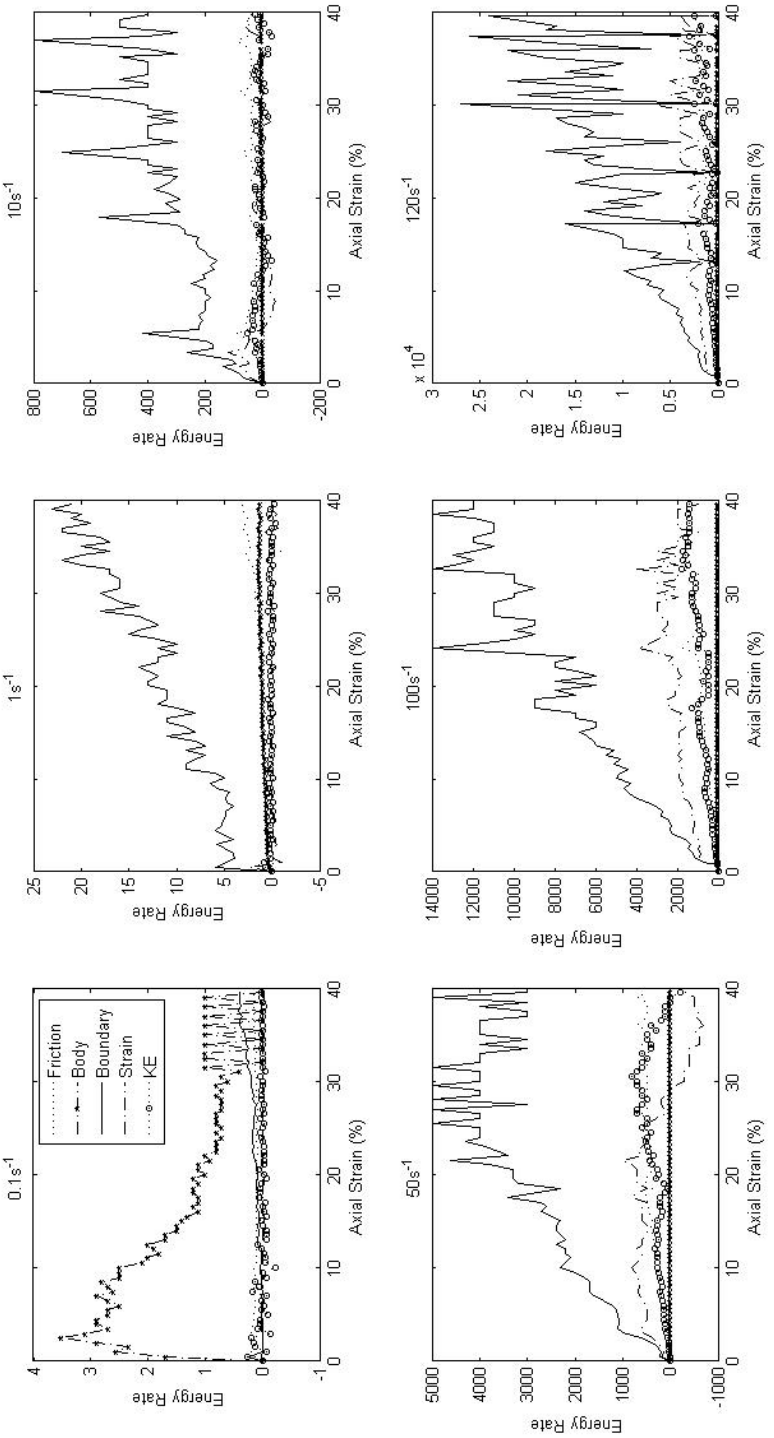

Figure C.18: Energy rate responses for specimen 4 at 4N bond strength

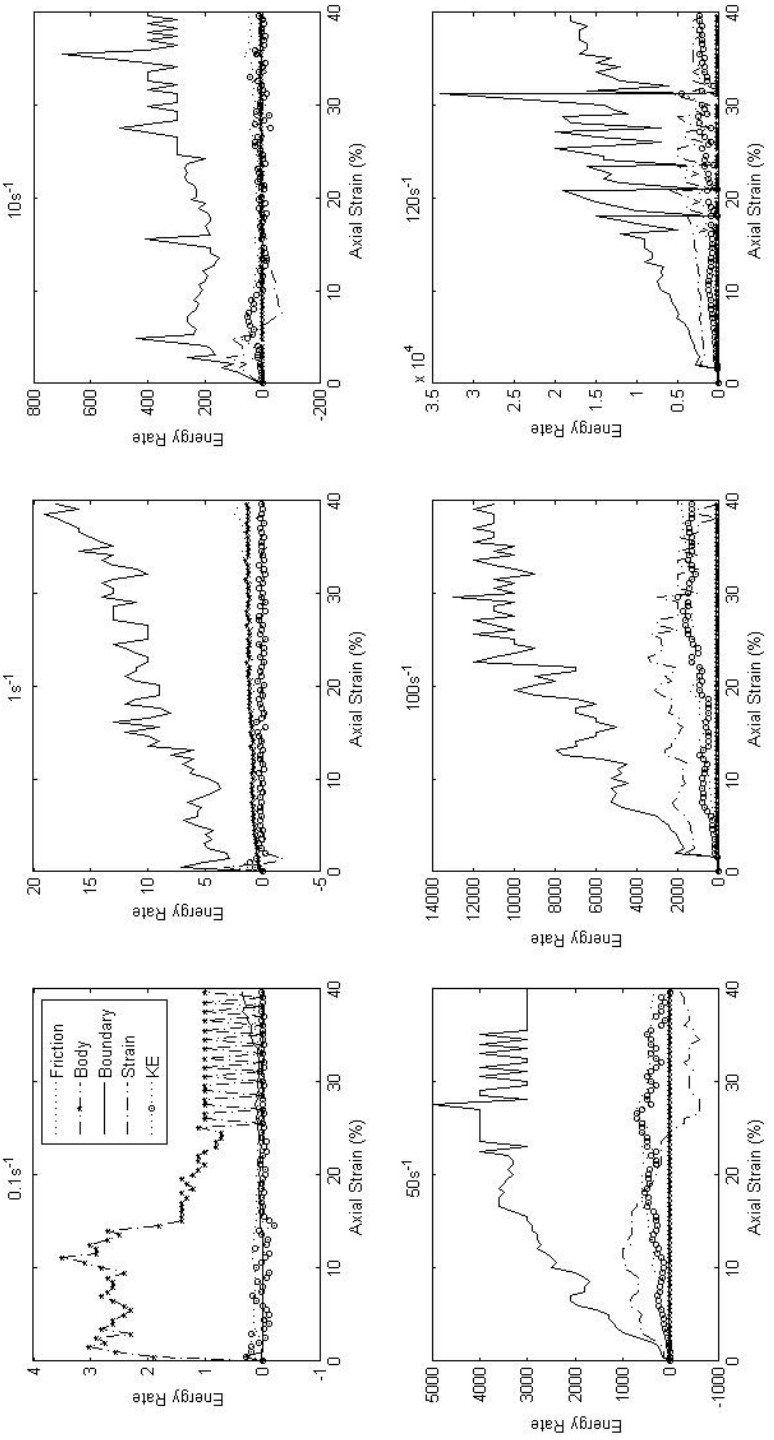

Figure C.19: Energy rate responses for specimen 5 at 4N bond strength

C.1.2 4kN Bond Strength

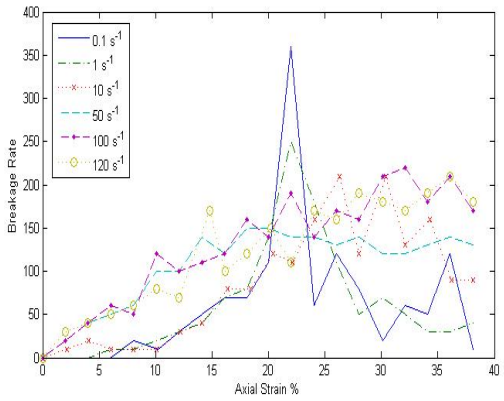

(a) Specimen 2

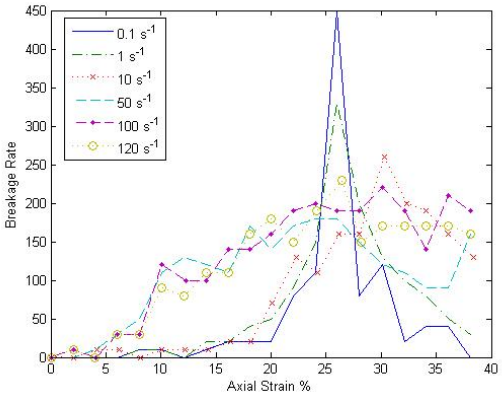

(b) Specimen 3

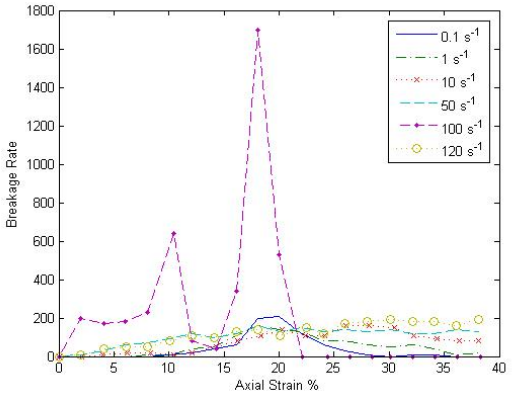

(c) Specimen 4

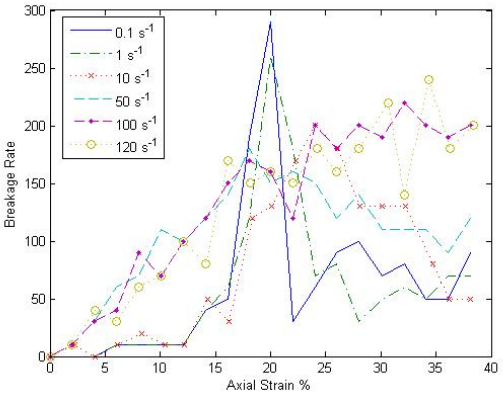

(d) Specimen 5

Figure C.20: Breakage rate

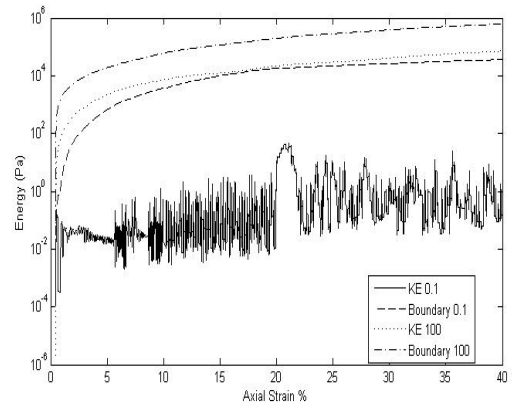

(a) Specimen 2

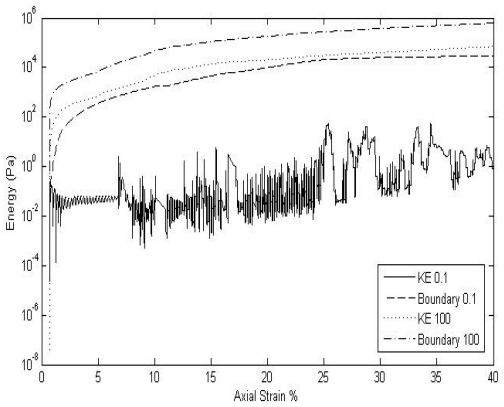

(b) Specimen 3

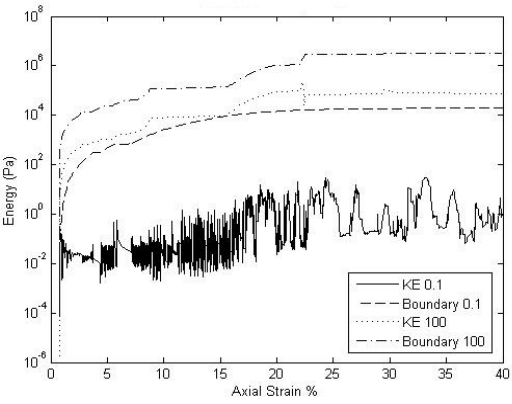

(c) Specimen 4

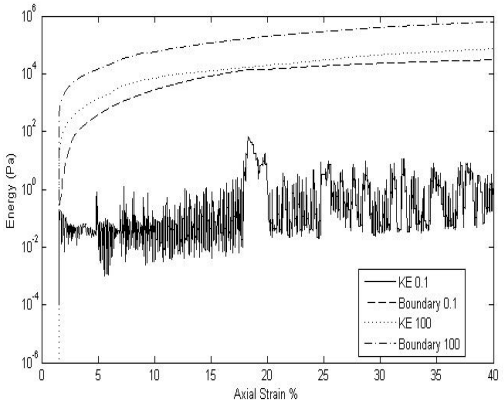

(d) Specimen 5

Figure C.21: Kinetic and boundary energy comparison

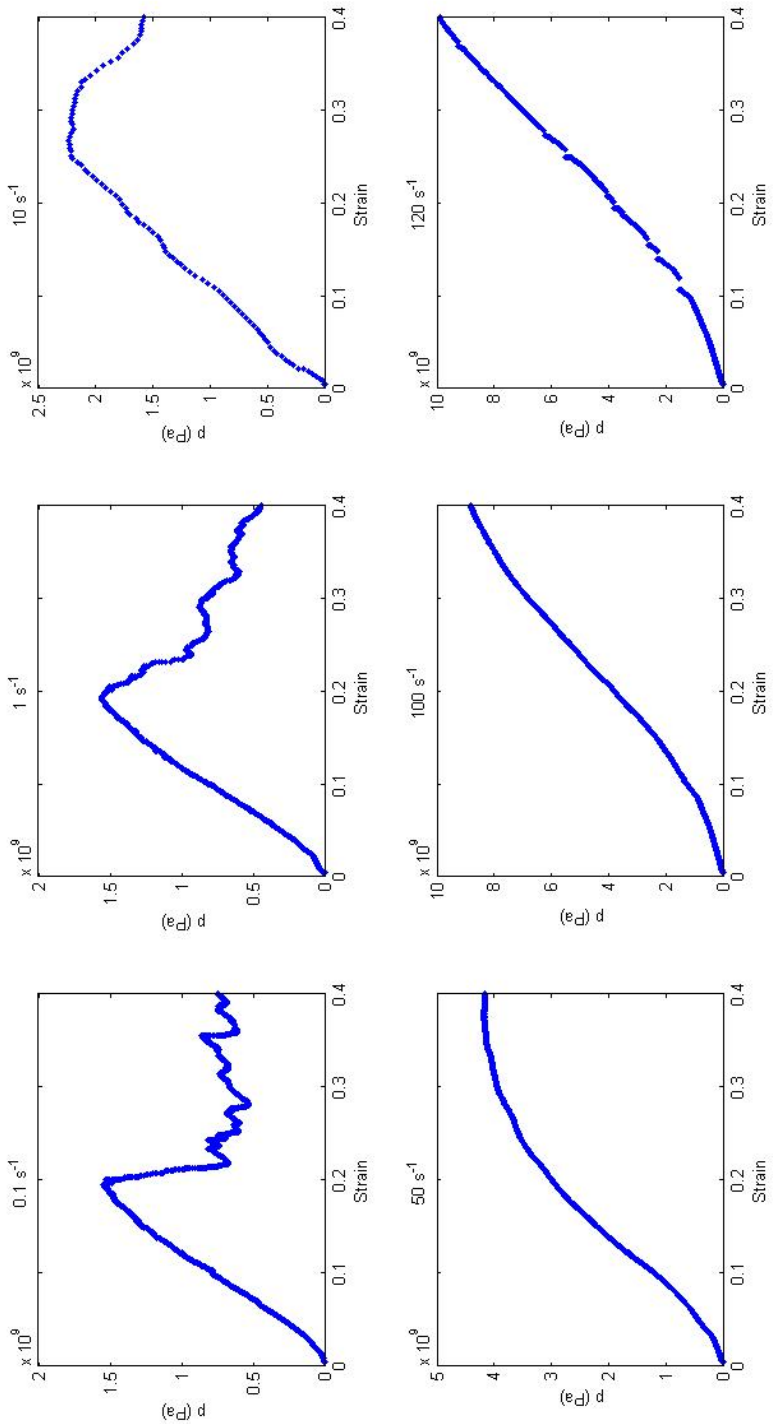

Figure C.22: Mean stress response for specimen 2 at 4kN bond strength

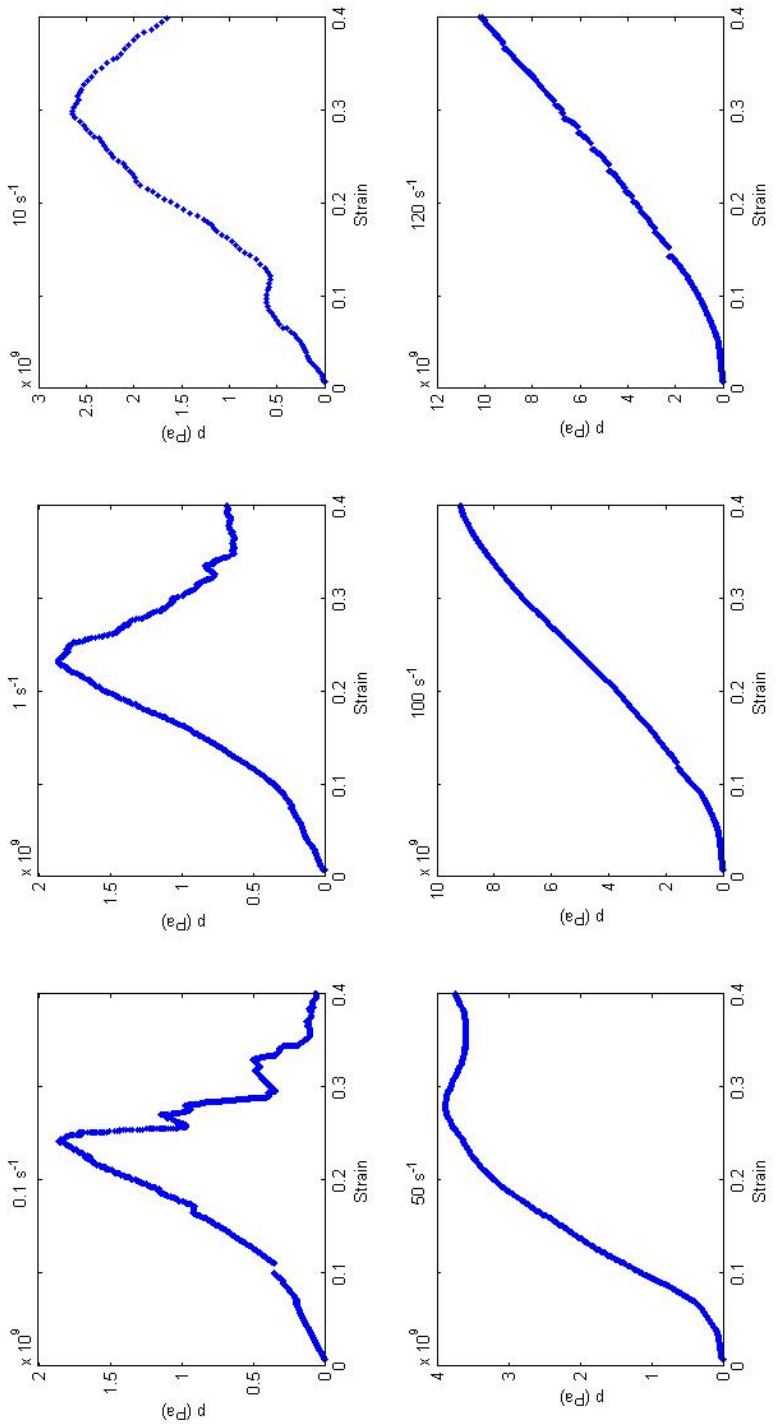

Figure C.23: Mean stress response for specimen 3 at 4kN bond strength

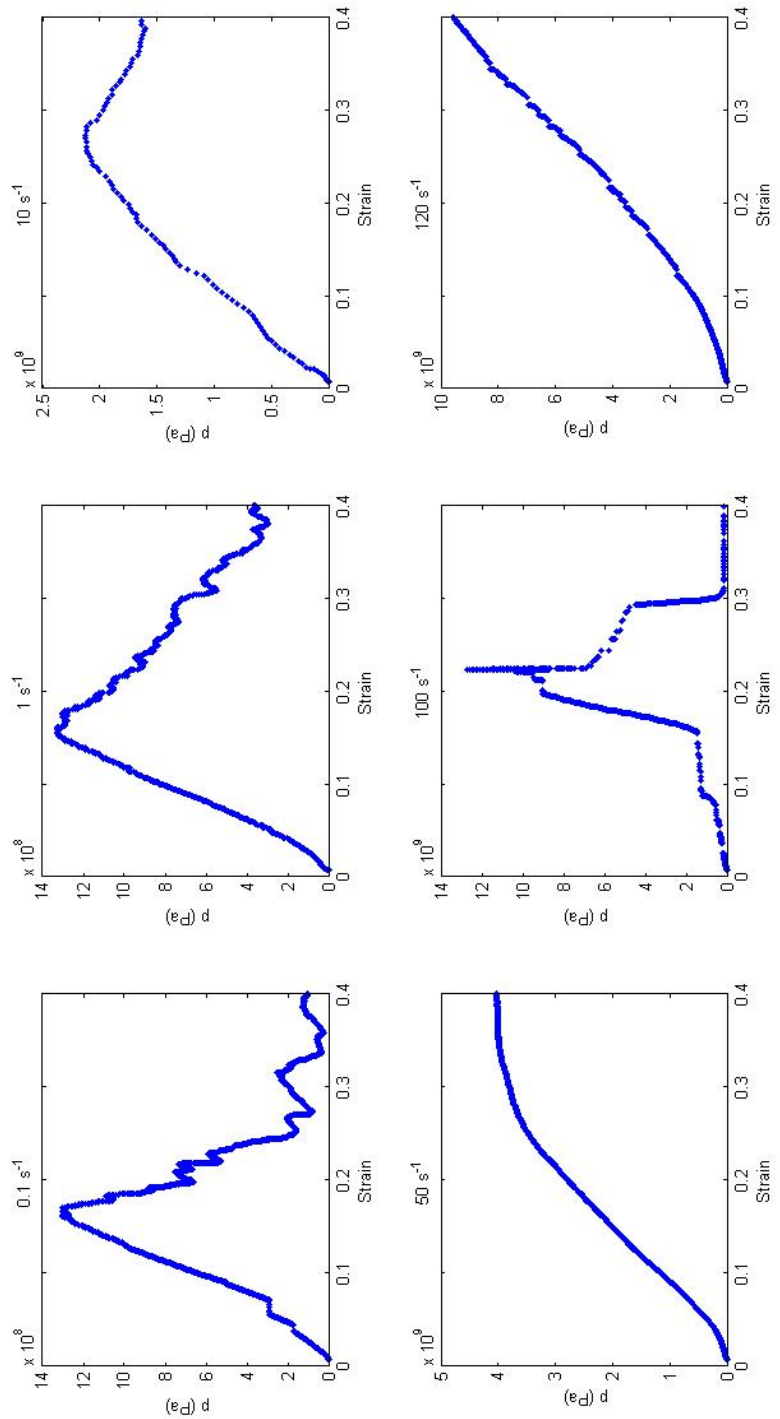

Figure C.24: Mean stress response for specimen 4 at 4kN bond strength

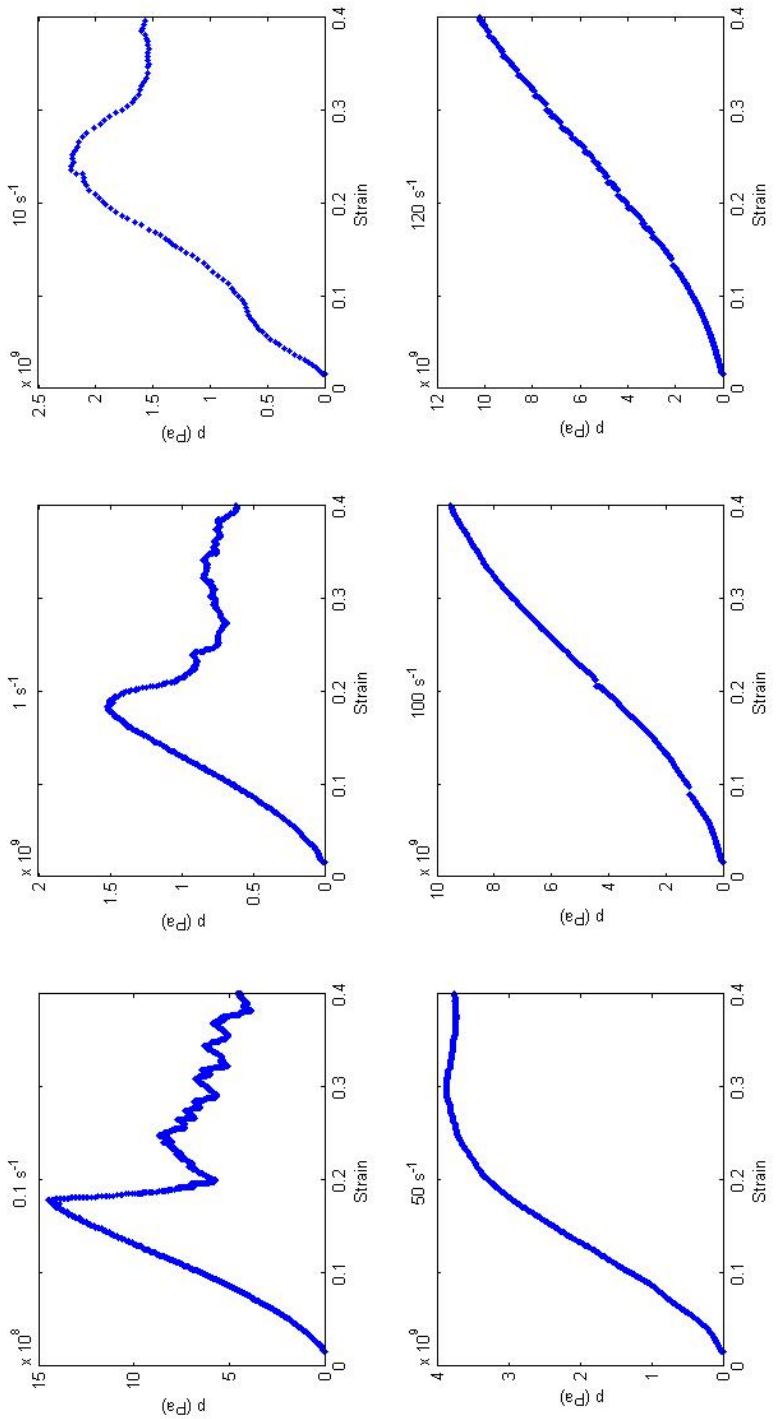

Figure C.25: Mean stress response for specimen 5 at 4kN bond strength

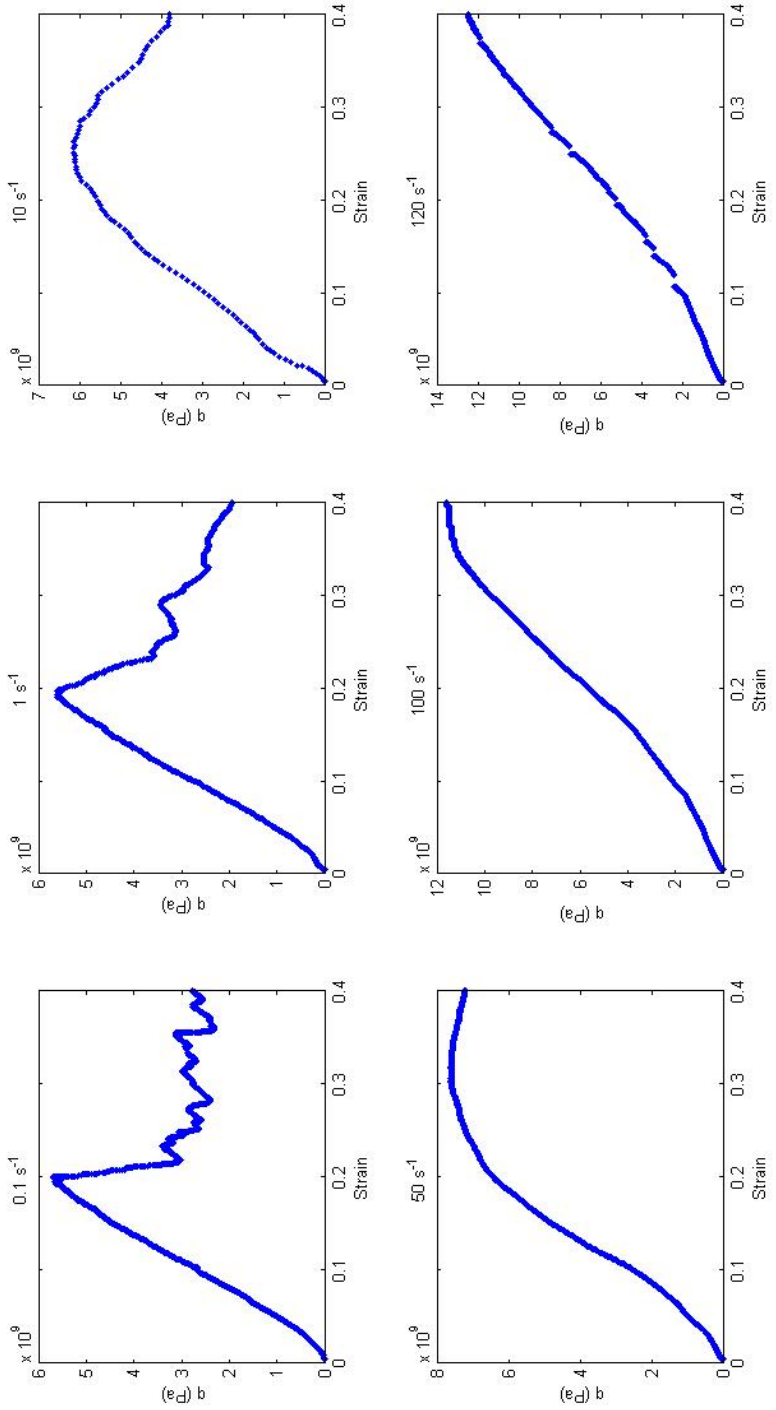

Figure C.26: Deviatoric stress response for specimen 2 at 4kN bond strength

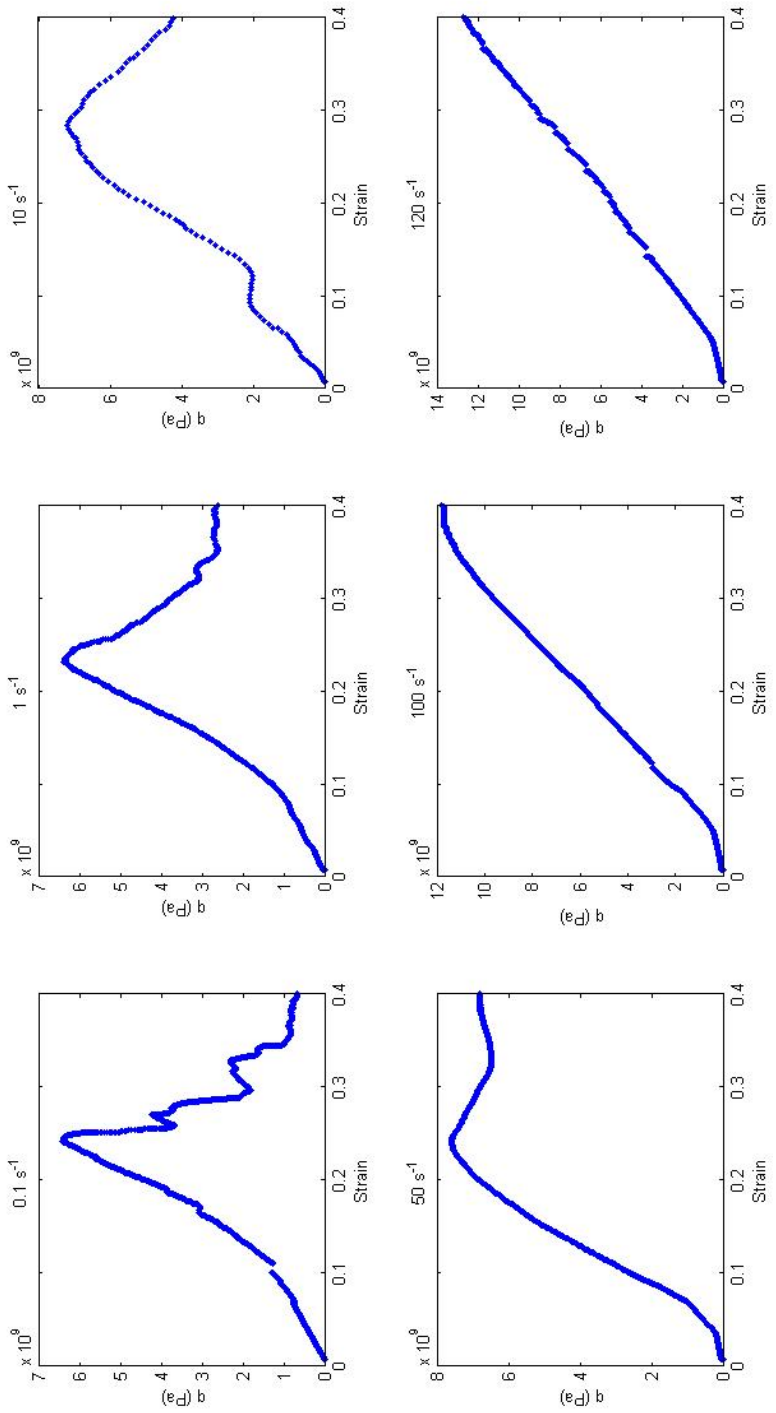

Figure C.27: Deviatoric stress response for specimen 3 at 4kN bond strength

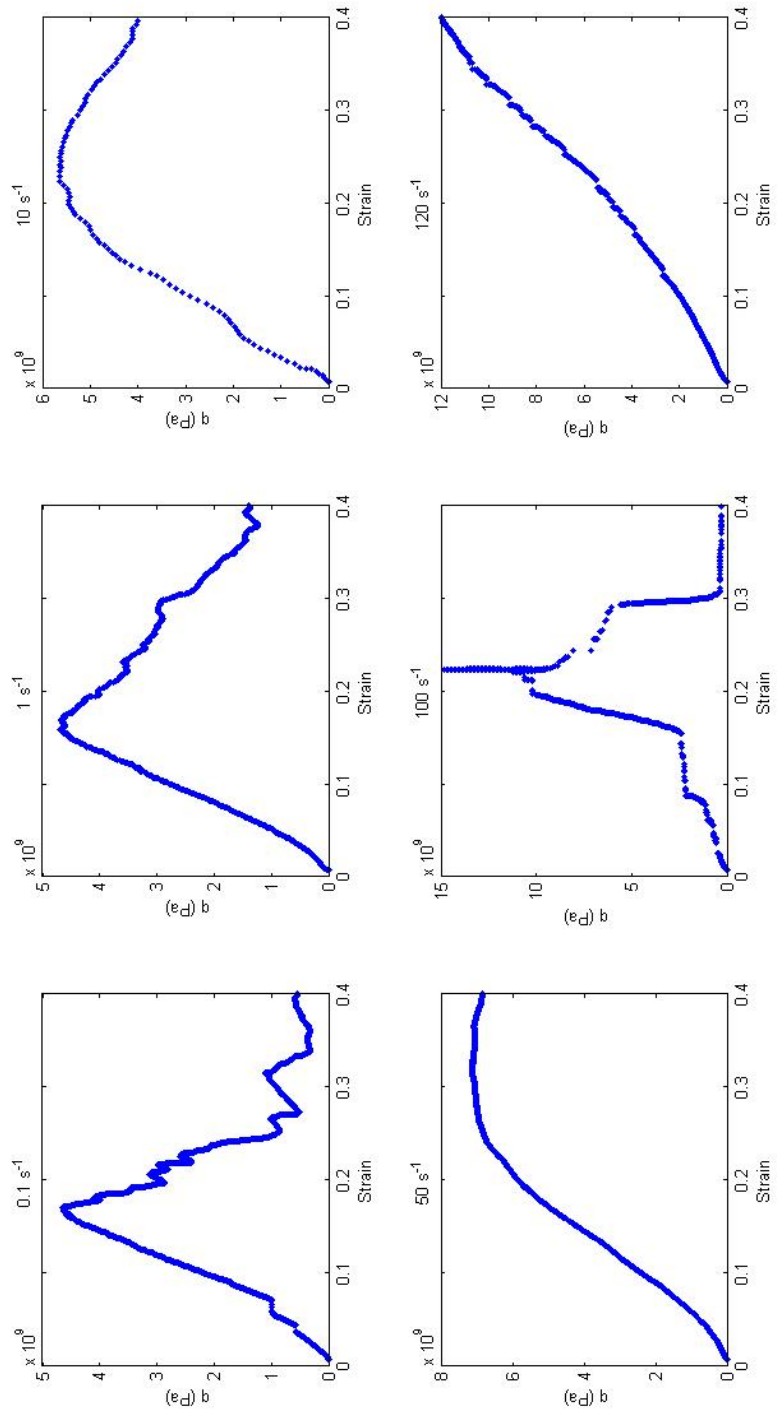

Figure C.28: Deviatoric stress response for specimen 4 at 4kN bond strength

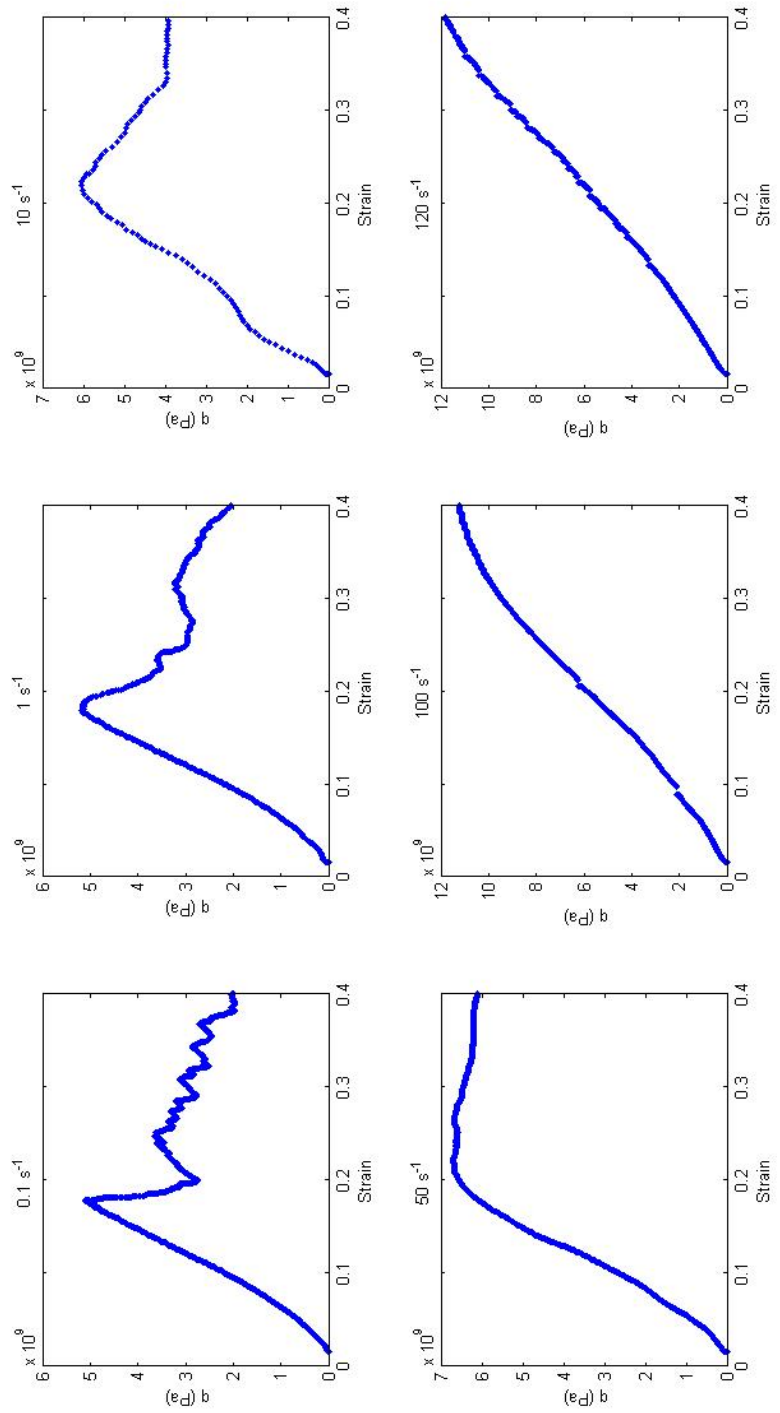

Figure C.29: Deviatoric stress response for specimen 5 at 4kN bond strength

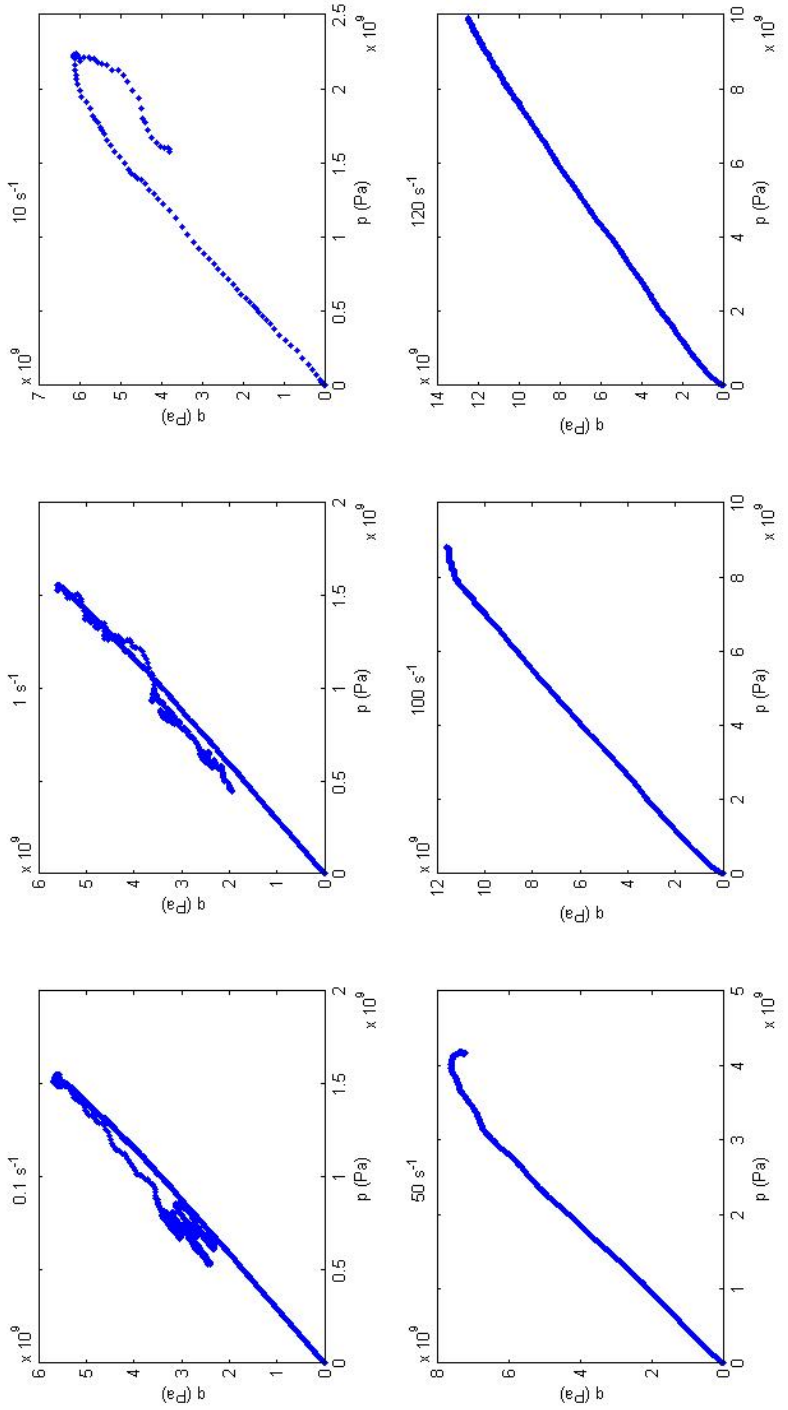

Figure C.30: Stress path for specimen 2 at 4kN bond strength

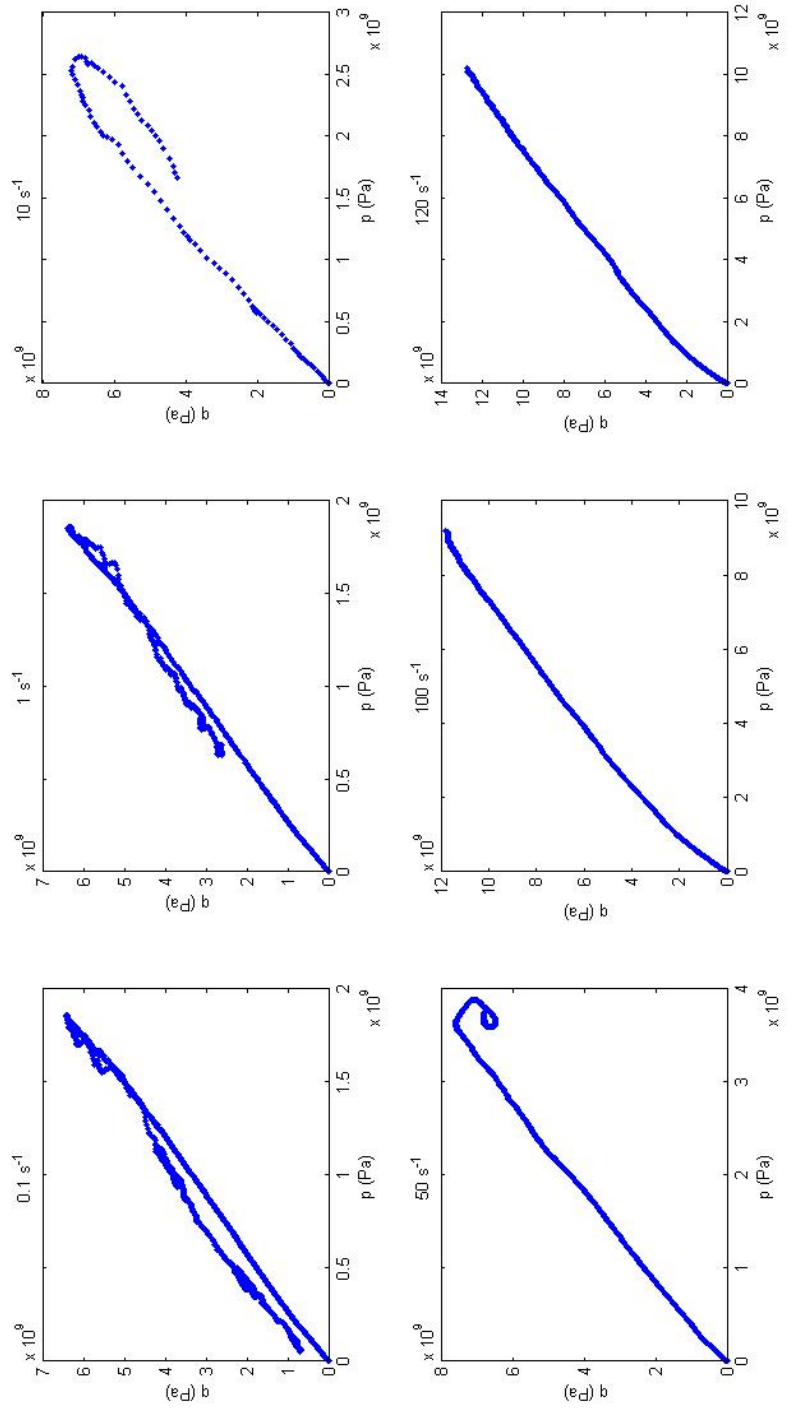

Figure C.31: Stress path for specimen 3 at 4kN bond strength

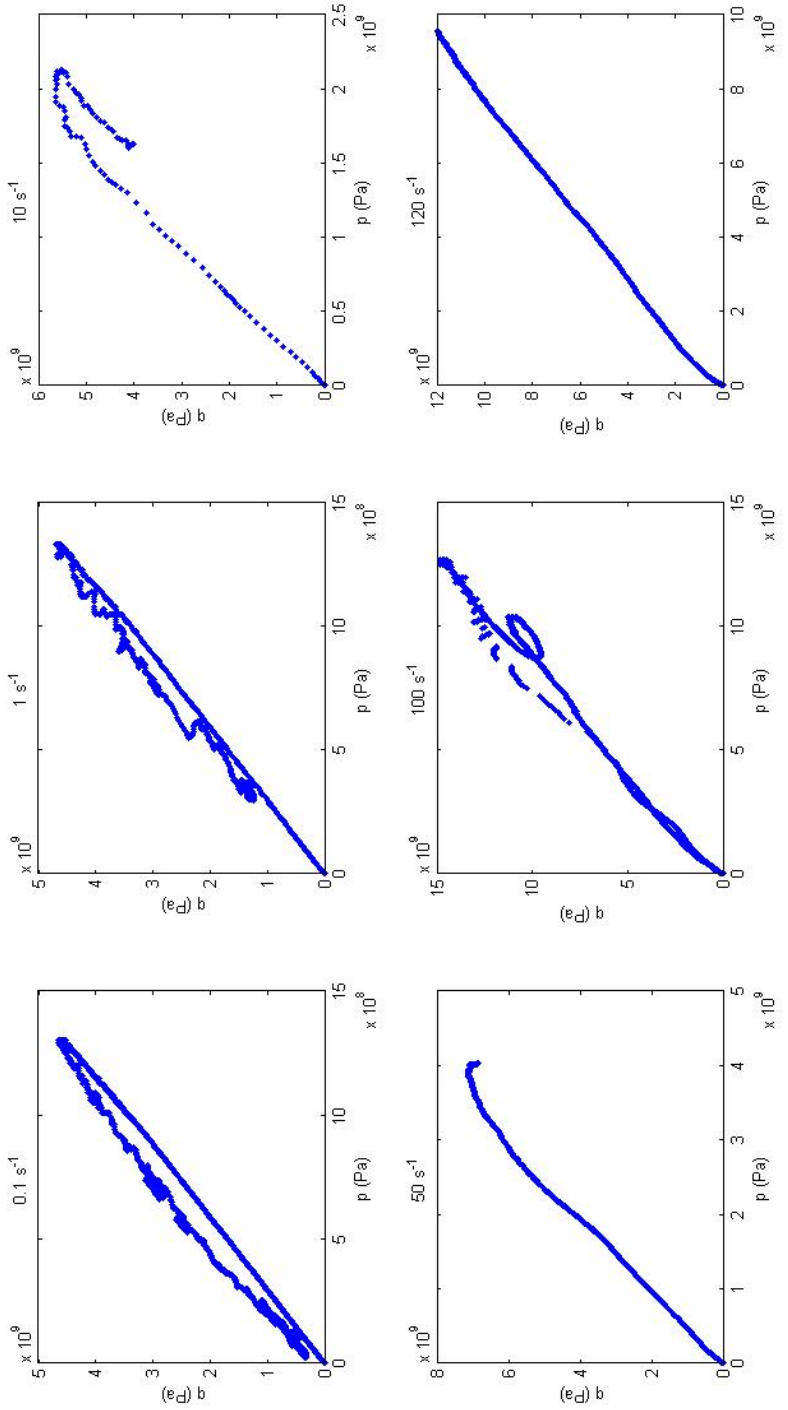

Figure C.32: Stress path for specimen 4 at 4kN bond strength

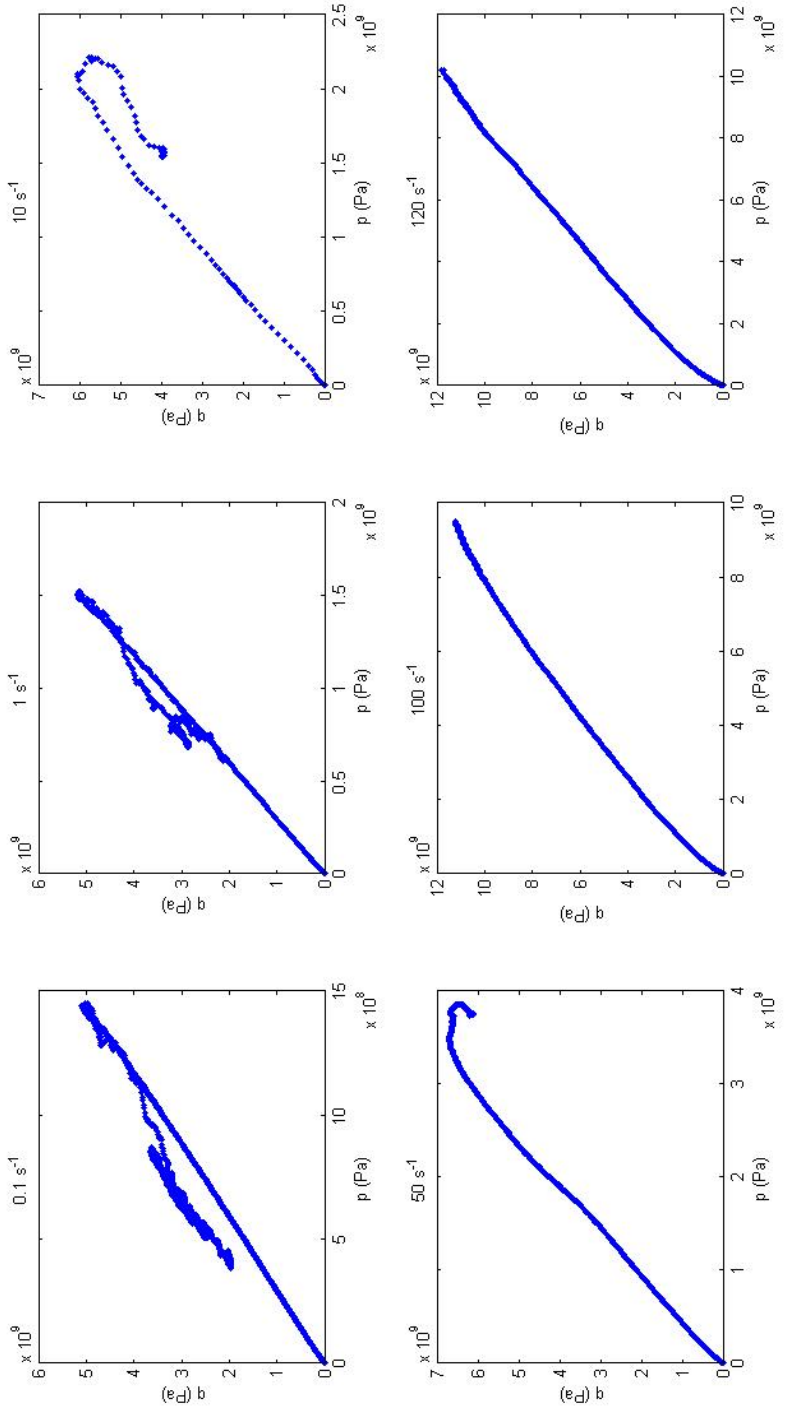

Figure C.33: Stress path for specimen 5 at 4kN bond strength

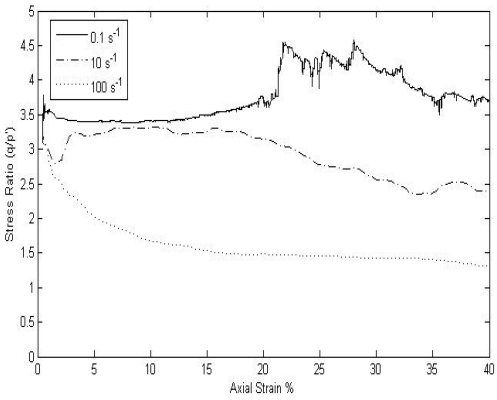

(a) Specimen 2

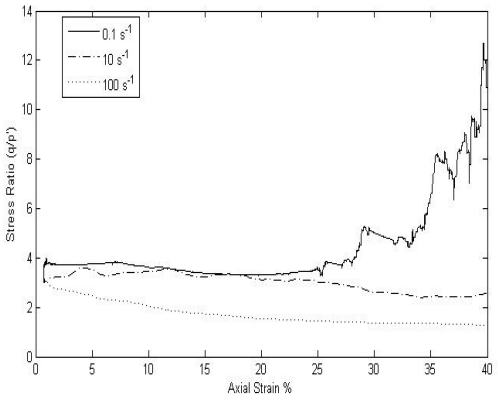

(b) Specimen 3

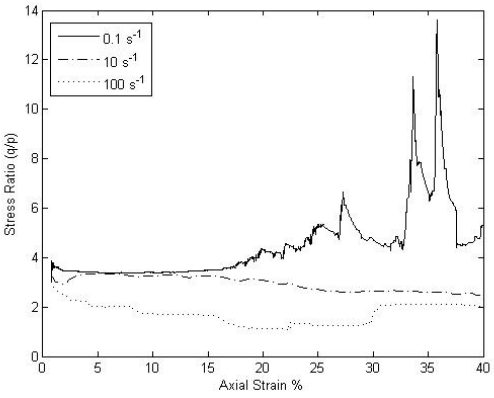

(c) Specimen 4

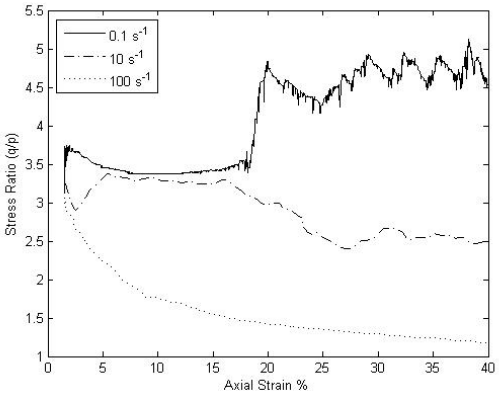

(d) Specimen 5

Figure C.34: $\frac{q}{p'}$ stress ratio

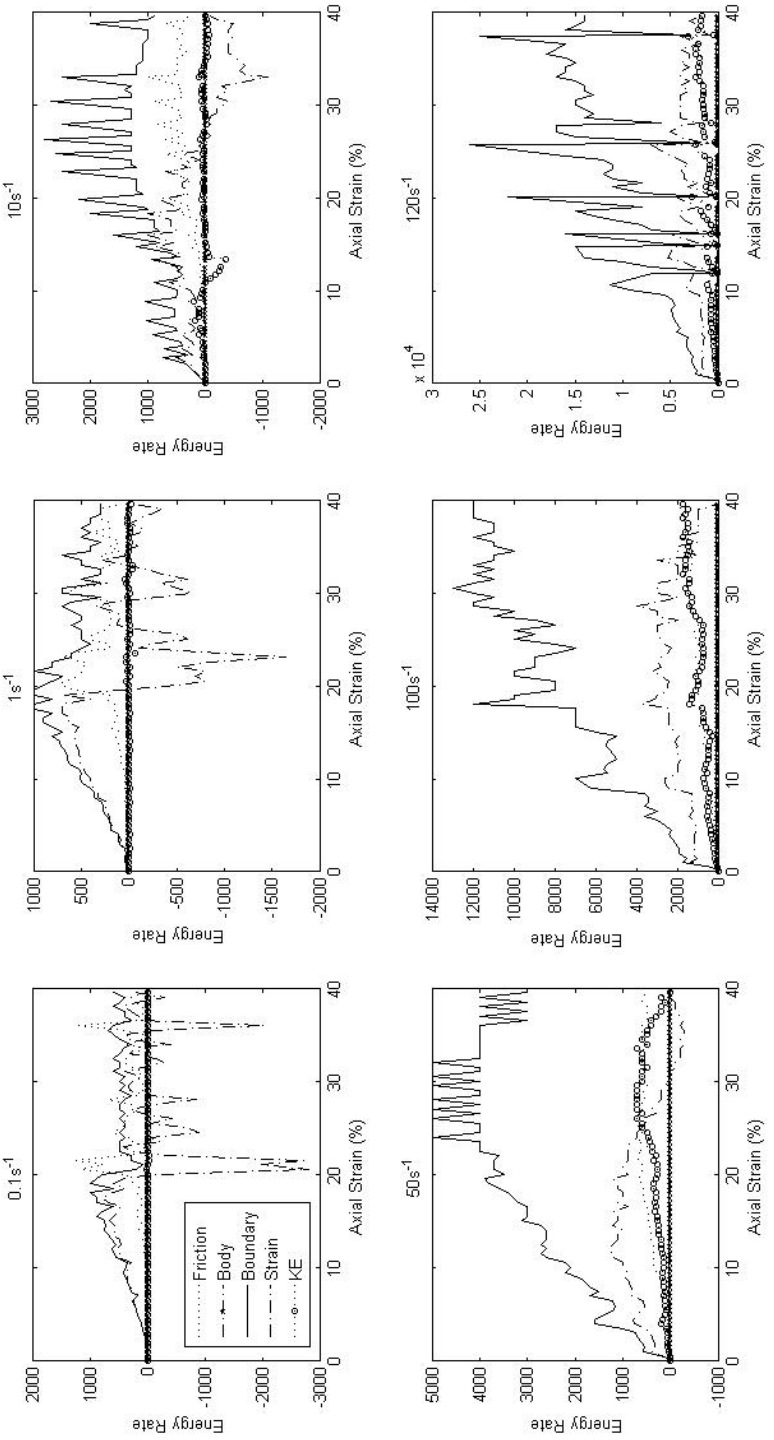

Figure C.35: Energy rate responses for specimen 2 at 4kN bond strength

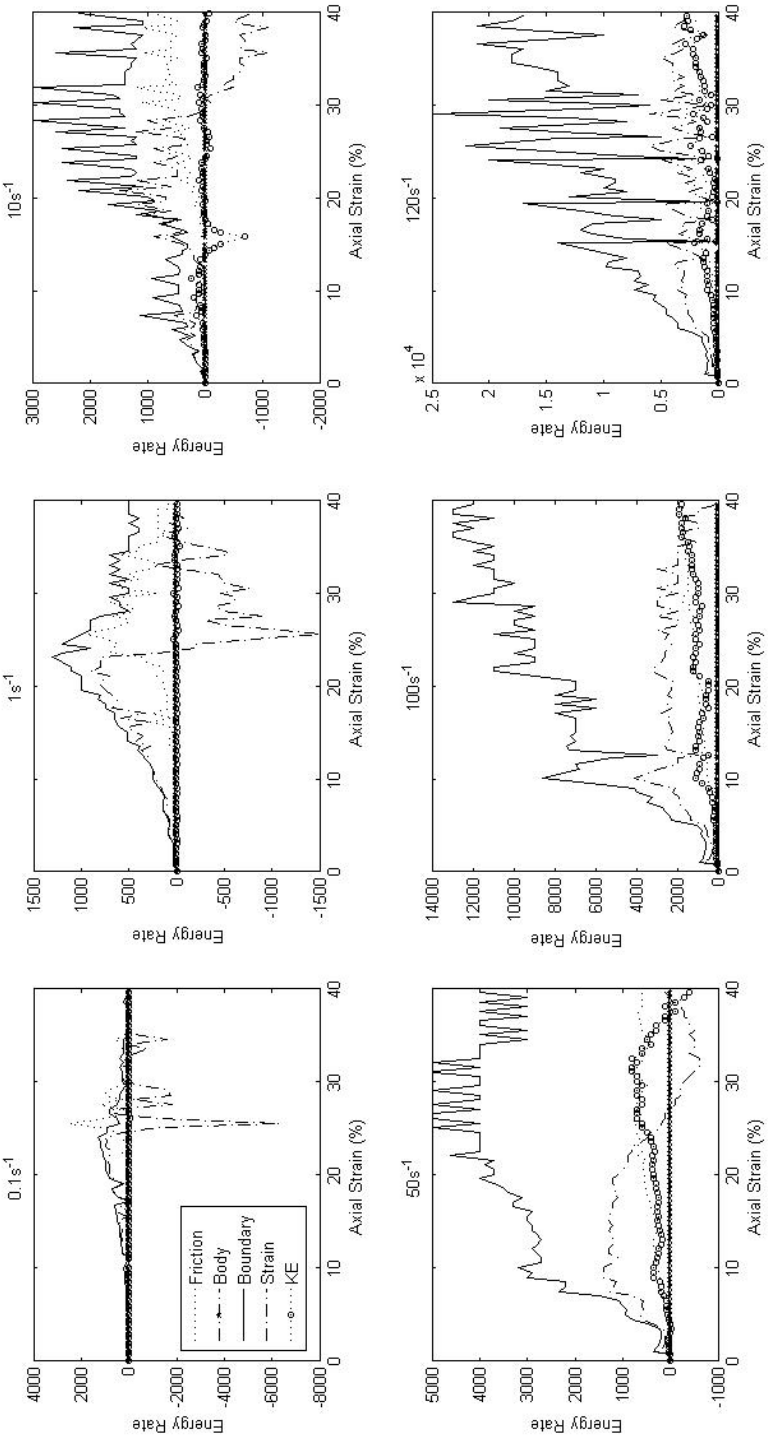

Figure C.36: Energy rate responses for specimen 3 at 4kN bond strength

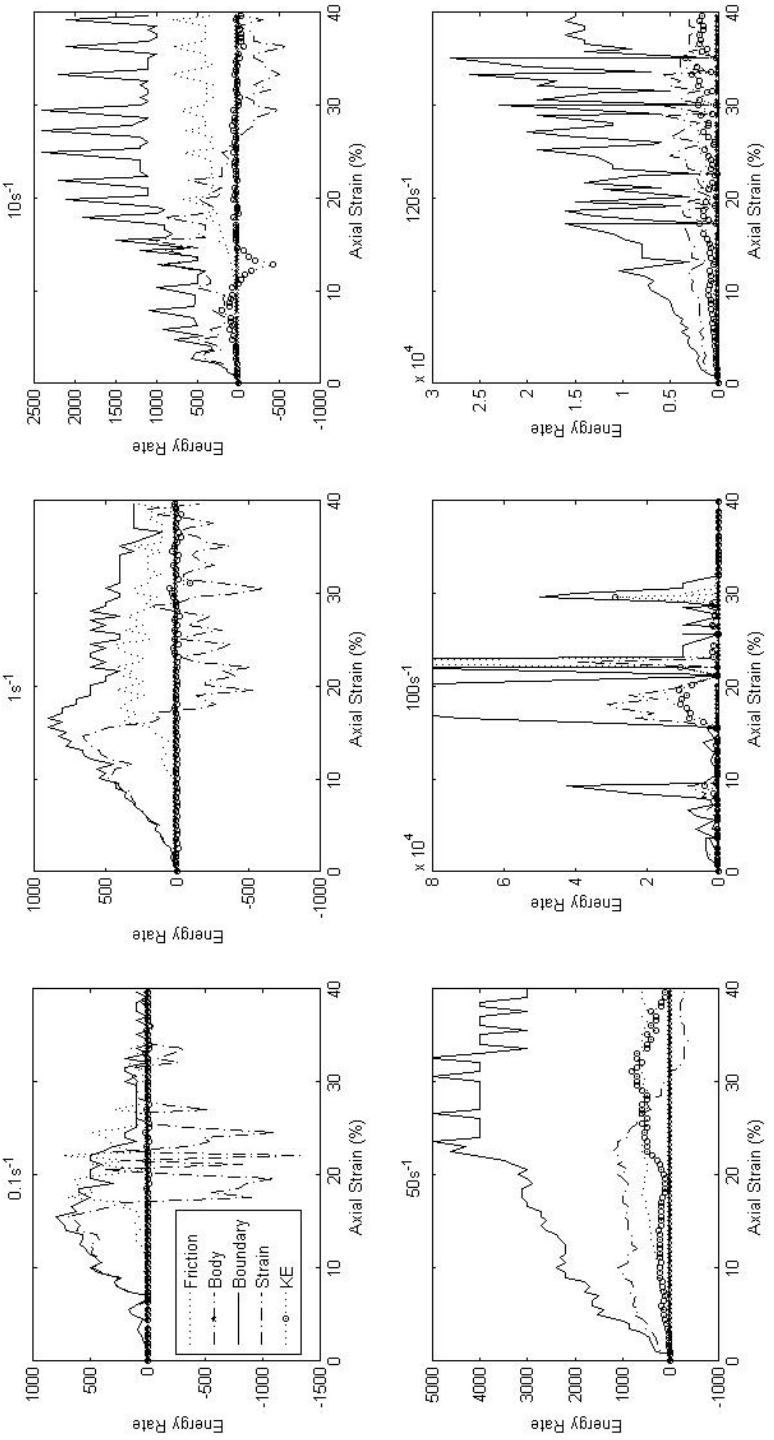

Figure C.37: Energy rate responses for specimen 4 at 4kN bond strength

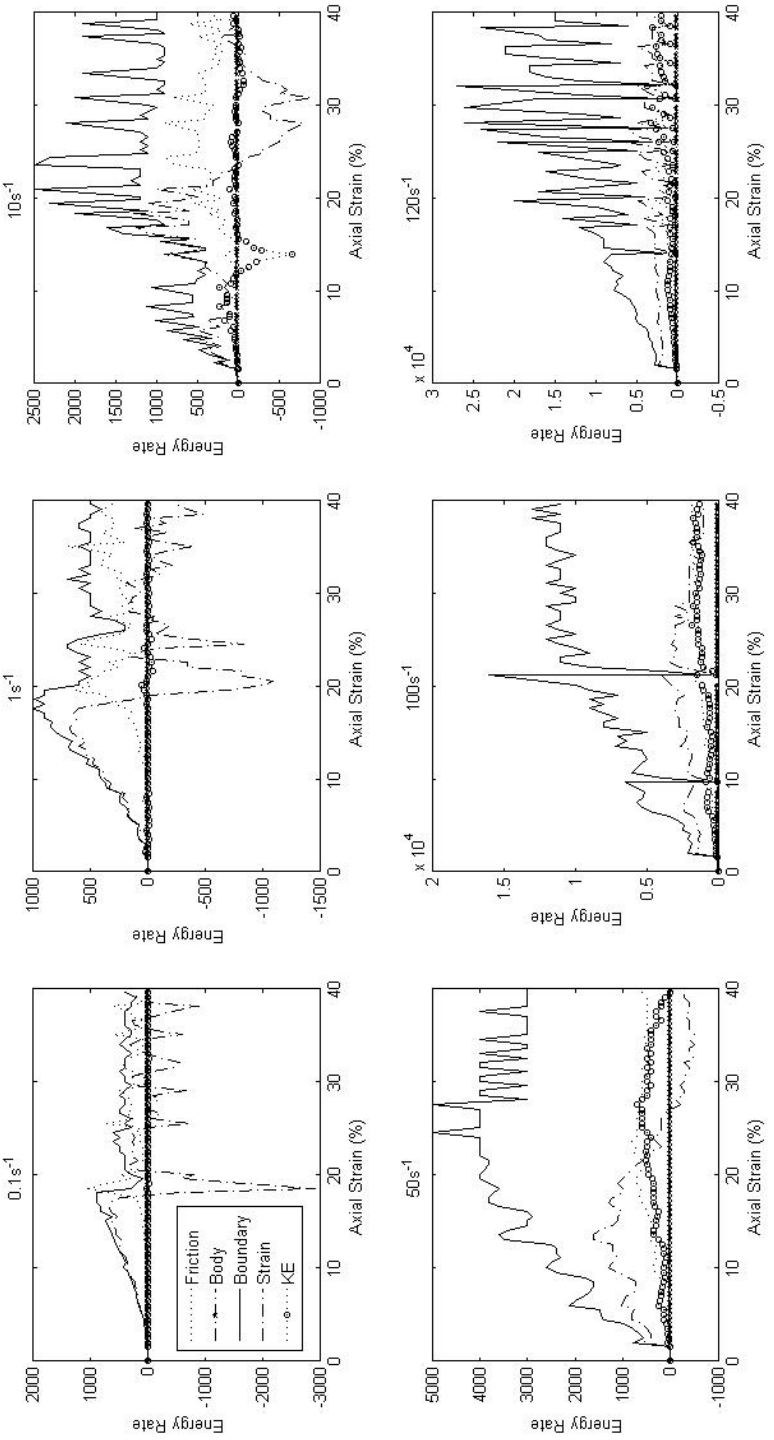

Figure C.38: Energy rate responses for specimen 5 at 4kN bond strength

C.2 HCP Agglomerates

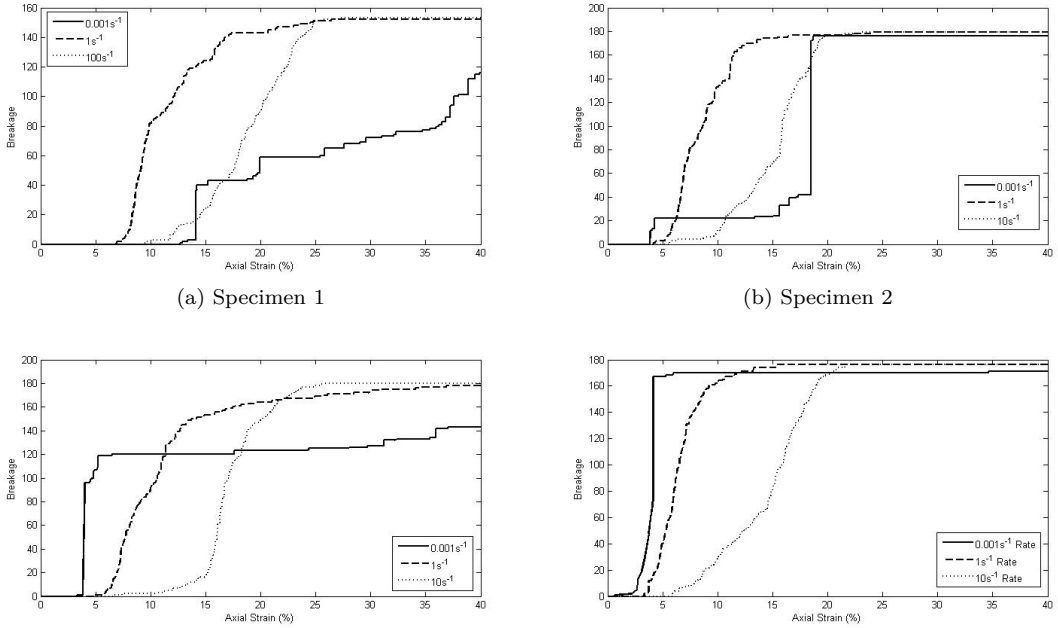

(a) Specimen 1

(b) Specimen 2

(c) Specimen 4

(d) Specimen 5

Figure C.39: Central boulder breakage

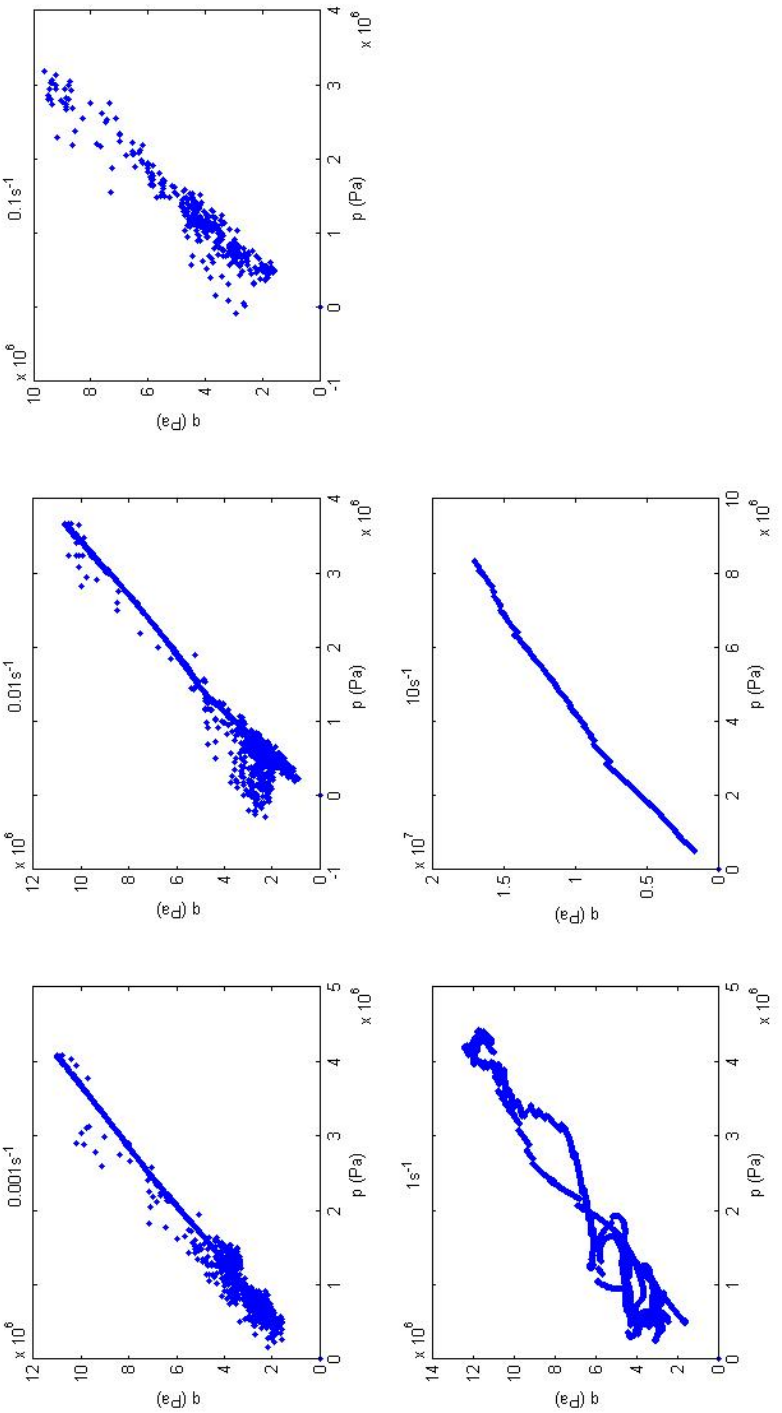

Figure C.40: Stress path for specimen 1

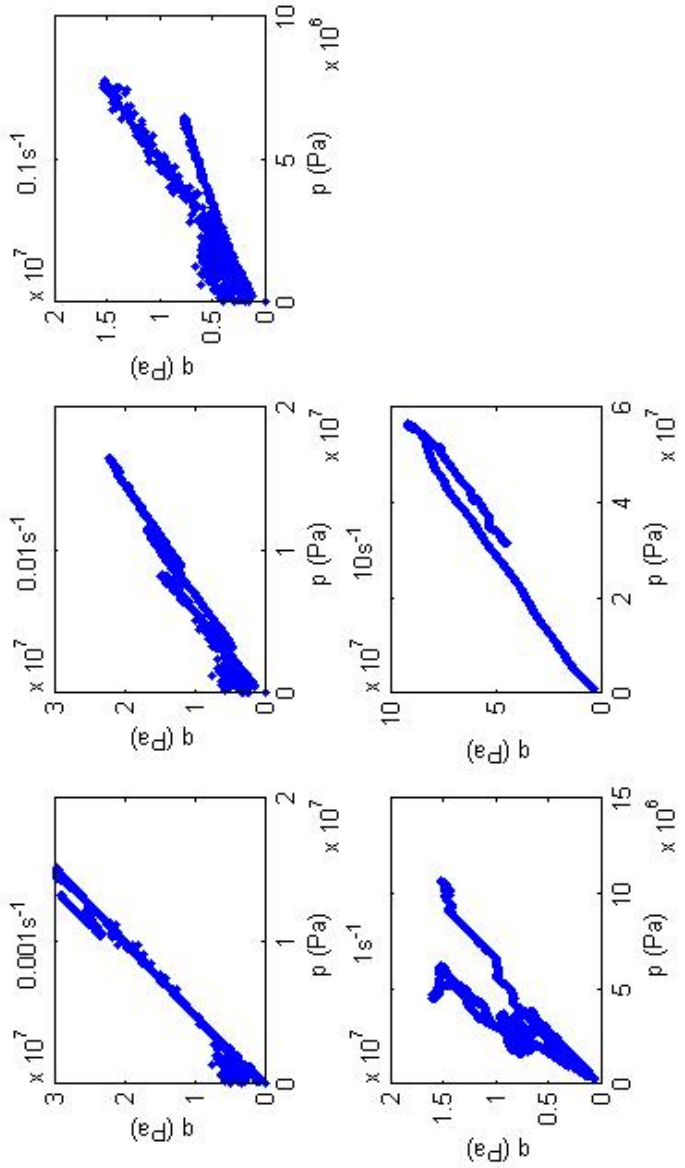

Figure C.41: Stress path for specimen 2

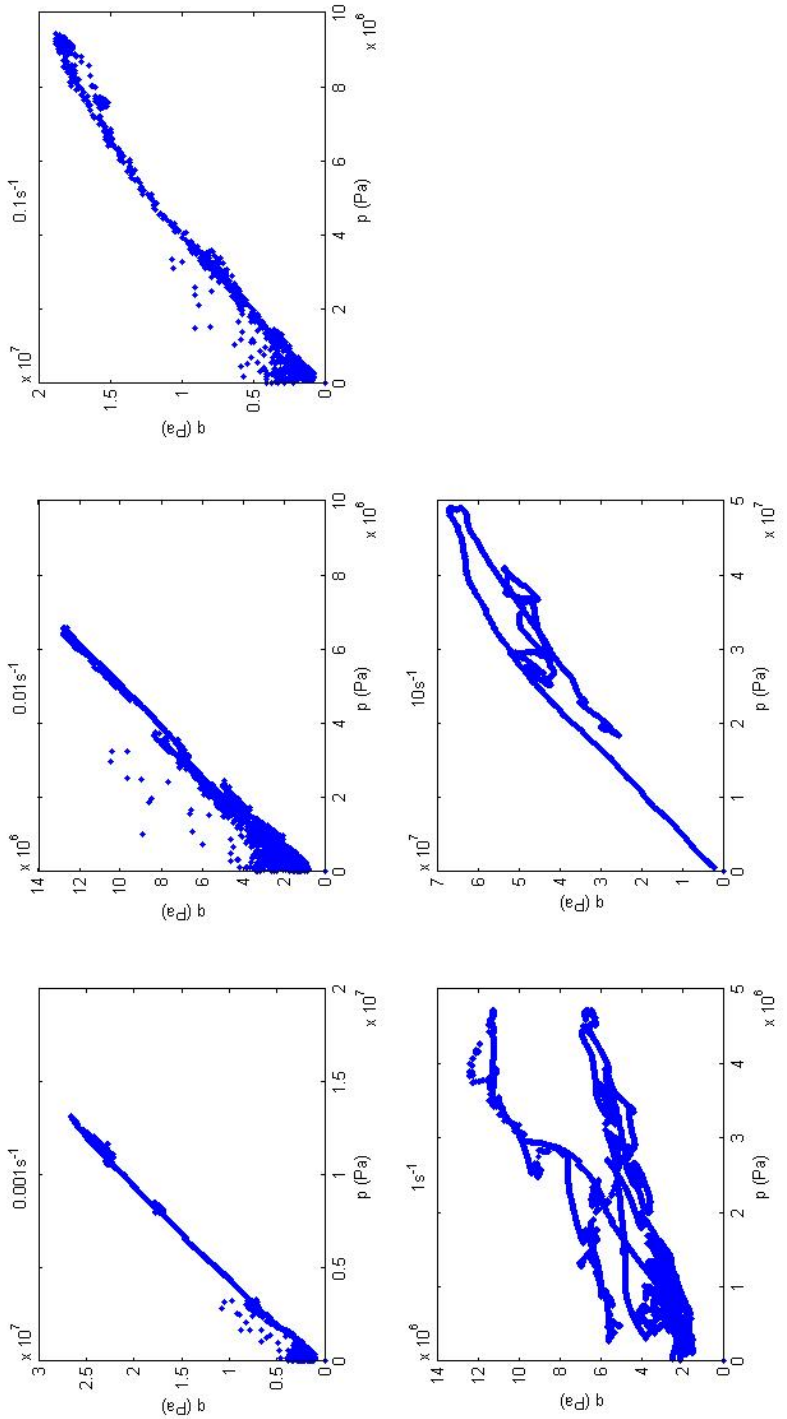

Figure C.42: Stress path for specimen 4

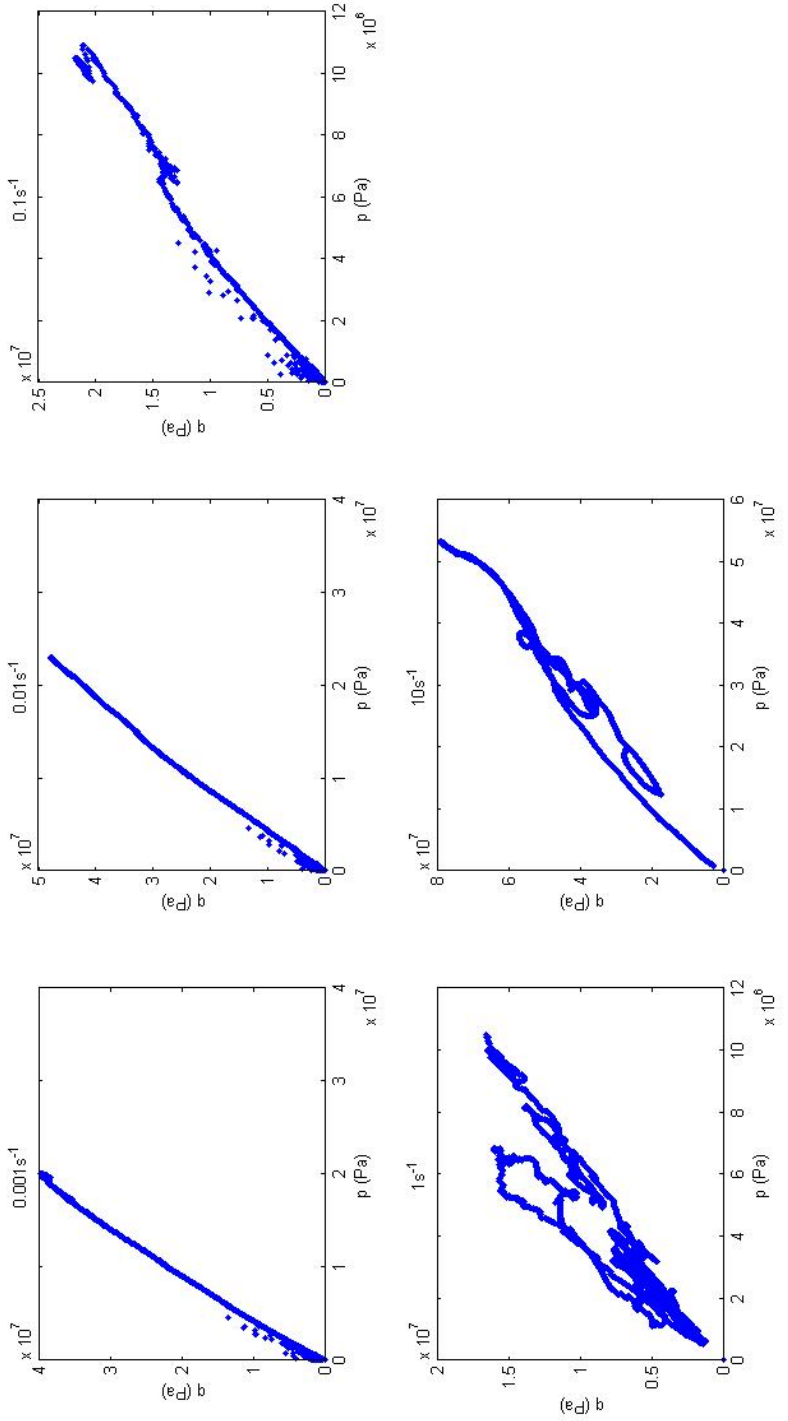

Figure C.43: Stress path for specimen 5

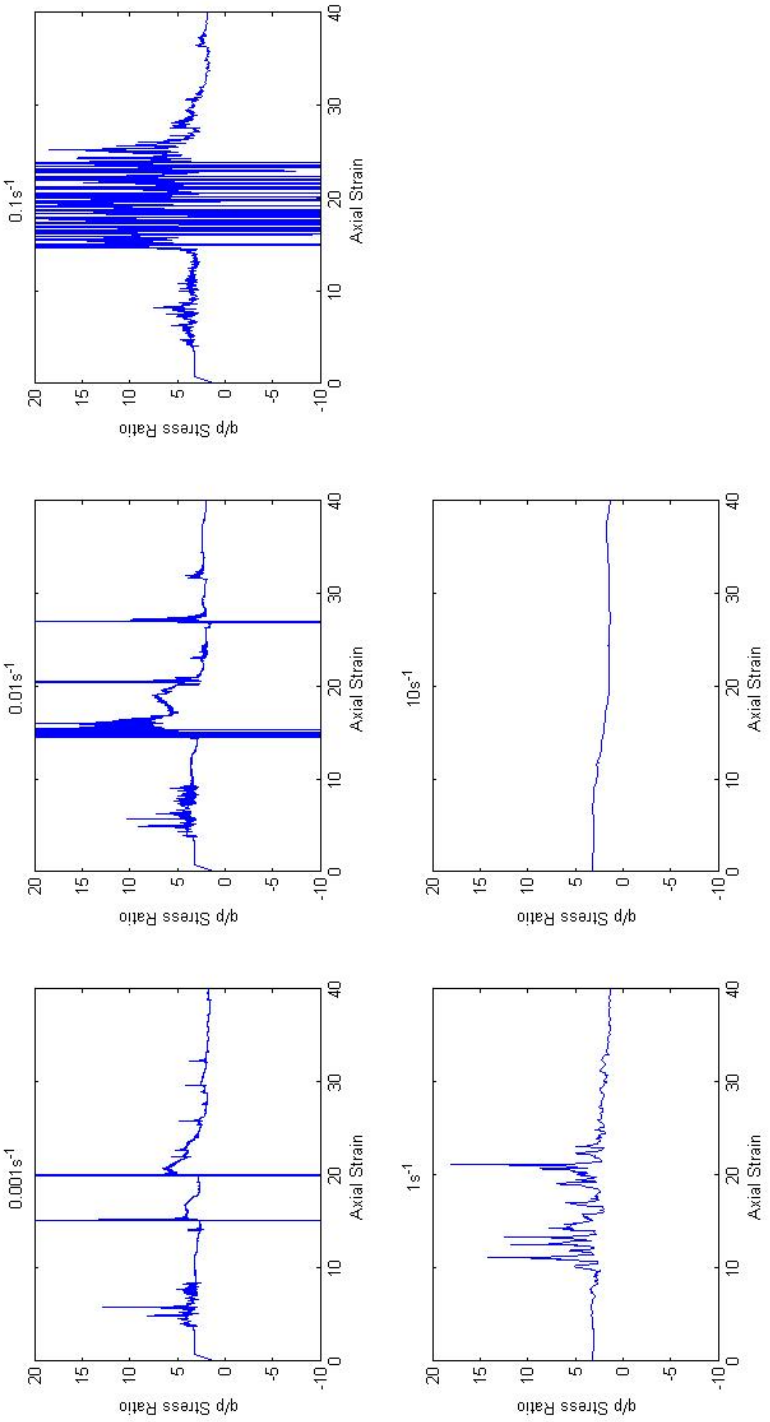

Figure C.44: $\frac{q}{p'}$ stress ratio for specimen 1

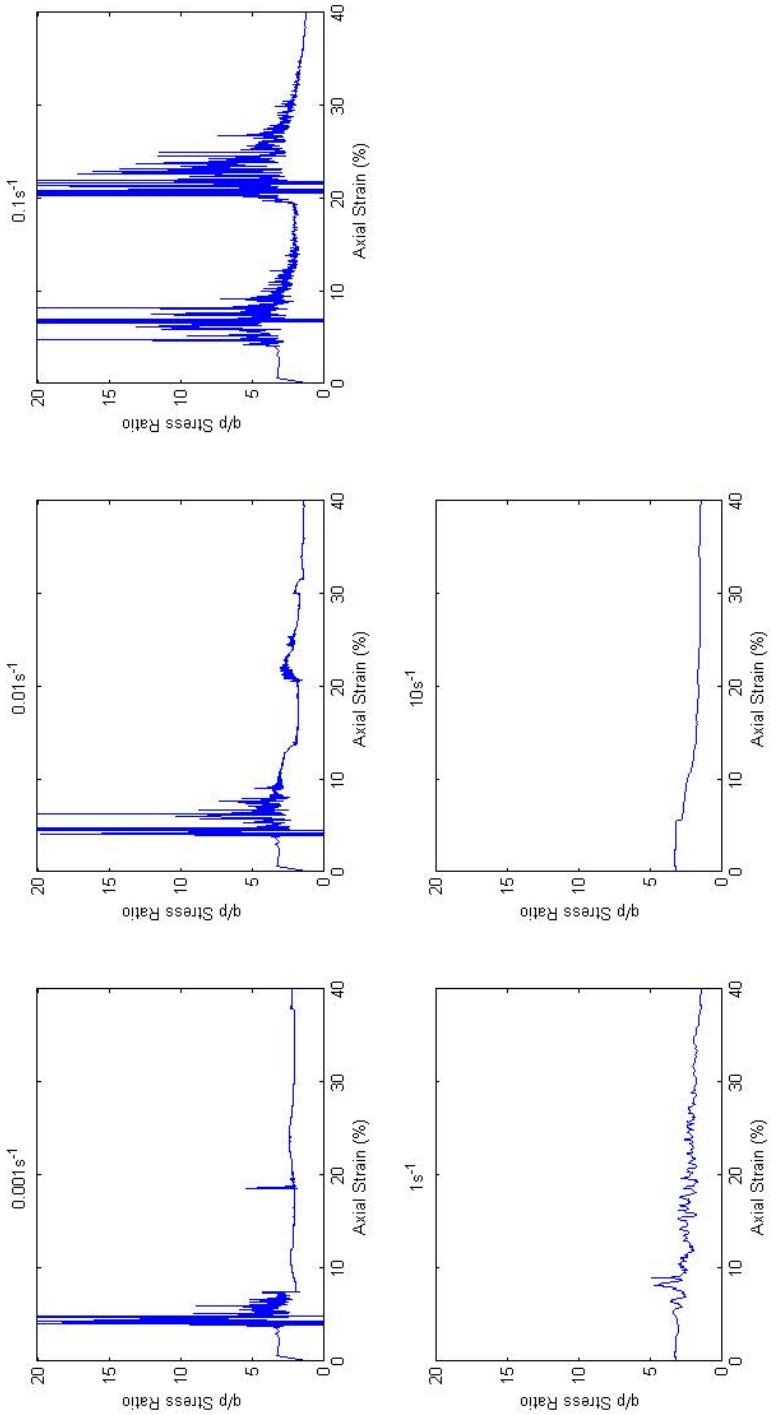

Figure C.45: $\frac{q}{p'}$ stress ratio for specimen 2

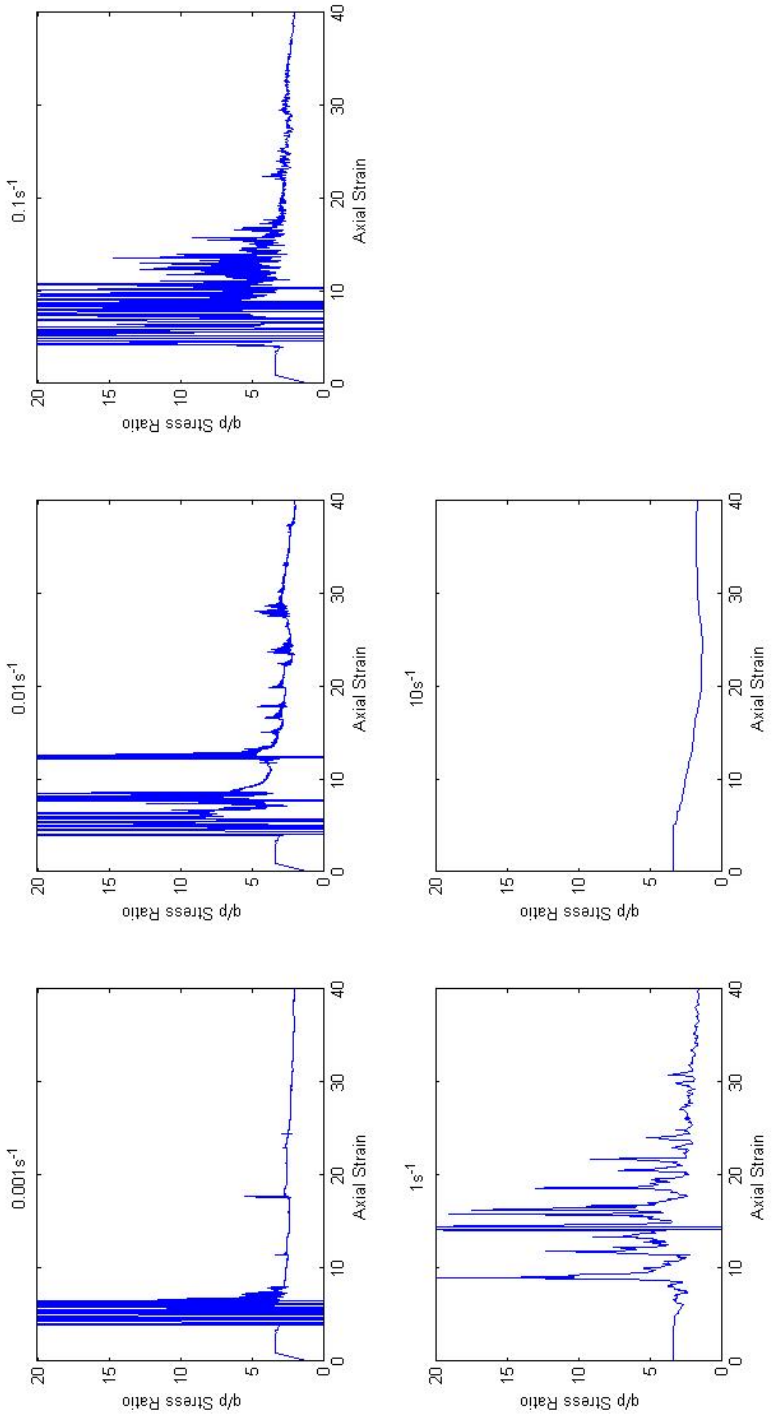

Figure C.46: $\frac{q}{p'}$ stress ratio for specimen 4

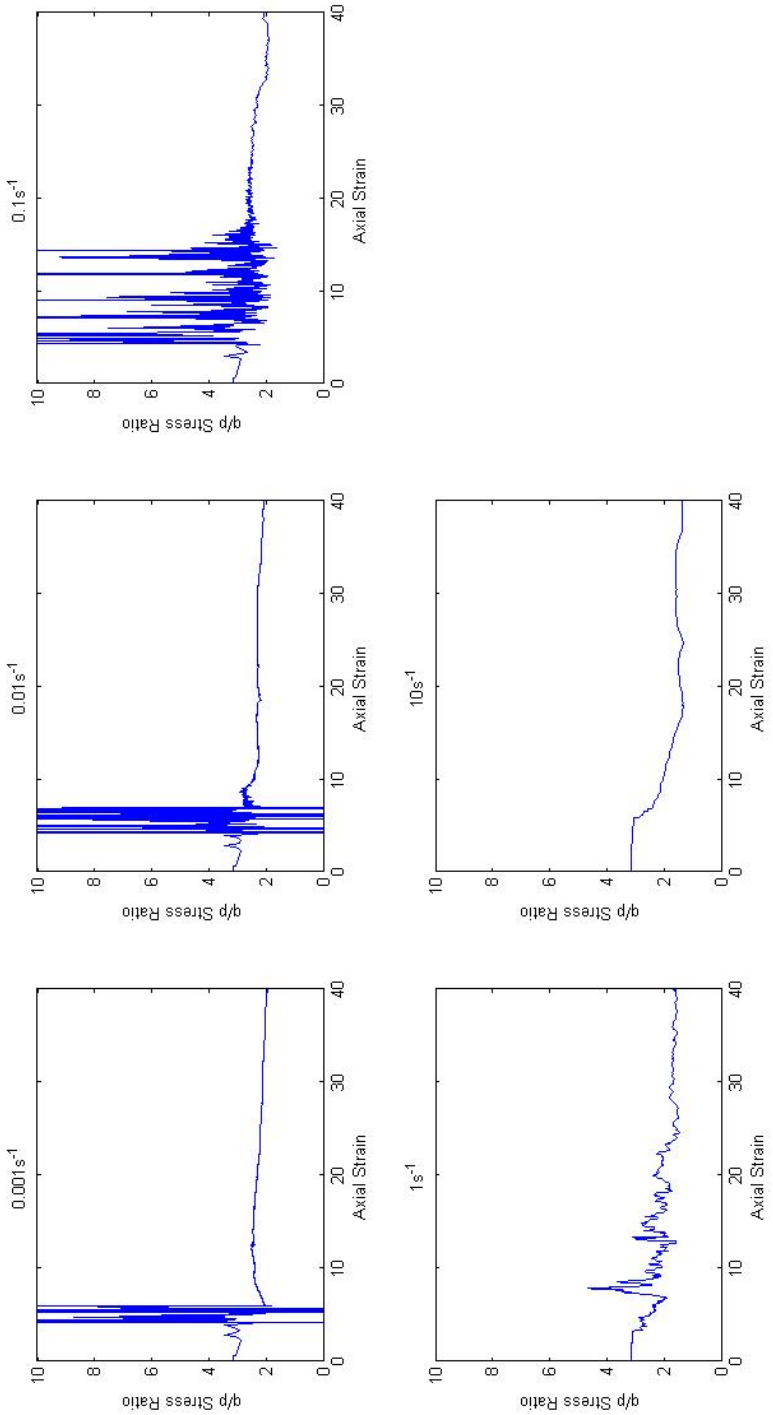

Figure C.47: $\frac{q}{p'}$ stress ratio for specimen 5

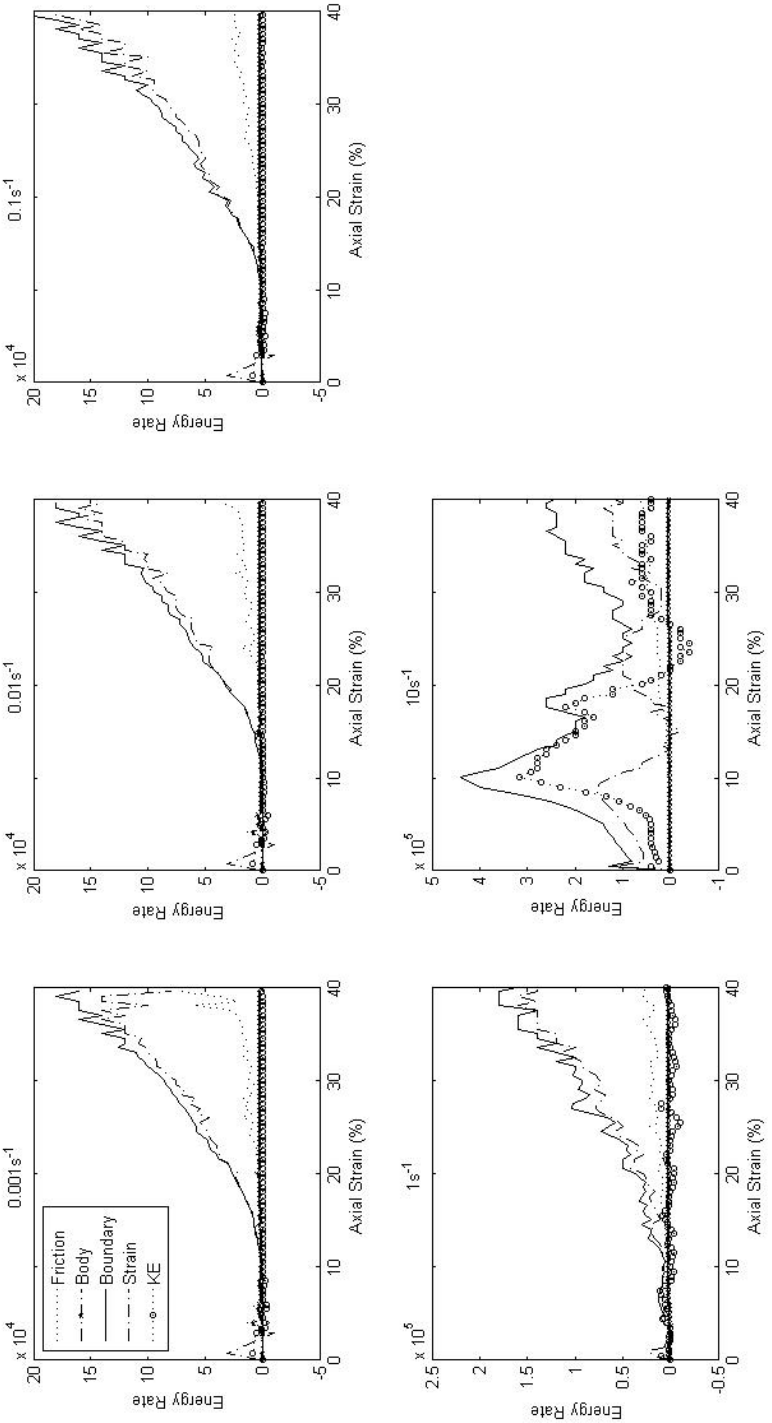

Figure C.48: Energy rate responses for specimen 1

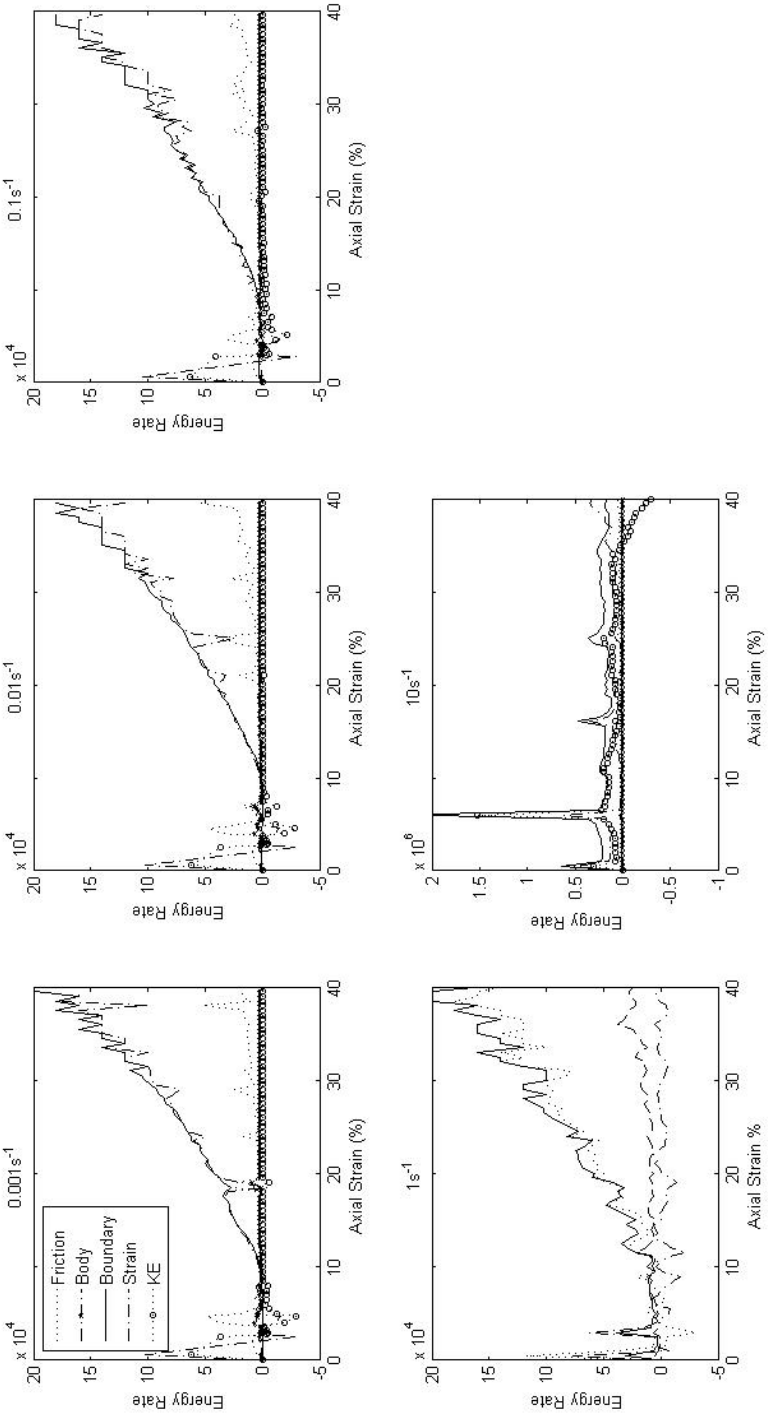

Figure C.49: Energy rate responses for specimen 2

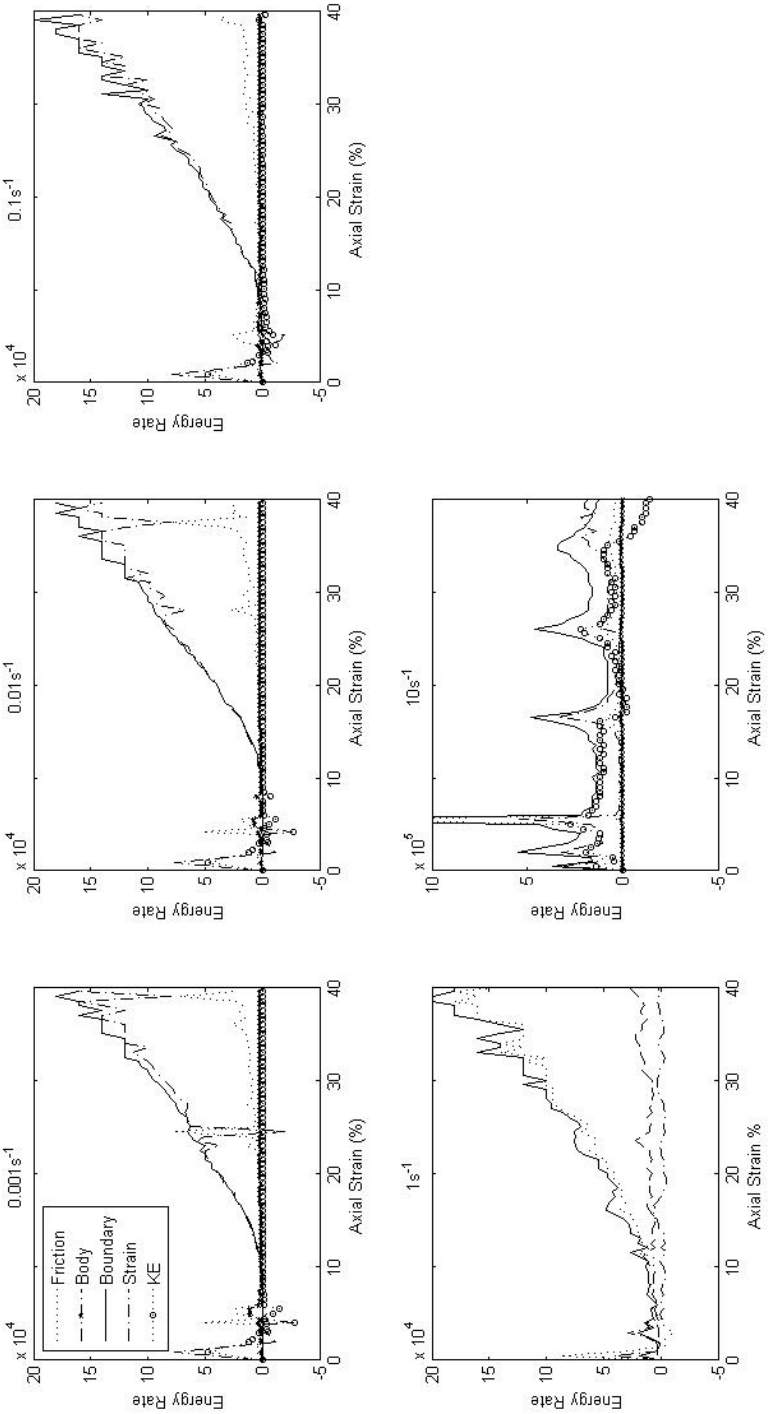

Figure C.50: Energy rate responses for specimen 4

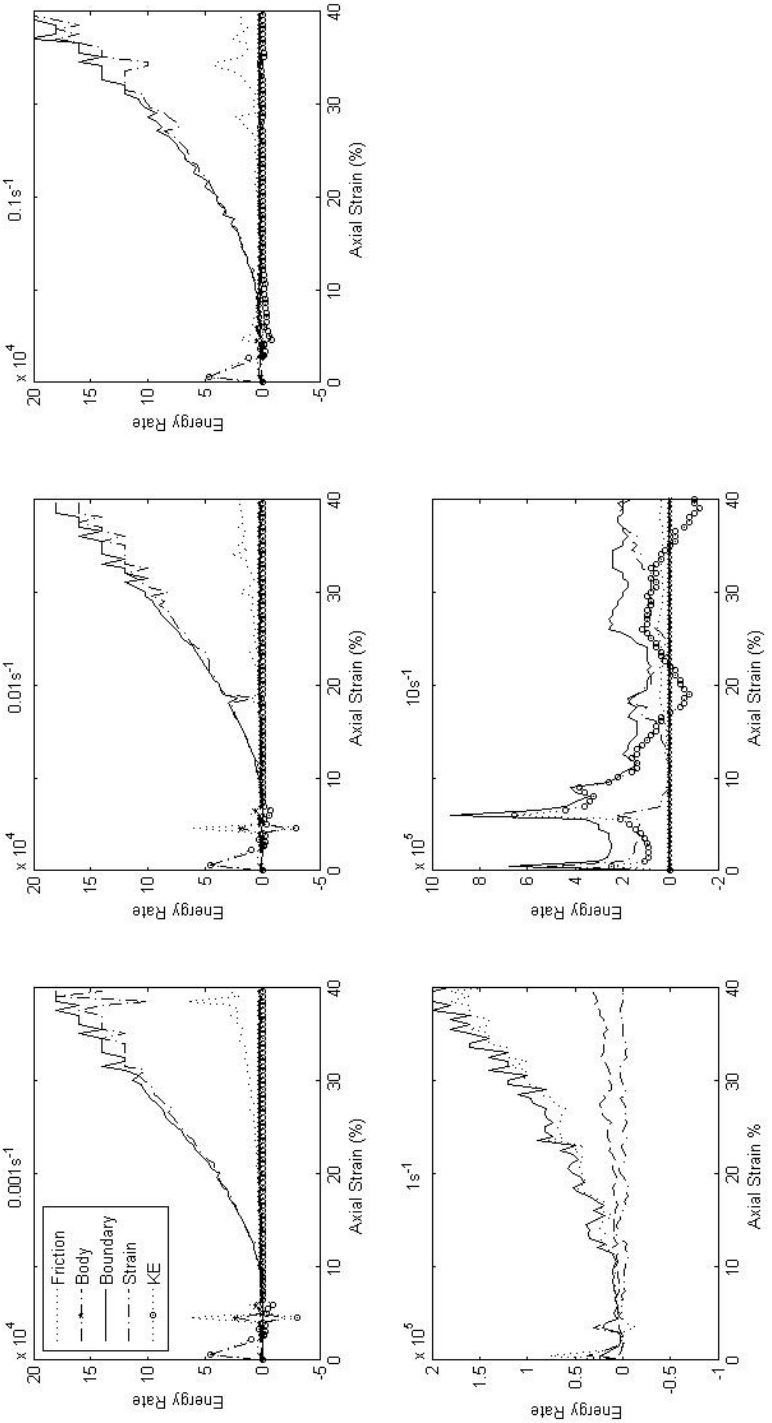

Figure C.51: Energy rate responses for specimen 5

Appendix D

Oedometric Testing - Sandstone

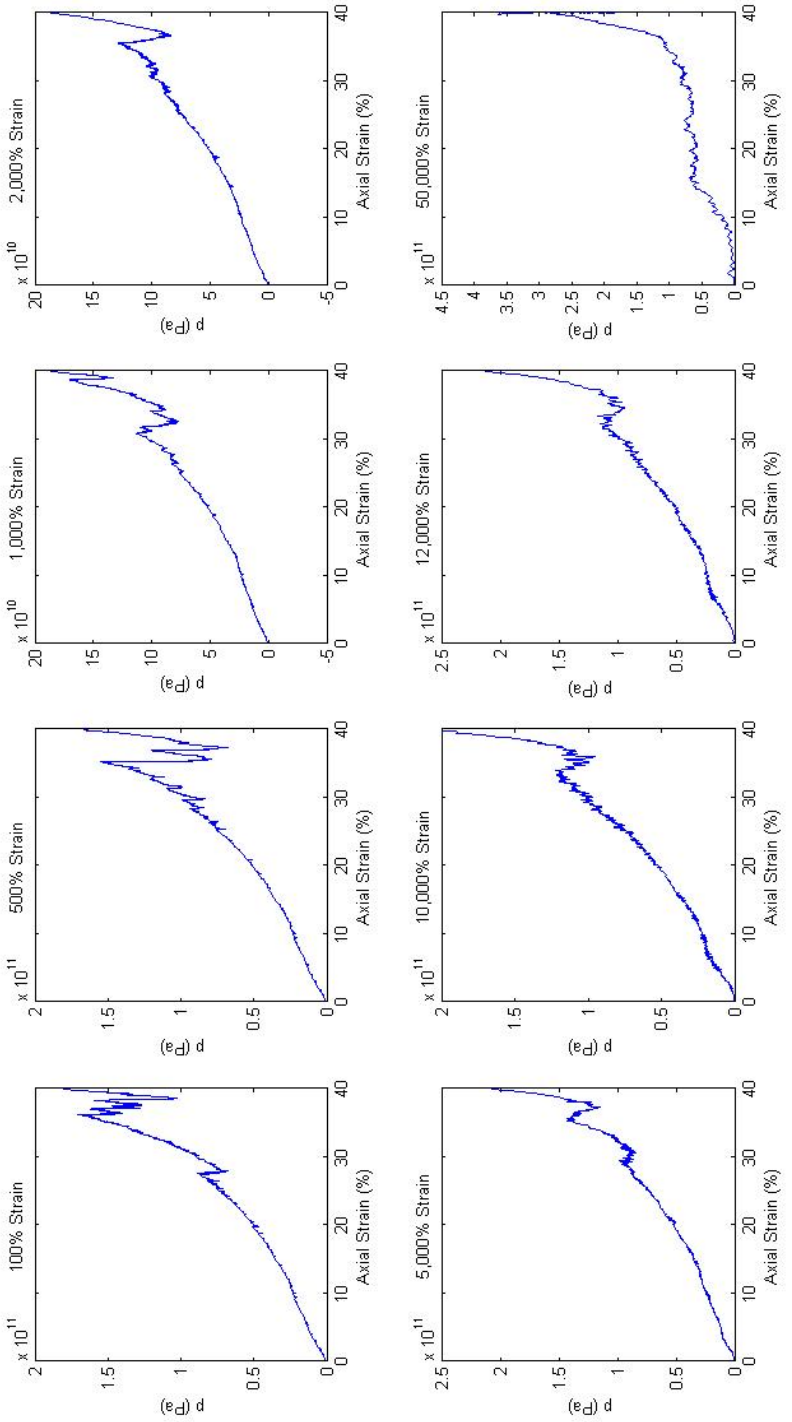

Figure D.1: Mean stress response for sandstone specimen 2

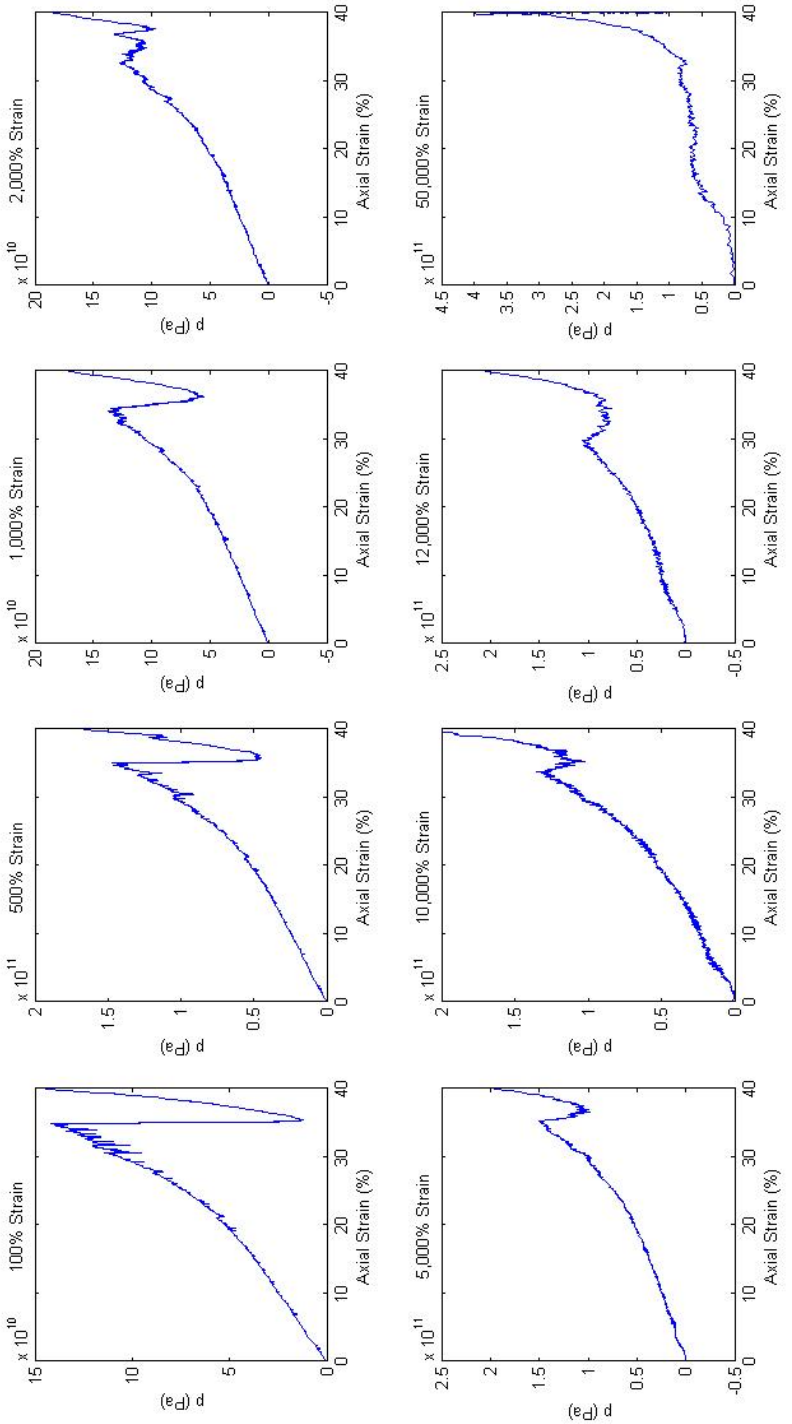

Figure D.2: Mean stress response for sandstone specimen 3

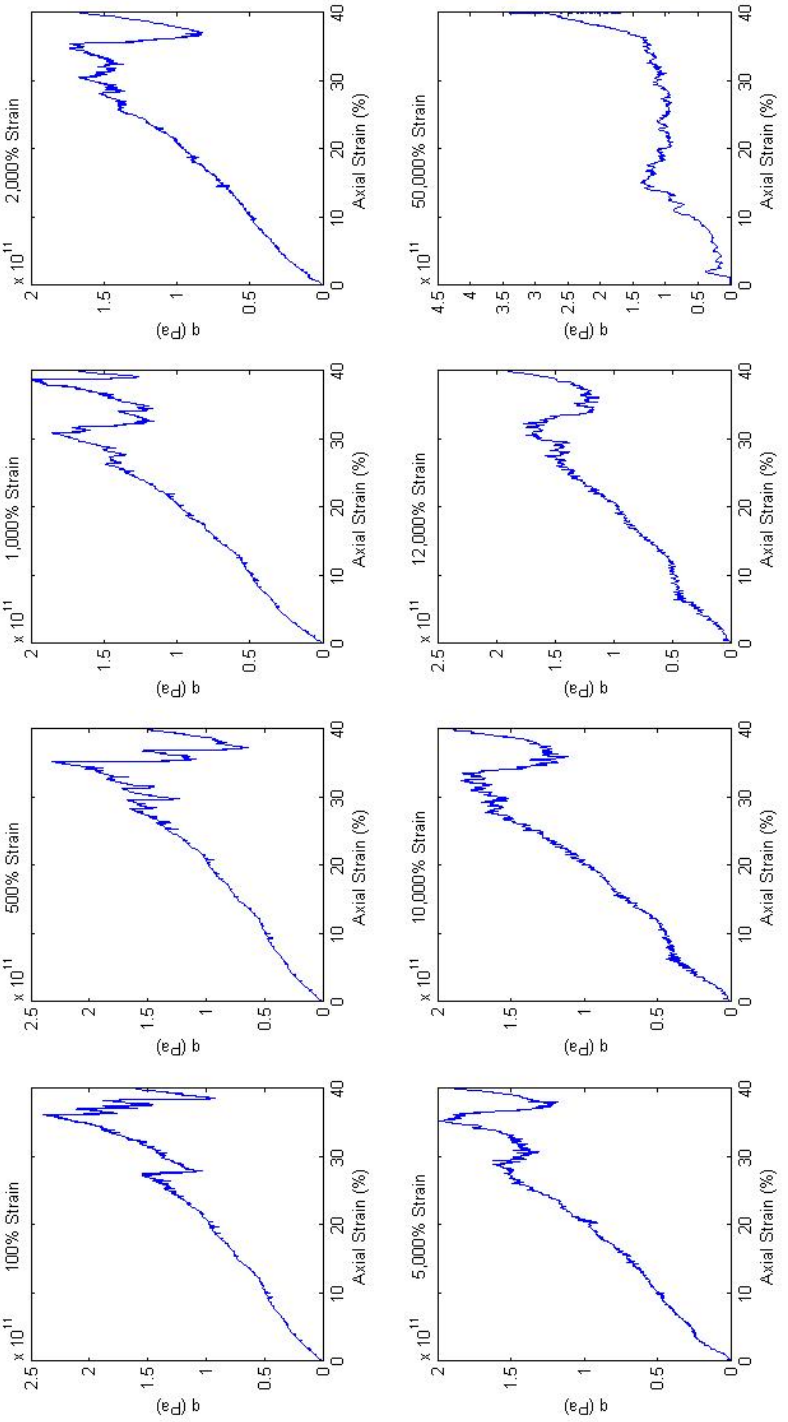

Figure D.3: Deviatoric stress response for sandstone specimen 2

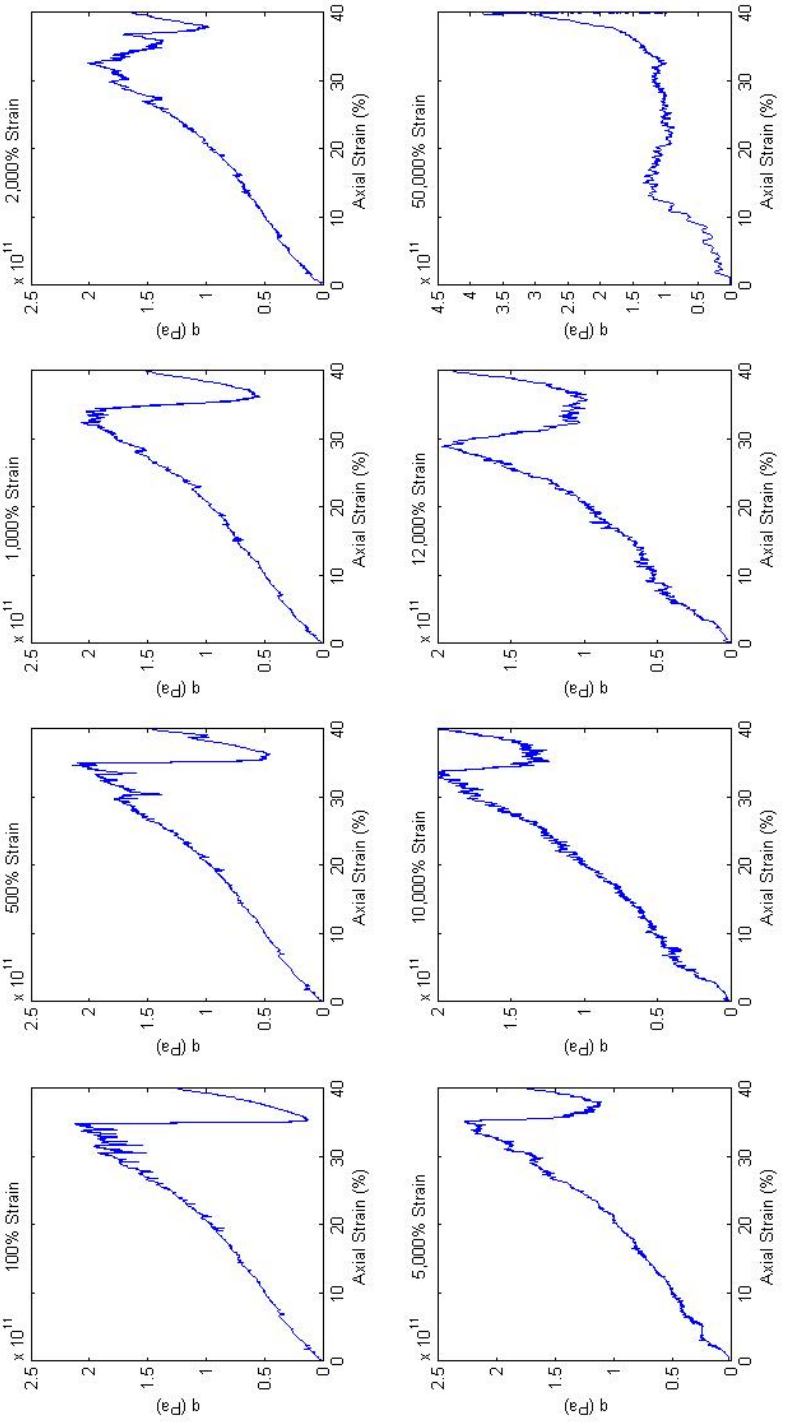

Figure D.4: Deviatoric stress response for sandstone specimen 3

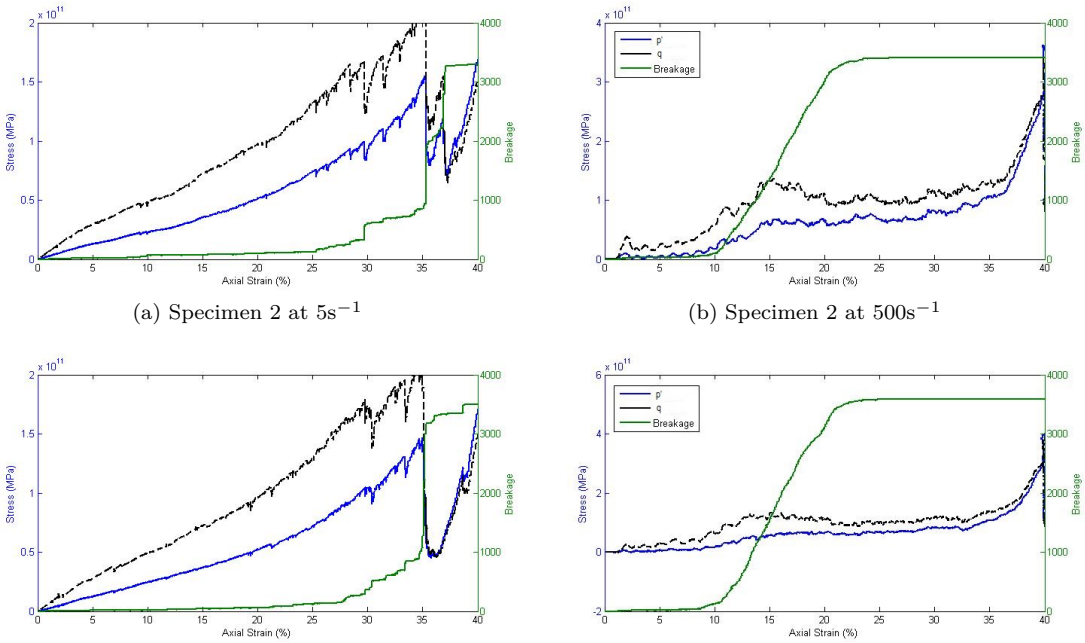

(a) Specimen 2 at $5s^{-1}$

(b) Specimen 2 at $500s^{-1}$

(c) Specimen 3 at $5s^{-1}$

(d) Specimen 3 at $500s^{-1}$

Figure D.5: Breakage compared with mean and deviatoric stress responses

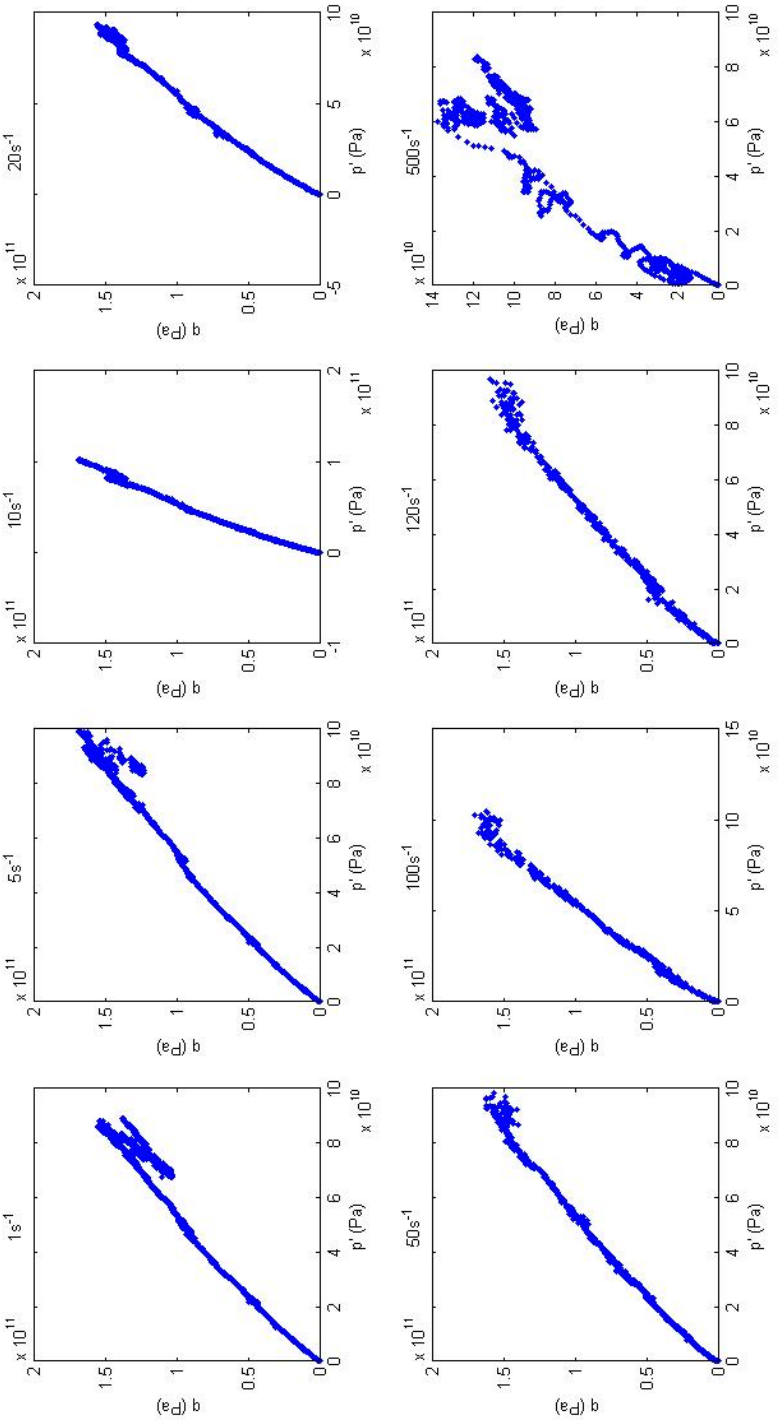

Figure D.6: Stress paths for sandstone specimen 2

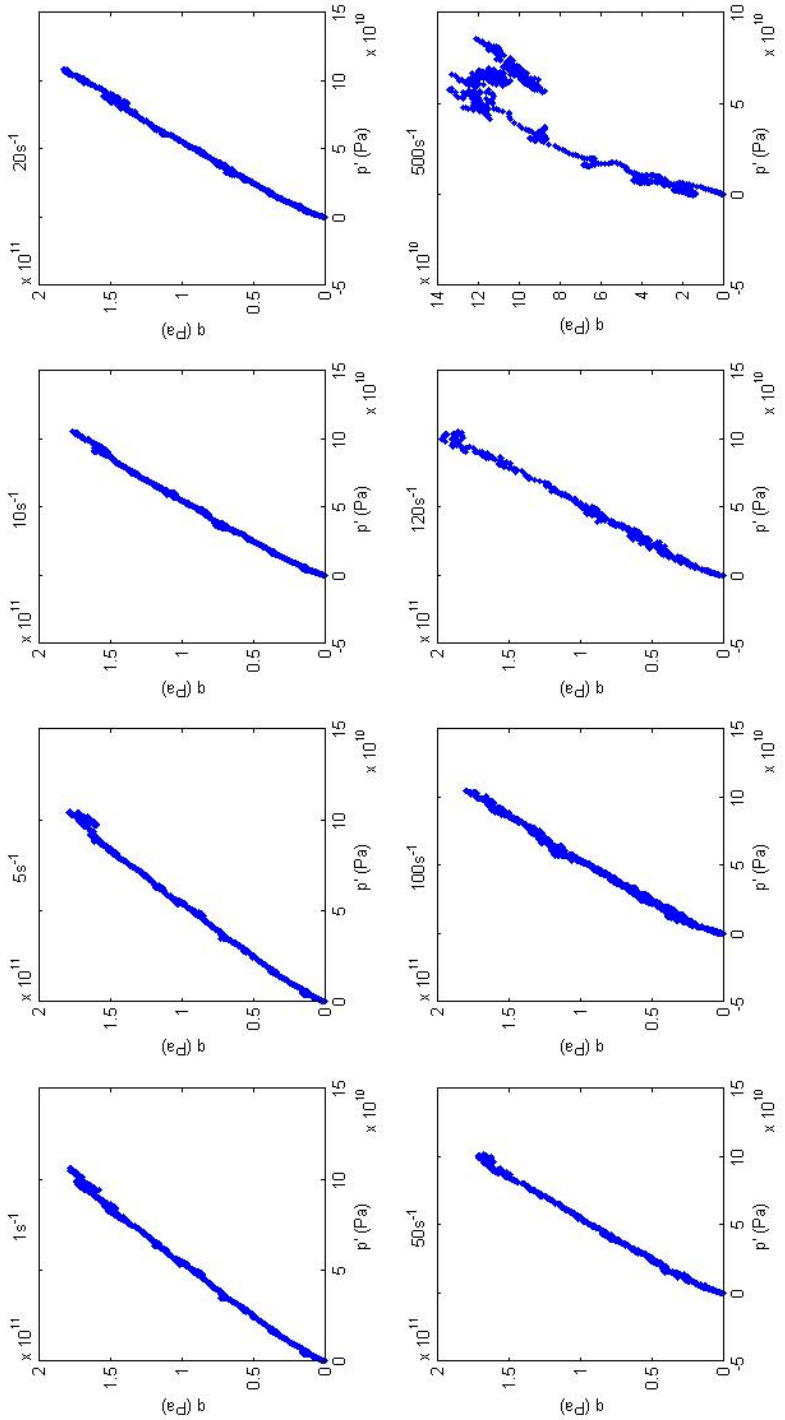

Figure D.7: Stress paths for sandstone specimen 3

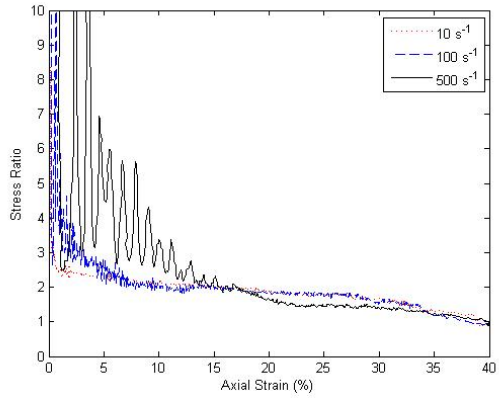

(a) Specimen 2

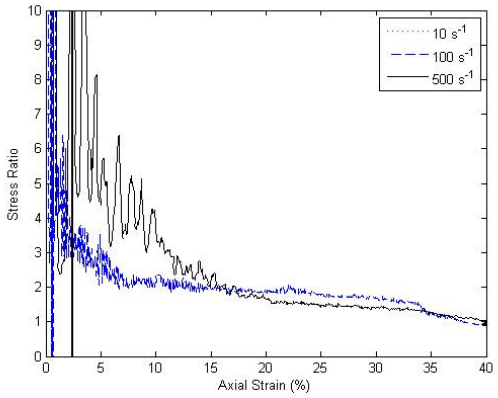

(b) Specimen 3

Figure D.8: $\frac{q}{p'}$ stress ratio

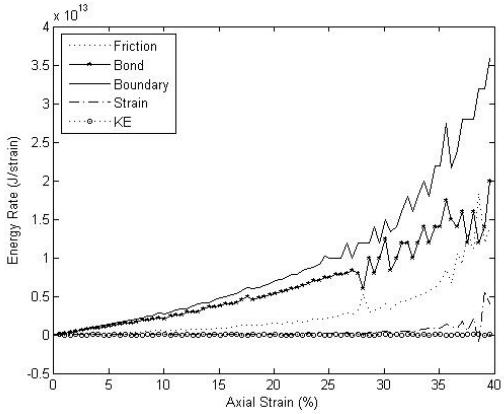

(a) $1s^{-1}$

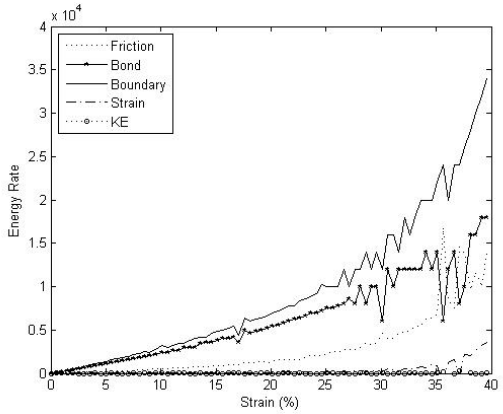

(b) $5s^{-1}$

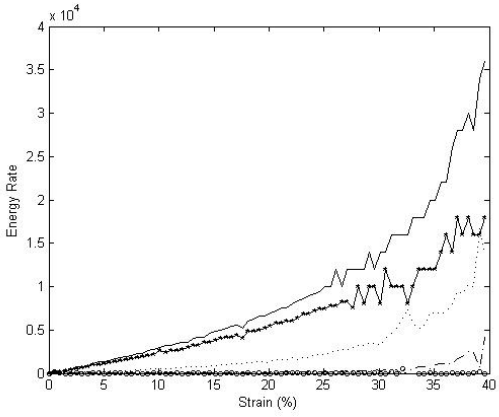

(c) $10s^{-1}$

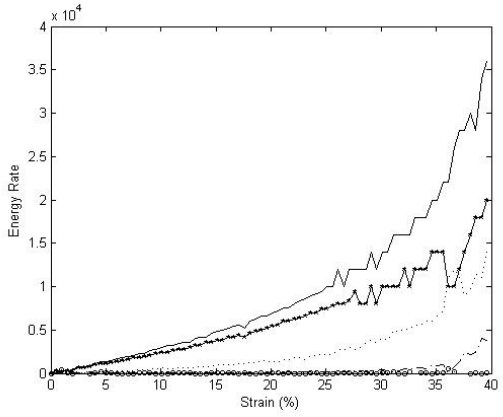

(d) $20s^{-1}$

Figure D.9: Energy rate responses for $1s^{-1}$ to $20s^{-1}$ strain rates for sandstone specimen 2

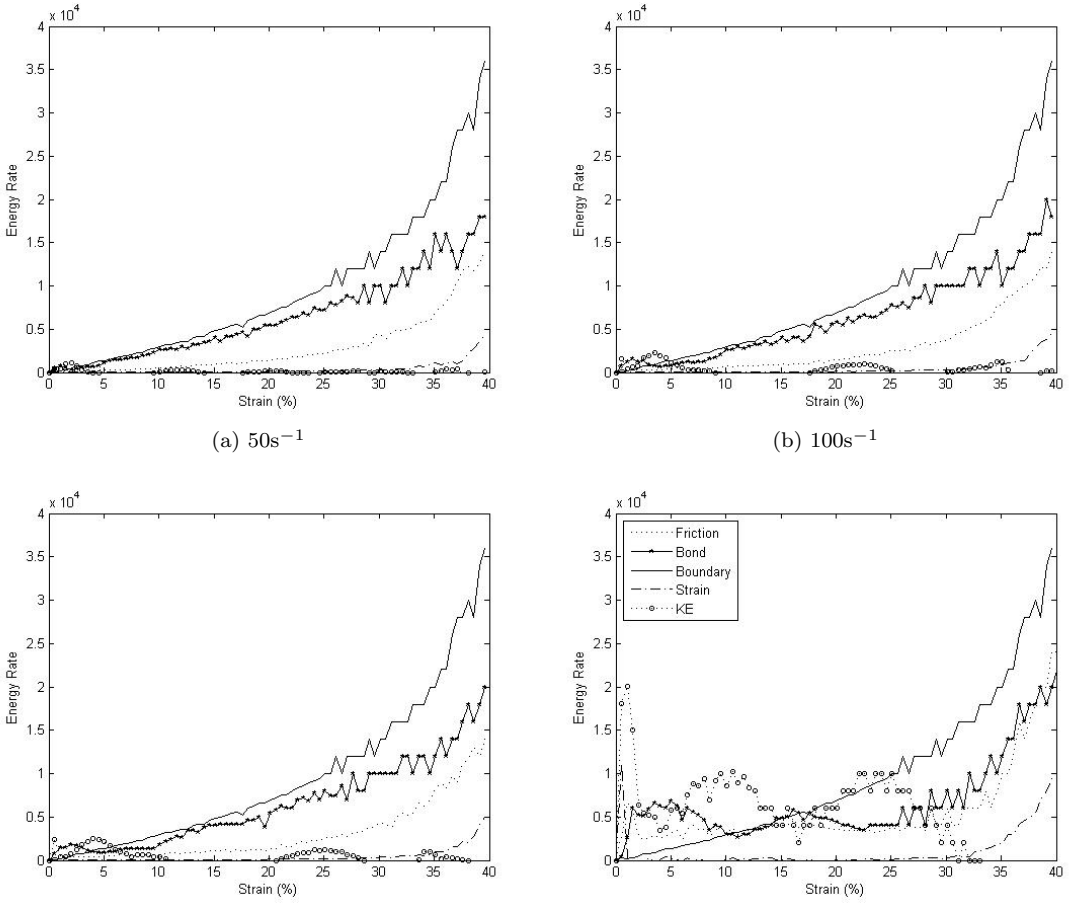

(a) $50s^{-1}$ (b) $100s^{-1}$

(c) $120s^{-1}$ (d) $500s^{-1}$

Figure D.10: Energy rate responses for $50s^{-1}$ to $500s^{-1}$ strain rates for sandstone specimen 2

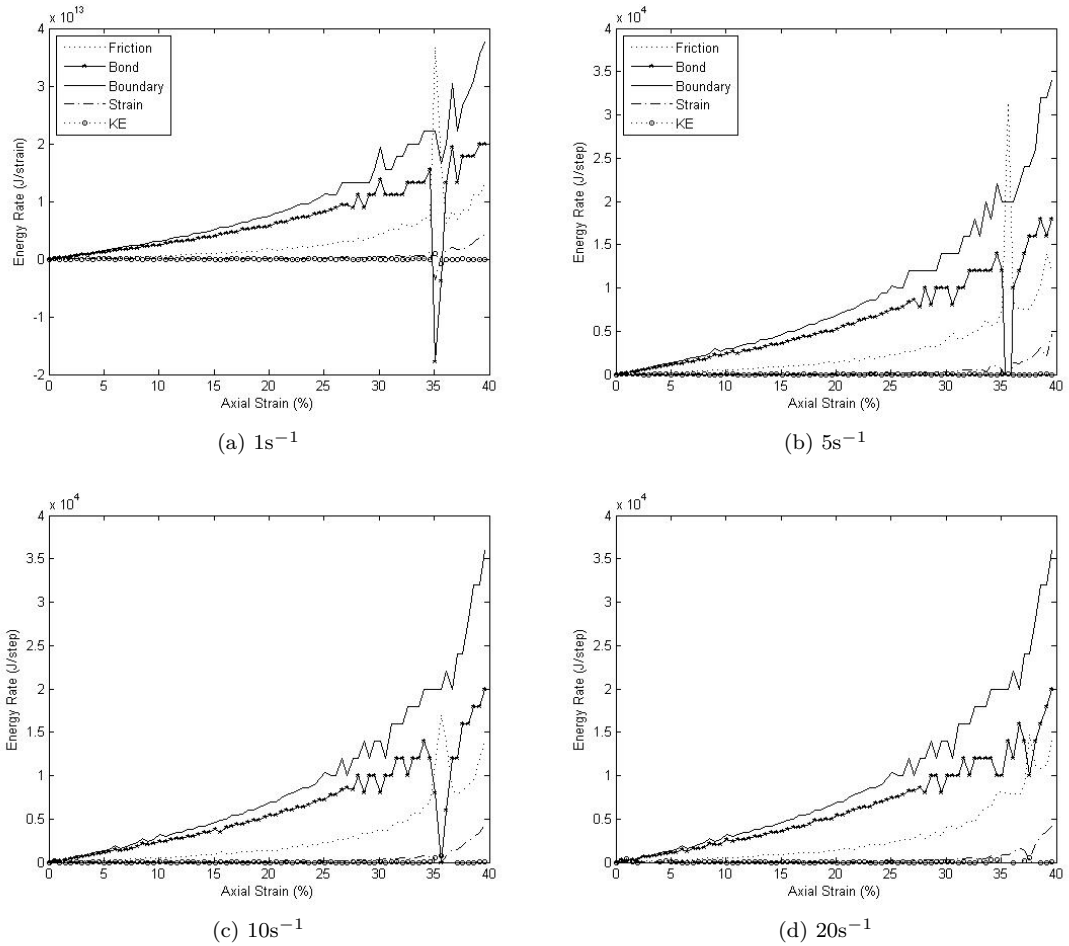

(a) $1s^{-1}$ (b) $5s^{-1}$

(c) $10s^{-1}$ (d) $20s^{-1}$

Figure D.11: Energy rate responses for $1s^{-1}$ to $20s^{-1}$ strain rates for sandstone specimen 3

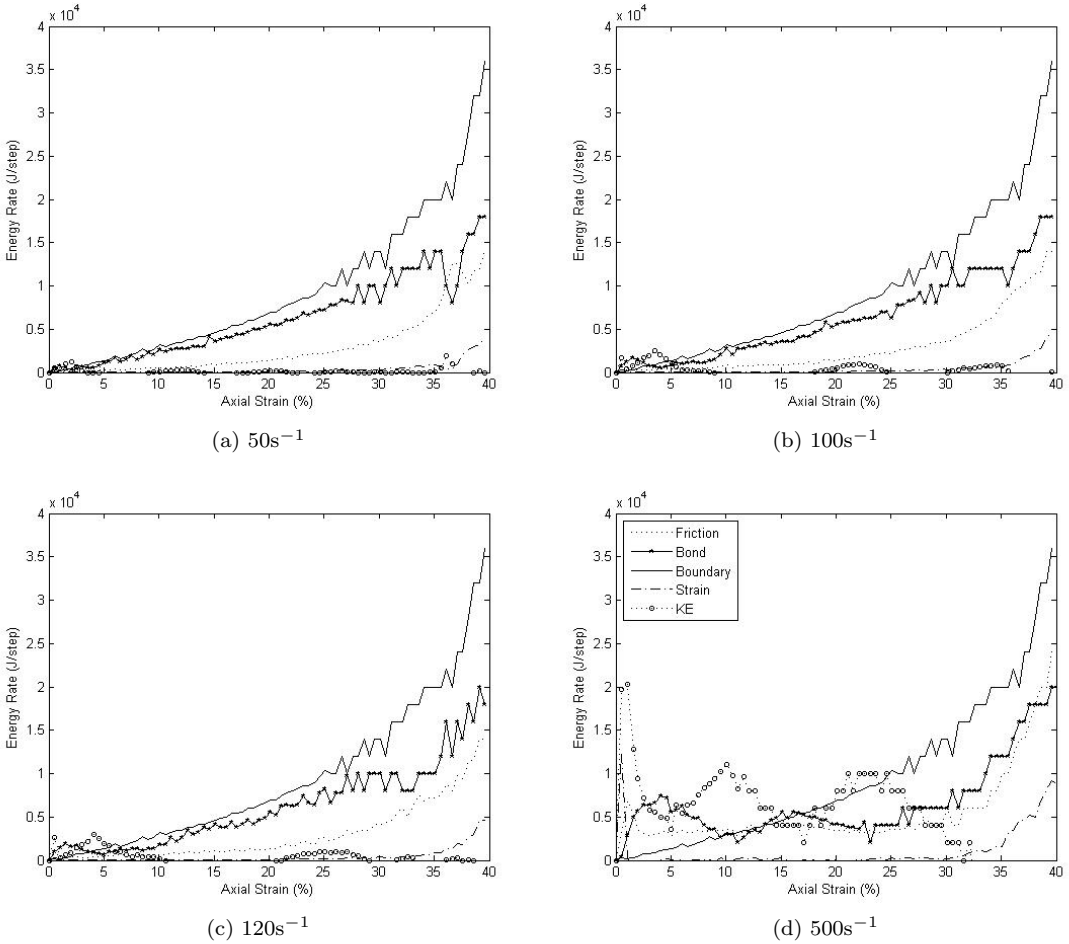

(a) $50s^{-1}$ (b) $100s^{-1}$

(c) $120s^{-1}$ (d) $500s^{-1}$

Figure D.12: Energy rate responses for $50s^{-1}$ to $500s^{-1}$ strain rates for sandstone specimen 3

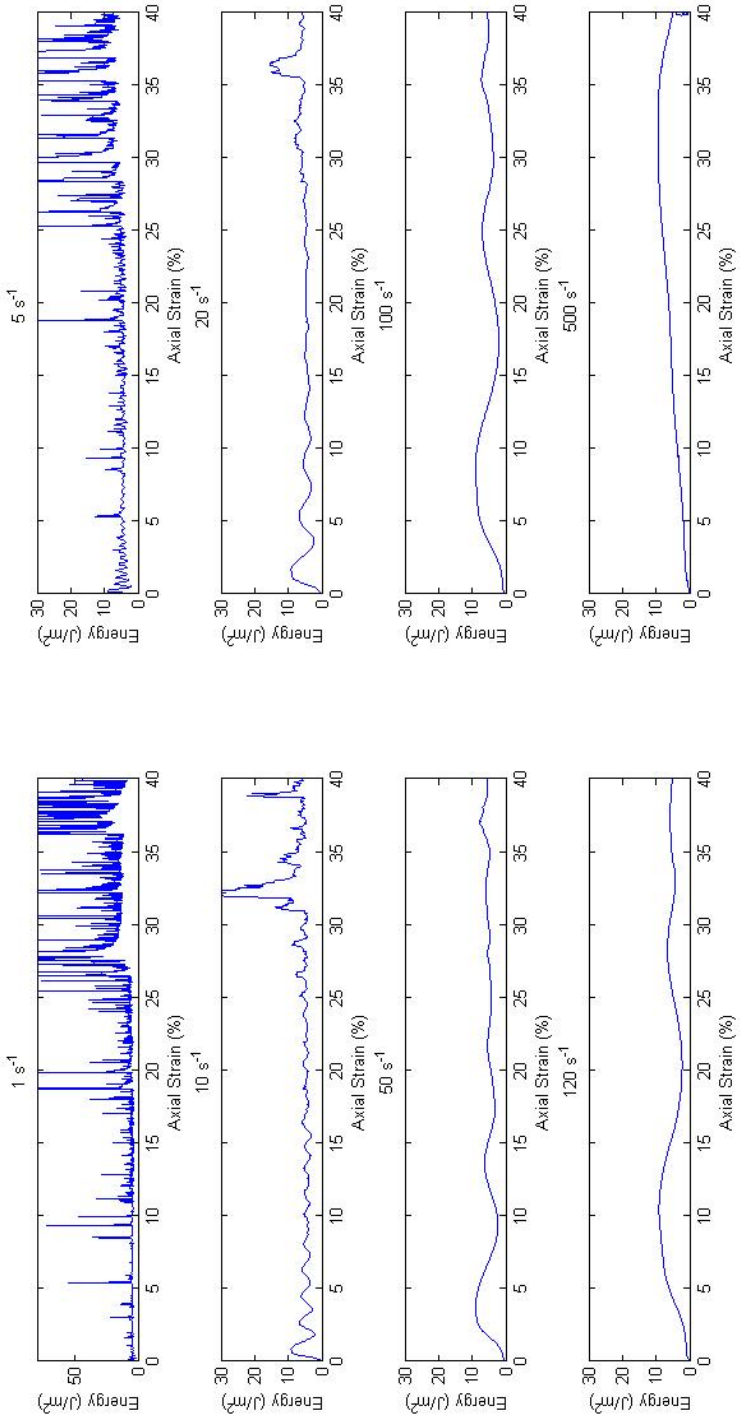

Figure D.13: Normalised kinetic energy for sandstone specimen 2

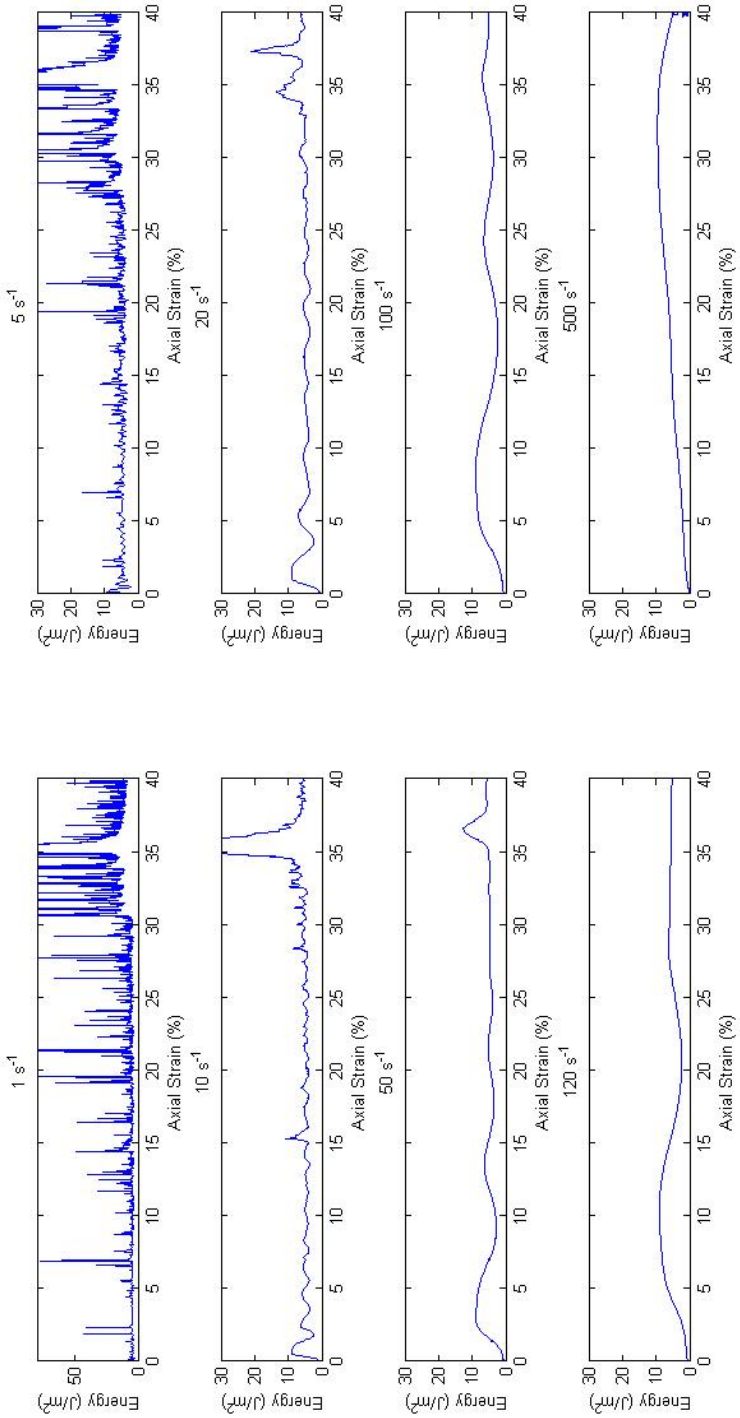

Figure D.14: Normalised kinetic energy for sandstone specimen 3

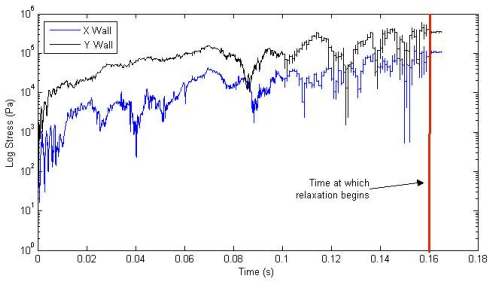

(a) Sandstone 2 at $5s^{-1}$

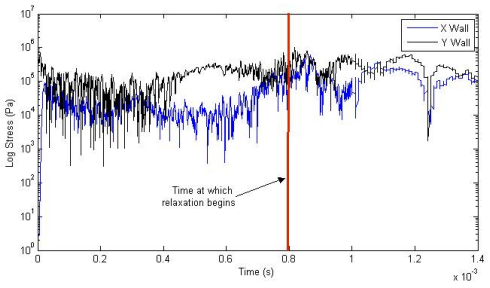

(b) Sandstone 2 at $500s^{-1}$

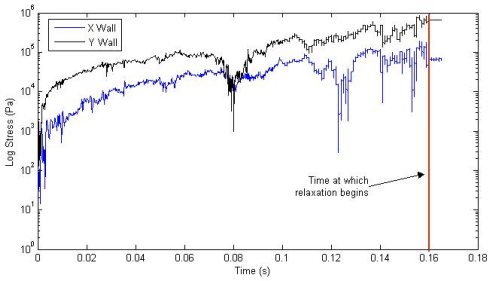

(c) Sandstone 3 at $5s^{-1}$

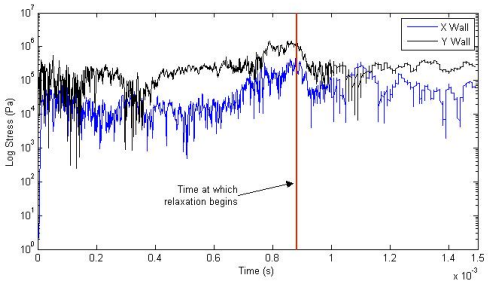

(d) Sandstone 3 at $500s^{-1}$

Figure D.15: Wall stress behaviour over time

Appendix E

Oedometric Testing - Weak Chalk

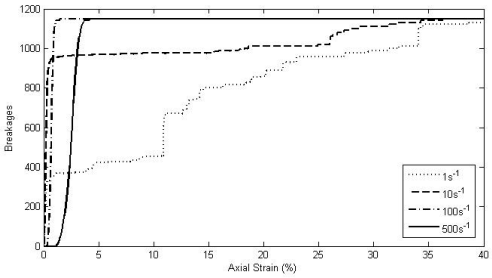

(a) Breakage weak chalk 2

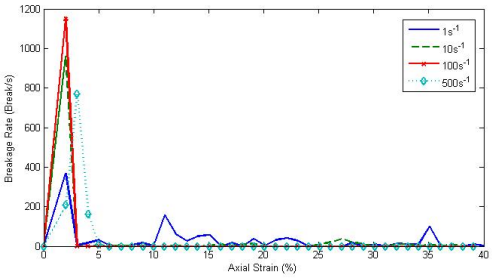

(b) Breakage rate weak chalk 2

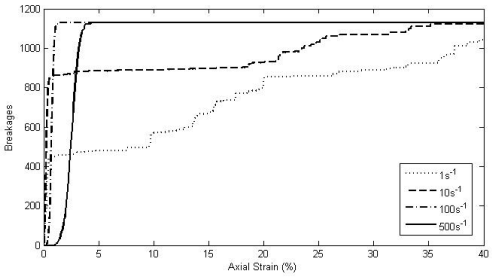

(c) Breakage weak chalk 3

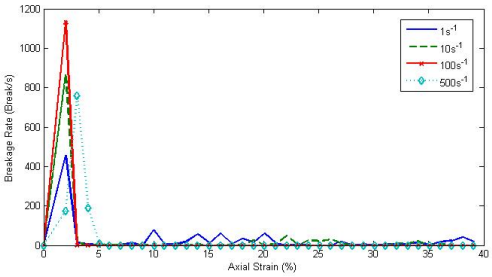

(d) Breakage rate weak chalk 3

Figure E.1: Breakage and breakage rate

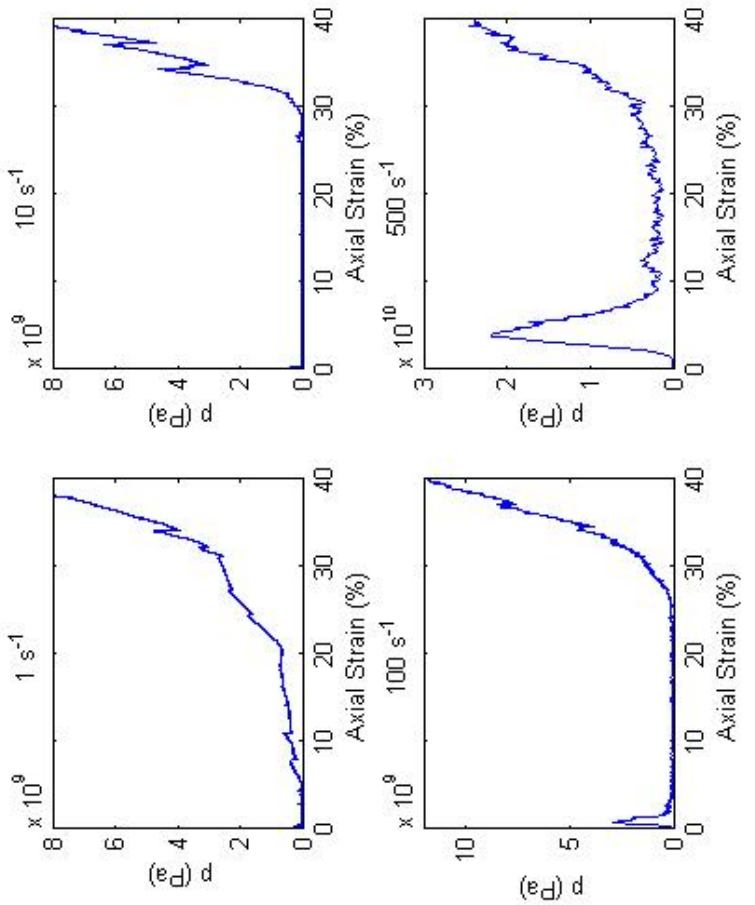

Figure E.2: Mean stress response for weak chalk specimen 2

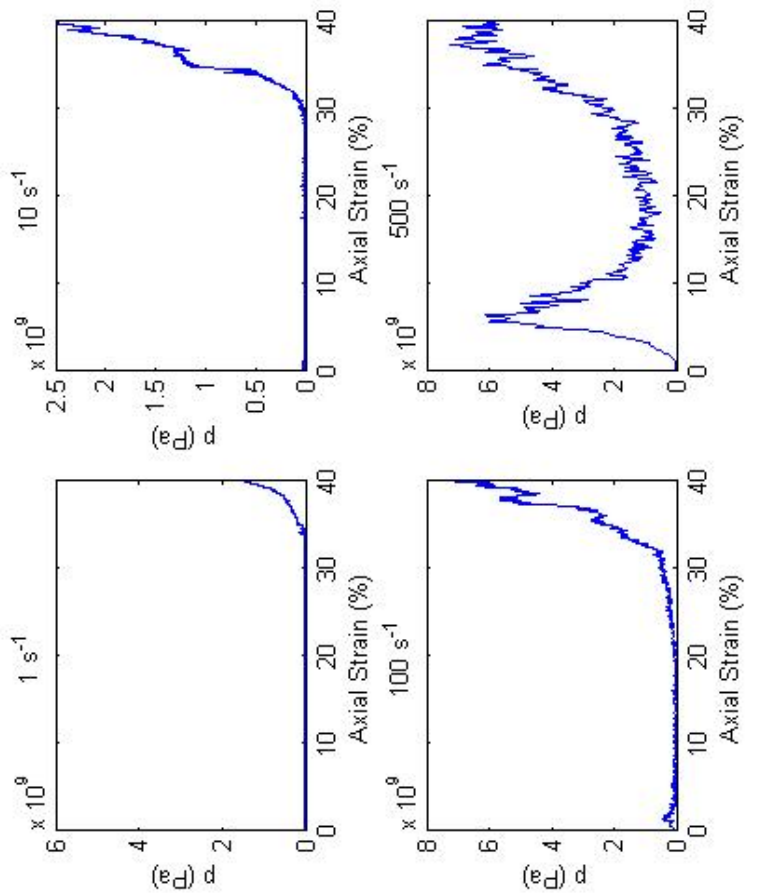

Figure E.3: Mean stress response for weak chalk specimen 3

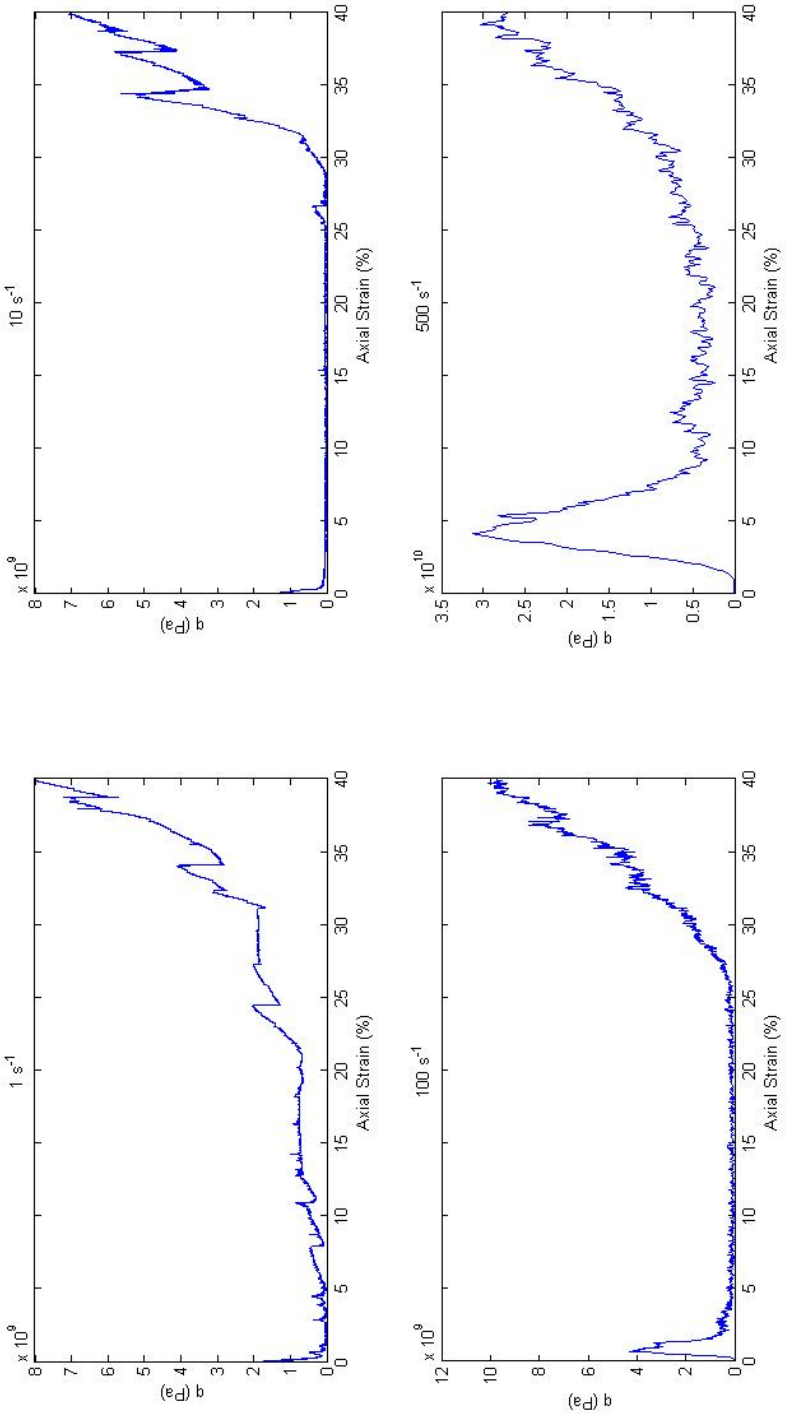

Figure E.4: Deviatoric stress response for weak chalk specimen 2

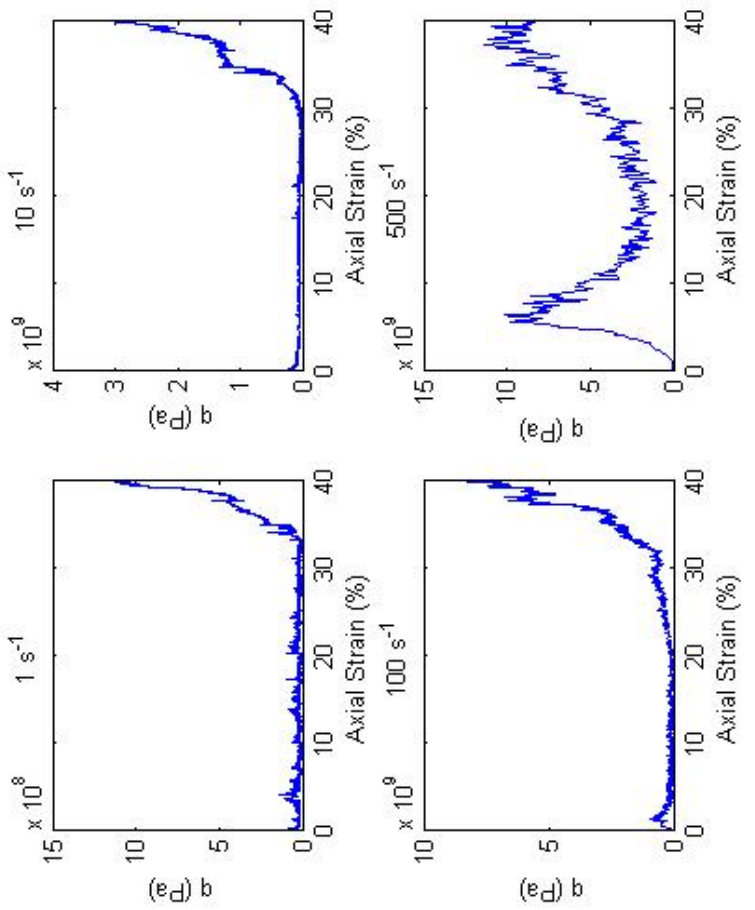

Figure E.5: Deviatoric stress response for weak chalk specimen 3

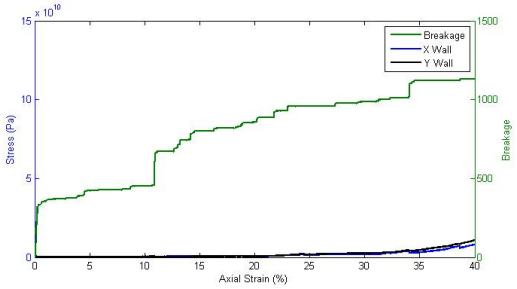

(a) $1s^{-1}$

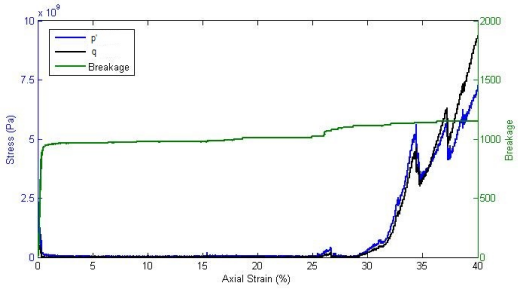

(b) $10s^{-1}$

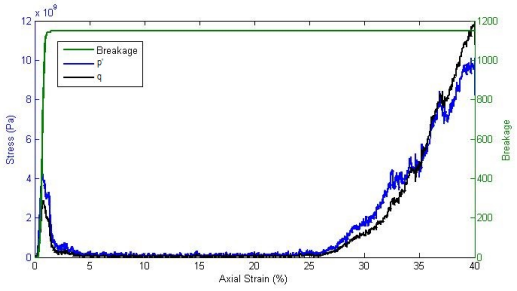

(c) $100s^{-1}$

Figure E.6: Breakage compared with mean and deviatoric stress responses for weak chalk 2

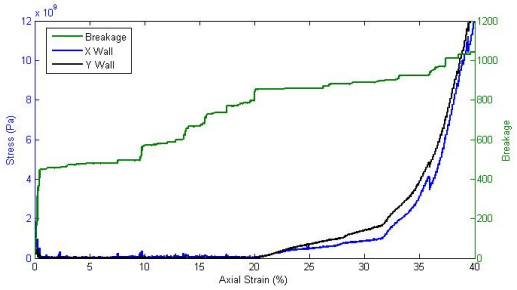

(a) $1s^{-1}$

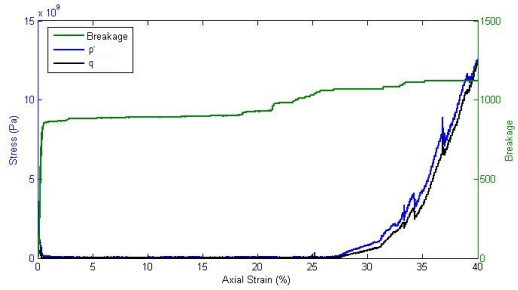

(b) $10s^{-1}$

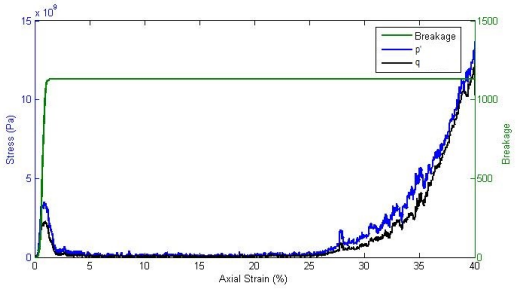

(c) $100s^{-1}$

Figure E.7: Breakage compared with mean and deviatoric stress responses for weak chalk 3

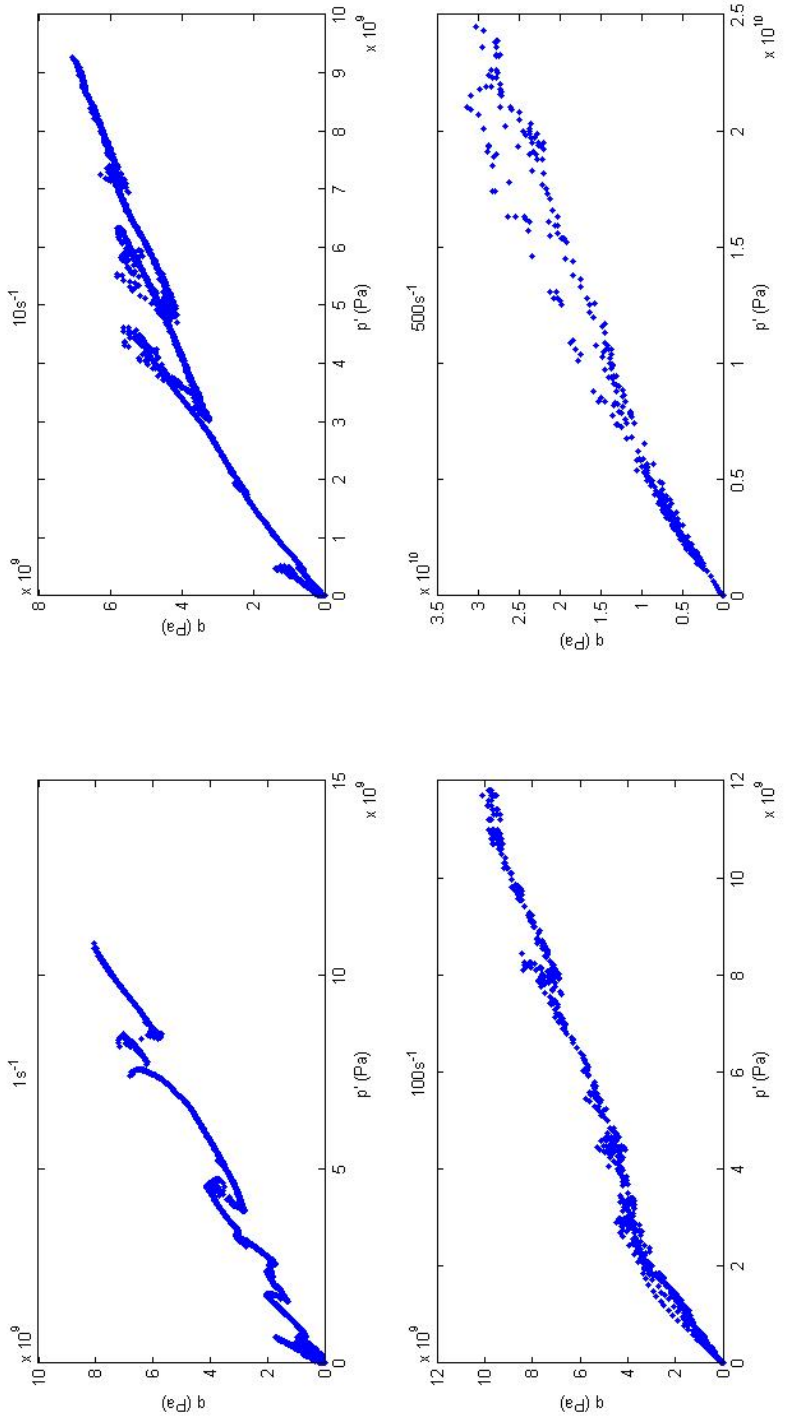

Figure E.8: Stress paths for weak chalk specimen 2

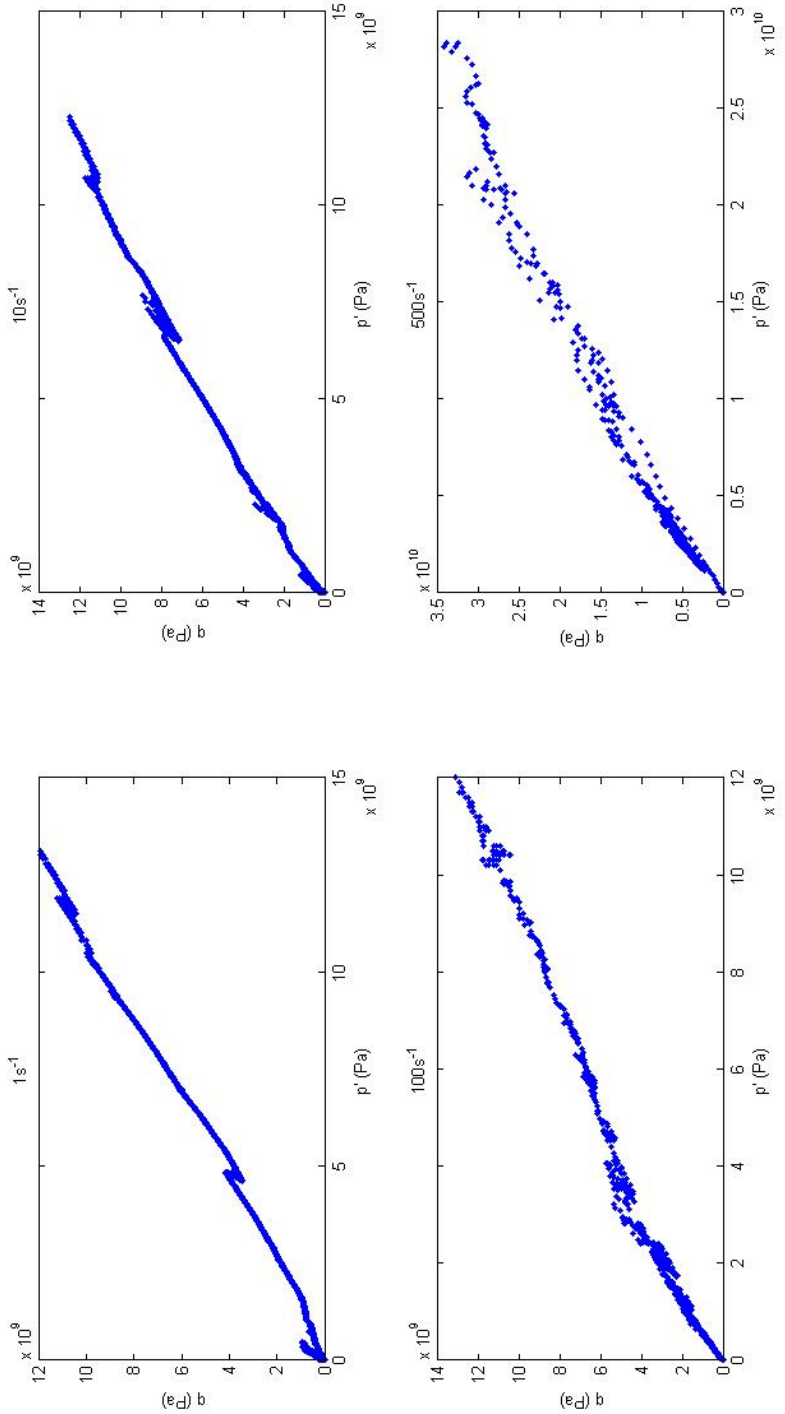

Figure E.9: Stress paths for weak chalk specimen 3

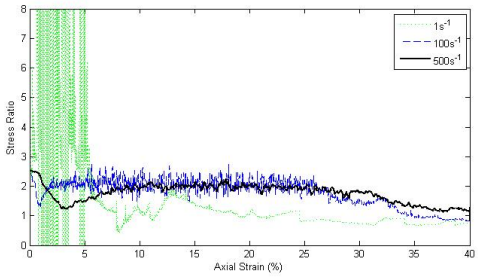

(a) Specimen 2

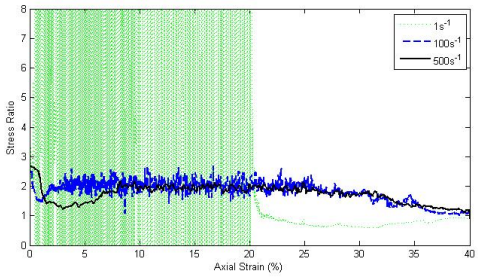

(b) Specimen 3

Figure E.10: $\frac{q}{p'}$ stress ratio

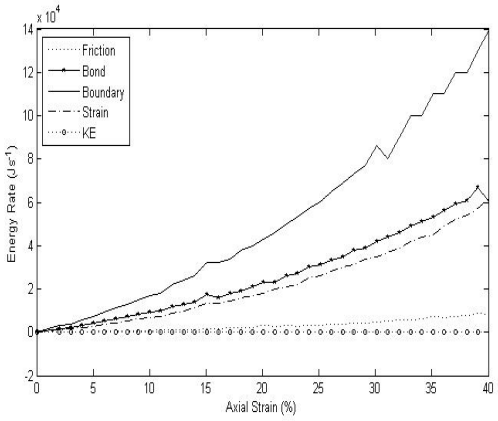

(a) $1s^{-1}$

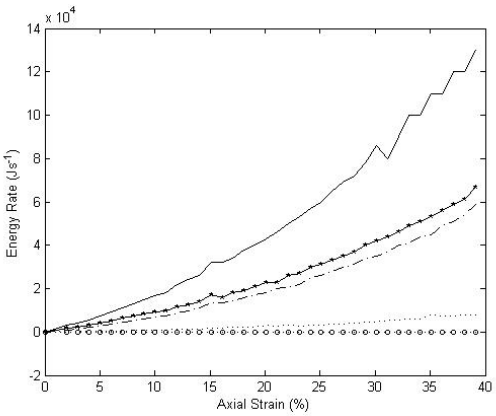

(b) $10s^{-1}$

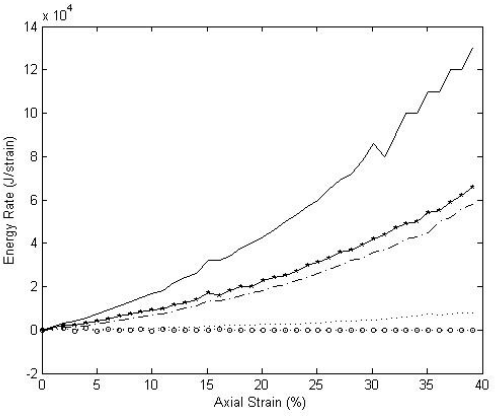

(c) $100s^{-1}$

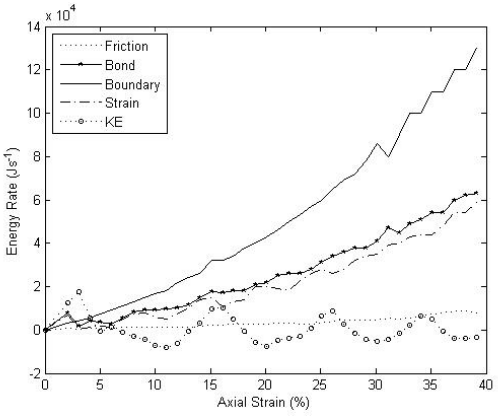

(d) $500s^{-1}$

Figure E.11: Energy rate responses for weak chalk specimen 2

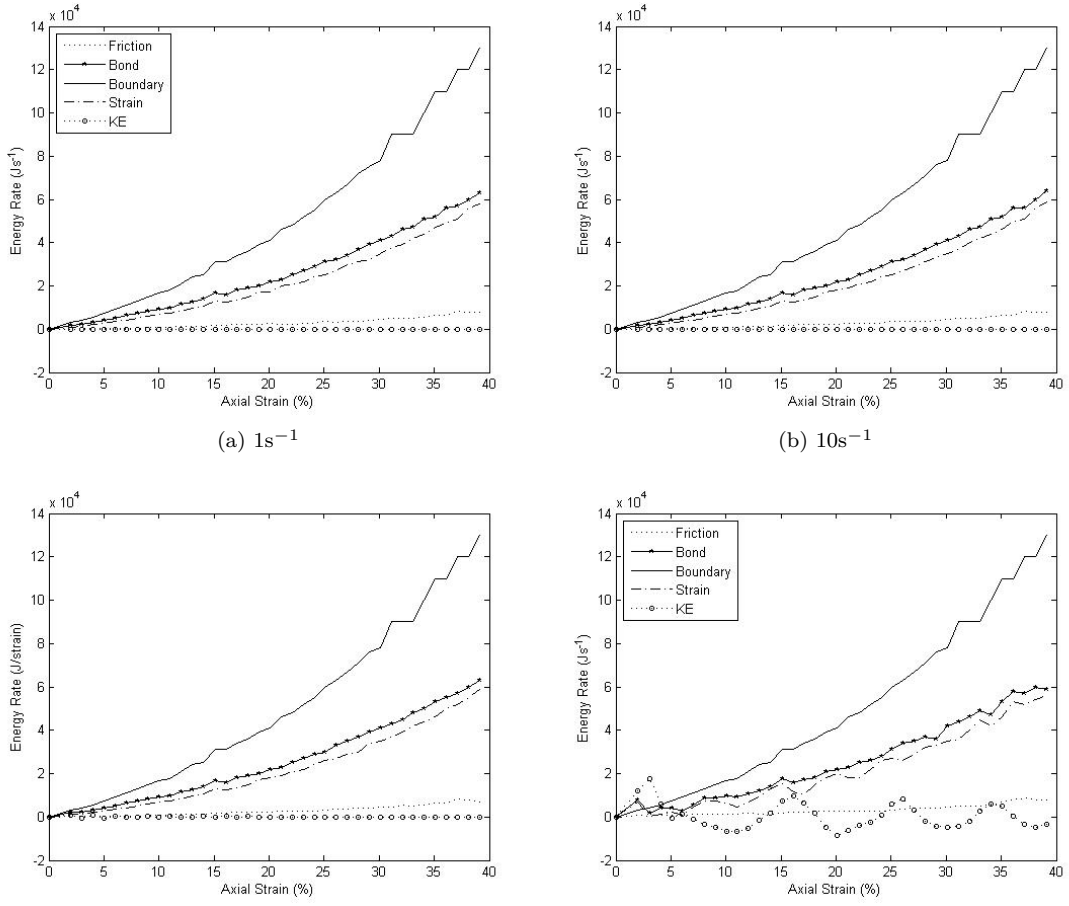

(a) $1s^{-1}$

(b) $10s^{-1}$

(c) $100s^{-1}$

(d) $500s^{-1}$

Figure E.12: Energy rate responses for weak chalk specimen 3

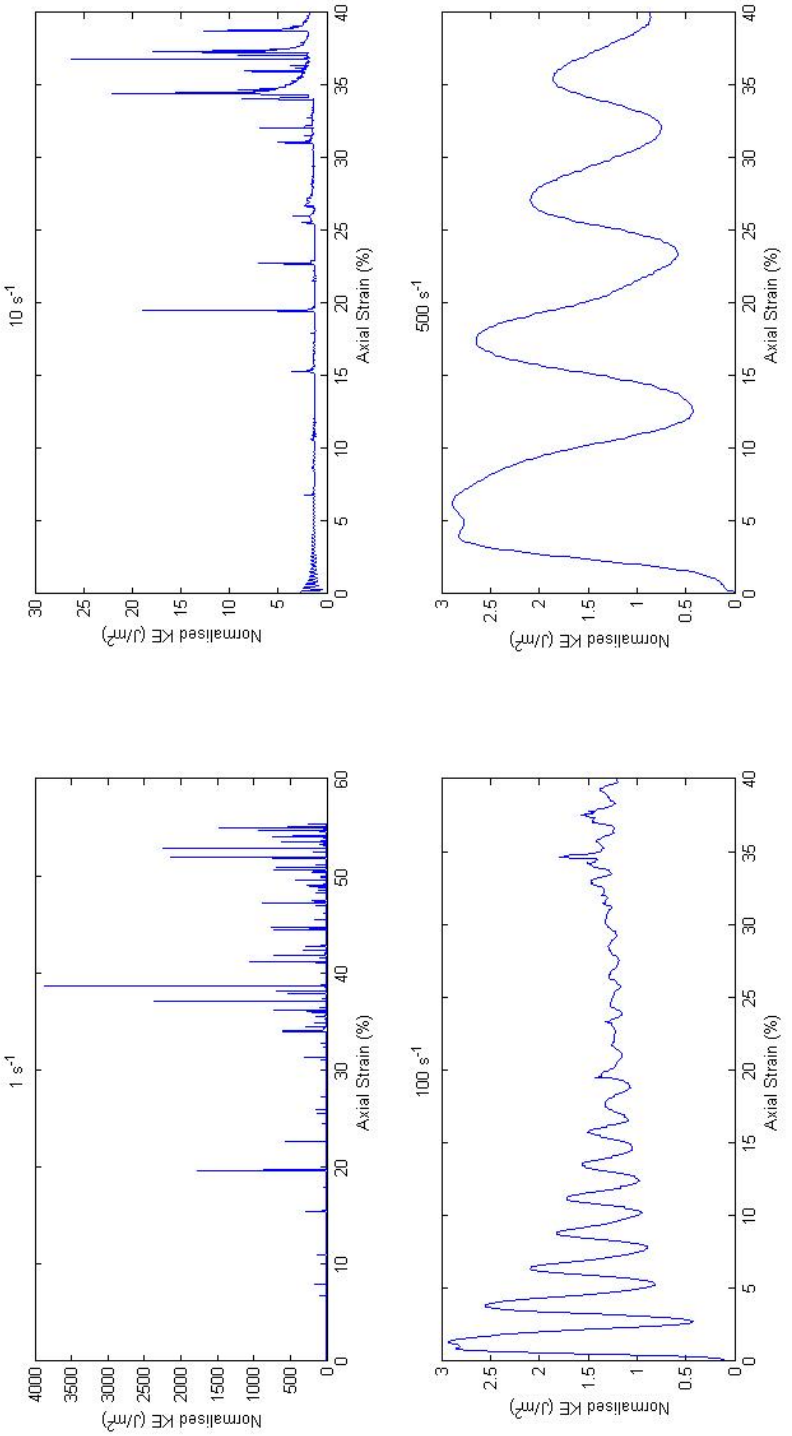

Figure E.13: Normalised kinetic energy for weak chalk specimen 2

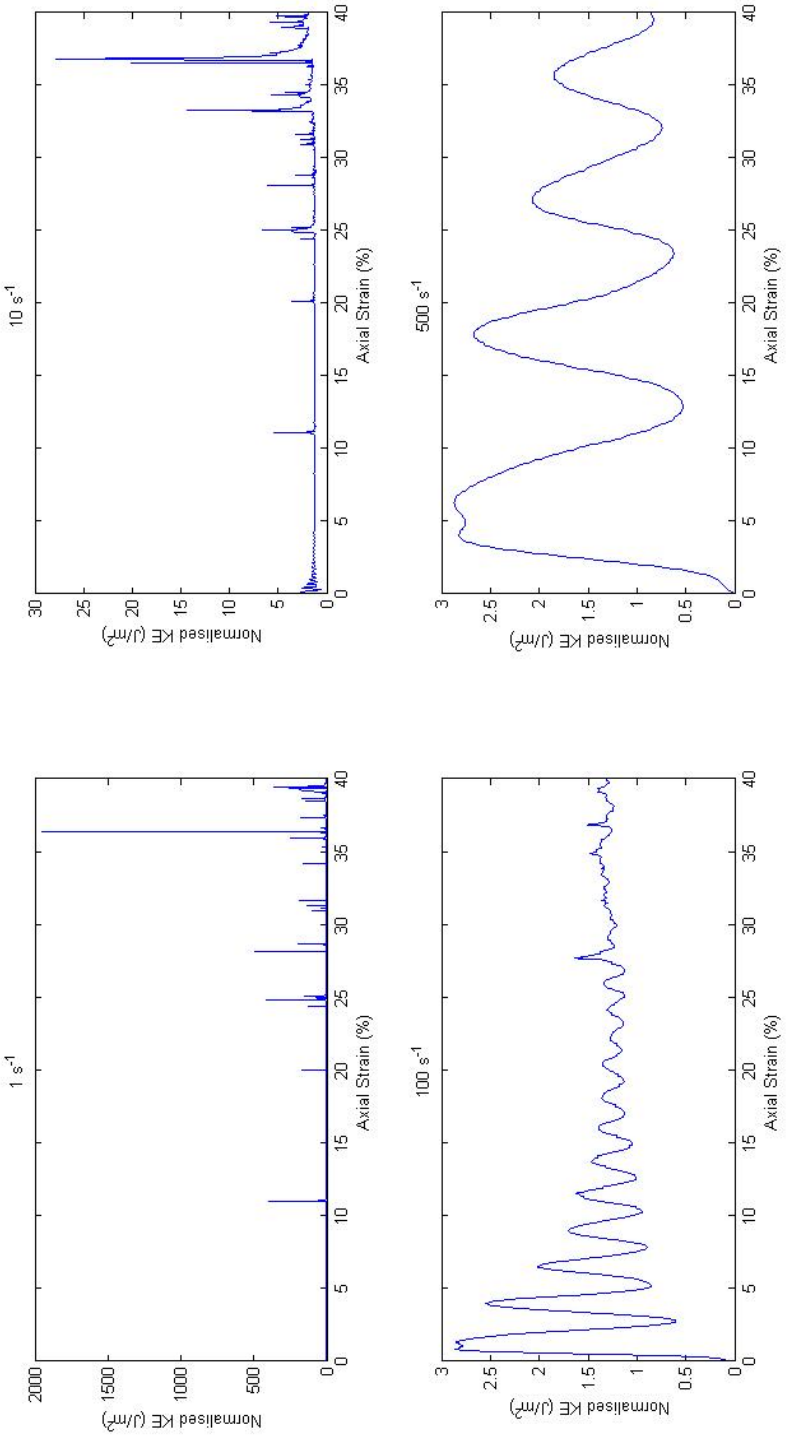

Figure E.14: Normalised kinetic energy for weak chalk specimen 3

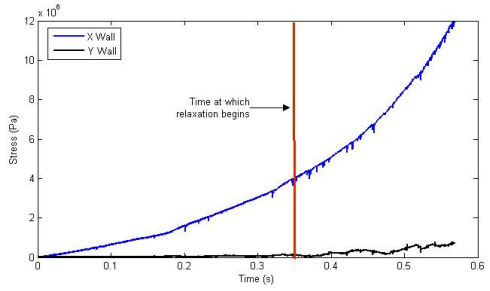

(a) Weak chalk 2 at $1s^{-1}$

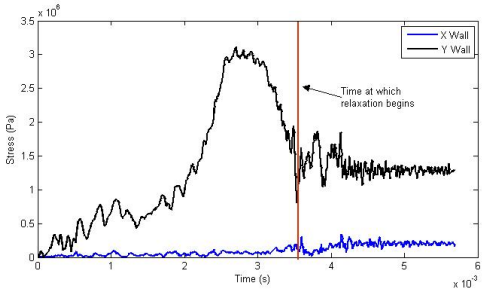

(b) Weak chalk 2 at $100s^{-1}$

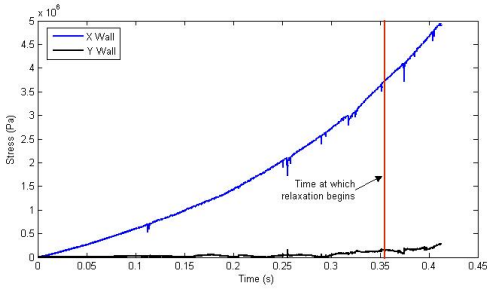

(c) Weak chalk 3 at $1s^{-1}$

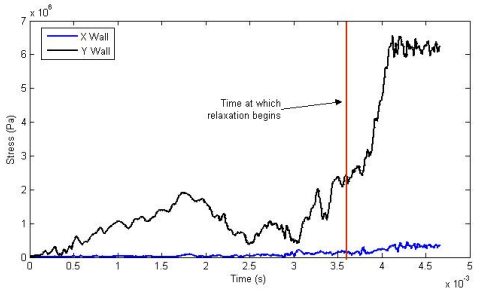

(d) Weak chalk 3 at $100s^{-1}$

Figure E.15: Wall stress behaviour over time

Appendix F

Oedometric Testing - Extremely Weak Chalk

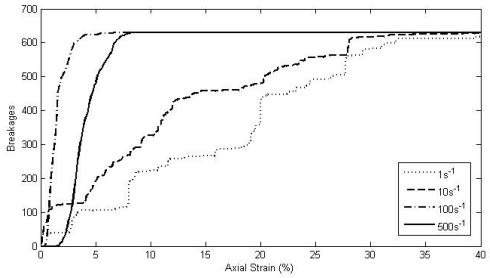

(a) Breakage extremely weak chalk 2

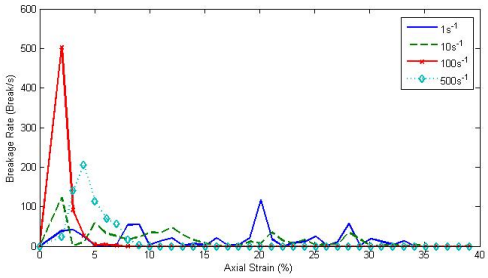

(b) Breakage rate extremely weak chalk 2

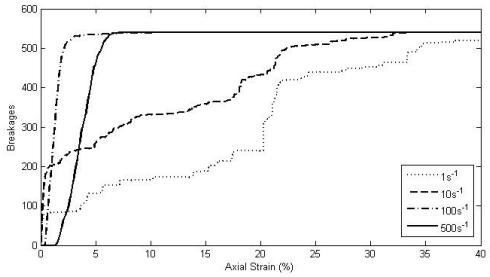

(c) Breakage extremely weak chalk 3

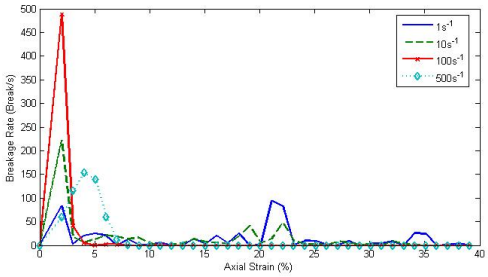

(d) Breakage rate extremely weak chalk 3

Figure F.1: Breakage and breakage rate

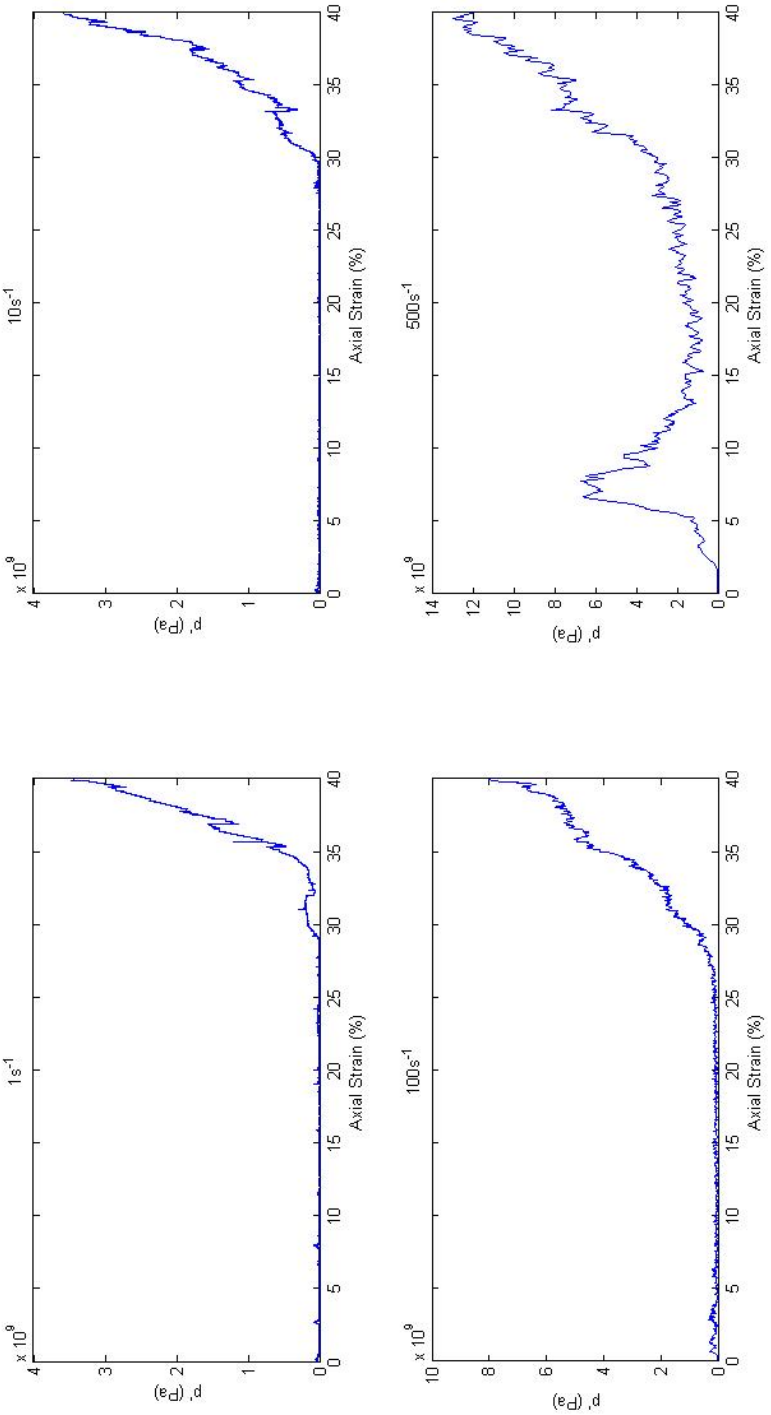

Figure F.2: Mean stress response for extremely weak chalk specimen 2

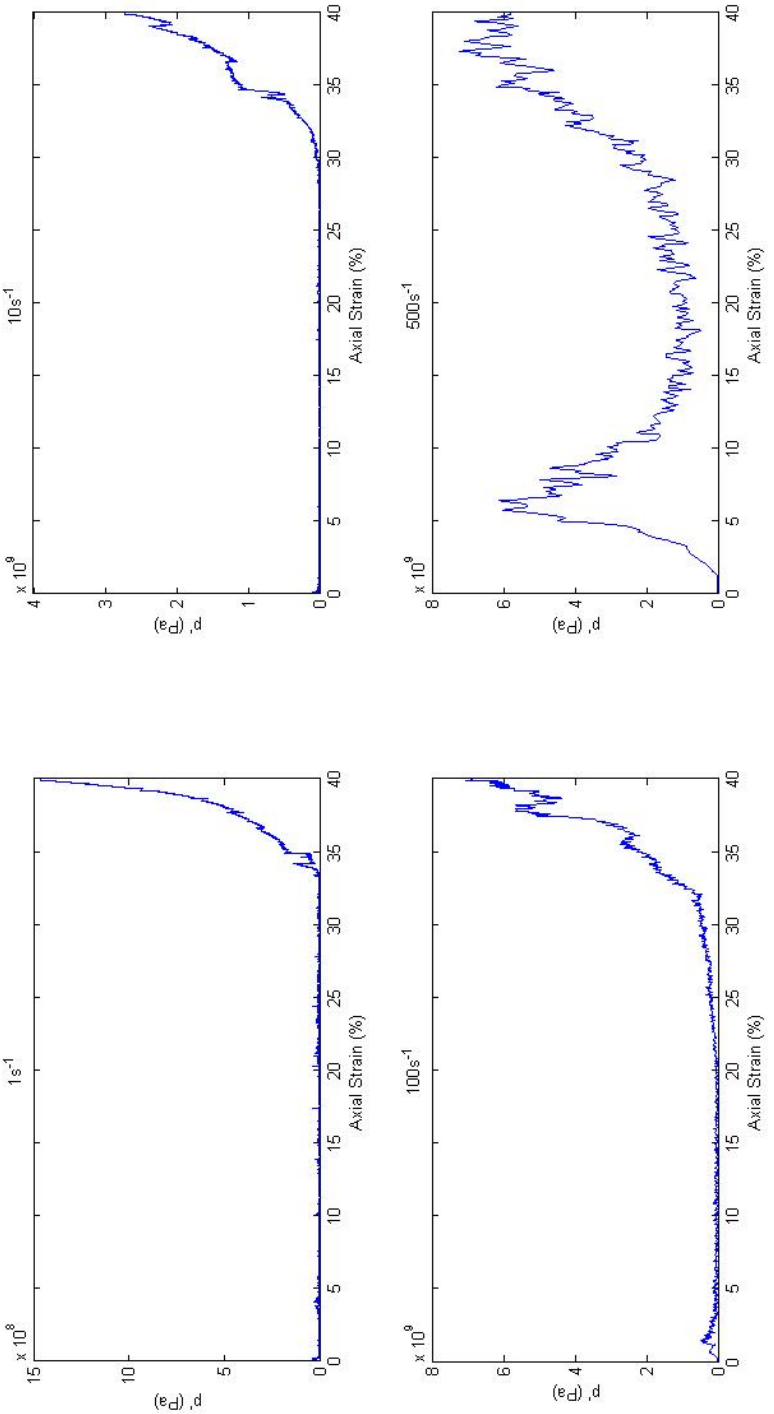

Figure F.3: Mean stress response for extremely weak chalk specimen 3

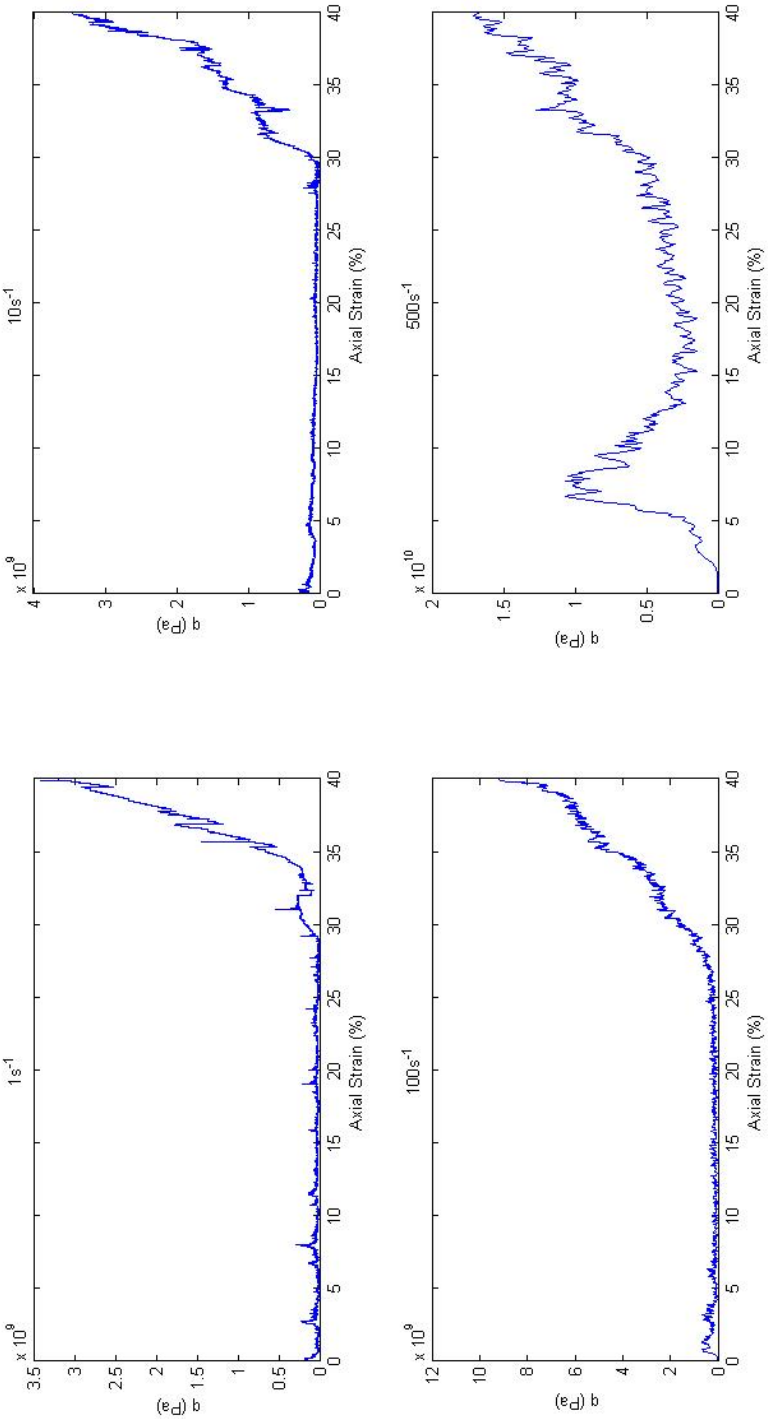

Figure F.4: Deviatoric stress response for extremely weak chalk specimen 2

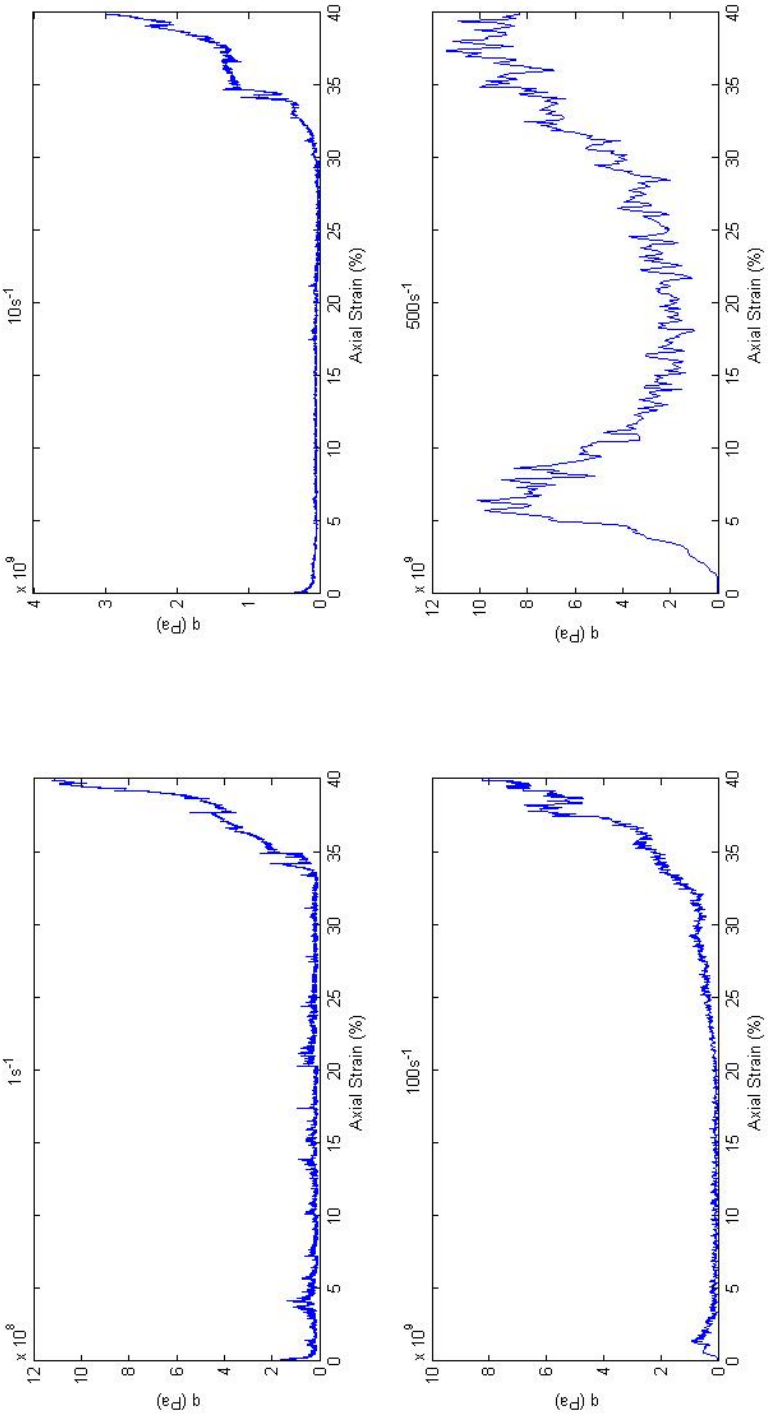

Figure F.5: Deviatoric stress response for extremely weak chalk specimen 3

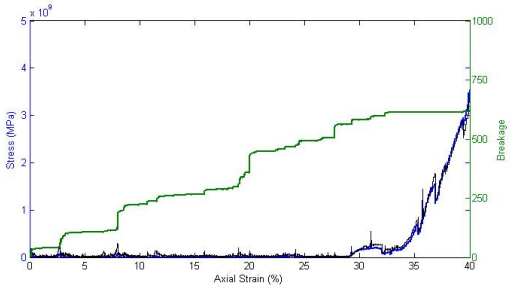

(a) $1s^{-1}$

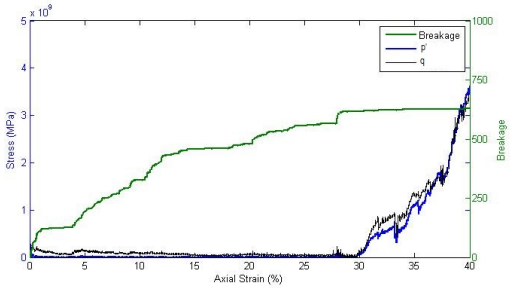

(b) $10s^{-1}$

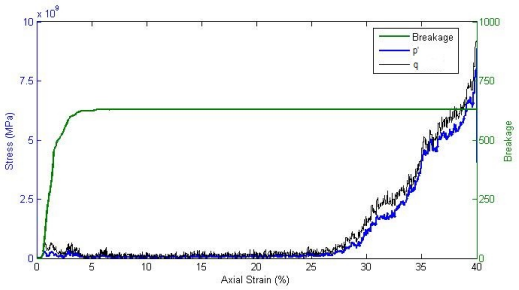

(c) $100s^{-1}$

Figure F.6: Breakage compared with mean and deviatoric stress responses for extremely weak chalk 2

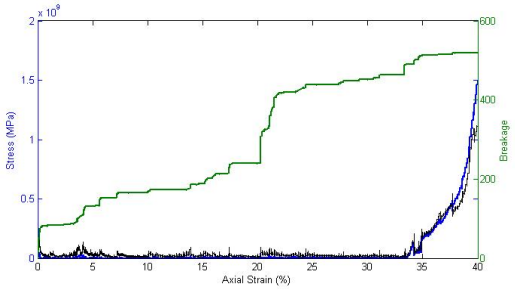

(a) $1s^{-1}$

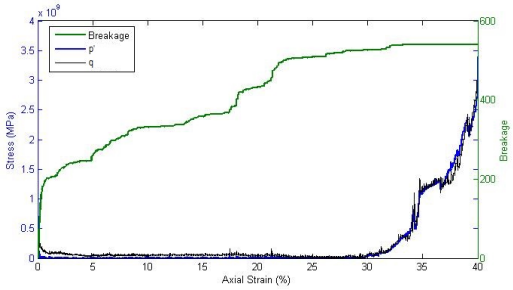

(b) $10s^{-1}$

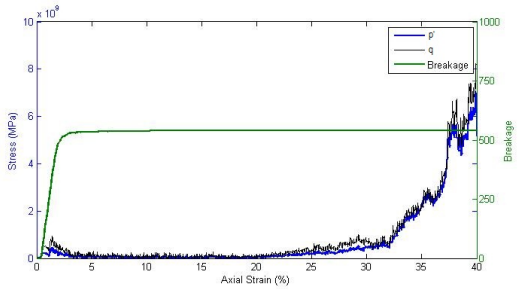

(c) $100s^{-1}$

Figure F.7: Breakage compared with mean and deviatoric stress responses for extremely weak chalk 3

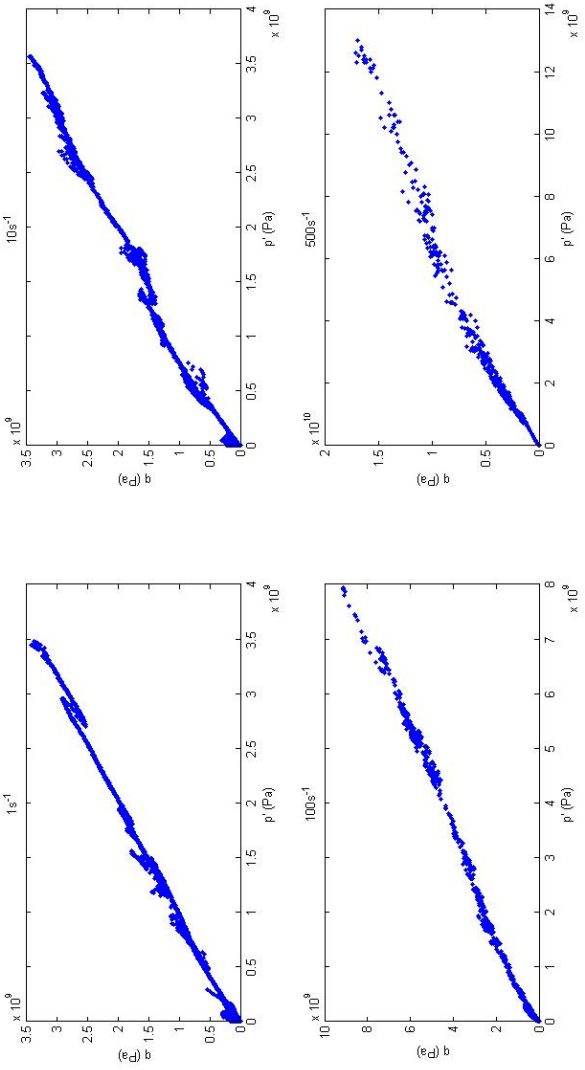

Figure F.8: Stress paths for extremely weak chalk specimen 2

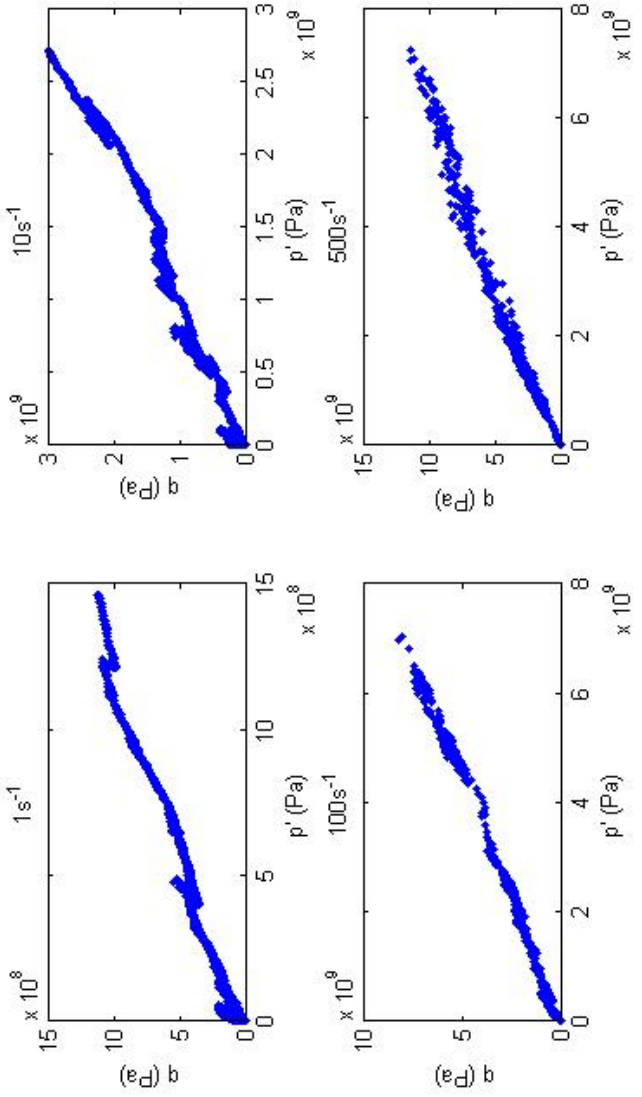

Figure F.9: Stress paths for extremely weak chalk specimen 3

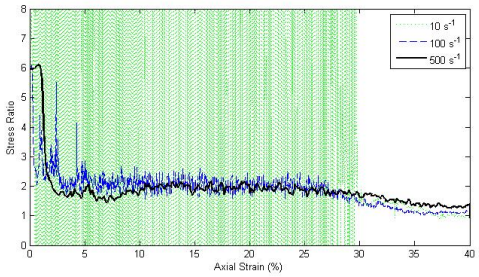

(a) Specimen 2

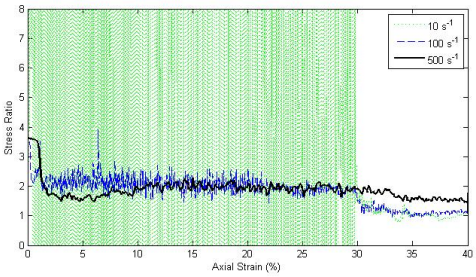

(b) Specimen 3

Figure F.10: $\frac{q}{p'}$ stress ratio

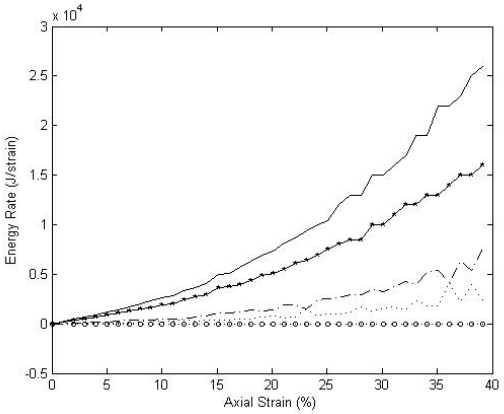

(a) $1s^{-1}$

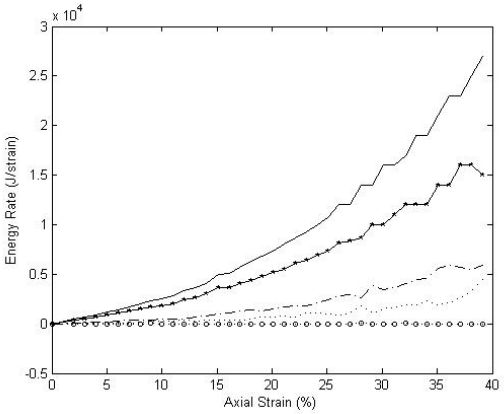

(b) $10s^{-1}$

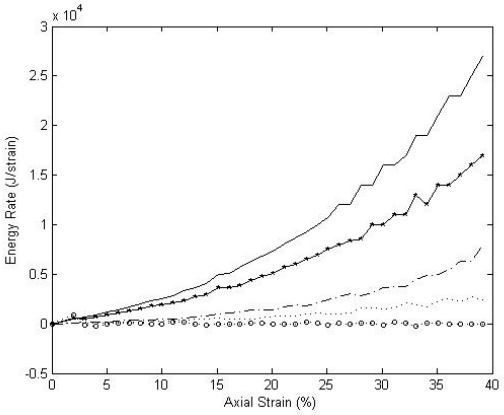

(c) $100s^{-1}$

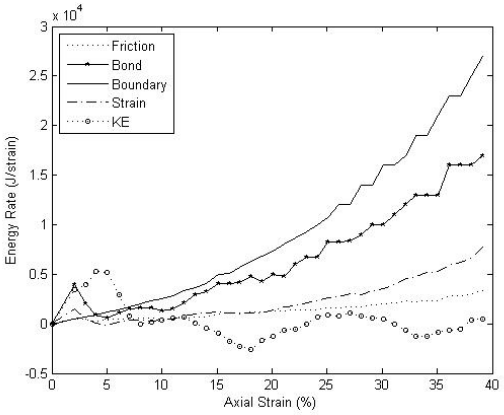

(d) $500s^{-1}$

Figure F.11: Energy rate responses for extremely weak chalk specimen 2

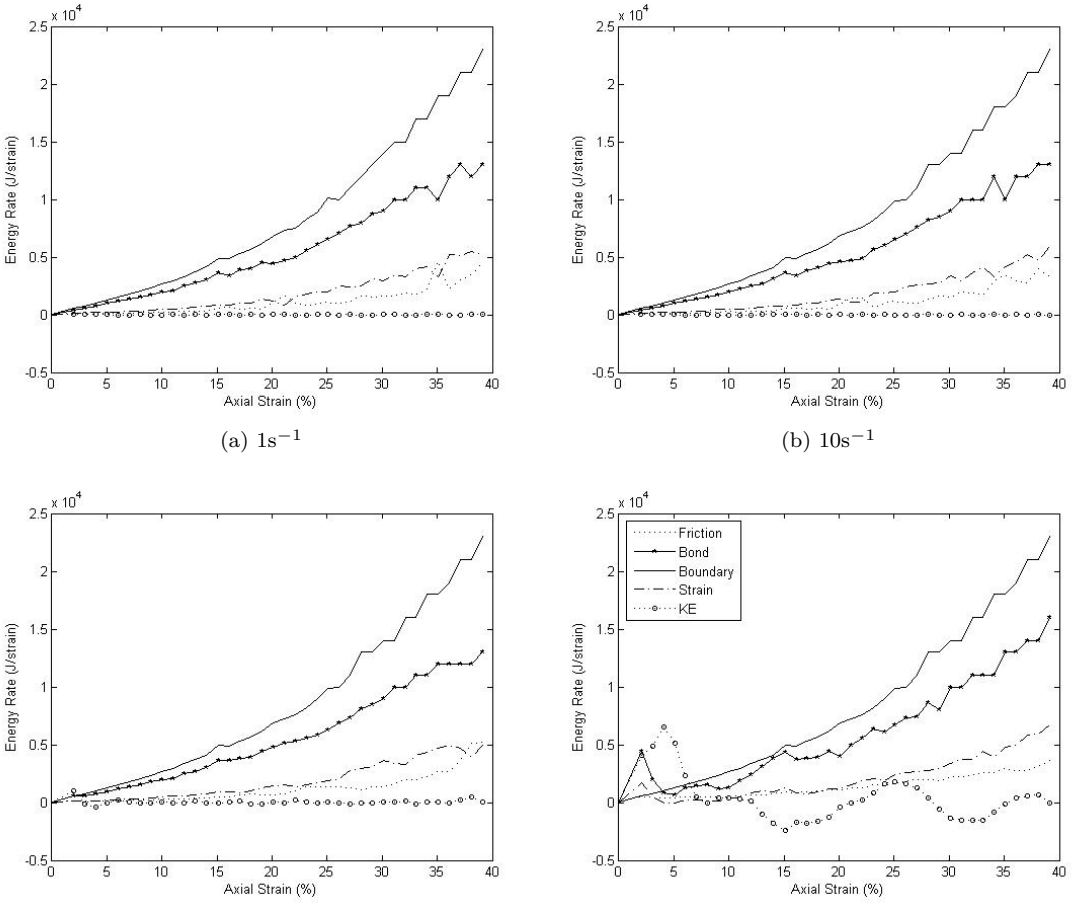

(a) $1s^{-1}$ (b) $10s^{-1}$

(c) $100s^{-1}$ (d) $500s^{-1}$

Figure F.12: Energy rate responses for extremely weak chalk specimen 3

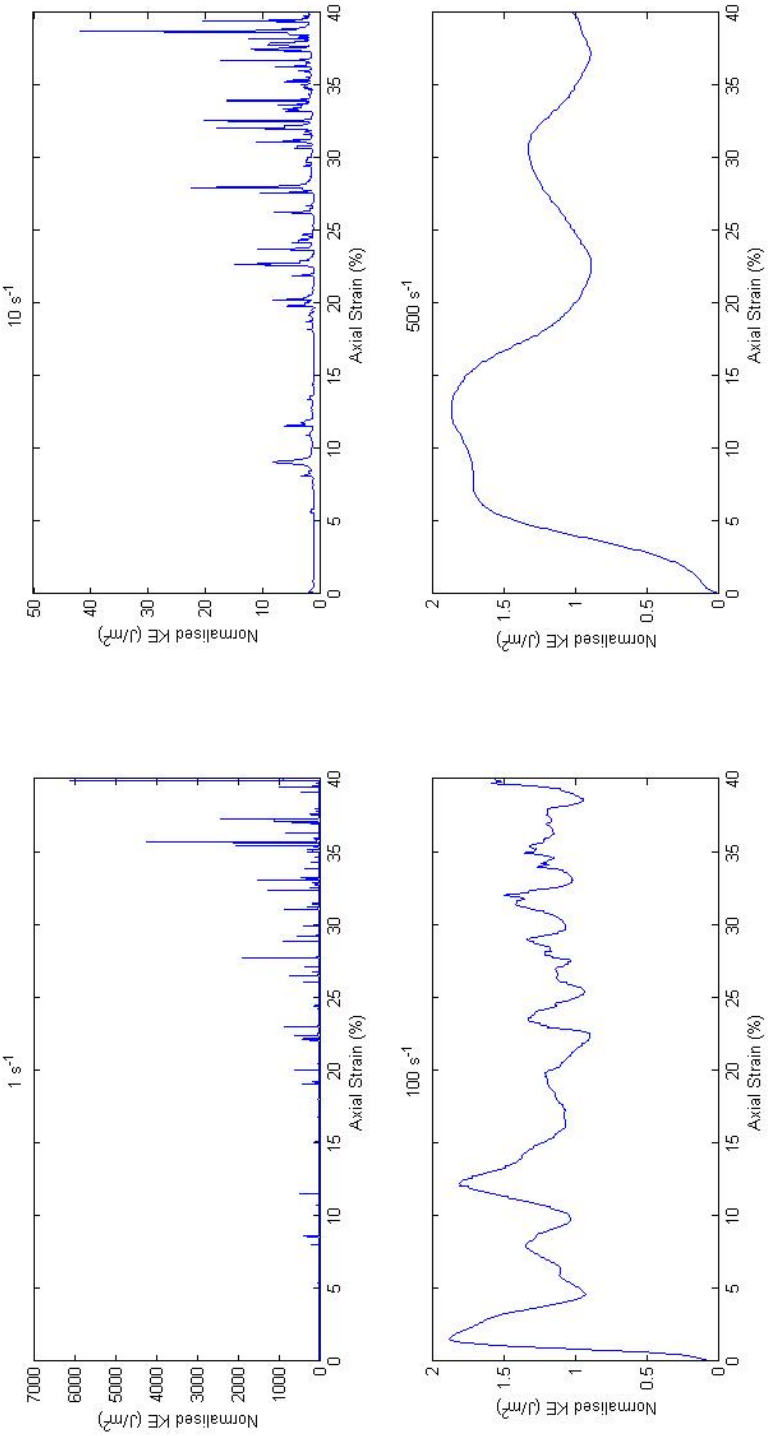

Figure F.13: Normalised kinetic energy for extremely weak chalk specimen 2

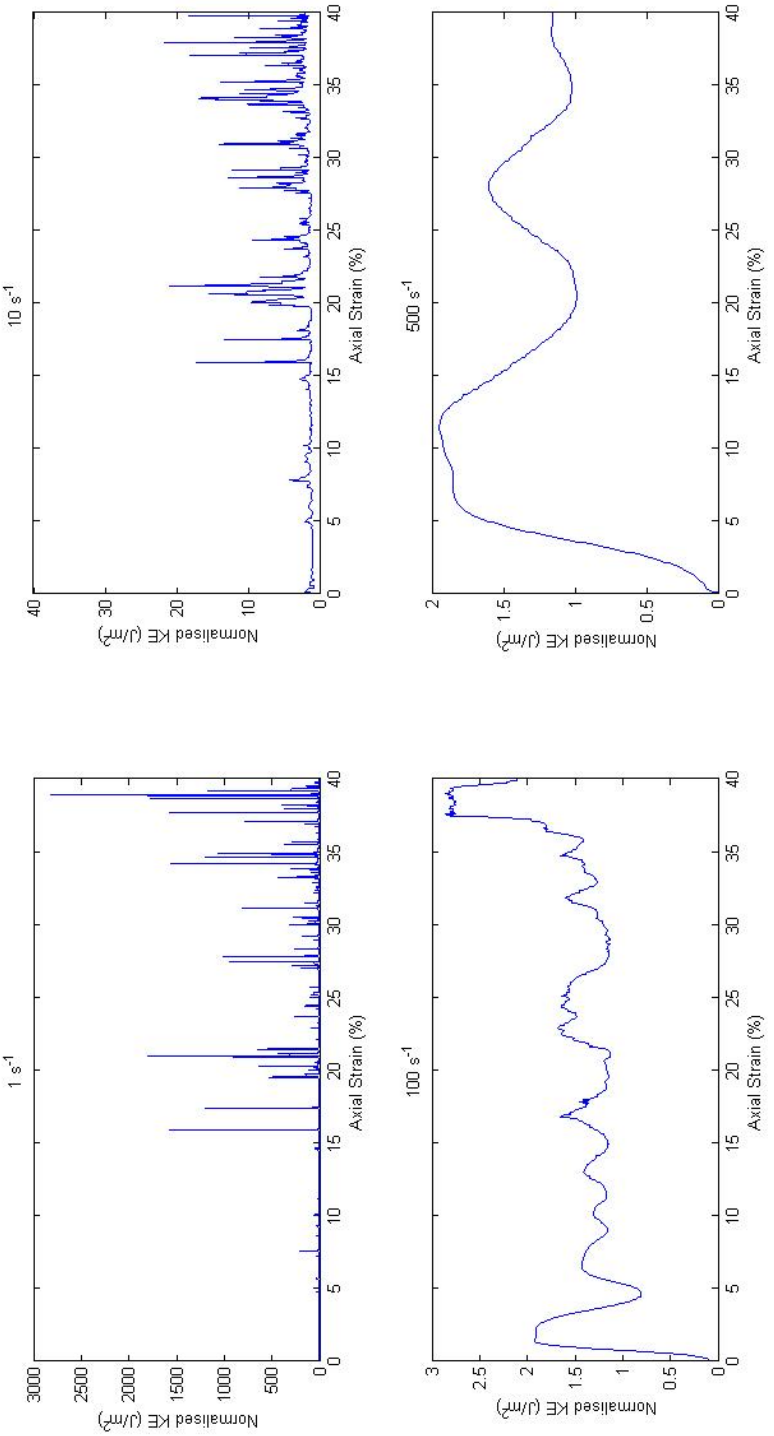

Figure F.14: Normalised kinetic energy for extremely weak chalk specimen 3

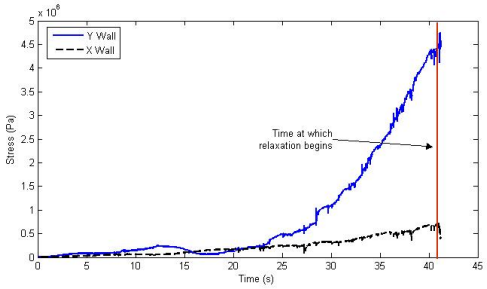

(a) Extremely weak chalk 2 at $1s^{-1}$

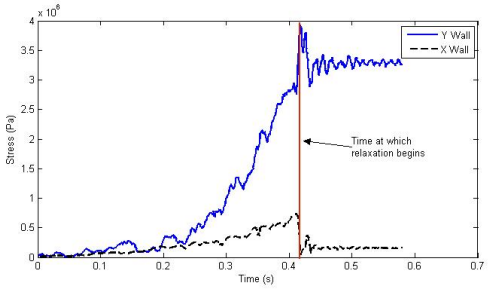

(b) Extremely weak chalk 2 at $100s^{-1}$

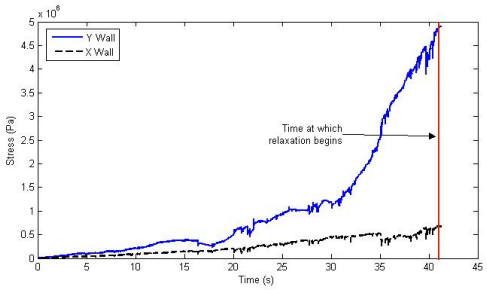

(c) Extremely weak chalk 3 at $1s^{-1}$

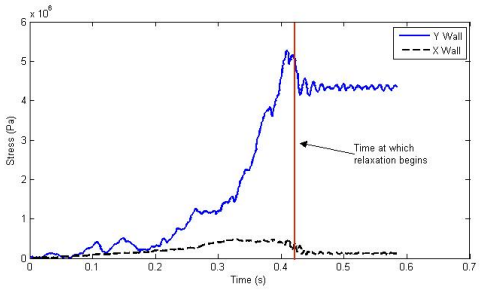

(d) Extremely weak chalk 3 at $100s^{-1}$

Figure F.15: Wall stress behaviour over time

Appendix G

Shear Testing - Sandstone

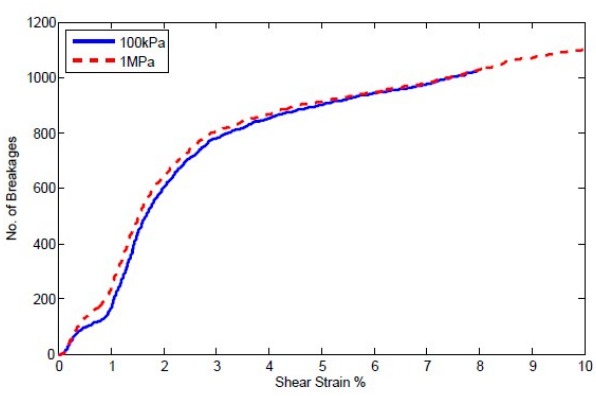

(a) Quasi-static breakage

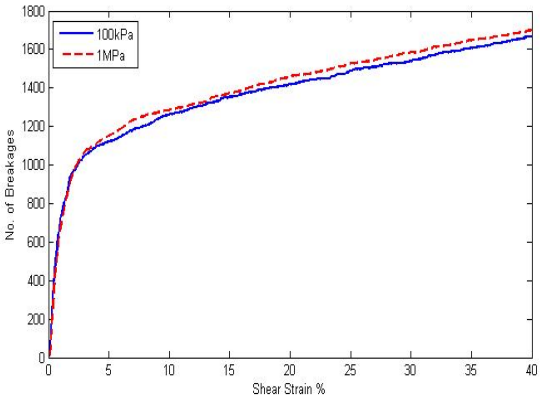

(b) Dynamic breakage

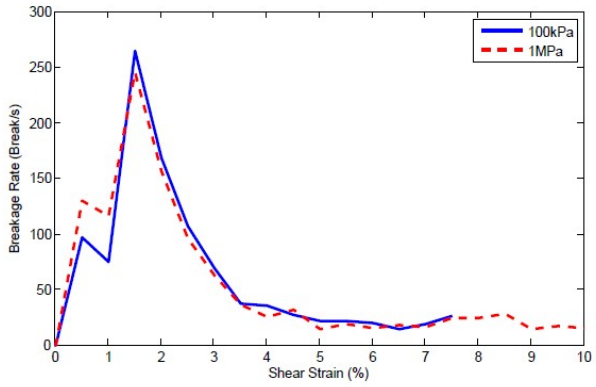

(c) Quasi-static breakage rate

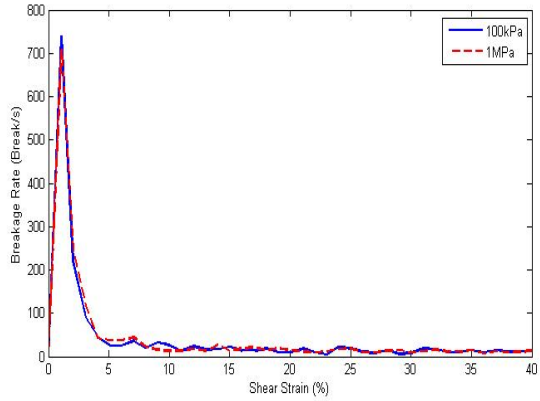

(d) Dynamic breakage rate

Figure G.1: Breakage under shear testing for sandstone specimen 2.

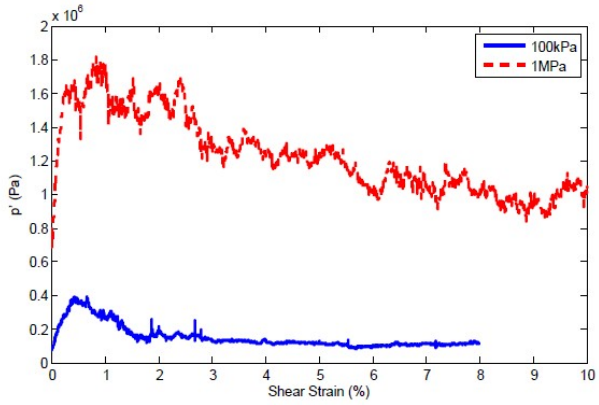

(a) Quasi-static mean stress p′

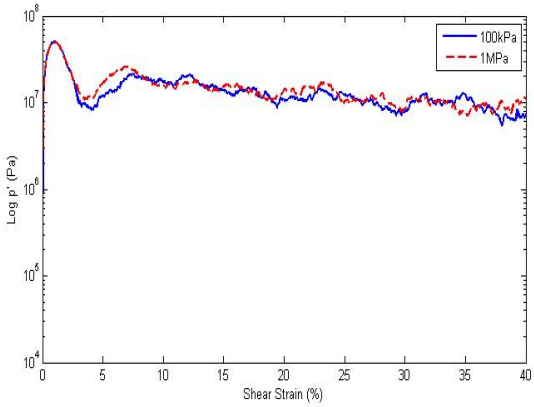

(b) Dynamic mean stress p′

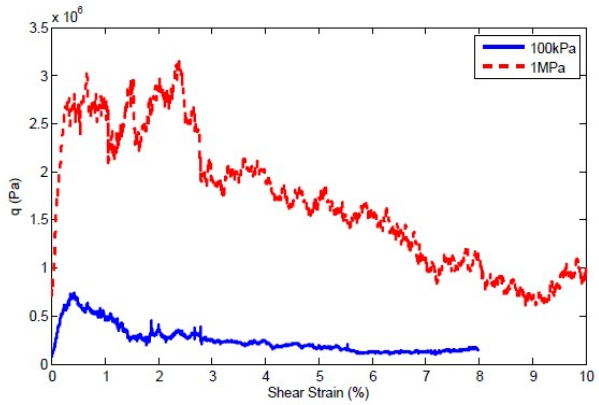

(c) Quasi-static deviatoric stress q

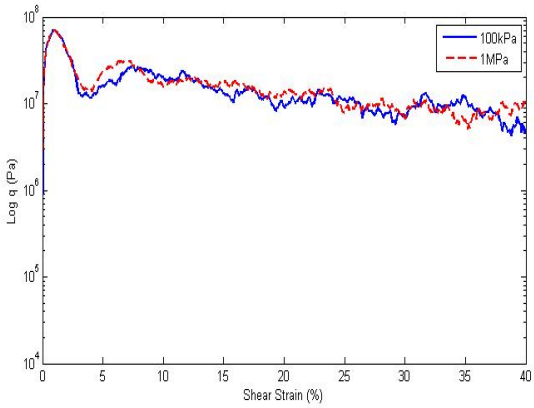

(d) Dynamic deviatoric stress q

Figure G.2: Mean effective and deviatoric stress responses within the boulders under shear testing for sandstone specimen 2.

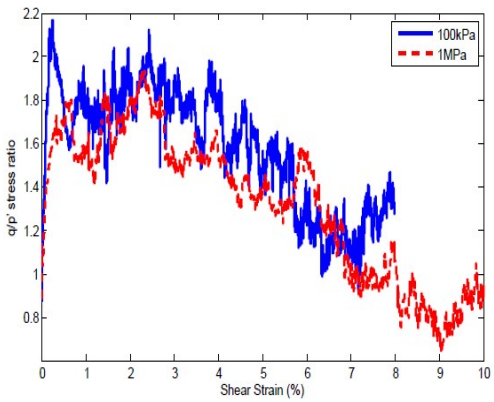

(a) Quasi-static $\frac{q}{p'}$ stress ratio

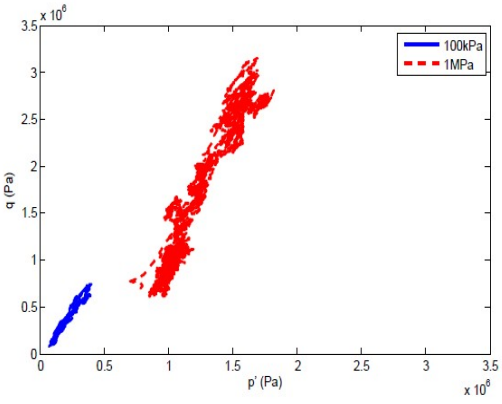

(b) Quasi-static stress path

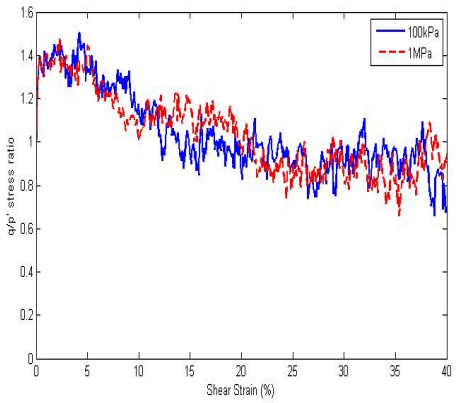

(c) Dynamic $\frac{q}{p'}$ stress ratio

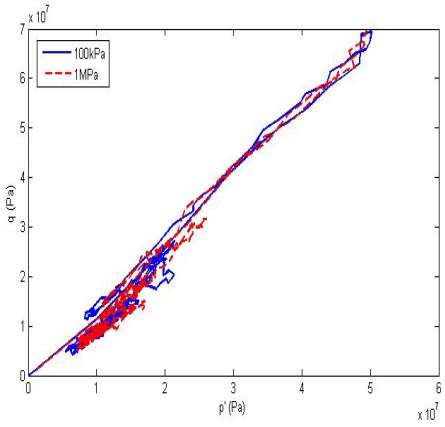

(d) Dynamic stress path

Figure G.3: $\frac{q}{p'}$ stress ratio of the boulders and stress path response under shear testing for sandstone specimen 2.

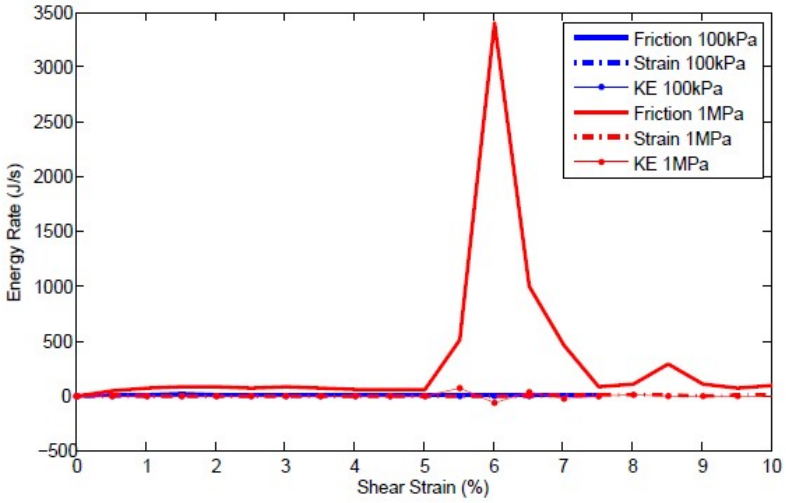

(a) Quasi-static

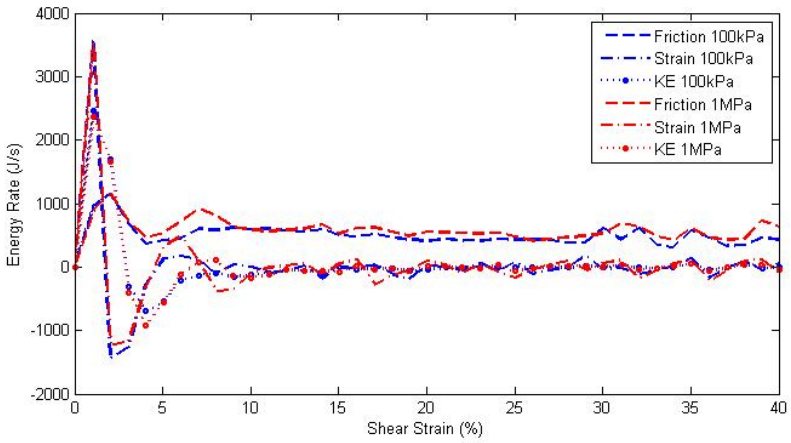

(b) Dynamic

Figure G.4: System energy rates from shear testing of sandstone specimen 2.

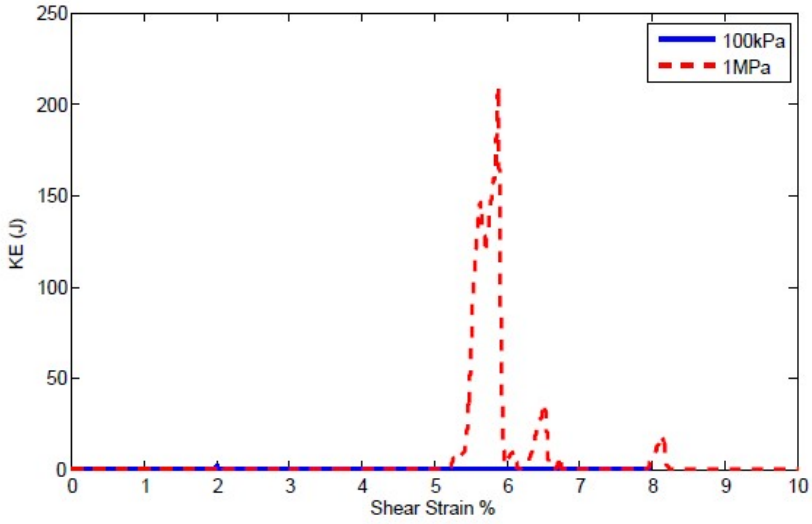

(a) Quasi-static

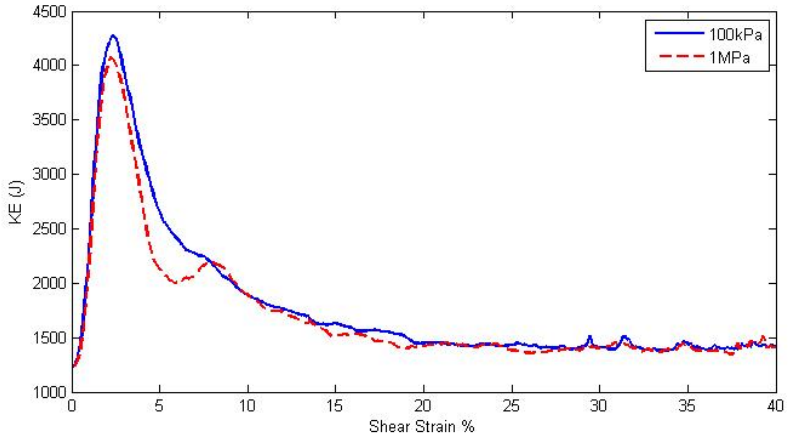

(b) Dynamic

Figure G.5: System kinetic energy response from shear testing of sandstone specimen 2.

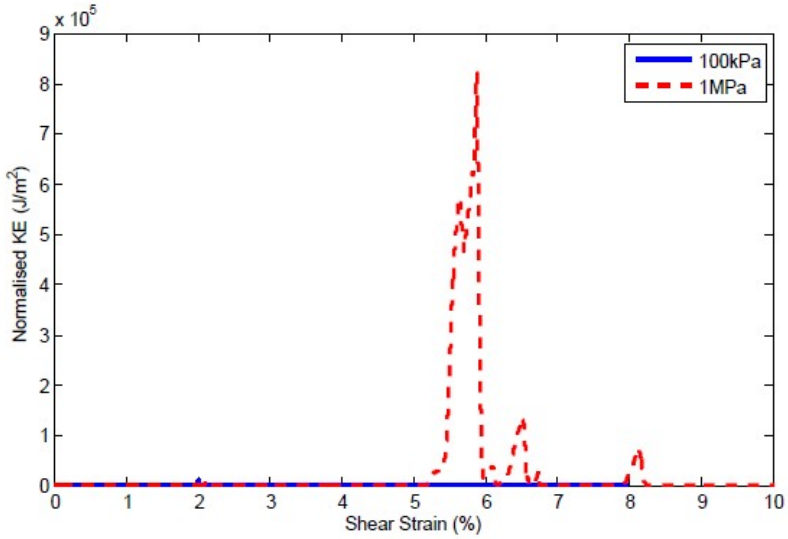

(a) Quasi-static

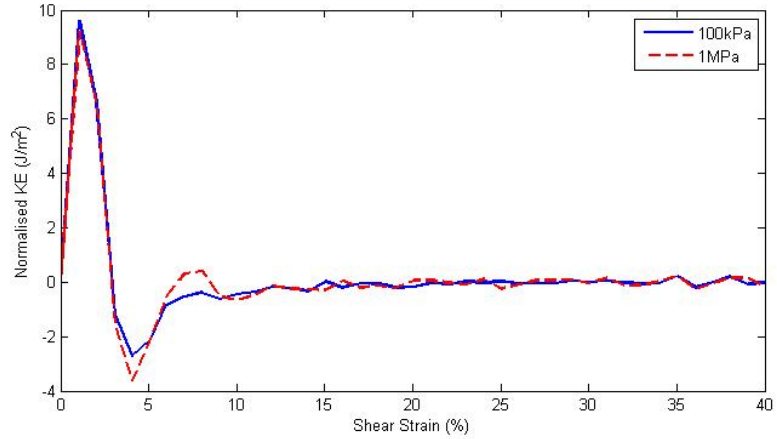

(b) Dynamic

Figure G.6: Kinetic energy rate normalised by the square of the platen velocity for sandstone specimen 2.

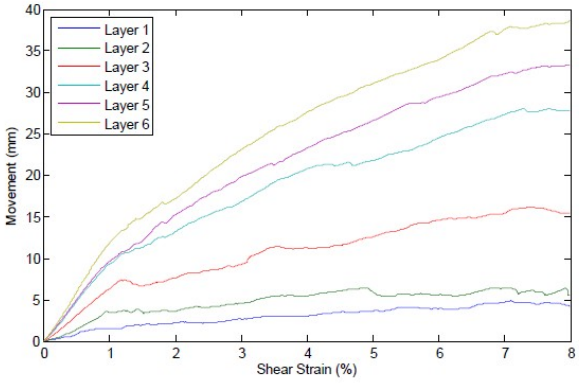

(a) Quasi-static 100kPa

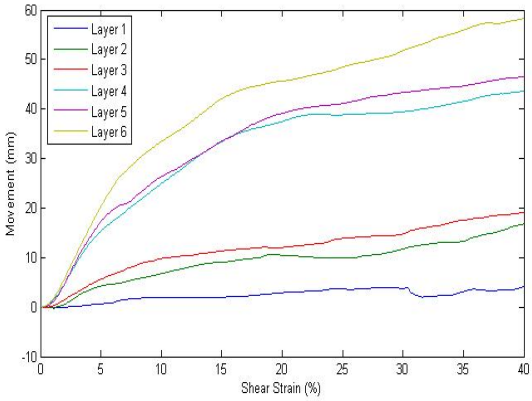

(b) Dynamic 100kPa

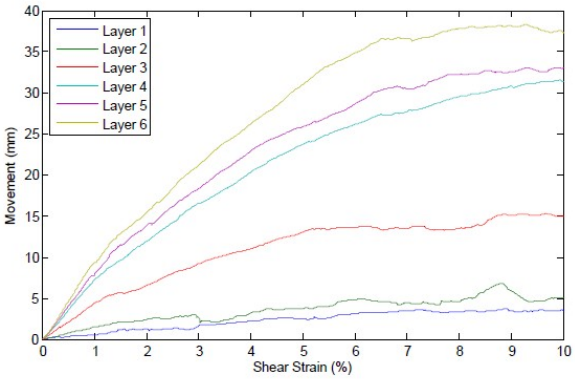

(c) Quasi-static 1MPa

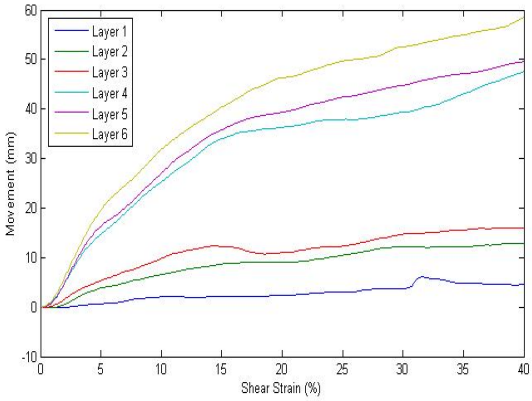

(d) Dynamic 1MPa

Figure G.7: Dilation of sandstone specimen 2 as measured by gauge particles.

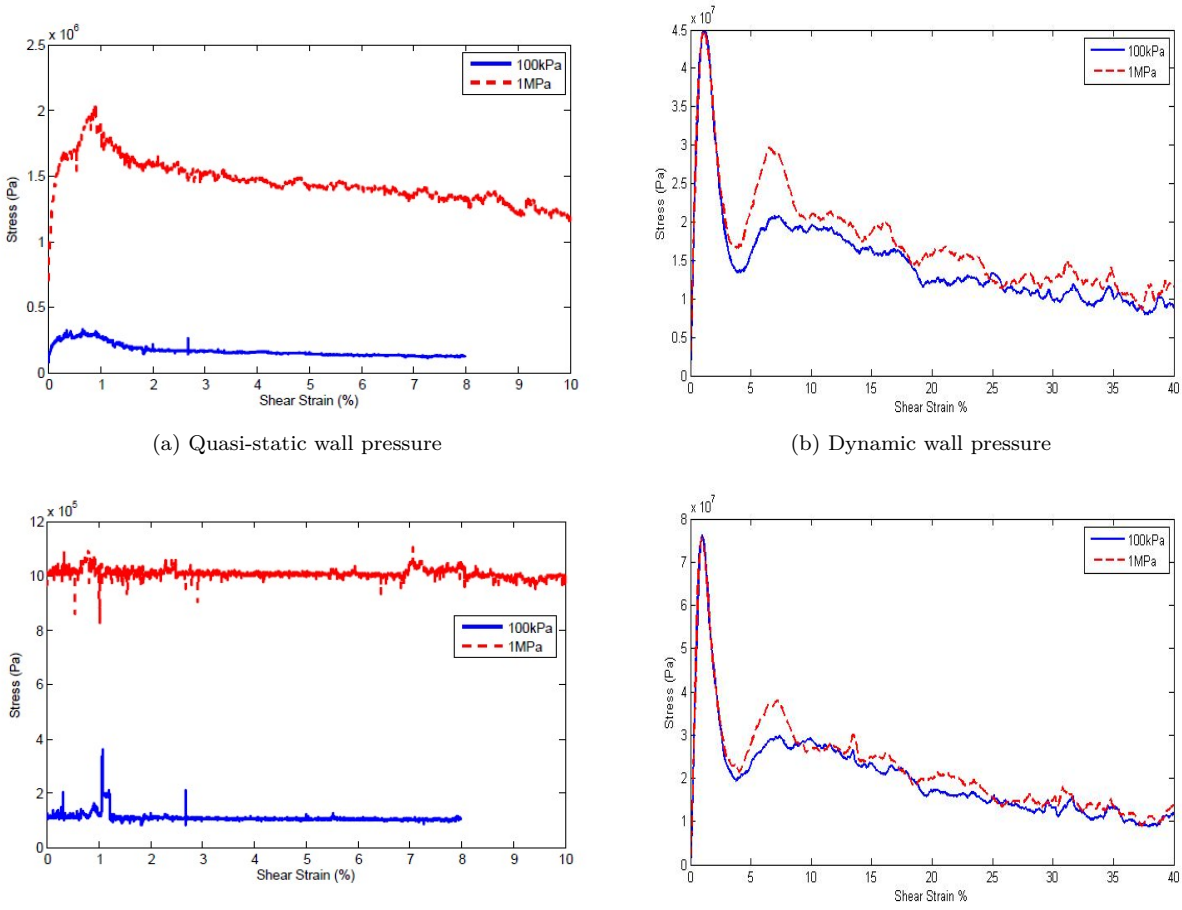

(a) Quasi-static wall pressure

(b) Dynamic wall pressure

(c) Quasi-static base pressure

(d) Dynamic base pressure

Figure G.8: Plane strain confining wall pressures and base wall pressures for sandstone specimen 2.

Appendix H

Shear Testing - Weak Chalk

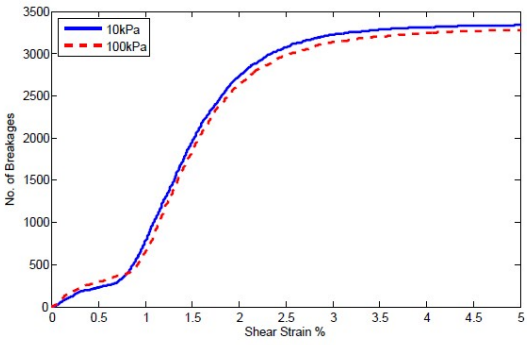

(a) Quasi-static breakage

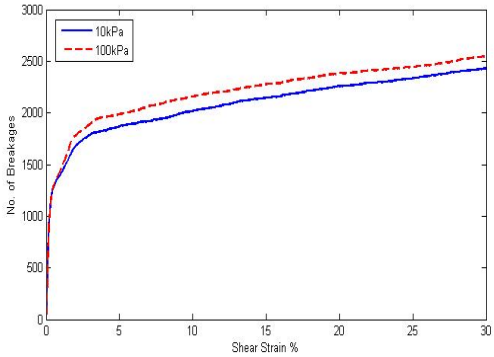

(b) Dynamic breakage

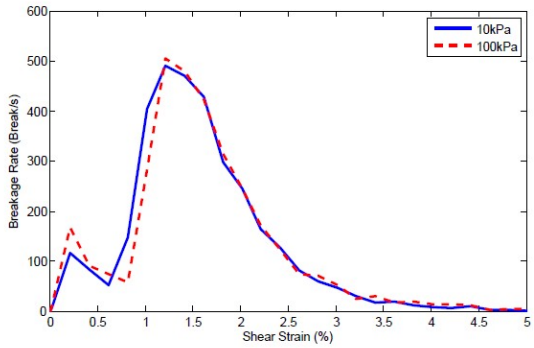

(c) Quasi-static breakage rate

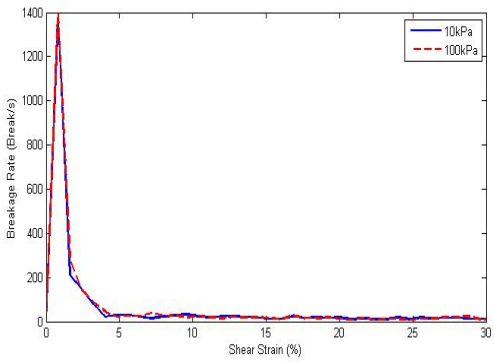

(d) Dynamic breakage rate

Figure H.1: Breakage under shear testing for weak chalk specimen 2.

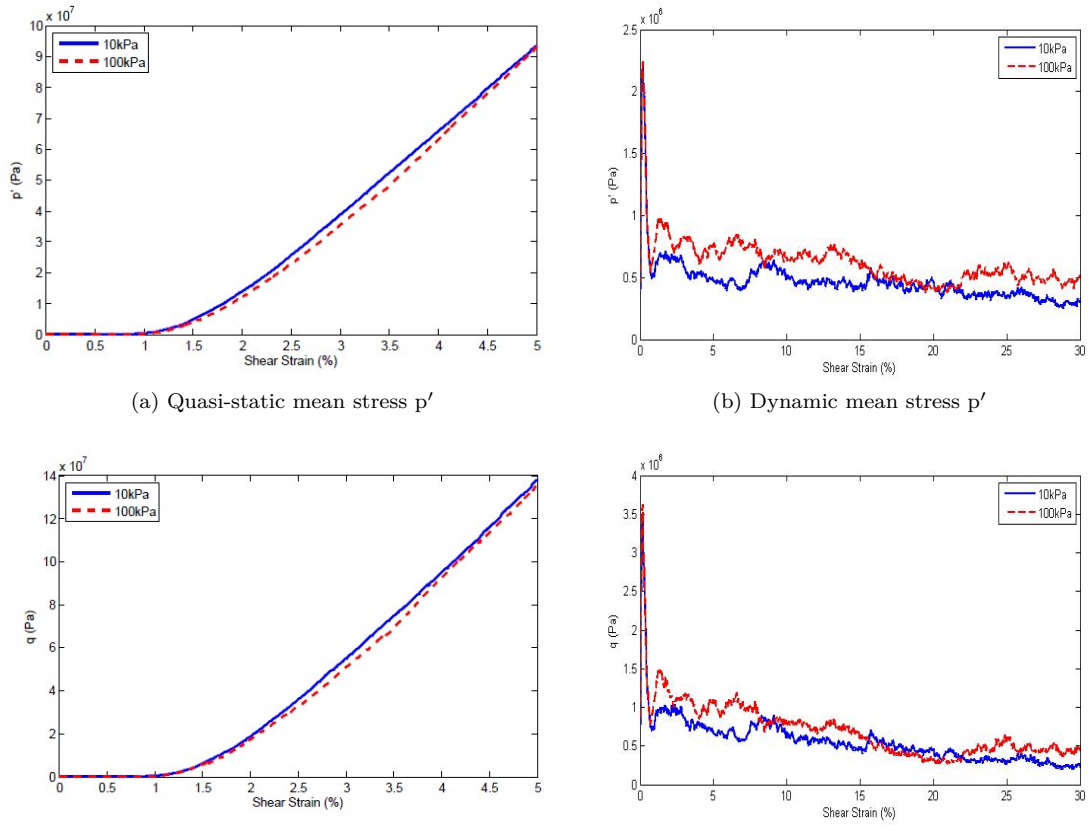

(a) Quasi-static mean stress p′

(b) Dynamic mean stress p′

(c) Quasi-static deviatoric stress q

(d) Dynamic deviatoric stress q

Figure H.2: Mean and deviatoric stress response under shear testing for weak chalk specimen 2.

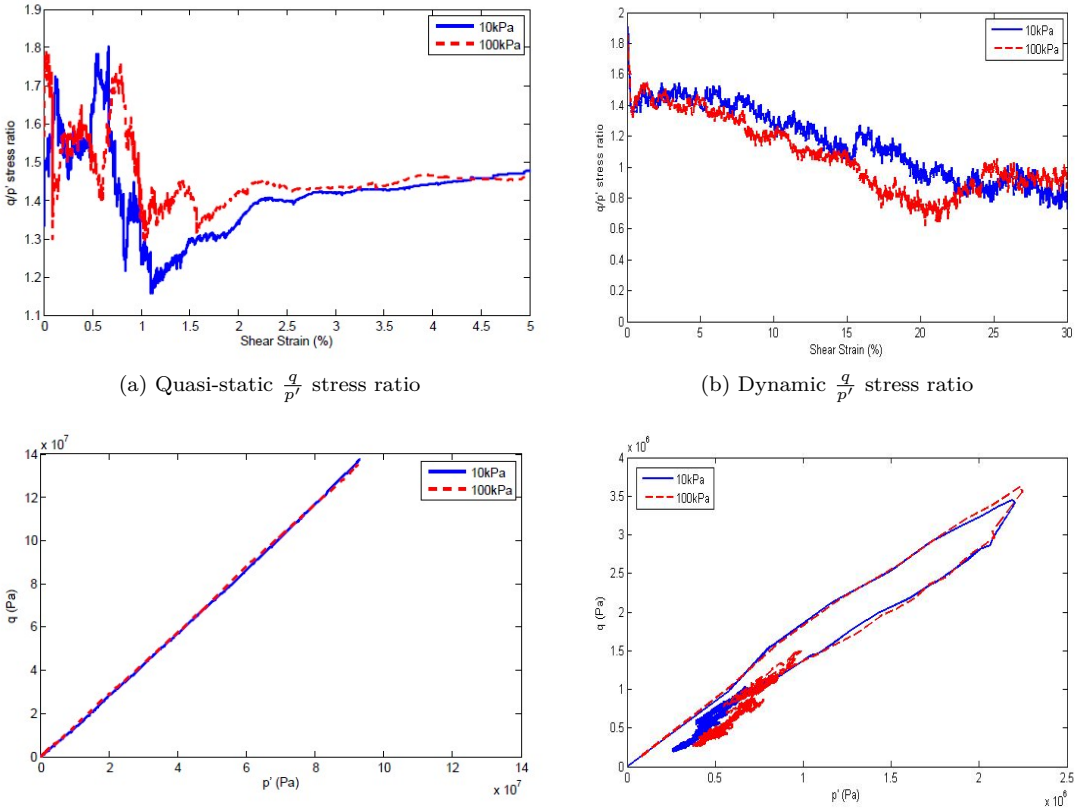

(a) Quasi-static $\frac{q}{p'}$ stress ratio

(b) Dynamic $\frac{q}{p'}$ stress ratio

(c) Quasi-static stress path

(d) Dynamic stress path

Figure H.3: $\frac{q}{p'}$ stress ratio and stress path response under shear testing for weak chalk specimen 2.

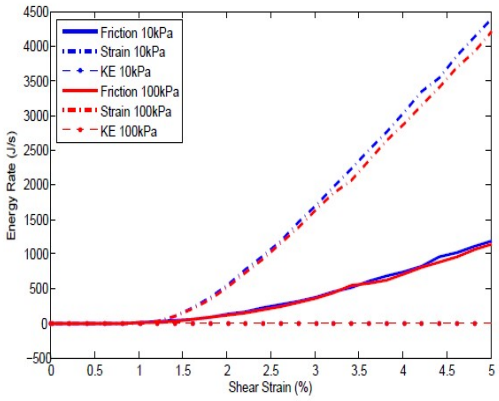

(a) Quasi-static

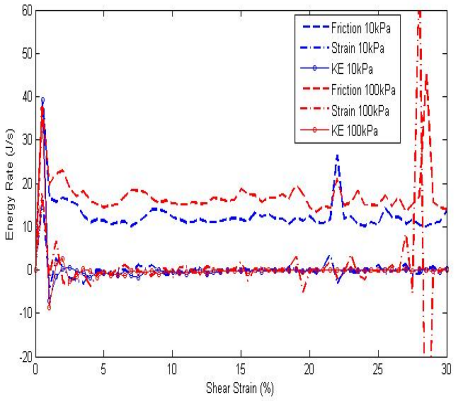

(b) Dynamic

Figure H.4: System energy rates from shear testing of weak chalk specimen 2.

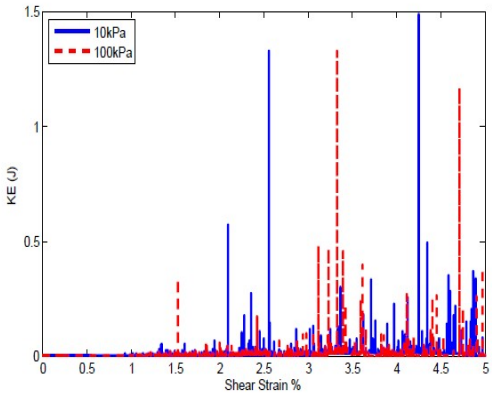

(a) Quasi-static

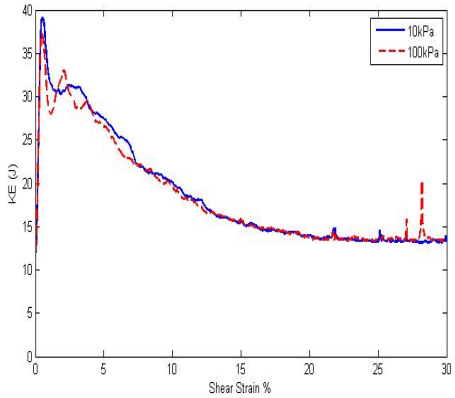

(b) Dynamic

Figure H.5: System kinetic energy response from shear testing of weak chalk specimen 2.

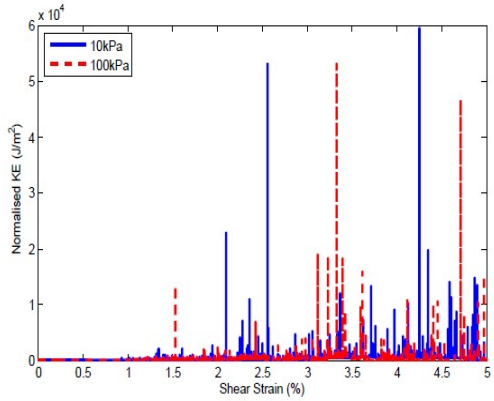

(a) Quasi-static

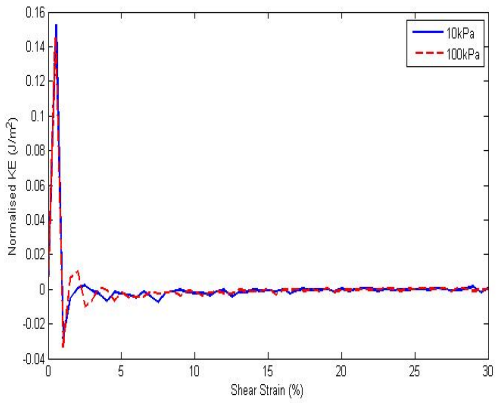

(b) Dynamic

Figure H.6: Kinetic energy rate normalised by the square of the shear velocity for weak chalk specimen 2.

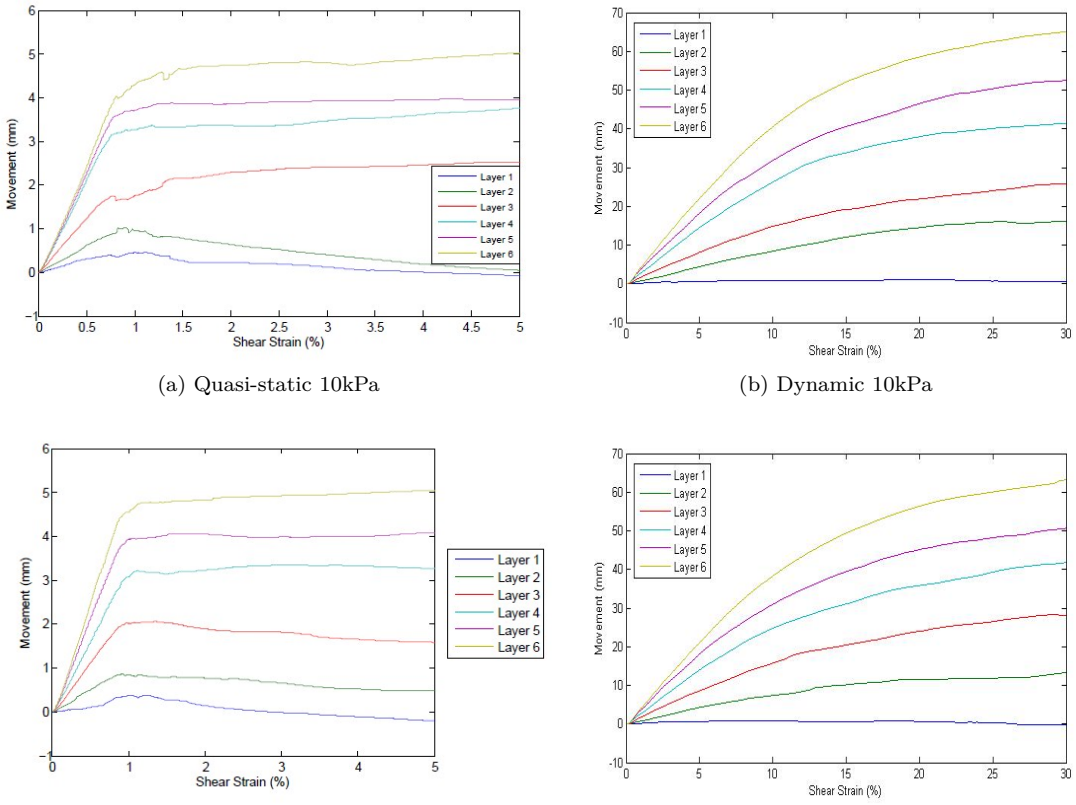

(a) Quasi-static 10kPa

(b) Dynamic 10kPa

(c) Quasi-static 100kPa

(d) Dynamic 100kPa

Figure H.7: Dilation of weak chalk specimen 2 from gauge particles.

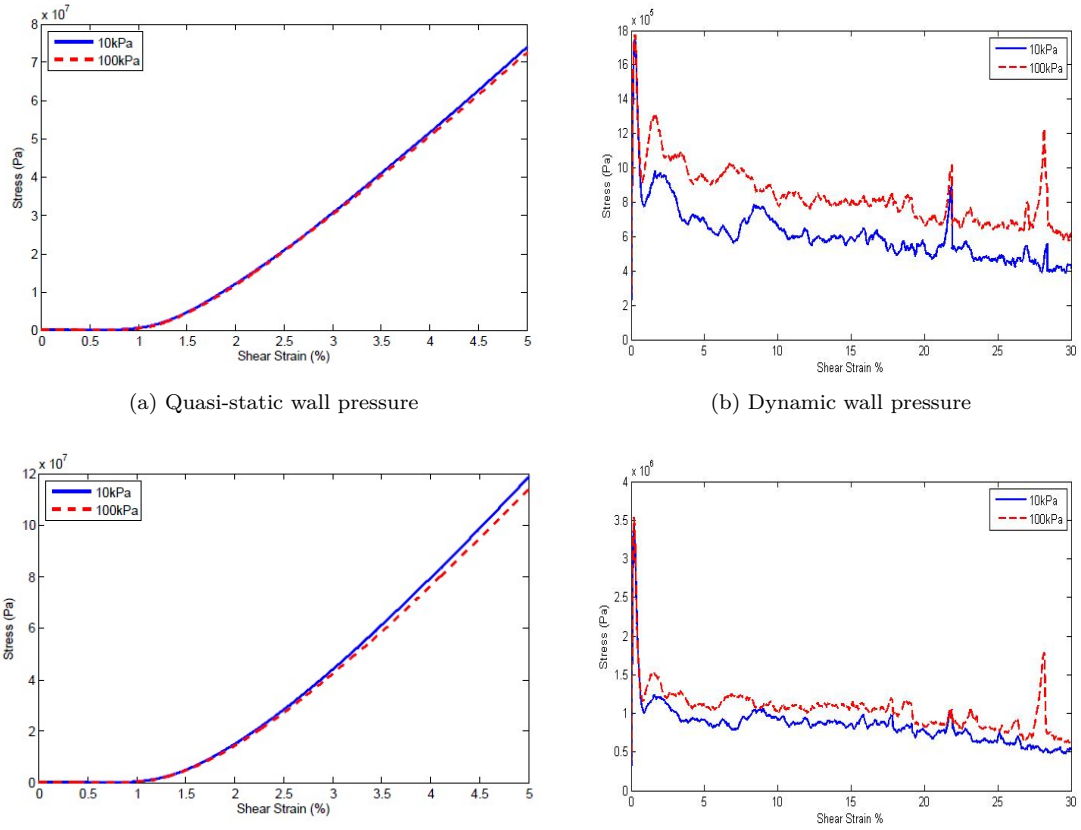

(a) Quasi-static wall pressure

(b) Dynamic wall pressure

(c) Quasi-static base pressure

(d) Dynamic base pressure

Figure H.8: Plane strain confining wall pressures and base wall pressures for weak chalk specimen 2.

Appendix I

Shear Testing - Extremely Weak Chalk

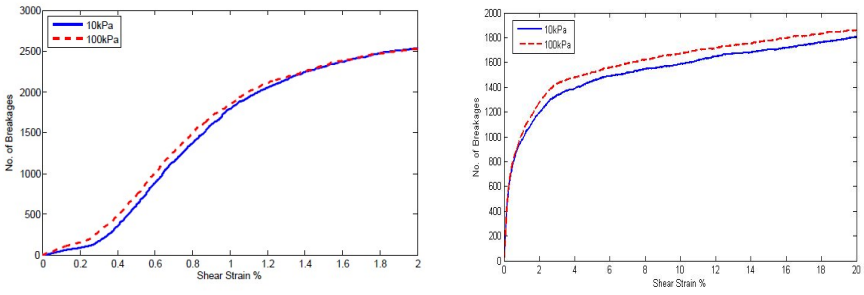

(a) Quasi-static breakage

(b) Dynamic breakage

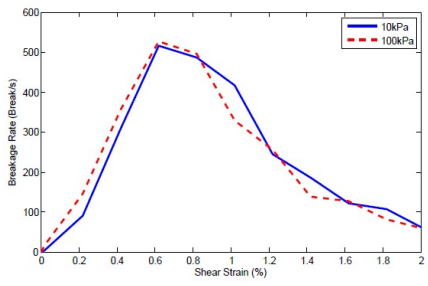

(c) Quasi-static breakage rate

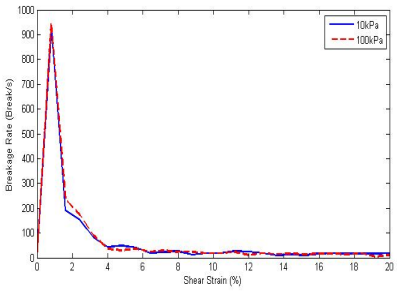

(d) Dynamic breakage rate

Figure I.1: Breakage under shear testing for extremely weak chalk specimen 1.

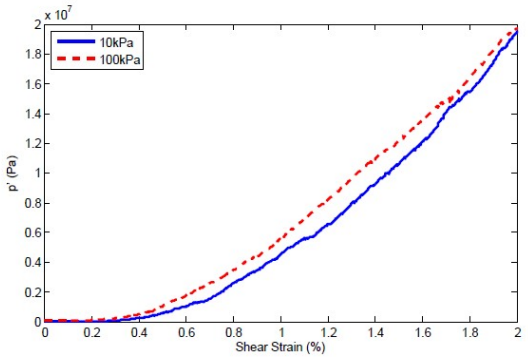

(a) Quasi-static mean stress p′

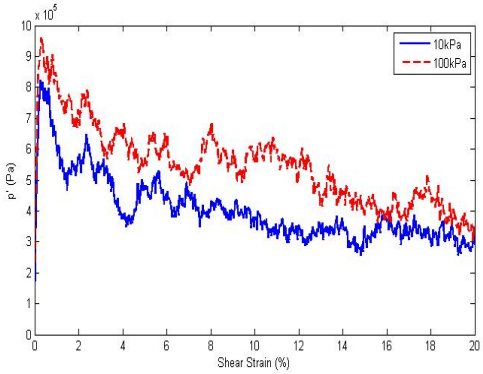

(b) Dynamic mean stress p′

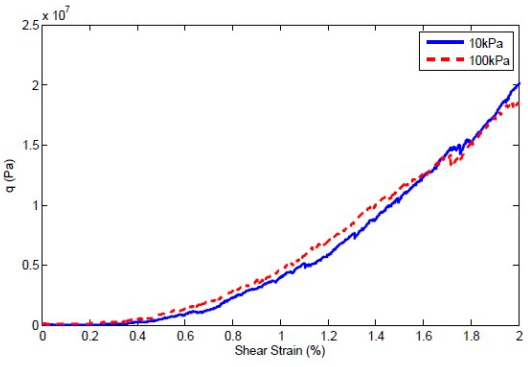

(c) Quasi-static deviatoric stress q

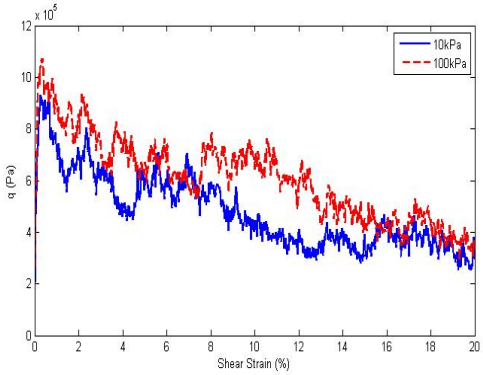

(d) Dynamic deviatoric stress q

Figure I.2: Mean effective and deviatoric stress response under shear testing for extremely weak chalk specimen 1.

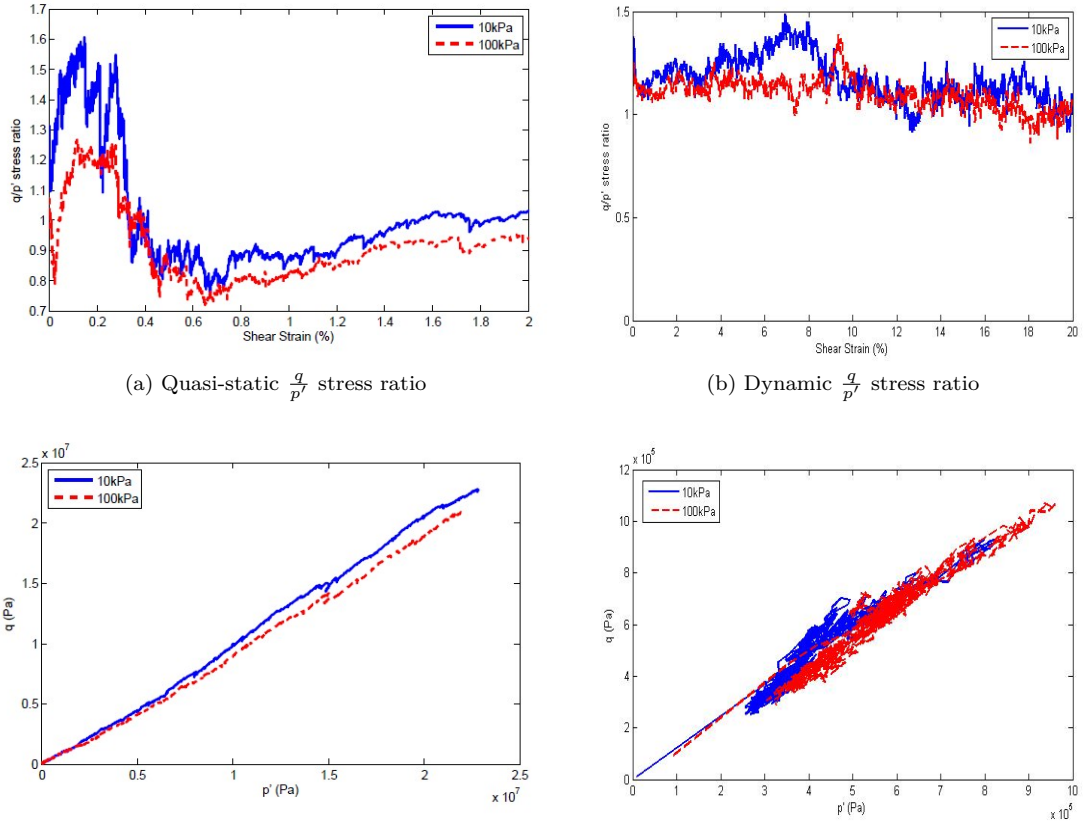

(a) Quasi-static $\frac{q}{p'}$ stress ratio

(b) Dynamic $\frac{q}{p'}$ stress ratio

(c) Quasi-static stress path

(d) Dynamic stress path

Figure I.3: $\frac{q}{p'}$ stress ratio and stress path response under shear testing for extremely weak chalk specimen 1.

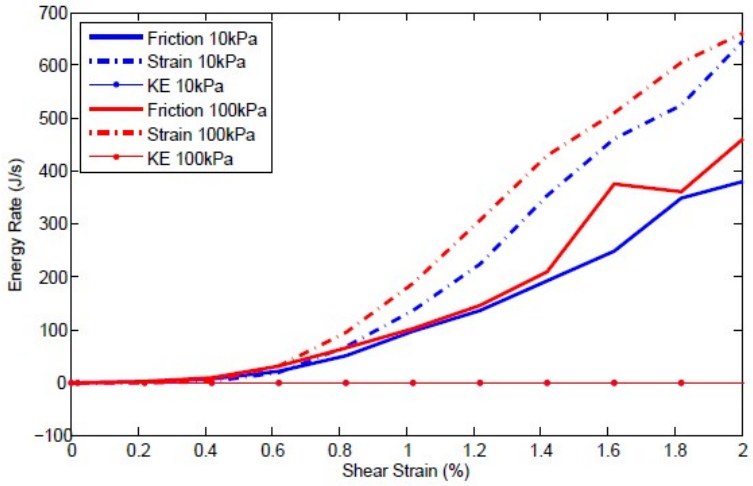

(a) Quasi-static energy rates

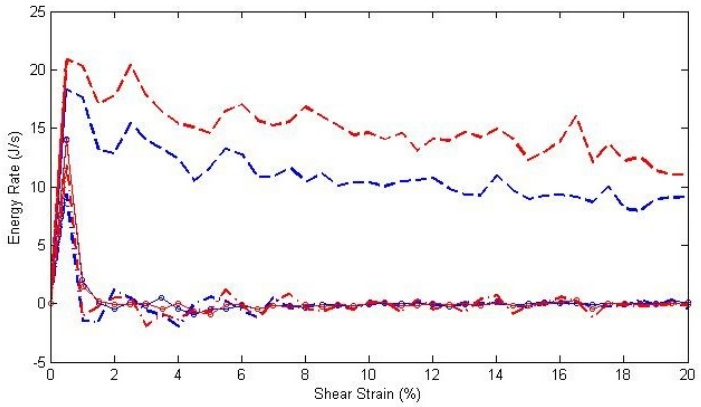

(b) Dynamic energy rates

Figure I.4: System energy rates from shear testing of extremely weak chalk specimen 1.

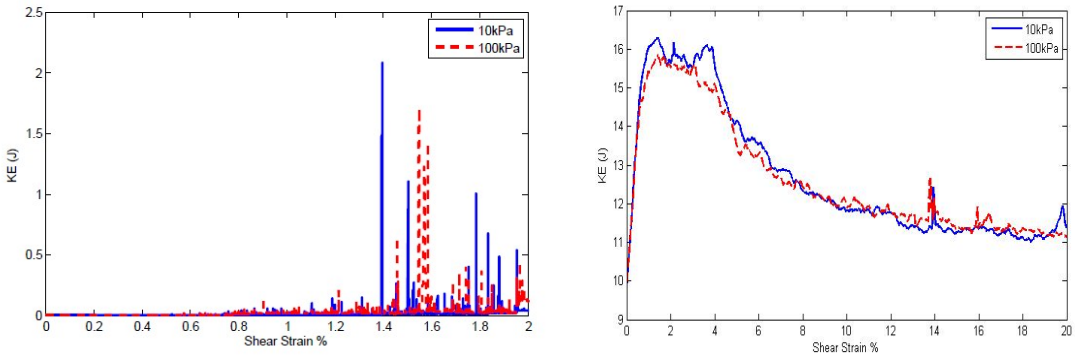

(a) Quasi-static

(b) Dynamic

Figure I.5: System kinetic energy response from shear testing of extremely weak chalk specimen 1.

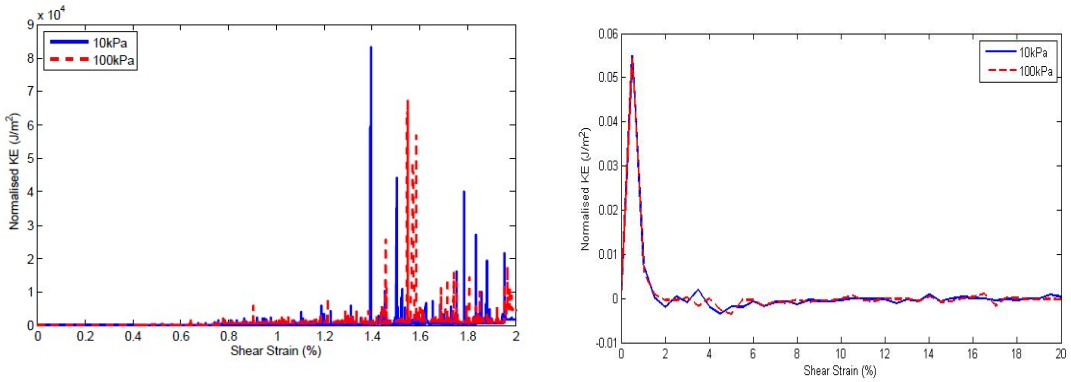

(a) Quasi-static (b) Dynamic

Figure I.6: Kinetic energy rate normalised by the square of the platen velocity for extremely weak chalk specimen 1.

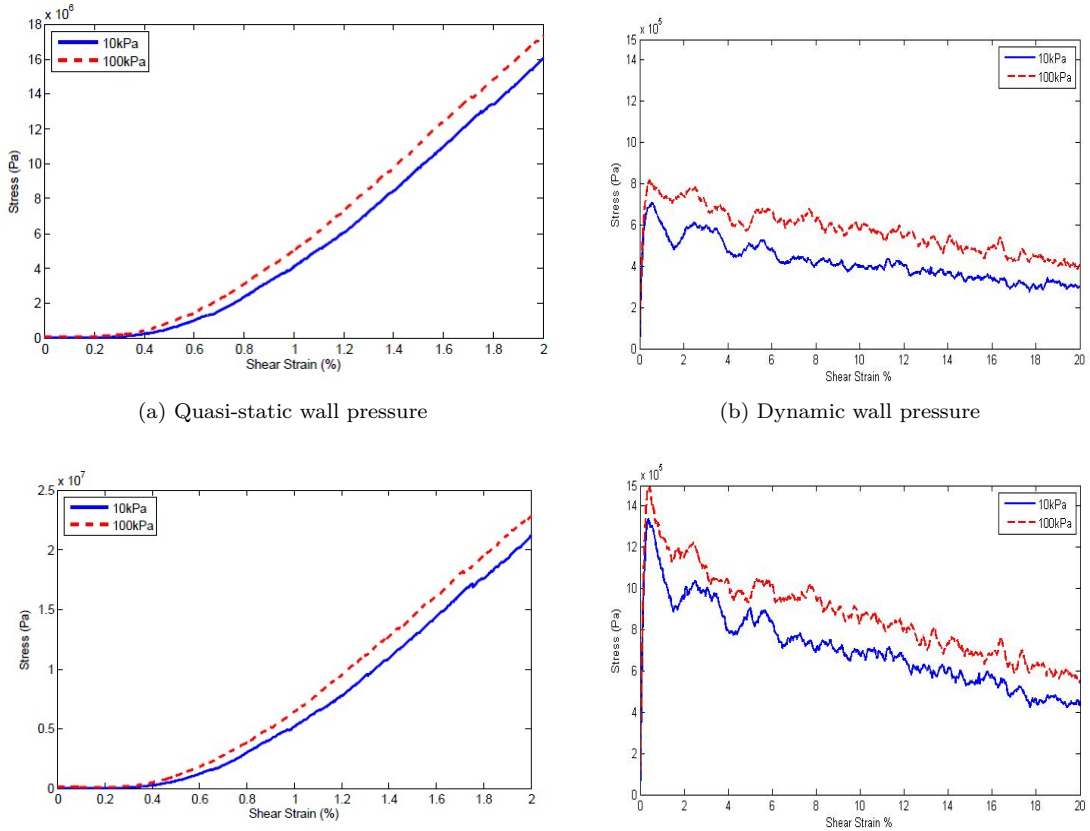

(a) Quasi-static wall pressure (b) Dynamic wall pressure

(c) Quasi-static base pressure (d) Dynamic base pressure

Figure I.7: Plane strain confining wall pressures and base wall pressures for extremely weak chalk specimen 1.

Bibliography

Ashby, M. and Jones, D. (2012). *Engineering Materials I: An Introduction to Properties, Applications and Design*. Elsevier Science, Oxford.

Bagnold, R. A. (1954). Experiments on a gravity-free dispersion of large solid spheres in a Newtonian fluid under shear. *Proceedings of the Royal Society of London Series A-Mathematical and Physical Sciences*, 225(1160):49–63.

Banton, J., Villard, P., Jongmans, D., and Scavia, C. (2009). Two-dimensional discrete element models of debris avalanches: Parameterization and the reproducibility of experimental results. *Journal of Geophysical Research-Earth Surface*, 114(F4):2156–2202.

Bell, F. G., Cripps, J. C., Edmonds, C. N., and Culshaw, M. G. (1990). Chalk fabric and its relation to certain geotechnical properties. In Burland, J., Mortimore, R., Roberts, L., Jones, B., and Corbett, B., editors, *Chalk. Proceedings of the International Chalk Symposium, Brighton Polytechnic, 1989*, pages 187–194, London. Thomas Telford.

Bell, F. G., Culshaw, M. G., and Cripps, J. C. (1999). A review of selected engineering geological characteristics of english chalk. *Engineering Geology*, 54(3-4):237–269.

Bieniawski, Z. T. (1967). Mechanism of brittle fracture of rock, part I - Theory of the fracture process. *International Journal of Rock Mechanics and Mining Sciences*, 4:395–406.

Bolton, M. D., Nakata, Y., and Cheng, Y. P. (2008). Micro- and macro-mechanical behaviour of DEM crushable materials. *Geotechnique*, 58(6):471–480.

Bowman, E. T. and Take, W. A. (2014). The runout of chalk cliff collapses in England and France — case studies and physical model experiments. *Landslides*, 12(2):225–239.

Bowman, E. T., Take, W. A., Rait, K. L., and Hann, C. (2012). Physical models of rock avalanche spreading behaviour with dynamic fragmentation. *Canadian Geotechnical Journal*, 49(4):460–476.

Brace, W. F. (1960). An extension of the Griffith theory of fracture to rocks. *Journal of Geophysical Research*, 65(10):3477–3480.

Cagnoli, B. and Piersanti, A. (2015). Grain size and flow volume effects on granular flow mobility in numerical simluations: 3-D discrete element modeling of flows of angular rock fragments. *Journal of Geophysical Research: Solid Earth*, 120:2350–2366.

Cagnoli, B. and Romano, G. P. (2010). Effect of grain size on mobility of dry granular flows of angular rock fragments: An experimental determination. *Journal of Volcanology and Geothermal Research*, 193(1-2):18–24.

Campbell, C. S. (1989). Self-lubrication for long runout landslides. *Journal of Geology*, 97(6):653–665.

Campbell, C. S., Cleary, P. W., and Hopkins, M. (1995). Large-scale landslide simulations. Global deformation, velocities and basal friction. *Journal of Geophysical Research*, 100(B5):8267–8283.

Carolan, A. M. and O'Sullivan, C. (2006). The influence of particle crushing on material response in the direct shear box using DEM. In *17th European Young Geotechnical Engineers Conference*, Croatia.

Cheng, Y. P., Bolton, M. D., and Nakata, Y. (2004). Crushing and plastic deformation of soils simulated using DEM. *Geotechnique*, 54(2):131–141.

Cheng, Y. P., Nakata, Y., and Bolton, M. D. (2003). Discrete element simulation of crushable soil. *Geotechnique*, 53(7):633–641.

Cheng, Y. P., Peng, Q., and Hughes, L. (2008). Shear band and strength of crushable agglomerates in direct shear box simulations of Discrete Element Method. In Burns, S., Mayne, P., and Santamarina, J., editors, *Deformation Characteristics of Geomaterials, Vols 1 and 2*, pages 357–364, Atlanta, Georgia.

Cheung, G. (2010). *Micromechanics of Sand Production in Oil Wells*. PhD thesis, Imperial College, London.

Cheung, G. and O'Sullivan, C. (2008). Effective simulation of flexible lateral boundaries in two- and three-dimensional DEM simulations. *Particuology*, 6(6):483–500.

Chugunov, V. A., Gray, J., and Hutter, K. (2008). Exact solutions of the Savage-Hutter equations for one-dimensional granular flows. *Newton Preprint NI03077*, page 26.

Clayton, C. R. I. (1990). The mechanical properties of the chalk. In Burland, J. B., Mortimore, R. N., Roberts, L. D., Jones, D. L., and Corbett, B. O., editors, *Chalk. Proceedings of the International Chalk Symposium, Brighton Polytechnic, 1989*, pages 213–232, London. Thomas Telford.

Cleary, P. W. and Campbell, C. S. (1993). Self-lubrication for long runout landslides - examination by computer simulation. *Journal of Geophysical Research-Solid Earth*, 98(B12):21911–21924.

Coe, J. A., Baum, R. L., Allstadt, K. E., Kochevar Jr, B. F., Schmitt, R. G., Morgan, M. L., White, J. L., Stratton, B. T., Hayashi, T. A., and Kean, J. W. (2016). Rock-avalanche dynamics revealed by large-scale field mapping and seismic signals at a highly mobile avalanche in the West Salt Creek valley, western Colorado. *Geosphere*, 12(2):607–631.

Cook, G. (2001). Rock mass structure and intact rock strength of New Zealand greywackes. Master's thesis, Masters Thesis, University of Canterbury, Christchurch, New Zealand.

Cook, N. G. W. (1965). The failure of rock. *International Journal of Rock Mechanics and Mining Sciences*, 2:389–403.

Cook, N. G. W. and Hodgson, K. (1965). Some detailed stress-strain curves for rock. *Journal of Geophysical Research*, 70(12):2883–2888.

Crosta, G. B., Frattini, P., and Fusi, N. (2007). Fragmentation in the Val Pola rock avalanche, Italian Alps. *Journal of Geophysical Research-Earth Surface*, 112(F1).

Cruden, D. M. and Hungr, O. (1986). The debris of the Frank slide and theories of rockslide avalanche mobility. *Canadian Journal of Earth Sciences*, 23(3):425–432.

Cruden, D. M. and Krahn, J. (1978). Frank Rockslide, Alberta, Canada. In Voight, B., editor, *Rockslides and Avalanches, Volume I.*

Cui, L. and O'Sullivan, C. (2006). Exploring the macro- and micro-scale response of an idealised granular material in the direct shear apparatus. *Geotechnique*, 56(7):455–468.

Cundall, P. A. (1988). Formulation of a 3-dimensional distinct element model - Part 1 a scheme to detect and represent contacts in a system composed of many polyhedral blocks. *International Journal of Rock Mechanics and Mining Sciences and Geomechanics Abstracts*, 25(3):107–116.

Cundall, P. A. and Strack, O. D. L. (1979). Discrete numerical model for granular assemblies. *Geotechnique*, 29(1):47–65.

Dade, W. B. and Huppert, H. E. (1998). Long-runout rockfalls. *Geology*, 26(9):803–806.

Darby, R. (2001). *Chemical Engineering Fluid Mechanics*. Taylor & Francis, London.

Daudon, D., Villard, P., Richefeu, V., and Mollon, G. (2010). Influence of the morphology of slope and blocks on the energy dissipations in a rock avalanche. *Bulletin of Volcanology*, 72(8):933–944.

Davies, T., McSaveney, M., and Kelfoun, K. (2010). Runout of the Socompa volcanic debris avalanche, Chile: A mechanical explanation for low basal shear resistance. *Bulletin of Volcanology*, 72(8):933–944.

Davies, T. R. and McSaveney, M. J. (1999). Runout of dry granular avalanches. *Canadian Geotechnical Journal*, 36(2):313–320.

Davies, T. R. and McSaveney, M. J. (2002). Dynamic simulation of the motion of fragmenting rock avalanches. *Canadian Geotechnical Journal*, 39(4):789–798.

Davies, T. R. and McSaveney, M. J. (2008). The role of rock fragmentation in the motion of large landslides. *Engineering Geology*, 109(1-2):67–79.

Davies, T. R., McSaveney, M. J., and Boulton, C. J. (2012). Elastic strain energy release from fragmenting grains: Effects on fault rupture. *Journal of Structural Geology*, 38:265–277.

Davies, T. R., McSaveney, M. J., and Deganutti, A. (2007). Dynamic rock fragmentation causes low rock-on-rock friction. In Eberhardt, E., Stead, D., and Morrison, T., editors, *Rock Mechanics: Meeting Society's Challenges and Demands, Vol 1*, Vancouver, Canada. Taylor and Francis.

Davies, T. R., McSaveney, M. J., and Hodgson, K. A. (1999). A fragmentation-spreading model for long-runout rock avalanches. *Canadian Geotechnical Journal*, 36(6):1096–1110.

De Blasio, F. V. (2011). Dynamical stress in force chains of granular media on a bumpy terrain and the fragmentation of rock avalanches. *Acta Mechanica*, 221:375–382.

De Blasio, F. V. and Crosta, G. B. (2015). Fragmentation and boosting of rock falls and rock avalanches. *Geophysical Research Letters*, 42:8463–8470.

Deganutti, A. (2008). *The Hypermobility of Rock Avalanches*. PhD thesis, Universita' Degli Studi di Padova, Italy.

Denlinger, R. P. and Iverson, R. M. (2001). Flow of variably fluidized granular masses across three-dimensional terrain 2. Numerical predictions and experimental tests. *Journal of Geophysical Research-Solid Earth*, 106(B1):553–566.

Donath, F. and Fruth, L. (1971). Dependence of strain-rate effects on deformation mechanism and rock type. *The Journal of Geology*, 79(3):347–371.

Donohue, S., O'Sullivan, C., and Long, M. (2009). Particle breakage during cyclic triaxial loading of a carbonate sand. *Geotechnique*, 59(5):477–482.

Dufresne, A., Bösmeier, A., and Prager, C. (2016). Sedimentology of rock avalanche deposits - Case study and review. *Earth Science Reviews*, 163:236–259.

Dufresne, A., Davies, T. R., and McSaveney, M. J. (2010). Influence of runout-path material on emplacement of the Round Top rock avalanche, New Zealand. *Earth Surface Processes and Landforms*, 35(2):190–201.

Dunning, S. A., Rosser, N. J., McColl, S. T., and Reznichenko, N. V. (2015). Rapid sequestration of rock avalanche deposits within glaciers. *Nature Communications*, 6:7964.

Duperret, A., Genter, A., Mortimore, R. N., Delacourt, B., and De Pomerai, M. R. (2002). Coastal rock cliff erosion by collapse at Puys, France: The role of impervious marl seams within chalk of NW Europe. *Journal of Coastal Research*, 18(1):52–61.

Eberhardt, E., Stimpson, B., and Stead, D. (1999). Effects of grain size on the initiation and propagation thresholds of stress-induced brittle fractures. *Rock Mechanics and Rock Engineering*, 32(2):81–99.

Erismann, T. H. (1979). Mechanisms of large landslides. *Rock Mechanics*, 12(1):15–46.

Evans, S. G., Hungr, O., and Enegren, E. (1994). The Avalanche Lake rock avalanche, Mackenzie Mountains, Northwest Territories, Canada: description, dating and dynamics. *Canadian Geotechnical Journal*, 31:749–768.

Friedmann, S. J., Kwon, G., and Losert, W. (2003). Granular memory and its effect on the triggering and distribution of rock avalanche events. *Journal of Geophysical Research-Solid Earth*, 108(B8):2380–2391.

Friedmann, S. J., Taberlet, N., and Losert, W. (2006). Rock-avalanche dynamics: Insights from granular physics experiments. *International Journal of Earth Sciences*, 95(5):911–919.

Fromm, W. (1981). *Der Bergsturz von Elm*. Heinrich Stussi, Linthal.

Grady, D. (1998). Shock-wave compression of brittle solids. *Mechanics of Materials*, 29:181–203.

Grady, D., Hollenbach, R. E., Schuler, K. W., and Callender, J. F. (1977). Strain rate dependence in dolomite inferred from impact and static compression studies. *Journal of Geophysical Research*, 82(8):1325–1333.

Grady, D. and Kipp, M. E. (1985). Mechanisms of dynamic fragmentation: Factors governing fragment size. *Mechanics of Materials*, 4:311–320.

Grady, D. E. (1981). Fragmentation of solids under impulsive stress loading. *Journal of Geophysical Research*, 86(NB2):1047–1054.

Grady, D. E. (1982). Local inertial effects in dynamic fragmentation. *Journal of Applied Physics*, 53(1):322–325.

Grady, D. E. and Kipp, M. (1987). Dynamic rock fragmentation. In Atkinson, B., editor, *Fracture Mechanics of Rock*, London. Academic Press Geology Series.

Grady, D. E. and Olsen, M. L. (2003). A statistics and energy based theory of dynamic fragmentation. In *Hypervelocity Impact Symposium*, pages 293–306, Noordwijk, Netherlands. Pergamon-Elsevier Science Ltd.

Gray, J., Tai, Y. C., and Noelle, S. (2003). Shock waves, dead zones and particle-free regions in rapid granular free-surface flows. *Journal of Fluid Mechanics*, 491:161–181.

Guo, Y. and Morgan, J. K. (2007). Fault gouge evolution and its dependence on normal stress and rock strength - Results of discrete element simulations: Gouge zone properties. *Journal of Geophysical Research-Solid Earth*, 112(B10).

Guo, Y. G. and Morgan, J. K. (2004). Influence of normal stress and grain shape on granular friction: Results of discrete element simulations. *Journal of Geophysical Research-Solid Earth*, 109(B12).

Guo, Y. G. and Morgan, J. K. (2006). The frictional and micromechanical effects of grain comminution in fault gouge from distinct element simulations. *Journal of Geophysical Research-Solid Earth*, 111(B12).

Guo, Y. G. and Morgan, J. K. (2008). Fault gouge evolution and its dependence on normal stress and rock strength - Results of discrete element simulations: Gouge zone micromechanics. *Journal of Geophysical Research-Solid Earth*, 113(B8).

Hancox, G. T. and Thomson, R. (2013). The January 2013 Mt Haast rock avalanche and Ball Ridge rock fall in Aoraki/Mt Cook National Park, New Zealand. Technical report, GNS Science Report 2013/33.

Hardin, B. (1985). Crushing of soil particles. *Journal of Geotechnical Engineering*, 111(10):1177–1192.

Hazzard, J. F., Young, R. P., and Maxwell, S. C. (2000). Micromechanical modeling of cracking and failure in brittle rocks. *Journal of Geophysical Research-Solid Earth*, 105(B7):16683–16697.

He, C., Okubo, S., and Nishimatsu, Y. (1990). A study on the Class II behaviour of rock. *Rock Mechanics and Rock Engineering*, 23:261–273.

Heim, A. (1882). Der bergsturz von Elm. *Zeitschrift der Deutschen Geologischen Gesellschaft*, 34:74–115.

Hoek, E. and Bieniawski, Z. T. (1965). Brittle fracture propagation in rock under compression. *International Journal of Fracture Mechanics*, 1(3):137–155.

Holt, R. M. (2001). Particle vs. laboratory modelling of in situ compaction. *Physics and Chemistry of the Earth Part a-Solid Earth and Geodesy*, 26(1-2):89–93.

Hsu, K. J. (1975). Catastrophic debris streams (sturzstroms) generated by rockfalls. *Geological Society of America Bulletin*, 86(1):129–140.

Hsu, K. J. (1978). Albert Heim: Observations on landslides and relevance to modern interpretations. In Voight, B., editor, *Rockslides and Avalanches, Volume I.*

Hudson, J. A. and Harrison, J. P. (1997). *Engineering Rock Mechanics: An Introduction to the Principles.* Elsevier Science, Oxford.

Hungr, O. (1995). A model for the runout analysis of rapid flow slides, debris flows and avalanches. *Canadian Geotechnical Journal*, 32(4):610–623.

Hungr, O. (2008). Simplified models of spreading flow of dry granular material. *Canadian Geotechnical Journal*, 45(8):1156–1168.

Hungr, O. and Evans, S. G. (1996). Rock avalanche runout prediction using a dynamic model. In Senneset, K., editor, *7th International Symposium on Landslides*, pages 233–238, Trondheim, Norway.

Hungr, O. and Morgenstern, N. R. (1984). High-velocity ring shear tests on sand. *Geotechnique*, 34(3):415–421.

Hutchinson, J. N. (2002). Chalk flows from the coastal cliffs of northwest Europe. In Evans, S. G. and DeGraff, J. V., editors, *Catastrophic landslides: effects, occurrence and mechanisms*, Geological Society of America Reviews in Engineering Geology, pages 257–302. Geological Society of America, Boulder, Colorado.

Hutter, K., Wang, Y. Q., and Pudasaini, S. P. (2005). The Savage-Hutter avalanche model: How far can it be pushed? *Philosophical Transactions of the Royal Society*, pages 1507–1528.

Imre, B., Laue, J., and Springman, S. M. (2010). Fractal fragmentation of rocks within sturzstroms: Insight derived from physical experiments within the ETH geotechnical drum centrifuge. *Granular Matter*, 12(3):267–285.

Itasca (2008). *Particle Flow Code in Three Dimensions.* Itasca Consulting Group Inc.

Iverson, R. M. (1997). The physics of debris flows. *Reviews of Geophysics*, 35(3):245–296.

Iverson, R. M. and Denlinger, R. P. (2001). Flow of variably fluidized granular masses across three-dimensional terrain 1. Coulomb mixture theory. *Journal of Geophysical Research-Solid Earth*, 106(B1):537–552.

Jackson, K., Kingman, S. W., Whittles, D. N., Lowndes, I. S., and Reddish, D. J. (2008). The effect of strain rate on the breakage behaviour of rock. *Archives of Mining Sciences*, 53(1):3–22.

Janach, W. (1976). The role of bulking in brittle failure of rocks under rapid compression. *International Journal of Rock Mechanics and Mineral Sciences*, 13:177–186.

Jibson, R. W., Harp, E. L., Schulz, W., and Keefer, D. K. (2006). Large rock avalanches triggered by the M 7.9 Denali Fault, Alaska, earthquake of 3 November 2002. *Engineering Geology*, 83(1-3):144–160.

Johnson, B. C., Campbell, C. S., and Melosh, H. J. (2016). The reduction of friction in long runout landslides as an emergent phenomenon. *Journal of Geophysical Research: Earth Surface*, 121:881–889.

Kafui, K. D. and Thornton, C. (2000). Numerical simulations of impact breakage of a spherical crystalline agglomerate. *Powder Technology*, 109(1-3):113–132.

Kelfoun, K. and Davies, T. R. (2011). Comment on "a random kinetic energy model for rock avalanches: Eight case studies" by T. Preuth et al. *Journal of Geophysical Research*, 116:F01014.

Kelfoun, K. and Druitt, T. H. (2005). Numerical modeling of the emplacement of Socompa rock avalanche, Chile. *Journal of Geophysical Research-Solid Earth*, 110(B12).

Kent, P. E. (1966). Transport mechanism in catastrophic rock falls. *Journal of Geology*, 74(1):79–83.

Khazaei, C., Hazzard, J., and Chalaturnyk, R. (2015). Damage quantification of intact rocks using acoustic emission energies recorded during uniaxial compression test and discrete element modelling. *Computers and Geotechnics*, 67:94–102.

Kilburn, C. R. J. (1999). The flow of giant rock landslides. In Briegel, U. and Xiao, W. J., editors, *Symposium on Paradoxes in Modern Geology*, pages 245–265, Beijing, Peoples R China.

Kipp, D. E. and Grady, M. E. (1985). Dynamic fracture growth and interaction in one dimension. *Journal of the Mechanics Physics of Solids*, 33(4):399–415.

Kipp, M. E. and Grady, D. E. (1978). Continuum model of strain-rate dependent rock fracture. *Bulletin of the American Physical Society*, 23(1):71–71.

Kipp, M. E., Grady, D. E., and Chen, E. P. (1980). Strain-rate dependent fracture initiation. *International Journal of Fracture*, 16(5):471–478.

Kuhn, M. R. (1999). Structured deformation in granular materials. *Mechanics of Materials*, 31(6):407–429.

Lajtai, E., Duncan, E., and Carter, B. (1991). The effect of strain rate on rock strength. *Rock Mechanics and Rock Engineering*, 24:99–109.

Langlois, V., Quiquerez, A., and Allemand, P. (2015). Collapse of a two-dimensional brittle granular column: Implications for understanding dynamic rock fragmentation in a landslide. *Journal of Geophysical Research: Solid Earth*, 120:1866–1880.

Legros, F. (2002). The mobility of long-runout landslides. *Engineering Geology*, 63(3-4):301–331.

Li, X., Zou, Y., and Zhou, Z. (2014). Numerical simulation of the rock SHPB test with a special shape striker based on the discrete element method. *Rock Mechanics and Rock Engineering*, 47:1693–1709.

Lim, W. L. and McDowell, G. R. (2005). Discrete element modelling of railway ballast. *Granular Matter*, 7(1):19–29.

Lim, W. L. and McDowell, G. R. (2007). The importance of coordination number in using agglomerates to simulate crushable particles in the discrete element method. *Geotechnique*, 57(8):701–705.

Lindholm, U., Yeakley, L., and A., N. (1974). The dynamic strength and fracture properties of Dresser basalt. *International Journal of Rock Mechanics and Mining Sciences and Geomechanics Abstracts*, 11(5):181–191.

Liu, S. H. (2006). Simulating a direct shear box test by DEM. *Canadian Geotechnical Journal*, 43(2):155–168.

Lo, C. Y., Bolton, M. D., and Cheng, Y. P. (2009). Discrete element simulation of granular column collapse. In Nakagawa, M. and Luding, S., editors, *6th International Conference on Micromechanics of Granular Media*, Colorado, USA. AIP Conference Proceedings.

Lobo-Guerrero, S. and Vallejo, L. E. (2005). Crushing a weak granular material: experimental numerical analyses. *Geotechnique*, 55(3):245–249.

Locat, P., Couture, R., Leroueil, S., Locat, J., and Jaboyedoff, M. (2006). Fragmentation energy in rock avalanches. *Canadian Geotechnical Journal*, 43(8):830–851.

Lundberg, B. (1976). Split Hopkinson Bar study of energy absorption in dynamic rock fragmentation. *International Journal of Rock Mechanics and Mining Sciences*, 13(6):187–197.

Mair, K. and Hazzard, J. F. (2007). Nature of stress accommodation in sheared granular material: Insights from 3D numerical modeling. *Earth and Planetary Science Letters*, 259(3-4):469–485.

Manzella, I. (2008). *Dry Rock Avalanche Propagation: Unconstrained Flow Experiments with Granular Materials and Blocks at Small Scale*. PhD thesis, Ecole Polytechnique Federale de Lausanne, Switzerland.

Manzella, I. and Labiouse, V. (2008). Qualitative analysis of rock avalanches propagation by means of physical modelling of non-constrained gravel flows. In *International Conference on Computer Methods and Advances in Geomechanics*, pages 133–151, Torino, Italy.

Manzella, I. and Labiouse, V. (2009). Flow experiments with gravel and blocks at small scale to investigate parameters and mechanisms involved in rock avalanches. *Engineering Geology*, 109(1-2):146–158.

Mars Ivars, D., Pierce, M. E., Darcel, C., Reyes-Montes, J., Potyondy, D. O., Young, R. P., and Cundall, P. A. (2011). The synthetic rock mass approach for jointed rock mass modelling. *International Journal of Rock Mechanics and Mining Sciences*, 48(2):219–244.

Masson, S. and Martinez, J. (2001). Micromechanical analysis of the shear behavior of a granular material. *Journal of Engineering Mechanics-ASCE*, 127(10):1007–1016.

Matthews, M. and Clayton, C. (1993). Influence of intact porosity on the engineering properties of a weak rock. In Anagnostopoulos, A., Schlosser, F., Kalteziotis, N., and Frank, R., editors, *International Symposium on Geotechnical Engineering of Hard Soils - Soft Rocks*, Athens, Greece. AA Balkema, Rotterdam.

McConnell, R. and Brock, R. (1904). Report on the great landslide at Frank, Alberta, Canada. Technical report.

McDougall, S. and Hungr, O. (2004). A model for the analysis of rapid landslide motion across three-dimensional terrain. *Canadian Geotechnical Journal*, 41(6):1084–1097.

McDowell, G. R. and Bolton, M. D. (1998). On the micromechanics of crushable aggregates. *Geotechnique*, 48(5):667–679.

McDowell, G. R., Bolton, M. D., and Robertson, D. (1996). The fractal crushing of granular materials. *Journal of the Mechanics and Physics of Solids*, 44(12):2079–2102.

McDowell, G. R. and Harireche, O. (2002a). Discrete element modelling of soil particle fracture. *Geotechnique*, 52(2):131–135.

McDowell, G. R. and Harireche, O. (2002b). Discrete element modelling of yielding and normal compression of sand. *Geotechnique*, 52(4):299–304.

McSaveney, M. J. (1978). Sherman Glacier Rock Avalanche, Alaska, U.S.A. In Voight, B., editor, *Rockslides and Avalanches, Volume I.*

McSaveney, M. J. (2015). Fragmenting granular flow: A personal account of the concept. In Lollino, G., Giordan, D., Crosta, G. B., Corominas, J., Azzam, R., Wasowski, J., and Sciarra, N., editors, *Engineering Geology for Society and Territory, Volume 2*, pages 1741–1744.

McSaveney, M. J. and Davies, T. (1999). The Falling Mountain Rock Avalanche of 1929, Arthur's Pass National Park, New Zealand. Technical report, GNS.

McSaveney, M. J. and Davies, T. R. (2007). Rockslides and their motion. In Sassa, K., Fukuoka, F., and Wang, G., editors, *Progress in Landslide Science*, pages 113–133.

McSaveney, M. J. and Davies, T. R. (2008). Surface energy is not one of the energy losses in rock comminution. *Engineering Geology*, 109(1-2):109–113.

McSaveney, M. J., Davies, T. R., and Hodgson, K. (2000). A contrast in deposit style and process between large and small rock avalanches. In Bromhead, E., Dixon, N., and Ibsen, M., editors, *8th International Symposium on Landslides*, pages 1053–1058, Cardiff, Wales. Thomas Telford.

Mead, S. and Cleary, P. (2015). Validation of DEM prediction for granular avalanches on irregular terrain. *Journal of Geophysical Research: Earth Surface*, 120:1724–1742.

Melosh, H. J. (1983). Acoustic fluidization. *American Scientist*, 71(2):158–165.

Melosh, H. J. (1986). The physics of very large landslides. *Acta Mechanica*, 64(1-2):89–99.

Mercier, M., Cossart, E., Decaulne, A., Feuillet, T., Jónsson, H. P., and Sæmundsson, Þ. (2012). The Höfðahólar rock avalanche (sturzström): Chronological constraint of paraglacial landsliding on an Icelandic hillslope. *The Holocene*, 23(3):432–446.

Meyer, M. (1994). *Dynamic behaviour of materials*. Wiley, New York.

Millar, M. (2000). *The Stress-Strain Behaviour of Jointed Chalk*. PhD thesis, University of Brighton, England.

Mishra, B. K. and Thornton, C. (2001). Impact breakage of particle agglomerates. *International Journal of Mineral Processing*, 61(4):225–239.

Mollon, G., Richefeu, V., Villard, P., and Daudon, D. (2015). Discrete modelling of rock avalanches: Sensitivity to block and slope geometries. *Granular Matter*, 17:645–666.

Moreau, J. J. (1994). Some numerical methods in multibody dynamics - application to granular materials. *European Journal of Mechanics and Solids*, 13:93–114.

Moreno, F., Jaboyedoff, M., Pedrazzini, A., Charriere, M., and Humair, F. (2011). Frank slide and Turtle Mountain early warning system technical tour guidebook. Technical report.

Moreno, R., Ghadiri, M., and Antony, S. J. (2003). Effect of the impact angle on the breakage of agglomerates: A numerical study using DEM. *Powder Technology*, 130:132–137.

Mortimore, R. N., Stone, K. J., Lawrence, J., and Duperret, A. (2004). *Chalk physical properties and cliff instability*, pages 75–88. Geological Society Engineering Geology Special Publication.

Muir Wood, D. (1990). *Soil Behaviour and Critical State Soil Mechanics*. Cambridge University Press, Cambridge.

Omdal, E. (2010). *The Mechanical Behaviour of Chalk Under Laboratory Conditions Simulating Reservoir Operations*. PhD thesis, University of Stavanger, Norway.

O'Sullivan, C. (2011). *Particulate Discrete Element Modelling: A Geomechanics Perspective*. Spon Press, Oxon.

O'Sullivan, C. and Bray, J. D. (2004). Selecting a suitable time step for discrete element simulations that use the central difference time integration scheme. *Engineering Computations*, 21(2-4):278–303.

Park, J. W. and Song, J. J. (2009). Numerical simulation of a direct shear test on a rock joint using a bonded-particle model. *International Journal of Rock Mechanics and Mining Sciences*, 46(8):1315–1328.

Passman, S. L., Grady, D. E., and Rundle, J. B. (1980). The role of inertia in the fracture of rock. *Journal of Applied Physics*, 51(8):4070–4075.

Pedersen, S. A. S., Larsen, L. M., Dahl-Jensen, T., Jepsen, H. F., Pedersen, G. K., Nielsen, T., Pedersen, A. K., von Platen-Hallermun, F., and Weng, W. (2002). Tsunami-generating rock fall and landslide on the south coast of Nuussuaq, central West Greenland. *Geology of Greenland Survey Bulletin*, 191:73–83.

Pirulli, M. (2009). The Thurwieser rock avalanche (Italian Alps): Description and dynamic analysis. *Engineering Geology*, 109(1-2):80–92.

Pirulli, M. and Mangeney, A. (2008). Results of back-analysis of the propagation of rock avalanches as a function of the assumed rheology. In *International Conference on Computer Methods and Advances in Geomechanics*, pages 59–84, Torino, Italy.

Plafker, G. and Ericksen, G. (1978). Nevados Huascaran Avalanches, Peru. In Voight, B., editor, *Rockslides and Avalanches, Volume I*.

Poisel, R. and Preh, A. (2008). 3D landslide run out modelling using the Particle Flow Code PFC3D. In Chen, Z., Zhang, J., Wu, F., and Ho, K., editors, *Landslides and Engineered Slopes: From the Past to the Future*, Xi'an, China.

Pollet, N., Cojean, R., Couture, R., Schneider, J. L., Strom, A., Voirin, C., and Wassmer, P. (2005). A slab-on-slab model for the Flims rockslide (Swiss Alps). *Canadian Geotechnical Journal*, 42(2):587–600.

Potyondy, D. O. and Cundall, P. A. (2004). A bonded-particle model for rock. *International Journal of Rock Mechanics and Mining Sciences*, 41(8):1329–1364.

Potyondy, D. O., Cundall, P. A., and Sarracino, R. S. (1996). Modeling of shock- and gas-driven fractures induced by a blast using bonded assemblies of spherical particles. In *Rock Fragmentation by Blasting*, pages 55–62.

Powrie, W. (2004). *Soil Mechanics - Concepts and Applications*. Spon Press, Oxon, second edition.

Powrie, W., Ni, Q., Harkness, R. M., and Zhang, X. (2005). Numerical modelling of plane strain tests on sands using a particulate approach. *Geotechnique*, 55(4):297–306.

Rait, K. L. and Bowman, E. T. (2010). Dynamic fragmentation in rock avalanches: A numerical model of micromechanical behaviour. In Benz, T. and Nordal, S., editors, *7th European Conference on Numerical Methods in Geotechnical Engineering*, Trondheim, Norway. Taylor & Francis Group.

Rait, K. L., Bowman, E. T., and Hann, C. (2011). Removing the Coriolis effect from centrifuge model data of high-speed rock avalanche spreading. In Khalili, N. and Oeser, M., editors, *13th International Conference of the International Association of Computer Methods and Advances in Geotechnics*, Melbourne, Australia. Centre for Infrastructure Engineering and Safety.

Rait, K. L., Bowman, E. T., and Lambert, C. (2012). Dynamic fragmentation of rock clasts under normal compression in sturzstrom. *Geotechnique Letters*, 2:167–172.

Refahi, A., Mohandesi, J. A., and Rezai, B. (2010). Discrete element modeling for predicting breakage behavior and fracture energy of a single particle in a jaw crusher. *International Journal of Mineral Processing*, 94(1-2):83–91.

Rinehart, J. S. (1966). Fracture of rocks. *International Journal of Fracture Mechanics*, 2(3):534–551.

Robertson, D. (2000). *Computer simulations of crushable aggregates*. PhD thesis, University of Cambridge, England.

Robinson, T. R., Davies, T. R. H., and Reznichenko, N. V., D. P. G. P. (2014). The extremely long-runout Komansu rock avalanche in the Trans Alai range, Pamir Mountains, southern Kyrgyzstan. *Landslides*, 12:523–535.

Ruban, A. V., Skriver, H. L., and Norskov, J. K. (2002). Local equilibrium properties of metallic surface alloys. In Woodruff, D. P., editor, *Surface Alloys and Alloy Surfaces*.

Sandhu, R. S. and Huang, S. W. (1975). Application of Griffith's theory to analysis of progressive fracture. *International Journal of Fracture*, 11(1):107–121.

Savage, S. B. and Hutter, K. (1989). The motion of a finite mass of granular material down a rough incline. *Journal of Fluid Mechanics*, 199:177–215.

Savage, S. B. and Hutter, K. (1991). The dynamics of avalanches of granular materials from initiation to runout. part I: Analysis. *Acta Mechanica*, 86(1-4):201–223.

Savage, S. B. and Sayed, M. (1984). Stresses developed by dry cohesionless granular materials sheared in an annular shear cell. *Journal of Fluid Mechanics*, 142(MAY):391–430.

Scheidegger, A. E. (1973). On the prediction of the reach and velocity of catastrophic landslides. *Rock Mechanics*, 5:231–236.

Schulz, W. H., Harp, E. L., and Jibson, R. W. (2008). Characteristics of large rock avalanches triggered by the november 3, 2002 Denali Fault earthquake, Alaska, USA. In Chen, Z., Zhang, J., Li, Z., Wu, F., and Ho, K., editors, *Landslides and Engineered Slopes: From the Past to the Future, Vols 1 and 2*, pages 1447–1453.

Shams Alam, M., Chakraborty, T., Matsagar, V., Rao, K., Sharma, P., and Singh, M. (2015). Characterization of Kota sandstone under different strain rates in uniaxial loading. *Geotechnical and Geological Engineering*, 33(1):143–152.

Shockey, D. A., Curran, D. R., Seaman, L., Rosenber, J. T., and Petersen, C. F. (1974). Fragmentation of rock under dynamic loads. *International Journal of Rock Mechanics and Mining Sciences*, 11(8):303–317.

Shreve, R. L. (1968). Leakage and fluidization in air-layer lubricated avalanches. *Geological Society of America Bulletin*, 79(5):653–657.

Staron, L. (2008). Mobility of long-runout rock flows: a discrete numerical investigation. *Geophysical Journal International*, 172(1):455–463.

Staron, L. and Hinch, E. J. (2007). The spreading of a granular mass: role of grain properties and initial conditions. *Granular Matter*, 9(3-4):205–217.

Subero, J., Ning, Z., Ghadiri, M., and Thornton, C. (1998). Effect of interface energy on the impact strength of agglomerates. In *9th European Symposium on Comminution and Classification*, pages 66–73, Albi, France.

Taboada, A. and Estrada, N. (2009). Rock-and-soil avalanches: Theory and simulation. *Journal of Geophysical Research-Earth Surface*, 114.

Terzaghi, K. and Peck, R. B. (1967). *Soil Mechanics in Engineering Practice, 2nd Edition.* John Wiley & Sons, Inc, New York.

Thompson, N., Bennett, M. R., and Petford, N. (2009). Analyses on granular mass movement mechanics and deformation with distinct element numerical modeling: implications for large-scale rock and debris avalanches. *Acta Geotechnica*, 4(4):233–247.

Thornton, C., Ciomocos, M. T., and Adams, M. J. (1998). Numerical simulations of agglomerate impact breakage. In *9th European Symposium on Comminution and Classification*, pages 74–82, Albi, France.

Thornton, C., Yin, K. K., and Adams, M. J. (1996). Numerical simulation of the impact fracture and fragmentation of agglomerates. *Journal of Physics D-Applied Physics*, 29(2):424–435.

Tommasi, P., Campedel, P., Consorti, C., and Ribacchi, R. (2008). A discontinuous approach to the numerical modelling of rock avalanches. *Rock Mechanics and Rock Engineering*, 41(1):37–58.

Valentino, R., Barla, G., and Montrasio, L. (2008). Experimental analysis and micromechanical modelling of dry granular flow and impacts in laboratory flume tests. In *International Conference on Computer Methods and Advances in Geomechanics*, pages 153–177, Torino, Italy.

Wasantha, P., Ranjith, P., Zhao, J., Shao, S., and Permata, G. (2015). Strain rate effect on the mechanical behaviour of sandstones with different grain sizes. *Rock Mechanics and Rock Engineering*, 48:1883–1895.

Wawersik, W. R. and Fairhurst, C. (1970). A study of brittle rock fracture in laboratory compression experiments. *International Journal of Rock Mechanics and Mining Sciences*, 7:561–575.

Weidinger, J. T., Korup, O., Munack, H., Altenberger, U., Dunning, S. A., Tippelt, G., and Lottermoser, W. (2014). Giant rockslides from the inside. *Earth and Planetary Science Letters*, 389:62–73.

Williams, R. B., Robinson, D. A., Dornbusch, U., Foote, Y. L., Moses, C. A., and Saddleton, P. R. (2004). A sturzstrom-like cliff fall on the chalk coast of Sussex, UK. In Mortimore, R. N. and Duperret, A., editors, *Coastal Chalk Cliff Instability*, Geological Society Engineering Geology Special Publication, pages 89–97.

Wittel, F. K., Carmona, H. A., Kun, F., and Herrmann, H. J. (2008). Mechanisms in impact fragmentation. *International Journal of Fracture*, 154:105–117.

Zhang, L. and Thornton, C. (2007). A numerical examination of the direct shear test. *Geotechnique*, 57(4):343–354.

Zhang, M., Yin, Y., and McSaveney, M. (2016). Dynamics of the 2008 earthquake-triggered Wenjiagou Creek rock avalanche, Qingping, Sichuan, China. *Engineering Geology*, 200:75–87.

Zhang, Q. B. and Zhao, J. (2014). A review of dynamic experimental techniques and mechanical behaviour of rock materials. *Rock Mechanics and Rock Engineering*, 47:1411–1478.

Zhang, X. P. and Wong, L. N. Y. (2014). Choosing a proper loading rate for bonded-particle model of intact rock. *International Journal of Fracture*, 189:163–179.